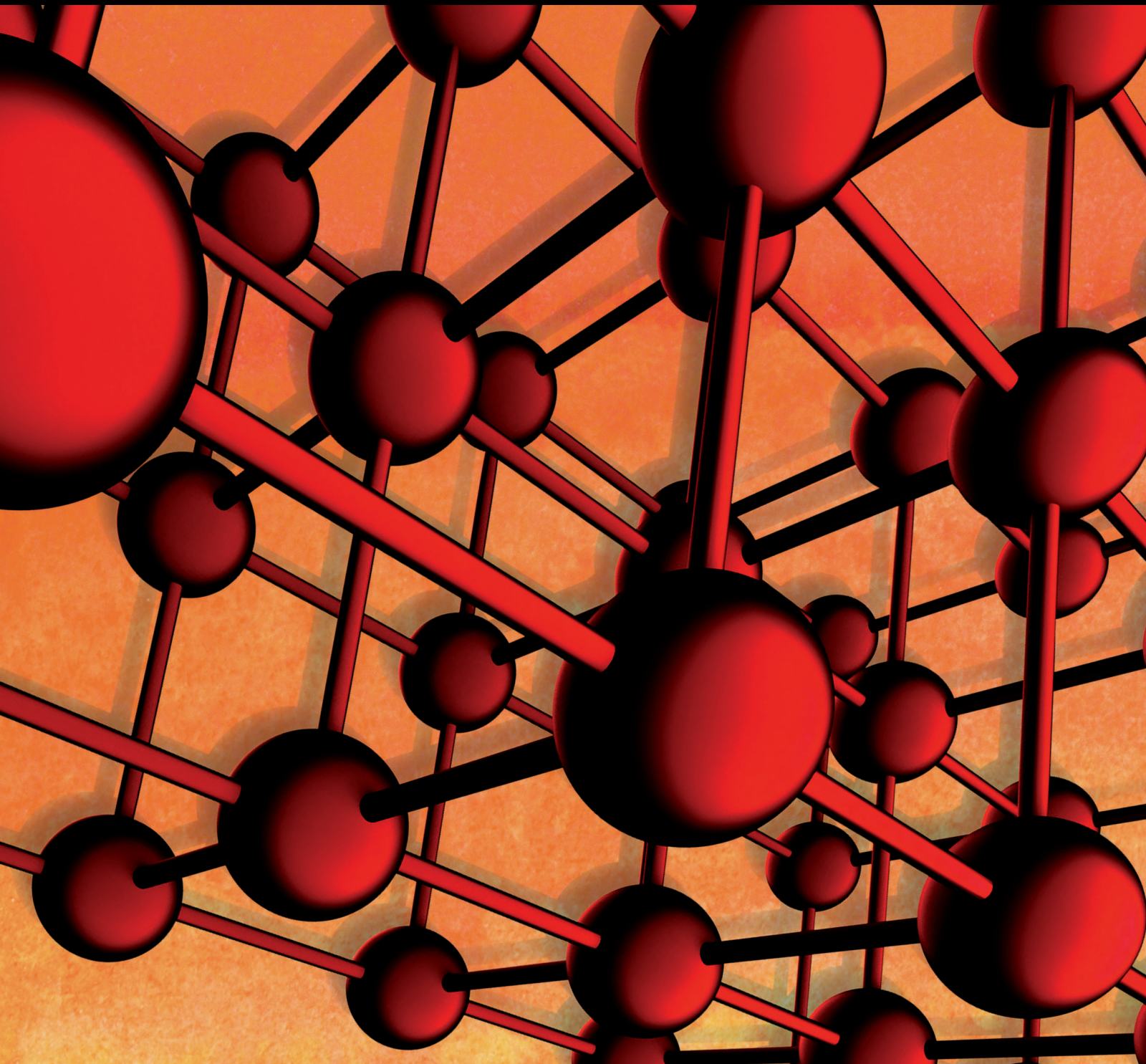


Advances in Materials Science and Engineering

Earth Materials and Environmental Applications

Guest Editors: Zhaohui Li, Hanlie Hong, and Guocheng Lv





Earth Materials and Environmental Applications

Advances in Materials Science and Engineering

Earth Materials and Environmental Applications

Guest Editors: Zhaohui Li, Hanlie Hong, and Guocheng Lv



Copyright © 2015 Hindawi Publishing Corporation. All rights reserved.

This is a special issue published in “Advances in Materials Science and Engineering.” All articles are open access articles distributed under the Creative Commons Attribution License, which permits unrestricted use, distribution, and reproduction in any medium, provided the original work is properly cited.

Editorial Board

Dimitrios G. Aggelis, Belgium
Jarir Aktaa, Germany
K. G. Anthymidis, Greece
Amit Bandyopadhyay, USA
Arun Bansil, USA
Massimiliano Barletta, Italy
Jozef Bednarcik, Germany
Avi Bendavid, Australia
Jamal Berakdar, Germany
Giovanni Berselli, Italy
Alessandra Bianco, Italy
Susmita Bose, USA
Heinz-Günter Brokmeier, Germany
Steve Bull, UK
Peter Chang, Canada
Daolun Chen, Canada
Gabriel Cuello, France
Narendra B. Dahotre, USA
João P. Davim, Portugal
Francesco Delogu, Italy
Seshu B. Desu, USA
Yong Ding, USA
Aziz Dinia, France
Kaveh Edalati, Japan
Gilbert Fantozzi, France
Massimo Fresta, Italy
E. Freysz, France
Sergi Gallego, Spain
Santiago Garcia-Granda, Spain
Filippo Giannazzo, Italy
Salvatore Grasso, UK
Daniel Guay, Canada
Hiroki Habazaki, Japan
Joke Hadermann, Belgium
Satoshi Horikoshi, Japan
Rui Huang, USA
Jacques Huot, Canada
Michele Iafisco, Italy

Richard W. Jones, UK
Maarit Karppinen, Finland
Katsuyuki Kida, Japan
Jae-Ho Kim, Korea
Akihiko Kimura, Japan
Takayuki Kitamura, Japan
Hongchao Kou, China
Prashant Kumta, USA
Luciano Lamberti, Italy
Heinrich Lang, Germany
Bradley Layton, USA
Pavel Lejcek, Czech Republic
Cristina Leonelli, Italy
Markku Leskela, Finland
Ying Li, USA
Ying Liu, USA
Yunqi Liu, China
Wei Liu, France
Jun Liu, China
Meilin Liu, Georgia
Fernando Lusquiños, Spain
Peter Majewski, Australia
Philippe Miele, France
Hossein Moayedi, Malaysia
Paul Munroe, Australia
Rufino M. Navarro, Spain
Luigi Nicolais, Italy
Hiroshi Noguchi, Japan
Chérif Nouar, France
José L. Ocaña, Spain
Tsutomu Ohzuku, Japan
Olanrewaju Ojo, Canada
Xiaoqing Pan, USA
Anna Paradowska, Australia
Bart Partoens, Belgium
Gianluca Percoco, Italy
Jean-Francois Pierson, France
Simon C. Potter, Canada

Manijeh Razeghi, USA
Anna Richelli, Italy
Antonio Riveiro, Spain
Pascal Roussel, France
Timo Sajavaara, Finland
Antti Salminen, Finland
Fawzy H. Samuel, Canada
Carlo Santulli, Italy
Franz-Josef Schmitt, Germany
Jainagesh A. Sekhar, USA
Fridon Shubitidze, USA
Charles C. Sorrell, Australia
Costas M. Soukoulis, USA
Sam-Shajing Sun, USA
Kohji Tashiro, Japan
Philippe Thomas, France
Somchai Thongtem, Thailand
Achim Trampert, Germany
Filip Tuomisto, Finland
Stuart Turner, Belgium
Krystyn Van Vliet, USA
Rui Vilar, Portugal
Holger von Wenckstern, Germany
Rong Wang, USA
Qiang Wang, China
Rui Wang, China
Lu Wei, China
Jörg Wiezorek, USA
Wei Wu, USA
Hemmige S. Yathirajan, India
Wenbin Yi, China
Belal F. Yousif, Australia
Ming-Xing Zhang, Australia
Li Zhang, China
Jinghuai Zhang, China
Wei Zhou, China

Contents

Earth Materials and Environmental Applications, Zhaohui Li, Hanlie Hong, and Guocheng Lv
Volume 2015, Article ID 404561, 2 pages

Research on Wetting-Drying Cycles' Effect on the Physical and Mechanical Properties of Expansive Soil Improved by OTAC-KCl, Bao-tian Wang, Can-hong Zhang, Xue-lian Qiu, En-yue Ji, and Wen-hui Zhang
Volume 2015, Article ID 304276, 7 pages

Preparation and Characterization of Barite/TiO₂ Composite Particles, Hong Zhou, Mengmeng Wang, Hao Ding, and Gaoxiang Du
Volume 2015, Article ID 878594, 8 pages

Triaxial Test and Mechanical Analysis of Rock-Soil Aggregate Sampled from Natural Sliding Mass, Shuling Huang, Xiuli Ding, Yuting Zhang, and Wei Cheng
Volume 2015, Article ID 238095, 14 pages

Preparation and Mechanism of a New Enhanced Flocculant Based on Bentonite for Drinking Water, Feng-shan Zhou, Jie Li, Lin Zhou, and Yang Liu
Volume 2015, Article ID 579513, 8 pages

Preparation of Cementitious Material Using Smelting Slag and Tailings and the Solidification and Leaching of Pb²⁺, Dan Zhang, Shiliu Shi, Chengbiao Wang, Xiacong Yang, Lijie Guo, and Shanshan Xue
Volume 2015, Article ID 352567, 7 pages

First-Principles Study on the Structural and Electronic Properties of N Atoms Doped-Rutile TiO₂ of Oxygen Vacancies, Zhong-Liang Zeng
Volume 2015, Article ID 670243, 10 pages

Experimental Study on Low-Strength Similar-Material Proportioning and Properties for Coal Mining, Shaojie Chen, Hailong Wang, Junwen Zhang, Huilin Xing, and Huaiyuan Wang
Volume 2015, Article ID 696501, 6 pages

Enhanced Viscosity of Aqueous Palygorskite Suspensions through Physical and Chemical Processing, Feng-shan Zhou, Tian-qi Li, Yun-hua Yan, Can Cao, Lin Zhou, and Yang Liu
Volume 2015, Article ID 941580, 7 pages

Interactions between Phosphoric/Tannic Acid and Different Forms of FeOOH, Lefu Mei, Libing Liao, Zise Wang, and Chunchun Xu
Volume 2015, Article ID 250836, 10 pages

Resource Distribution, Interprovincial Trade, and Embodied Energy: A Case Study of China, Sanmang Wu, Yalin Lei, and Li Li
Volume 2015, Article ID 910835, 10 pages

Adsorption Mechanism of Ciprofloxacin from Water by Synthesized Birnessite, Xuebing Xing, Jingwen Feng, Guocheng Lv, Kenan Song, Lefu Mei, Libing Liao, Xiaoyu Wang, and Ben Xu
Volume 2015, Article ID 148423, 7 pages

Seismic Earth Pressures of Retaining Wall from Large Shaking Table Tests, Changwei Yang, Jian Jing Zhang, Qu Honglue, Bi Junwei, and Liu Feicheng
Volume 2015, Article ID 836503, 8 pages

Preparation and Coagulation Behavior of a Novel Multiple Flocculant Based on Cationic Polymer, Hydroxy Aluminum, and Clay Minerals, Feng-shan Zhou, Xi Wang, Lin Zhou, and Yang Liu
Volume 2015, Article ID 581051, 8 pages

Composition Optimization of Glass-Like Casing and Its Novel Application in Mending Instable Borehole Wall, Zhi-jun Li, Yu Wang, Bao-lin Liu, and Chun Yang
Volume 2015, Article ID 945475, 7 pages

The Experimental Investigation of Hydraulic Fracture Propagation Characteristics in Glutenite Formation, Zhihong Zhao, Jianchun Guo, and Shou Ma
Volume 2015, Article ID 521480, 5 pages

Compositional Effects and Mechanical Parametric Analysis of Outwash Deposits Based on the Randomised Generation of Stone Blocks, Chong Shi and Jinzhou Bai
Volume 2015, Article ID 863915, 13 pages

Effect of Sintering Temperature on Membranes Manufactured with Clays for Textile Effluent Treatment, Mirele Costa da Silva, Hélio de Lucena Lira, Rosa do Carmo de Oliveira Lima, and Normanda Lino de Freitas
Volume 2015, Article ID 371697, 7 pages

Tunable Upconversion Luminescence and Energy Transfer Process in $\text{BaLa}_2\text{ZnO}_5\text{:Er}^{3+}/\text{Yb}^{3+}$ Phosphors, Lefu Mei, Jing Xie, Libing Liao, Ming Guan, and Haikun Liu
Volume 2015, Article ID 380936, 5 pages

The Evaluation of Groundwater Resources Value of Beijing Based on Emery Theory, Ling Wang and Qing He
Volume 2015, Article ID 743136, 9 pages

Critical Damage Analysis of WC-Co Tip of Conical Pick due to Coal Excavation in Mines, Saurabh Dewangan, Somnath Chattopadhyaya, and Sergej Hloch
Volume 2015, Article ID 292046, 7 pages

Preparation of N-Doped $\text{TiO}_2\text{-ZrO}_2$ Composite Films under Electric Field and Heat Treatment and Assessment of Their Removal of Methylene Blue from Solution, Lefu Mei,
Ranfang Zuo, Jing Xie, Libing Liao, and Hao Ding
Volume 2014, Article ID 129540, 4 pages

Experimental Study and Numerical Solution of Poly Acrylic Acid Supported Magnetite Nanoparticles Transport in a One-Dimensional Porous Media, M. Golzar, S. F. Saghavani, and M. Azhdari Moghaddam
Volume 2014, Article ID 864068, 8 pages

Photocatalytic Degradation of Methylene Blue Using TiO_2 Impregnated Diatomite,
Ranfang Zuo, Gaoxiang Du, Weiwei Zhang, Lianhua Liu, Yanming Liu, Lefu Mei, and Zhaohui Li
Volume 2014, Article ID 170148, 7 pages

Editorial

Earth Materials and Environmental Applications

Zhaohui Li,^{1,2} Hanlie Hong,³ and Guocheng Lv¹

¹Beijing Key Laboratory of Materials Utilization of Nonmetallic Minerals and Solid Wastes, National Laboratory of Mineral Materials, School of Materials Science and Technology, China University of Geosciences, 29 Xueyuan Road, Beijing 100083, China

²Geosciences Department, University of Wisconsin–Parkside, Kenosha, WI 53144, USA

³Faculty of Earth Science, China University of Geosciences, Wuhan 436400, China

Correspondence should be addressed to Zhaohui Li; li@uwp.edu

Received 22 January 2015; Accepted 22 January 2015

Copyright © 2015 Zhaohui Li et al. This is an open access article distributed under the Creative Commons Attribution License, which permits unrestricted use, distribution, and reproduction in any medium, provided the original work is properly cited.

Earth materials refer to the naturally occurring materials including rocks, minerals, and soils. Traditionally, the studies of Earth materials including mineralogy (the study of minerals), petrology (the study of rocks), and pedology (the study of soil) were limited to their occurrence, characterization, and resource utilization. The interactions between Earth materials and anthropogenic compounds (most of them are contaminants) only attracted recent attentions. This is the area that has experienced accelerated research since 1990. Still, due to the use and misuse of emerging compounds (ECs), many are on the targeted watch list and more studies are in great need to explore their fate and transport in the natural environment. In addition to the interactions between of the ECs and Earth materials, development of cost-efficient or energy efficient materials from raw Earth materials for environmental application also picked up recently due to advancement of modern technology. Moreover, studies on mechanical responses of Earth materials to natural and anthropogenic-induced hazards may guide for better structural design and hazard prevention.

In this special issue, we have a collection of 23 papers covering the topics of the following general areas: (1) materials (13 papers), including materials, resources, innovation, and utilization for environmental application, and (2) engineering applications (10 papers), including soils and foundation stabilization and and rhyology improvements.

In the area of materials, the materials innovation studies addressed either new preparation methods of current Earth materials for new environmental applications in contaminant removal and water treatment or new applications in

energy transfer processes. A unique method for the synthesis of $\text{BaLa}_2\text{ZnO}_5:\text{Er}^{3+}/\text{Yb}^{3+}$ was developed and the tunable up-conversion luminescence and energy transfer process between Yb^{3+} and Er^{3+} was demonstrated. A TiO_2 - ZrO_2 composite film with the grain size of 50 nm was synthesized by electric field and heat treatments and then doped with nitrogen atoms. Photocatalytic experiments using this composite film resulted in significant increase in methylene blue degradation under visible light irradiation.

Simulation using first principle on the structural and electronic properties of nitrogen doped rutile TiO_2 of oxygen vacancies showed that the impurity elements do not affect the migration of Fermi level while the conduction band of metal atoms move to the Fermi level, forming the N-type semiconductor material. A TiO_2 /diatomite composite prepared by loading TiO_2 on the surface of diatomite resulted in a good photocatalytic enhancement through absorbing organic compounds with diatomite and degrading them by TiO_2 and the composite was more active than nano- TiO_2 for the degradation of methylene blue. For the heavy metal removal side composite cementations materials were prepared with lead-zinc tailings and lead-zinc smelting slag mixed with cement clinker with low lead leaching potential over a large pH range. To make full use of barite mineral and obtain composite material bearing, the property of both barite and TiO_2 was developed by coating barite surface with TiO_2 via a solution method and hydrolysis process. The hiding power and oil absorption value of the composite powder were similar to TiO_2 alone. In addition to these new solid materials, a new enhanced flocculent based on

bentonite and formulated with addition of polymeric chloride aluminum, cationic polyacrylamide, ferrous sulfate, and aluminum sulfate was developed for potential application in drinking water in Karamay City, Xinjiang. The treated water reached or exceeded the drinking water standard of China in decolorization and deodorization as well as heavy metal removal.

From materials utilizations studies, several Earth materials were utilized for the removal of contaminants. Uptake of ciprofloxacin on synthesized birnessite was mainly via surface adsorption, instead of cation exchange and quantum mechanics simulation showed that the final energy of the interactions between ciprofloxacin and birnessite was decreased under the condition when the average oxidation states of Mn were lower. Studies on the effect of sintering temperature on membranes performance showed that increases in sintering temperature of the membranes raised the average pores diameter from 0.116 to 0.179 μm but decreased the porosity of the membrane from 40.30 to 25.16%, which reduced the water permeated flux for temperatures from 900 to 1100°C. Studies on interactions between phosphoric/tannic acid and different forms of FeOOH showed that 3% tannic acid +10% phosphoric acid +FeOOH was the most suitable formula for rust stabilizer and its reaction products were made up of iron phosphate and chelate of iron and tannin. The results provided optimal combinations for the preservation of iron, especially iron cultural relics. The experimental and simulated breakthrough curves showed that classical colloid filtration theory is able to predict the transport and fate of iron oxide nanoparticles stabilized with PAA up to 500 ppm in a porous media.

As an Earth material or resource, groundwater was evaluated based on Energy theory for Beijing area. In terms of monetary value of groundwater in Beijing, it was 7.64, 6.00, and 3.25 billion Yuan, accounting for 45.24%, 35.52%, and 19.24% of the total value, respectively. Based on the data from 2007 input-output tables for each province in China, energy embodied in China's interprovincial trade through input-output analysis was estimated. The results showed that a sizable transfer of energy from the central and western provinces to the eastern and coastal provinces is embodied in China's interprovincial trade.

In the area of environmental application on stabilities of soil and foundations, the rock-soil aggregate sampled from the deep layer of sliding mass at Jinpingzi area of Wudongde hydropower plant on Yangtze River was investigated for its mechanical behavior. Results from large-scale laboratory triaxial tests show that variation of stone content and gradation affected the mechanical characteristics of rock-soil aggregate considerably. Results of studies on hydraulic fracture propagation characteristics in glutenite formation by a series of servocontrolled triaxial large-scale fracturing experiments showed that the fractures extended along the gravel and sandstone cementing face, the extension pressure was fluctuating, and the degree of fluctuation was more drastic with the gravel diameter increase in the process of the fracture extension. An orthogonal study on low-strength similar materials comprising sand, fly ash, and plaster and the sensitivity analyses suggested that their compression strength

and elastic modulus decreased as the sand-binder ratio or cement ratio increases. Numerical experiments of biaxial compression using the granular discrete element method were performed in the macro- and microparametric analyses to study the influences of strength of the cementation as affected by the sizes of stone blocks and the content of stone blocks on the peak compressive and shear strength. The seismic response of retaining wall in the Wenchuan earthquake was tested on large shaking table and an acceleration record was acted in 3 directions. The results showed that the dynamic earth pressure increases with the increase of ground shaking from 0.1g to 0.9g and the relationship is nonlinear. A glass-like casing was developed to mend the instable borehole due to its great similarities in compositions and structure. Different wt% aluminum and quartz sand were added into the composition, in order to boost the casing's mechanical properties and lower its cost. Investigation of coal/rock intermixing, cracking and crushing of WC grains, and adhesion of rock particles suggested that coal/rock materials penetrate the cracks of the coal cutting tools to enter inside the base material and degrade it. An introduction of a modifier OTAC-KCl at a combination of ameliorant 0.3% STAC and 3% KCl improved the wetting and drying cycles on engineering properties of expansive soil after 14-day curing time, while the untreated soil specimens collapsed when they were immersed in water.

Finally, studies on coagulation behavior showed that cationic polymer, hydroxy aluminum, and clay minerals are three flocculants with different action mechanisms and a more cost-efficient multiple flocculent could be prepared by compositing them through appropriate technology. The viscosity of an aqueous palygorskite suspension could be increased via physical and chemical processing and the contribution of MgO to viscosity caused the reinforcing of flocculation and, in drilling applications, the higher viscosity value would provide better cutting suspension and carrying capacity.

Acknowledgments

We would like to thank all the authors who have submitted their papers to this special issue and also to all the reviewers for their invaluable contributions to the reviewing process.

Zhaohui Li
Hanlie Hong
Guocheng Lv

Research Article

Research on Wetting-Drying Cycles' Effect on the Physical and Mechanical Properties of Expansive Soil Improved by OTAC-KCl

Bao-tian Wang,^{1,2} Can-hong Zhang,^{1,2} Xue-lian Qiu,³ En-yue Ji,^{1,2} and Wen-hui Zhang^{1,2}

¹Key Laboratory of Ministry of Education for Geotechnics and Embankment Engineering, Hohai University, Nanjing, Jiangsu 210098, China

²Institute of Geotechnical Engineering, Hohai University, Nanjing, Jiangsu 210098, China

³China Coal Technology and Engineering Group, Nanjing Design and Research Institute Co. Ltd., Nanjing, Jiangsu 210031, China

Correspondence should be addressed to Can-hong Zhang; 2008zhangcanhong@163.com

Received 21 August 2014; Revised 7 November 2014; Accepted 15 November 2014

Academic Editor: Guocheng Lv

Copyright © 2015 Bao-tian Wang et al. This is an open access article distributed under the Creative Commons Attribution License, which permits unrestricted use, distribution, and reproduction in any medium, provided the original work is properly cited.

Expansive soil experiences periodic swelling and shrinkage during the alternate wet and dry environments, which will result in severe damage to the slope stability. In this study, a promising modifier OTAC-KCl is introduced, which has a good diffusivity and is soluble in water or other solvents easily. Firstly, a reasonable combination of ameliorant 0.3% STAC and 3% KCl is chosen referring to the free swell test. Then, the best curing period, 14 days, is gotten from UCS tests. The effect of wetting and drying cycles on engineering properties of expansive soil improved by OTAC-KCl admixtures after 14-day curing is also studied accordingly. Both treated and untreated expansive soil samples are prepared for the cyclic wetting-drying tests which mainly include cyclic swelling potential and cyclic strength tests. Experimental results show that the swelling potential of expansive soil samples stabilized with OTAC-KCl is suppressed efficiently, and the untreated soil specimens will collapse when immersed in water while the treated specimens keep in good conditions. Moreover, expansive soil samples modified with 0.3% OTAC + 3% KCl show enough durability on the swelling ability, shear strength, and unconfined compressive strength, which means, that both the physical and the mechanical properties of stabilized expansive soil have been improved effectively.

1. Introduction

Expansive soil is a kind of high plasticity clay which has obvious swell-shrink characteristics. It also has the engineering properties of shrinking and cracking due to water loss and the swelling and softening due to the moisture content increase [1, 2]. Expansive soil problem mainly comes from its water stability.

Recently, numerous researchers have investigated the influence of wetting-drying cycles on the engineering properties of natural clay [3, 4]. The work of Ring [5] indicated that the specimens' height during 4 wetting and drying cycles is the same and the initial compaction conditions are even independent. Popescu [6], Osipov et al. [7], and Basma et al. [8] studied expansive soil basic properties with full shrinkage method and found that the swelling ability of specimens increases with the number of wetting and drying cycles. Such

cyclic swelling and shrinkage potentials of the ground will cause severe damage to the overlying structures such as the pavements and embankment [2, 3]. So it is important to improve the hydrophilic, physical, and mechanical properties of expansive soil for slope stability of embankment and highway engineering and reducing the cost of investment [9].

In recent decades, geotechnical engineers have made great effort to find different methods to improve expansive soil engineering properties [3]. Chemical stabilization is one of the alternative solutions to overcome the undesirable swell-shrink potentials of the expansive soils, which has been extensively used [10]. When amendment is added into soils, the reaction with clay particles will lead to the improvement in many expansive soil engineering properties [11]. In addition, various methods of chemical modifier have been developed. Among them, inorganic admixture such as lime, fly ash, and cement and organic stabilization like

TABLE 1: Physical properties of expansive soil.

Dry density	Free swell ratio (%)	Natural water content (%)	Liquid limit (%)	Plastic limit (%)	Specific gravity
1.53	55.0	20.2	54.0	25.0	2.74

ISS, HEC, K^+ , and polyvinyl alcohol are the most widely applied methods for controlling the swell-shrink potentials [10, 12–16]. On the other hand, new methods are still being developed to increase the strength properties and to reduce the swell potential of expansive soils [4]. With the intensive study of expansion mechanism of expansive soil as well as the continuous exploration of the amendment, a new kind of stabilizer has come to light.

Because of the lowest hydration energy, K^+ is regarded as the best hydration swelling inhibitors [17]. However, it works with hydrous expansive soil and the effect of the single role is limited [18]. A kind of cationic surfactant named octadecyl trimethyl ammonium chloride (chemical formula $C_{21}H_{46}NCl$) or TC-8/OTAC for short is considered. It has a good compatibility with other additives, and the synergistic effect is significant [19]. Therefore, a new stabilizer OTAC-KCl is developed. This new ameliorant can be soluble in water or other solvents. The solution is sprayed on the surface of natural expansive soil slope and diffuses throughout the soil internal by permeation, and then the soil properties can be improved efficiently.

This study aims to clarify the influence of cyclic wetting and drying on the swelling behavior and strength properties of natural expansive soils improved by OTAC-KCl. Thus, an attempt to intermingle OTAC-KCl with expansive soil for physical and mechanical properties studying is presented in this paper.

2. Materials, Mechanism, Optimum Ameliorant Content, and Curing Period Determination

As a prerequisite of this research, the engineering properties of the expansive soil used, swelling potential, shear strength, and unconfined compressive strength are determined in the laboratory according to the pertinent tests specified in GB/T 50123-1999 [20].

2.1. Materials. Expansive soil used in this study is from Nanjing. It is a typical clayey soil extensively distributed in Eastern China, which will cause damage to the slope safety. All representative soil samples are subjected to engineering properties measurements, including hydrometer tests, Atterberg limits, and free swell tests. All the results are presented in Table 1.

2.2. Mechanism. Expansive soil used in this study is mainly composed of hydrophilic clay minerals, which are montmorillonite, illite, and so forth. Montmorillonite, which is with a high cation exchange capacity, plays a decisive role in swell-shrink characteristic of expansive soil [21]. It is a kind of layered aluminosilicate minerals, and its unit cell

consists of a silicon-oxygen tetrahedron and an aluminum-oxygen octahedron. Si^{4+} in the tetrahedron and Al^{3+} in the octahedron can be replaced easily by low cation; thus, the equivalent negative charge increases in the crystal structure, and then the surrounding cations are adsorbed to balance the extra negative charge. Meanwhile, oxygen bridge between montmorillonite crystal layers is very weak and cationic and water molecules can easily get into and expand the interlayer. KCl and OTAC can dissociate amount of K^+ and NH_4^+ when reacting with water in soil. K^+ and NH_4^+ near to the clay crystal can extrude water molecules and reform stronger links by intercalating into the crystal. The inhibiting effect on the swell-shrink is notable due to the lowest hydration energy of these two positive ions. OTAC is a kind of cationic surfactant and long-chain polymer, which can produce series of physical and chemical reactions to improve expansive soil engineering properties and turn the soil's hydrophilicity into hydrophobicity. The mechanism of OTAC-KCl can be divided into two aspects. Firstly, the hydrophilic radical with positive charge is absorbed on the surface of clay mineral; thus, the hydrophobicity of soil gets strengthened and the reaction of soil and water becomes weakened, and then the swelling ability is suppressed. Secondly, due to the reaction between amendment and soil, firm space grid structures are formed among particles; the expansive soil strength will be improved [22].

2.3. Free Swell Test and the Optimum Proportion of OTAC and KCl. The expansive soil is air-dried and then the calcareous concretions were removed. After these, it is pulverized with a plastic mallet to crush the lumps and sieved at 2 mm. The different dosages of OTAC and KCl by taking into account mass ratio of the dried soil are prepared. The ameliorants are dissolved in water and sprayed on the expansive soil surface; eventually, they permeate through soil. Three types of mixtures, namely, soil-OTAC, soil-KCl, and soil-OTAC-KCl, are prepared. The water contents of natural soil and three types of improved specimens are all controlled with the standard of 20% or so according to the initial moisture content. All the prepared samples are sealed in plastic bags for 48 h.

Once the amelioration period is achieved, the soil is removed from the sealed container and dried carefully; then it is pulverized until all the particles passed a 0.5 mm sieve. Free swell test of all the soil samples is conducted to measure the improved effect of different ameliorants and dosage. The effect of different content of amendments on the free swell ratio of clayey soil samples is shown in Table 2.

Table 2 shows that, as KCl works alone, free swell ratio decreases a little in the case of a high content. As for OTAC, the rate can reduce to the desired value with a high dosage of 1.5%. Big consumption brings a higher cost. Therefore, KCl and OTAC combination is more reasonable. Considering

TABLE 2: Free swell rate of improved soil.

Modifier types and dosage		Free swell ratio δ_{ef} (%)
OTAC (%)	KCl (%)	
—	6	47
1.5	—	36
1.0	—	41
0.5	1	40
0.5	2	33
0.5	4	31
0.5	6	30
0.5	8	27
0.3	2	34
0.3	3	31
0.3	6	25

the improved effect and economy cost, the combination of 0.3% OTAC + 3% KCl is chosen.

2.4. Unconfined Compressive Strength Test and Optimum Curing Period. Soil specimens are prepared according to the procedure represented in Section 2.3. Improved specimens are prepared by adding 0.3% OTAC and 3% KCl to the clayey soil. After a thorough permeation, both untreated and treated soil specimens are compacted into cylindrical soil samplers with 50 mm diameter and 50 mm height. All specimens are prepared at the initial moisture contents 20% and dry density 1.53 g/cm^3 . Then each kind of sample is divided into 3 groups and cured in wet sand curing box for 7 days, 14 days, and 28 days, respectively.

The samples are saturated before tests. Because the vacuum saturation apparatus is inappropriate for UCS specimens' size, process of saturation is simplified. The cured samples are taken from curing box and then soaked in water for 48 h to saturate fully. Before the UCS test, the side and bottom of the samples are coated with vaseline to prevent moisture evaporation during the experiment. Unconfined compression strengths test is performed on these samples with the strain rate of 0.4 mm/min until specimens failed during 7–15 min. When the dynamometer peak is gotten, tests will be ended after axial strain growths 3%~5%. Otherwise, the tests will be stopped until axial strain reducing 20%. Every group carries out two sets of tests to ensure the accuracy. The UCS values of untreated and treated samples for different curing times are presented in Table 3 and the UCS curves with axial strain are shown in Figure 1.

No matter maintained or not, all of the untreated samples crack when soaking in water within a few minutes. Uncured improved samples damage a little within one hour and lose strength after two hours. The improved samples maintained 7 days are in good conditions basically; the samples maintained integrity when soaking in water for 48 hours and there are little peelings on the specimens. Treated samples are cured for 14 or 28 days without any peelings or cracks in the process of soaking. From Table 3 and Figure 1, it can be observed that the best curing duration of treated soils is 14 days. Comparing 7 days with 14 days, we conclude that

TABLE 3: Unconfined compressive strength of untreated and treated soil under different curing periods.

Curing time (d)	Unconfined compressive strength (kPa)	
	Natural soil	0.3% 1831 + 3% KCl improved soil
0	Damage	Damage
7	—	32.92
14	—	47.73
28	—	50.28

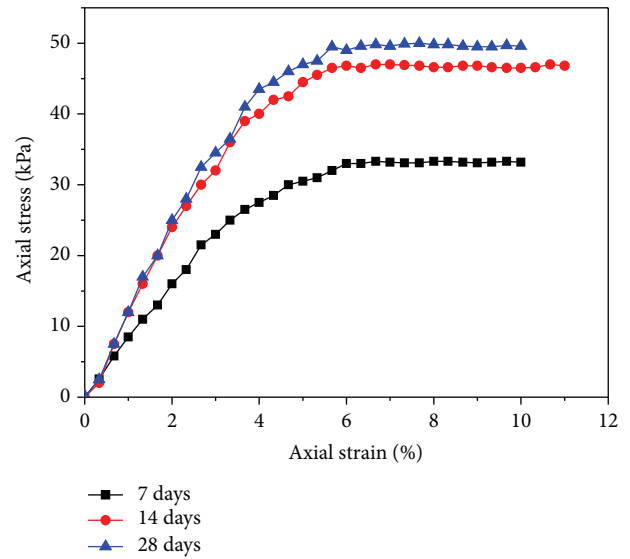


FIGURE 1: Unconfined compressive strength curves of improved soil with axial strain under different curing times.

the unconfined compressive strength increases with the curing period. However, when the soil samples are maintained 28 days, the UC strength does not have any obvious increase. Soil specimens maintain stability after 14-day curing time.

Cyclic wetting-drying experiments are carried out in this research to measure the physical and mechanical properties of the expansive soil improved by 0.3% STAC + 3% KCl combinations after 14-day curing time.

3. Testing Program and Results

The wetting-drying cycle test has the greatest advantage of being repeatable on the same samples [4, 23–25]. Water stability of stabilized soil under wetting-drying cycles is investigated by two approaches. The first one takes the swelling stability into account, and the other one measures the loss of shear strength and unconfined compression strength [26].

3.1. Cyclic Swelling Potential Test. Soil specimens are prepared following the procedure described in Section 2.3. Improved specimens are prepared by mixing the clayey soil with 0.3% OTAC and 3% KCl. Soil specimens with a diameter of

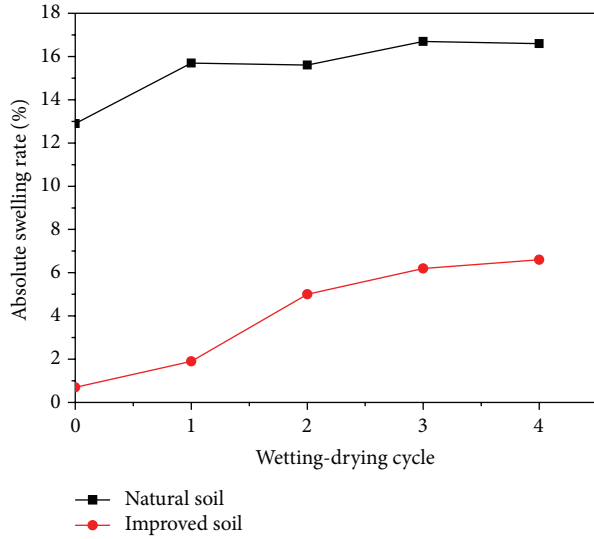


FIGURE 2: Absolute swelling ratio trends of the natural soil and improved soil.

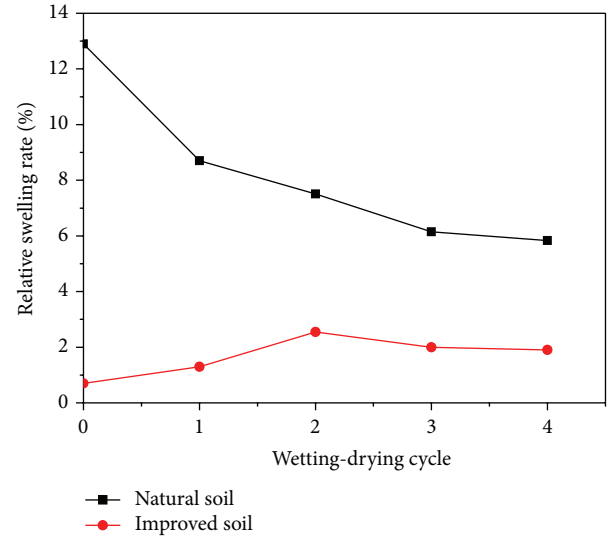


FIGURE 3: Relative swelling ratio trends of the natural soil and improved soil.

61.8 mm and height of 20 mm are made by cylindrical thin-wall samplers. The samples are cured in wet sand curing box for 14 days. After the curing process, all samples are subjected to 4 cycles of wetting-drying. A wetting-drying cycle consists of submerging in water until saturation and air-drying to the initial moisture content of 20% (by the weight of the samples). The cured cutting-ring specimens are saturated with a vacuum saturation apparatus. Specimens are put in the apparatus and soaked in water for 48 hours. This phase is defined as the 0th cycle. Then, the wetted samples are taken out and air-dried to the initial moisture content about 20%. So far, a complete cycle is finished.

Initial height of the specimens at the beginning of swell-shrink cycle marked h_0 is then manually measured by vernier caliper. Then, the heights of saturated specimens named h_{w1} and air-dried samples named h_1 are all measured. According to Liu et al. [27] and Wu et al. [28], the absolute swelling ratio and relative ratio are defined to quantitative analysis the regularity and reversibility of swell-shrink characteristics during cyclic wetting-drying process.

Definition of the absolute swelling ratio is the following: $\delta_a : \delta_a = ((h_w - h_0)/h_0) \times 100\%$, where h_0 is the initial height and h_w is the height after expansion.

Definition of the relative swelling ratio is the following: $\delta_r : \delta_r = ((h_w - h_i)/h_i) \times 100\%$, where h_w is the height after expansion and h_i is the height before certain wet-dry cycle.

The tests are carried on until the end of four cycles, and the results are given in Figures 2 and 3 after 4 wetting and drying cycles.

From Figures 2 and 3, it can be concluded that the absolute swelling ratio of modified soil is always smaller than natural soil and the suppression of swelling in stabilized specimens is obvious. The absolute swelling ratio reaches equilibrium at the 4th cycle of wetting-drying and increases with increasing wetting and drying cycles for both kinds of soil samples. The values are 16.5% and 6.54%, respectively,

after 4 cycles, while the initial values are 12.9% and 0.59%. As for relative swelling ratio, natural soil decreases with increasing cyclic wetting and drying, while improved soil increases during the first two cycles, a peak occurs in the second loop, and then relative swelling ratio reduces to be stable gradually. This result shows that the expansion of the soil is not entirely reversible.

According to the results of experiment, soil stabilized with 0.3% OTAC and 3% KCl has a quite low swelling ratio even wetting-drying for 4 times. The effect of ameliorants on the swelling ability during wetting-drying cycles is notable compared with natural soil.

3.2. Cyclic Direct Shear Test. Natural and improved soil samples are made by cutting ring molds and cured for 14 days in wet sand curing box. Each kind of soil sample is divided into four groups and saturated with a vacuum saturation apparatus. This is called the 0th cycles. The first wetting-drying cycle is completed after air-drying the saturated samples to initial moisture content about 20%. Direct shear tests are carried out by quadruple strain controlled direct shear apparatus (Nanjing Soil Instrument Factory Co. Ltd.), soil samples are placed in a shear testing device, and normal loads of 50, 100, 150, and 200 kPa are applied and sheared immediately. In these tests, the natural and stabilized soil specimens are subjected to 4 cycles of alternate wetting-drying. In order to get the trend of strength change during cycles, the samples are tested at the 0th cycles and the 2nd and 4th cycles. Results are described in Figures 4 and 5 and Table 4.

The figures indicate that the shear strength of soil modified with 0.3% OTAC + 3% KCl is improved significantly. Shear strength reduces with increasing wetting-drying cycles while it increases with vertical pressure for both soils. The shear strength of a soil can be expressed by two parameters as the cohesion (c) and the internal friction angle (φ).

TABLE 4: The results of shear strength parameters during cyclic wetting-drying process.

Types of soil	Shear strength under different vertical pressures (kPa)				Internal friction angle $\phi/^\circ$	Cohesion c/kPa	Note
	50	100	150	200			
Natural soil							
0th cycle	19.1	29.6	37.6	40.7	8.3	13.5	
2nd cycle	15.8	24.3	32.1	36.1	7.8	9.9	
4th cycle	11.6	16.5	25.7	30.7	7.6	4.5	
Improved soil							Saturated samples
0th cycle	41.9	50.3	58.6	74.4	12.0	29.8	
2nd cycle	36.9	43.6	49.8	65.3	10.4	26.0	
4th cycle	30.4	36.4	43.2	56.1	9.5	20.6	

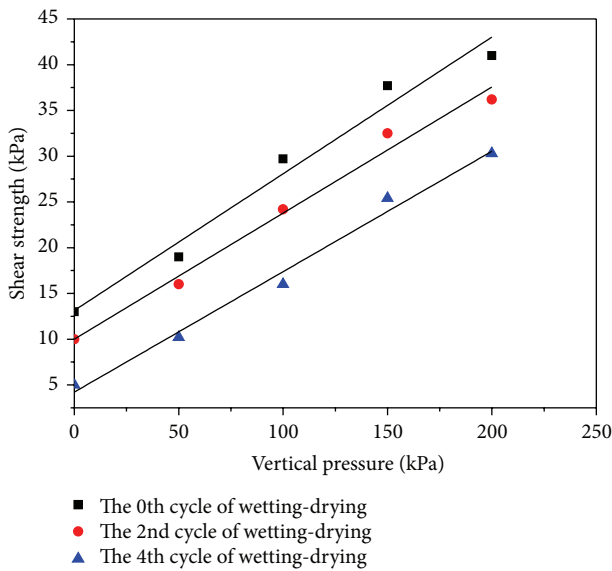


FIGURE 4: Shear strength of natural soil during wetting-drying cycles.

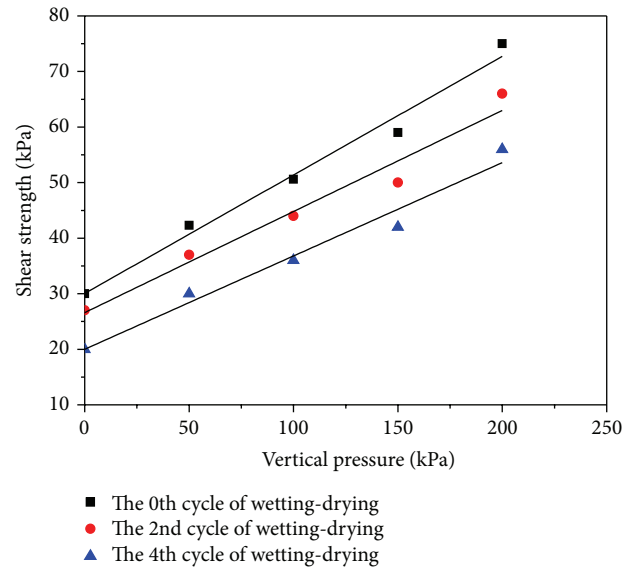


FIGURE 5: Shear strength of improved soil during wetting-drying cycles.

Mean c and ϕ of the studied expansive soil and stabilized soil are presented in Table 4, respectively. Cohesions are all diminished with the cycles while internal friction strengths changed a little. Comparing with the natural soil, the 0.3% OTAC + 3% KCl amended soil has significantly higher c values. Expansive soil improved by STAC combined with KCl shows good water stability based on shear strength.

3.3. *Cyclic Unconfined Compressive Strength Test.* Multiple modified specimens are prepared at optimum OTAC-KCl dosages and the initial moisture contents. Samples are cured in wet sand curing box for 14 days and immersed in water for 48 h. The influence of additive on the strength behavior of treated soils is examined by performing UCS studies on the same soils at the 0th cycles, 2nd cycle, and 4th cycle. In comparison, untreated soils are also tested at the same cycles. The procedure is the same as mentioned in Section 2.4. The cylindrical samples taken out from UCS apparatus and air-dried to initial water content are used for the next wetting and drying cycle. The wetting-drying procedure is terminated



FIGURE 6: Natural samples disintegrate after 48-hour immersion in water.

after 4 cycles of wetting-drying. The UCS values of untreated and treated samples for different wet-dry cycle times are presented in Table 5 and the photos taken in the process of experiments are shown in Figures 6, 7, 8, and 9.

TABLE 5: Results of unconfined compressive strength during cyclic wetting-drying process.

Types of soil	Cycles	Unconfined compressive strength (kPa)	Strength loss (%)	Conditions of samples immersed in water
Natural soil	0th cycles	—	—	Cracking after 10-minute immersion in water
	—	—	—	
Improved soil	0th cycles	47.73	—	Keeping good conditions without peelings
	2nd cycle	41.24	13.6	In good conditions basically, with a little amount of peelings on the edges
	4th cycle	37.33	21.8	In good conditions overall, with a little amount of cracks on the surface and peelings on the edges

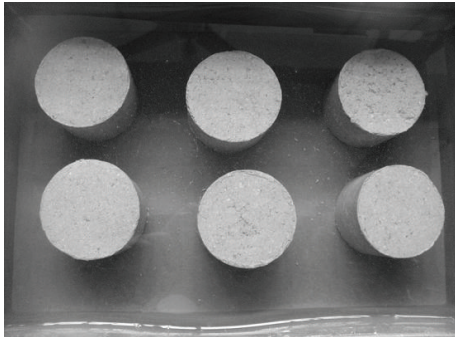


FIGURE 7: Improved samples immersed in water for 48 h at 0 wetting-drying cycles.

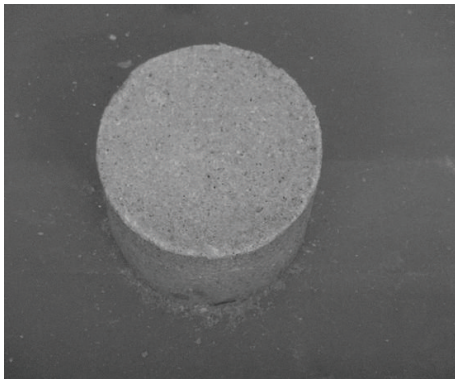


FIGURE 8: Improved samples immersed in water for 48 h at 2nd cycle of wetting-drying.

As shown in Table 5, the results obtained from UCS tests indicate that, for the particular proportions of OTAC and KCl in soil, an increase in wet-dry cycles induces a gradual weakness in strength, and the strength loss is 21.8%. The UCS values of improved soil samples increase a lot comparing with the natural soil samples and the gain of durability is noticeable.

Figures 6 to 9 show that water stabilities of untreated specimens are quite poor and they collapse after immersing in water for the first 48 hours. Because the untreated samples disintegrate after being immersed in water, all the untreated samples fail in the water stability test. However, soil samples



FIGURE 9: Improved samples immersed in water for 48 h at 4th cycle of wetting-drying.

improved by OTAC-KCl can go through numerous wetting-drying cycles. Due to the admixtures, samples keep a good condition until the end of the test.

4. Conclusions

Based on the study, the effect on the swelling potential, shear strength, and unconfined compressive strength behavior of expansive soils improved with 0.3% OTAC – 3% KCl during wetting-drying cycles has been investigated and the main conclusions are as follows.

Comparing with the natural expansive soil samples, it is found that the improved soil samples will have a lower swelling ability and a higher strength. The absolute swelling ratio increases with the increasing wetting-drying cycles while the relative swelling rates decrease with the cycles, and both of them reach the final equilibrium at the last cycle for the natural and modified soil samples. By the application of the wetting-drying cycles on both untreated and treated soils, the shear strength will reduce. Expansive soil improved by OTAC-KCl has significantly higher c values; stabilized soil shows enough water stability based on shear strength. Untreated specimens have poor water stability, which will collapse after immersion in water at the first cycle. However, for the modified soil, an increase in wetting-drying cycle will induce a gradual weakness in strength; the strength loss is 21.8% after 4 cycles. Soil samples improved by OTAC-KCl

can bear numerous wetting-drying cycles and keep a good condition until the end of the test.

Conflict of Interests

The authors declare that there is no conflict of interests regarding the publication of this paper.

Acknowledgments

This research is supported by the Fundamental Research Funds for the Central Universities (no. 2013B34914), which is greatly appreciated. The laboratory portion of this research was carried out in Key Laboratory of Ministry of Education for Geotechnics and Embankment Engineering of Hohai University. The authors also like to acknowledge the authorities of the Civil Engineering Department.

References

- [1] C. Gallage, M. Cochrane, and J. Ramanujam, "Effects of lime content and amelioration period in double lime application on the strength of lime treated expansive sub-grade soils," in *Proceedings of the 2nd International Conference on Transportation Geotechnics (ICTG '12)*, pp. 99–104, September 2012.
- [2] S. B. Ikizler, M. Vekli, E. Dogan, M. Aytekin, and F. Kocabas, "Prediction of swelling pressures of expansive soils using soft computing methods," *Neural Computing and Applications*, vol. 24, no. 2, pp. 473–485, 2014.
- [3] F. Yazdandoust and S. S. Yasrobi, "Effect of cyclic wetting and drying on swelling behavior of polymer-stabilized expansive clays," *Applied Clay Science*, vol. 50, no. 4, pp. 461–468, 2010.
- [4] E. Kalkan, "Impact of wetting-drying cycles on swelling behavior of clayey soils modified by silica fume," *Applied Clay Science*, vol. 52, no. 4, pp. 345–352, 2011.
- [5] W. G. Ring, "Shrink-Swell potential of soils," Highways Research Record 119, National Academy of Science-National Research Council Publication no. 1360, Washington, DC, USA, 1966.
- [6] M. Popescu, "Behavior of expansive soils with crumb structure," in *Proceedings of the 4th International Conference on Expansive Soils*, vol. 1, pp. 158–171, ASCE, New York, NY, USA, 1980.
- [7] V. I. Osipov, N. N. Bik, and N. A. Rumjantseva, "Cyclic swelling of clays," *Applied Clay Science*, vol. 2, no. 4, pp. 363–374, 1987.
- [8] A. A. Basma, A. S. Al-Homoud, A. I. H. Malkawi, and M. A. Al-Bashabsheh, "Swelling-shrinkage behavior of natural expansive clays," *Applied Clay Science*, vol. 11, no. 2–4, pp. 211–227, 1996.
- [9] Z. J. Wang and J. B. Liang, "Engineering characteristics of expansive soil and its improved research development," *Advanced Materials Research*, vol. 884–885, pp. 657–661, 2014.
- [10] T. Thyagaraj, S. M. Rao, P. Sai Suresh, and U. Salini, "Laboratory studies on stabilization of an expansive soil by lime precipitation technique," *Journal of Materials in Civil Engineering*, vol. 24, no. 8, pp. 1067–1075, 2012.
- [11] Y. Cai, B. Shi, C. W. W. Ng, and C. S. Tang, "Effect of polypropylene fibre and lime admixture on engineering properties of clayey soil," *Engineering Geology*, vol. 87, no. 3–4, pp. 230–240, 2006.
- [12] J.-Q. Yu, R.-L. Hu, H.-M. Shang, F.-P. Cui, and M.-L. Yang, "Synergistic reaction of K⁺ and polyvinyl alcohol on restraining swelling and hydrating behavior of expansive soil," *Chinese Journal of Geotechnical Engineering*, vol. 30, no. 6, pp. 900–905, 2008 (Chinese).
- [13] L.-J. He and X.-Y. Tang, "Laboratory studies on expansive soil improved by HEC," *Yellow River*, vol. 32, no. 9, pp. 148–151, 2010 (Chinese).
- [14] Q. B. Liu, W. Xiang, and D. S. Cui, "Effect of ionic soil stabilizer on bound water of expansive soils," *Chinese Journal of Geotechnical Engineering*, vol. 34, no. 10, pp. 1887–1895, 2012 (Chinese).
- [15] S. Saride, A. J. Puppala, and S. R. Chikyala, "Swell-shrink and strength behaviors of lime and cement stabilized expansive organic clays," *Applied Clay Science*, vol. 85, no. 1, pp. 39–45, 2013.
- [16] P. Voottipruex and P. Jamsawang, "Characteristics of expansive soils improved with cement and fly ash in Northern Thailand," *Geomechanics and Engineering*, vol. 6, no. 5, pp. 437–453, 2014.
- [17] C. Huang, S.-Y. Liu, C.-G. Zhang, X.-G. Mo, and D.-J. Sun, "Inhibition behavior of NH₄⁺, urea and polyethylene glycol on swelling of montmorillonite," *Acta Chimica Sinica*, vol. 61, no. 7, pp. 983–988, 2003 (Chinese).
- [18] B.-T. Wang and F.-H. Zhang, *Improvement Technology and Engineering Application of Expansive Soil*, Science Press, Beijing, China, 2008 (Chinese).
- [19] J. Qiu, F.-F. Yang, J.-J. Li, and X.-J. Lu, "Study on the conditions of preparing organic montmorillonite under the synergic effect of tetraethyl ammonium bromide and octadecyltrimethyl ammonium chloride," *Industrial Minerals Processing*, vol. 7, pp. 12–15, 2006 (Chinese).
- [20] Ministry of Construction P.R. China, "Standard for soil test method," Tech. Rep. GB/T 50123-1999, Ministry of Construction P.R. China, Beijing, China, 1999, (Chinese).
- [21] J. M. Montenegro, M. Celemín-Matachana, J. Cañizal, and J. Setién, "Ladle furnace slag in the construction of embankments: expansive behavior," *Journal of Materials in Civil Engineering*, vol. 25, no. 8, pp. 972–979, 2013.
- [22] X.-L. Qiu and B.-T. Wang, "Experimental research on chemical modification of expansive soil and its application in slope engineering," *Journal of Water Resources and Architectural Engineering*, vol. 11, no. 2, pp. 190–195, 2013 (Chinese).
- [23] A. S. Al-Homoud, A. A. Basma, A. I. H. Malkawi, and M. A. Al-Bashabsheh, "Cyclic swelling behavior of clays," *Journal of Geotechnical Engineering*, vol. 121, no. 7, pp. 562–565, 1995.
- [24] Y. Guney, D. Sari, M. Cetin, and M. Tuncan, "Impact of cyclic wetting-drying on swelling behavior of lime-stabilized soil," *Handbook of Environmental Chemistry*, vol. 42, no. 2, pp. 681–688, 2007.
- [25] K. S. Subba Rao, S. M. Rao, and S. Gangadhara, "Swelling behavior of a desiccated clay," *Geotechnical Testing Journal*, vol. 23, no. 2, pp. 193–198, 2000.
- [26] U. Calik and E. Sadoglu, "Classification, shear strength, and durability of expansive clayey soil stabilized with lime and perlite," *Natural Hazards*, vol. 71, no. 3, pp. 1289–1303, 2014.
- [27] S. Liu, P. Ji, and L. Fang, "Approach to cyclic swelling behavior of compacted expansive clays," *Chinese Journal of Geotechnical Engineering*, vol. 21, no. 1, pp. 9–13, 1999 (Chinese).
- [28] J. Wu, J. Yuan, S. Yang, and T. Lu, "Experimental study on swell-shrinking performance of expansive soil under wetting-drying cycles," *Advances in Science and Technology of Water Resources*, vol. 33, no. 1, pp. 62–73, 2013 (Chinese).

Research Article

Preparation and Characterization of Barite/TiO₂ Composite Particles

Hong Zhou, Mengmeng Wang, Hao Ding, and Gaoxiang Du

School of Materials Science and Engineering, China University of Geosciences, Beijing 100083, China

Correspondence should be addressed to Hao Ding; dinghao@cugb.edu.cn

Received 26 July 2014; Revised 19 September 2014; Accepted 7 October 2014

Academic Editor: Hanlie Hong

Copyright © 2015 Hong Zhou et al. This is an open access article distributed under the Creative Commons Attribution License, which permits unrestricted use, distribution, and reproduction in any medium, provided the original work is properly cited.

To make full use of barite mineral and obtain a kind of composite particles material which has the property of both barite and TiO₂, the composite particles material with TiO₂ coated on the surface of barite particle was prepared by the method of TiOSO₄ solution chemical hydrolysis and precipitation to form hydrolysis composite, removing the impurities of hydrolysis composite, drying, and calcination in this study. The results were evaluated by the covering power of composites. Composite structure and properties were characterized by means of XRD, SEM, FTIR, and XPS. The results showed that the surface of barite had been coated with rutile TiO₂ uniformly and compactly and the hiding power value and oil absorption value of the composite powder were 18.50 g/m² and 15.5 g/100 g, respectively, which had similar pigment performances to TiO₂. The results also showed that it was mainly the strong chemical bond between barite and TiO₂ that combined them firmly in barite/TiO₂ composite particle (B/TCP).

1. Introduction

The resource consumption, environmental pollution, cost ascension, and strong demand problems brought about during the production and application of TiO₂ limit its development seriously. To alleviate these problems and reduce the actual dosage of titanium dioxide, preparing white mineral/TiO₂ composite particle materials with similar pigment properties to TiO₂ caused a widespread concern. Many studies show that mineral surface-coated TiO₂ composite particles can be prepared by adding white mineral, such as kaolinite [1–4], wollastonite [5, 6], montmorillonite [7], sericite [8–10], tourmaline [11], and talc [12, 13] to the titanium salt solution [14]. To make titanium salt solution hydrolyzate (hydrated titanium dioxide, TiO₂·H₂O) crystallize, the production needs to be calcined at about 600°C to 900°C. The studies above mainly researched the photocatalytic properties, pigment performance, and UV shielding performance of nanotitanium dioxide. As a result of the selected minerals which were more different from titanium dioxide in density, the prepared composites were easy to layer when mixed with other components and could not be used effectively.

Barite with the main component of BaSO₄ and similar density to titanium dioxide is a significant white nonmetallic mineral. Its high reservation, chemical stability, and low cost in China make it extensively applied in chemical raw materials, drilling mud raw materials, glass raw material, chemical fillers, and so on [15]. This is barite as mineral-TiO₂ composite particles substrate provides the basis. The density of barite was close to TiO₂, and both were 4.3 and 4.4 g/cm³, and the oil absorption is low; therefore, preparing barite/TiO₂ composite powder paint is expected to obtain good effect.

There have been studies in preparing functional composite particles by coating metal oxide on surface of barite particles. Yang et al. [16] prepared Sb-SnO₂/BaSO₄ conductive powder by chemical precipitation method. Zhou [17] prepared barite loaded with nano-TiO₂ composites using TiOSO₄ and TiCl₄ as titanium source in process of methyl orange degradation. Wang et al. [18] prepared barite/TiO₂ composite particles by coating anatase TiO₂ on the surfaces of barite particles through mechanochemical method. These results showed that the prepared composite powders had certain kind of pigment performance and it was mainly the strong electrostatic attraction between barite and TiO₂ that combined them firmly and then formed B/TCP. Therefore,

the composites' pigment performance and the combination extent between barite and TiO_2 need to be improved.

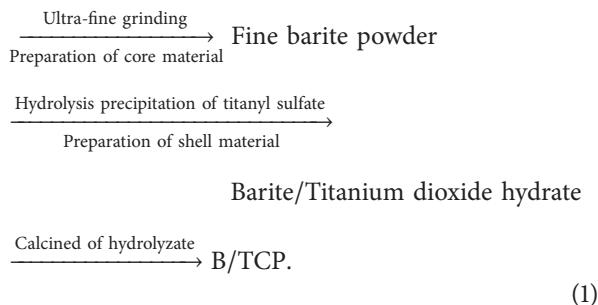
To prepare barite coated with TiO_2 composite particles and combine them firmly, chemical precipitation method was used and the technology was studied in this paper. The preparation process conditions, pigment properties of composites, the structure of B/TCP, and the interaction mechanism between TiO_2 and barite particles were also investigated in this paper.

2. Experimental

2.1. Raw Materials and Reagents. The barite (particle size of less than $10\ \mu\text{m}$) used was provided by Antai Minerals Co., Ltd, Hebei Province, China. TiOSO_4 solution (concentration of $152\ \text{g}/1000\ \text{mL}$) was produced by Jiaozuo Chemical Plant, Henan Province, China. Concentrated sulfuric acid and sodium hydroxide (analytical grade) were both purchased from Jingwen Huabo Commerce Center, Beijing, China.

2.2. Chemical Precipitation Coating Process. The process of preparing B/TCP by chemical precipitation method could be expressed as follows:

Barite



Firstly, a certain amount of barite, grinding media, and distilled water were put into a stirred mill (Type GSDM-003, 3L, Beijing Gosdel Powder & Technology Co., Ltd.) and stirred at a speed of $1000\ \text{r}\cdot\text{min}^{-1}$. The ratio of the grinding media to powder fed and the concentration of barite slurry were 4:1 and 45%, respectively. The particle size under different grinding time was measured by BT-1500 type centrifugal sedimentation particle size analyzer. Then the effects of grinding time on performance of B/TCP were studied.

Secondly, the barite powders after grinding for a certain time and distilled water were put into 800 mL of flask and stirred at a certain temperature. Then TiOSO_4 solution was added in five times. The pH value of the reaction solution was adjusted to 2.5 by adding H_2SO_4 and NaOH aqueous solution. When the reaction time was reached, the stir was stopped. The precipitate was washed with 70°C distilled water until it was neutral. After that the washed precipitate was filtrated and then dried.

Finally, the dried samples were calcined in muffle furnace at 800°C for 1 h. The as-prepared B/TCP samples were kept in a desiccator for characterization.

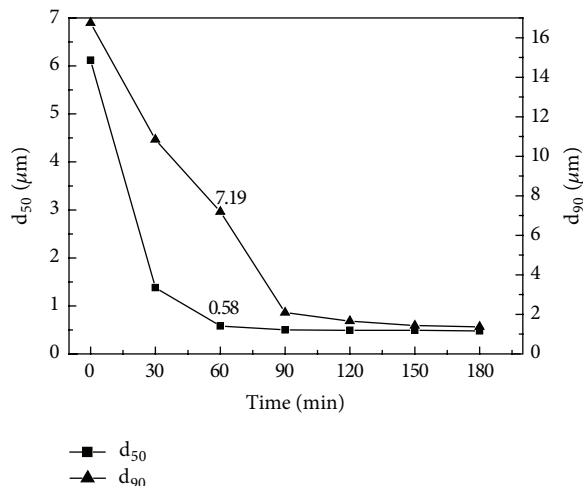


FIGURE 1: Effect of grinding time on granularity about d_{50} and d_{90} of barite.

2.3. Performance and Structure Research Means. The pigment properties of B/TCP were evaluated and the preparation conditions were optimized by measuring hiding power and oil absorption comprehensively. The hiding power (the minimum mass of pigment used to cover evenly a unit area of background surface when just hiding up its color, $\text{g}\cdot\text{m}^{-2}$) and oil absorption value were measured according to the National Standards GB1709-79 and GB1712-79, respectively.

D/MAX 2000 X-ray powder diffractometer (XRD), made in Rigaku Company, was used to analyze the crystalline phase of B/TCP, and field emission scanning electron microscope, model JSM-7001F, made in Japanese Electronics Company, was used to observe the morphology of raw materials and composite particles. The infrared spectra of powder and the combined form between barite and titanium dioxide were measured by NICOLET 750 type infrared spectroscopy and ESCALAB 250 Xi type X-ray photoelectron spectroscopy spectrometer (XPS), respectively.

3. Results and Discussion

3.1. The Pigment Properties and Structure of B/TCP. The appropriate proportion between barite and TiO_2 was the premise of coating TiO_2 on barite effectively. Hydrolysis complex with barite under different grinding time was prepared. The preparation conditions were as follows: titanyl sulfate solution dosage: TiO_2 (included in TiOSO_4 solution):barite = 1:1 (by mass), hydrolysis temperature 90°C , hydrolysis time 90 min, matrix slurry concentration of barite 1.0%, and the pH value about 2.5. Then B/TCP was prepared after hydrolysis complex was calcined at 800°C for 1 h. The effects of grinding time and granularity of barite on pigment properties of B/TCP were evaluated by hiding power value and oil absorption value comprehensively. The effects of grinding time on granularity of barite and pigment properties of B/TCP were shown in Figures 1 and 2, respectively.

Figure 1 showed that the granularity about d_{50} and d_{90} of barite decreased gradually with grinding time increasing,

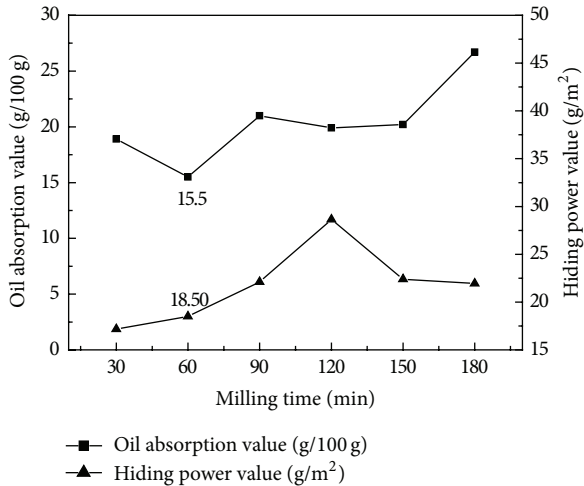


FIGURE 2: Effect of grinding time of barite on pigment properties of B/TCP.

indicating that the particle size was gradually refining. The granularity stabilized to a fixed value 90 min later, indicating that it might turn into a stable state. As shown in Figure 2, the hiding power value of B/TCP prepared first gradually increased and then declined, while the oil absorption value showed an upward trend. When the grinding time of barite reached 60 min, both of the hiding power value and oil absorption value of B/TCP prepared stabilized to a low value, showing that the pigment property was optimal. The granularity about d_{50} and d_{90} of barite prepared was $0.58 \mu\text{m}$ and $7.19 \mu\text{m}$, respectively. The hiding power and oil absorption value of B/TCP prepared under optimal conditions were 18.50 g/m^2 and 15.5 g/100 g , respectively. The pigment property of B/TCP prepared was better than the results of B/TCP prepared through mechanochemical method by Wang et al. [18].

Figure 3 showed the SEM images of naked barite and B/TCP prepared with barite under different times.

3.2. Grinding Time. It was shown that the naked barite particle had regular square state and smooth surface without tiny covering, while the composite particle with regular state was covered with tiny covering in different degree. It could be deduced that composite particle was composed of barite particle as matrix and the tiny covering was TiO_2 . Compared with the samples, it could be found that, after barite grinding for 30 min, 60 min, and 90 min, the composite particle had more TiO_2 which was uniformly and compactly covering its surface, in which after 60 min of grinding and TiO_2 coating, the composite particles had best covering effect. The result here corresponded to that of Figure 2, which also showed the relevance between structure and properties of B/TCP.

When barite grinding time continued to 120 min and 150 min, there was much area with barite naked on the surface of B/TCP, so TiO_2 covering degree was lower with worse covering effect. Apparently, the barite grinding time should not be too long during the preparation of B/TCP.

TABLE 1: EDS energy spectrum of naked barite and B/TCP.

Element	Weight percent	Atom percent
O	26.40	63.19
Mg	2.84	4.47
S	12.26	14.65
Ca	2.03	1.94
Ba	56.47	15.75
Total quality	100.00	
C	4.68	12.84
O	28.67	59.03
S	7.32	7.52
Ti	14.23	9.79
Ba	45.10	10.82
Total quality	100.00	

3.3. X-Ray Diffraction Analysis. The XRD patterns of naked barite, rutile and anatase TiO_2 , and B/TCP prepared from barite- TiOSO_4 hydrolysis complex after calcination at different temperature were shown in Figure 4. It showed that the XRD peaks appearing at $2\theta = 25.8, 26.8, 28.8, 31.5,$ and 43.0 were ascribed to that of barite; the XRD peaks appearing at $2\theta = 27.4, 36.8, 42.6, 54.3,$ and 56.6° were ascribed to that of rutile TiO_2 ; the XRD peaks appearing at $2\theta = 25.3, 37.8, 48.1,$ and 55.1° were ascribed to that of anatase TiO_2 . Otherwise, little anatase TiO_2 diffraction peaks were generated when hydrolysis complex was calcined at less than 700°C , without rutile TiO_2 characteristic peak. It could be deduced that there was little TiOSO_4 hydrolysate on the surface of barite transformed into anatase crystalline phase. Almost all of TiO_2 on the surface of composite changed into rutile TiO_2 when calcined temperature increased to 750°C and 800°C and the diffraction peaks were strong. Meanwhile, the reflections of barite substrate decreased greatly, indicating that composite particle surface had mainly consisted of rutile TiO_2 and the barite surface was basically covered with TiO_2 .

3.4. Scanning Electron Microscope and EDS Energy Spectrum Analysis. The SEM images of naked barite and B/TCP were shown in Figure 5, and the corresponding EDS spectrum analysis results were shown in Table 1.

Figure 5 showed that barite raw material was composed of regular square particles with smooth surface. It corresponded to the characteristic of orthogonal (oblique) crystal which existed in the form of thick plate-like, columnar, or granular aggregate. While B/TCP was composed of small TiO_2 particles uniformly and densely, it could be deduced that B/TCP was composed of TiO_2 coated with barite and TiO_2 was not aggregate. Obviously, barite was like a crystal core for the generated $\text{TiO}_2 \cdot \text{H}_2\text{O}$ growing and attached uniformly. And then the Barite- $\text{TiO}_2 \cdot \text{H}_2\text{O}$ composite particles were washed, stirred, filtered, and calcined at high temperature many times during the preparing process. But most of TiO_2 coating on the surface of barite did not drop off and had regular shape, compact arrangement, and fixed crystal type, indicating that TiO_2 and barite particle were combined firmly, which corresponded to XRD results.

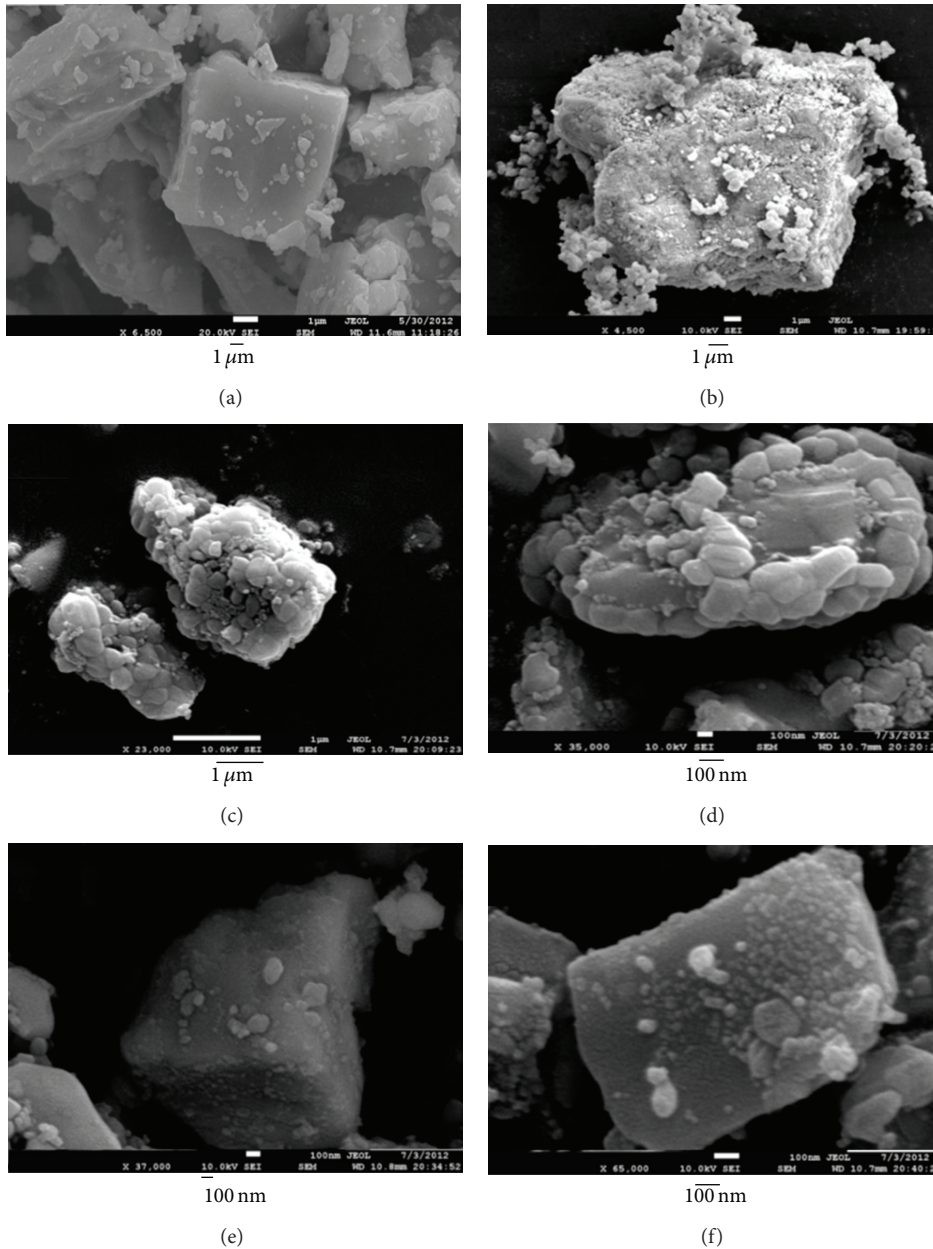


FIGURE 3: SEM images of naked barite (a), 30 min of grinding (b), 60 min of grinding (c), 90 min of grinding (d), 120 min of grinding (e), and 150 min of grinding (f).

As shown in Table 1, the EDS data of barite raw material was consistent with its elements, just a little Ca and Mg, indicating that it was pure. By comparing the EDS spectrum analysis of B/TCP and barite raw material, it could be found that the weight percent of S and Ba significantly decreased, while Ti increased obviously (the weight percent of 14.23%). It was deduced that quantity of TiO_2 was generated on surface of composites, which corresponded to XRD and the SEM results.

3.5. IR Spectrum Analysis. IR spectrograms of rutile TiO_2 , B/TCP (prepared by calcining at 800°C for 1h), and barite

were shown in Figure 6. In the spectrogram of rutile TiO_2 , the IR absorption bands at 674 cm^{-1} and 473 cm^{-1} corresponded to vibration of Ti-O. In the spectrogram of barite, the bands at 1177 cm^{-1} , 1115 cm^{-1} , and 1076 cm^{-1} were assigned to the asymmetric stretching vibration of S-O, resulting from threefold degeneracy of S-O. 983 cm^{-1} band was assigned to the symmetric stretching vibration of S-O, while bands at 635 cm^{-1} and 612 cm^{-1} corresponded to the bending vibration of S-O, which was also from the threefold degeneracy [19]. Therefore, it could be inferred that the IR spectrogram of this section mainly showed the inner vibration mode of SO_4 group. By comparing Figure 6 (a, b, and c) curve, it

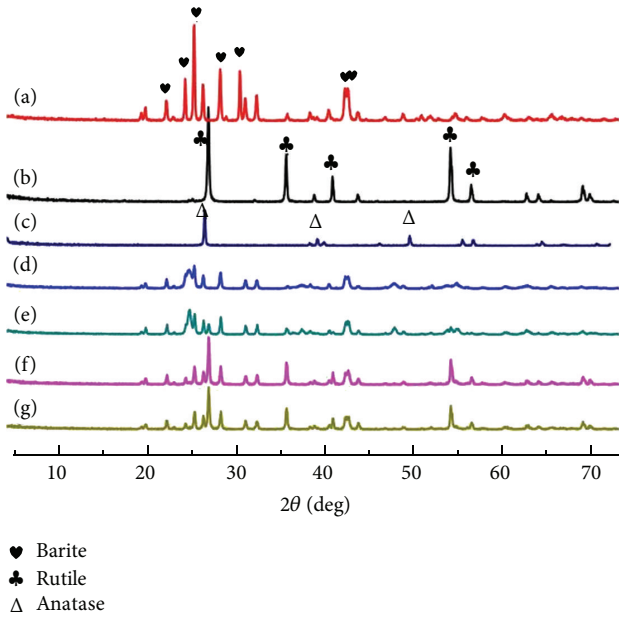


FIGURE 4: XRD patterns of the naked barite (a), rutile TiO_2 (b), anatase TiO_2 (c), and barite coated with TiO_2 powders ((d), (e), (f), and (g)) calcined at 600, 700, 750, and 800 °C for 1 h.

was shown that the bands of B/TCP at 883 cm^{-1} , 728 cm^{-1} , and 1440 cm^{-1} disappeared. Deducing from the above phenomenon, there were some free hydroxyls on the surface of B/TCP before being calcined and then they dropped off after being calcined. It could also be found that the peak at 612 cm^{-1} in Figure 6(b) turned wider than that in Figure 6(c), deducing that the banding form of Ba^{2+} and hydroxyl on the surface of B/TCP might have changed and a new chemical bond Ti-O-Ba was formed.

3.6. XPS Analysis. As Figures 7, 8, and 9 show, to prove the binding energy of each main characteristic element before and after B/TCP being formed and deduce Ti-O-Ba chemical bond formed, the naked barite, rutile TiO_2 , and B/TCP were characterized with XPS under a $\text{CuK}\alpha$ -radiation, a power of 150 W, and a background pressure of 6.5×10^{-10} mbar including all elements spectrum diagram and Ba, S, and Ti elements spectrum diagram. The binding energy of Ba_{3d} in naked barite was 779.61 eV, while it changed into 780.74 eV in TiO_2 -coated barite powders. Therefore, the binding energy of Ba_{3d} shifted to a higher value about 1.13 eV, indicating that the chemical environment around Ba atom changed. Moreover, the binding energy of S_{2p} in raw barite and Ti_{2p} in rutile TiO_2 was 169.00 eV and 458.44 eV, respectively. However, the value changed into 170.02 eV and 458.46 eV, respectively, in B/TCP. Comparing with the binding energy in barite and rutile TiO_2 , the binding energy of S_{2p} and Ti_{2p} shifted to a higher value about 1.02 eV and 0.02 eV. From the change above, it could be indicated that the chemical environment around S atom in barite changed apparently after barite covering with TiO_2 . The binding energy shift of Ti_{2p} was lower, deducing that it still combined with O firmly in the form of Ti-O bond.

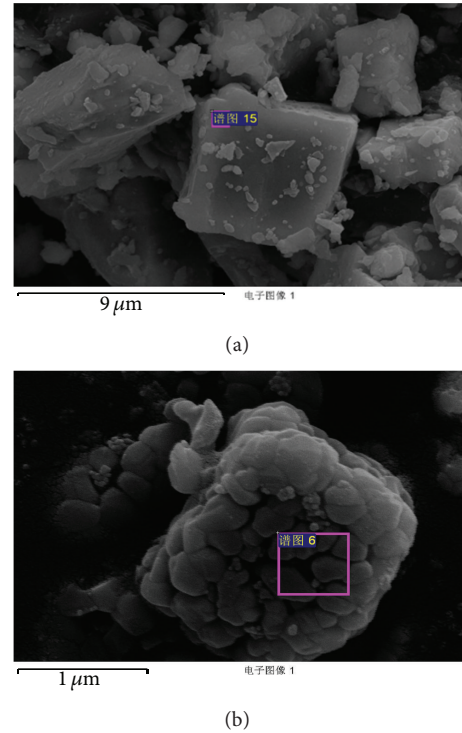


FIGURE 5: SEM images of naked barite (a) and B/TCP (b).

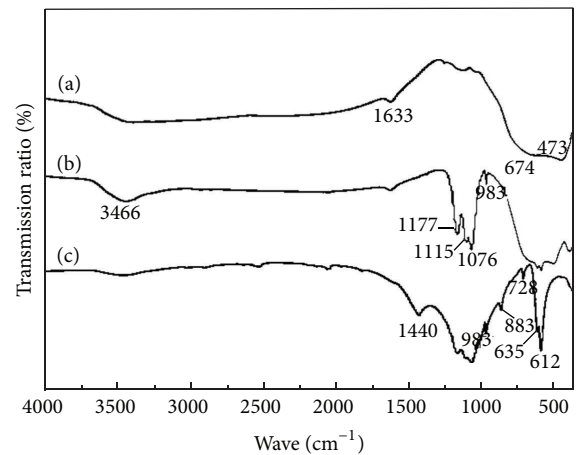


FIGURE 6: IR spectrum of samples: (a) the IR spectrogram of TiO_2 ; (b) the IR spectrogram of B/TCP; and (c) the IR spectrogram of barite.

As a result of some free hydroxyl groups around Ba atom and Ti atom which exist in barite- $\text{TiO}_2 \cdot \text{H}_2\text{O}$, Ba atom and Ti atom were combined by dropping off hydrogen and hydroxyl, forming Ti-O-Ba bond. The chemical shift is generated due to the environmental changes of atoms, which is mainly from the potential energy changes caused by valence electron transfer. Valence electron transfer is closely related to the electronegativity of corresponding element [20]. The inner electrons of the atoms are mainly attracted through Coulomb force by nucleus, which makes the electron have a certain binding energy. Meanwhile, the inner electron is

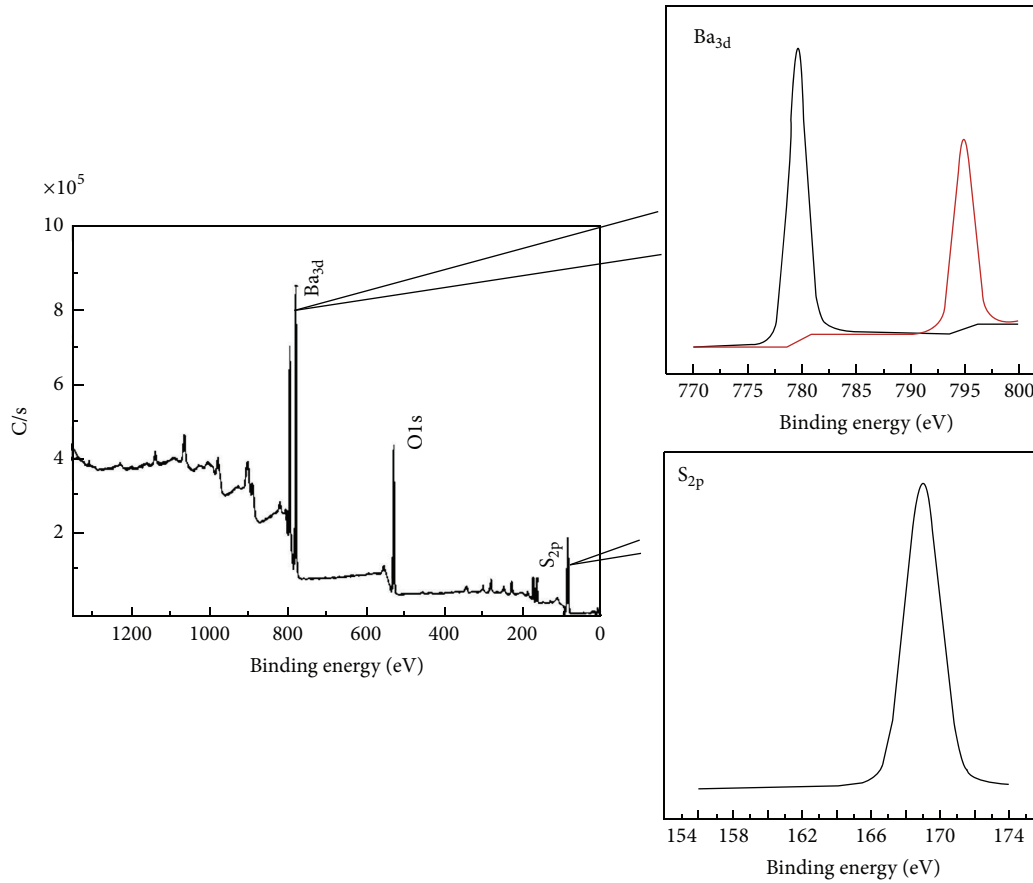


FIGURE 7: XPS spectrum of all elements of barite and XPS spectrum of Ba and S.

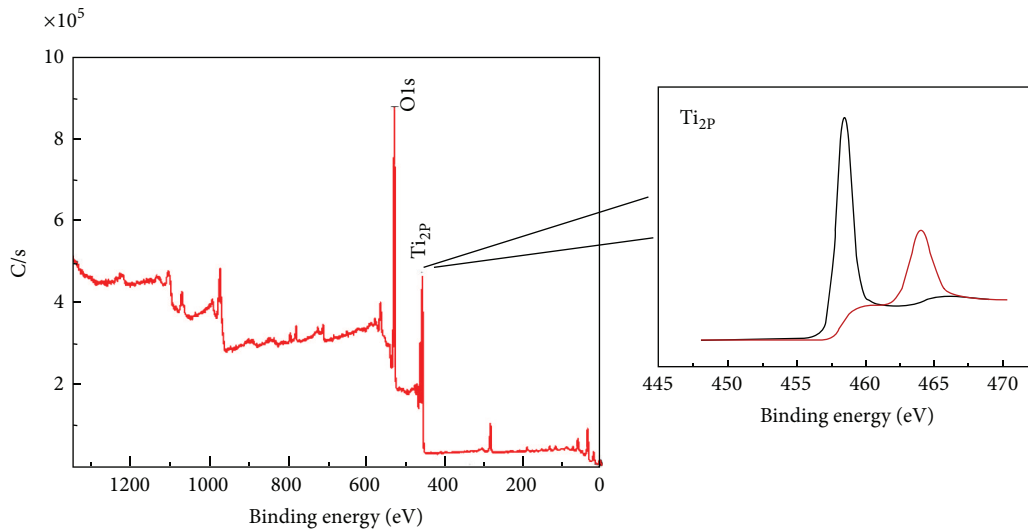


FIGURE 8: XPS spectrum of all elements of rutile TiO₂ and XPS spectrum of Ti.

shielded by the outer electron. Therefore, when the valence electrons shift to the large electronegativity atom, whose electron concentration is increased, the shielding effect is enhanced and the binding energy is decreased. On the contrary, the binding capacity will increase. Due to the larger

electronegativity of Ti than that of Ba, the electron around Ba transfers to O-Ti, and then the electron concentration around Ti is increased, the shielding effect is enhanced, and the binding energy is decreased, while the binding energy of Ba is increased.

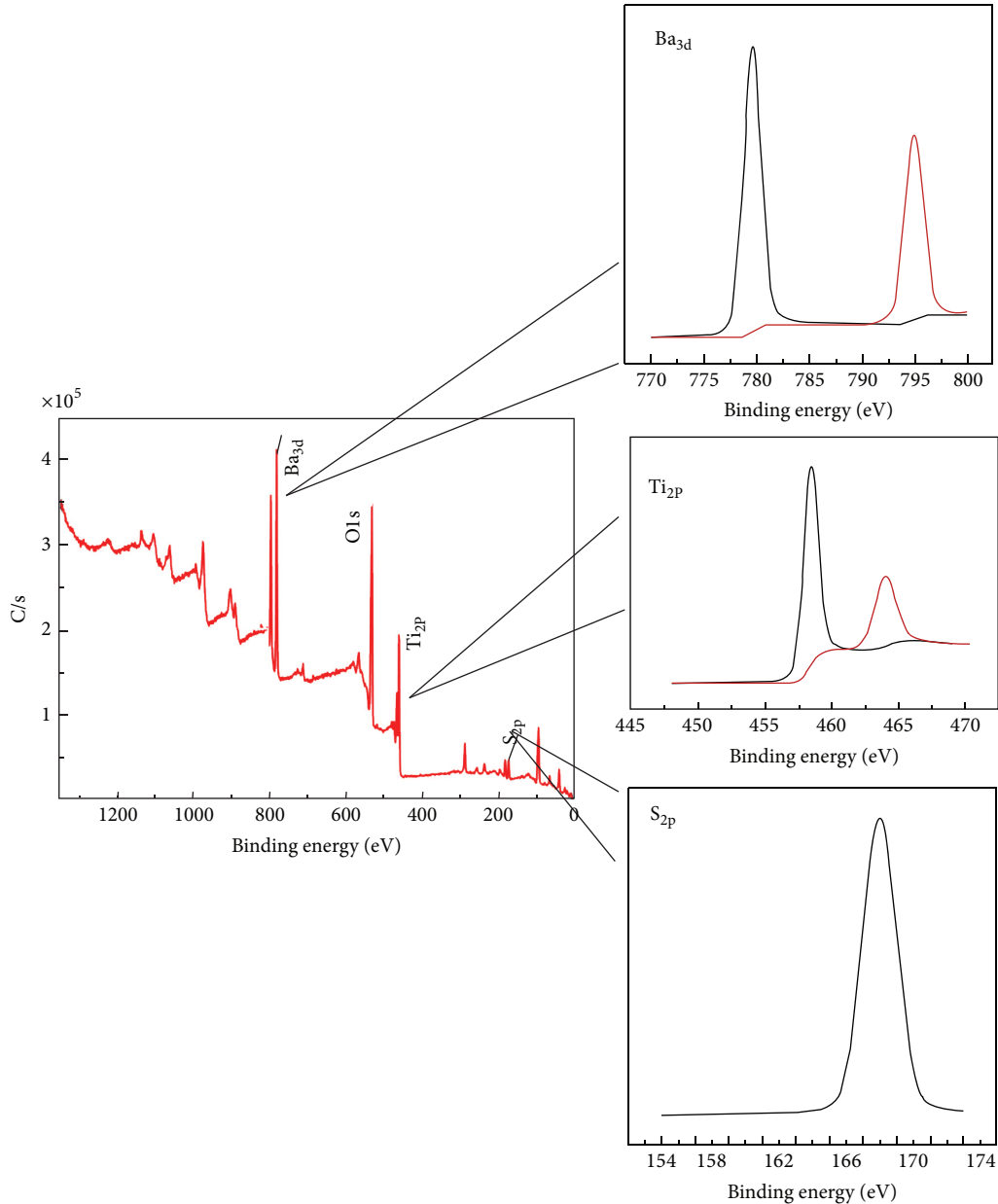


FIGURE 9: XPS spectrum of all elements of B/TCP and XPS spectrum of Ba, S, and Ti.

4. Conclusion

(1) B/TCP was prepared through TiOSO_4 hydrolysis, $\text{TiO}_2 \cdot \text{H}_2\text{O}$ depositing and coating on the surfaces of barite, and composite particles calcined method in TiOSO_4 hydrolysis system including barite. The results showed that the composite powder had similar pigment performances with titanium dioxide and the oil absorption value and hiding power value were 15.5 g/100 g and 18.50 g/m², respectively.

(2) The structure and properties of B/TCP were influenced greatly by the granularity of barite and the calcined temperature of hydrolysis complex. The composite particles with TiO_2 coating on the surface of barite uniformly and compactly were prepared when the granularity about d_{50} and

d_{90} of barite was 0.58 μm and 7.19 μm , respectively. When the calcined temperature of hydrolysis complex was over 700°C, the TiO_2 on the surface of composite particle was rutile crystalline.

(3) By analyzing the results of IR and XPS, we deduce that barite and TiO_2 were combined with Ti–O–Ba chemical bond in B/TCP, which made TiO_2 coat on the surface of barite uniform, compact, and firm.

(4) In the process of preparation of B/TCP, the pigment performance of B/TCP would be more better, when TiO_2 coated on the surface of barite the more uniformly and compactly, and they combined the more firmly. Therefore, the results show that this study is very useful to improve the pigment performance of B/TCP.

Conflict of Interests

The authors declare that there is no conflict of interests regarding the publication of this paper.

References

- [1] Y. Zhang, H. Gan, and G. Zhang, "A novel mixed-phase TiO₂/kaolinite composites and their photocatalytic activity for degradation of organic contaminants," *Chemical Engineering Journal*, vol. 172, no. 2-3, pp. 936–943, 2011.
- [2] K. Mamulová Kutlákova, J. Tokarský, P. Kovář et al., "Preparation and characterization of photoactive composite kaolinite/TiO₂," *Journal of Hazardous Materials*, vol. 188, no. 1-3, pp. 212–220, 2011.
- [3] L. Hai, *Research on the Technology and Theory of Preparing Substitute Product of Titanium Dioxide by Use of Calcined Coal Kaolin*, Beijing University of Technology and Science, Beijing, China, 1999.
- [4] L. Hai, "Research on the technology of coating TiO₂ film on the surface of ultra-fine calcined coal kaolin powder," *China Mining Magazine*, vol. 9, pp. 60–64, 2000.
- [5] J.-W. Lee, S. Kong, W.-S. Kim, and J. Kim, "Preparation and characterization of SiO₂/TiO₂ core-shell particles with controlled shell thickness," *Materials Chemistry and Physics*, vol. 106, no. 1, pp. 39–44, 2007.
- [6] M. Yuan, S. Ren, Y. Guo, X. Zhao, and Y. Liu, "Preparation and characterization of TiO₂/SiO₂ composites," *Journal of Ji Lin University (Science Edition)*, vol. 45, pp. 857–860, 2007.
- [7] H. Qian, *Research on the Preparation and Degradation Characteristic of Nanometer TiO₂/Montmorillonite Composite Photocatalytic Materials*, Wuhan University of Technology, Wuhan, China, 2006.
- [8] M. Ren, H. Yin, Z. Lu, A. Wang, L. Yu, and T. Jiang, "Evolution of rutile TiO₂ coating layers on lamellar sericite surface induced by Sn⁴⁺ and the pigmentary properties," *Powder Technology*, vol. 204, no. 2-3, pp. 249–254, 2010.
- [9] M. Ren, H. Yin, A. Wang et al., "Evolution of TiO₂ coating layers on lamellar sericite in the presence of La³⁺ and the pigmentary properties," *Applied Surface Science*, vol. 254, no. 22, pp. 7314–7320, 2008.
- [10] R. Jun, *Study on Preparation of Sericite/TiO₂ Composite Particles Material by Hydrolyzing-Coating Method*, China University of Geosciences, Beijing, China, 2008.
- [11] X. Yan, Z. Ji, J. Wang et al., "Preparation and characterization of nano-TiO₂ tourmaline," *Rare Metal Materials and Engineering*, vol. 33, pp. 66–68, 2004.
- [12] N. M. Ahmed and M. M. Selim, "Anticorrosive performance of titanium dioxide-talc hybrid pigments in alkyd paint formulations for protection of steel structures," *Anti-Corrosion Methods and Materials*, vol. 57, no. 3, pp. 133–141, 2010.
- [13] P. Liu, *Preparation and Ultraviolet Shielding Research on Nano-TiO₂/Talc*, Tianjin University, Tianjin, China, 2005.
- [14] H. Lin and Y. Hu, "Mechanism of coating TiO₂ film on the surface of ultra-fine industrial mineral particles," *The Chinese Journal of Process Engineering*, vol. 2, pp. 151–155, 2002.
- [15] H. Ma, *Industrial Mineral and Rock*, Geological Publishing House, Beijing, China, 2001.
- [16] H. Yang, Y. Hu, H. Zhang, and C. Du, "Preparation and characterization of Sb-SnO₂/BaSO₄ conductive powder," *Journal of the Chinese Ceramic Society*, vol. 34, no. 7, pp. 776–781, 2006.
- [17] H. Zhou, *Preparation and Photocatalytic Activity of TiO₂/BaSO₄ Composite Material*, Hebei Normal University, Shijiazhuang, China, 2010.
- [18] B. Wang, H. Ding, Y. Wang et al., "Preparation of Barite/TiO₂ composite particle and interaction mechanism between TiO₂ and Barite particles," *Rare Metal Materials and Engineering*, vol. 40, pp. 193–197, 2011.
- [19] W. Lu, W. Liang, Z. Zhang et al., *Mineral infrared spectroscopy [M.S. thesis]*, Chongqing University Publishing House, Chongqing, China, 1989.
- [20] Y. Lin, T. Wang, and C. Tan, "Organically modified silica-alumina oxide-coated titanium dioxide particles," *Chemical Journal of Chinese Universities*, vol. 22, pp. 104–107, 2001.

Research Article

Triaxial Test and Mechanical Analysis of Rock-Soil Aggregate Sampled from Natural Sliding Mass

Shuling Huang,¹ Xiuli Ding,¹ Yuting Zhang,¹ and Wei Cheng²

¹Key Laboratory of Geotechnical Mechanics and Engineering of Ministry of Water Resources, Changjiang River Scientific Research Institute, Wuhan, Hubei 430010, China

²Sichuan Forestry Inventory and Planning Institute, Chengdu 610081, China

Correspondence should be addressed to Shuling Huang; huangsl_2014@163.com

Received 25 August 2014; Accepted 21 November 2014

Academic Editor: Guocheng Lv

Copyright © 2015 Shuling Huang et al. This is an open access article distributed under the Creative Commons Attribution License, which permits unrestricted use, distribution, and reproduction in any medium, provided the original work is properly cited.

Rock-soil aggregate, as a specific geomaterial, exhibits complicated mechanical behavior. The rock-soil aggregate sampled from the deep layer of sliding mass at Jinpingzi area of Wudongde hydropower plant on Yangtze River is investigated to understand its mechanical behavior. Large-scale laboratory triaxial tests are conducted considering different gradations, stone contents and confining pressures. The results show that variation of stone content and gradation considerably affects the mechanical characteristics of rock-soil aggregate. Further, the influences of stone content, and gradation variation on stress-strain curve, Mohr-Coulomb criterion based shear strength parameters, Duncan-Chang model based deformation parameters, and internal friction angle are analyzed. A modified Rowe's stress-dilatancy equation describing the mechanical response of rock-soil aggregate is then suggested.

1. Introduction

The rock-soil aggregate is emerging as a new concept as the accumulation layered sliding mass receives increasing attention. Geomaterials, therefore, are further categorized into three existence forms, which are soil, rock, and rock-soil aggregate [1]. Rock-soil aggregates are widely distributed on the planet and already spotted in many engineering construction cases. Due to this practical need, the mechanical properties of rock-soil aggregate have been extensively addressed by many scholars. Particularly during the past decades, rock-soil aggregate gains its popularity as a hot issue in geotechnical scope.

Rock-soil aggregate in accumulation layered sliding mass is a natural geomaterial. It is composed of blocks, gravels, and fine grained soil of various dimensions. Due to this unique composition, it is characterized by high nonuniformity and discontinuity [2, 3]. Its mechanical characteristics and deformation failure mechanism are therefore different from conventional geomaterials, such as soil and rock blocks [4–6]. The fabric features of rock-soil aggregate, including its granular composition, particle properties, and patterns

of spatial distribution, have significant influences on its mechanical characteristics [7, 8].

For laboratory tests, researches are usually conducted based on a series of tests, including large-scale in situ shear test, laboratory shear test, laboratory uniaxial compressive test, and seepage test [9–12]. Strength and seepage parameters can be then obtained and adopted by engineering constructions. As for in situ test, the natural features of stone content, stone spatial distribution, and its gradation are maintained. However, rock-soil aggregates are randomly distributed. Due to this fact, as well as the restrictions caused by representativeness, operability, and financial cost, in situ tests cannot be conducted in large amounts. Moreover, for landslide occurring at deep layer with a sliding mass thickness greater than 25 m, the stress state and stress path of rock-soil aggregate have significant impact on the evolution process of landslide. It is therefore not practical for in situ tests to provide different stress state and stress path conditions.

As for triaxial test, the successful development of laboratory large-scale triaxial testing equipment makes it possible to conduct indoor tests for geomaterials containing coarse grained particles. Moreover, stress state provided by

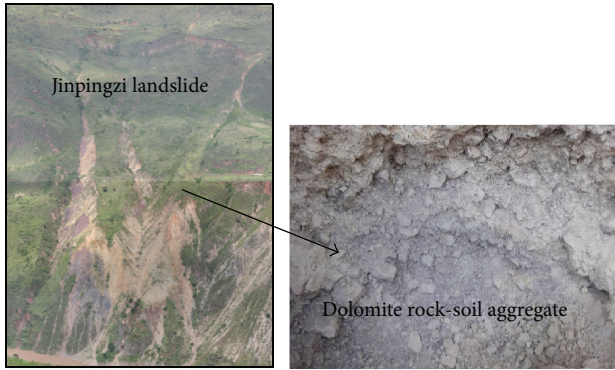


FIGURE 1: Dolomite rock-soil aggregate in Jinpingzi landslide.

large-scale triaxial test is close to real situation and multiple stress paths can be imposed. As a result, the measured parameters are then rational and reliable and can well reflect the inherent features of rock-soil aggregate. So far, researches based on large-scale triaxial test focusing on the mechanical characteristics of rock-soil aggregate sampled from natural sliding mass are rarely reported.

The Jinpingzi landslide took place at Wudongde hydro-power plant in Southwest China. The volume of the sliding mass is about $2,700 \times 10^4 \text{ m}^3$ and its thickness is about 45~100 m. It is a deep layer sliding mass whose main contents are ancient gully of gravelly soil and dolomite rock-soil aggregates. The studied dolomite rock-soil aggregates are sampled from this sliding mass (Figure 1). By performing laboratory large-scale triaxial tests, the mechanical characteristics and deformation failure patterns of the rock-soil aggregates are analyzed.

2. Materials and Methods

2.1. Materials. The front side of the sliding mass in Jinpingzi landslide is chosen as the sampling area. The obtained sample has rich gradation (Figure 2(a)). Its particles have various shapes, which are mostly angular and subangular. Most rock block size ranges from 2 cm to 7 cm and the maximum size reaches 15 cm. The rock-soil aggregates are primarily composed of Z2d dolomite and siliceous dolomite, which have high mechanical strength.

Laboratory particle analysis is conducted on the samples of rock-soil aggregate firstly. The equivalent substitution method is employed to reduce the scale of the oversized particles. Particles with a diameter range of 5~60 mm are used to equivalently substitute for those oversized particles whose diameter exceeds 60 mm. The proportion of particles whose diameters are less than 5 mm remains unchanged. The obtained gradation used for test is plotted as the average line in Figure 2(a). Gradations 1, 2, 4, and 5 are adjusted as wide gradation for the test.

2.2. Large-Scale Triaxial Shear Apparatus and Test Methodologies. The dimension of the sample is arranged as $\Phi 300 \text{ mm} \times 600 \text{ mm}$. The test is conducted on the large-scale triaxial test machine and plotted in Figure 2(b).

The samples used in the triaxial test are in saturation state. At the start of the test, the samples are all restored to their natural stress state. The confining pressures are arranged as 0.4 MPa, 0.8 MPa, 1.2 MPa, and 1.6 MPa. The densities of saturated samples are obtained by compaction test (Table 1). The compactness degree of all samples is controlled as 90%.

The consolidated-drained triaxial shear test is strain-controlled. The shear velocity is fixed at 0.25 mm/min (or 2.5%/h). The sample size, dry density, and gradation are all calculated in accordance with test requirements. The rock-soil aggregate samples are then weighed and mixed uniformly.

3. Results and Discussions

3.1. Test Results. Large-scale saturated consolidated-drained shear tests are performed on the prepared samples which are arranged in 5 fixed gradations. The stress to strain curves and volumetric strain to axial strain curves are then obtained. The curves of different gradation samples are plotted in Figures 3 and 4.

The following findings can be summarized after analyzing the triaxial test results.

- (1) Remarkable nonlinearity is observed in the stress to strain curve of rock-soil aggregate samples. The maximum principal difference value, denoted by $(\sigma_1 - \sigma_3)_f$, increases as the confining pressure increases.
- (2) When the confining pressure is low ($\sigma_3 = 0.4 \text{ MPa}$), rock-soil aggregate exhibits slight strain softening effect. The strain-hardening degree increases as the confining pressure increases. When the confining pressure approaches larger value ($\sigma_3 = 0.8 \text{ MPa}$), rock-soil aggregate takes on strain-hardening effect. The stress-strain curves based on 20 samples all have wide range of approximately horizontal distributions near peak point. This indicates that rock-soil aggregate has remarkable ductile plastic deformation features.
- (3) By observing the volumetric strain to axial strain curve, it is found that the shear contraction deformation increases as the confining pressure increases. When the confining pressure is low ($\sigma_3 = 0.4 \text{ MPa}$), the samples firstly show shear contraction and then show shear dilation. As the confining pressure increases, the degree of shear dilation decreases. When the confining pressure is high ($\sigma_3 \geq 1.2 \text{ MPa}$), the samples basically exhibit shear contraction. As the loading increases, the increasing extent of shear contraction deformation becomes smaller.

The above observed macroscopic deformation findings have close relevance to the adjustments of mesoscopic fabric and particle rupture of rock-soil aggregate during loading process. When the confining pressure is low, the resistance against particle movements is small. Therefore, when samples are under shear state, particles are easy to overcome the resistance and turn over adjacent particles, thus causing dislocated slips. As a result, remarkable shear dilation deformation is observed and the strain softening effect of stress to strain

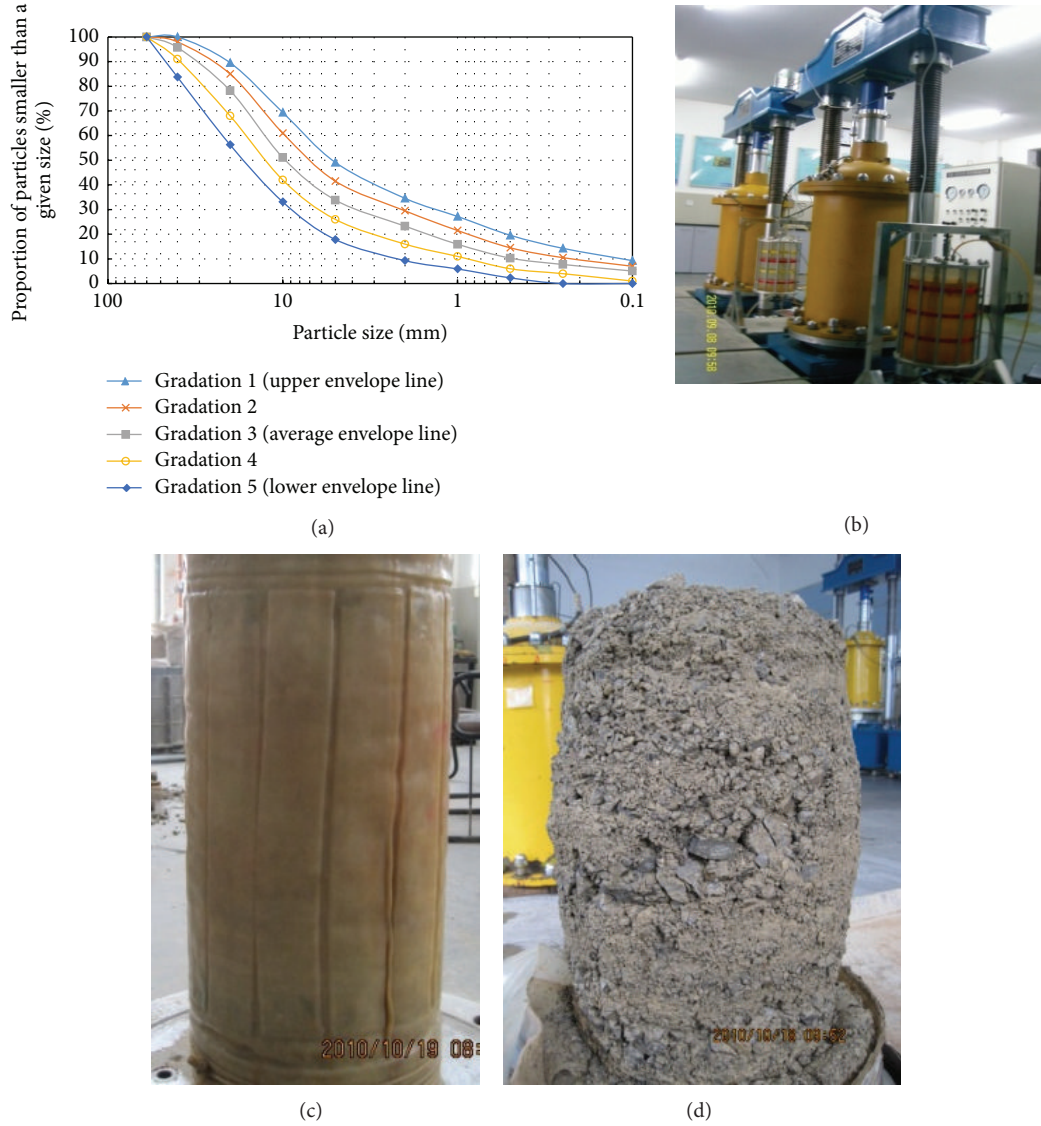


FIGURE 2: Laboratory triaxial test: (a) gradation of rock-soil aggregate; (b) stress-controlled large-scale triaxial test; (c) test sample of rock-soil aggregate; (d) failure mode.

TABLE 1: Dry density of rock-soil aggregate samples.

Gradation	Gradation 1	Gradation 2	Gradation 3	Gradation 4	Gradation 5
Dry density (g/cm ³)	2.102	2.135	2.144	2.128	2.073
Rock proportion (P5)	50.89%	58.50%	66.16%	74.00%	82.17%

curve is weaker. When the confining pressure is high, the constraining effects among particles and resistance against movements are considerable during shear failure process. Therefore, when samples are under shear state, it is difficult for particles to overcome the resistance, thus lowering the possibility of dislocated slips. As a result, shear dilation degree is lowered. As particles cannot turn over adjacent particles, stress concentration is induced. It then leads to particle ruptures and rearrangements. The stress to strain curve is hardening type and the volumetric strain is primarily condensed.

3.2. Effects of Gradation and Stone Content

Stress-Strain Curves. To analyze the differences of deformation features among different samples, the stress to strain curves and volumetric strain to axial strain curves obtained from samples of different gradation groups are plotted in Figures 5 and 6. The curves are all obtained from tests under the same confining pressure.

It is found from Figures 5 and 6 that, under the same confining pressure, the stress to strain curve obtained from

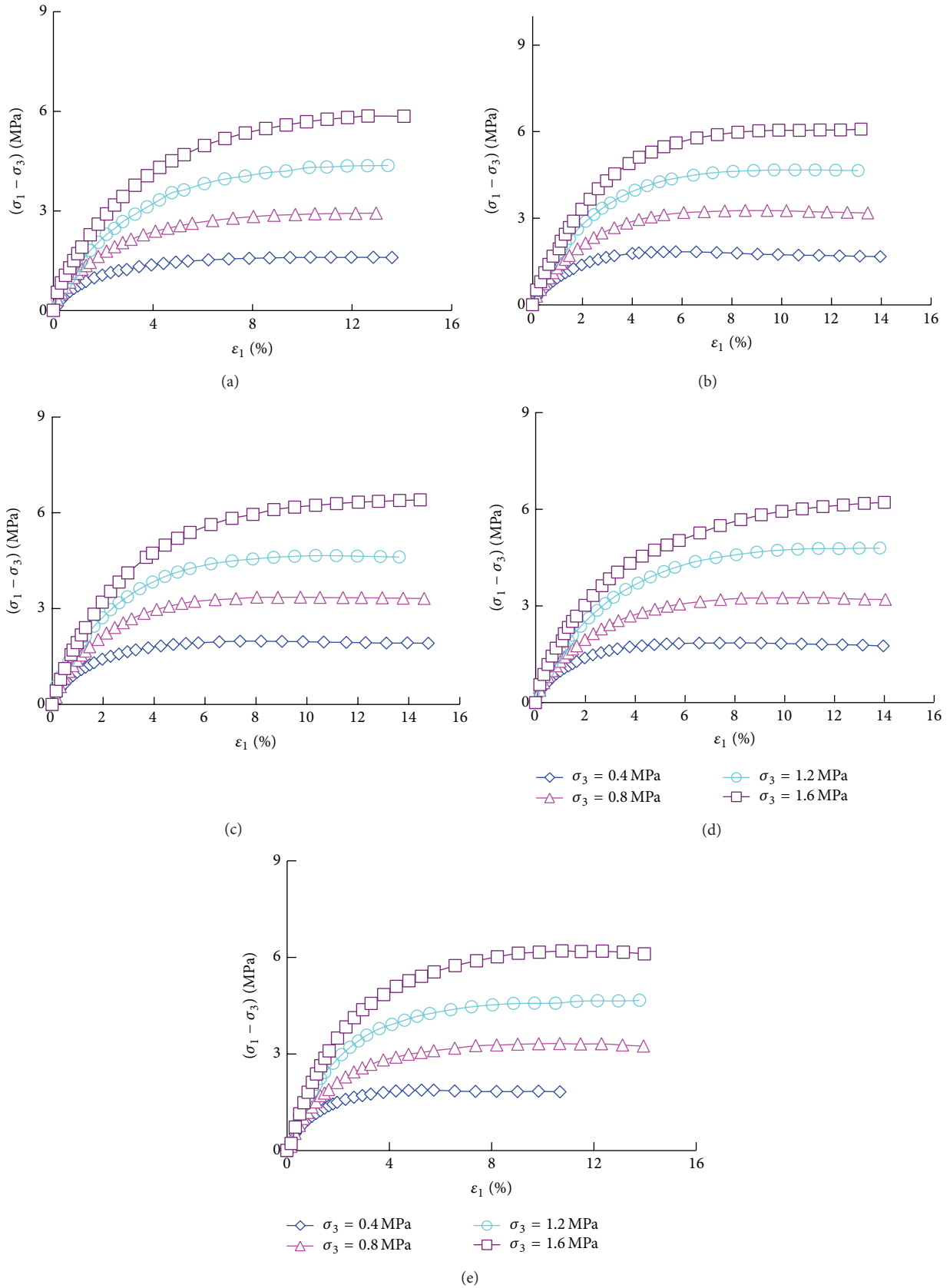


FIGURE 3: Stress-strain curve under different confining pressure: (a) gradation 1, rock proportion (P5), 50.89%; (b) gradation 2, rock proportion (P5), 58.50%; (c) gradation 3, rock proportion (P5), 66.16%; (d) gradation 4, rock proportion (P5), 74.00%; (e) gradation 5, rock proportion (P5), 82.17%.

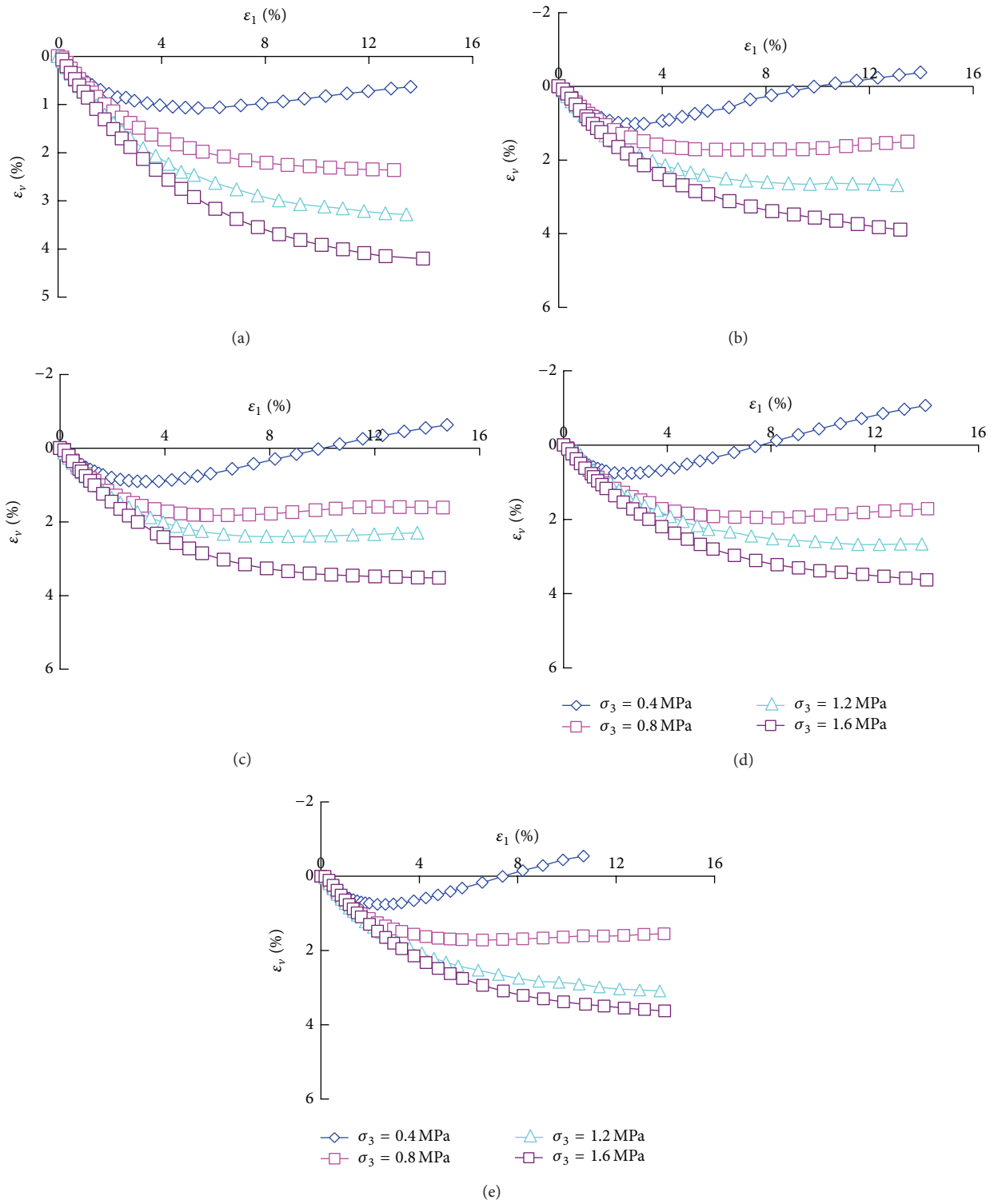


FIGURE 4: Volumetric strain to axial strain curve under different confining pressure: (a) gradation 1, rock proportion (P5), 50.89%; (b) gradation 2, rock proportion (P5), 58.50%; (c) gradation 3, rock proportion (P5), 66.16%; (d) gradation 4, rock proportion (P5), 74.00%; (e) gradation 5, rock proportion (P5), 82.17%.

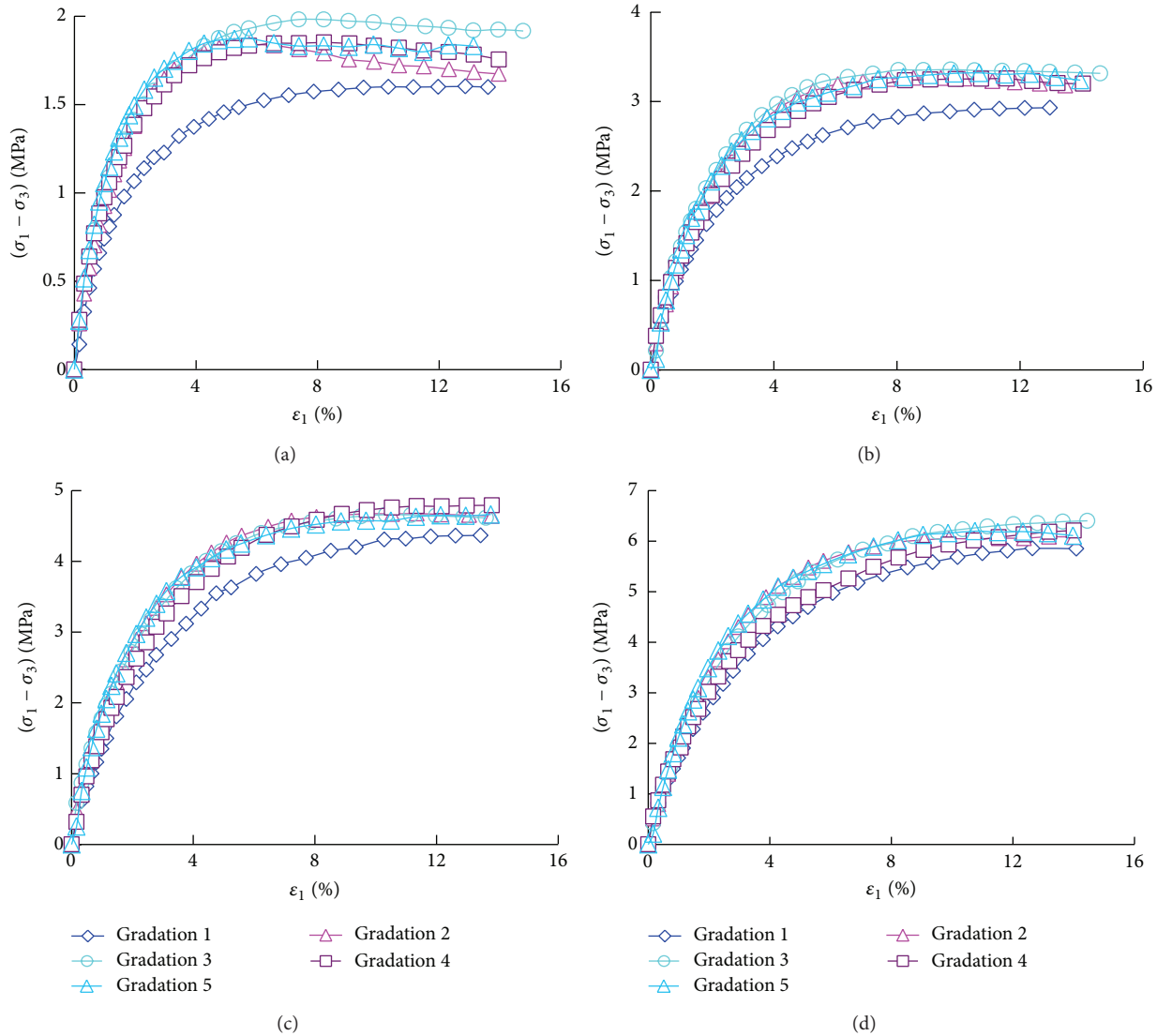


FIGURE 5: Stress-strain curve under different gradation: (a) $\sigma_3 = 0.4$ MPa; (b) $\sigma_3 = 0.8$ MPa; (c) $\sigma_3 = 1.2$ MPa; (d) $\sigma_3 = 1.6$ MPa.

gradation number 1 sample is considerably lower with large deviation extent compared to other curves, while other curves obtained from gradation number 2 to number 5 samples are basically identical.

Under low confining pressure, the stress to strain curve of gradation 1 is remarkably lower than curves of gradations 2~5. As the confining pressure increases, curve of gradation 1 gradually approaches the curves of other gradations. Under high confining pressure, curve distribution of all gradations is basically similar.

For volumetric strain to axial strain relation, the shear contraction effect of gradation 1 is more observable than other gradations. Particularly for confining pressure lower than 0.4 MPa, the volumetric strain of gradations 2~5 samples firstly increases and then quickly decreases, turning the volumetric strain magnitude from positive value into negative value. Equally, during the process, shear contraction firstly

takes place and then remarkable shear dilation takes place. On the other hand, although the volumetric strain of gradation 1 sample is also firstly increasing and then decreasing, the decreasing speed is lower and volumetric strain magnitude maintains positive value during the whole process. Compared to other gradations, dilation effect of gradation 1 sample is not obvious. As the confining pressure increases, shear dilation effect of all gradations gradually becomes less observable. Particularly, when the confining pressure exceeds 0.8 MPa for gradation 1, shear contraction effect occurs and shear dilation effect no longer exists. For other gradations under confining pressure of 0.8 MPa, shear contraction effect is also observed and shear dilation effect becomes less observable. When the confining pressure is above 1.2 MPa, gradations 2~5 samples take on shear contraction effect and shear dilation effect no longer existed. In a word, under high confining pressure, the volumetric strain to axial strain curves

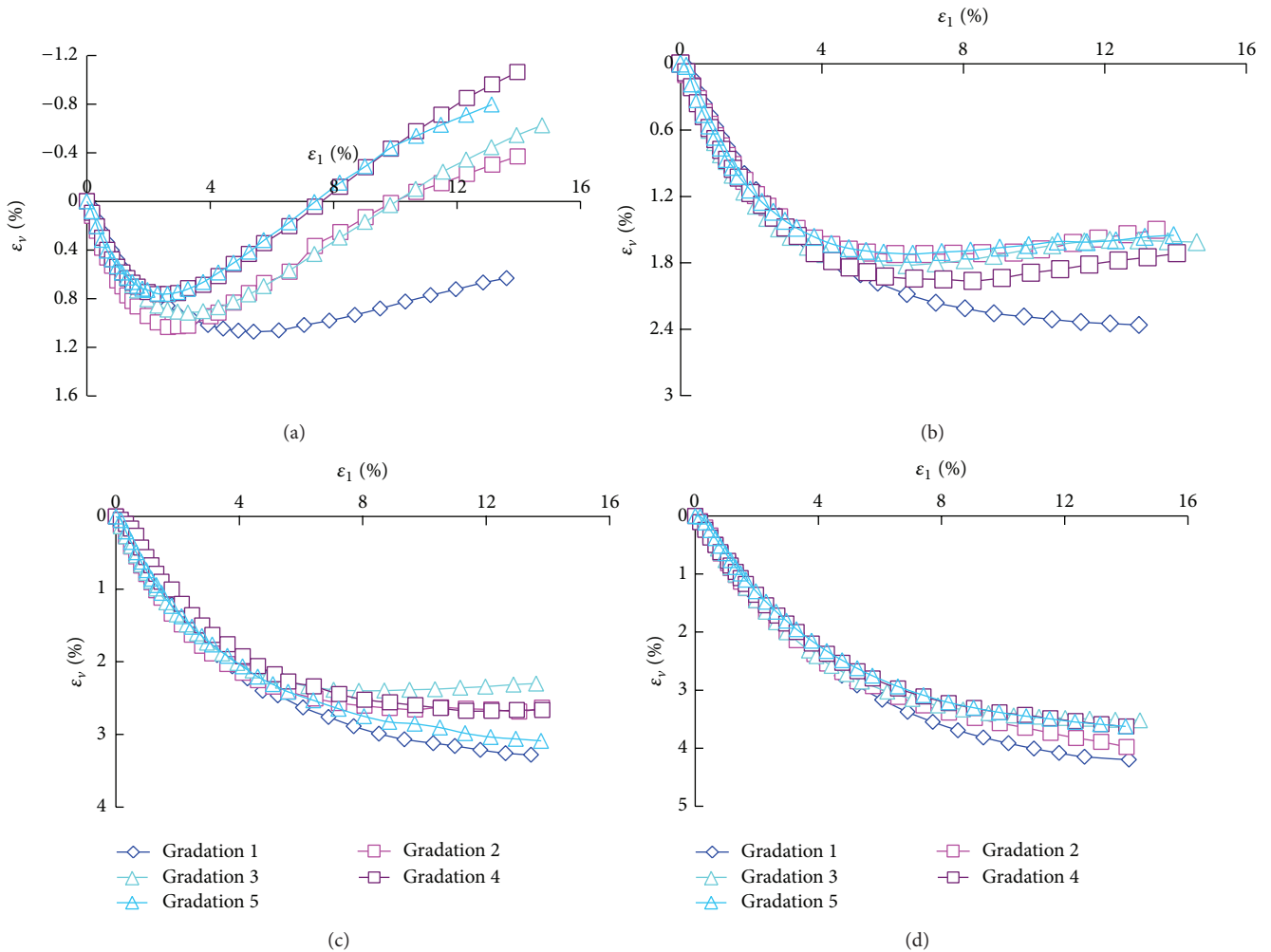


FIGURE 6: Volumetric strain to axial strain curve under different gradation: (a) $\sigma_3 = 0.4$ MPa; (b) $\sigma_3 = 0.8$ MPa; (c) $\sigma_3 = 1.2$ MPa; (d) $\sigma_3 = 1.6$ MPa.

of all gradations are observed to distribute uniformly. This feature is basically consistent with that of stress to strain curves.

The reason is that the proportion of fine grained particle with diameters smaller than 5 mm accounts for 49.11%. Therefore, the skeleton effect provided by coarse grained particles is not obvious. On the other hand, the rock proportion ranges from 60% to 80% in gradation number 2 to number 5 samples. Coarse and fine grained particles can attain fully mutual contact. Coarse grained particles can form skeletons and fine grained particles can fully fill the voids inside skeletons, thus making it possible to reach an optimum composition and produce considerable bite force. Therefore, the deviatoric stress is larger. From the start of loading to the arrival of maximum loading value, the stress to strain curves of gradations number 2, number 3, and number 4 almost coincide with that of gradation number 5. It indicates that when rock proportion ranges from 60% to 80%, its variation has small influences on the stress to strain curves before reaching the maximum value. After reaching the maximum loading value, the stress to strain

curves develop dispersedly. As the composition of coarse and fine particles of gradation number 3 sample reaches optimal state, the maximum deviatoric stress is observed. When the confining stress is low, the volumetric strain curves of all samples exhibit remarkable shear contraction (or shear dilation) characteristics.

Shear Strength Parameters. It is observed that the strength envelope lines are typically linear under the condition of confining pressure 0.4 MPa~1.6 Mpa (Figure 7). Mohr-Coulomb failure criterion has been adopted for determining shear strength parameters c and ϕ . The variation laws of shear strength parameters c and ϕ with the variation of rock proportion are plotted in Figure 8 and given in Table 2.

With the increase of the amount of stone, values of shear strength parameter ϕ of different sample gradations show a slowly increasing trend but values of shear strength parameter c show a slowly downward trend. For no sticky granular medium such as rock-soil aggregate, its shear strength is primarily provided by the bite forces among particles. As the voids inside coarse particles of gradation number 3

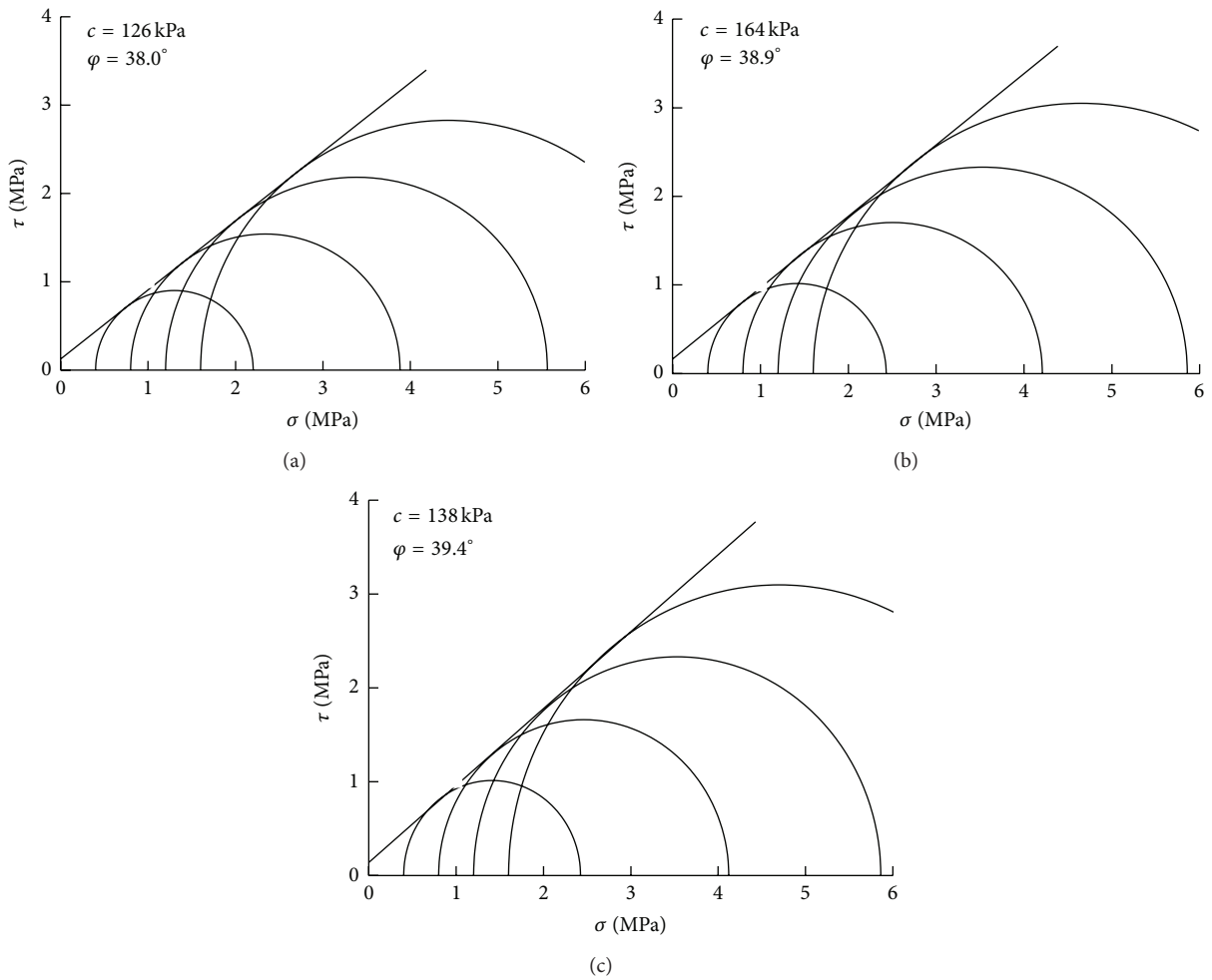


FIGURE 7: Mohr-Coulomb failure envelopes and Mohr circles: (a) gradation 1; (b) gradation 3; (c) gradation 5.

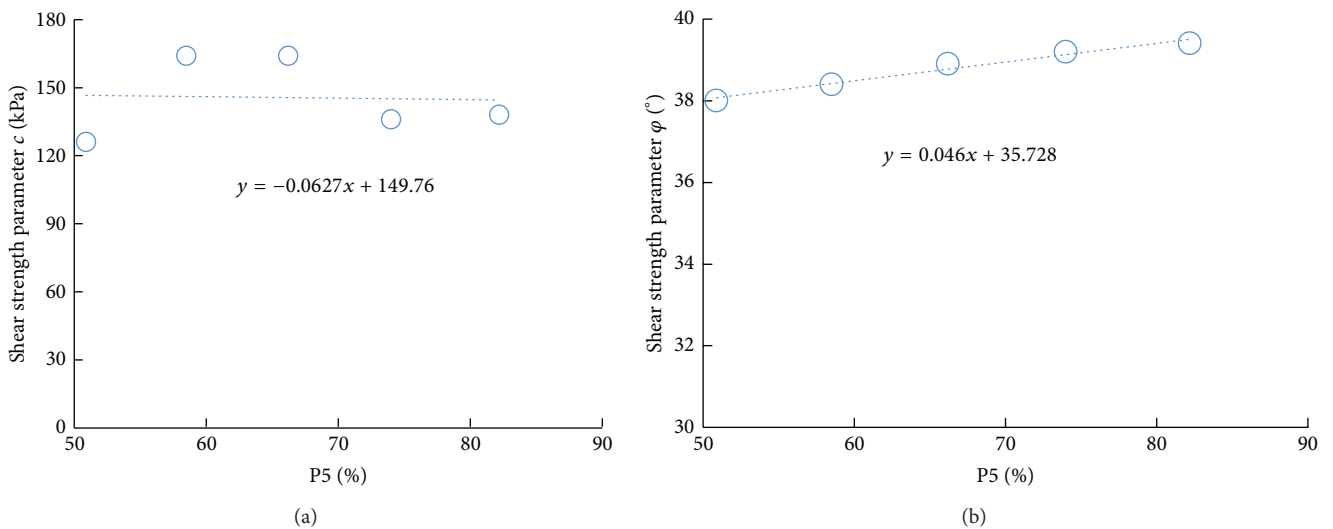


FIGURE 8: Shear strength parameters to rock proportion curve: (a) shear strength parameter c ; (b) shear strength parameter φ .

TABLE 2: Parameters of Duncan-Chang model, including E - B model and E - μ model.

P5/%	c /MPa	Φ /°	K	n	K_b	m	R_f	G	F	D
50.9	126	38.0	919	0.333	355	0.284	0.869	0.435	0.238	4.303
58.5	164	38.4	1009	0.394	456	0.295	0.830	0.295	0.138	5.760
66.2	164	38.9	1076	0.376	470	0.274	0.845	0.351	0.178	5.618
74	136	39.2	1100	0.314	493	0.232	0.825	0.360	0.155	4.542
82.2	138	39.4	1094	0.347	455	0.337	0.814	0.256	0.054	5.742

and number 4 samples can be well filled by fine particles and meanwhile coarse particles can mutually form favorable skeletons, the bite forces of these two samples can reach maximum value. As the rock proportions of gradation number 4 and number 5 samples are comparatively larger, the coarse and fine particles are able to contact closely. Therefore, their bite forces and shear strength are also considerable. The proportion of fine particles in gradation number 1 samples is comparatively larger than other samples; thus its shear strength is smaller. The shear strength parameter φ ranges from 38.0° to 39.4°, which is not remarkably affected by P5.

Deformation Parameters. As mentioned above, rock-soil aggregate behaves highly nonlinearly. A hyperbolic model known as Duncan-Chang model is an incremental nonlinear stress-dependent model which is suggested by Duncan and Chang [13]. Mohr-Coulomb is its failure criteria which includes two strength parameters c and φ . This model including E - μ mode and E - B model describes nonlinearity and stress-dependent and inelastic behavior. Tangential elastic modulus and tangential Poisson's ratio can be described using expressions proposed by E - μ model as follows [13]:

$$E_t = E_i \left[1 - \frac{R_f (\sigma_1 - \sigma_3) (1 - \sin \varphi)}{2c \cos \varphi + 2c\sigma_3 \sin \varphi} \right]^2, \quad (1)$$

$$\mu_t = \frac{\mu_i}{(1 - A)^2},$$

$$A = D (\sigma_1 - \sigma_3) \left(K p_a \left(\frac{\sigma_3}{p_a} \right) \times \left[1 - \frac{R_f (\sigma_1 - \sigma_3) (1 - \sin \varphi)}{2c \cos \varphi + 2c\sigma_3 \sin \varphi} \right] \right)^{-1},$$

where c is cohesion and φ is internal friction angle. R_f is the principal stress ratio when failure occurs. D is the lateral expansive strain increment induced by deviatoric stress increment.

Moreover, when E - B model is used, bulk modulus B_t of rock-soil aggregate can be calculated by [14]

$$B_t = K_b p_a \left(\frac{\sigma_3}{p_a} \right)^m, \quad (2)$$

where K_b is the ratio of initial bulk modulus to p_a when confining pressure is normal atmosphere. m is an index describing the increasing extent of bulk modulus as confining pressure increases.

The relationship between initial elastic modulus E_i and confining pressure, as well as the relationship between initial Poisson's ratio μ_i and confining pressure, is given in Figure 9. It is found that as the confining pressure increases, the initial elastic modulus increases too. As $\lg(E_i)$ and $\lg(\sigma_3/p_a)$ are linearly related, the relationship between E_i and confining pressure can be described as a stress-dependent parameter using a power law formulation suggested by Janbu [15]:

$$E_i = K p_a \left(\frac{\sigma_3}{p_a} \right)^n, \quad (3)$$

where p_a is normal atmosphere and K is the ratio of E_i to p_a when the confining pressure is normal atmosphere. n is an index describing the increasing extent of E_i when confining pressure increases.

It is also found from Figure 9 that the initial Poisson's ratio μ_i decreases as the confining pressure increases and is linearly related to $\lg(\sigma_3/p_a)$ as

$$\mu_i = G - F \lg \left(\frac{\sigma_3}{p_a} \right), \quad (4)$$

where G is the initial tangential Poisson's ratio under normal atmosphere. F is an index describing the increasing extent of tangential Poisson's ratio when confining pressure increases.

It is found that the axial stress-strain curve of rock-soil aggregate under medium and high confining pressure is nonlinear and can be described using hyperbolic curve, from Figure 10.

The relationship between deformation parameters and stone content P5 is given in Table 2 on the basis of (1)~(4). With the increase of stone content P5, deformation parameters K , K_b , and D generally increase. This indicates that higher value of stone content leads to stronger framework supporting effect produced by coarse grained particles and larger bulk modulus. The values of G and F are both decreasing as P5 increases. The values of m , n , and R_f are not remarkably affected by P5.

Internal Friction Angle. The index of internal friction angle of rock-soil aggregate is related to gradation, stone content, and other factors. The cohesion of the sampled sliding mass is assumed zero. Then the internal friction angle φ can be obtained using

$$\varphi = \sin^{-1} \frac{\sigma_1 - \sigma_3}{\sigma_1 + \sigma_3}, \quad (5)$$

where σ_1 and σ_3 are measured value of the first and the third principal stress in test. The relationship between φ and

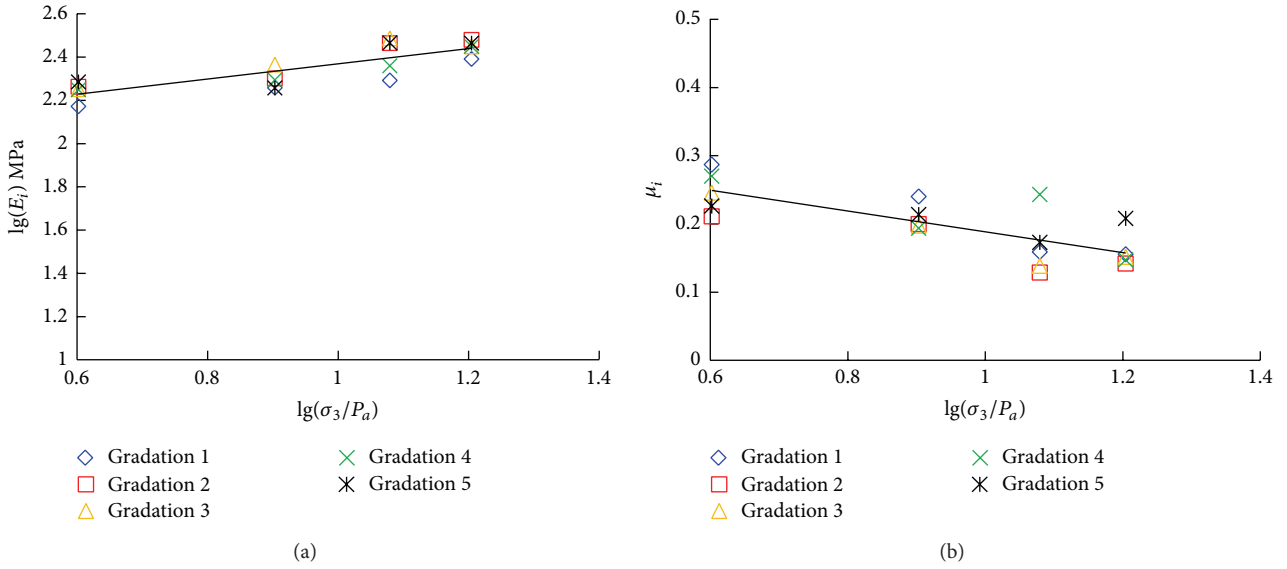


FIGURE 9: Influence of confining pressure on initial deformation modulus and Poisson's ratio in initial loading stage: (a) initial deformation modulus; (b) initial Poisson's ratio.

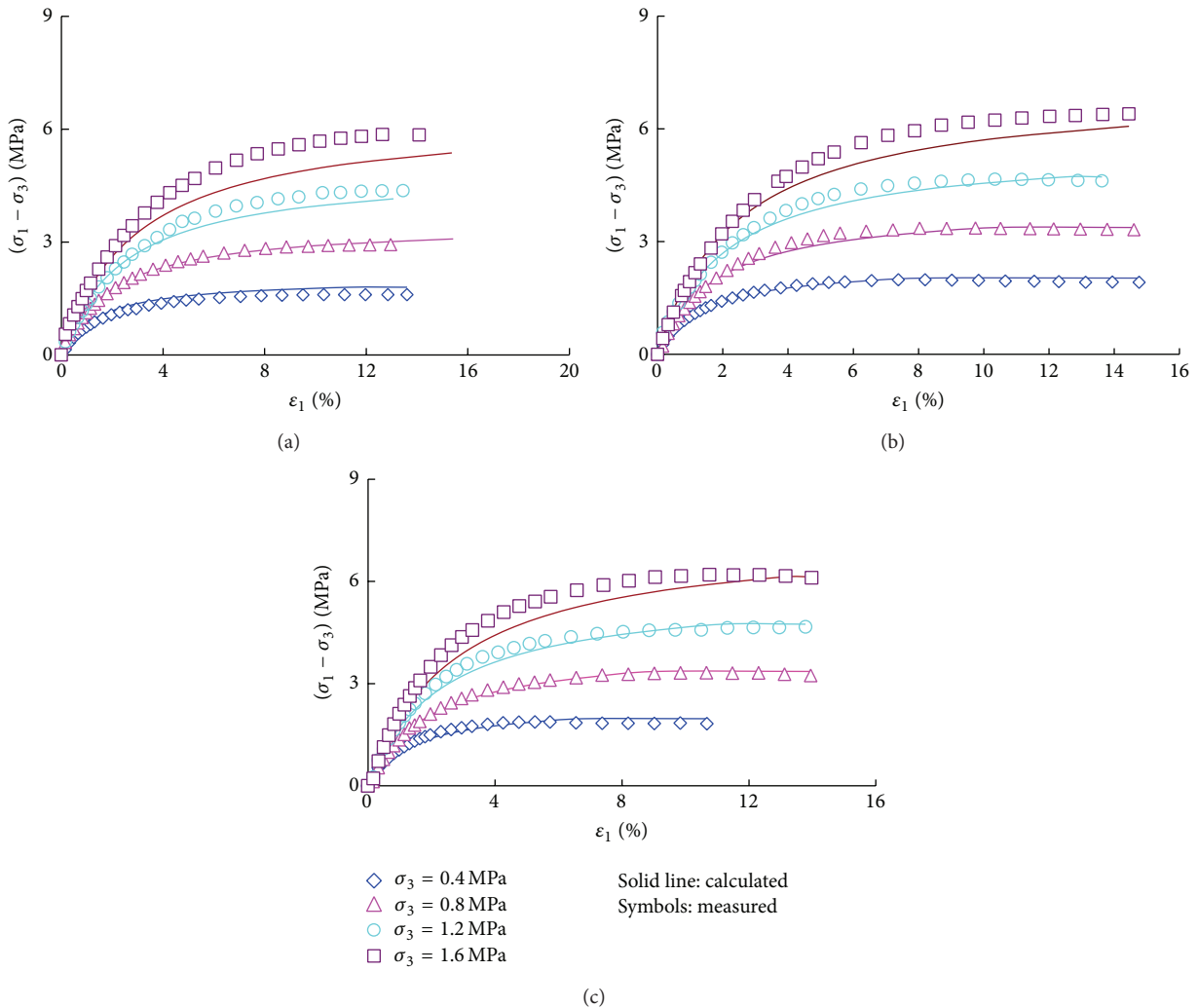


FIGURE 10: Stress difference versus axial strains: (a) gradation 1; (b) gradation 3; (c) gradation 5.

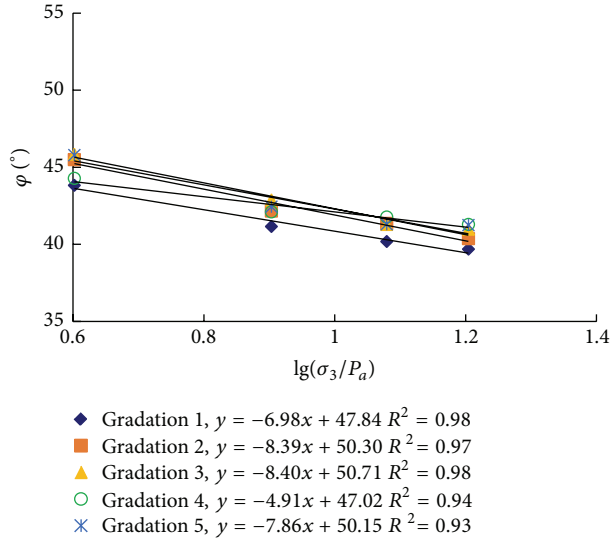


FIGURE 11: Influence of confining pressure on the angle of internal friction.

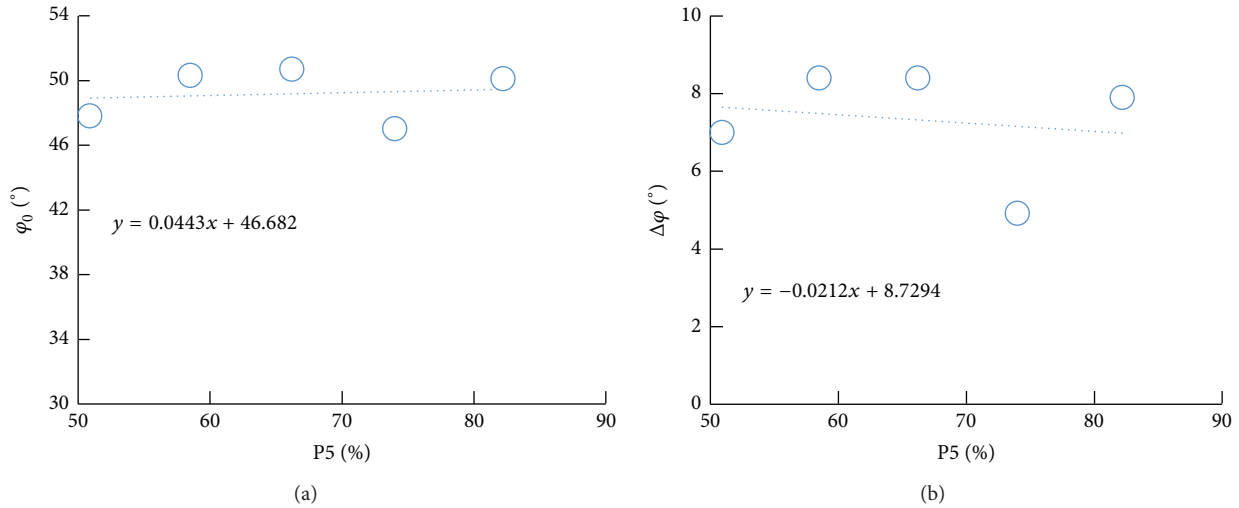


FIGURE 12: Internal friction angle to rock proportion curve: (a) internal friction angle when confining pressure equals normal atmosphere; (b) gradual decrement of internal friction angle.

confining pressure is given in Figure 11. It is found from Figure 11 that, as the increase of confining pressure, the internal friction angle gradually decreases and is basically log-linearly related to confining pressure as

$$\phi = \phi_0 - \Delta\phi \lg\left(\frac{\sigma_3}{P_a}\right), \quad (6)$$

where ϕ_0 is internal friction angle when confining pressure is normal atmosphere. $\Delta\phi$ is gradual decrement of internal friction angle. When confining pressure is low, internal friction angle reaches its maximum. Based on (5) and (6), the fitted values of ϕ_0 and $\Delta\phi$ are shown in Figure 12. The variation of these values with stone content is given in Figure 12. It is found that, in general, ϕ_0 and $\Delta\phi$ show gradual increasing trend as stone content increases. When stone content varies within 50% to 80%, the value of ϕ_0 ranges from

47° to 51° and $\Delta\phi$ ranges from 4.9° to 8.5°, indicating that stone content variation does not have significant influences on the values of ϕ_0 and $\Delta\phi$. The variation law of peak internal friction angle ϕ as confining pressure varies, presented in the above expression, is suitable for rock-soil aggregate sampled from natural sliding mass.

3.3. Stress-Dilatancy Behavior of Rock-Soil Aggregate. Charles and Watts' research [16] indicates that when principal stress reaches its maximum, dilation rate, namely $(d\epsilon_v/d\epsilon_1)_p$, is related to the maximum value of ratio of the first principal stress to the third principal stress, namely $(\sigma_1/\sigma_3)_p$. Here, the peak dilation coefficient is defined by the expression $D_p = 1 - (d\epsilon_v/d\epsilon_1)_p$. According to Indraratna's study [17], the hyperbolic curve is recommended to describe this relationship between $(\sigma_1/\sigma_3)_p$ and $(d\epsilon_v/d\epsilon_1)_p$, based on the

TABLE 3: Parameters of stress-dilatancy equation.

P5/%	Rowe's stress-dilatancy equation		Modified Rowe's stress-dilatancy equation		
	1/K	K	α	β	R_d
50.9	0.1933	5.17	0.1027	1.4462	4.82
58.5	0.1836	5.45	0.0542	1.8047	5.03
66.2	0.1826	5.48	0.0516	1.8165	5.11
74	0.1904	5.25	0.0716	1.6493	4.95
82.2	0.1819	5.50	0.0453	1.9152	5.03

condition that the confining pressure ranges from 1kPa to 240 kPa. Rowe proposed the linear stress-dilatancy equation [18, 19]. Based on the assumption of rigid plastic of rock-soil aggregate, the equation is written as [18]

$$R = KD \quad \text{or} \quad D = \frac{R}{K}, \quad (7)$$

where R is the principal stress ratio and is calculated by σ_1/σ_3 , D is dilation coefficient and is calculated by $1 - (d\varepsilon_v/d\varepsilon_1)$, and K is related to an angle of friction. Figure 13 shows the fitting results of $D \sim R$ for all samples with different gradations. According to the test results (Table 3), the value of K for rock-soil aggregate ranges from 5.17 to 5.50, indicating that stone content variation does not have significant influences. Also, it is obvious from Figure 13 that Rowe's stress-dilatancy equation obviously overestimated the dilatancy of rock-soil aggregate, and the stress-dilatancy behavior does not have significant influences on the stress level.

From another point of view, it is found from Figure 13(a) that when the confining pressure ranges from 0.4 MPa to 1.6 MPa, R exhibits a power function relationship with D for all samples with different gradations. In order to model the dilatancy during deformation of rock-soil aggregate, the modified stress-dilatancy relationship becomes

$$D = \alpha R^\beta, \quad (8)$$

where α and β are parameters obtained in tests. Let $\alpha = (1/R_d)^\beta$; then (8) can be written as

$$D = \left(\frac{R}{R_d} \right)^\beta. \quad (9)$$

Obviously, the value of β reflects the influence of the stress ratio R on the dilatancy of rock-soil aggregate. Particularly, when $\beta = 1$, (9) is the original Rowe's stress-dilatancy equation, and at this time $R_d = K$.

Figure 13 shows that the modified stress-dilatancy equation can be used to describe the volume deformation characteristics of rock-soil aggregate. The values of β and R_d under different gradations are given in Table 3, in which the value of R_d for rock-soil aggregate ranges from 4.82 to 5.11, indicating that rock content variation does not have significant influences. The value of β ranges from 1.4462 to 1.9152, which implied that the β value is affected by rock content variation, which mainly shows that when the rock

content variation is low, the β value is small; when the rock content variation is higher, β value is larger.

Figure 14 shows the dilatancy-contraction relationship of rock-soil aggregate expressed by formula (9). Under the low confining pressure condition, when $R < R_d$, rock-soil aggregate shows shear contraction; when $R > R_d$, the rock-soil aggregate shows shear dilatancy; when $R = R_d$, $d\varepsilon_v/d\varepsilon_1$ is equal to 0. So formula (9) inherently assumes that the R_d value of rock-soil aggregate not only is the demarcation point of contraction and dilatancy but also is stress ratio of critical state corresponding to constant volume deformation. Under high confining pressure, R is always smaller than R_d and contraction occurs for rock-soil aggregate. When R becomes larger and approaches R_d , rock-soil aggregate gradually comes to critical state and remains constant volume deformation.

4. Conclusions

The following understandings can be noted after we analyzed the loading test results of rock-soil aggregate derived from Jinpingzi sliding mass.

- (1) Under the confining pressure of 0.4 MPa, rock-soil aggregate exhibits slight strain softening effect and remarkable shear dilation effect. When confining pressure exceeds 0.8 MPa, the sample exhibits strain-hardening effect and shear contraction effect. Under low confining pressure condition, the variation of stone content and gradation has significant influences on stress-strain curve and volumetric strain-axial strain curve. However, under high confining pressure condition, stress-strain curves and volumetric strain-axial strain curves of different gradations and stone contents are basically similar, indicating that the influences of gradation and stone content are smaller. In general, rock-soil aggregate sampled from sliding mass has both high bearing capacity and considerable ductile plastic deformation characteristics.
- (2) Initial elastic moduli $\lg(E_i)$ and $\lg(\sigma_3/P_a)$ are linearly related. Initial Poisson's ratio and $\lg(\sigma_3/P_a)$ are negatively linearly related. When confining pressure varies within medium and high values, hyperbolic curve can be used to describe the axial stress-strain relation of rock-soil aggregate. When confining pressure ranges from 0.4 MPa to 1.6 MPa, the Mohr strength envelope line is typical linear style. When stone content ranges from 50% to 80%, shear strength parameter φ obtained from Mohr-Coulomb strength criterion gradually increases and shear strength parameter c gradually decreases as stone content increases. Internal friction angle is in negative linear relation to $\lg(\sigma_3/P_a)$. Their relationship can be described using the Duncan proposed expression. Moreover, under low confining pressure, the internal friction angle reaches its maximum value. This index also maintains large magnitude with high stone content and favorable gradation.

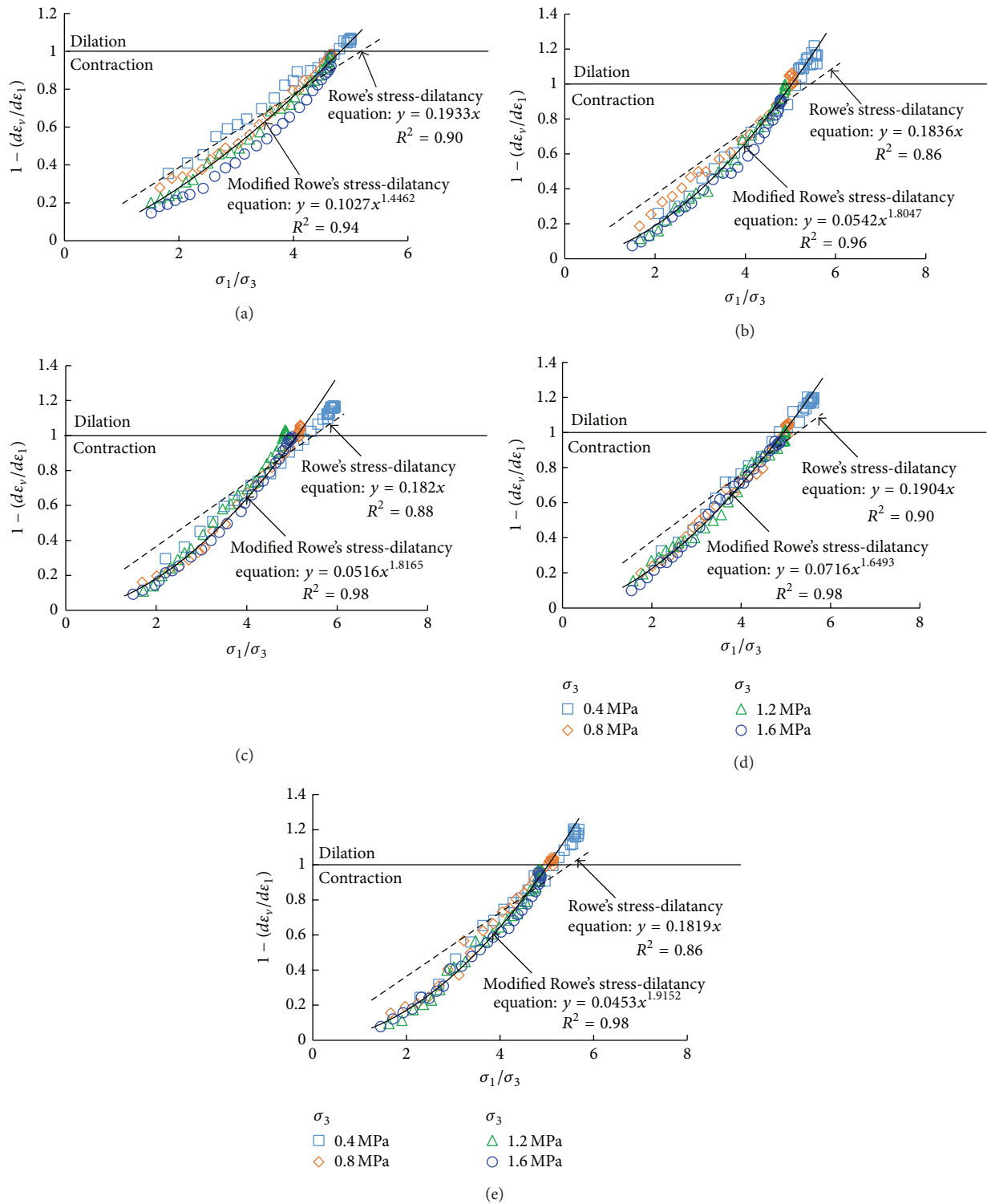


FIGURE 13: Relationship between principal stress ratio and dilatancy rate under different gradations: (a) gradation 1, rock proportion (P5), 50.89%; (b) gradation 2, rock proportion (P5), 58.50%; (c) gradation 3, rock proportion (P5), 66.16%; (d) gradation 4, rock proportion (P5), 74.00%; (e) gradation 5, rock proportion (P5), 82.17%.

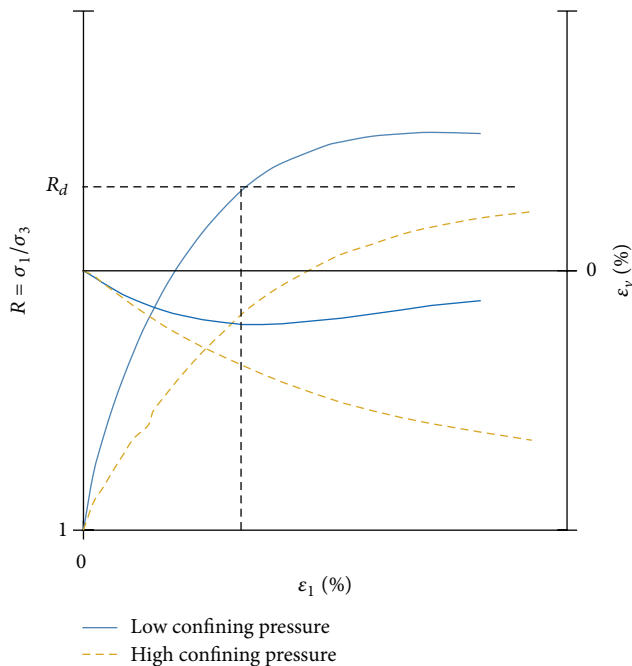


FIGURE 14: Dilatancy-contraction relationship of rock-soil aggregate expressed by the formula.

- (3) Based on studying the volumetric deformation characteristics of rock-soil aggregate and the relationship between volumetric deformation and principal stress ratio, a modified Rowe's stress-dilatancy equation suitable for rock-soil aggregate is suggested.

In summary, Duncan-Chang model is to certain extent suitable for describing the deformation characteristics of rock-soil aggregate. Future study will be conducted on how to propose a practical constitutive model suitable for rock-soil aggregate by combining Duncan-Chang model and the proposed modified Rowe's stress-dilatancy equation.

Conflict of Interests

The authors declare that there is no conflict of interests regarding the publication of this paper.

Acknowledgments

This study was supported by the National Basic Research Program of China (no. 2011CB710600) and the National Natural Science Foundation of China (nos. 51379022, 51179013, and 51209021). These supports are greatly acknowledged and appreciated.

References

- [1] X. U. Wenjie and H. U. Ruilin, "Conception, classification and significations of soil-rock mixture," *Hydrogeology & Engineering Geology*, vol. 4, no. 6, pp. 50–56, 2009.
- [2] G. Sun and B. Yao, *Study on Landslide Disaster in China*, Science Press, Beijing, China, 1988.

- [3] E. Medley, *The engineering characterization of melanges and similar block-in-matrix rocks (Bimrocks) [Ph.D. thesis]*, University of California, Berkeley, Calif, USA, 1994.
- [4] X. Li, Q. L. Liao, and J. M. He, "In-situ tests and a stochastic structural model of rock and soil aggregate in the three gorges reservoir area, China," *International Journal of Rock Mechanics and Mining Sciences*, vol. 41, no. 1, pp. 2–6, 2004.
- [5] Q. Liao, X. Li, Z. Hao et al., "Current status and future trends of studies on rock and soil aggregates," *Journal of Engineering Geology*, vol. 14, no. 06, pp. 801–807, 2006.
- [6] X. You and J. Tang, "Research on horizontal push-shear in-situ test of soil and rock- mixture," *Chinese Journal of Rock Mechanics and Engineering*, vol. 21, no. 10, pp. 1537–1540, 2002.
- [7] X. Wang, *Research on influence factors of mechanics characteristics and characteristics failure mechanism of soil-rock mixture [M.S. thesis]*, Changjiang Scientific Research Institute, 2010.
- [8] W. Cheng, *Study on mechanical properties test and constitutive relationship of colluvial landslide soil-rock mixture [M.S. thesis]*, Hohai University, 2011.
- [9] W.-S. Li, X.-L. Ding, A.-Q. Wu, and S.-H. Xiong, "Shear strength degeneration of soil and rock mixture in Three Gorges Reservoir bank slopes under influence of impounding," *Rock and Soil Mechanics*, vol. 28, no. 7, pp. 1338–1342, 2007.
- [10] Z. Zhou, H.-L. Fu, B.-C. Liu, H.-H. Tan, and W.-X. Long, "Orthogonal tests on permeability of soil-rock-mixture," *Chinese Journal of Geotechnical Engineering*, vol. 28, no. 9, pp. 1134–1138, 2006.
- [11] W. Xu, R. Hu, Z. Q. Yue, R. Zhang, and G. Wang, "Research on relationship between rock block proportion and shear strength of soil-rock mixtures based on digital image analysis and large direct shear test," *Chinese Journal of Rock Mechanics and Engineering*, vol. 27, no. 5, pp. 996–1007, 2008.
- [12] O. Zhenhua, L. Shihai, and D. Zhisheng, "On the Influence factors of mechanical properties for soil-rock mixture," *Journal of Experimental Mechanics*, vol. 25, no. 1, pp. 61–67, 2010.
- [13] J. M. Duncan and C.-Y. Chang, "Nonlinear analysis of stress and strain in soil," *ASCE Journal of the Soil Mechanics and Foundations Division*, vol. 96, pp. 1629–1653, 1970.
- [14] M. J. Duncan, P. Byren, K. Wong et al., "Strength, stress-strain and bulk modulus parameters for finite element analysis of stress and movements in soils masses," Report No. UCB/ GT/ 80001[R], University of California, Berkeley, Calif, USA, 1980.
- [15] N. Janbu, "Soil compressibility as determined by oedometer and triaxial tests," in *Proceedings of the European Conference on Soil Mechanics and Foundations Engineering*, vol. 1, pp. 19–25, Wiesbaden, Germany, 1963.
- [16] J. A. Charles and K. S. Watts, "The influence of confining pressure on the shear strength of compacted rockfill," *Geotechnique*, vol. 30, no. 4, pp. 353–367, 1980.
- [17] B. Indraratna, D. Ionescu, and H. D. Christie, "Shear behavior of railway ballast based on large-scale triaxial tests," *Journal of Geotechnical and Geoenvironmental Engineering*, vol. 124, no. 5, pp. 439–449, 1998.
- [18] P. W. Rowe, "The stress dilatancy relation for static equilibrium of an assembly of particles in contact," *Proceedings of the Royal Society of London A*, vol. 269, no. 1339, pp. 500–527, 1962.
- [19] P. W. Rowe, "Theoretical meaning and observed values of deformation parameters for soil," in *Proceedings of the Stress-Strain Behaviour of Soils, Roscoe Memorial Symposium*, R. H. G. Parry, Ed., pp. 143–194, Cambridge University, The Whitefriars Press Ltd, London, UK, 1971.

Research Article

Preparation and Mechanism of a New Enhanced Flocculant Based on Bentonite for Drinking Water

Feng-shan Zhou, Jie Li, Lin Zhou, and Yang Liu

Beijing Key Laboratory of Materials Utilization of Nonmetallic Minerals and Solid Wastes, National Laboratory of Mineral Materials, School of Materials Science and Technology, China University of Geosciences, Beijing 100083, China

Correspondence should be addressed to Feng-shan Zhou; zhousf@cugb.edu.cn

Received 12 July 2014; Revised 29 October 2014; Accepted 14 November 2014

Academic Editor: Hanlie Hong

Copyright © 2015 Feng-shan Zhou et al. This is an open access article distributed under the Creative Commons Attribution License, which permits unrestricted use, distribution, and reproduction in any medium, provided the original work is properly cited.

Bentonite is characterized by the large specific surface, good adsorption, ion exchange ability, and nontoxicity. An enhanced bentonite base composite flocculant (BTA) can be prepared from treating the calcium base bentonite and compositing various functional additives. Bentonite was firstly treated by citric acid, then the talc and activated carbon turned to be acid part and simultaneously the part that was treated by sodium bicarbonate and calcium hydroxide turned to be alkaline part, and finally the acid bentonite part and alkaline bentonite part were mixed up with preground powder of polymeric chloride aluminium (PAC), cationic polyacrylamide (CPAM), ferrous sulfate, and aluminum sulfate, and after all of the processing flocculant BTA was obtained. The optimum preparation process of flocculant BTA has shown 29.5% acid bentonite part, 29.5% alkaline bentonite part, 15% PAC, 1% CPAM, 5% ferrous sulfate, and 20% aluminum sulfate. BTA was used to treat drinking water with high turbidity and metal ion in Karamay City, Xinjiang. The treated water was surely up to the drinking water standard of China in decolorization rate, deodorization rate, heavy metal ion removal rate, and so forth, and contents of residual aluminum ions and acrylamide monomer in drinking water were considerably decreased.

1. Introduction

China is facing water shortage and severe water pollution. In order to reduce the harm of water pollution, improve and protect environment, and achieve higher water quality, domestic as well as industrial water was often purified. Among various water treatment agents, flocculants have been found to be with wide application due to their satisfying purification performance, low cost, and convenience. Flocculants are the most widely used agents with the largest consumption in water treatment and mainly include inorganic flocculant, organic polymer flocculant, microbial flocculant, and composite flocculants [1].

In recent years, based on investigation of surface activity, ultrafine effect, chemical component, and crystal structure of natural minerals, minerals are found to have good environment attributes and natural minerals were applied in water pollution management due to their self-purification in various pollutants [2–6]. As flocculants, mineral materials have the advantage in wide varieties, abundant reserve, low cost,

and little secondary pollution. The frequently used minerals include montmorillonite, sepiolite, zeolite, kieselguhr, and attapulgite [7–15].

Si^{4+} in Si–O tetrahedron and Al^{3+} in Al–O octahedron of bentonite could be replaced by low valence states of Li^+ , Mg^{2+} , and Fe^{2+} , thus making the unbalanced electrovalence of bentonite unit cell, so bentonite interlayer is negatively charged. In interlayer, the negatively charged surface will often balance with exchangeable hydrated cations which are unstable and also tend to exchange with other ions. Consequently, bentonite has good adsorption and ion exchange ability, cohesiveness, hydrophilicity, and large specific surface [10, 11, 15], and, above all, it is nontoxic.

Bentonite was often used as adsorbent in water treatment mainly due to its good adsorption and ion exchange ability and this adsorption includes both exchange adsorption and physical absorption [12].

There were a lot of researches on bentonite being water treatment agent. For example, Liao and Wang used bentonite

as adsorbent to prepare purifier to treat sewage of winery and the rate of turbidity was reported as 37.6% at 5% purifier dosage [13]. Combining bentonite with flocculant PAC or PAM, Yuan et al. treated oily sewage and compared the oil removal performance of different kinds of bentonite and organic modified bentonite. They found that oil removal rate was as high as 90% at calcium base bentonite dosage of 2.5 g/L and PAC dosage of 400 ppm [14, 15]. Srinivasan [6] and many other researchers [16–18] made a detailed and comprehensive investigation on the applications of natural clay minerals including bentonite in removing biological, organic, and inorganic contaminants in drinking water.

2. Materials and Methods

2.1. Instruments and Materials. 101-1 Electric Blast Drying Oven (Tianjin Qin Shite Instrument Co., Ltd); ZDM-50 Vibration Mill (Tianjin Keqi Technology Co., Ltd); and SGE-2 Digital Turbidity Meter (Shanghai Yuefeng Instruments Co., Ltd.) were used.

All of the industrial produced samples in our work such as calcium bentonite (Ningcheng, Inner Mongolia), polyaluminum chloride (PAC) (Gongyi, Henan), Talc (Dandong, Liaoning), activated carbon (Gongyi, Henan), polyacrylamide (PAM), and cationic polyacrylamide (CPAM) (Xitao, Beijing) obtained from China chemical market. All of the chemical pure samples such as citric acid (chemically pure, CP), sodium bicarbonate (CP), ferrous sulfate (CP), aluminium sulfate (CP), and calcium hydroxide (analytical reagent, AR) were obtained from Beijing chemical reagent supply and marketing Co.

2.2. Methods

2.2.1. Pretreatment of Raw Material

Pretreatment. Calcium base bentonite activation adopts the thermal activation method. Calcium base bentonite was heated for 24 h at 300°C and then ground to 100–200 mesh by vibrating mill for spare.

Pretreatment of the Additives. Additives including citric acid, talc, activated carbon, sodium bicarbonate, calcium hydroxide, ferrous sulfate, and aluminum sulfate were ground, respectively, to passing 200 mesh screen for spare.

Pretreatment of the Flocculants. PAC, PAM, and CPAM were ground, respectively, to passing 100 mesh screen for spare.

2.2.2. Preparation of Flocculant Base Powder. Acid powder A and basic powder B were firstly prepared, respectively, and then powder A and powder B were mixed up in a proper ratio to form AB component. As diatomite with pH = 7 was used in evaluation tests to simulate suspension liquid, the optimized mass ratio of powder A and powder B was 1:1. After system optimization, the compositions and mass ratio of component A and component B were shown in Table 1.

TABLE 1: The compositions and the mass ratio of acid component A and basic component B.

Acid component A		Basic component B	
Raw materials	Content (wt%)	Raw materials	Content (wt%)
Ca-bentonite	80	Ca-bentonite	80
Citric acid	10	Sodium bicarbonate	10
Talc	9.5	Calcium hydroxide	10
Activated carbon	0.5		

2.2.3. Preparation of Flocculant BTA

- (1) Weigh raw material referring to Table 1 and then after being extruded by extruder, dried and ground for 10 min to passing 100 mesh screen, powder A and powder B were obtained.
- (2) Mix powder A and powder B at the mass ratio of 1:1 and then powder AB was obtained.
- (3) Weigh PAC, PAM, ferrous sulfate, and aluminum sulfate in a certain proportion and then mix them up with powder AB; vibrating grind for 10 min, the enhanced flocculant BTA was obtained.

2.2.4. Mechanism of Preparation of Flocculant BTA. The preferred composition of the present product was manufactured in two separately manufactured portions or subcomponents (acid First Portion A and alkaline Second Portion B) by extruding a calcium bentonite component that was not acid-activated, together with an acid and optionally an alkali, separately from the sodium bentonite component, to prevent the acid and alkali components from interacting or reacting with the sodium bentonite component of the composition, while the calcium bentonite-containing portion of the composition should be extruded to activate the calcium bentonite and bind any acid and alkali to the calcium bentonite, thereby preventing any acid and alkali from interacting with the sodium bentonite. It was not necessary to extrude the sodium bentonite containing portion of the composition.

All components of the composition may be extruded, so long as any acid and alkali components are maintained separately from the sodium bentonite during the extrusion process. Next, when extruded with calcium bentonite, the acid and alkali disperse more quickly in the waste water to prepare the waste water for later flocculation by the sodium bentonite. Dispersing the acid as early as possible, prior to dispersing the sodium bentonite, is important to break up the oil and grease emulsions. Dispersing the alkali as early as possible and prior to dispersing the sodium bentonite is important for precipitation of dissolved metals, so that the bentonite, later dispersed, can flocculate the oil, grease, and precipitated metals, together with the flocculating agent. Of all examples, various compositions were manufactured by extruding all composition components in two separate composition portions and then grinding the two extruded composition portions into a desired granular particle size distribution with other adding agents.

The extruded calcium bentonite pellets, including bound acid and optionally alkali, were ground to a desired granular particle size distribution in the range of about 200 μm to 1000 μm , and the ground granules from both portions of the composition were combined into a single composition, together with some other enhanced flocculating additives.

3. Results and Discussion

According to the composite principle, factors that could affect the performances of flocculant BTA mainly included the content of inorganic polymer flocculant PAC, type and content of precipitating aid, pH value of water in flocculation, and content of ferrous sulfate and aluminum sulfate. These four factors were investigated, respectively, and then compositions and their ratios in BTA system were determined.

3.1. Influence of Inorganic Flocculant PAC on BTA Performances. Inorganic flocculant PAC with the largest consumption was the most widely used and has excellent absorption and bridging effect and charge neutralization performance. PAC used in the test also functions as flocculant and therefore investigating its influence rule on turbidity removal matters much.

As shown in Figure 1, flocculation effect of BTA was enhanced as a function of PAC content but the increase degree slows down. According to the data, the increase degree accelerated generally when PAC content was lower than 45% and rate of deturbidity reached 95.1% at PAC content of 40%, while when PAC content was 50%, rate of deturbidity only increased to 96.9%. Consequently, taking cost into consideration, PAC content in BTA was determined as 40%.

3.2. Influence of Organic Precipitating Aid on BTA Performances. All derivatives of polyacrylamide were excellent precipitating aid. The influences of anionic polyacrylamide (PAM) and cationic polyacrylamide (CPAM) on flocculation effect of BTA were investigated in tests, shown in Figure 2.

It was shown in Figure 2 that precipitating aid performance of cationic polyacrylamide (CPAM) significantly outperformed that of anionic polyacrylamide (PAM) in both rate of deturbidity and settling time. The performance and structure of bentonite indicate that its interlayer was negatively charged permanently. If the enhanced flocculant BTA contained bentonite, cationic polyacrylamide was more apt to adsorb and bridge with bentonite while anionic polyacrylamide will not react with bentonite obviously.

It was also found that only small amount of CPAM could promote the flocculation effect of BTA greatly and flocculation effect of BTA could be completely reflected. It was observed that the alum grains of enhanced flocculant BTA were larger than that of flocculant PAC, since the settling velocity of BTA was fast and it took only about 40 s for its floccules to settle completely while it took 2 to 3 min for PAC to settle completely. Referring to test results, flocculation precipitating aid adopted CPAM and its content accounts for 1% (mass fraction) of BTA system.

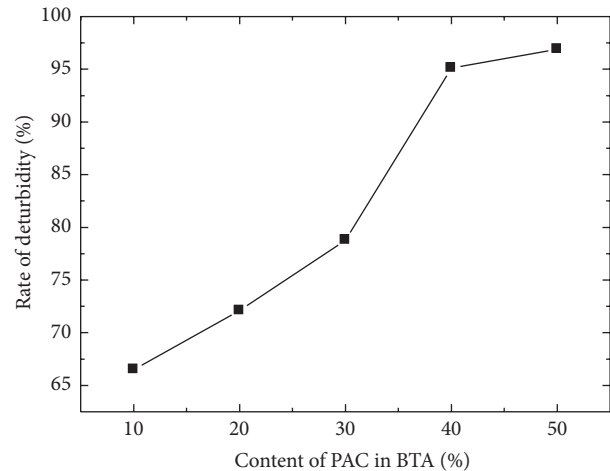


FIGURE 1: The effect of PAC in BAT on the rate of deturbidity.

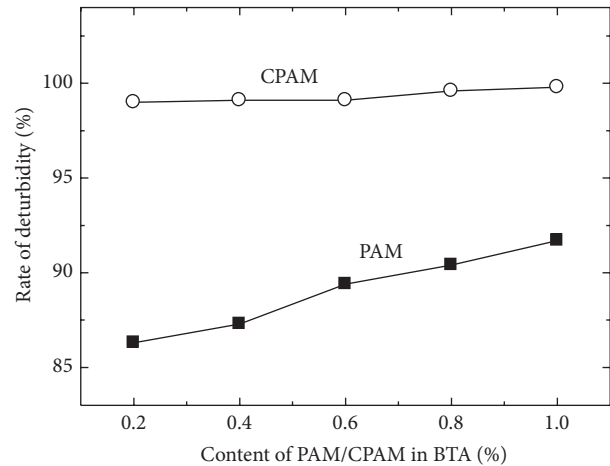


FIGURE 2: The effects of PAM/CPAM in BAT on the rate of deturbidity.

3.3. Influence of Flocculation Precipitating Aid on BTA Performance. Results showed that when the proportion of bentonite base powder, PAC, and CPAM in enhanced flocculant BTA system was 59%, 40%, and 1%, respectively, the flocculation effect could be as good as that of solid PAC and flocculating settling velocity is faster than that of solid PAC. However, as the dosage of enhanced flocculant was often large, thus costs in subsequent sludge treatment would increase and domestic flocculants were cheap, so it was necessary to control the costs of flocculants. Consequently, PAC content in the system should be reduced on condition that the flocculation effect was as good as the deturbidity effect of solid PAC and the settling velocity of sludge was faster than that of solid PAC. Meanwhile, ferrous sulfate and aluminum sulfate were considered to be added in the system as flocculation aid.

The flocculation effects of flocculation precipitating aids with PAC content of 10%, 15%, 20%, and 30% were shown in Tables 2, 3, 4, and 5, respectively. By adjusting the proportion

TABLE 2: The influence of additives on coagulation behaviors of BTA while PAC content was 10% (200NTU diatomite suspension).

AB (%)	Aluminium sulfate (%)	BTA (mg/L)	Rate of deturbidity (%)	Settling time (s)
5	25	100	99.2	20
10	20	100	99.1	20
15	15	100	95.3	60
20	10	100	95.8	60
25	5	100	95.1	60
—	—	PAC (100)	98.1	60

TABLE 3: The influence of additives on coagulation behaviors of BTA while PAC content was 15% (200NTU diatomite suspension).

Ferrous sulfate (%)	Aluminium sulfate (%)	BTA (mg/L)	Rate of deturbidity (%)	Settling time (s)
0	25	100	98.8	20
5	20	100	98.7	20
10	15	100	98.7	60
15	10	100	98.3	60
20	5	100	98.4	60
25	0	100	98.0	60
—	—	PAC (100)	98.5	60
—	—	PAC (50)	97.7	90

TABLE 4: The influence of additives on coagulation behaviors of BTA with 20% PAC (200NTU diatomite suspension).

Ferrous sulfate (%)	Aluminium sulfate (%)	BTA (mg/L)	Rate of deturbidity (%)	Settling time (s)
0	20	100	98.0	40
5	15	100	98.2	40
10	10	100	98.1	40
15	5	100	97.7	40
20	0	100	97.7	50
—	—	PAC (100)	98.4	60
—	—	PAC (50)	97.6	90

TABLE 5: The influence of additives on coagulation behaviors of BTA with 30% PAC (200NTU diatomite suspension).

Ferrous sulfate (%)	Aluminium sulfate (%)	BTA (mg/L)	Rate of deturbidity (%)	Settling time (s)
0	10	100	98.9	30
5	5	100	98.7	30
10	0	100	98.7	30
—	—	PAC (100)	98.5	90
—	—	PAC (50)	98.2	120

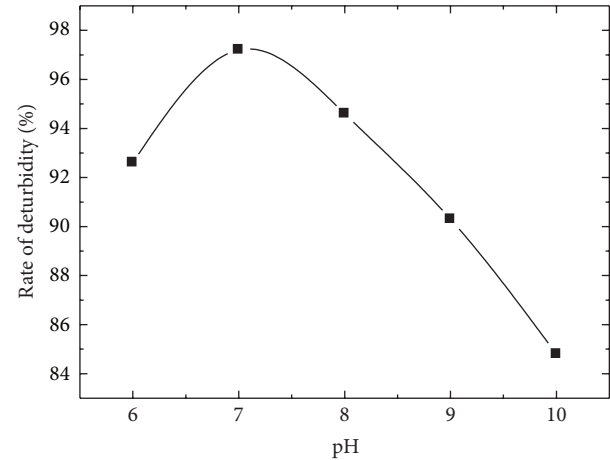


FIGURE 3: The influence of pH on coagulation behaviors of BTA.

of ferrous sulfate and aluminum sulfate and comparing with PAC, the optimal blending ratio of BTA was determined.

Results showed that generally rate of deturbidity changes little when PAC content ranges from 10% to 30%, but it could be observed in tests that floccules of BTA were small at PAC content of 10%. Consequently, the content of PAC in the system was finally determined as 15%.

According to the influence of ferrous sulfate and aluminum sulfate, flocculation effect generally got better as a function of aluminum sulfate content. However, as ferrous sulfate could increase the compactness of floccules and decrease the function of COD, it was an indispensable part of the system. Combining turbidity removal performance and economic effect, the optimized compositions of enhanced flocculant BTA were shown in Table 6.

3.4. Influence of pH on BTA Performance. It could be known from flocculating mechanism that flocculation was caused by hydrolysis of flocculant in water. BTA contained some flocculants, for example, PAC, and the flocculation effect was directly affected by pH of water, and therefore the suitable environment of enhanced flocculant BTA should be determined. Diatomite suspension with pH of 6 to 10 was prepared, respectively, to simulate sewage and then the suitable environment could be found by observing the change of flocculation effect, as shown in Figure 3. The best flocculation effect of BTA was observed at pH 7, which agreed with the suitable environment of PAC.

3.5. Application of Flocculant BTA in Treating Moderately Polluted Drinking Water. Karamay City, located in Junggar Basin of northwestern Xinjiang, is an industrial city that mainly depends on oil industry. According to random inspection results, only 53.4% of drinking water in average met the quality standard and that percentage in rain season and dry season was 45.6% and 61.9%, respectively. It was reported that domestic drinking water of citizens came in sequence from natural raw water, processed water from drinking water treatment plant, tap water of water supply network, and secondary

TABLE 6: The optimized compositions of BTA.

Component	Acid part A	Basic part B	PAC	CPAM	Ferrous sulfate	Aluminium sulfate
Content (%)	29.5	29.5	15	1	5	20

TABLE 7: The treatment effect for Xinjiang Karamay City drinking water with enhanced flocculant BTA.

Number	Testing items	China National Standard (China GB 5749-2006)	Testing results (SN. G2013024)	Unit
1	Chromaticity	≤15	<5	Degree
2	Turbidity	≤1 or ≤3	<0.5	NTU
3	Odor and taste	No foreign order and taste	No	
4	Visible matter	No	No	
5	pH	6.5–8.5	7.92	
6	Total hardness (as CaCO ₃)	≤450	189	mg/L
7	Iron	≤0.3	<0.005	mg/L
8	Manganese	≤0.1	<0.022	mg/L
9	Copper	≤1.0	<0.0015	mg/L
10	Zinc	≤1.0	<0.0015	mg/L
11	Cadmium	≤0.005	<2.0 × 10 ⁻⁶	mg/L
12	Lead	≤0.01	<5.0 × 10 ⁻⁵	mg/L
13	Volatile phenol (as phenol)	≤0.002	<0.002	mg/L
14	Composite anionic detergent	≤0.3	<0.05	mg/L
15	Sulfate	≤250	93.82	mg/L
16	Chloride	≤250	109.38	mg/L
17	Total dissolved solids	≤1000	304	mg/L
18	Fluoride	≤1.0	0.38	mg/L
19	Cyanide	≤0.05	<0.002	mg/L
20	Arsenic	≤0.01	<9.0 × 10 ⁻⁴	mg/L
21	Selenium	≤0.01	<9.0 × 10 ⁻⁴	mg/L
22	Mercury	≤0.001	<9.0 × 10 ⁻⁵	mg/L
23	Chromium (hexavalent)	≤0.05	<0.004	mg/L
24	Nitrate (as nitrogen)	≤10	0.45	mg/L
25	Trichloromethane	≤0.06	<2.0 × 10 ⁻⁴	mg/L
26	Tetrachloromethane	≤0.002	<1.0 × 10 ⁻⁴	mg/L
27	Bacterial colony number	≤100	30	CFU/mL
28	Total α radioactivity	≤0.5	<0.016	Bq/L
29	Total β radioactivity	≤1	0.038	Bq/L
30	Oxygen consumption (as O ₂)	≤3	1.75	mg/L
31	Aluminum	≤0.2	0.092	mg/L

water supply in high-rise housing. Processed water referred to water being treated in drinking water treatment plant, and tap water of supply network meant water branched from main water supply line, while secondary water supply meant providing domestic drinking water for residents indirectly by secondary water supply facilities, for example, impounding reservoir and its attaching pipeline, valve, pumping unit, and pressure tank. As raw water quality was unchangeable, the drinking water quality cannot meet the standard all the year round.

Tests on using enhanced flocculant BTA to treat the source water of No. 2 Water Purification Plant of Xinjiang

Oilfield Company were carried out in 2013. The processed water quality was tested by Water Quality Supervision and Inspection Station, Xinjiang Petroleum Administration Bureau. As shown in Table 7, the treated water was surely up to the drinking water standard of China in decolorization and deodorization rate, removal rate of heavy metal ion, and so forth, and contents of residual aluminum ions and acrylamide monomer in drinking water were considerably decreased, thus reflecting the powerful adsorption property of bentonite as natural mineral material and showing a great prospect of the enhanced bentonite base flocculant in drinking water treatment.

TABLE 8: The costing evaluation for flocculant BTA based on the price of raw materials purchased from Beijing chemical market in 2013.

Raw material	Content (wt%)	Price (RMB¥/t)	Cost (RMB¥/t)
PAC	15.0	2000	300
Ca-bentonite	47.2	500	236
Talc	2.95	600	17
Calcium hydroxide	2.95	700	20
Citric acid	2.95	5000	147
Sodium bicarbonate	2.95	1500	44
Ferrous sulfate	5.0	400	20
Aluminum sulfate	20.0	800	160
CPAM	1.0	25000	250
Total cost of raw materials (RMB¥/t)			1194
Estimated total produced cost (RMB¥/t)			200
Total cost of flocculant BTA (RMB¥/t)			1400

3.6. *Applied Cost of Flocculant BTA.* The main raw materials of the new enhanced flocculant BTA used natural clay mineral bentonite, which is abundant in our country, combined with simple production process to get the excellent coagulation behavior, so BTA had a good economic feasibility. Table 8 listed the raw materials of BTA and their market prices. Due to the low cost and simple production process of BTA, the solid medicament was convenient for transportation and sewage rate significantly faster than conventional PAC, especially suitable for the modern small sewage treatment needs. Therefore the new enhanced flocculant BTA would have good applications in the future.

Using the new enhanced flocculant BTA to treat the source water of No. 2 Water Purification Plant of Xinjiang Karamay City in 2013, the original treatment price was 0.09~0.12RMB¥ per ton drinking water which included about PAC 0.10RMB¥ coupled with the CPAM 0.01RMB¥. If we used PAC only, the treated water quality could not meet the drinking water standard. When the BTA flocculant was used singly to treat the source water of above water plant, the processed cost was only 0.03~0.06RMB¥ per ton drinking water, and the treated water quality was better.

3.7. Mechanism of Bentonite Based Flocculant Enhancing Flocculation

3.7.1. *PAC, CPAM, and Their Interactions.* PAC and CPAM really are typical and effective flocculants widely used in water treatment sites. Their excellent coagulation properties had been well studied and widely accepted.

The main coagulating function of PAC was its high charge, which made it more effective at destabilizing and removing suspended materials than other aluminium salts such as aluminium sulfate and aluminium chloride, in which the aluminium structure results in a lower net charge than aluminium chlorohydrate. Aluminium chlorohydrate was the best representative described as an inorganic polymer and as

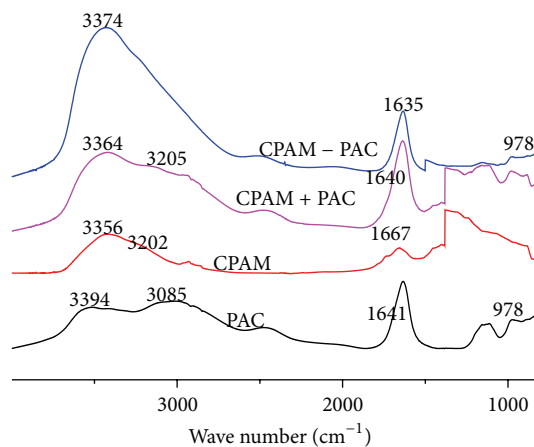


FIGURE 4: The FTIR of PAC after enhanced reaction of modification with cationic PAM.

such was difficult to structurally characterise. However, techniques such as gel permeation chromatography, X-ray crystallography, and ^{27}Al -NMR have been used in researches and had been shown such that the material was based on Al_{13} units with a Keggin ion structure and that this base unit then underwent complex transformations to form larger polyaluminium complexes [18, 19].

The primary role of CPAM was characterized by its macromolecular chains, because the macromolecular chains had a variety of lively groups, which will capture many nucleophilic substances by hydrogen bonds in the macromolecular chains especially for negatively charged colloid particles. CPAM was mainly used for turbidity, bleaching, adsorption, adhesion, and other functions in water purification process [18–20].

Figure 4 was the infrared structure changes of PAC modified with PAM (formed PAC-PAM composite) before and after enhanced modified reaction, which included physical superposition infrared spectra of PAC + PAM with OMNIC 5.0 software. It was shown that Al interacted with $-\text{O}-$ on $-\text{CONH}_2$, weakening the effect of PAM molecular chain $\text{C}=\text{O}$. The characteristic absorption peak of PAM in $1561\sim 1667\text{ cm}^{-1}$, that is, amide I belt and amide II belt, decreased significantly in the spectra of PAC-PAM, and the absorption peak of PAM in 3202 cm^{-1} has already disappeared in PAC-PAM too. We can also see that the IR spectra of PAM + PAC and the IR spectra of PAM, PAC were significantly different, which was enough to prove that the PAM used as coagulant aid was through the chemical reaction between the PAM and PAC to play a role rather than just physical blend. It revealed that the essence of PAM composite synergistic PAC was indeed to generate a greater molecular weight of the new polymer (because of PAM, PAC flocculation characteristics compared with PAC had greatly increased), and that was not the traditional flocculation theory, which was considered such that PAM only had a physical bridging role, and the enlargement alum floc flowers formed just through mechanical netting [21, 22].

3.7.2. Bentonite, Flocculating Additives, and Their Interactions.

Enhanced bentonite base flocculant BTA contained five kinds of key material with different function, that is, clay mineral to quickly form flocculation core, inorganic polymer flocculant to supply electrical neutralization, organic polymer to aid precipitating functioning, and acid and alkaline bentonite components to help adjusting pH of water. The flocculation performance of this composite flocculant would not be affected by clay minerals. On the contrary, clay minerals would be improved flocculation and accelerate settling velocity. This composite flocculant was equipped with excellent flocculation and turbidity removal performance and fast settling, and it overcame the disadvantage of PAC in difficult settling as a result of its light flocules, so it was suitable for rapid treatment (i.e., enhanced flocculation) of sewage and drinking water of various turbidities [23, 24].

Based on heterogeneous nucleation theory and differential flocculation model, bentonite, clay mineral with excellent hydrophilicity, was selected as base in tests and mineral base composite flocculant BTA was prepared by compositing conventional inorganic polymer flocculant PAC, organic polymer precipitating aid PAM, and other flocculation aids. Composite flocculant BTA contained many flocculation cores and could produce flocculation core efficiently in the presence of water. Meanwhile, bentonite could adsorb other micromolecules and colloid pollutants effectively due to its good adsorption capacity [25, 26]. Enhanced flocculant BTA made full use of the heterogeneous nucleation and adsorption capacity of clay minerals, electrical neutralization of inorganic polymer flocculant, and adsorption and bridging capacity of organic polymer. Therefore, BTA, as a new functional composite flocculant, would indeed enhance flocculation performance and promoted flocculation efficiency.

4. Conclusions

Based on heterogeneous nucleation theory and differential flocculation model, factors affecting flocculation performance were analyzed comprehensively. Calcium base bentonite being treated as the main base, a new functional bentonite base composite flocculant BTA aiming at enhancing flocculation rapidly, was prepared by compositing conventional inorganic polymer flocculant, organic polymer precipitating aid, and other flocculation aids. Evaluation results of flocculation performance showed that turbidity removal performance of BTA was as good as that of PAC while settling time of its flocules was one time faster than that of PAC's flocules. When BTA was used to treat drinking water with high turbidity and metal ion content, the treated water was surely up to the drinking water standard of China in discoloration and deodorization rate, heavy metal ion removal rate, and so forth and contents of residual aluminum ions and acrylamide monomer in drinking water were considerably decreased, thus reflecting the powerful adsorption property of bentonite as environmental mineral material. Due to its cheap raw materials, easily available material source, and simple preparation process, the special enhanced bentonite base flocculant showed a great prospect in drinking water treatment.

Conflict of Interests

The authors declare that there is no conflict of interests regarding the publication of this paper.

Acknowledgment

This research was supported by National High Technology Research and Development Program of China (863 Program 2012AA06A109).

References

- [1] F.-S. Zhou, S.-H. Wang, J.-Y. Li, and J.-G. Wu, "Progress in researches of polysilicate-containing composite inorganic polymer flocculants," *Oilfield Chemistry*, vol. 19, no. 4, pp. 391–394, 2002.
- [2] S. Triantafyllou, E. Christodoulou, and P. Neou-Syngouna, "Removal of nickel and cobalt from aqueous solutions by Na-activated bentonite," *Clays and Clay Minerals*, vol. 47, no. 5, pp. 567–572, 1999.
- [3] S.-H. Lin and R.-S. Juang, "Heavy metal removal from water by sorption using surfactant-modified montmorillonite," *Journal of Hazardous Materials*, vol. 92, no. 3, pp. 315–326, 2002.
- [4] K. G. Bhattacharyya and S. S. Gupta, "Adsorption of a few heavy metals on natural and modified kaolinite and montmorillonite: a review," *Advances in Colloid and Interface Science*, vol. 140, no. 2, pp. 114–131, 2008.
- [5] C. Cooper and R. Burch, "Mesoporous materials for water treatment processes," *Water Research*, vol. 33, no. 18, pp. 3689–3694, 1999.
- [6] R. Srinivasan, "Advances in application of natural clay and its composites in removal of biological, organic, and inorganic contaminants from drinking water," *Advances in Materials Science and Engineering*, vol. 2011, Article ID 872531, 17 pages, 2011.
- [7] Z. P. Ren and Z. Z. Yang, "The environmental protection function of minerals and its application perspective," *Conservation and Utilization of Mineral Resources*, vol. 2001, no. 3, pp. 44–48, 2001.
- [8] X. F. Xie and J. G. Wang, "Application of clay mineral materials in water treatment," *Metallic Ore Dressing Abroad*, vol. 2001, no. 1, pp. 22–25, 2001.
- [9] X. Q. Cui, X. J. Lv, and G. H. Zhou, "The property and application of bentonite," *China Non-Metallic Mining Industry Herald*, vol. 2000, no. 2, pp. 6–9, 2000.
- [10] X. Q. Zeng and W. P. Liu, "Advance in synthesis of inorgano-organo-montmorillonites and their utilization in water treatment," *Techniques and Equipment for Environmental Pollution Control*, vol. 2, no. 2, pp. 9–10, 2001.
- [11] X. J. Peng, J. Z. Yuan, and M. L. Cao, "Application of modified bentonite in wastewater treatment," *China Non-Metallic Mining Industry Herald*, vol. 2005, no. 5, pp. 40–41, 2005.
- [12] F. C. Yi and J. Yang, "The properties and preparation of water purifying agent with bentonite," *Multipurpose Utilization of Mineral Resources*, vol. 1999, supplement 1, pp. 27–28, 1999.
- [13] X. F. Liao and Z. L. Wang, "Adsorption and flocculation of bentonite to emulsified oil wastewater," *Environmental Pollution & Control*, vol. 21, supplement 1, pp. 78–79, 1999.
- [14] Z. X. Yuan, H. L. Zheng, and X. W. Shu, "Advancement of coagulation science and technology," *Journal of Chongqing*

- University (Natural Science Edition)*, vol. 24, no. 2, pp. 143–147, 2001.
- [15] C. Cao, F. Zhou, Z. Zhang et al., “Preparation and evaluation of high yield sodium-modified calcium base bentonite,” *Earth Science Frontiers*, vol. 20, no. 5, pp. 220–226, 2013.
- [16] D. Thakre, S. Rayalu, R. Kawade, S. Meshram, J. Subrt, and N. Labhsetwar, “Magnesium incorporated bentonite clay for defluoridation of drinking water,” *Journal of Hazardous Materials*, vol. 180, no. 1–3, pp. 122–130, 2010.
- [17] S. P. Kamble, P. Dixit, S. S. Rayalu, and N. K. Labhsetwar, “Defluoridation of drinking water using chemically modified bentonite clay,” *Desalination*, vol. 249, no. 2, pp. 687–693, 2009.
- [18] B. J. Xu, *Contemporary Water Supply and Wastewater Treatment Principle*, Higher Education Press, Beijing, China, 1992.
- [19] H. X. Tang and Z. K. Luan, “The differences of behavior and mechanism between pre-polymeric inorganic flocculants and traditional coagulants,” in *Chemical Water and Wastewater Treatment IV*, H. H. Hahn, Ed., vol. 9, Springer, Berlin, Germany, 1996.
- [20] H. X. Tang, Z. K. Luan, D. S. Wang, and B. Y. Gao, “Composite inorganic polymer flocculants,” in *Chemical Water and Wastewater Treatment V*, H. H. Hahn, E. Hoffman, and H. Odegaard, Eds., pp. 25–34, Springer, Berlin, Germany, 1998.
- [21] F.-S. Zhou, S.-H. Wang, J.-Z. Su et al., “Structural characteristics of infrared spectra for polyaluminum chloride in enhanced reactions of modification,” *Spectroscopy and Spectral Analysis*, vol. 24, no. 5, pp. 532–535, 2004.
- [22] F.-S. Zhou, S.-H. Wang, J.-Z. Su et al., “The infrared spectra and characteristics of PMC—a multicore inorganic polymer flocculant,” *Fine Chemicals*, vol. 20, no. 10, pp. 615–620, 2003.
- [23] J.-Q. Jiang and C. G. Kim, “Comparison of algal removal by coagulation with clays and Al-based coagulants,” *Separation Science and Technology*, vol. 43, no. 7, pp. 1677–1686, 2008.
- [24] C. S. Choi and T. I. Yun, “Rapid coagulation-flocculation and sedimentation type waste water treatment method,” United States Patent 6447686, 2002.
- [25] H. H. Murray, “Traditional and new applications for kaolin, smectite, and palygorskite: a general overview,” *Applied Clay Science*, vol. 17, no. 5-6, pp. 207–221, 2000.
- [26] G. J. Churchman, “Formation of complexes between bentonite and different cationic polyelectrolytes and their use as sorbents for non-ionic and anionic pollutants,” *Applied Clay Science*, vol. 21, no. 3-4, pp. 177–189, 2002.

Research Article

Preparation of Cementitious Material Using Smelting Slag and Tailings and the Solidification and Leaching of Pb²⁺

Dan Zhang,^{1,2} Shiliu Shi,³ Chengbiao Wang,¹ Xiaocong Yang,²
Lijie Guo,² and Shanshan Xue²

¹School of Engineering Technology, China University of Geosciences, Beijing 100083, China

²Beijing General Research Institute of Mining & Metallurgy, Beijing 110160, China

³School of Materials Sciences and Technology, China University of Geosciences, Beijing 100083, China

Correspondence should be addressed to Dan Zhang; dzdxzd@163.com

Received 11 July 2014; Accepted 16 September 2014

Academic Editor: Zhaohui Li

Copyright © 2015 Dan Zhang et al. This is an open access article distributed under the Creative Commons Attribution License, which permits unrestricted use, distribution, and reproduction in any medium, provided the original work is properly cited.

The composite cementitious materials were prepared with lead-zinc tailings, lead-zinc smelting slag, and cement clinker. The effect of material ratio on the mechanical properties, the phase analysis, and microstructures were investigated. The effect of the pH and stripping time on the leaching amount of lead ion was discussed. The results show that the additive amount of the tailings should be minimized for the cementitious materials meeting the strength requirements, controlled within 10%. The leaching amount of cementitious materials remains low in a larger range of pH, which can effectively reduce the leaching of heavy metal lead. The leaching kinetics of lead ions in the three kinds of samples could be better described by the pseudo-second-model.

1. Introduction

In the process of exploiting and utilizing of mineral resource, a series of environmental problems have been arisen. The exploitation of the mine will produce a lot of waste rock and gob, resulting in waste of resources and security risks. The stacking of tailings from concentration and smelting slag, sludge, and dust from metallurgical process have stolen the land resources which produce a serious pollution to the environment. Filling the gobs with tailings and other solid waste can not only realize the control of solid waste pollution and improve the utilization of the land but also prevent the surface subsidence and improve the mining index. However, if tailings and other solid waste are directly used to fill the gobs, it will be prone to oxidation and ion release in the rain, the sun, and other natural stress; toxic substances and heavy metal ions can be released to the environment as well. A tailings dam leakage occurred in Spanish Aznalcollar sulfur iron mine in April 1998, resulting in the decline of the pH values in the vicinity of the local underground water and the concentration of heavy metal ions Zn, Mn, Co, Pb, Cd, and Tl in underground water and soil was significantly increased

[1]. Sharma and Al-Busaidi investigated the changes of underground water metal ion concentration and pH value through the analysis of 12 years monitoring data of soil and water around the copper mine tailings of Oman Mine Company [2, 3] and confirmed the pollution of groundwater tailings. Shaw monitored that the Hg concentrations in surface water and groundwater continued to rise although the Murray Brook gold mine in Canada had been closed for 10 years [4]. Therefore, the tailing cannot be used to fill the gobs directly. It had been confirmed that heavy metals could be solidified in cement clinker crystalline lattice in the process of cement kiln incinerating solid waste. These elements would be compacted in the C-S-H consolidation gel or exist in small pores after cement hydration and were not willing to release under natural conditions. Via the use of the cement, heavy metals and other harmful substances are not released into the environment which can eliminate the hidden dangers of pollution. The preparation of cementitious material with tailings to replace a part of cement can not only meet the requirement of structure and high strength but also reduce the cost. The purpose of effectively recycling tailings and other waste was achieved [5].

TABLE 1: Chemical composition of raw materials/%.

Composition	CaO	SiO ₂	Al ₂ O ₃	MgO	Fe ₂ O ₃	MnO	K ₂ O	TiO ₂	FeO	Pb	Zn	Na ₂ O	S	LOI
Gangue	2.19	69.92	10.41	1.39	1.89	0.51	2.17	0.57	5.38	0.17	0.12	0.51	0.55	3.68
Smelting slag	13.54	27.72	11.32	6.12	1.69	1.79	1.12	0.6	25.28	0.92	3.2	3.25	2.15	0.57

Lead-zinc tailings lead and zinc smelting slag and cement clinker were used in the experiment to prepare composite cementitious material. The effect of the species and quantities of hydration products under different ratio of raw materials on mechanical properties was studied, which laid the theoretical foundation for how to prepare cementitious material and optimize its strength. Because external pH is the main factor affecting the heavy metal leaching, the lead ion leaching of tailings, smelting slag, and tailings-smelting slag cementitious materials under different pH conditions were studied, respectively, providing basis of suitable environment for the prepared composite cementitious materials.

2. Experimental

2.1. Materials and Equipment. In this experiment, the raw materials were lead-zinc tailings, smelting slag, and cement clinker. The additives mainly contained gypsum. The XRD analysis indicated that the main components in the tailings were quartz and kaolinite, and the activation was not difficult. Lead and zinc smelting slag was composed of SiO₂, FeO, CaO, Al₂O₃, and MgO; the main mineral composition was glass phase which meant it was a potential hydraulic material with high activity. The cement clinker came from a cement factory of Baoding, Hebei province. The main compositions are tricalcium silicate, dicalcium silicate, and calcium iron oxide. Chemical composition of lead-zinc tailings and lead-zinc smelting slag was shown in Table 1.

2.2. Experimentation

2.2.1. Preparation of Composite Cementing Material. Pre-grinding the lead and zinc smelting slag for the raw smelting slag is coarse. Add gypsum and clinker in the fine smelting slag when it was grinded to a certain degree; the final specific surface area of the mixture is 480~720 m²/kg. Standard mortar specimen was made according to the "test for cement mortar strength" (ISO, GB/T 17671-1999), and then the specimens were mold unloading and were maintained in (20 ± 1)°C and humidity above 90% for 28 days.

2.2.2. Leaching Test. Use a static immersion method to simulate the tailings, smelting slag, and cement products, respectively. In each leaching experiment, 2 g samples were soaked in a 100 mL conical flask by the solid to liquid ratio of 1:25. The experiment was carried out at room temperature. In order to study the effect of soaking time and initial pH value on ion release, tailings, smelting slag, and the cement products were soaked in the soaking liquid of the initial pH values 1, 2, 3, 4, 5, 6, 7, 8, 9, 10, 11, and 12, respectively. The initial pH values were adjusted with NaOH and HCl solutions; the immersion time was 24 h. The pH value was adjusted every

TABLE 2: The ratio of materials for smelting slag cementitious.

Number	Materials		
	Additive	Smelting slag	Cement clinker
1	5	55	40
2	5	60	35
3	5	65	30
4	5	70	25
5	10	55	35
6	10	60	30
7	10	65	25
8	10	70	20

8 h during the leaching process to ensure the stability of pH value.

2.2.3. Analytic Technique. The strength of the sample was tested using a microcomputer controlled electrohydraulic servo pressure testing machine from Changchun new testing machine Co. Ltd. The concentration of lead ions was determined by the two xylenol orange spectrophotometric method at the wavelength of 575 nm by a T6 ultraviolet visible spectrophotometer from Beijing Puxi General Instrument Corp. The pH value was measured by PHS-3C pH meter produced by Shanghai Leici instrument factory. The test parameters of scanning electron microscope are as follows: HV 20 KV, mag 10000 times, WD 10.1 mm, spot3.0, mode SEI, DET ETD, and HFW 15 μm. The XRD pattern was determined by X-ray diffraction in the scanning speed of 40 kV × 100 mA and 8°/min conditions.

3. Result and Discussion

3.1. Strength Test and Analysis

3.1.1. Smelting Slag Cementitious Material. Smelting slag cementitious material consists of zinc smelting slag, clinker, and additive. In order to study the influence of smelting slag admixture on the strength of cementitious materials, change the ratio of slag and cement when the amount of admixture is 5%; the specific mixture ratio and property were shown in Table 2 and Figure 1. It can be seen from the chart that the cementitious material bending strength and compressive strength gradually decreased with the increase of smelting waste content. Because of the latent activity of the slag, cement clinker can be used as alkali activator to destroy the vitreous structure of smelting slag. The active SiO₂ and Al₂O₃ reacted with Ca(OH)₂ to form hydrated calcium silicate and hydrated calcium aluminates, resulting in increased strength. The increase of smelting slag resulted in the reduction of

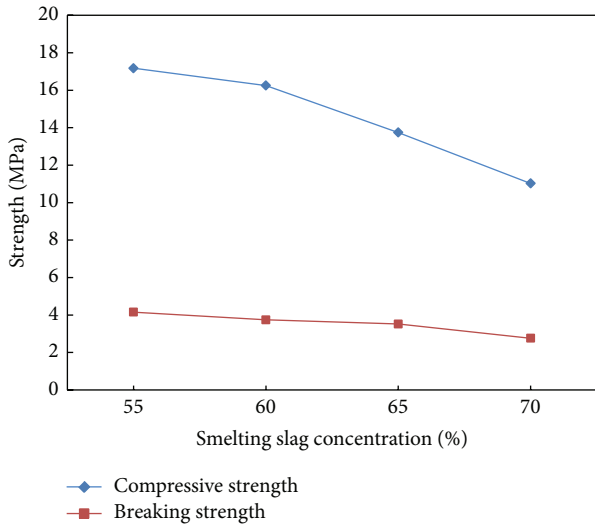


FIGURE 1: Strength among cementitious materials with various smelting concentration.

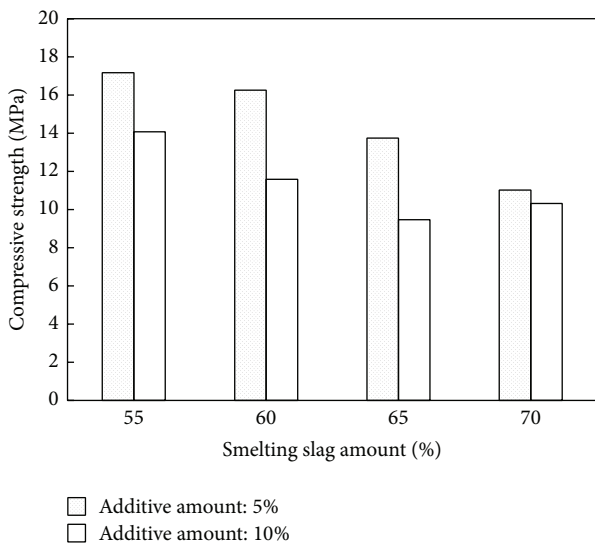


FIGURE 2: Comparison of compressive strength of smelting slag cementitious materials with different additive content.

the proportion of cement clinker in raw materials. When the content of gypsum was too low to inspire all smelting slag, smelting slag existed in hydration and hardening body in the form of low intensity, which led to the decrease of strength of cementitious materials. The influence of different additive dosage on the strength of cementitious materials was shown in Figure 2. On the condition of same smelting slag content, the compressive strength of cementitious material became weak as the additive content increased from 5% to 10%. The existence of gypsum made it easier to form ettringite when the additive agent was plenty, so that the activity of smelting slag can be taken full advantage of, but, at the same time, the reduced amount of cement clinker in the system led to less calcium hydroxide.

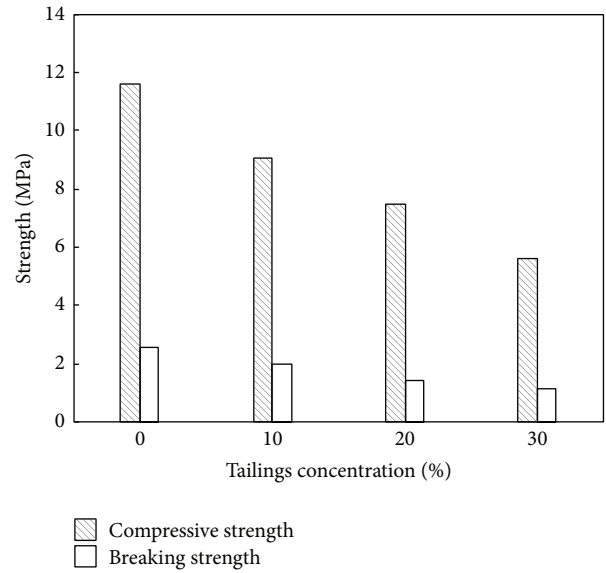


FIGURE 3: Comparison of strength among cementitious materials with different tailing content.

3.1.2. Tailings-Smelting Slag Cementitious Material. For the optimization of comprehensive utilization of solid waste and the comprehensive consideration of economic cost and strength and other factors, appropriately add tailings in the mixture of the proportion of 60% zinc smelting slag, 30% cement clinker, and 10% additive to develop a colored solid waste cementitious material with certain mechanical strength. Figure 3 showed the change of strength with different amount of tailings added when the proportion of smelting slag/clinker/additive was 6/3/1. As can be seen from the figure, the material strength decreased after the tailings were added, which indicated that the addition of the lead-zinc tailings goes against the improvement of the mechanical properties of cementitious material. In order to meet the strength requirements, the tailings added in cementitious materials should be limited [6].

3.1.3. SEM Analysis. The scanning electron micrographs of different smelting slag admixture cementitious material when the amount of additive was 10% was shown (Figure 4), and the magnification was 1000 times. The microstructure of smelting slag cementitious material can be briefly described as follows: needle shaped ettringite crystals and flocculent C-S-H gel overlapped to form a spatial network structure, and it filled the surface and holes and simultaneously mixed the unreacted dehydrate gypsum and slag particles together to form a whole. When the slag content was 55%, the hydration products were ettringite, which was in the initial stage of growth, and fiber was short and dense; independent existence of slag almost cannot be seen; when the slag content was 60%, the hydration products were C-S-H gel and flaky calcium hydroxide; when the slag content increased up to 65%, the structure of the material was loose and the raw material component was exposed; part of C-S-H gel and ettringite were produced. When the content of smelting slag was 55%,

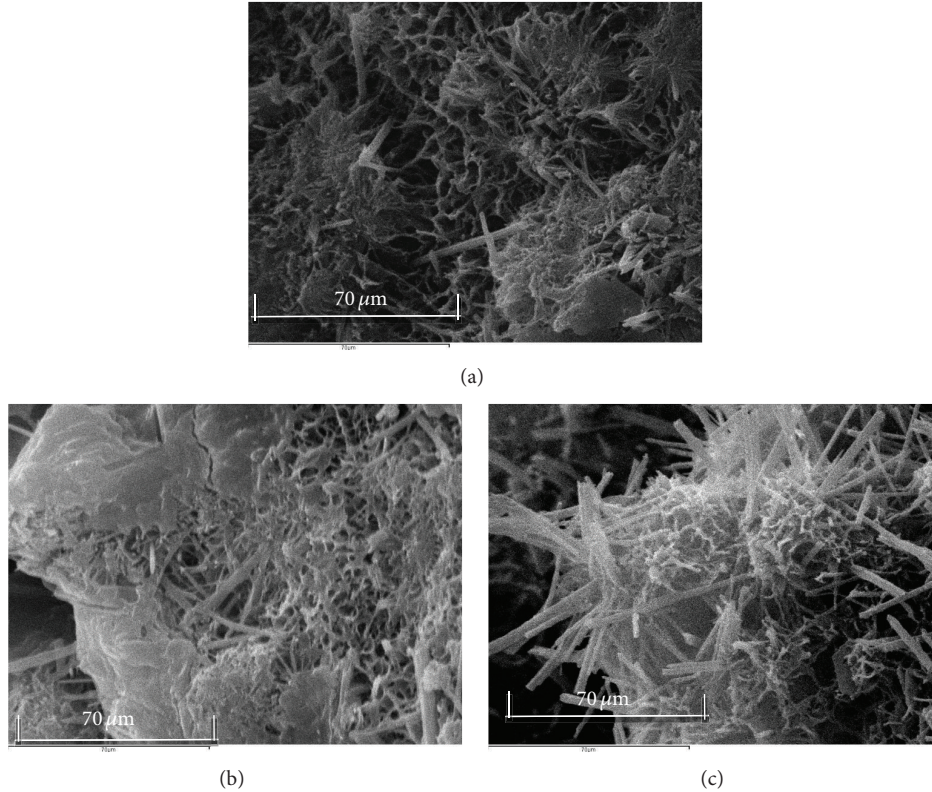


FIGURE 4: SEM photos of hydration products with different smelting slag content: (a) 55%; (b) 60%; (c) 65%.

needle-like AFt crystals in the mortar formed skeleton, and the structure of hardened pastes continuously compacting through the well-distributed filling of C-S-H gel, thus increasing the strength of cementing filling material; this explained the reason why the strength of mortar with 55% smelting slag content was higher than that of the other samples from the point of microstructure, while with the increase of smelting slag in the sample, $\text{Ca}(\text{OH})_2$ crystal increased, calcium silicate hydrate (C-S-H) gel decreased, and the structure was more loose; this also explained the gradual decrease of compressive strength of the samples from the point of microstructure.

3.2. Leaching Experiment

3.2.1. Effect of pH on Lead Ion Leaching Amount. Generally, pH value of the leaching solution is an important factor influencing heavy metal leaching process, for the pH value can affect not only the physicochemical properties of the adsorbent surface but also the existence state of heavy metal ions after being leached. The leaching of lead ion of tailings, smelting slag and tailings, smelting slag cementitious materials under different pH conditions was studied in this experiment. The pH value was installed in the range of 1 to 12 and the experimental results were shown in Figure 5. It was not difficult to find out that in the same pH environment, lead ion leaching smelting slag quantity > lead ion leaching tailings in quantity > lead ion leaching cementitious materials body weight. Therefore, making the smelting slag and tailings

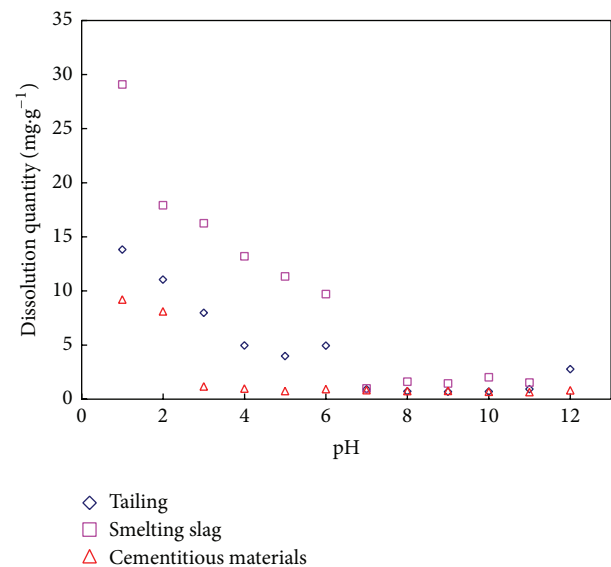


FIGURE 5: The influence of pH on leaching amount.

into cementitious materials fixed lead ions and reduced the leaching. With the increase of pH value of leaching liquids, the trend of lead ion leaching from tailings and metallurgical slag were decreased alike. When the pH < 7, the lead ion leaching amount was quite high and decreased significantly

with the increase of pH value; when the $\text{pH} \geq 7$, the lead ion leaching rate was maintained at a low level. This was because, in an acidic environment, it was easy for metal to form soluble metal oxides, and stronger solubility made lead ions more susceptible to leaching, while heavy metals might combine with OH^- or silicate and form into calcium salts in the alkaline environment, existed in a state of stable insoluble [7], so that the leaching amount of lead ion reduced. In addition, the curve of lead ion leaching from cementitious materials versus pH showed that when $\text{pH} < 3$, lead ion leaching amount obviously decreased with the increase of pH, and when $\text{pH} \geq 3$, lead ion leaching quantity slightly decreased with the increase of pH and kept at a low level; therefore, the preparation of smelting waste and tailings being made into cementitious materials can not only reduce the amount of lead ion leaching but also keep a low leaching amount of lead ion from cementing material in arrange of pH 3–12.

3.2.2. Effect of Time on the Leaching of Lead Ions. Under the condition of pH environment ($\text{pH} = 9\sim 10$) of the leaching solution, solid to liquid ratio was 1:25 and 293 (± 1) constant temperature, the effect of leaching time on the lead ion leaching from smelting slag, tailings, and cementitious materials was studied, and the experimental results were shown in Figure 6. The equilibrium times of lead ion leaching from smelting slag, tailings, and cementitious materials, respectively, were 60 min, 80 min, and 40 min, the lead ion leaching amount when the balance was achieved: smelting slag > tailings > cementitious materials. Hence one can see that preparing cementitious materials by smelting slag and tailings can effectively reduce the leaching of heavy metals of lead ions; this is because the alkaline slag cementitious material hydration products t ($\text{pH} = 12$) can urge heavy metal ions such as Pb to form insoluble metal oxides and hydroxides, thereby adsorbed on the surface of charged ettringite or precipitated in C-S-H sol pore; this reaction was also the main mechanism of cement solidification of heavy metals. In addition, the additive containing anhydrous gypsum caused the high concentration of sulfate in hydration products of cementitious materials, and in the high concentration of sulfate, heavy metal ions are contained by ettringite crystal [8]. Compare the condition of less sulfate concentration in cement; it can be considered that the high sulfate concentration in HAS hydration products is the reason of low concentration of heavy metal filtrate of cementitious material solidified body.

For the better comparison of leaching process of 3 samples to reach equilibrium, the experimental data was fitted by the quasi-two-level dynamic model; the equation is as follows [9]:

$$\frac{t}{q_t} = \frac{1}{K_s q_e^2} + \frac{1}{q_e} t, \quad (1)$$

where q_e and q_t are, respectively, the equilibrium time and adsorption amount of HA when the time is t (min) and K_s ($\text{g} \cdot (\text{mg} \cdot \text{min})^{-1}$) is the quasi-two-level kinetic constant.

The quasi-two-level dynamic simulation curves of each lead ion leaching samples were shown in Figure 7. According

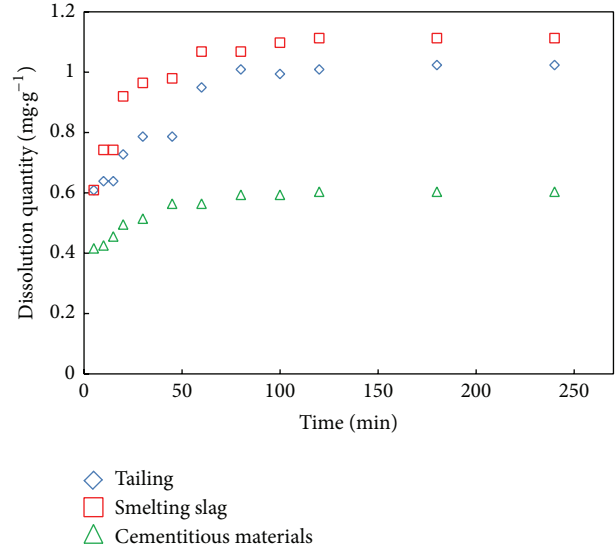


FIGURE 6: Dissolution quantity of different sample with time.

to the slope and intercept of the curve, quasi-two-level kinetic constant K_s and the theoretical leaching amount of equilibrium $q_{e(\text{cal})}$ and determination coefficient R^2 can be calculated, and the actual leaching amount of equilibrium $q_{e(\text{exp})}$ was shown in Table 3. The determination coefficient R^2 value of three kinds of samples measured by the quasi-two-level dynamic model fitting curve was 0.9981, 0.9996, and 0.9998, and the leaching amount of balance theory and the actual amount is consistent thus quasi-two-stage dynamic model can be used to describe the leaching behavior of lead ion of the three kinds of samples. It can be calculated by comparison of kinetic constants that $K_{sC} > K_{sS} > K_{sT}$. The tailings and metallurgical slag prepared into cementitious materials can shorten the equilibrium time required for lead ion leaching, which can reduce the amount of lead ions.

4. Conclusion

Making smelting slag and lead-zinc tailings as the basic components, mixed with right amount of clinker and gypsum additive, can prepare a cementitious material with good performance and have a fixed effect on the heavy metal lead in the smelting slag and tailings to reduce the leaching amount of lead ion.

- (1) The strength of gel materials decline with the increase of smelting slag content.
- (2) The addition of this kind of lead-zinc tailings goes against the improvement of the mechanical properties of the cementitious material so that the dosage should be controlled within 10%.
- (3) The preparation of composite cementitious materials by smelting slag and tailings can effectively reduce the leaching of heavy metals lead and can keep low leaching quantity in a wide range of pH value.

TABLE 3: The quasi-two-level dynamic model equation data.

Sample	$q_{e(\text{exp})}/\text{mg}\cdot\text{g}^{-1}$	$q_{e(\text{cal})}/\text{mg}\cdot\text{g}^{-1}$	$K_s/\text{g}\cdot(\text{mg}\cdot\text{min})^{-1}$	R^2
Tailing	1.0234	1.0656	0.1130	0.9981
Smelting slag	1.1123	1.1446	0.1586	0.9996
Cementitious materials	0.6033	0.6169	0.3716	0.9998

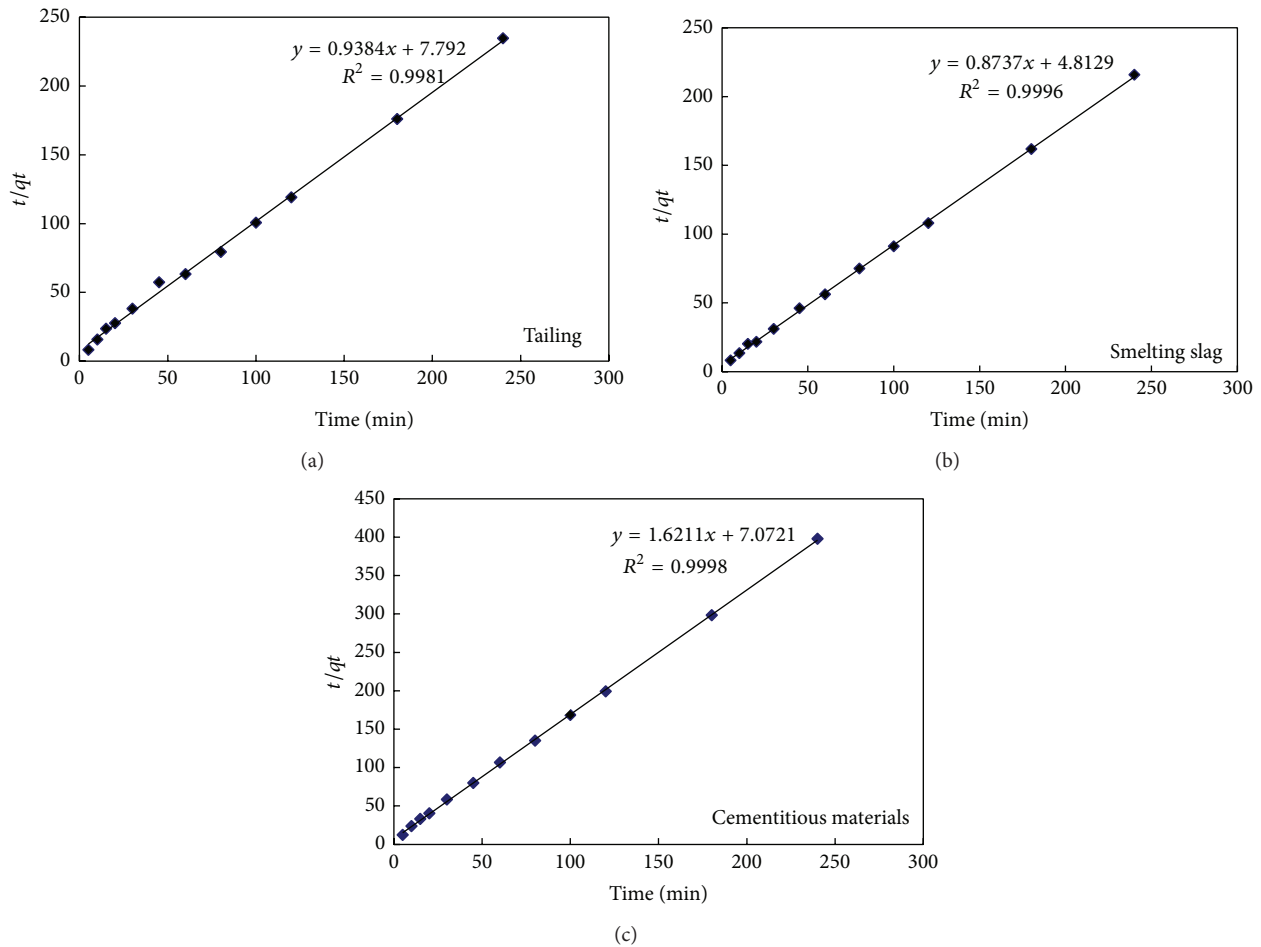


FIGURE 7: The quasi-two-level dynamic model of three samples.

- (4) The quasi-two-level dynamic model can fit well with the leaching curves of lead ion leach from smelting slag, tailings, and cementitious materials by the time. The model can be used to describe leaching behavior of lead ion in the three samples.

Conflict of Interests

The authors declare that there is no conflict of interests regarding the publication of this paper.

Acknowledgment

This research was funded by International S & T Cooperation (no. 2014DFA70760).

References

- [1] M. Manzano, C. Ayora, C. Domenech, P. Navarrete, A. Garralon, and M.-J. Turrero, "The impact of the Aznalcollar mine tailing spill on groundwater," *Science of the Total Environment*, vol. 242, no. 1-3, pp. 189-209, 1999.
- [2] R. S. Sharma and T. S. Al-Busaidi, "Groundwater pollution due to a tailings dam," *Engineering Geology*, vol. 60, no. 1-4, pp. 235-244, 2001.
- [3] S. Yin, A. Wu, K. J. Hu, Y. Wang, and Y. Zhang, "The effect of solid components on the rheological and mechanical properties of cemented paste backfill," *Minerals Engineering*, vol. 35, pp. 61-66, 2012.
- [4] S. A. Shaw, T. A. Al, and K. T. B. MacQuarrie, "Mercury mobility in unsaturated gold mine tailings, Murray Brook mine, New Brunswick, Canada," *Applied Geochemistry*, vol. 21, no. 11, pp. 1986-1998, 2006.

- [5] A. Allahverdi and S. Ahmadnezhad, "Mechanical activation of silicomanganese slag and its influence on the properties of Portland slag cement," *Powder Technology*, vol. 251, pp. 41–51, 2014.
- [6] S. H. Yin and Y. Wang, "Influence of mud height on the concentration of the fine tailing," *Science and Technology Review*, vol. 30, no. 7, pp. 29–33, 2012.
- [7] R. D. Spence, *Chemistry and Microstructure of Solidified Waste Forms*, CRC Press, 1992.
- [8] R. K. Vempati, M. Y. A. Mollah, A. K. Chinthala, D. L. Cocke, and J. H. Beeghly, "Solidification/stabilization of toxic metal wastes using coke and coal combustion by-products," *Waste Management*, vol. 15, no. 5-6, pp. 433–440, 1995.
- [9] G. Lü, J. Hao, L. Liu et al., "The adsorption of phenol by lignite activated carbon," *Chinese Journal of Chemical Engineering*, vol. 19, no. 3, pp. 380–385, 2011.

Research Article

First-Principles Study on the Structural and Electronic Properties of N Atoms Doped-Rutile TiO_2 of Oxygen Vacancies

Zhong-Liang Zeng

College of Earth Sciences, China University of Geosciences, Wuhan 430074, China

Correspondence should be addressed to Zhong-Liang Zeng; dillon117@163.com

Received 18 March 2014; Revised 19 July 2014; Accepted 22 July 2014

Academic Editor: Guocheng Lv

Copyright © 2015 Zhong-Liang Zeng. This is an open access article distributed under the Creative Commons Attribution License, which permits unrestricted use, distribution, and reproduction in any medium, provided the original work is properly cited.

For the propose of considering the actual situation of electronic neutral, a simulation has been down on the basis of choosing the position of dual N and researching the oxygen vacancy. It is found that the reason why crystal material gets smaller is due to the emergence of impurity levels. By introducing the oxygen vacancy to the structure, the results show that while the oxygen vacancy is near the two nitrogen atoms which have a back to back position, its energy gets the lowest level and its structure gets the most stable state. From its energy band structure and density, the author finds that the impurity elements do not affect the migration of Fermi level while the oxygen vacancy has been increased. Instead of that, the conduction band of metal atoms moves to the Fermi level and then forms the N-type semiconductor material, but the photocatalytic activity is not as good as the dual N-doping state.

1. Introduction

Since the discovery of TiO_2 Fujisima-Honda [1] effect exists, different preparation methods have been used to further enhance the photocatalytic performance of TiO_2 . N doped TiO_2 catalyst which is used for improving the ability of visible light shows good effect [2–10]. But in the TiO_2 photocatalytic material preparation process, the oxygen vacancy is an intrinsic defect, that is very easy to occur [11], though researchers have done a lot of research on it [12–21]. However, the different methods of calculation results are not totally unanimous.

Research shows that the most common form of a defect of three-dimensional periodic crystals is vacancy defects, which will affect the physical properties of the material, and the oxygen vacancies are also more prone to N doped TiO_2 system [22–24]. However, effect of oxygen vacancy on the electronic structure and optical activity is still not very clear. On one hand, the oxygen vacancy is the key factor causing visible light photocatalytic activity [25–29]. But it is discussed by Irie et al. [30] that, with increasing N content, the amounts of oxygen vacancies act as recombination centers electron hole, which reduces the visible light photocatalytic activity. It is N doped TiO_2 with oxygen vacancies which

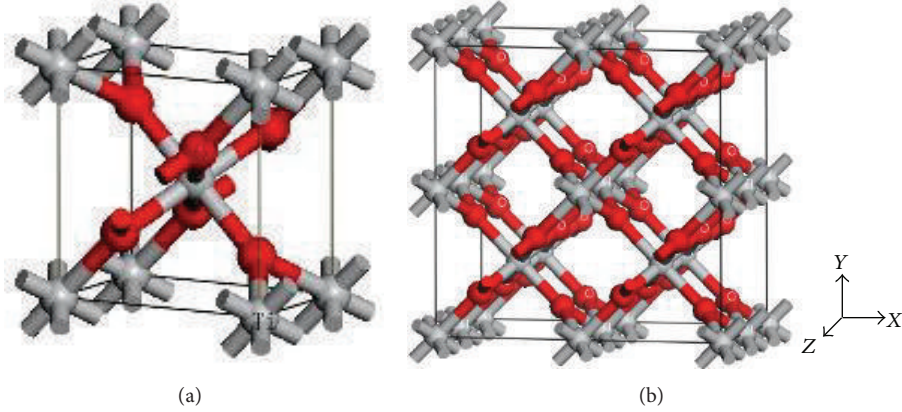
is studied through theoretical and experimental methods by Wang et al. [31]. They believe that the doping of N and Vo both can cause the red shift of absorption edge to visible light region. However, as oxygen vacancies and Ti^{3+} act as a recombination center electron hole, it is not conducive to visible light photocatalytic activity increase. So the electronic structure of point defects in the study that will be important for understanding the characteristics of TiO_2 materials plays a role.

Although the photocatalytic effect of single rutile is not as good as anatase [32], in fact, rutile TiO_2 also has higher photocatalytic activity in the degradation of some pollutants; under certain conditions, rutile and anatase particles can be synergistic [33–35]. Therefore, research on doped rutile has some practical needs.

Based on the density functional theory (DFT), the plane-wave ultrasoft pseudopotential method has been successfully applied to study the electronic structure and dynamical properties for variety of materials [36–42] in order to more clearly reveal the influence of N element and oxygen vacancies of rutile geometry and electronic structure. Based on the first-principles density functional theory of energy band calculation method and the super cell model, this paper has taken a geometrical optimization for the rutile- TiO_2

TABLE 1: Comparisons of lattice constants between calculation (including those obtained in another work) and experiment.

	Exp. [47]	This work	Relative error	Another work [45]
a/nm	0.45929 ± 0.00005	0.4594	$2.3950 \times 10^{-2}\%$	0.4594
c/nm	0.29591 ± 0.00003	0.2959	$3.3794 \times 10^{-3}\%$	0.2959
U	0.03056 ± 0.00006	0.03059	$9.8168 \times 10^{-2}\%$	0.03059

FIGURE 1: (a) The structure of rutile TiO₂ primitive cell. (b) The super cell structure of rutile TiO₂ (2 × 2 × 2).

doped N elements and analyzes the geometric structure and electronic structure of the double nitrogen. After that, the paper theoretically analyzes the oxygen vacancy doping cases and its related properties.

2. The Computational Model and Method

Rutile TiO₂ has a tetragonal crystal structure, with a space group of P42/MNM. In this paper, we employed the rutile-phase TiO₂ single cell and super cell (2 × 2 × 2) models as shown in Figures 1(a) and 1(b). The super cell model consists of eight single cells, which were arrayed along the x -axis, y -axis, and z -axis. The crystal structure formula is Ti₁₆O₃₂.

The calculation in this paper is based on the wavelet plane ultrasoft pseudopotential method. In order to minimize the number of plane waves, we apply ultrasoft pseudopotential to describe the ion-core interaction with the valence electrons. In the reciprocal k -space, the cut-off energy is selected as 300 eV, the generalized gradient approximation (GGA) [43] method is used in the work. The integral calculation of total system energy and charge density which works in the Brillouin zone takes the Monkhorst-Pack scheme to select the k grid as 2 × 2 × 7. In the calculation, the involved valence electron configurations are O 2s²2p⁴, N 2s²2p³, and Ti 3s²3p⁶3d²4s. The calculation is accomplished by employing CASTEP [44] quantum mechanics module which is based on density functional theory, and the software package is MS4.4 version.

3. The Calculation Results

3.1. Pure Rutile Lattice Constant and Electronic Structure. Firstly, we carry out structural optimization of TiO₂ and then

we obtain the rutile phase TiO₂ lattice constants and energy band structures. The lattice constant parameters are listed in Table 1, and the experimental data are also included in the table. Apparently, Our calculation results are well consistent with the experimental and the predecessors' simulated results.

The rutile TiO₂ band structure and density of states are shown in Figure 2, the Fermi level has been chosen at zero-point energy, which is shown as dotted line in the figure. The calculated band gap is 2.048 eV, which is less than the experimental value of 3.0 eV, while it matches the band gap of 1.9 eV calculated by Song et al. [45]. As we all know that a certain degree of bias by DFT [45, 46] in the calculation of electronic band structure.

Based on the above calculation of pure rutile, we can determine that the method of calculation is suitable for doped TiO₂ System.

For comparison, we also optimized a single N atom doped-rutile structure; then we obtained its geometric structure and electronic properties. Figure 3 shows the models of geometry diagram about a N atom and two-N-atom doped TiO₂ on different positions. By optimizing the geometries, then we calculated the total energy, energy band gap, and the distances between the two impurity N atoms; the related parameters are listed in Table 2.

For the two-N-atom doped TiO₂, for convenience, in this paper, we take a Ti atom as the benchmark calibration; in the three models of two-N-atom doped structure, the N atoms in the same position are labeled N1, N atoms changes in position are written as N2. Through geometry optimization, it can be found that when the two doped N atoms have a minimum distance (the minimum is 0.2546 nm), the structure has the lowest energy, with the highest stability. This indicates that if N atoms doped in rutile TiO₂, it will take the nearest neighbor

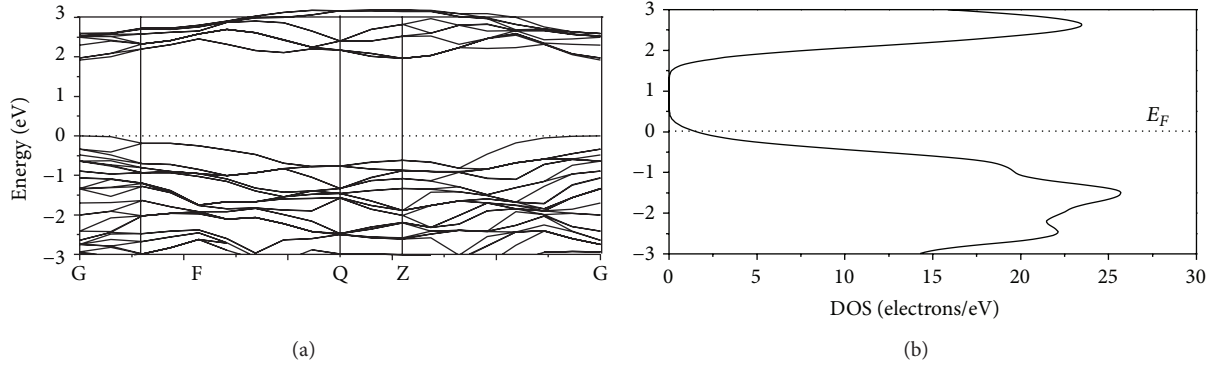


FIGURE 2: (a) The band structure of rutile TiO_2 . (b) The total density of rutile TiO_2 .

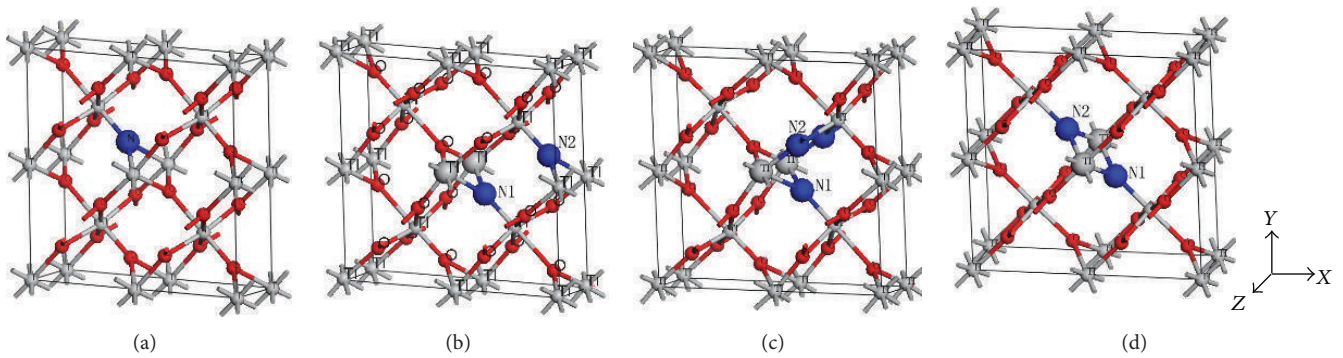


FIGURE 3: The structures of single N doped and double N doped-rutile TiO_2 . (a) Single N doped TiO_2 ; (b) Model A of double N doped- TiO_2 ; (c) Model B of double N doped TiO_2 ; (d) Model C of double N doped- TiO_2 .

occupancy mode. By comparing Figures 3(b), 3(c), 3(d), and 1(b) we find that doping will result in different levels of local deformation. Comparing the data in Table 2, it seems that when the location of N atoms is in the adjacent position, the two doped N atoms will affect one another.

Considering N atom has one electron less than O atom, the two N atoms in the adjacent position can share electrons more easily and then reach a steady state; from the optimized model in Figure 3(b), we also found that if two N atoms are close to each other, the N-N bond has the shortest distance; the structural optimization parameters are consistent with the above analysis.

3.2. Comparative Analysis of Six Kinds of $\text{Ti}_{16}\text{O}_{30}\text{N}_2$ Model. When creating a dual N super cell $\text{Ti}_{16}\text{O}_{32}$ for orthodoping, taking into account the bond lengths, bond angles, and symmetry, it is still possible to build six different types of doping methods. This paper considers mainly six kinds of geometrical and electronic structure analysis.

3.2.1. The Geometrical Structure of the Six Models of $\text{Ti}_{16}\text{O}_{30}\text{N}_2$. Figure 4 is a pair of N-atom super cells in $\text{Ti}_{16}\text{O}_{32}$ oxygen doping orthosubstitution optimized geometric structure. By optimizing calculation, the total energy, energy band gap, and the distance between the two impurity atoms have been listed in Table 3. After the geometry optimization, by

Energy band analyzing and the size of the bond angle between N-O-N and the atomic distance of N-N, we identified six calibration models which are named Model 1 ($\text{Ti}_{16}\text{O}_{30}\text{N}_2$ -1), Model 2 ($\text{Ti}_{16}\text{O}_{30}\text{N}_2$ -2), Model 3 ($\text{Ti}_{16}\text{O}_{30}\text{N}_2$ -3), Model 4 ($\text{Ti}_{16}\text{O}_{30}\text{N}_2$ -4), Model 5 ($\text{Ti}_{16}\text{O}_{30}\text{N}_2$ -5), and Model 6 ($\text{Ti}_{16}\text{O}_{30}\text{N}_2$ -6).

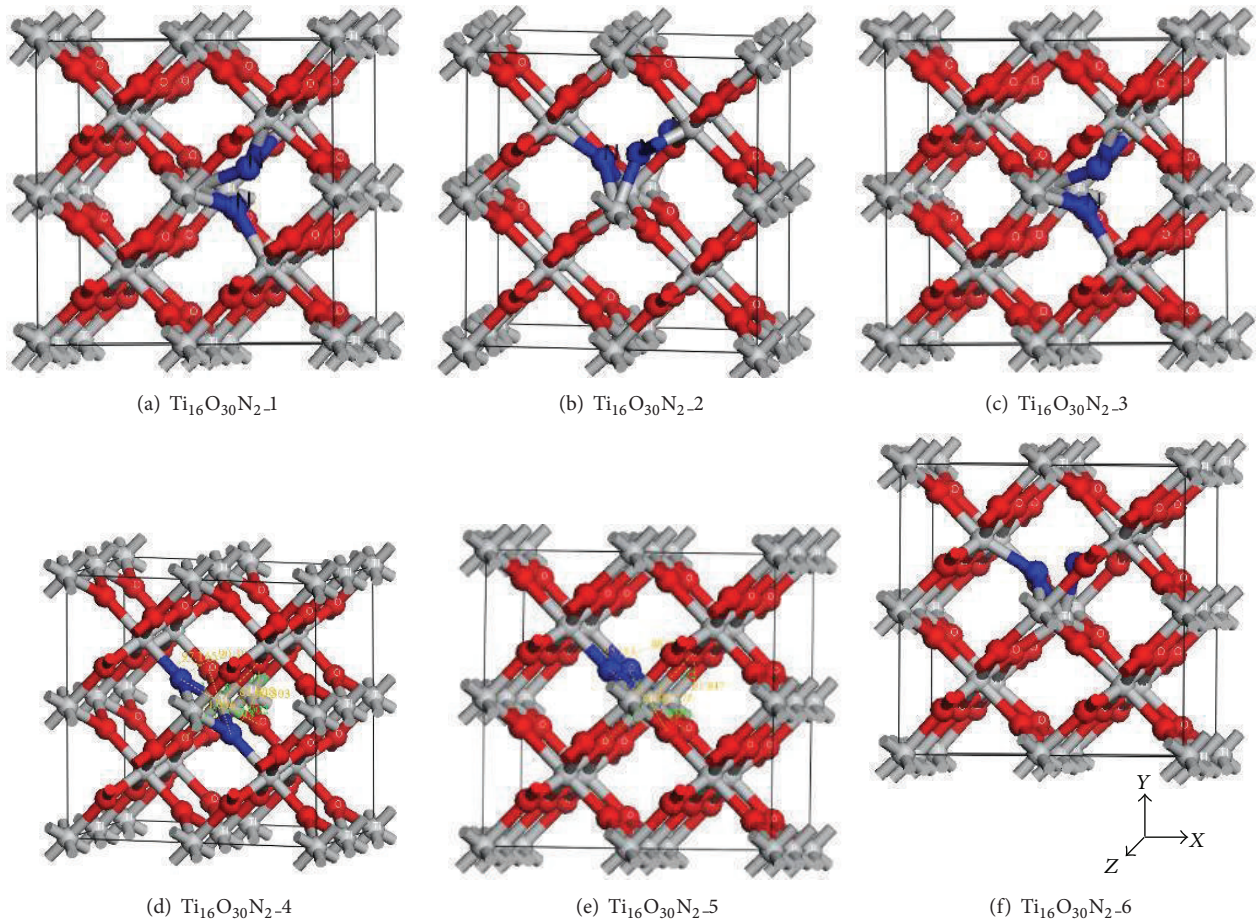
The results show that the pure direct band gap of $\text{Ti}_{16}\text{O}_{32}$ is 1.887 eV which is different from the band gap Ti_8O_{16} (1.921 eV). As we get the result under a professional analysis, the calculation is precise. Therefore, it must comply with the same initial conditions and computing platform when we make a horizontal contrast. For the same object we can exclude the difference caused by different software versions. Qualitative analysis has been used to analyze the property of the six different models. After having a geometry optimization, the distance between the two nitrogen atoms gets its minimum. When the minimum gets 0.1372 nm, the smallest band gap becomes 1.498 eV. It indicates that while the N atom doped into rutile, it will occupy the nearest neighbor position. By comparing Figures 4(a), 4(b), 4(c), 4(d), and 4(f) with Figure 1, we find there is a replacement bit with different degree of local deformation replacement. With the data in Table 3, take into account that O atoms lack one electron than N atoms, while two N atoms that are in adjacent positions can be better sharing electrons and it is easier to achieve steady state. From Table 3 we also found $\text{Ti}_{16}\text{O}_{30}\text{N}_2$ -1 minimum total energy model, and it is also more stable. Combining with

TABLE 2: The total energy and band gaps of rutile and four kinds of N-doped rutile TiO_2 and the bond distance between the two doped N-N.

	Final free energy (eV)	Energy gaps (eV)	Atomic distance of N-N (nm)
Ti_8O_{16}	-19890.0596	2.048	—
$\text{Ti}_8\text{O}_{15}\text{N}$	-19678.9163	1.553	—
Model A	-19552.3673	1.63	0.3377
Model B	-19552.8169	1.24	0.2546
Model C	-19552.2915	1.28	0.2715

TABLE 3: The total energy and band gaps of rutile and six kinds of N-doped rutile TiO_2 and the bond distance between the two doped N-N and Angle of N-Ti-N.

	Final free energy (eV)	Energy gap (eV)	Atomic distance of N-N (nm)	Angle of N-Ti-N
$\text{Ti}_{16}\text{O}_{32}$	-39780.209	1.887	0.2780 (O-O)	90.000 (O-Ti-O)
$\text{Ti}_{16}\text{O}_{30}\text{N}_2-1$	-39444.4974	1.508	0.1373	39.968
$\text{Ti}_{16}\text{O}_{30}\text{N}_2-2$	-39444.4952	1.501	0.1373	39.924
$\text{Ti}_{16}\text{O}_{30}\text{N}_2-3$	-39444.4928	1.498	0.1372	39.975
$\text{Ti}_{16}\text{O}_{30}\text{N}_2-4$	-39444.4949	1.502	0.1372	39.914
$\text{Ti}_{16}\text{O}_{30}\text{N}_2-5$	-39442.4369	0.182	0.2602	84.036
$\text{Ti}_{16}\text{O}_{30}\text{N}_2-6$	-39442.4177	0.208	0.2959	95.114

FIGURE 4: The structures of six kinds of $\text{Ti}_{16}\text{O}_{30}\text{N}_2$.

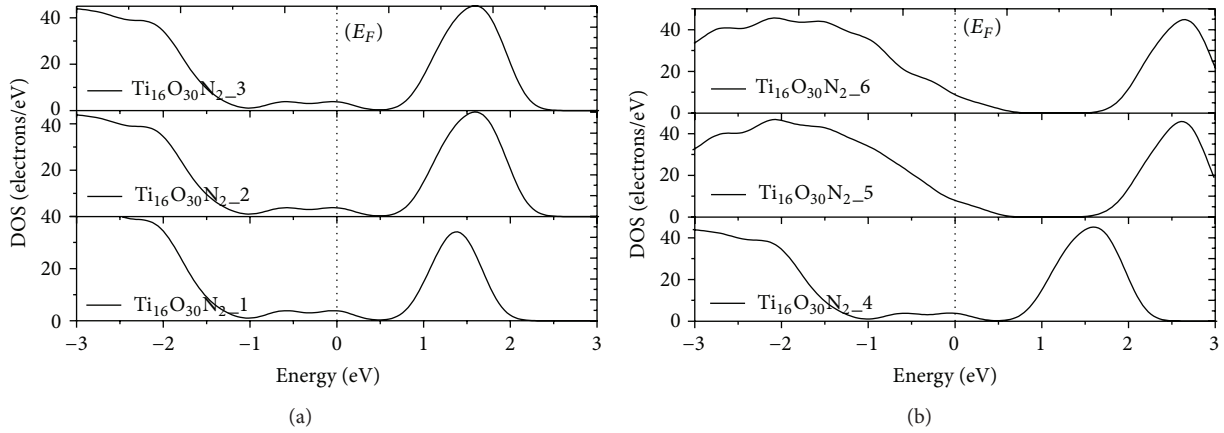


FIGURE 5: The total density of states of six kinds of $Ti_{16}O_{30}N_2$ model.

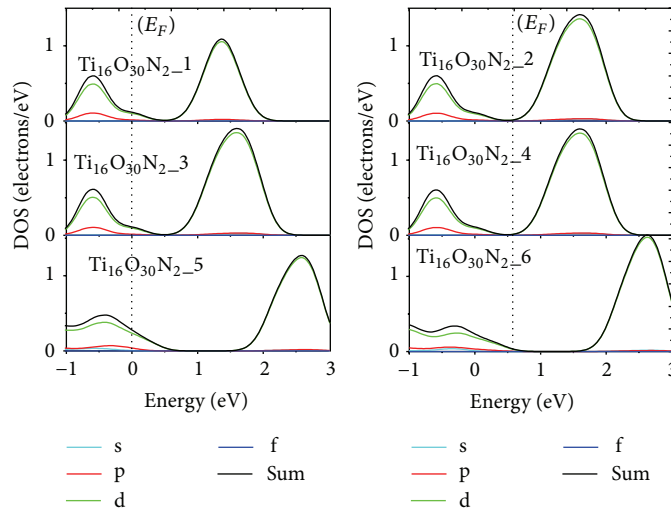


FIGURE 6: The density of states of Ti atom.

the author's dual N doped in the conclusions of the study, he finds that $Ti_{16}O_{30}N_2_1$ may be more closer to the actual state.

3.2.2. The Electronic Structure of Six Kinds of $Ti_{16}O_{30}N_2$ Model. Figure 5 shows the density graph of six models. From Figures 5 and 4(a) we find that the band gap of TiO_2 has been changed. The calculated band gap has been shown in Table 3. The generated doping which occurred during O atoms replaced N atoms has been apparently reduced. However, it shows band gap minimum in Model 5 and Model 6 which is much lower than the normal band gap. It is due to the Fermi level caused through the band. From the energy band structure of the state we saw that a small amount of energy level cross the Fermi energy level, since the band gap cannot be accurately obtained.

From Figure 5 we can see the density graph of Model 5 and Model 6 is different from the other four models. It is mainly reflected by smaller direct band gap, which is farther from band Fermi level. The valence band is closer to Fermi level which is only 0.208 eV. This is because the Fermi level has

crossed the band level, so the material gets metallic character. We can no longer classify it as a semiconductor material and the band gap cannot be given directly.

Figures 6 and 7 show us the density graph of N-atom and Ti atom. From Figure 7, we see N 2p orbital located in the middle band, which forms an intermediate level. It indicates that the introduction of N atom will better change the band gap. Since the density near the Fermi energy of Model 1, Model 2, Model 3, and Model 4 is low, and the band gap is small there, thus they will more likely result in excitation phenomenon. The density of N atoms of Models 5 and 6 near the Fermi energy is very large, but its band gap is wide. With Figures 5, 6, and 7 we can conclude that the dope of the first four models may affect the valence of Ti atom. The valence band energy level may have a certain extension to higher level, but there are not any prominent changes in conduction band. Besides, the width and lower restrict of the guiding band do not change significantly, while near the Fermi level it showed a more gentle impurity energy level. For Models 5 and 6, their conduction band has been removed away from Fermi level. According to the contents in Table 3, we found that when

TABLE 4: The total energy and band gaps of rutile and eight kinds of neutral doped rutile TiO_2 and the bond distance between the two doped N–N and angle of N–Ti–N.

	Final free energy (eV)	Energy gap (eV)	Atomic distance of N–N (nm)	Angle of N–Ti–N
$\text{Ti}_{16}\text{O}_{29}\text{N}_2\text{-1}$	–39003.2719	—	0.1369	39.934
$\text{Ti}_{16}\text{O}_{29}\text{N}_2\text{-2}$	–39004.1026	0.014	0.1373	39.968
$\text{Ti}_{16}\text{O}_{29}\text{N}_2\text{-3}$	–39003.568	—	0.1388	40.475
$\text{Ti}_{16}\text{O}_{29}\text{N}_2\text{-4}$	–39003.7126	—	0.1372	39.914
$\text{Ti}_{16}\text{O}_{29}\text{N}_2\text{-5}$	–39003.5715	0.008	0.1373	39.968
$\text{Ti}_{16}\text{O}_{29}\text{N}_2\text{-6}$	–39003.7321	0.040	0.1371	40.104
$\text{Ti}_{16}\text{O}_{29}\text{N}_2\text{-7}$	–39004.4015	—	0.1420	42.348
$\text{Ti}_{16}\text{O}_{29}\text{N}_2\text{-8}$	–39004.1177	0.014	0.1367	38.307

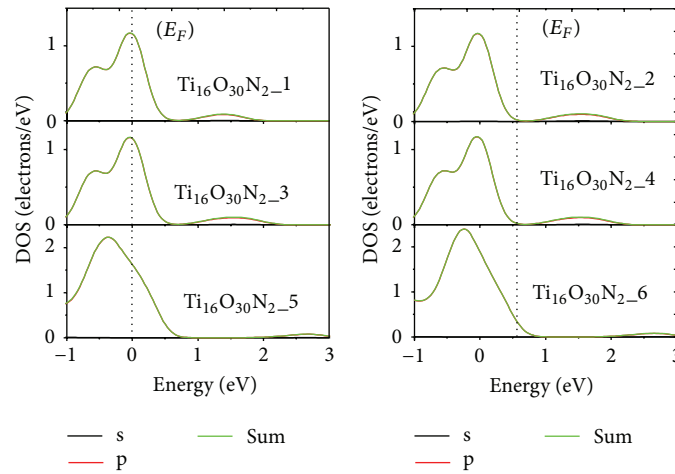


FIGURE 7: The density of states of neighbors bit N atom.

the super cell was $(2 \times 2 \times 2)$, the NN neighbor position would have a different doping effect which has a close relationship with the distance of the two N atoms. From Figure 4 the structure optimized model also shows us the two atoms become more stable and closer to each other. So, we take Model 1 as our basis in the follow-up study of electrical neutral doping while we continue an electrical neutral study.

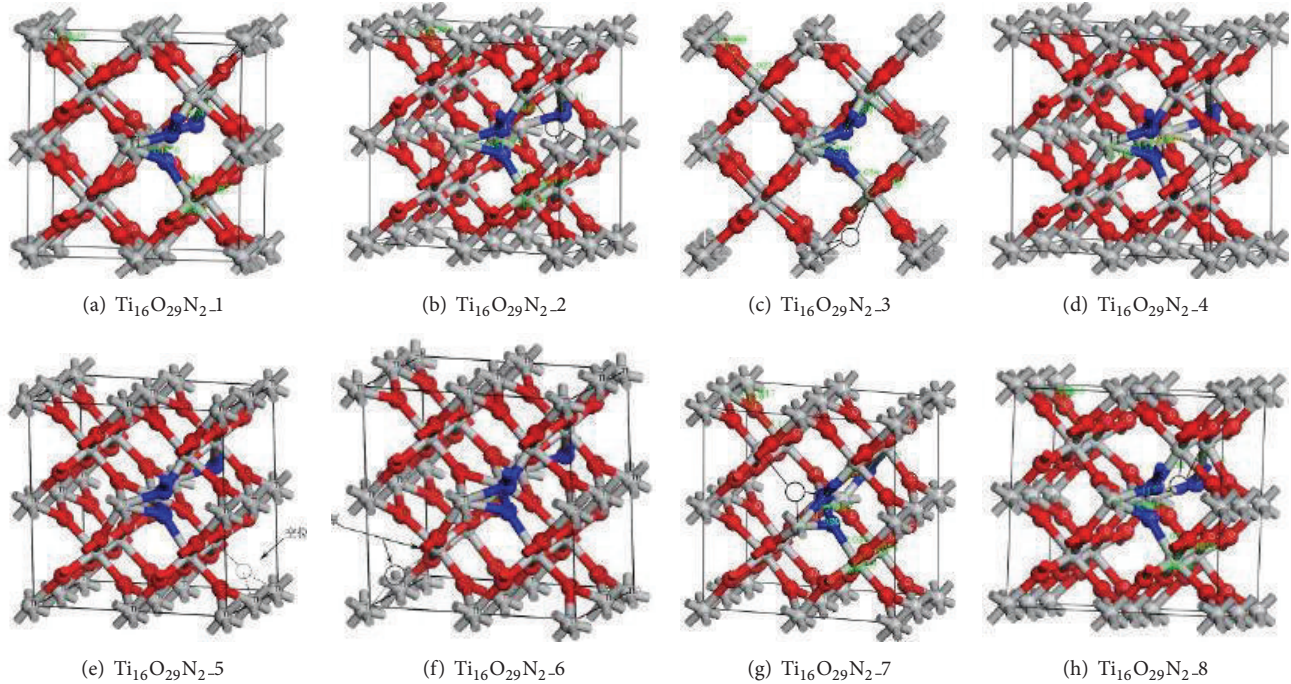
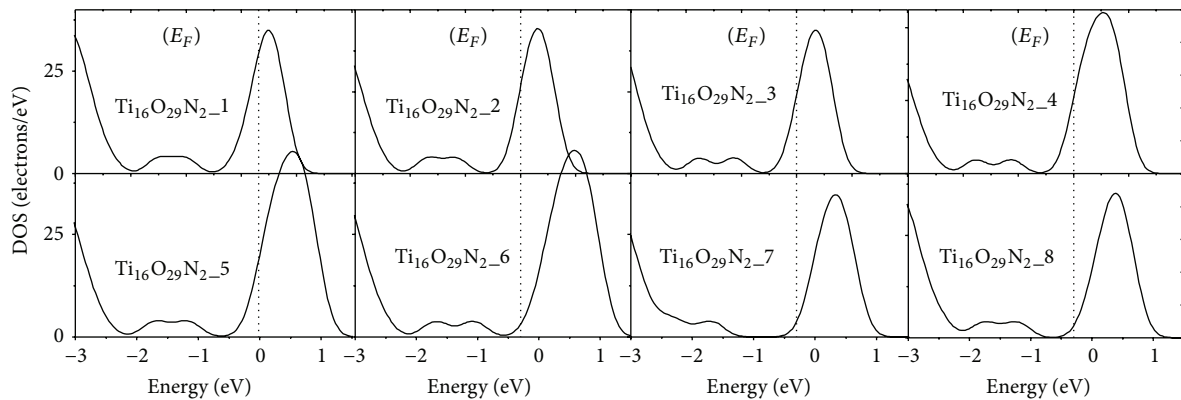
3.3. Comparative Analysis of Electrical Neutral Doping $\text{Ti}_{16}\text{O}_{29}\text{N}_2$ Model. Based on the partial results of the analysis, we select model 1 in Figure 4 in this section as a basic doping blueprint and then consider the case when the position of the oxygen is vacancy.

3.3.1. Eight Geometrical Structure Models of $\text{Ti}_{16}\text{O}_{29}\text{N}_2$. On the basis of the distance between an O atom and a Ti atom and their corresponding angle, we set 8 models of comparative analysis. As the selected super cell still follows in the previous section, thus the initial parameters are still without any change.

The black circle in Figure 8 is the missing oxygen atoms. Black lines represent the oxygen atoms which form a bond before they miss. We found that oxygen deletion does not cause big changes in the crystal structure. That means the geometry of the optimization is still in the acceptable range

which corresponds to the actual situation, From this state, we discover that in daily growth of the crystal, oxygen atoms in rutile crystal will be easier to form such kind of vacancy, but when the oxygen has been lost, catalytic reaction may get lower effect and lower oxidation resistance. When research of impurity atoms appeared, whether it can be more effective to inhibit oxygen atoms will be the focus of it. In physics, it was easier to explain through their electronic structure.

By analyzing the results in Table 4, it is easy to see each doping crystal in the electronic structure tends to move to the valence band from Fermi level. If the impurity level gets through the Fermi level, it becomes more sensitive to light. Meanwhile, from Table 4, we know Model 7 has the lowest total energy. After analyzing the N–N distance and the angle between N–O–N atoms, we find different oxygen vacancies in different positions may cause different forms though dual N atoms are in the same position. Obviously, for Model 7 the distance between two atoms is significantly increased. Comparing the geometry of the model 7, we find the vacancy of oxygen atom is in Adjacent positions of the two N atoms. Compared to the distance of Model 1, Model 3, Model 4, Model 5, and Model 6, its deformation is relatively small, as the vacant positions are in the opposite angle between the two N atoms. Missing 2 electrons, two N atoms have to fill the vacancy position, so the two N atoms must move to fill the vacancy, which actually opened the distance between

FIGURE 8: The structures of eight kinds of $\text{Ti}_{16}\text{O}_{29}\text{N}_2$.FIGURE 9: The total density of states of eight kinds of $\text{Ti}_{16}\text{O}_{29}\text{N}_2$ model.

two atoms which comply with the conclusion of the previous section. It has been reflected that crystals among atoms are all mutually shared electrons as they all lose necessary electrons; then it may achieve electronic balance. In this section, because of the absence of electrons, atoms around the vacant position have to coshare their electrons. Without a doubt, in actual situation, N atoms still present in the form of doped ions. Thus, the anionic dopants obtain more advantages than cation in specific tests.

3.3.2. The Electronic Structure of Eight Kinds of $\text{Ti}_{16}\text{O}_{29}\text{N}_2$ Models. In the former part, a qualitative analysis is taken from the geometry optimized structure from the figure of eight models. Then, a further analysis is taken from the perspective of the electronic structure to study the interaction among atoms which have electronic structure changes.

From Figure 9 we can see the total density of eight models is very different from the density graph where oxygen is not vacant. They have smaller band gap. For Fermi level has got into the conduction band, it indicates that the introduction of oxygen vacancy makes the eight models form a typically *n*-type semiconductor. The occupation of conduction band spread all super cells. By analyzing the occupation of conduction band, it is known that excess electrons near oxygen vacancies have made great contribution to the valence band, which have caused changes of valence band.

Figures 10 and 11 give us the N-atom and Ti atom which is in the orthoposition of the density of states. From Figure 11, we can see that N 2p's orbital is in the valence band, and its valence band level has been reduced which cannot form intermediate level. The state indicates contribution of the N atoms to light catalytic is not as good as vacant oxygen atoms.

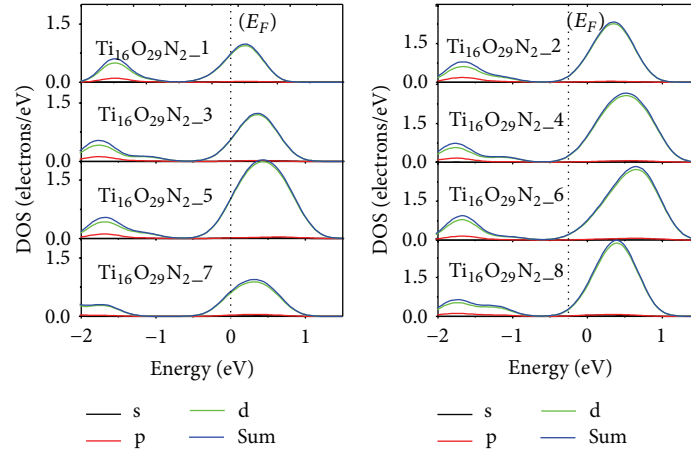


FIGURE 10: The DOS of Ti atom of eight kinds.

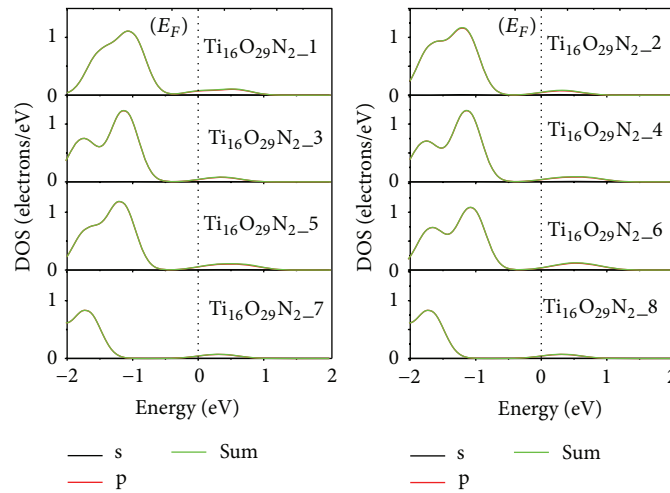


FIGURE 11: The DOS of N atom of eight kinds.

Figure 9 shows that the model 7, the model 8 significantly reduced the number of electrons in the valence band, and the band gap is large. The valence band and the conduction band electrons of Ti of model 7 are also reduced accordingly in Figure 10. Consider a large number of electrons need to be compensated to fill the oxygen vacancies, thus leading the conduction band moves to the Fermi level. To the whole trend, Model 7 also has some semiconductor properties, and there remains a certain band gap. However, as the impurity levels are near the Fermi energy, we cannot clearly calculate the forbidden band of the state.

4. Conclusion

In this paper, the study concludes that the growth of rutile in the natural process always rises oxygen vacancy. By theoretical calculation and analysis, we found reasons for its formation are consistent with the scientific premise.

By means of the N-doping research in the first part, it has the lower total energy, but not necessarily the smallest

band gap when the dual N doped is in the nearest neighbor position. Smallest band gap appears in symmetrical position. After further research we found that the band gap becomes smaller as impurity energy level appeared in the Fermi level, while the bandwidth between conduction band and the valence band is not reduced obviously. We selected one of the models to continue the study of objects. The second part is for the selected model, where we introduce an oxygen vacancy situation to show that when the two neighboring oxygen atoms and nitrogen atoms are in its back position, the energy is the lowest and most stable. From the band structure and density analysis it is also found that the increase of the vacancy doping leads the metal atoms to move to Fermi level and then generate the N type semiconductor material. The effort of impurity elements is limited, but the catalytic activity is not as good as dual N situation. This is consistent with reality. As the rutile crystal growth usually causes daily oxygen vacancies, the oxygen vacancy has to be taken carefully, be reduced as good as we can, and then increased the doping density of ion.

Conflict of Interests

The author declares that there is no conflict of interests regarding the publication of this paper.

References

- [1] A. Fujishima and K. Honda, "Electrochemical photolysis of water at a semiconductor electrode," *Nature*, vol. 238, no. 5358, pp. 37–38, 1972.
- [2] R. M. Dreizler and E. K. Geoss, *Density Functional Theory*, Springer, Berlin, Germany, 1990.
- [3] W. E. Pickett, "Pseudopotential methods in condensed matter applications," *Computer Physics Reports*, vol. 9, no. 3, pp. 115–197, 1989.
- [4] P. Hohenberg and W. Kohn, "Inhomogeneous electron gas," *Physical Review B*, vol. 136, pp. B864–B871, 1964.
- [5] R. G. Parr and W. Yang, in *Density-Functional Theory of Atoms and Molecules*, Oxford University Press, Oxford, UK, 1989.
- [6] J. Zhu, F. Chen, J. Zhang, H. Chen, and M. Anpo, "Fe³⁺-TiO₂ photocatalysts prepared by combining sol-gel method with hydrothermal treatment and their characterization," *Journal of Photochemistry and Photobiology A: Chemistry*, vol. 180, no. 1-2, pp. 196–204, 2006.
- [7] S.-X. Wu, Z. Ma, Y.-N. Qin, X.-Z. Qi, and Z.-C. Liang, "Photocatalytic redox activity of doped nanocrystalline TiO₂," *Acta Physico-Chimica Sinica*, vol. 20, no. 2, pp. 138–143, 2004 (Chinese).
- [8] P. Cheng, M. Y. Gu, and Y. P. Jin, "Recent progress in titania photocatalyst operating under visible light," *Progress in Chemistry*, vol. 17, no. 1, pp. 8–14, 2005.
- [9] W. Zhang, Y. Li, S. Zhu, and F. Wang, "Copper doping in titanium oxide catalyst film prepared by dc reactive magnetron sputtering," *Catalysis Today*, vol. 93-95, pp. 589–594, 2004.
- [10] J. T. Chang, Y. F. Lai, and J. L. He, "Photocatalytic performance of chromium or nitrogen doped arc ion plated-TiO₂ films," *Surface and Coatings Technology*, vol. 200, no. 5-6, pp. 1640–1644, 2005.
- [11] U. Diebold, "The surface science of titanium dioxide," *Surface Science Reports*, vol. 48, no. 5–8, pp. 53–229, 2003.
- [12] C. di Valentin, G. Pacchioni, and A. Selloni, "Theory of carbon doping of titanium dioxide," *Chemistry of Materials*, vol. 17, no. 26, pp. 6656–6665, 2005.
- [13] S. Na-Phattalung, M. F. Smith, K. Kim et al., "First-principles study of native defects in anatase TiO₂," *Physical Review B*, vol. 73, no. 12, Article ID 125205, 2006.
- [14] G. Mattioli, F. Filippone, P. Alippi, and A. A. Bonapasta, "Ab initio study of the electronic states induced by oxygen vacancies in rutile and anatase TiO₂," *Physical Review B*, vol. 78, no. 24, Article ID 241201, 2008.
- [15] E. Cho, S. Han, H.-S. Ahn, K.-R. Lee, S. K. Kim, and C. S. Hwang, "First-principles study of point defects in rutile TiO_{2-x}," *Physical Review B: Condensed Matter and Materials Physics*, vol. 73, no. 19, Article ID 193202, 2006.
- [16] M. Cococcioni and S. de Gironcoli, "Linear response approach to the calculation of the effective interaction parameters in the LDA+U method," *Physical Review B—Condensed Matter and Materials Physics*, vol. 71, no. 3, Article ID 035105, 2005.
- [17] H. Iddir, S. Öğüt, P. Zapol, and N. D. Browning, "Diffusion mechanisms of native point defects in rutile TiO₂: Ab initio total-energy calculations," *Physical Review B*, vol. 75, no. 7, Article ID 073203, 2007.
- [18] J. He, R. K. Behera, M. W. Finnis et al., "Prediction of high-temperature point defect formation in TiO₂ from combined ab initio and thermodynamic calculations," *Acta Materialia*, vol. 55, no. 13, pp. 4325–4337, 2007.
- [19] E. Finazzi, C. Di Valentin, G. Pacchioni, and A. Selloni, "Excess electron states in reduced bulk anatase TiO₂: comparison of standard GGA, GGA+U, and hybrid DFT calculations," *Journal of Chemical Physics*, vol. 129, no. 15, Article ID 154113, 2008.
- [20] K. Yang, Y. Dai, B. Huang, and Y. P. Feng, "Density-functional characterization of antiferromagnetism in oxygen-deficient anatase and rutile TiO₂," *Physical Review B: Condensed Matter and Materials Physics*, vol. 81, no. 3, Article ID 033202, 2010.
- [21] Z. Lin, A. Orlov, R. M. Lambert, and M. C. Payne, "New insights into the origin of visible light photocatalytic activity of nitrogen-doped and oxygen-deficient anatase TiO₂," *Journal of Physical Chemistry B*, vol. 109, no. 44, pp. 20948–20952, 2005.
- [22] Y. Nakano, T. Morikawa, T. Ohwaki, and Y. Taga, "Deep-level optical spectroscopy investigation of N-doped TiO₂ films," *Applied Physics Letters*, vol. 86, no. 13, Article ID 132104, pp. 1–3, 2005.
- [23] C. Di Valentin, G. Pacchioni, and A. Selloni, "Origin of the different photoactivity of N-doped anatase and rutile TiO₂," *Physical Review B: Condensed Matter and Materials Physics*, vol. 70, no. 8, Article ID 85116, 2004.
- [24] H. Noda, K. Oikawa, T. Ogata, K. Matsuki, and H. Kamata, "Preparation of titanium (IV) oxides and its characterization," *Journal of the Chemical Society of Japan*, no. 8, pp. 1084–1090, 1986 (Japanese).
- [25] I. Justicia, P. Ordej, G. Canto et al., "Designed self-doped titanium oxide thin films for efficient visible-light photocatalysis," *Advanced Materials*, vol. 14, p. 1399, 2002.
- [26] I. Nakamura, N. Negishi, S. Kutsuna, T. Ihara, S. Sugihara, and K. Takeuchi, "Role of oxygen vacancy in the plasma-treated TiO₂ photocatalyst with visible light activity for NO removal," *Journal of Molecular Catalysis A: Chemical*, vol. 161, no. 1-2, pp. 205–212, 2000.
- [27] T. Ihara, M. Miyoshi, Y. Iriyama, O. Matsumoto, and S. Sugihara, "Visible-light-active titanium oxide photocatalyst realized by an oxygen-deficient structure and by nitrogen doping," *Applied Catalysis B: Environmental*, vol. 42, no. 4, pp. 403–409, 2003.
- [28] T. Ihara, M. Ando, and S. Sugihara, "Preparation of visible light active TiO₂ photocatalysis using wet method," *Photocatalysis*, vol. 5, p. 19, 2001.
- [29] A. K. Rumaiz, J. C. Woicik, E. Cockayne, H. Y. Lin, G. H. Jaffari, and S. I. Shah, "Oxygen vacancies in N doped anatase TiO₂: experiment and first-principles calculations," *Applied Physics Letters*, vol. 95, no. 26, Article ID 262111, 2009.
- [30] H. Irie, Y. Watanabe, and K. Hashimoto, "Nitrogen-concentration dependence on photocatalytic activity of TiO_{2-x}N_x powders," *The Journal of Physical Chemistry B*, vol. 107, no. 23, pp. 5483–5486, 2003.
- [31] J. Wang, D. N. Tafen, J. P. Lewis et al., "Origin of photocatalytic activity of Nitrogen-doped TiO₂ nanobelts," *Journal of the American Chemical Society*, vol. 131, no. 34, pp. 12290–12297, 2009.
- [32] E. Obuchi, "Titania photocatalytic," *Journal of the Electrochemical Society*, vol. 143, no. 9, pp. 191–193, 1996.
- [33] A. L. Linsebigler, G. Lu, and J. T. Yates Jr., "Photocatalysis on TiO₂ surfaces: principles, mechanisms, and selected results," *Chemical Reviews*, vol. 95, no. 3, pp. 735–758, 1995.

- [34] M. Wu, W. Zhang, Z. Du, and Y. Huang, "Structural transformation in nanophase titanium dioxide," *Modern Physics Letters B*, vol. 13, no. 5, pp. 167–174, 1999.
- [35] T. Ohno, K. Tokieda, S. Higashida, and M. Matsumura, "Synergism between rutile and anatase TiO_2 particles in photocatalytic oxidation of naphthalene," *Applied Catalysis A: General*, vol. 244, no. 2, pp. 383–391, 2003.
- [36] G. Zheng, S. J. Clark, P. R. Tulip, S. Brand, and R. A. Abram, "Ab initio dynamics study of poly-para-phenylene vinylene," *Journal of Chemical Physics*, vol. 123, no. 2, Article ID 024904, 2005.
- [37] G. Zheng, S. J. Clark, S. Brand, and R. A. Abram, "First-principles studies of the structural and electronic properties of poly-para-phenylene vinylene," *Journal of Physics Condensed Matter*, vol. 16, no. 47, pp. 8609–8620, 2004.
- [38] G. Zheng, S. J. Clark, S. Brand, and R. A. Abram, "Lattices dynamics of polymer PPyV and PANI: first-principles determination," *Physical Review B*, vol. 74, Article ID 165210, 2006.
- [39] K. H. He, G. Zheng, G. Chen, T. Lü, M. Wan, and G. F. Ji, "Effects of single oxygen vacancy on electronic structure and ferromagnetism for V-doped TiO_2 ," *Solid State Communications*, vol. 144, no. 1-2, pp. 54–57, 2007.
- [40] W. Xue D, J. Cai, M. Wang X et al., "First-principle study on SrTiO_3 film oxygen imperfection," *Journal of Atomic and Molecular Physics*, vol. 24, no. 4, pp. 875–878, 2007.
- [41] Q. Feng, X. Q. Wang, and G. B. Liu, "First-principles study of point defects in rutile TiO_2 ," *Journal of Physics B: Atomic and Molecular Physics*, vol. 25, no. 5, article 1096, 2008 (Chinese).
- [42] Y. G. Liu, M. X. Song, L. Bian, T. Zhou, and X. Zhao, "Ab initio band gap calculation of rare earth doped rutile TiO_2 ," *Journal of Atomic and Molecular Physics*, vol. 25, no. 5, p. 1141, 2008 (Chinese).
- [43] J. P. Perdew, K. Burke, and M. Ernzerhof, "Generalized gradient approximation made simple," *Physical Review Letters*, vol. 77, no. 18, pp. 3865–3868, 1996.
- [44] M. D. Segall, P. J. D. Lindan, M. J. Probert et al., "First-principles simulation: ideas, illustrations and the CASTEP code," *Journal of Physics Condensed Matter*, vol. 14, no. 11, pp. 2717–2744, 2002.
- [45] Q. T. Song, P. Yang, J. B. Wang, X. Lu, and N. Huang, "First-principles study on the rutile TiO_2 doped with phosphorus," *Journal of Materials Science & Engineering*, vol. 26, no. 3, pp. 435–437, 2008.
- [46] Q. L. Chen and C. Q. Tang, "Ab initio band calculations of transition metals doped rutile TiO_2 ," *Journal of Materials Science & Engineering*, vol. 24, no. 4, p. 514, 2006.
- [47] J. G. Traylor, H. G. Smith, R. M. Nicklow, and M. K. Wilkinson, "Lattice dynamics of rutile," *Physical Review B*, vol. 3, no. 10, pp. 3457–3472, 1971.

Research Article

Experimental Study on Low-Strength Similar-Material Proportioning and Properties for Coal Mining

Shaojie Chen,^{1,2} Hailong Wang,¹ Junwen Zhang,³ Huilin Xing,² and Huaiyuan Wang¹

¹State Key Laboratory of Mine Disaster Prevention and Control, Shandong University of Science and Technology, Qingdao 266590, China

²Centre for Geosciences Computing, School of Earth Sciences, The University of Queensland, Brisbane, QLD 4072, Australia

³School of Mining Engineering, Heilongjiang University of Science and Technology, Harbin 150022, China

Correspondence should be addressed to Shaojie Chen; csjwyb@163.com

Received 14 May 2014; Revised 19 November 2014; Accepted 20 November 2014

Academic Editor: Guocheng Lv

Copyright © 2015 Shaojie Chen et al. This is an open access article distributed under the Creative Commons Attribution License, which permits unrestricted use, distribution, and reproduction in any medium, provided the original work is properly cited.

Similar-material simulation test is an effective tool to study the practical problems in mining and civil engineering. This paper conducts an orthogonal study on low-strength similar materials comprising sand, fly ash, and plaster and analyses the sensitivity of the materials. The mechanical properties of the similar materials strongly depend on the proportioning ratio, and they can satisfy different similar-material simulation tests. The compression strength and elastic modulus of the similar material decrease as the sand-binder ratio or cement ratio increases. There are approximately linear relations between the compression strength/elastic modulus and sand-binder ratio and approximately power relations between the compression strength/elastic modulus and sand-binder ratio. Sensitivity analysis employing the range method shows that the effects of the cement ratio on the compression strength and elastic modulus are more obvious than the effects of the sand-binder ratio. Finally, one of similar materials is used in a simulation test of coal backfill mining.

1. Introduction

Some large-scale projects, such as the underground coal mining that reduce the strength of the strata and are subjected to deformation failure, are difficult to study on-site. Although these complex problems can be investigated through theoretical analysis and numerical modelling, most problems need to be investigated by conducting geomechanical simulation tests [1–5], such as similar-material simulations. A geomechanical simulation test is the representation of real physical objects, with the materials having mechanical properties similar to those of a prototype according to a certain proportionality relation. The model has all or most of the major characteristics of the prototype, and an experiment can be duplicated using the model in less time and at lower cost, and visual results can be obtained. To obtain results that are more convincing, the selected similar materials must have very similar physical and mechanical properties for the physical model and engineering prototype [6]. The materials and mixing ratio strongly affect the properties of the physical model, which is critical to the success of simulation tests.

With the help of similar-material simulation test, Gao et al. studied the time series system for induced caving of roof in continuous mining under complex backfill in ore body number 92 of Tongkeng Tin Mine [7]; Li et al. simulated the “domino effect” of the stope pillar unstable failure of gently inclined and medium thick phosphate rock under pillar and room caving [8] and the deformation behaviour of overburden rocks and mining pressure of the deep ore body of mining [9].

Moreover, Meguid et al. conducted physical modelling of tunnels in soft ground using a mixture of barite powder, sand, plaster powder, water, and liquid laundry detergent [10], and Fei et al. employed a temperature-analogue material to simulate the decreasing strength of the weak interlayer but did not obtain desired results [11]. A new similar material mixed using sand, barite powder, talc powder, cement, Vaseline, and silicone oil for fluid-solid coupling was developed by Li et al. to simulate the tunnel under Qingdao Kiaochow Bay in China [12], and the effects of the sand-binder ratio, binder proportions on similar materials of limestone was

studied by Zuo et al. [13]. Zhang et al. developed a similar material of collapsible loess for simulation testing [14], and Hui et al. presented the similarity criterion analysis of goaf in a similar-material simulation [15], where the cement, sand, water, activated carbon, and coal powder were selected as the raw material to mix the coal similar material [16].

Although similar-material simulations have been widely employed, a new similar material is urgently required in the increasingly wide range of geomechanical engineering projects. For example, as coal resources are developed, there is an increasing focus on environmental protection. Backfill is increasingly carried out in coal mining to protect the environment and replace resources, and the backfill body has lower strength than the coal-bearing sedimentary rocks.

In order to find a new similar material to simulate rock mass with low strength in mining engineering, such as filling paste, this paper conducts an orthogonal study of low-strength similar materials comprising sand, fly ash, and plaster in a similar-material simulation test and analyses the sensitivity of the materials. One of similar materials is used in a simulation test of coal backfill mining, and the test result shows that the mixture of artificial materials is appropriate for the simulation test.

2. Sample Preparation of Similar Material with Lower Strength

The similar material with lower strength in this experiment is mixed with sand, fly ash, and plaster.

Considering that the similar material in the simulation model has lower strength, generally less than 120 kPa, similar materials with a larger sand-binder ratio and cement ratio are tested in an orthogonal study. To investigate the effect of the sand-binder ratio and cement ratio on mechanical properties of the materials, 16 groups of samples were tested for two factors and four levels (Table 1). The suitable similar material with lower strength can be mixed through a small adjustment to the mixing ratios. The quality concentration of the similar material in different levels is 80%.

The samples of similar materials are standard cylindrical specimens with dimensions of $\Phi 50 \text{ mm} \times 100 \text{ mm}$. A PVC tube with diameter of 50 mm was cut into simple moulds each with length of 100 mm, as shown in Figure 1. A vertical gap was cut in the middle of each mould to allow the removal of the standard sample. The original materials are clean river sand common gypsum and fly ash from a power plant. Appropriate proportions of aggregate and cementing materials were stirred evenly with a cement paste mixer, and water was then quantitatively added to the mixture. The mixture was put into the sample moulds and tamped. The standard specimens were obtained after three days. There were 48 samples in 16 groups, some of which are shown in Figure 2.

3. Analysis of Uniaxial Compression Test Results

3.1. Uniaxial Compression Test Results. Sixteen standard specimens were tested under uniaxial compression using

TABLE 1: Orthogonal study of similar materials.

Level	Factor	
	Sand-binder ratio (A)	Cement ratio fly ash : gypsum (B)
1	6 : 1	8 : 2
2	7 : 1	7 : 3
3	8 : 1	6 : 4
4	9 : 1	5 : 5



FIGURE 1: Moulds for making standard specimens.



FIGURE 2: Standard specimens.

an AG-X250 electronic universal testing machine. The uniaxial compressive strength and elasticity modulus of similar materials with different mixing ratios are given in Table 2, where the number denoting the mixing ratio comprises three digits. When the number denoting the mixing ratio is “682,” for example, “6” represents the sand-binder ratio and “82” represents the cement ratio.

The uniaxial compressive strengths of similar material with different mixing ratios are between 28.542 and 100.407 kPa, and the elasticity moduli are between 813.918 and 4008.291 kPa, which are values that meet the requirements of most lower strength similar-material simulation tests [12]. At the same time, the required mixing ratio of the similar material can be selected from the results of the orthogonal experiment using the mechanical parameters of a single experimental model.

Typical failure specimens are shown in Figure 3, and stress-strain curves of similar-material specimens are presented in Figures 4 and 5.

3.2. Effects of the Sand-Binder Ratio and Cement Ratio on the Mechanical Properties. The variations in the strength of the similar materials with a change in the sand-binder ratio and cement ratio are shown in Figures 6 and 7. The strength of the similar materials clearly experiences a decrease as the sand-binder ratio or cement ratio increases. The relation between

TABLE 2: Results of the orthogonal experiment on similar materials with different mixing ratios.

Specimen number	Diameter/mm	Height/mm	Number of mixing ratios	Uniaxial compressive strength/kPa	Elasticity modulus/kPa
P11	46.58	102.32	682	51.93	1110.083
P12	46.16	101.16	673	58.388	1754.256
P13	46.82	103.48	664	78.818	3401.377
P14	46.64	102.70	655	100.407	4008.291
P21	46.38	100.52	782	44.100	961.323
P22	46.18	102.02	773	52.478	1698.07
P23	46.58	103.04	764	64.009	2629.804
P24	46.22	102.38	755	88.600	3862.366
P31	46.46	101.22	882	37.667	830.820
P32	46.64	102.66	873	43.958	1548.728
P33	46.52	102.42	864	53.935	2252.316
P34	46.50	102.48	855	72.092	3480.833
P41	46.58	101.54	982	28.542	813.918
P42	46.56	102.86	973	38.673	1311.437
P43	46.76	102.72	964	48.199	2133.269
P44	46.28	100.26	955	58.487	2941.296



FIGURE 3: Typical failure specimens.

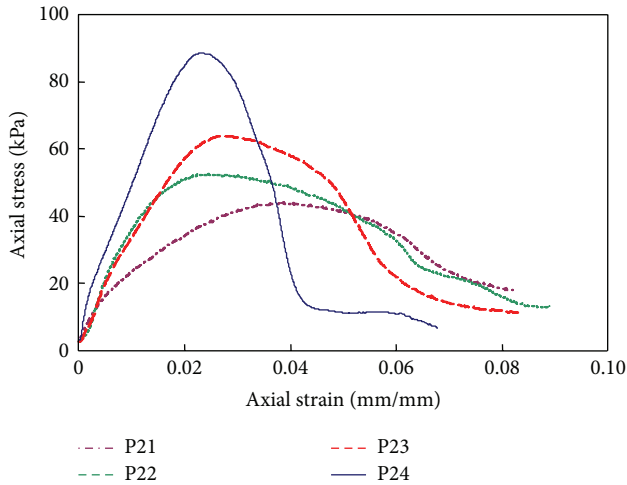


FIGURE 4: Stress-strain curves of material (sand-binder ratio of 7 : 1).

the sand-binder ratio and compression strength is linear; for example, the relation in the cement ratio case of 6 : 4 satisfies

$$y = -14.227x + 186.6, \tag{1}$$

where y is the compressive strength and x is the sand-binder ratio.

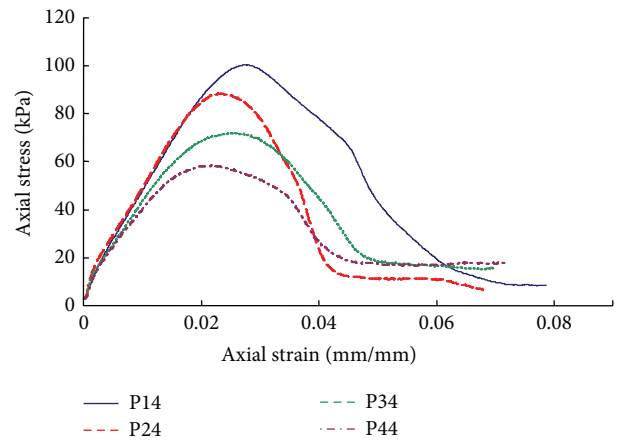


FIGURE 5: Stress-strain curves of material (cement ratio of 5 : 5).

The relation between the cement ratio and compression strength satisfies an exponential growth; for example, the relation in the sand-binder ratio case of 8 : 1 is

$$y = 68.303x^{-0.462}, \tag{2}$$

where y is the compressive strength and x is the cement ratio.

The variations in the elasticity modulus of the similar material with a change in the sand-binder ratio and cement ratio are shown in Figures 8 and 9. Similar to the strength of the similar materials, the elasticity modulus of the material also experiences a reduction as the sand-binder ratio or cement ratio increases. A linear correlation between the sand-binder ratio and elasticity modulus is observed. In particular, the relation in the cement ratio case of 7 : 3 is

$$y = -6.7665x + 99.123, \tag{3}$$

where y is the elasticity modulus and x is the sand-binder ratio.

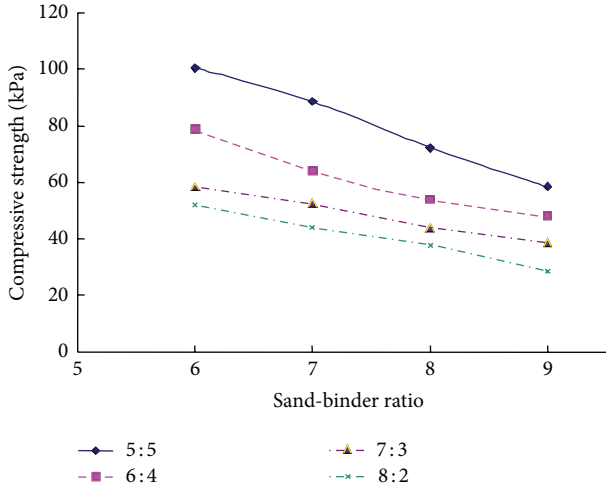


FIGURE 6: Effect of the sand-binder ratio on strength.

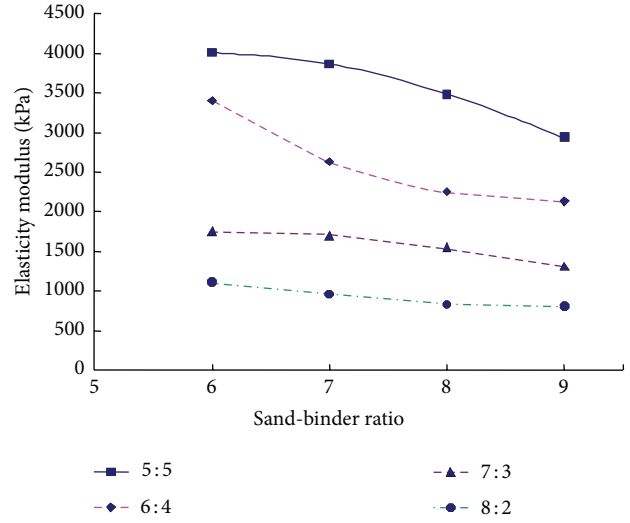


FIGURE 8: Effect of the sand-binder ratio on the elastic modulus.

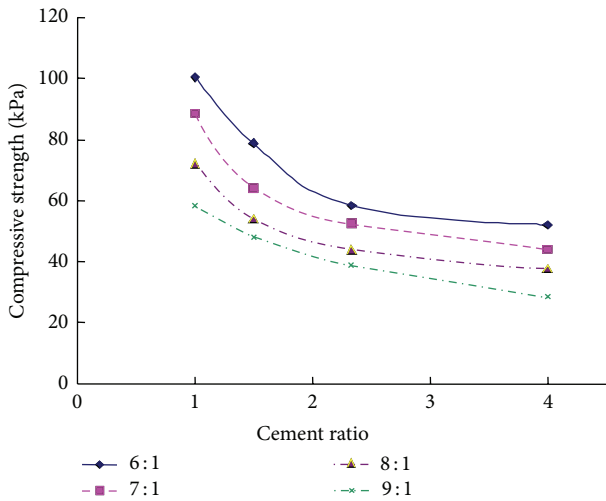


FIGURE 7: Effect of the cement ratio on strength.

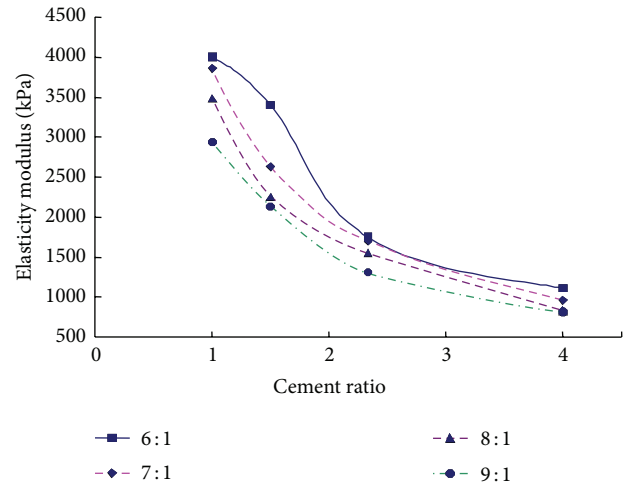


FIGURE 9: Effect of the cement ratio on the elastic modulus.

The relation between the cement ratio and elasticity modulus satisfies an exponential growth; for example, the relation in the sand-binder ratio case 7:1 is

$$y = 3912.5x^{-1.004}, \tag{4}$$

where y is the elasticity modulus and x is the cement ratio.

4. Analysis of the Two Factors

The mean and range of each factor at each level that affect the compressive strength and elasticity modulus of the similar materials are given in Table 3. The range of factor A (sand-binder ratio) is smaller than the range of factor B (cement ratio), and the effects of the cement ratio on the compression strength and elastic modulus are more remarkable than the effect of the sand-binder ratio.

To analyse the effect of various factors on the compressive strength and elasticity modulus intuitively, according to

Table 3, the relationships between factors and mechanical parameters of the similar material are presented in direct analysis charts, as shown in Figures 10 and 11. Both the compression strength and elastic modulus of the similar material decrease as the sand-binder ratio or cement ratio increases.

5. Lower Similar Material Used in Backfill Mining Simulation

In this test, the referred prototype is the backfill mining of Daizhuang coal mine in China. If the low-strength similar material can simulate the deformation and supporting role of filling body and the overlying strata movement and failure mode are consistent with the practical project, the test can be seen as a success.

The aim of this test is to study the overlying strata movement and failure mode qualitatively. The scale effect between simulation experiment and practical engineering is

TABLE 3: Range analysis.

Compressive strength/kPa			Elasticity modulus/kPa		
Level	Sand-binder ratio (A)	Fly ash : gypsum (B)	Level	Sand-binder ratio (A)	Fly ash : gypsum (B)
1	72.386	40.560	1	2568.502	929.036
2	62.297	48.374	2	2287.891	1578.123
3	51.913	61.240	3	2028.174	2604.192
4	43.475	79.897	4	1799.980	3573.197
Range	28.911	39.337	Range	768.522	2644.161

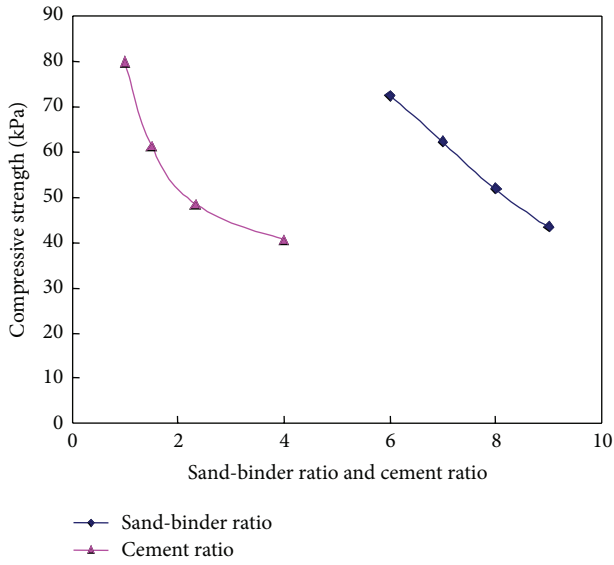


FIGURE 10: Sensitivity analysis of factors affecting strength.

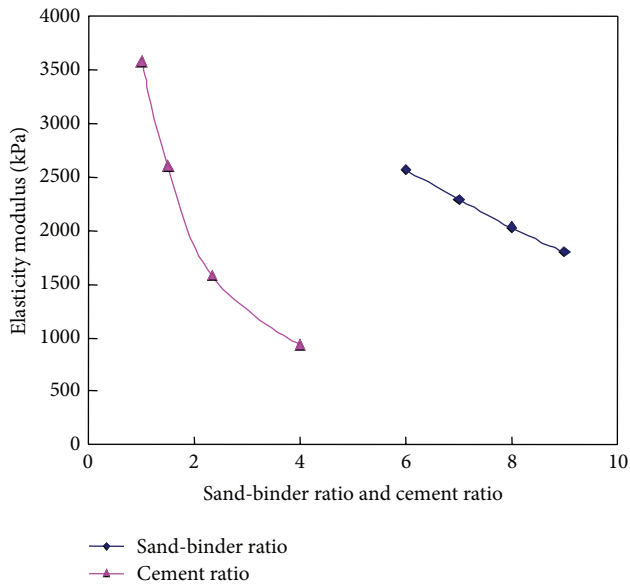


FIGURE 11: Sensitivity analysis of factors affecting the elastic modulus.



FIGURE 12: Similar-material simulation test of backfill mining.

not considered. According to the theory of similarity, similar-material simulation models must satisfy a series of similarity requirements in terms of geometry, physical-mechanical properties, boundary conditions, and initial stress conditions. The reduced scale of dimension in the simulation test is selected as 100. According to the similarity theory, the general law of similarity between the prototype parameters and the model parameters can be deduced. The reduced scale of volume-weight is selected as 1.5 and the reduced scale of stress is selected as 150. The uniaxial compression strength of backfill paste obtained in site of Daizhuang coal mine is 5.436 MPa, and the strength of the similar material is 37.67 kPa. Thereby, the number of mixing ratios of the similar material is 8 : 8 : 2 (see Table 2).

The two strip working faces are mined firstly in the experiment, and then the strip pillars are changed by the filling body. The simulation test of backfill mining is shown in Figure 12. After the strip pillars are changed, the equilibrium around the goaf is disrupted; then the overlying strata deform, move, and even damage. If it is not filled, the overlying strata will cave and break. After it is filled, the backfill pastes restrict the movement of roofs, and the overlying strata only bend and sink but not cave or break.

The backfill pastes have large deformation but control the overlying strata movement effectively, which are different from pillars. The experiment reproduced the real situation in field, and the low-strength backfill paste similar material played a right role in the simulation experiment.

6. Conclusions

- (1) A new low-strength similar material was mixed from sand, fly ash, and plaster. The uniaxial compressive strengths of similar materials with different mixing ratios ranged from 28.542 to 100.407 kPa,

and the elasticity modulus ranged from 813.918 to 4008.291 kPa. This similar material can meet the requirements of most similar-material simulation tests.

- (2) The compression strength and elastic modulus of the similar material both decrease as the sand-binder ratio or cement ratio increases. A linear relation was found between the sand-binder ratio and compression strength of the material and between the sand-binder ratio and elastic modulus as well. The relation between the cement ratio and compression strength and that between the cement ratio and elastic modulus both satisfy an exponential growth.
- (3) The sensitivities of the sand-binder ratio and cement ratio were analysed by employing the range method and the relationship between factors and parameters were studied using direct analysis charts where the factors affect the mechanical indexes. The effects of the cement ratio on the compression strength and elastic modulus are more remarkable than the effects of the sand-binder ratio.
- (4) The effects of the sand-binder ratio and cement ratio on the mechanical properties of the materials were analysed in a uniaxial compression experiment but without consideration of the effects of material physical and chemical reactions among the sand, fly ash, and plaster, which will be studied in the future work.
- (5) Based on the orthogonal test, one of similar materials is used in a simulation test of coal backfill mining. The experiment reproduced the real situation in field, and the low backfill paste similar material played a right role in the simulation experiment.

Conflict of Interests

The authors declare that there is no conflict of interests regarding the publication of this paper.

Acknowledgments

This study was supported by National Natural Science Foundation of China (nos. 51104094 and 51474134), Program for New Century Excellent Talents (NCET-13-0880), and Shandong Provincial Natural Science Foundation (ZR2013EEZ001).

References

- [1] S. H. Kim, H. J. Burd, and G. W. E. Milligan, "Model testing of closely spaced tunnels in clay," *Geotechnique*, vol. 48, no. 3, pp. 375–388, 1998.
- [2] D. N. Chapman, S. K. Ahn, D. V. L. Hunt, and A. H. C. Chan, "The use of model tests to investigate the ground displacements associated with multiple tunnel construction in soil," *Tunnelling and Underground Space Technology*, vol. 21, no. 3, p. 413, 2006.
- [3] J. Lemaitre, "A continuous damage mechanics model for ductile fracture," *Journal of Engineering Materials and Technology*, vol. 107, no. 1, pp. 83–89, 1985.
- [4] M. C. He, W. L. Gong, H. M. Zhai, and H. P. Zhang, "Physical modeling of deep ground excavation in geologically horizontal strata based on infrared thermography," *Tunnelling and Underground Space Technology*, vol. 25, no. 4, pp. 366–376, 2010.
- [5] S. Jeon, J. Kim, Y. Seo, and C. Hong, "Effect of a fault and weak plane on the stability of a tunnel in rock—a scaled model test and numerical analysis," *International Journal of Rock Mechanics and Mining Sciences*, vol. 41, supplement 1, pp. 658–663, 2004.
- [6] F. Huang, H. Zhu, Q. Xu, Y. Cai, and X. Zhuang, "The effect of weak interlayer on the failure pattern of rock mass around tunnel—scaled model tests and numerical analysis," *Tunnelling and Underground Space Technology*, vol. 35, pp. 207–218, 2013.
- [7] F. Gao, K.-P. Zhou, W.-J. Dong, and J.-H. Su, "Similar material simulation of time series system for induced caving of roof in continuous mining under backfill," *Journal of Central South University of Technology*, vol. 15, no. 3, pp. 356–360, 2008.
- [8] Y.-J. Li, X.-S. Li, G.-Z. Yin, and J.-W. Yao, "Similar material experimental study on the "domino effect" of the stope pillar unstable failure of gently inclined and medium thick phosphate rock under pillar and room caving," *Disaster Advances*, vol. 5, pp. 77–82, 2012.
- [9] X. Li, Y. Li, M. Wang, and J. Wang, "Similar material experimental study on the deformation behavior of overburden rocks and mining pressure of the deep ore body of mining of Yunnan phosphate chemical group CO., LTD," *Disaster Advances*, vol. 6, pp. 363–369, 2013.
- [10] M. A. Meguid, O. Saada, M. A. Nunes, and J. Mattar, "Physical modeling of tunnels in soft ground: a review," *Tunnelling and Underground Space Technology*, vol. 23, no. 2, pp. 185–198, 2008.
- [11] W.-P. Fei, L. Zhang, and R. Zhang, "Experimental study on a geo-mechanical model of a high arch dam," *International Journal of Rock Mechanics and Mining Sciences*, vol. 47, no. 2, pp. 299–306, 2010.
- [12] S.-C. Li, Y. Zhou, L.-P. Li et al., "Development and application of a new similar material for underground engineering fluid-solid coupling model test," *Chinese Journal of Rock Mechanics and Engineering*, vol. 31, no. 6, pp. 1128–1137, 2012.
- [13] B.-C. Zuo, C.-X. Chen, C.-H. Liu, Q. Shen, G.-F. Xiao, and X.-W. Liu, "Research on similar material of slope simulation experiment," *Rock and Soil Mechanics*, vol. 25, no. 11, pp. 1805–1808, 2004.
- [14] Y. Zhang, X. Wang, Q. Liang, D. Jiang, and X. Ma, "Development of model test similar material of collapsible loess," *Chinese Journal of Rock Mechanics and Engineering*, vol. 32, no. 2, pp. 4019–4024, 2013.
- [15] W. Hui, X. Jian, G. Yu-Kun, and H. Qi-qi, "Similarity criterion analysis of goaf similar material simulation," in *Proceedings of the International Colloquium on Safety Science and Technology*, vol. 34, pp. 11–14, Shenyang, China, 2012.
- [16] L. C. Dai, "Research on simulation test of coal similar material," *Advanced Materials Research*, vol. 850–851, pp. 847–850, 2014.

Research Article

Enhanced Viscosity of Aqueous Palygorskite Suspensions through Physical and Chemical Processing

Feng-shan Zhou,¹ Tian-qi Li,¹ Yun-hua Yan,² Can Cao,¹ Lin Zhou,¹ and Yang Liu¹

¹ School of Materials Science and Technology, China University of Geosciences (Beijing), Beijing 100083, China

² The Key Laboratory of Orogenic Belts and Crustal Evolution, School of Earth and Space Sciences, Peking University, Beijing 100871, China

Correspondence should be addressed to Feng-shan Zhou; zhousf@cugb.edu.cn

Received 12 July 2014; Revised 14 August 2014; Accepted 14 August 2014

Academic Editor: Zhaohui Li

Copyright © 2015 Feng-shan Zhou et al. This is an open access article distributed under the Creative Commons Attribution License, which permits unrestricted use, distribution, and reproduction in any medium, provided the original work is properly cited.

Palygorskite has remarkable rheological properties and was used to increase the stability and viscosity of aqueous suspensions. The effects of different physical and chemical processing methods on the apparent viscosity and plastic viscosity of the palygorskite suspensions such as pressing, ultrasound scattering, acidification, and chemical additives have been released. The pressing and ultrasound scattering indicated that the dispersed state of palygorskite could be increased effectively after treatment, and the apparent viscosity of treated-palygorskite samples increased almost 2-3 times compared to that of before. The viscosity of the acid-treated palygorskite suspension was not increased. The viscosity increased with the content of bentonite in the mixture of bentonite and palygorskite in fresh water. It seemed to be not worthy to add a certain amount of bentonite to palygorskite in order to enhance viscosity and vice versa. Chemical additives appeared to have good effects on the rheological behavior of palygorskite suspension. Magnesium oxide revealed great contribution to viscosity enhancement. The main mechanism was the electrostatic attractive interaction between magnesium oxide particles with positive charges and the palygorskite rods with negative charges. This interacted force has an impact on the structural inversion of palygorskite rods and even caused the reinforcing of flocculation.

1. Introduction

Clay minerals have remarkable rheological properties and are used to increase the stability and viscosity of flowing suspensions. They tend to form gel-like structures at low solid contents [1]. This property is of great importance in a very wide range of applications for drilling fluids, paints, liquid fertilizers, wild-fire suppressants, foundry coatings, animal flowing feeds, molecular sieve binders, and a lot of aqueous suspensions in which rheological properties play a significant role [1–5].

Palygorskite forms gel structures in fresh and salt water by establishing a lattice structure of particles connected through hydrogen bonds. In the drilling industry, these properties enable the clay suspension to suspend the large dense particles of the drilling cuttings and require relatively low pump power during water circulation [1, 7]. Palygorskite, unlike bentonite, will form gel structures in salt water and is

used in special salt-water drilling mud for drilling formations contaminated with salt [8]. Palygorskite particles can be considered as charged particles with zones of positive (+) and negative (–) charges. It is the bonding of these alternating charges that allows them to form gel suspensions in salt and fresh water.

Although most clay minerals form stable and viscous suspensions when dispersed in water, the mechanisms of gel formation for each clay mineral differ because of their unique structures, particle size and shape, and composition [9, 10].

Unlike the swelling clay minerals such as montmorillonite, palygorskite as a fibrous nonswelling clay mineral, the fibre length and number of silanol groups on the surface of the fibre play an important role in aggregating fibres together [11] and forming a random network that entraps water and increases viscosity [12].

Neaman and Singer [13–15] systematically studied the rheological properties of six palygorskite samples, used them

TABLE 1: The chemical compositions, the physical properties, and the theoretical crystal structural formula of the palygorskite sample in present work.

Components	SiO ₂	Al ₂ O ₃	TiO ₂	Fe ₂ O ₃	FeO	MgO	CaO	Na ₂ O	K ₂ O	P ₂ O ₅	SO ₃
Content/wt%	64.89	12.95	1.26	8.19	0.16	9.11	1.48	0.07	1.33	0.43	0.02
Crystal structural formula: (Mg _{0.81} Al _{0.73} Fe ³⁺ _{0.36} Ca _{0.09} Ti _{0.06})(Si _{3.83} Al _{0.17})O ₁₀ (OH)·4H ₂ O Cation exchange capacity (CEC): 49.8 meq/100 g Specific surface area: 462.0 m ² /g											

as a kind of common thixotropic modifier in aqueous suspensions, and focused on the influence factors including the ratio of crystal length to diameter, concentration of sodium chloride (NaCl), and pH. The effects of pressing modification and adding magnesium oxide (MgO) [16, 17], ultrasound scattering [18, 19], acidification [6, 20], and even the mixed palygorskite-bentonite suspensions [21] on the rheological properties of palygorskite suspensions also have been studied.

High-pressure homogenization process with solvent and electrolytes with dispersion properties of palygorskite were investigated in detail by Xu et al. [22–24]. They dispersed the natural palygorskite in six solvents including distilled water, methanol, ethanol, isopropanol, dimethyl formamide, and dimethyl sulfoxide and then carried out high-pressure homogenization. They confirmed that colloidal stability and suspension viscosity were affected by the solvent nature, and a much higher viscosity was obtained by dispersing palygorskite in isopropanol, but the good colloidal stability was obtained in dimethyl sulfoxide (DMSO) solvent. A series of palygorskite samples modified with inorganic potassium electrolytes including KCl, KBr, KI, KH₂PO₄, KHSO₄, K₂HPO₄, K₂SO₄, and K₃PO₄ were prepared with the aid of high-pressure homogenization. A stable suspension was obtained when palygorskite was dispersed in K₂SO₄ solutions. Because the requirement of the viscosity is more than the stability for palygorskite suspension, obviously, high prices and toxic solvents in their works would be limiting the value of industrial applications.

However, no one had systematically studied the influence of viscosity and the methods of enhanced viscosity for palygorskite gel. The purpose of the present work is to study the effects of different physical and chemical processing methods, such as pressing, ultrasound scattering, acidification, and chemical additives, on the apparent viscosity and plastic viscosity of the aqueous palygorskite suspensions.

2. Materials and Methods

2.1. Materials. Palygorskite mineral sample with purity greater than 95% was received from Mingguang Palygorskite Mining Co., Ltd. (Anhui, China). The average length of the palygorskite rods is around 1 μm, and the average aspect ratio is about 20. The chemical compositions, the physical properties, and the theoretical crystal structural formula of the palygorskite sample in present work are listed in Table 1.

There are two bentonite mineral samples used in this work. One bentonite sample was obtained from Sinopec Shengli Oilfield Co., Ltd. (Shandong, China). Another bentonite containing palygorskite sample from Iraq Anbar was

obtained from Beijing Taihua Bentonite Science & Technology Development Co., Ltd. (Beijing, China). Industrial grade magnesium oxide (also named calcined magnesia; light-burned magnesia) (MgO) and magnesium hydroxide (Mg(OH)₂) samples were obtained from Dandong Yilong High Science & Technological Materials Co., Ltd. (Liaoning, China).

2.2. Instruments. The experiment of pressing palygorskite was conducted on Jinniu JL-80 vertical grinder (1.5 KW; Hualian Industry Co., Ltd.) (Beijing, China). The ultrasonic dispersion test was carried out by JY92-IIDN ultrasonic cell crusher (20–24 KHz, 650 W; Ningbo Scientz Biotechnology Co., Ltd.) (Zhejiang, China). The modified palygorskite was filtrated by SHB-III water circulation pumps (180 W; Xi'an Taikang Biotechnology Co., Ltd.) (Shaanxi, China) and dried by a 101-3 electric blast drying oven (300°C maximum; Shanghai Rolling-gen Equipment Co., Ltd.) (Shanghai, China). The gelation of samples dispersion was prepared after being stirred by GJ-2S digital display high-speed agitator (180 W, 4000–11000 rpm). The rheological parameters of suspensions were conducted by ZNN-D6A six-speed rotary viscometer (speed: 3, 6, 100, 200, 300, and 600 rpm, viscosity range: 0–300 mPa·s). Both of the latter instruments were manufactured by Qingdao Haitongda Special Instrument Co., Ltd. (Shandong, China).

2.3. Methods

2.3.1. Palygorskite Modification

Pressing. A certain amount of palygorskite and tap-water was mixed and pressed by a vertical extruder. After that, the palygorskite was collected, dried, and ground.

Ultrasound Scattering. 25 g palygorskite and a certain amount of tap-water were added into an 80 mL beaker, stirred, and then loaded onto the platform of an ultrasonic cell crusher. The time of ultrasound scattering on the platform of ultrasonic cell crusher was 10 min and repeated 2-3 times to make a better dispersion.

Acidification. The clay mineral was treated with hydrochloric acid at a concentration of 2 mol/L by liquid and a solid ratio of 10 to 1 in the flask, under mechanical stirring (550 rpm) in dispersion at room temperature for 1 h. Then the sample was filtrated, followed by washing with distilled water until a pH value 3-4 was reached.

TABLE 2: The effect of pressing on the rheological parameters of palygorskite suspension.

Samples of palygorskite	Rheological parameters					
	θ_{600} (dia)	θ_{300} (dia)	AV (mPa·s)	PV (mPa·s)	YP (Pa)	YP/PV (Pa/mPa·s)
Unpressing	39	35	19.5	4.0	15.84	3.96
Unpressing with 1% MgO	59	44	29.5	15.0	14.82	2.00
Pressing without MgO	48	41	24.0	7.0	17.37	2.48
Pressing with 1% MgO	85	75	42.5	10.0	33.22	3.32

Chemical Additives. Certain amounts of additives were added into 6.4 w/v% palygorskite dispersions. The dosage of chemical additives (%) in the tables and the figures was the ratio of mass between chemicals and palygorskite.

The dispersions were stirred mechanically at 8000 rpm for 20 min at room temperature and hydration was conducted for 24 h. The term of hydration was an ageing process of water penetrating the interlayer spaces and concomitant adsorption with the clay swelling and colloidization.

2.3.2. Rheological Parameters Measurement. Darley and George [8] concluded the common composition and properties of drilling and completion fluids. According to the American Petroleum Institute (API) recommended practice (2009) [25], the parameters of the palygorskite gel in the drilling fluid suspension samples were prepared and measured under the specification and standard procedures. The viscosity and gel strength of the modified gels were tested by a rotating viscometer (ZNN-D₆S). The hydrated gels underwent mechanical stirring at 8000 rpm for a further 20 min. This preparation step before measuring the viscosity was to make the dispersion even and flowing. And then the viscosity was measured at different shear rates (different stirring velocity).

2.3.3. Rheological Theory. According to Bingham-plastic model, the rheological parameters, including AV (apparent viscosity), PV (plastic viscosity), YP (yield point), and RYP (ratio of yield and plastic viscosity), were calculated with the dial readings of 300 rpm and 600 rpm using the following formulas according to the API recommended practice of standard procedures [25]:

$$\begin{aligned}
 AV &= 0.5\theta_{600} \text{ (mPa} \cdot \text{s)} \\
 PV &= \theta_{600} - \theta_{300} \text{ (mPa} \cdot \text{s)} \\
 YP &= 0.511 (\theta_{300} - PV) \text{ (Pa)} \\
 RYP &= \frac{YP}{PV} \text{ (Pa/mPa} \cdot \text{s)},
 \end{aligned} \tag{1}$$

where θ_{600} (dia) was the dial reading of rotating viscometer at 600 rpm and θ_{300} (dia) was the dial reading of rotating viscometer at 300 rpm.

2.3.4. Microscopic Examination. The morphology of the palygorskite and modified palygorskite with additives was

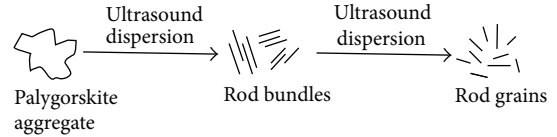


FIGURE 1: The mechanism of ultrasound scattering dispersion for palygorskite aggregates.

observed in a Quanta 200FEG environmental scanning electron microscope (SEM). All of the raw minerals were firstly made to powder samples, which were dried from dilute 0.2% dispersions before the SEM examination. The modified palygorskite gel samples were also dried out from the same concentration before SEM measurement.

3. Results and Discussion

3.1. Pressing Effect. Pressing as an effective way to break up close and compact bulks of natural palygorskite rods could more easily disperse palygorskite fibers in water. Experimental measurement of viscosity of pressed palygorskite showed that the apparent viscosity increased from 19.5 mPa·s to 42.5 mPa·s (Table 2).

Pressing can be applied as a useful approach to enhance better dispersion of palygorskite particles, especially for raw palygorskite aggregates. However, in our opinion, compared to effective viscosity enlarging by using small amount of chemical, the pressing with the inefficient and high cost was not a suitable technique for enhanced viscosity of palygorskite suspension in some applications with low added value such as drilling fluids.

3.2. Ultrasound Scattering Effect. Song et al. [18] found that after treatment with ultrasound the palygorskite crystal bundles were crushed into crystal needles, generating palygorskite nanoparticles. What is more, Zhao et al. [19] studied the dispersion of palygorskite in a polypropylene matrix, and their SEM and TEM analysis results showed that ultrasonic oscillation promoted the dispersion of palygorskite particles (Figure 1).

Under the condition of ultrasound dispersion, the apparent viscosity was raised rapidly from 19.5 mPa·s to 54 mPa·s (Table 3). The enhancement of viscosity was related to the fact that ultrasonic cavitation could cause local high temperature and high pressure. The shock wave and microjet in dispersion brought about intense collisions of palygorskite aggregates

TABLE 3: The effect of ultrasound scattering on the rheological parameters of palygorskite suspension.

Samples of palygorskite	Rheological parameters					
	θ_{600} (dia)	θ_{300} (dia)	AV (mPa·s)	PV (mPa·s)	YP (Pa)	YP/PV (Pa/mPa·s)
No ultrasound scattering	39	35	19.5	4	15.84	3.96
Ultrasound scattering	108	92	54.0	16	38.84	2.43

in aqueous suspensions just like the same dispersion mechanism in polypropylene matrix described in Figure 1.

3.3. Acidification Effect. Many practices using acid to purify palygorskite have been reported in the literature. For example, Neaman and Singer [20] used acid to remove carbonates and other cement impurities. Other researchers used acidification to break up the cluster of closely bound fibers to increase specific surface area for good dispersion and absorption. The raw material in the experiment was of high purity. Octahedral cations dissolved and crystal structure was even changed because of the high concentration of acid and reaction time. Chen et al. [6] investigated the structural changes of palygorskite with reaction to acid; their results indicated that dissolution of octahedral reactions increased with an increase in acid concentration and reaction time. When octahedral cations were dissolved completely, the final product was mesoporous amorphous silica-fiber (Figure 2).

The study showed that the gel of the acidified palygorskite in dispersion came to serious sedimentation after hydration. Initially, with the ratio of acid to palygorskite being 10 to 1 and concentration of HCl being 2 mol/L, the apparent viscosity value was only 5 mPa·s. By reducing the concentration and amount of acid solution (weight ratio of acid to palygorskite was 4 to 1; concentration of HCl was 1 mol/L), the AV still measured only 10 mPa·s. Obviously, acidizing palygorskite viscosity was not enhanced in the present work; the opposite is the case.

3.4. Effects of Bentonite. Several studies have been carried out in the past to understand the rheological properties of standard clays [9, 10, 13–15, 26–28]. However, there are a lot of works on the rheological properties of mixed clay suspensions in recent years. The influence of montmorillonite addition on the rheological behaviour of palygorskite suspensions was investigated by Neaman and Singer [13–15]. Rheological properties of palygorskite-bentonite mixed clay suspensions were studied by Chemedda et al. [21].

The limited information is considered important because most clay used such as in drilling fluid applications usually contains more than one type of clay minerals along with nonclay minerals. For example, palygorskite occurs in association with smectite in most of the known world palygorskite deposits [6]. Therefore it is worthwhile to understand the rheological behavior of suspensions containing mixtures of clay minerals.

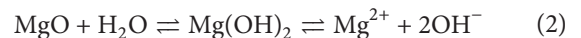
The most difference of rheological properties between palygorskite and bentonite was that palygorskite can be used in fresh water and salt water, but the bentonite is only

used in fresh water. Figure 3 shows the effects of bentonite addition on the viscosity of bentonite-palygorskite mixture. The viscosity of the mixture increased with the increase of content of bentonite in mixture in fresh water. But the viscosity of the mixture decreased with the increase of content of bentonite in mixture in salt water because of the poor salt tolerance of bentonite. Taking into account the effect, nature, and the price ratio, it was not worthy to add a certain amount of bentonite to palygorskite, because the palygorskite is normally used in salt water condition. For the same reason, it was also worthless to add a certain amount of palygorskite to bentonite.

In contrast to the admixture of bentonite and palygorskite, some kinds of natural coexisting bentonite-palygorskite clay mixture would have a very high viscosity (Figure 4), because their random network structures were formed more easily which entrapped water and increased viscosity. But for some others, the same viscosity behavior does not appear [6]; the real reason is still unknown.

3.5. Effects of Magnesium Oxide. The experimental measurements of samples with chemical additives (Figure 5) exhibited that the sample added MgO showed an increased viscosity value with lower MgO content. This higher viscosity value exhibited better cuttings suspension and carrying capacity in drilling fluids.

When MgO particles were added to water, the reaction happened as follows:



The cation exchange ability of Mg^{2+} was better than Na^+ . The Mg^{2+} entered into the channels of clay mineral particles and caused shrinkage of the electrical double layer. The shrinkage of the electrical double layer easily formed face-face aggregation. At the same time, the absorbed Mg^{2+} bridged edge and face formed edge-edge and edge-face flocculation.

As already stated above, the PV reflected the internal friction of suspended particles, the liquid phase, and their interface. Flocculation reinforced the suspension network structure with expression of an increase on viscosity.

SEM micrographs of the palygorskite with $\text{Mg}(\text{OH})_2$ and MgO (Figure 6) revealed that the palygorskite had a fibrous morphology and that $\text{Mg}(\text{OH})_2$ and MgO particles with positive charge dispersed in the palygorskite scaffolding structure with negative charge. The electrostatic attractive interaction also reinforced the palygorskite structure, confirming the increase in viscosity.

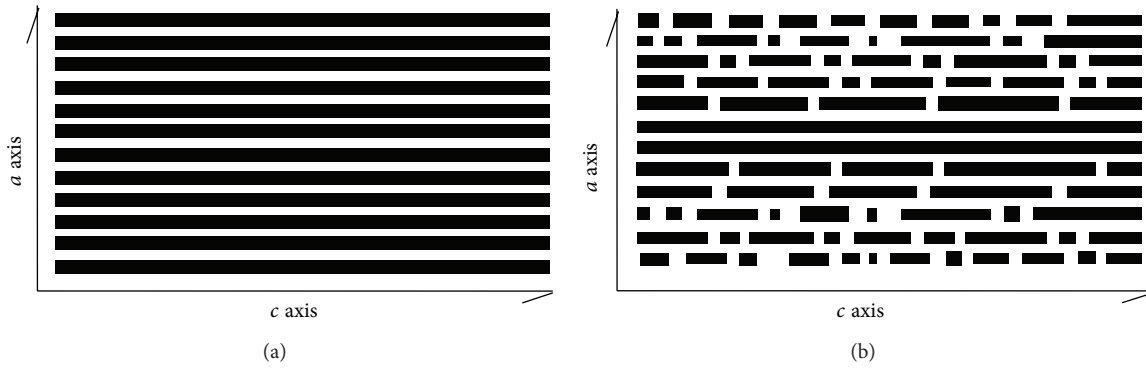


FIGURE 2: The channel structure change of palygorskite with acidification treatment [6]. (a) The original channel structure of palygorskite. (b) The channel structure of palygorskite after acidification with hydrochloric acid.

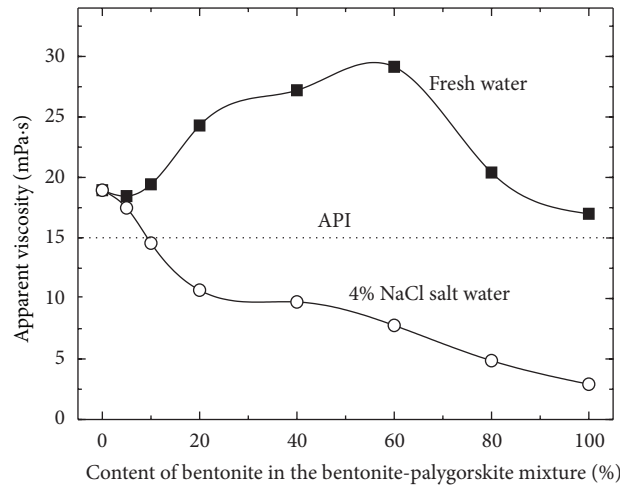


FIGURE 3: The effects of bentonite addition on the viscosity of suspension of bentonite-palygorskite mixture in fresh water and salt water.

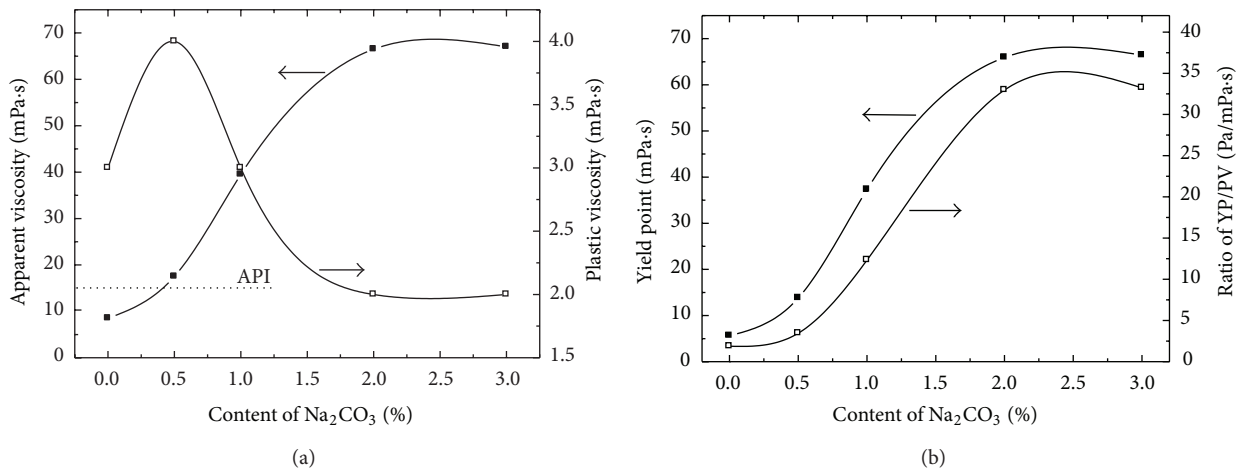


FIGURE 4: The viscosity of a natural coexisting clay mixture sample with 7% palygorskite and 57% sodium-calcium based hybrid bentonite from Iraq Anbar. (a) The apparent viscosity and plastic viscosity of the natural coexisting clay mixture. (b) The yield point and ratio of YP/PV of the natural coexisting clay mixture.

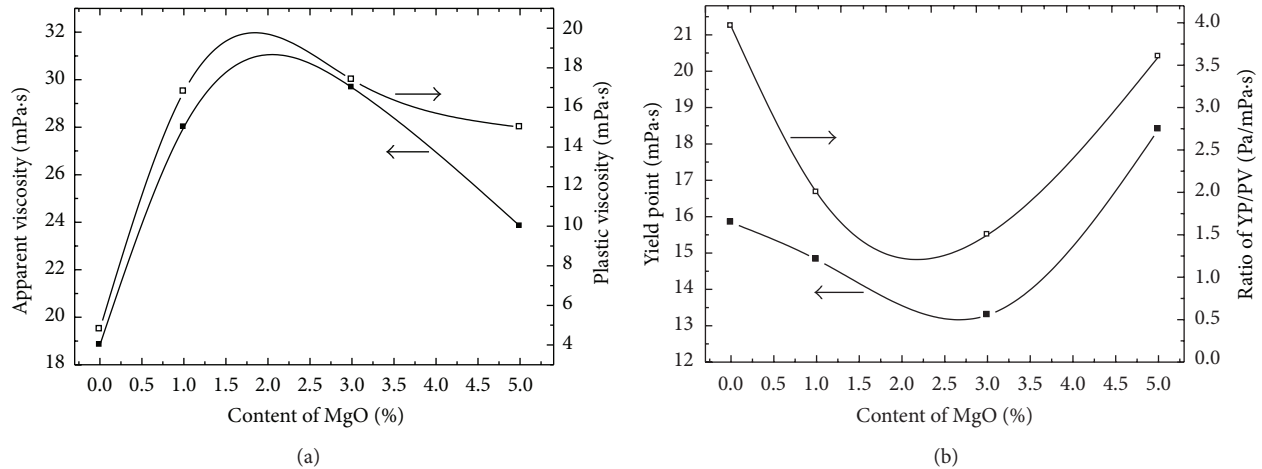


FIGURE 5: The effects of MgO on the rheological parameters of palygorskite suspension. (a) The apparent viscosity and plastic viscosity of palygorskite suspension. (b) The yield point and ratio of YP/PV of palygorskite suspension.

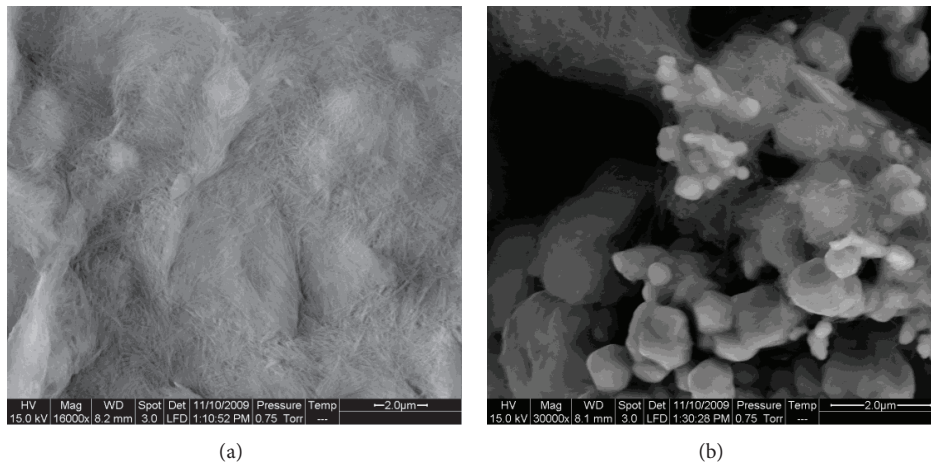


FIGURE 6: The change of scanning electron microscope photograph of palygorskite processed with magnesium oxide. (a) SEM micrograph of original unmodified palygorskite. (b) SEM micrograph of palygorskite modified adding MgO.

4. Conclusions

The results of the pressing and ultrasound scattering effect studies indicated that the dispersed state and increasing viscosity of clay mineral gel could be adjusted by the two methods effectively. The mechanisms were that pressing broke up close and compact palygorskite rods clusters, and ultrasonic cavitations caused intense collisions within the palygorskite aggregate. Consequently, pressing and ultrasound scattering could be used as useful modification methods for improving the viscosity of the aqueous suspension of palygorskite.

The acidification effect would not increase the viscosity of palygorskite, perhaps because the high concentration acidification was harmful for gelation and dispersion of palygorskite.

The viscosity of the mixture of bentonite and palygorskite increased with the increase of content of bentonite in fresh water. But the viscosity of the mixture decreased with the increase of content of bentonite in salt water because of the

poor salt tolerance of bentonite. It seemed to be not worthy to add a certain amount of bentonite to palygorskite in order to enhance viscosity.

Chemical additives showed good effects on the rheological and thixotropic behavior of palygorskite suspension. The results of adding MgO revealed that the contribution of MgO to viscosity caused the reinforcing of flocculation. Furthermore, the analysis showed that electrostatic attractive interaction between MgO particles dispersed in the scaffolding structure with positive charges and the palygorskite rods with negative charges had impact on the inversion of palygorskite rods configuration. In drilling applications, this higher viscosity value will provide better cuttings suspension and carrying capacity.

Conflict of Interests

The authors declare that there is no conflict of interests regarding the publication of this paper.

Acknowledgment

Thanks are due to Dr. Susan Turner (Brisbane) for the helpful comments on the paper and for improving the English language.

References

- [1] P. F. Luckham and S. Rossi, "The colloidal and rheological properties of bentonite suspensions," *Advances in Colloid and Interface Science*, vol. 82, no. 1–3, pp. 43–92, 1999.
- [2] N. P. Chafé and J. R. de Bruyn, "Drag and relaxation in a bentonite clay suspension," *Journal of Non-Newtonian Fluid Mechanics*, vol. 131, no. 1–3, pp. 44–52, 2005.
- [3] E. Galan, "Properties and applications of palygorskite-sepiolite clays," *Clay Minerals*, vol. 31, no. 4, pp. 443–453, 1996.
- [4] E. Galan and A. Singer, *Developments in Palygorskite-Sepiolite Research, A New Outlook on these Nanomaterials*, vol. 3 of *Developments in Clay Science*, Elsevier, New York, NY, USA, 2011.
- [5] H. H. Murray, "Occurrences, processing and application of kaolins, bentonites, palygorskite-sepiolite, and common clays," in *Developments in Clay Science*, vol. 2 of *Applied Clay Mineralogy*, Elsevier, 2007.
- [6] T. H. Chen, Y. L. Feng, and X. Shi, "Study on products and structural changes of reaction of palygorskite with acid," *Journal of the Chinese Ceramic Society*, vol. 31, no. 10, pp. 959–964, 2004.
- [7] V. C. Kelessidis, C. Tsamantaki, and P. Dalamarinis, "Effect of pH and electrolyte on the rheology of aqueous Wyoming bentonite dispersions," *Applied Clay Science*, vol. 38, no. 1–2, pp. 86–96, 2007.
- [8] H. C. H. Darley and R. G. George, *Composition and Properties of Drilling and Completion Fluids*, Gulf Professional, Houston, Tex, USA, 6th edition, 2011.
- [9] H. Heller and R. Keren, "Rheology of Na-rich montmorillonite suspension as affected by electrolyte concentration and shear rate," *Clays and Clay Minerals*, vol. 49, no. 4, pp. 286–291, 2001.
- [10] E. Paineau, L. J. Michot, I. Bihannic, and C. Baravian, "Aqueous suspensions of natural swelling clay minerals. 2. Rheological characterization," *Langmuir*, vol. 27, no. 12, pp. 7806–7819, 2011.
- [11] T. C. Simonton, S. Komarneni, and R. Roy, "Gelling properties of sepiolite versus montmorillonite," *Applied Clay Science*, vol. 3, no. 2, pp. 165–176, 1988.
- [12] G. E. Christidis, P. Katsiki, A. Pratikakis, and G. Kacandes, "Rheological properties of palygorskite—smectite suspensions from the Ventzia basin, W. Macedonia, Greece," *Bulletin of the Geological Society of Greece*, vol. 43, pp. 2562–2569, 2011.
- [13] A. Neaman and A. Singer, "Kinetics of hydrolysis of some palygorskite-containing soil clays in dilute salt solutions," *Clays and Clay Minerals*, vol. 48, no. 6, pp. 708–712, 2000.
- [14] A. Neaman and A. Singer, "Rheology of mixed palygorskite—montmorillonite suspensions," *Clays and Clay Minerals*, vol. 48, no. 6, pp. 713–715, 2000.
- [15] A. Neaman and A. Singer, "Rheological properties of aqueous suspensions of palygorskite," *Soil Science Society of America Journal*, vol. 64, no. 1, pp. 427–436, 2000.
- [16] J. Zhou, L. J. Liu, N. Liu, and X. F. Liu, "Effects of Mg(OH)₂ and MgO on rheological behavior of attapulgite clay-water suspensions," *Journal of Hefei University of Technology*, no. 6, pp. 58–63, 1999.
- [17] J. Zhou, N. Liu, Y. Li, and Y. J. Ma, "Microscopic structure characteristics of attapulgite," *Bulletin of the Chinese Ceramic Society*, vol. 18, no. 6, pp. 50–55, 1999.
- [18] R. F. Song, L. Y. Yang, J. Sheng, N. X. Shen, and T. W. Kang, "The surface modification and characterization of nano-attapulgite," *Bulletin of the Chinese Ceramic Society*, vol. 22, no. 3, pp. 36–39, 2003.
- [19] L. Zhao, Q. Du, G. Jiang, and S. Guo, "Attapulgite and ultrasonic oscillation induced crystallization behavior of polypropylene," *Journal of Polymer Science B: Polymer Physics*, vol. 45, no. 16, pp. 2300–2308, 2007.
- [20] A. Neaman and A. Singer, "Possible use of the Sacalum (Yucatan) palygorskite as drilling muds," *Applied Clay Science*, vol. 25, no. 1–2, pp. 121–124, 2004.
- [21] Y. C. Chemedá, G. E. Christidis, N. M. Tauhid-Khan, E. Koutsopoulou, V. Hatzistamou, and V. Kelessidis, "Rheological properties of palygorskite—bentonite and sepiolite—bentonite mixed clay suspensions," *Applied Clay Science*, vol. 90, pp. 165–174, 2000.
- [22] J. Xu, W. Wang, and A. Wang, "Effects of solvent treatment and high-pressure homogenization process on dispersion properties of palygorskite," *Powder Technology*, vol. 235, pp. 652–660, 2013.
- [23] J. Xu, W. Wang, and A. Wang, "Superior dispersion properties of palygorskite in dimethyl sulfoxide via high-pressure homogenization process," *Applied Clay Science*, vol. 86, pp. 174–178, 2013.
- [24] J. Xu, W. Wang, and A. Wang, "Influence of anions on the electrokinetic and colloidal properties of palygorskite clay via high-pressure homogenization," *Journal of Chemical and Engineering Data*, vol. 58, no. 3, pp. 764–772, 2013.
- [25] ANSI/API Recommended Practice 13B-1, *Recommended Practice for Field Testing Water-Based Drilling Fluids*, American Petroleum Institute, 4th edition, 2009.
- [26] S. Abend and G. Lagaly, "Sol-gel transitions of sodium montmorillonite dispersions," *Applied Clay Science*, vol. 16, no. 3–4, pp. 201–227, 2000.
- [27] L. V. Amorim, C. M. Gomes, H. L. Lira, K. B. Franca, and H. C. Ferreira, "Bentonites from Boa Vista, Brazil: physical, mineralogical and rheological properties," *Materials Research*, vol. 7, no. 4, pp. 583–593, 2004.
- [28] G. E. Christidis, A. E. Blum, and D. D. Eberl, "Influence of layer charge and charge distribution of smectites on the flow behaviour and swelling of bentonites," *Applied Clay Science*, vol. 34, no. 1–4, pp. 125–138, 2006.

Research Article

Interactions between Phosphoric/Tannic Acid and Different Forms of FeOOH

Lefu Mei,¹ Libing Liao,¹ Zise Wang,² and Chunchun Xu³

¹School of Material Sciences and Technology, China University of Geosciences, Beijing 100083, China

²China Science and Technology Museum, Beijing 100029, China

³School of Material Sciences and Technology, Beijing University of Chemical Technology, Beijing 100029, China

Correspondence should be addressed to Lefu Mei; mlf@cugb.edu.cn and Libing Liao; clayl@cugb.edu.cn

Received 23 July 2014; Accepted 17 September 2014

Academic Editor: Zhaohui Li

Copyright © 2015 Lefu Mei et al. This is an open access article distributed under the Creative Commons Attribution License, which permits unrestricted use, distribution, and reproduction in any medium, provided the original work is properly cited.

Alpha, beta, gamma, and delta hydroxyl ferric oxides (FeOOH), as the most common rust layers on iron surface, play different roles in iron preservation. Using modern surface analysis technologies such as X-ray diffraction (XRD), infrared spectra (IR), X-ray photoelectron spectroscopy (XPS), and scanning electron microscopy (SEM), we studied the interactions between these four types of synthetic FeOOH and phosphoric and tannic acid of different concentrations and proportions. A 3% tannic acid + 10% phosphoric acid + FeOOH was the most suitable formula for rust stabilizer and its reaction products were made up of iron phosphate and chelate of iron and tannin. This research provided technical basis in distinguishing FeOOH and selecting rust layer stabilizer for the preservation of iron, especially iron cultural relics.

1. Introduction

Structure and composition of corrosion products on iron are two important factors of causing its further corrosion, apart from environmental factors, iron components, and defect and inclusion in iron. There are two types of rust layers: a loose outer rust layer and a dense inner rust layer. The former was composed of α -FeOOH, γ -FeOOH, magnetite (Fe_3O_4), H_2O , and amorphous ferric oxyhydroxide ($\text{FeO}_x(\text{OH})_{3-2x}$, $x = 0-1$), while the latter was composed mainly of Fe_3O_4 with a little α -FeOOH [1, 2]. The β -FeOOH is a typical product of FeCl_3 hydrolysis, whereas α -FeOOH is that of $\text{Fe}(\text{NO}_3)_3$ hydrolysis and under specific conditions these hydrolytic products may transform to α - Fe_2O_3 [3–5]. The δ -FeOOH is a type of amorphous hydroxyl oxide rust layer on iron material surface [6], forming a compact rust layer that enhances corrosion resistance of the steel [7].

The underlying corrosion of carbon steel was dependent on the inherent properties of the rust layers formed under different conditions such as composition and structure with β -FeOOH exerting significant influence among all the iron oxides [8]. In terms of reaction with $\text{Fe}(\text{OH})_2$ to produce

Fe_3O_4 , the following order was observed: β -FeOOH > α -FeOOH \gg γ -FeOOH [9].

Rust converters are chemical formulations that can be applied to corroded surfaces causing their passivation and elimination of possible further attack after the application of a coating [10]. To reduce the effects of hydroxyl ferric oxide on steel preservation, surface stabilizing treatment of rust layer has been widely used in the steel anticorrosion field. By employing a processing method of a chemical conversion film, the hydroxyl oxide rust layer on the iron may undertake a chemical conversion and form porous membrane barrier with good ventilation property and water permeability [11]. The excellent atmospheric corrosion resistance of the phosphoric Dhar pillar iron was attributed to the formation of a protective passive film on the surface [12]. Chemical conversion film, as inoxidizing coating of metal, reduces chemical activity of the metal and increases thermodynamic stability of steel in environmental medium. In addition, the surface products may also play a certain role in metal isolation from environmental medium. Chemical conversion films such as thin layer, exquisite crystallization, and porosity, may be combined with sealing materials. Accordingly, industrial

anticorrosion methods provide research foundation for surface stabilizing treatment of iron relics.

The chromate salt passivation treatment method [13] is an effective chemical conversion technology. In spite of a good corrosion prevention effect, its use is limited by environmental regulations, due to high toxicity and carcinogenicity of hexavalent chromium [14–16].

Phosphate covering by forming a phosphate film on metals using phosphoric acid or zinc phosphate, manganese phosphate, or iron phosphate solution possesses many advantages, such as anticorrosion, wear-resisting, antifriction, increasing lubricity, and promoting base adhesion between coating and metal [17]. Phosphorus processing, therefore, is widely applied in processing steel parts, especially coating layer process [18]. Separately, pretreatment of reinforced steel surface with tannic acid based rust converter prior to the application of zinc rich coating improved the corrosion resistance appreciably [19, 20].

As one of metal surface treatment methods, tannins have potential application prospects, with low toxicity, low pollution, low usage volume, and even color with excellent corrosion-resistant performance [21]. Tannins as corrosion inhibitors were applied both in solvent and waterborne pretreatment formulations [22]. These formulations could be applied on partially rusted substrates, reducing the effort needed for cleaning the surface by methods which proved to be expensive and are not applicable in many situations [21]. Thus, combination of phosphoric acid and tannic acid may provide a synergistic effect on corrosion resistance of iron cultural relics.

In this study, X-ray diffraction (XRD), infrared spectroscopy (IR), X-ray photoelectron spectrometry (XPS), and transmission electron microscopy (TEM) were used to characterize the four types of FeOOH, as well as to investigate the interactions between FeOOH and mixed solutions containing different concentrations and proportions of phosphoric acid and tannic acid in order to provide technical basis to distinguish these types of FeOOH and enable rust layer stabilizer selection for preservation of steel, especially for iron cultural relics.

2. Experimental Details

2.1. Preparation of α -, β -, γ -, and δ -FeOOH. Rust analyses revealed the presence of crystalline magnetite ($\text{Fe}_{3-x}\text{O}_4$), α - Fe_2O_3 (haematite), goethite (α -FeOOH), lepidocrocite (γ -FeOOH), akaganeite (β -FeOOH), and amorphous δ -FeOOH phases [12]. Thus, the four FeOOH polymorphs were prepared to investigate their effects on iron rust.

The α -FeOOH was prepared using a solution containing 40 g of FeSO_4 and 8 g of NaOH per liter of deionized (DI) water. The temperature was adjusted to 50°C and pH to 13 with 10 wt% NaOH. The solution was fluxed with oxygen for 8 h. The precipitates were washed with 10 portions of DI water until the filtrate became neutral in pH before being dried at 100°C.

The γ -FeOOH was prepared using a solution made of 60 g of $\text{FeCl}_2 \cdot 4\text{H}_2\text{O}$ in 1 L of DI water. Meanwhile, 84 g of

urotropine and 21 g of NaNO_2 each were dissolved in 300 mL of DI water. After the $\text{FeCl}_2 \cdot 4\text{H}_2\text{O}$ solution was mixed with urotropine solution, NaNO_2 was added into the mixture under constant stir at room temperature. The mixture was heated to 60°C under constant stir for 3 h. The precipitates were washed with hot water and dried at 60°C.

The β -FeOOH was prepared using a 0.2 M FeCl_3 solution heated to 60°C for 5 h. Then, small quantities of 3.175 mM EDTA and ammonia were added. The precipitates were washed with DI water until no Cl^- was detected before being dried at 70°C for 24 h.

The δ -FeOOH was prepared using a solution made of 40 g FeSO_4 and 8 g NaOH per liter of DI water. A 10 wt% NaOH solution was added dropwise till abundant brown precipitates were formed at room temperature. Then, small quantities of EDTA were added before the precipitates were filtered out.

2.2. Test on the Influence of β -FeOOH and γ -FeOOH on Iron Rusting. Archaize iron was used as the experimental material. It had a composition of (wt%) 4.17% C, 0.59% Si, 0.32% Mn, 0.087% S, and 0.017% P. The samples were cut into coupons each with a dimension of 15 mm \times 15 mm \times 3 mm. A corrosion cell with a dimension of 10 mm \times 10 mm \times 0.5 mm was cut in the middle (Figure 1). One g synthetic β -FeOOH powder and one g synthetic γ -FeOOH powder were added into separate cells. The FeOOH powder was pressed with a glass slide. A drop of each of the following corrosion media was added to the corresponding cell each day Monday through Friday for 10 months: 0.01 mol/L NO_3^- , 0.01 mol/L Cl^- , 0.01 mol/L HSO_4^- , and 0.01 mol/L $\text{Cl}^- + 0.01$ mol/L HSO_4^- . At the end of the experiment the specimens were encapsulated into epoxy resin. The resin was carefully ground till the rust layer and iron clearly appeared. Observation of propagation of rust under the influence of NO_3^- , Cl^- , HSO_4^- , and $\text{Cl}^- + \text{HSO}_4^-$ was made using scanning electron microscope (SEM).

2.3. Interactions between FeOOH and Phosphoric Acid/Tannic Acid. To each test tube, 2 g of β -FeOOH, γ -FeOOH, or δ -FeOOH was added. Then, 20 mL of tannic acid + phosphoric acid solution of different concentrations was added (Table 1). The tubes were sealed and shaken for varying amounts of time and then were allowed left aside for a while to ensure complete reaction inside. At the end of reaction, the products were filtered, washed with DI water repeatedly, and dried at 50°C.

2.4. Characterization of FeOOH. Phase identification was conducted using an XRD-6000 X-ray diffractometer (Shimadzu, Japan) with a $\text{CuK}\alpha$ radiation ($\lambda = 1.5418 \text{ \AA}$) at 40 kV and 30 mA, a scanning speed of 5°/min, and a scan range of 3–90°. FTIR spectra were acquired on a Bruker VECTOR 22 infrared spectrometer at a resolution of 2 cm^{-1} and a scan range of 4000–400 cm^{-1} with a KBr pressing method. The morphology of FeOOH was characterized by a TEM. Power samples were added to anhydrous ethanol and ultrasonicated for 30 minutes. A little drip of suspension was put onto a copper mesh and dried naturally before TEM observation.

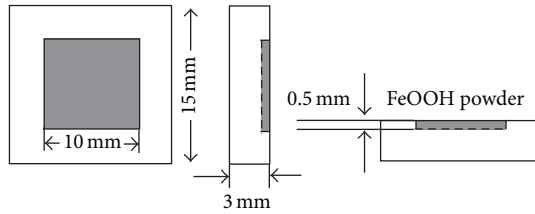


FIGURE 1: Test device for the study of iron corrosion in the presence of different types of FeOOH.

TABLE 1: The combinations of tannic acid/phosphoric acid (wt%).

Number	Tannic acid/phosphoric acid	Labeling
1	3% tannic acid + 10% phosphoric acid	3T-10P
2	3% tannic acid + 20% phosphoric acid	3T-20P
3	3% tannic acid + 30% phosphoric acid	3T-30P
4	5% tannic acid + 10% phosphoric acid	5T-10P
5	5% tannic acid + 20% phosphoric acid	5T-20P
6	5% tannic acid + 30% phosphoric acid	5T-30P

The elemental composition and valence state of elements were investigated by XPS (British VG's MCROLAB MK II X-ray photoelectron spectroscopy). Magnesium was used as X-ray photon source with a power of 160 W. The energy analyser was set at 50 eV. The focusing voltage was 3 kV. An argon pressure of 1×10^{-4} Pa and a vacuum pressure of 0.5×10^{-6} Pa were used for sputtering. The angle between Ar^+ ions sputtering gun and sample surface was 45° . Scan started 5 min after Ar^+ ions sputtering.

3. Results and Discussion

3.1. Microstructures and Structures of FeOOH. FTIR spectra of the samples prepared in the present work showed typical features of α -, β -, γ -, and δ -FeOOH (Figure 2). The FTIR bands recorded at 1628 cm^{-1} were ascribed to the $-\text{OH}$ stretching vibration, whereas the bands at 883 and 795 cm^{-1} were ascribed to the $-\text{OH}$ bending modes in α -FeOOH [23]; bands at 847 and 696 cm^{-1} were ascribed to the $-\text{OH}$ bending modes in β -FeOOH [24]; nearby bands at 1020 and 750 cm^{-1} were the bending vibration of $-\text{OH}$ modes in γ -FeOOH [12]; and bands at 1120 and 975 cm^{-1} were the bending vibration of OH modes in δ -FeOOH [25]. The four types of FeOOH were also confirmed by XRD analyses (Figure 3). Under the TEM observation, the α -FeOOH was granular, β -FeOOH appeared as rod-shaped, while γ -FeOOH looked like fine needles, and δ -FeOOH was irregularly cotton-like (Figure 4). Different types of corrosion products would cause different degrees of iron corrosion. As α -FeOOH is relatively stable, it may attribute to nondetrimental rust. On the other hand, the club-shaped β -FeOOH and fine needle-like γ -FeOOH had loose texture that could store large amounts of moisture, resulting in more iron corrosion.

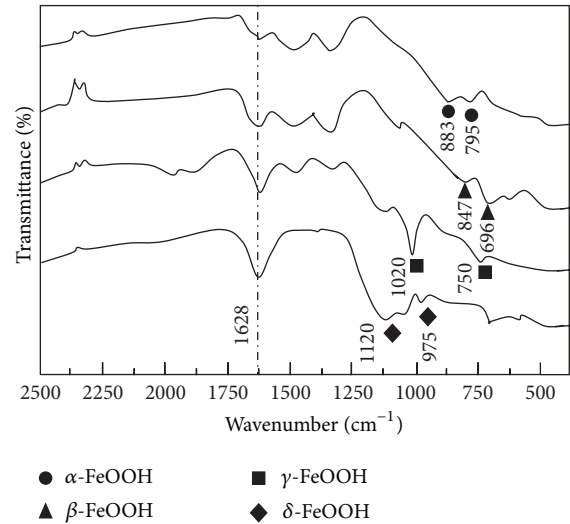


FIGURE 2: FTIR spectra of different forms of FeOOH. ●: α -FeOOH; ▲: β -FeOOH; ■: γ -FeOOH; ◆: δ -FeOOH.

3.2. Influence of β -FeOOH and γ -FeOOH on Corrosion of Archaeological Iron. Corrosion morphologies of the surface between cast iron and β -FeOOH or γ -FeOOH under the action of different ions NO_3^- , Cl^- , HSO_4^- , and $\text{Cl}^- + \text{HSO}_4^-$ were illustrated in Figure 5. FeOOH was sandwiched in between epoxide resin on top and cast iron on bottom. The boundaries were marked with white lines to help delineate the rust surface.

The surface between γ -FeOOH and cast iron varied significantly with different types of ions. The surface was relatively flat when NO_3^- was used (Figure 5(a)). Similar to NO_3^- , a clear γ -FeOOH layer could be seen under the action of Cl^- (Figure 5(c)). When HSO_4^- was added, the interface became fuzzy (Figure 5(e)), indicating that HSO_4^- could lead to more serious corrosion. The interface became more irregular under the influence of $\text{Cl}^- + \text{HSO}_4^-$ (Figure 5(g)). More corrosion of the cast iron was observed, when the freshly formed rust layer was connected to γ -FeOOH layer. In the presence of Cl^- and SO_4^{2-} , green rust would form which had little protection on iron and was just an intermediate Fe(II)-Fe(III) hydroxyl-salt via which ferrous hydroxide $\text{Fe}(\text{OH})_2$ usually oxidizes into different ferric oxyhydroxides [26].

The change in surface morphology of β -FeOOH was similar to that of γ -FeOOH. When NO_3^- was added, the surface was relatively flat (Figure 5(b)). The surface corrosion became more serious as the anion was changed from Cl^- to HSO_4^- (Figures 5(d) and 5(f)). When $\text{Cl}^- + \text{HSO}_4^-$ was acting on β -FeOOH, corrosion of the interface was so serious that it connected to the original β -FeOOH layers (Figure 5(h)).

The above observations showed that when either γ -FeOOH or β -FeOOH adhered to iron surface, it was unable to prevent different anions from reaching the iron surface. In another word, the two hydroxy-oxide rust layers were not strong enough to provide a good protection and prevent iron from further corrosion. With relatively loose textures, γ -FeOOH and β -FeOOH not only failed to stop anions from

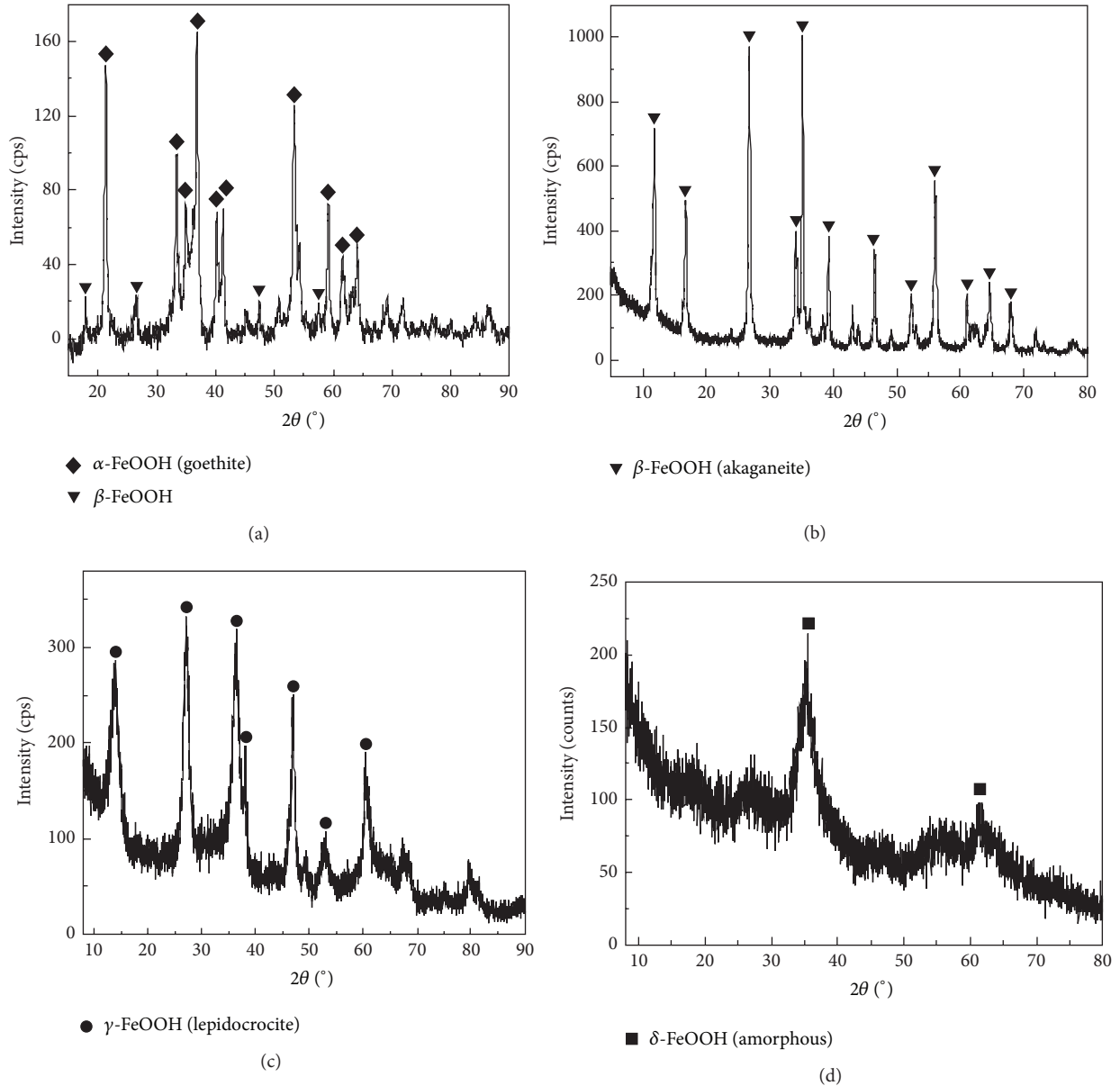


FIGURE 3: X-ray diffraction patterns of different forms of FeOOH. ◆: α -FeOOH; ▼: β -FeOOH; ●: γ -FeOOH; ■: δ -FeOOH.

corroding the iron, but also became a storage area for anions and moisture, resulting in strong adsorption. Meanwhile, it slowed down the evaporation rate of moisture and extended the corrosion cycle of moisture, thus promoting corrosive ions acting on the cast iron.

Moreover, among the common anions in atmosphere that would cause corrosion, NO_3^- had the weakest corrosion power on cast iron. The corrosive power increased progressively, following the order $\text{Cl}^- + \text{HSO}_4^- > \text{HSO}_4^- > \text{Cl}^-$. Under the combined action of Cl^- and HSO_4^- , the corrosion of cast iron was much more serious than any other ions used alone, indicating synergistic activities between Cl^- and HSO_4^- . β -FeOOH was produced exclusively in the presence of Cl^- [27] which had weaker iron protection and resulted in more iron

rusting. The corrosion product of cast iron in contact with the FeCl_2 solution over 138 days was made up of three layers: α -FeOOH, Fe_3O_4 , and a little β -FeOOH in the inner layer, γ -FeOOH in the middle layer, and α -FeOOH in the outer layer [28].

3.3. Interactions between FeOOH and Different Combinations of Phosphoric Acid/Tannic Acid. Different states and colors of reaction products after filtrating, drying, and grinding were documented in Table 2. The yellow powder and tannic acid were identical in material phases and composition, suggesting that the yellow powder was excess tannins. As tannic acid dissolves γ -FeOOH and higher concentrations of tannic acid speeded up the dissolution [29], it is suggested that FeOOH

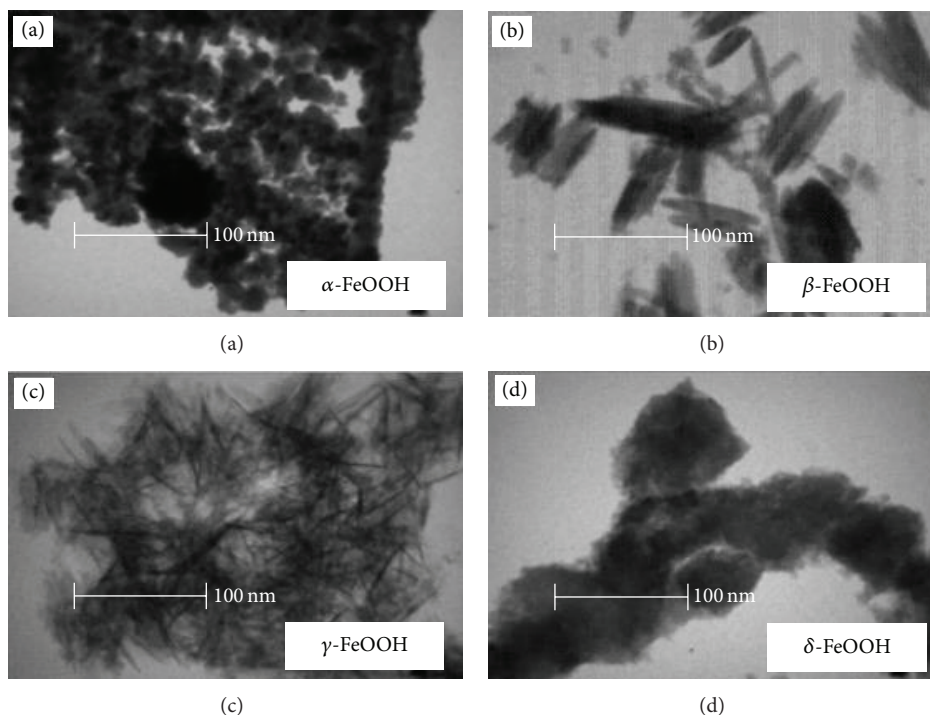


FIGURE 4: TEM images of different forms of FeOOH.

TABLE 2: The state and color of reaction products.

Phosphoric acid/tannic acid	β -FeOOH	γ -FeOOH	δ -FeOOH
3T-10P	Gray powder	Gray powder	Gray powder
3T-20P	Gray powder	Yellow powder	Less product, blue-gray
3T-30P	Less product, beige	Yellow powder	Yellow powder
5T-10P	Gray powder	Blue-gray, yellow	Blue-gray powder
5T-20P	Gray powder	Yellow powder	Blue-gray powder
5T-30P	Less product, beige	Less product, blue-gray	Yellow powder

was completely dissolved. Thus, these proportions were not suitable as a choice of rust stabilizer formula, due to accumulation of residual tannic acid after reaction. In addition, for some combinations, the reaction products were very limited, indicating that most of the FeOOH was dissolved under the action of phosphoric acid/tannic acid. Only a small amount of FeOOH was involved in chemical transformation. Thus, these combinations were also undesirable for rust stabilizer formula.

At the same time, according to protection standards of cultural relics, protection materials must be close to original artifacts to the maximum extent. Among the combinations in Table 2, only the product of the 3T-10P, namely, 3% tannic acid + 10% phosphoric acid and FeOOH, was gray, similar to the color of steel materials, suggesting that 3% tannic acid + 10% phosphoric acid was the most suitable formula for rust stabilizer. Previous studies showed that conventional anticorrosive paints or the painting schemes applied on steel previously treated with a primer formulated with pine tannins extend the duration of painting schemes more than 50% relative to the case without this chemical treatment [30].

The XRD pattern of reaction products of β -, γ -, and δ -FeOOH and 3T-10P was presented in Figure 6. A crystalline phosphate was the major product and it matched the XRD patterns of $\text{Fe}_3\text{P}_6\text{O}_2$ well. In contrast, the major constituents of the scale on Delhi iron pillar were crystalline iron hydrogen phosphate hydrate ($\text{FePO}_4 \cdot \text{H}_3\text{PO}_4 \cdot 4\text{H}_2\text{O}$) as well as α -, γ -, and δ -FeOOH and magnetite [30] or crystalline phosphate $\text{Fe}_2(\text{PO}_4)(\text{OH})$ [7]. No phases related to tannic acid were identified, suggesting that the transformation products of tannic acid and FeOOH were amorphous.

The transformation products from the reaction of tannic acid/phosphoric acid and FeOOH were further characterized by XPS. The reaction products between β -FeOOH and 3T-10P were mainly Fe, C, P, and O (Figure 7). The binding energy of $\text{Fe}2p_{3/2}$ was 712.42 eV, confirming the presence of Fe^{3+} in the product. The binding energy of C1s can be decomposed to 285.07, 286.89, and 288.50 eV, with the former corresponding to carbon and the combination of the latter two corresponding to standard spectral peaks of carboxide in tannic acid. The binding energy of O1s was 531.95 eV, corresponding to C-OH in tannic acid. In addition, the peak at 133.64 eV was

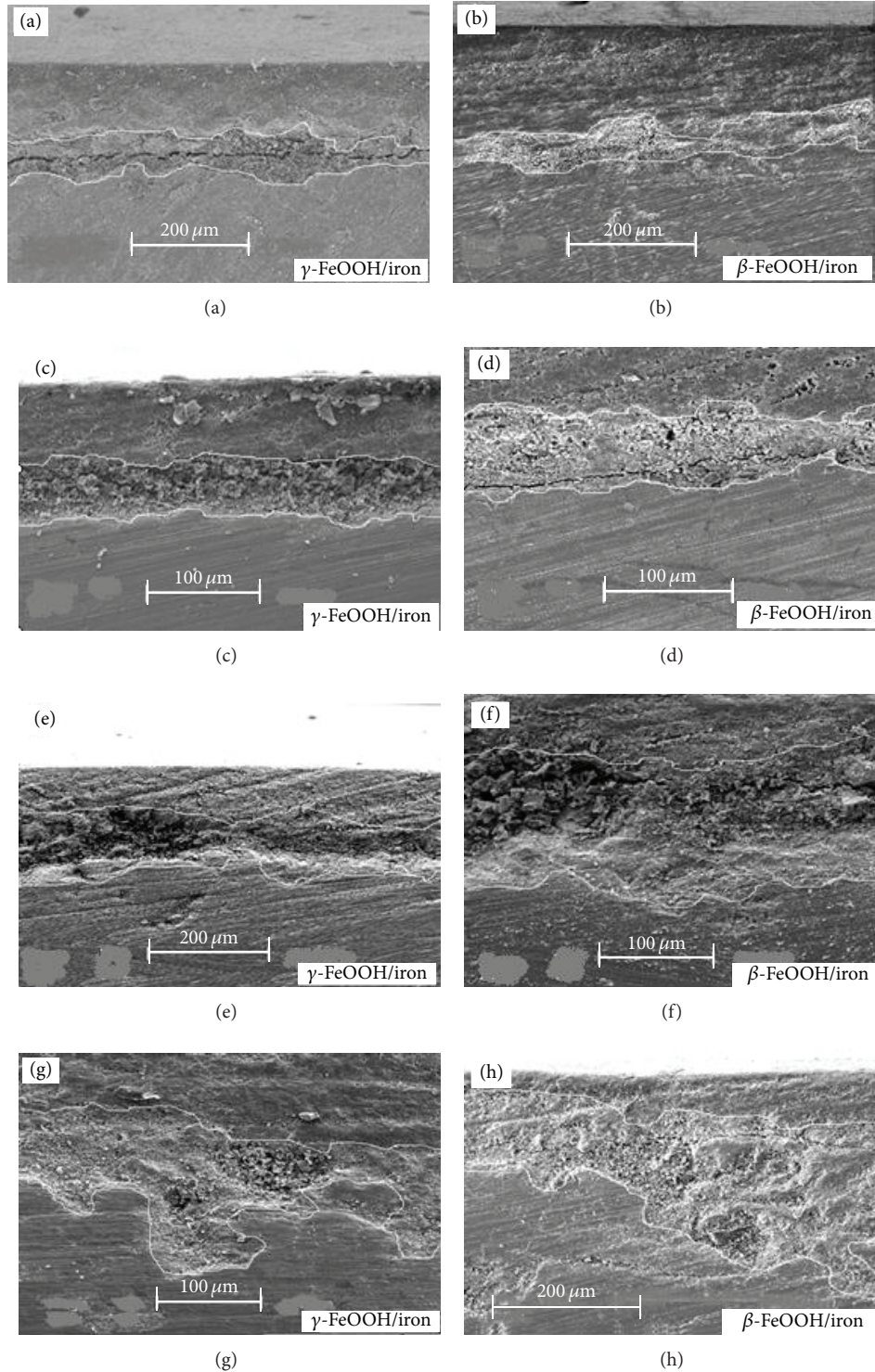


FIGURE 5: SEM images of rust powder/cast iron interface with the effects of NO_3^- ((a) and (b)); Cl^- ((c) and (d)); HSO_4^- ((e) and (f)); and $\text{Cl}^- + \text{HSO}_4^-$ ((g) and (h)).

originated from P2p, confirming the presence of phosphate. The peaks of $\text{Fe}2p_{3/2}$ in Fe^{3+} generally lie between 710.20 and 711.05 eV. However, the binding energy of $\text{Fe}2p_{3/2}$ in this study was 712.42 eV, resulting in a chemical shift of more than 1eV. Such a shift may suggest a change in chemical

environment of the elements, thus indicating formation of a new chemical bond between Fe^{3+} and other substances. Due to the presence of tannic acid, it may suggest the formation of chelate between iron and tannin [31] as illustrated in Scheme 1.

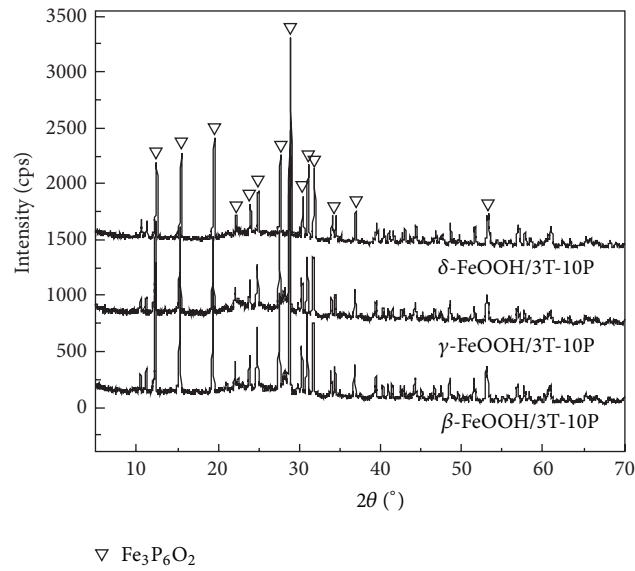


FIGURE 6: XRD patterns of the products formed from the reaction of FeOOH and 3T-10P.

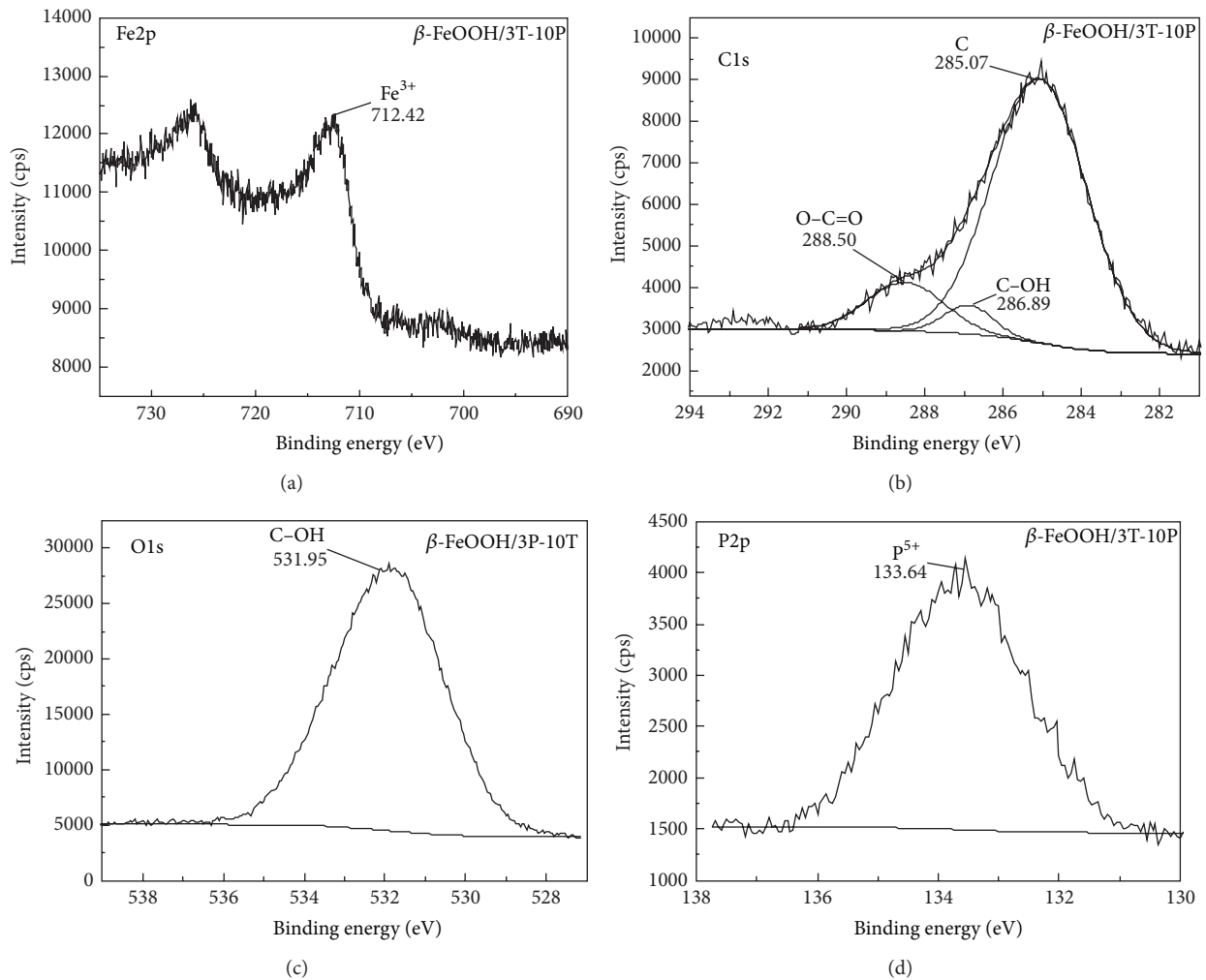


FIGURE 7: XPS spectra of the products formed from the reaction of $\beta\text{-FeOOH}$ and 3T-10P.

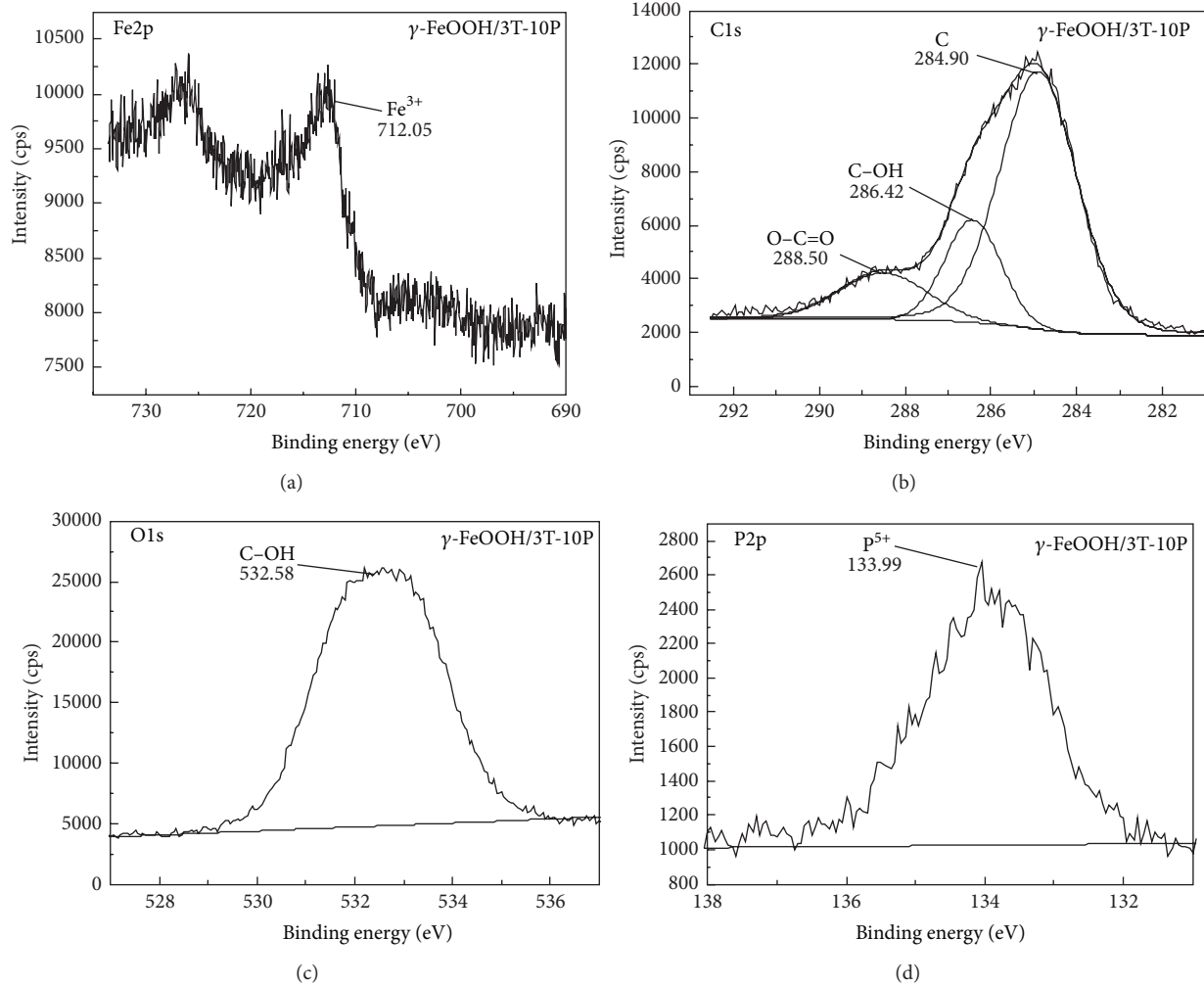
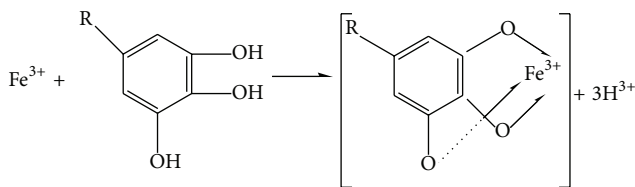


FIGURE 8: XPS spectra of the products formed from the reaction of γ -FeOOH and 3T-10P.



SCHEME 1: Single-chelate complex ion body.

Thus, it was speculated that the reaction products of β -FeOOH and 3T-10P were made up of iron phosphate and chelate of iron and tannin.

The results of XPS analyses of the reaction products generated by γ -FeOOH and 3T-10P and by δ -FeOOH and 3T-10P were illustrated in Figures 8 and 9. The composition of these two products was similar to the reaction products of β -FeOOH and 3T-10P, that is, was made mainly of Fe, C, P, and O and having about the same peak positions. Therefore, the reaction products were mainly made of iron phosphate and chelate of iron and tannin.

The structures of iron phosphate and chelate of iron and tannin are relatively stable. If acting as chemical conversion layer, the cast iron may develop strong corrosion resistance capacity. Meanwhile, the layer can enhance bonding between the coating and the substrate. These favorable physical and chemical properties could meet the need of coating and sealing treatment for iron artifact. However, the mechanisms of tannic acid/phosphoric acid rust conversion may need further study.

4. Conclusions

- (1) When cast iron was covered by β -FeOOH and γ -FeOOH corrosion, the rust layer was porous and not tight enough to provide a good protection against corrosion by NO_3^- , Cl^- , HSO_4^- , and $\text{Cl}^- + \text{HSO}_4^-$.
- (2) Among common anions tested, NO_3^- had the weakest corrosive power on cast iron. The corrosion power increased in the following sequence: Cl^- , HSO_4^- , and $\text{Cl}^- + \text{HSO}_4^-$. Meanwhile, synergistic corrosion could be enhanced when both Cl^- and HSO_4^- were present.

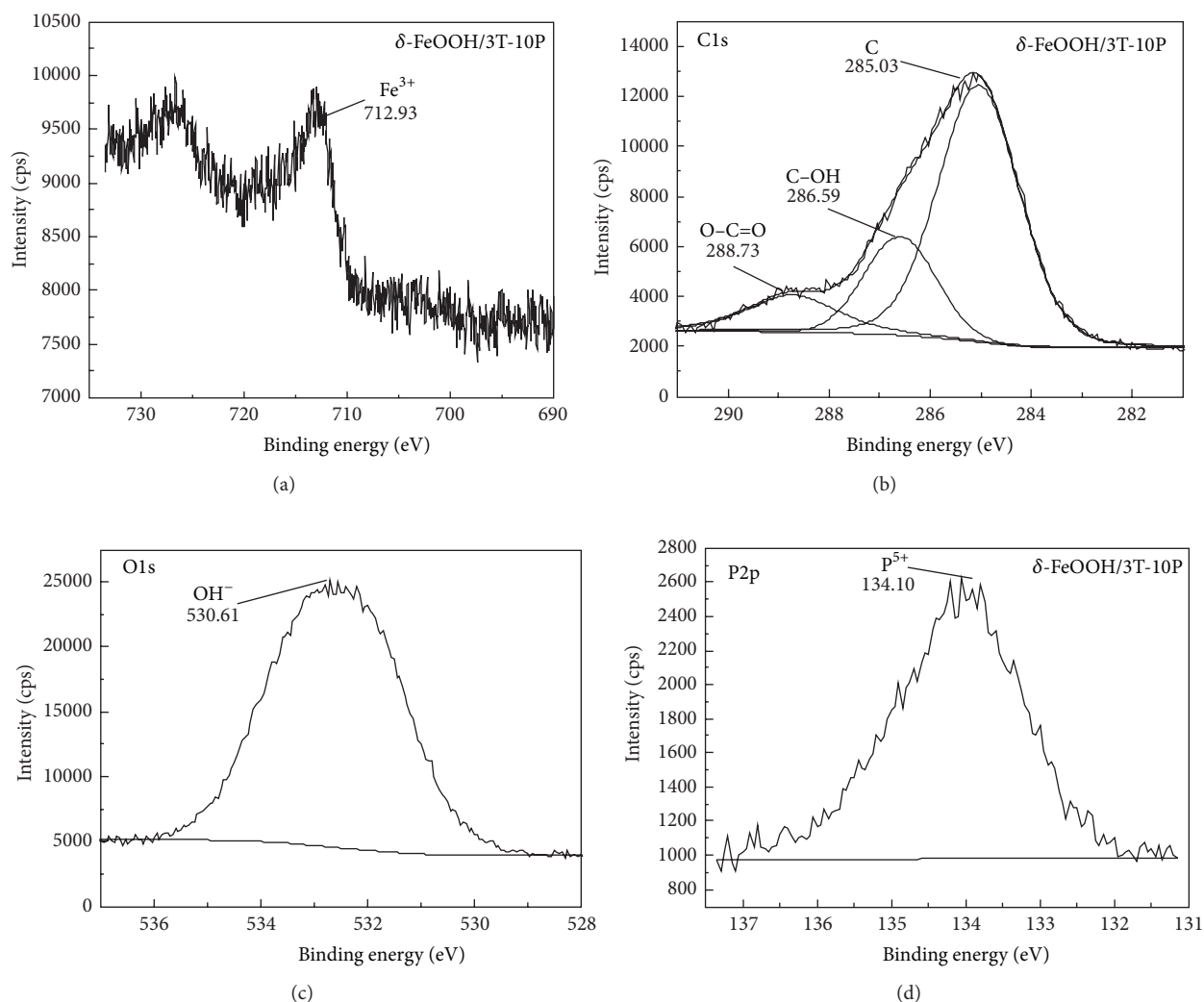


FIGURE 9: XPS spectra of the products formed from the reaction of δ -FeOOH and 3T-10P.

- (3) Analyses of the reaction products between FeOOH and different combinations of phosphoric acid/tannic acid showed that 3% tannic acid + 10% phosphoric acid was the most suitable formula as rust stabilizer.
- (4) The reaction products between β -FeOOH, γ -FeOOH, or δ -FeOOH and 3T-10P were made up of iron phosphate and chelate of iron and tannin.

Conflict of Interests

The authors declare that there is no conflict of interests regarding the publication of this paper.

Acknowledgments

This present work was supported by the National Natural Science Foundation of China (Grants nos. 51202226 and 51172216) and the Fundamental Research Funds for the Central Universities (Grant no. 2652013043).

References

- [1] W. Xu, K. Daub, X. Zhang, J. J. Noel, D. W. Shoesmith, and J. C. Wren, "Oxide formation and conversion on carbon steel in mildly basic solutions," *Electrochimica Acta*, vol. 54, no. 24, pp. 5727–5738, 2009.
- [2] X. Liu, G. Qiu, A. Yan, Z. Wang, and X. Li, "Hydrothermal synthesis and characterization of α -FeOOH and α -Fe₂O₃ uniform nanocrystallines," *Journal of Alloys and Compounds*, vol. 433, no. 1-2, pp. 216–220, 2007.
- [3] H. Abdel-Samad and P. R. Watson, "An XPS study of the adsorption of lead on goethite (α -FeOOH)," *Applied Surface Science*, vol. 136, no. 1-2, pp. 46–54, 1998.
- [4] C.-J. Jia, L.-D. Sun, Z.-G. Yan et al., "Single-crystalline iron oxide nanotubes," *Angewandte Chemie*, vol. 44, no. 28, pp. 4328–4333, 2005.
- [5] M. Žic, M. Ristić, and S. Musić, "The effect of temperature on the crystallization of α -Fe₂O₃ particles from dense β -FeOOH suspensions," *Materials Chemistry and Physics*, vol. 120, no. 1, pp. 160–166, 2010.

- [6] A. Jagminas, K. Mažeika, E. Juška, J. Reklaitis, and D. Baltrunas, "Electrochemical fabrication and characterization of lepidocrocite (γ -FeOOH) nanowire arrays," *Applied Surface Science*, vol. 256, no. 12, pp. 3993–3996, 2010.
- [7] P. Dillmann, R. Balasubramaniam, and G. Beranger, "Characterization of protective rust on ancient Indian iron using microprobe analyses," *Corrosion Science*, vol. 44, no. 10, pp. 2231–2242, 2002.
- [8] H. Tanaka, J. Wakatsuki, K. Kandori, T. Ishikawa, and T. Nakayama, "Role of zinc compounds on the formation, morphology, and adsorption characteristics of β -FeOOH rusts," *Corrosion Science*, vol. 52, no. 9, pp. 2973–2978, 2010.
- [9] T. Ishikawa, M. Kumagai, A. Yasukawa, K. Kandori, T. Nakayama, and F. Yuse, "Influences of metal ions on the formation of γ -FeOOH and magnetite rusts," *Corrosion Science*, vol. 44, no. 5, pp. 1073–1086, 2002.
- [10] A. Collazo, X. R. Nóvoa, C. Pérez, and B. Puga, "The corrosion protection mechanism of rust converters: an electrochemical impedance spectroscopy study," *Electrochimica Acta*, vol. 55, no. 21, pp. 6156–6162, 2010.
- [11] M. Žic, M. Ristić, and S. Musić, "Precipitation of α -Fe₂O₃ from dense β -FeOOH suspensions with added ammonium amidosulfonate," *Journal of Molecular Structure*, vol. 924–926, pp. 235–242, 2009.
- [12] C. Q. Cheng, J. Zhao, T. S. Cao, Q. Q. Fu, M. K. Lei, and D. W. Deng, "Facile chromaticity approach for the inspection of passive films on austenitic stainless steel," *Corrosion Science*, vol. 70, pp. 235–242, 2013.
- [13] A. I. Muñoz, J. G. Antón, J. L. Guiñón, and V. P. Herranz, "Inhibition effect of chromate on the passivation and pitting corrosion of a duplex stainless steel in LiBr solutions using electrochemical techniques," *Corrosion Science*, vol. 49, no. 8, pp. 3200–3225, 2007.
- [14] S. Powell, "Evaluation of alternative corrosion inhibitors to chromate for use in organic coatings using scanning reference electrode technique," *Surface Engineering*, vol. 16, no. 2, pp. 169–175, 2000.
- [15] B. J. Basu, A. Srinivasan, J. Manasa, and V. K. W. Grips, "Improved corrosion protection of aluminium alloy AA 2024 by sol-gel hybrid coatings after surface pretreatment by silanisation," *Surface Engineering*, vol. 28, no. 4, pp. 294–299, 2012.
- [16] Z. Liu, D. Yan, Y. Dong, Y. Yang, Z. Chu, and Z. Zhang, "The effect of modified epoxy sealing on the electrochemical corrosion behaviour of reactive plasma-sprayed TiN coatings," *Corrosion Science*, vol. 75, pp. 220–227, 2013.
- [17] A. M. Simões, J. Torres, R. Picciochi, and J. C. S. Fernandes, "Corrosion inhibition at galvanized steel cut edges by phosphate pigments," *Electrochimica Acta*, vol. 54, no. 15, pp. 3857–3865, 2009.
- [18] B. Gruss, "Iron phosphating," *Metal Finishing*, vol. 108, no. 11–12, pp. 33–37, 2010.
- [19] D. Singh and S. Yadav, "Role of tannic acid based rust converter on formation of passive film on zinc rich coating exposed in simulated concrete pore solution," *Surface and Coatings Technology*, vol. 202, no. 8, pp. 1526–1542, 2008.
- [20] B. Qian, B. Hou, and M. Zheng, "The inhibition effect of tannic acid on mild steel corrosion in seawater wet/dry cyclic conditions," *Corrosion Science*, vol. 72, pp. 1–9, 2013.
- [21] A. Ostovari, S. M. Hoseinie, M. Peikari, S. R. Shadizadeh, and S. J. Hashemi, "Corrosion inhibition of mild steel in 1 M HCl solution by henna extract: a comparative study of the inhibition by henna and its constituents (Lawson, Gallic acid, α -D-Glucose and Tannic acid)," *Corrosion Science*, vol. 51, no. 9, pp. 1935–1949, 2009.
- [22] K. W. Tan, M. J. Kassim, and C. W. Oo, "Possible improvement of catechin as corrosion inhibitor in acidic medium," *Corrosion Science*, vol. 65, pp. 152–162, 2012.
- [23] B. Yuan, J. Xu, X. Li, and M.-L. Fu, "Preparation of Si-Al/ α -FeOOH catalyst from an iron-containing waste and surface-catalytic oxidation of methylene blue at neutral pH value in the presence of H₂O₂," *Chemical Engineering Journal*, vol. 226, pp. 181–188, 2013.
- [24] S. Bashir, R. W. McCabe, C. Boxall, M. S. Leaver, and D. Mobbs, "Synthesis of α - and β -FeOOH iron oxide nanoparticles in non-ionic surfactant medium," *Journal of Nanoparticle Research*, vol. 11, no. 3, pp. 701–706, 2009.
- [25] L. Carlson and U. Schwertmann, "Natural occurrence of ferroxhyte (δ -FeOOH)," *Clays & Clay Minerals*, vol. 28, no. 4, pp. 272–280, 1980.
- [26] Z. Wang, C. Xu, and X. Dong, "Localized corrosion and phase transformation of simulated archaeological iron," *Chinese Journal of Chemical Engineering*, vol. 16, no. 2, pp. 299–305, 2008.
- [27] C. Rémazeilles and P. Refait, "On the formation of β -FeOOH (akaganéite) in chloride-containing environments," *Corrosion Science*, vol. 49, no. 2, pp. 844–857, 2007.
- [28] Z. Wang, C. Xu, X. Cao, and B. Xu, "The Morphology, phase composition and effect of corrosion product on simulated archaeological iron," *Chinese Journal of Chemical Engineering*, vol. 15, no. 3, pp. 433–438, 2007.
- [29] S. Nasrazadani, "The application of infrared spectroscopy to a study of phosphoric and tannic acids interactions with magnetite (Fe₃O₄), goethite (α -FeOOH) and lepidocrocite (γ -FeOOH)," *Corrosion Science*, vol. 39, no. 10–11, pp. 1845–1859, 1997.
- [30] R. Balasubramaniam, "On the corrosion resistance of the Delhi iron pillar," *Corrosion Science*, vol. 42, no. 12, pp. 2103–2129, 2000.
- [31] A. M. Al-Mayouf, "Inhibitors for chemical cleaning of iron with tannic acid," *Desalination*, vol. 121, no. 2, pp. 173–182, 1999.

Research Article

Resource Distribution, Interprovincial Trade, and Embodied Energy: A Case Study of China

Sanmang Wu, Yalin Lei, and Li Li

School of Humanities and Economic Management, China University of Geosciences, Beijing 100083, China

Correspondence should be addressed to Sanmang Wu; wusanmang@sina.com

Received 25 June 2014; Accepted 20 October 2014

Academic Editor: Hanlie Hong

Copyright © 2015 Sanmang Wu et al. This is an open access article distributed under the Creative Commons Attribution License, which permits unrestricted use, distribution, and reproduction in any medium, provided the original work is properly cited.

Based on data from 2007 input-output tables for each province, we estimated the energy embodied in China's interprovincial trade through input-output analysis. The results show that a sizable transfer of energy is embodied in China's interprovincial trade, and the transfer goes from the central and western provinces, which have higher energy endowments, to the eastern and coastal provinces, which have more developed economies. The provinces with the greatest net inflow of embodied energy via interprovincial trade were Zhejiang, Guangdong, Beijing, Shandong, and Jiangsu. The provinces with the greatest net outflow of embodied energy were Inner Mongolia, Shanxi, Shaanxi, Xinjiang, and Heilongjiang. To effectively reduce China's energy consumption, it is vital to adhere not only to the producer responsibility principle but also to the consumer responsibility principle. In particular, the economically developed provinces with substantial net inflows of embodied energy in interprovincial trade should provide support to the provinces from which the embodied energy outflows come.

1. Introduction

China's rapid economic development comes at the expense of enormous resources and environmental pollution. According to the World Energy Look 2010 of the International Energy Association [1], China's total energy consumption in 2009 was equivalent to 2.252 billion tons of crude oil, which was 4% greater than the energy consumption of the US in 2009. China is already the world's top energy consumer.

China's increasing total energy consumption has caused severe environmental pollution. China produces the most carbon emissions in the world, according to the International Energy Association [2]. In 2012, China contributed 300 million tons of carbon emissions. The Tyndall Centre for Climate Change Research [3] indicated that the top four regions producing the greatest amounts of carbon emissions in 2011 were China, US, the European Union, and India. The carbon emissions of these four regions accounted for 28%, 16%, 11%, and 7%, respectively, of the world's total emissions.

The rapid growth of China's carbon emissions has become a concern in the international community, and international pressures are increasing for emission reduction in China.

In this context, China is currently strengthening its energy-saving and emission reduction measures. In 2011, the Chinese government published the Plan for Energy Saving and Emission Reduction during the 12th Five-Year Plan Period (2011–2015). This plan proposed reducing energy consumption per unit of gross domestic product (GDP) by 16% between 2010 and 2015. The total emissions of chemical oxygen demand and sulfur dioxide will be reduced by 8%, and the total emissions of ammonia nitrogen and nitrogen oxides will be reduced by 10%. To achieve these goals, the State Council issued the Plan for Greenhouse Gas Emission Control during the 12th Five-Year Plan Period in 2011. This plan specifies the targets for energy consumption and carbon dioxide emission per unit of GDP for each province (excluding Hong Kong, Macao, and Taiwan, there are 22 provinces, five autonomous regions, and four municipalities directly under the central government in China. For simplicity's sake, all of them will be called provinces) during the 12th Five-Year Plan period. However, the public disputes the fairness of the plan's assignment of the energy-saving and emission reduction targets across the provinces because the targets were formulated in accordance

with the producer responsibility principle, not the consumer responsibility principle.

Some provinces may achieve energy-saving and emission reduction targets through the inflow of high-energy-consumption products (embodied energy) from other provinces, which is detrimental to the fulfillment of China's energy-saving and emission reduction goals on the whole. Thus, analysis of the embodied energy inflow and outflow via interprovincial trade in China is necessary to provide factual evidence for realizing the energy-saving and emission reduction goals in each district in China.

2. Literature Survey

After the signing of the Kyoto Protocol, countries with the task of greenhouse gas emission reduction may achieve their goals by increasing commodity imports from countries without such obligations. As a result of trade growth, carbon leakage will occur, leading to the constant growth of global greenhouse gas emissions. Embodied energy, embodied carbon emissions, and embodied pollutant emissions are topics of concern for researchers, who devote many empirical analyses to these issues. Input-output analysis, a useful analytical framework developed by Leontief [4], has been widely used to analyze the energy embodied in goods and services [5–7]. The following literature review shows that existing analyses primarily cover two major areas of interest.

One topic in existing research is the energy and carbon emissions embodied in a single country's international trade. Lenzen analyzed the primary energy and greenhouse gas contents in Australia's final consumption using input-output analysis and revealed that indirect energy consumption cannot be ignored in the commodity manufacturing process [8]. Sánchez-Chóliz and Duarte performed a sector-based calculation of carbon dioxide emissions that were associated with Spain's economic development and trade and evaluated the effect of each sector imports and exports on carbon dioxide emissions [9]. Mongelli et al. studied energy consumption in Italy's international commodity trade using input-output analysis and calculated the energy and carbon dioxide emissions embodied in Italy's commodity trade [10]. Peters and Hertwich investigated the energy and carbon emissions embodied in Norway's foreign trade [11].

A second topic of research interest is the embodiment of energy and carbon emissions in multilateral trade. Przybylinski analyzed the effect of bilateral trade between Poland and Germany on the two countries' environments and measured the total effect of bilateral trade between the two countries through input-output analysis [12]. Hayami and Nakamura used the input-output tables of Japan and Canada and bilateral trade data to calculate the carbon dioxide emissions in the trade between the two countries [13]. They found that greenhouse gas emissions could be reduced in both countries by redistributing technologies between the two countries. Lenzen and Munksgaard expanded the single-district model and proposed a multidistrict input-output model, which was used to calculate the energy and greenhouse gas emissions embodied in final consumer

products in Denmark [14]. Rhee and Chung studied the carbon dioxide transfer through international trade between Japan and Korea. Despite Korea's trade deficit with Japan, the carbon dioxide emissions embodied in the goods exported from Korea to Japan exceeded the emissions embodied in the goods exported from Japan to Korea. Thus, there was a carbon dioxide transfer from Korea to Japan through international trade [15].

For China, energy consumption has been investigated in a number of analyses [16–18]. Shui and Harriss performed an estimation of emissions embodied in US-China trade using input-output analysis [19]. The carbon dioxide export from China to the US rose from 213 tons in 1997 to 497 tons in 2003. However, there is very little carbon dioxide exported from the US to China. Shen estimated the effects of China's goods exports and imports on energy consumption from 2002 to 2005 using an input-output model [20]. Pan et al. calculated the energy and carbon emissions embodied in China's exported goods in 2002 using input-output analysis [21]. They calculated the complete energy use intensity for each industrial sector in China and the sector-based energy embodiment in China's imports and exports for 2002. Li and Hewitt used input-output analysis in analyzing the carbon emissions embodied in China's exports to the UK. With the import of industrial goods from China, UK had an 11% reduction of carbon emissions in 2004 compared with years in which there were no imports from China. However, Sino-UK trade resulted in a 117-ton increase in the world's carbon dioxide emissions in 2004 [22]. Lin and Sun used an input-output table to estimate China's carbon emissions in 2005 that were associated with consumption and production. The difference between the carbon dioxide export and import was as high as 1.024 billion tons, which means that carbon leakage occurred [23].

As the literature review demonstrates, input-output analysis is the tool most frequently used in estimating the energy and carbon emissions embodied in international trade. However, there have been few studies on the energy and carbon emissions embodied in trade between different regions within one country. China is territorially vast and shows a considerable gap in economic development across its regions. The provinces differ greatly in terms of economic development stages, industrial structures, and resource endowments. The embodied energy inflows and outflows occur in enormous quantities through interprovincial trade. Estimating the energy embodied in China's interprovincial trade is of great importance to scientifically formulate energy-saving and emission reduction targets for each district in China. Therefore, this study also adopted input-output analysis to estimate embodied energy inflows and outflows in China's interprovincial trade.

3. Research Methods and Data Sources

3.1. Research Methods. According to the following balance equation for the input-output table,

$$X_{11} + X_{12} + \dots + X_{1n} + Y_1 = X_1,$$

$$\begin{aligned}
X_{21} + X_{22} + \cdots + X_{2n} + Y_2 &= X_2, \\
X_{31} + X_{32} + \cdots + X_{3n} + Y_3 &= X_3, \\
&\vdots \\
X_{n1} + X_{n2} + \cdots + X_{nn} + Y_n &= X_n,
\end{aligned} \tag{1}$$

formula (1) is simplified as follows:

$$\sum_{j=1}^n X_{ij} + Y_i = X_i \quad (i = 1, 2, \dots, n). \tag{2}$$

Formula (2) is simplified as follows:

$$\sum_{j=1}^n a_{ij} X_{ij} + Y_i = X_i \quad (i = 1, 2, \dots, n), \tag{3}$$

where a_{ij} is the direct consumption coefficient.

Formula (3) is simplified as follows:

$$AX + Y = X, \tag{4}$$

where

$$A = \begin{bmatrix} a_{11} & a_{12} & \cdots & a_{1n} \\ a_{21} & a_{22} & \cdots & a_{2n} \\ \cdots & \cdots & \cdots & \cdots \\ a_{n1} & a_{n2} & \cdots & a_{nn} \end{bmatrix}, \quad X = \begin{bmatrix} X_1 \\ X_2 \\ \vdots \\ X_n \end{bmatrix}, \quad Y = \begin{bmatrix} Y_1 \\ Y_2 \\ \vdots \\ Y_n \end{bmatrix}. \tag{5}$$

Through a matrix operation, formula (4) becomes

$$X = (I - A)^{-1} Y. \tag{6}$$

In formula (6), X is the final output vector for each sector in a district. Some of the output is used in final consumption and some reenters the production sphere as raw material. There are some output outflows from production through trade. The outflowing output is expressed as E_x . By substituting Y with E_x in formula (6), the right side of the equation becomes the outflowing output from the district. The total product value input is expressed as X_e . Thus,

$$X_e = (I - A)^{-1} E_x. \tag{7}$$

Using the energy consumption data at hand, the sector-based energy consumption coefficients for each district were calculated (i.e., the energy consumed per unit of output value, denoted by e). The product of e and the X_e value of total products input to produce the outflowing goods is the energy consumption embodied in the outflowing goods, which is the embodied energy defined in this paper and denoted by E in the following equation:

$$E = e * [(I - A)^{-1} E_x]. \tag{8}$$

Based on formula (8), as long as the sector-based trade data between any two regions are available, the energy

embodied in the goods (including services) traded between two regions can be calculated. Suppose the two regions are a and b , and the value of products flowing from a to b is $E_{x(a,b)}$, which is the column vector of $n \times 1$ (where n is the number of sectors, as below). e_a is the unit energy consumption vector for each sector in a ; A_a is the direct energy consumption coefficient matrix for the input-output table in a ; $E_{a,b}$ is the energy embodied in all products flowing from a to b . Thus,

$$E_{a,b} = e_a * [(I - A_a)^{-1} E_{x(a,b)}]. \tag{9}$$

Formula (9) is the core formula for calculating the energy embodied in trades between provinces. Using formula (9), the energy embodied in interprovincial trade can be calculated. The calculation that results from formula (9) is a figure. By substituting $E_{x(a,b)}$ with the $n \times m$ matrix composed of the column vectors of the value of products flowing from a to other regions (where m is the number of regions), the calculation result becomes a row vector, indicating the embodied energy flowing from a to other regions. Using this method, the matrix of embodied energy flowing from one district to other regions can be obtained (i.e., the $m \times m$ matrix).

3.2. Data Sources. Estimating the energy embodied in China's interprovincial trade requires the input-output tables for each province, sector-based trade data, and final energy consumption coefficients. The latest available input-output tables are from 2007. Therefore, this study calculated the energy embodied in interprovincial trade for 2007. The specific data sources are listed in the subsections below.

3.2.1. Input-Output Tables for Each Province in 2007. This study's data are from the Input-Output Tables of China (2007) published by the Department of National Accounts, National Bureau of Statistics of China. Data from the Tibet Autonomous Region are not included in the input-output tables. Therefore, the energy embodied in interprovincial trade among 30 provinces (including 22 provinces, 4 autonomous regions, and 4 municipalities directly under the central government) was estimated.

3.2.2. Sector-Based Trade Data between Provinces in 2007. The sector-based interprovincial trade data in 2007 was obtained from the multiregional input-output (MRIO) table for 2007. In 1990, with the financial support of the United Nations Center for Regional Development, the National Bureau of Statistics of China, the Development Research Center of the State Council, and Tsinghua University jointly developed China's interregional input-output tables for nine sectors in seven regions for 1987, with Professors Ichimura and Wang Huijiong acting as the responsible parties. The Development Research Center of the State Council cooperated with the National Bureau of Statistics of China, Peking University, and other collaborators several times to develop China's MRIO tables for 2007. The Institute of Geographic Sciences and Natural Resources Research of the Chinese Academy of Sciences developed regional input-output tables

TABLE 1: The interprovincial trade matrix of a good (service).

	Beijing	Tianjin	Hebei	...	Qinghai	Ningxia	Xinjiang	Total
Beijing	$A_{1,2}$	$A_{1,3}$	$A_{1,4}$		$A_{1,28}$	$A_{1,29}$	$A_{1,30}$	RS_1
Tianjin	$A_{2,2}$	$A_{2,3}$	$A_{2,4}$		$A_{2,28}$	$A_{2,29}$	$A_{2,30}$	RS_2
Hebei	$A_{3,2}$	$A_{3,3}$	$A_{3,4}$		$A_{3,28}$	$A_{3,29}$	$A_{3,30}$	RS_3
⋮								⋮
Qinghai	$A_{28,2}$	$A_{28,3}$	$A_{28,4}$		$A_{28,28}$	$A_{28,29}$	$A_{28,30}$	RS_{28}
Ningxia	$A_{29,2}$	$A_{29,3}$	$A_{29,4}$		$A_{29,28}$	$A_{29,29}$	$A_{29,30}$	RS_{29}
Xinjiang	$A_{30,2}$	$A_{30,3}$	$A_{30,4}$		$A_{30,28}$	$A_{30,29}$	$A_{30,30}$	RS_{30}
Total	CS_1	CS_2	CS_3	...	CS_{28}	CS_{29}	CS_{30}	

for 30 provinces in 2007 [24], and the Fictitious Economy and Data Science Research Center of the Chinese Academy of Sciences also developed MRIO tables in 2007 [25].

This study used China's MRIO tables for 2007, which were jointly developed by the Development Research Center of the State Council and the National Bureau of Statistics of China. The MRIO table for 2007 is the most recent MRIO table for China. These MRIO tables cover 30 provinces and 42 sectors for each region (no input-output tables are available for Tibet, so Tibet was not included).

The estimation method for interprovincial trade is shown in Table 1. In Table 1, $A_{i,j}$ is the flow of a commodity (service) from region i to region j via interprovincial trade. The sum of rows (RS_i) represents the total value of the interprovincial exporting goods (services) in region i . The sum of columns (CS_j) represents the total value of the interprovincial importing goods (services) in region j . First, they estimated the RS_i and CS_j . Second, they estimated interprovincial trade using data (e.g., rail transportation) based on each province's input-output tables, and they got the initial matrix of trade $\bar{A}_{i,j}$. Last, they got the final trade matrix by using cross entropy. To facilitate the study, the 42 sectors were combined into 28 sectors.

3.2.3. Sector-Based Data for Each Province's Final Energy Consumption Coefficient in 2007. The sector-based data for each province's final energy consumption coefficient in 2007 were obtained by dividing the sector-based final total energy consumption for each province by the sector-based total output in the corresponding input-output table. The sector-based data for each province's final total energy consumption were from the Statistical Yearbook of 2008; however, relevant data were only available for 22 provinces. Moreover, there was a discrepancy in the sector classifications among the provinces. According to the classification of the 28 sectors listed in Table 1, there was uniform treatment for the provinces' sector-based final energy consumption data. The final total energy consumption data could not be determined from the Statistical Yearbook for eight provinces (Shanghai, Jiangsu, Zhejiang, Hebei, Shandong, Sichuan, Guangxi, and Heilongjiang). For these provinces, the following accommodation was made.

First, the final total energy consumption data for several sectors (agriculture, construction, transportation, warehousing/posts/communication, wholesale/retail trade/catering,

and other industries) were taken from the 2007 energy balance tables for Shanghai, Jiangsu, and Zhejiang. The final total industrial energy consumption data were also taken from the 2007 energy balance tables. Each sector's final total energy consumption data for 2007 were obtained by the following accommodation for these provinces: the sector-based final consumption data were collected for 2010. Assuming that these provinces' industrial energy consumption structure in 2007 was the same as in 2010, the final total energy consumption in the 2007 energy balance tables was assigned according to the energy consumption structure for the industrial sectors in 2010. In this way, the sector-based final total energy consumption data for these three provinces were obtained for 2007. The final energy consumption data for the five sectors (agriculture/forestry/husbandry/fishing, construction, transportation, warehousing/posts/communications, wholesale/retail trade/catering, and other industries) from these three provinces' energy balance tables were used. Thus, the sector-based data for the 28 sectors' final total energy consumption were obtained for Shanghai, Jiangsu, and Zhejiang in 2007.

Second, for five provinces (Hebei, Shandong, Sichuan, Guangxi, and Heilongjiang), the final energy consumption data for these sectors (agriculture/forestry/husbandry/fishing, construction, transportation, warehousing/posts/communications, wholesale/retail trade/catering, and other industries) came from the corresponding energy balance tables for 2007. The sector-based data for these five provinces' final energy consumption were obtained by the following method for 2007: the regions with industrial structures similar to these five provinces were identified (Table 2). For example, the industrial structures of Hebei and Liaoning were similar. Second, by referring to similar industrial energy structures in other districts, the final total industrial energy consumption for the five provinces was decomposed. Thus, the sector-based final energy consumption data for the five provinces were obtained. Third, the final energy consumption data for these sectors (agriculture/forestry/husbandry/fishing, construction, transportation, warehousing/posts/communications, wholesale/retail trade/catering, and other industries) from the energy balance tables of the five provinces were used. The final total energy consumption data of the 28 sectors for these five provinces were thus obtained for 2007.

TABLE 2: Provinces for which sector-based data were adjusted for 2007.

Provinces for which sector-based data were adjusted	Reference provinces
Hebei	Liaoning
Shandong	Liaoning
Hainan	Guangdong
Sichuan	Chongqing
Guangxi	Guizhou
Heilongjiang	Jilin

4. Results and Discussion

Based on these data, the energy embodied in China's inter-provincial trade in 2007 was estimated using formula (9).

4.1. Total Outflow and Unit Outflow of Embodied Energy in Interprovincial Trade

4.1.1. Total Embodied Energy Outflow in Interprovincial Trade. Table 2 reflects the total embodied energy outflow in inter-provincial trade between 30 provinces in 2007. As shown in Table 3, there were significant differences in the outflows of embodied energy via interprovincial trade. For example, there was an outflow of embodied energy via interprovincial trade equivalent to 77.23 million tons of standard coal from Hebei in 2007. For Hainan, the total outflow of embodied energy was 2.60 million tons of standard coal.

The five provinces with the greatest outflows of embodied energy via interprovincial trade in 2007 were Hebei, Inner Mongolia, Liaoning, Shanxi, and Heilongjiang. The total outflows were 77.23 million, 65.88 million, 58.95 million, 49.15 million, and 43.83 million tons of standard coal, respectively. Hebei and Liaoning had the greatest outflows of embodied energy via interprovincial trade. The high-energy-consumption sectors occupy a large proportion of these provinces' industrial structures, and the high-energy-consumption products are the major products traded. Hebei is China's major site of iron and steel production and the province where Handan Iron and Steel Group and Tangshan Iron and Steel Group Company Limited are headquartered. Since 2002, Hebei has ranked first nationwide in outputs of iron, steel, and steel products. Liaoning is China's important industrial base, with a proportion of heavy industry as high as 80% in 2012.

Inner Mongolia, Shanxi, and Heilongjiang also have high outflows of embodied energy via interprovincial trade because they are China's major sites of energy production (Table 4). Inner Mongolia and Shanxi are China's two largest sites of coal production. In 2013, their coal outputs were 994 million and 960 million tons, respectively. Heilongjiang is the most important oil production base, and coal and oil production consumes huge amounts of energy in the exploitation process. These regions' industries are developing with coal as their primary energy source. For example, the

gross output values of coal, coking, smelting, and electric power made up approximately 80% of the gross output industrial value in Shanxi. Along with the outflow of energy products, there is a massive outflow of energy-intensive products.

The destinations of the embodied energy outflows from the top five provinces were analyzed. The three provinces with the greatest inflows of embodied energy are listed in Table 5. The destinations of embodied energy outflows from the top five provinces were in the eastern region: Zhejiang, Guangdong, Beijing, Jiangsu, and Shandong (the eastern region includes Beijing, Tianjin, Hebei, Shanghai, Jiangsu, Zhejiang, Fujian, Shandong, Guangdong, and Hainan; the central region includes Shanxi, Anhui, Jiangxi, Henan, Hubei, and Hunan; the western region includes Inner Mongolia, Guangxi, Chongqing, Sichuan, Guizhou, Yunnan, Shanxi, Gansu, Qinghai, Ningxia, and Xinjiang; and the northeastern region includes Liaoning, Jilin, and Heilongjiang).

In 2007, the five provinces with the smallest outflows of embodied energy via interprovincial trade were Hainan, Qinghai, Fujian, Ningxia, and Yunnan. These provinces are not major energy producers. Moreover, Hainan, Qinghai, Ningxia, and Yunnan are economically underdeveloped regions. Their low level of industrial development means that there will be no outflow of energy embodied in inter-provincial trade products. Fujian has a more developed economy, but its industrial structure is dominated by the light industry, which has low energy intensity. Therefore, the embodied energy outflow via interprovincial trade was not substantial.

4.1.2. Unit Outflow of Embodied Energy in Interprovincial Trade. Each province's total embodied energy outflow via interprovincial trade was estimated in the previous section. There are two major reasons for the provinces' substantial total embodied energy outflows via interprovincial trade: the large proportion of high-energy-consumption industries and the large scale of the economy (although the regional industrial structure may be cleaner in terms of emissions). To reveal the source discrepancies in each province's embodied energy outflow, we further estimated the unit outflow of embodied energy via interprovincial trade. The unit outflow of embodied energy refers to the energy embodied in the unit value of commodity and service. It is calculated by dividing the total embodied energy outflow by the total value of outflowing commodities and services.

Figure 1 shows the unit outflow of embodied energy via interprovincial trade for 30 provinces in 2007. As shown in Figure 1, among the provinces, there were substantial differences in the unit outflows of embodied energy in interprovincial trade. The five provinces with the greatest unit outflows of embodied energy were Inner Mongolia, Shanxi, Guizhou, Ningxia, and Shanxi, with unit outflows of embodied energy of 53.444 thousand, 33.035 thousand, 32.544 thousand, 26.597 thousand, and 18.85 thousand tons of standard coal/10,000 RMB, respectively.

These provinces were the major producers of high-energy-consumption product outflows to other regions. The

TABLE 3: Outflows of embodied energy via China’s interprovincial trade (in millions of tons of standard coal).

District	Embodied energy total outflow	District	Embodied energy total outflow	District	Embodied energy total outflow
Hebei	77.23	Xinjiang	35.73	Guangxi	22.10
Inner Mongolia	65.88	Jiangsu	35.57	Tianjin	20.36
Liaoning	58.95	Hunan	34.76	Sichuan	13.72
Shanxi	49.15	Shandong	34.09	Jiangxi	12.59
Heilongjiang	43.83	Guizhou	28.24	Gansu	12.00
Zhejiang	41.79	Chongqing	28.12	Yunnan	11.23
Henan	40.80	Hubei	25.35	Ningxia	8.04
Shaanxi	40.49	Shanghai	25.14	Fujian	7.73
Anhui	39.04	Guangdong	24.86	Qinghai	3.88
Jilin	36.78	Beijing	24.60	Hainan	2.60

TABLE 4: China’s major sites of energy distribution.

Types of energy	Reserves	Major provinces of distribution	Total proportion (%)
Coal	Prospective reserves	Xinjiang, Inner Mongolia, Shaanxi, Shanxi	94.9
	Proven reserves	Shanxi, Inner Mongolia, Shaanxi, Xinjiang	80.5
Oil	Prospective reserves	Xinjiang, Heilongjiang, Shandong, Liaoning	85
	Proven reserves	Heilongjiang, Shandong, Liaoning, Hebei	70

Data source: Chinese mineral resources report, 2014 [26].

TABLE 5: Destinations of embodied energy outflows from the top five provinces.

Provinces with the greatest embodied energy outflows	Provinces with the greatest embodied energy inflows
Hebei	Shandong, Zhejiang, Beijing
Inner Mongolia	Beijing, Zhejiang, Guangdong
Liaoning	Hebei, Zhejiang, Shandong
Shanxi	Guangdong, Jiangsu, Shanghai
Heilongjiang	Hebei, Zhejiang, Jiangsu

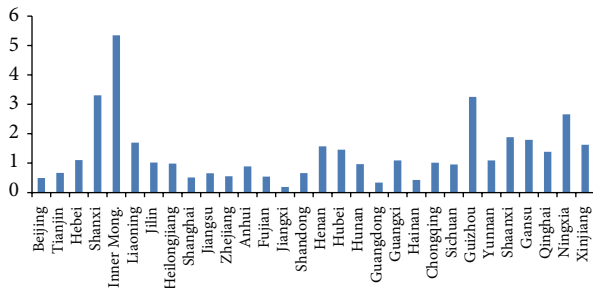


FIGURE 1: Unit outflow of embodied energy for each province in 2007 (in tons of standard coal/10,000 RMB).

high-energy-consumption sectors occupied a large proportion of the industrial structure. There was a considerable inconsistency in the top five provinces in terms of the unit outflows of embodied energy and the total embodied energy

outflows, which indicated that the provinces with substantial total embodied energy outflows might have had low unit outflows of embodied energy.

Zhejiang is China’s major manufacturer with a developed economy. In 2007, the total outflow of Zhejiang’s embodied energy via interprovincial trade ranked fourth in the country, but its unit outflow of embodied energy was very small. The reason for Zhejiang’s substantial embodied energy outflow was the high value of the outflowing products. Zhejiang’s industrial structure was not dominated by high-energy-consumption sectors.

In 2007, the five provinces with the smallest unit outflows of embodied energy via interprovincial trade were Jiangxi, Guangdong, Hainan, Beijing, and Shanghai, with unit outflows of 1.921 thousand, 3.381 thousand, 4.267 thousand, 4.963 thousand, and 5.103 thousand tons of standard coal/10,000 RMB, respectively. These values indicated that these provinces’ outflowing products consumed less energy in the production process. These provinces’ industrial structures were characterized by low energy consumption.

4.2. Total Inflow and Unit Inflow of Embodied Energy in Interprovincial Trade

4.2.1. Total Embodied Energy Inflow in Interprovincial Trade.

Table 6 shows the total embodied energy inflow in interprovincial trade for China’s 30 provinces in 2007. As shown in Table 6, there were substantial differences in the provinces’ total embodied energy inflows. For example, Hebei’s embodied energy inflow via interprovincial trade is 88.69 million tons of standard coal. Qinghai’s inflow is only 4.44 million tons of standard coal.

TABLE 6: Total embodied energy inflows via interprovincial trade for each province in 2007 (in millions of tons of standard coal).

District	Total embodied energy inflow	District	Total embodied energy inflow	District	Total embodied energy inflow
Zhejiang	88.69	Chongqing	31.02	Shaanxi	14.62
Hebei	66.19	Tianjin	25.24	Yunnan	12.46
Guangdong	65.43	Henan	24.86	Xinjiang	10.33
Shandong	55.75	Hubei	21.42	Gansu	10.20
Beijing	53.70	Guangxi	21.38	Inner Mongolia	8.82
Jiangsu	48.63	Hunan	20.23	Guizhou	7.16
Liaoning	40.79	Heilongjiang	20.14	Hainan	6.94
Jilin	39.05	Fujian	16.28	Shanxi	6.70
Shanghai	37.42	Jiangxi	15.72	Ningxia	5.61
Anhui	36.28	Sichuan	15.00	Qinghai	4.44

In 2007, the five provinces with the greatest energy inflows via interprovincial trade were Zhejiang, Hebei, Guangdong, Shandong, and Beijing. The inflows were 88.69 million, 66.19 million, 65.43 million, 55.75 million, and 53.70 million tons of standard coal, respectively. Zhejiang and Guangdong had substantial embodied energy inflows via interprovincial trade because both are major provinces in terms of manufacturing trade with strong economies. However, these two provinces are deficient in energy resources. The development of manufacturing trade requires substantial inflows of energy and non-energy-related and energy-intensive products from other regions. As a result, there will be significant embodied energy inflows.

As mentioned above, Hebei is China's major iron producer, and a large amount of coal is consumed in the manufacturing of iron products. In recent years, Hebei still needed a coal inflow from other provinces and regions. However, Hebei's coal products do not have the highest energy embodiment. Through the inflow of coal as the primary energy source, there was also a substantial embodied energy inflow.

Shandong's situation is similar to that of Hebei. Shandong is China's major iron product producer, and its crude steel production reached 59 billion tons in 2012, ranking third in the country. The reason for Beijing's substantial embodied energy inflow via interprovincial trade is that Beijing is not rich in energy resources. Given the high population intensity and economic output, as the capital of China, Beijing needs an energy inflow from other regions and an inflow of non-energy-intensive products.

The provinces with the greatest embodied energy inflows via interprovincial trade were analyzed. The top three provinces in terms of embodied energy inflow are listed in Table 6. As shown in Table 7, the embodied energy inflows to Zhejiang, Guangdong, Hebei, Shandong, and Beijing mainly came from Inner Mongolia, Hebei, Liaoning, and Hebei, respectively.

In 2007, the five provinces with the smallest embodied energy inflows via interprovincial trade were Qinghai, Ningxia, Shanxi, Hainan, and Guizhou. These provinces fall into two categories: provinces with small populations and less developed industry and coal producing provinces. In Qinghai, Ningxia, and Hainan, the population does not

TABLE 7: Sources of embodied energy inflows into the top five provinces.

Five provinces with the greatest embodied energy inflows	Provinces with the greatest embodied energy outflows
Zhejiang	Hebei, Liaoning, Inner Mongolia
Guangdong	Zhejiang, Hebei, Inner Mongolia
Hebei	Liaoning, Shanxi, Inner Mongolia
Shandong	Hebei, Liaoning, Hunan
Beijing	Inner Mongolia, Hebei, Tianjin

exceed 10 million, and there is less demand for products with high energy embodiments. In the provinces that are coal producers, such as Guizhou and Shanxi, there is less need for the inflow of direct energy products and energy-intensive products, which reduces the embodied energy inflow via interprovincial trade.

4.2.2. Unit Inflow of Embodied Energy via Interprovincial Trade. The unit inflow of embodied energy was further estimated for each province. The unit inflow of embodied energy refers to the energy embodied in the unit value of commodities and services. It is calculated by dividing the total embodied energy inflow by the total value of outflowing commodities and services. The unit inflow of embodied energy via interprovincial trade measures the average energy consumption level of inflowing products for the corresponding province.

Figure 2 shows each province's unit inflow of embodied energy via interprovincial trade in 2007. As indicated in Figure 2, there was a much less substantial difference in terms of each province's unit inflow of embodied energy compared with the unit outflow of embodied energy. The unit inflows of embodied energy for Guizhou, Shanxi, and Fujian were less than 8,000 tons/10,000 RMB. For all other provinces, the unit inflows of embodied energy ranged from 8,000 to 12,000 tons/10,000 RMB because each province maintained

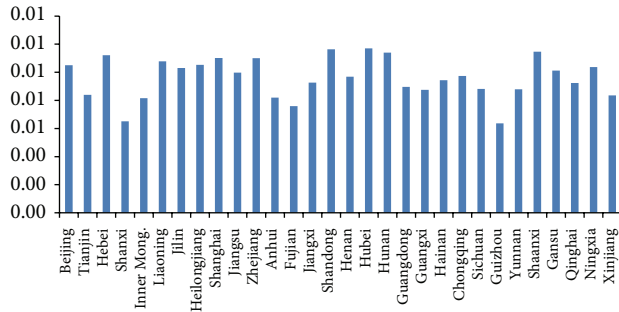


FIGURE 2: Unit inflow of embodied energy via interprovincial trade for each province in 2007 (in tons of standard coal/10,000 RMB).

a trading relationship with all other provinces. The diversity of the inflowing product sources ensured that there were no extremely large or small unit inflows of embodied energy.

The provinces' unit inflows and unit outflows of embodied energy were compared in 2007. The results show that the unit outflow of embodied energy for some provinces (e.g., Inner Mongolia, Shanxi, Guizhou, and Ningxia) exceeded the unit inflow of embodied energy. The unit outflow of embodied energy via interprovincial trade was 53.444 thousand tons of standard coal/10,000 RMB in Inner Mongolia. However, Inner Mongolia's unit inflow was only 8.163 thousand tons of standard coal/10,000 RMB.

In these provinces, the average energy consumption of the outflowing products was significantly higher than the average energy consumption of the inflowing products. These provinces' industrial structures were characterized by high energy consumption. For Jiangxi, Shanghai, Guangdong, and Beijing, the unit outflow of embodied energy via interprovincial trade was significantly smaller than the unit inflow. In Shanghai, the unit outflow of embodied energy was 5.103 tons of standard coal/10,000 RMB, whereas the unit inflow was 11.017 tons of standard coal/10,000 RMB. In these provinces, the average energy consumption of the inflowing products was much higher than the average energy consumption of the outflowing products. The industrial structures also tended to be cleaner.

4.3. Net Embodied Energy Inflow. To more comprehensively reflect the embodied energy inflow and outflow for each province, the net embodied energy inflow in 2007 was estimated (the total embodied energy inflow minus the total embodied energy outflow). The specific results are shown in Figure 3, which shows that the five provinces with the greatest net embodied energy inflow via interprovincial trade in 2007 were Zhejiang, Guangdong, Beijing, Shandong, and Jiangsu. The net inflows were 46.9 million, 40.57 million, 29.1 million, 21.66 million, and 13.06 million tons of standard coal, respectively. These provinces are strong economies in China's eastern coastal areas. According to data released by the National Bureau of Statistics, Guangdong, Jiangsu, Shandong, and Zhejiang were the top four provinces in terms of GDP in 2013. Beijing's economic output also ranked among the highest of the provinces. Except for Shandong, these

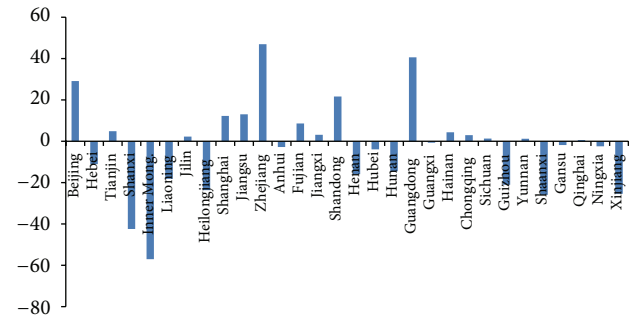


FIGURE 3: Net embodied energy inflow via interprovincial trade for each province in 2007 (in millions of tons of standard coal).

provinces' energy productions were low. In these regions, the direct energy products and energy-intensive products were needed in large quantities via interprovincial trade to sustain development.

In 2007, the net embodied energy inflow via interprovincial trade was negative for some provinces. The embodied energy outflows exceeded the embodied energy inflows in these provinces, which were the provinces with net embodied energy outflows. The five provinces with the greatest net embodied energy outflows were Inner Mongolia, Shanxi, Shaanxi, Xinjiang, and Heilongjiang, all of which are located in central and western China. The net outflows were 57.06 million, 42.45 million, 25.87 million, 25.4 million, and 23.69 million tons of standard coal, respectively. These provinces are all major energy producers. Inner Mongolia, Shanxi, Shaanxi, and Xinjiang are rich in coal resources, whereas Heilongjiang is a major site of oil production in China (Table 4).

5. Conclusions and Policy Implications

5.1. Conclusions. This study used input-output analysis to estimate the embodied energy in China's interprovincial trade for 2007. The following conclusions were obtained through analysis of the measurement results.

First, the eastern coastal provinces with developed economies (e.g., Zhejiang, Hebei, Guangdong, Shandong, and Beijing) had higher embodied energy inflows. The inflows were 88.69 million, 66.19 million, 65.43 million, 55.75 million, and 53.70 million tons of standard coal, respectively.

Second, the provinces with substantial embodied energy outflows via interprovincial trade were major producers of energy and iron and steel products. In 2007, the two provinces with the greatest embodied energy outflows via interprovincial trade were Hebei and Liaoning. The high-energy-consumption sectors occupy a large proportion of these provinces' industrial structures, and the high-energy-consumption products are the major products traded.

Third, the provinces with substantial net embodied energy inflows via interprovincial trade were Zhejiang, Guangdong, Beijing, Shandong, and Jiangsu. The net inflow was 46.9 million, 40.57 million, 29.1 million, 21.66 million, and 13.06 million tons of standard coal, respectively. These

provinces' common features include developed economies, low resource endowments, and the ability to produce products with high energy intensities. The embodied energy inflows via interprovincial trade were remarkably lower than the outflows in Inner Mongolia, Shanxi, Shaanxi, Xinjiang, and Heilongjiang.

Fourth, due to the diversity of trade partners, there were small differences in unit inflows of embodied energy among the provinces. However, the unit outflows of embodied energy were considerably different among the provinces. For example, Inner Mongolia, Shanxi, Guizhou, and Ningxia, which are rich in energy resources, had much higher unit outflows of embodied energy compared with those of other regions. These provinces' industrial structures are characterized by high energy consumption. The unit outflows of embodied energy via interprovincial trade were substantially lower than the unit inflows in Jiangxi, Shanghai, Guangdong, and Beijing. These provinces' industrial structures are cleaner.

5.2. Policy Implications. In summary, there is generally an embodied energy outflow via China's interprovincial trade from central and western provinces, where the energy resources are richer, to the provinces in coastal eastern region, where the economy is more developed. Thus, with the development of interprovincial trade, the embodied energy is transferred from central and western provinces to eastern provinces. If energy-saving and emission reduction goals can be formulated according to the producer responsibility principle, it will be difficult to save energy and reduce emissions for the provinces in central and western region. Transferring energy-intensive products from the central and western regions to the eastern region will relieve the pressures of energy saving and emission reduction.

In fact, the economically developed provinces in China's eastern coastal region are situated upstream in the industrial chain. Transferring the high-energy-consumption products (together with the embodied energy) from the less developed provinces in the central and western regions elevates their industrial structures and realizes the energy-saving and emission reduction requirements. The intensified dependency of provinces with high embodied energy outflows on the high-energy-consumption industries aggravates the pressures of energy saving and consumption reduction, which brings greater pressure to bear on overall energy saving and emission reduction in China.

The consumer responsibility principle should be introduced when formulating energy-saving and emission reduction goals. The economically developed provinces with substantial net embodied energy inflows should take responsibility for supporting the provinces with net embodied energy outflows. Outputs of advanced technologies, knowledge, and talents from the eastern region to the central and western regions should be encouraged. By introducing capital and advanced clean production technologies, the central and western regions can improve energy efficiency and industrial output and better meet energy-saving and energy consumption reduction targets, crucial for finally realizing China's overall energy-saving and emission reduction goals.

Conflict of Interests

The authors declare that there is no conflict of interests regarding the publication of this paper.

Acknowledgment

The authors are grateful for the support from the National Natural Science Foundation of China under Grant nos. 71003066, 71173200, and 71133003.

References

- [1] International Energy Association, World Energy Outlook, 2010.
- [2] International Energy Association, World Energy Outlook, 2013.
- [3] The Tyndall Centre for Climate Change Research, *Global Carbon Emissions Reach Record 10 Billion Tons—Threatening 2 Degree Target*, Nature Climate Change, 2012.
- [4] W. Leontief, "Composite commodities and the problem of index numbers," *Econometrica*, vol. 4, no. 1, pp. 39–59, 1936.
- [5] D. Hawdon and P. Pearson, "Input-output simulations of energy, environment, economy interactions in the UK," *Energy Economics*, vol. 17, no. 1, pp. 73–86, 1995.
- [6] Y. Kondo, Y. Moriguchi, and H. Shimizu, "CO₂ emissions in Japan: influences of imports and exports," *Applied Energy*, vol. 59, no. 2-3, pp. 163–174, 1998.
- [7] G. Machado, R. Schaeffer, and E. Worrell, "Energy and carbon embodied in the international trade of Brazil: an input-output approach," *Ecological Economics*, vol. 39, no. 3, pp. 409–424, 2001.
- [8] M. Lenzen, "Primary energy and greenhouse gases embodied in Australian final consumption: an input-output analysis," *Energy Policy*, vol. 26, no. 6, pp. 495–506, 1998.
- [9] J. Sánchez-Chóliz and R. Duarte, "CO₂ emissions embodied in international trade: evidence for Spain," *Energy Policy*, vol. 32, no. 18, pp. 1999–2005, 2004.
- [10] I. Mongelli, G. Tassili, and B. Notarnicola, "Global warming agreements, international trade and energy/carbon embodiments: an input-output approach to the Italian case," *Energy Policy*, vol. 34, no. 1, pp. 88–100, 2006.
- [11] G. P. Peters and E. G. Hertwich, "Pollution embodied in trade: the Norwegian case," *Global Environmental Change*, vol. 16, no. 4, pp. 379–387, 2006.
- [12] M. Przybylinski, "Pollution flows between Poland and Germany," in *Proceedings of the 14th International Conference on Input-Output Techniques*, Montreal, Canada, 2002.
- [13] H. Hayami and M. Nakamura, "CO₂ emission of an alternative technology and bilateral trade between Japan and Canada: relocating production and an implication for joint implementation," in *Proceedings of the 14th International Conference on Input-Output Techniques*, Montréal, Canada, 2002.
- [14] M. Lenzen and J. Munksgaard, "Energy and CO₂ life-cycle analyses of wind turbines—review and applications," *Renewable Energy*, vol. 26, no. 3, pp. 339–362, 2002.
- [15] H.-C. Rhee and H.-S. Chung, "Change in CO₂ emission and its transmissions between Korea and Japan using international input-output analysis," *Ecological Economics*, vol. 58, no. 4, pp. 788–800, 2006.
- [16] K. Fisher-Vanden, G. H. Jefferson, H. Liu, and Q. Tao, "What is driving China's decline in energy intensity?" *Resource and Energy Economics*, vol. 26, no. 1, pp. 77–97, 2004.

- [17] L. Hong, Z. P. Dong, and H. Chunyu, "Evaluating the effects of embodied energy in international trade on ecological footprint in China," *Ecological Economics*, vol. 62, no. 1, pp. 136–148, 2007.
- [18] G. P. Peters, C. L. Weber, D. Guan, and K. Hubacek, "China's growing CO₂ emissions—a race between increasing consumption and efficiency gains," *Environmental Science and Technology*, vol. 41, no. 17, pp. 5939–5944, 2007.
- [19] B. Shui and R. C. Harriss, "The role of CO₂ embodiment in US-China trade," *Energy Policy*, vol. 34, no. 18, pp. 4063–4068, 2006.
- [20] L. S. Shen, "The change of China's foreign trade structure is not favorable to energy-saving and emission reduction," *Management World*, vol. 45, pp. 167–186, 2007 (Chinese).
- [21] J. Pan, J. Phillips, and Y. Chen, "China's balance of emissions embodied in trade: approaches to measurement and allocating international responsibility," *Oxford Review of Economic Policy*, vol. 24, no. 2, pp. 354–376, 2008.
- [22] Y. Li and C. N. Hewitt, "The effect of trade between China and the UK on national and global carbon dioxide emissions," *Energy Policy*, vol. 36, no. 6, pp. 1907–1914, 2008.
- [23] B. Lin and C. Sun, "Evaluating carbon dioxide emissions in international trade of China," *Energy Policy*, vol. 38, no. 1, pp. 613–621, 2010.
- [24] W. Liu, J. Chen, and Z. Tang, *Theories and Practices of Development of China's Interregional Input-Output Tables of 30 Provinces/Cities in 2007*, China Statistics Press, 2012, (Chinese).
- [25] S. Minjun and Z. Zhuoying, *China's Interregional Input-Output Model and Regional Economic Connections*, Science Press, Beijing, China, 2012.
- [26] Ministry of Land and Resources of the People's Republic of China, *Chinese Mineral Resources Report*, 2014.

Research Article

Adsorption Mechanism of Ciprofloxacin from Water by Synthesized Birnessite

Xuebing Xing,¹ Jingwen Feng,¹ Guocheng Lv,¹ Kenan Song,² Lefu Mei,¹
Libing Liao,¹ Xiaoyu Wang,¹ and Ben Xu²

¹Beijing Key Laboratory of Nonmetallic Minerals and Material Utilization of Solid Wastes, School of Material Sciences and Technology, China University of Geosciences, Beijing 100083, China

²School of Materials Science and Engineering, Tsinghua University, Beijing 100084, China

Correspondence should be addressed to Guocheng Lv; guochenglv@cugb.edu.cn and Ben Xu; xu9ben@gmail.com

Received 11 August 2014; Revised 14 September 2014; Accepted 15 September 2014

Academic Editor: Zhaohui Li

Copyright © 2015 Xuebing Xing et al. This is an open access article distributed under the Creative Commons Attribution License, which permits unrestricted use, distribution, and reproduction in any medium, provided the original work is properly cited.

The efficiency of ciprofloxacin (CIP) adsorption on synthesized birnessite was systematically studied under varying physicochemical conditions, such as solution pH, contact time, initial CIP concentration, and different average oxidation states (AOS) of Mn in birnessite. X-ray diffraction (XRD), Fourier transform infrared (FTIR), and molecular simulations were employed to investigate the adsorption mechanism of CIP on birnessite. Experimental results showed that surface adsorption instead of cation exchange was responsible for the uptake of CIP on birnessite. The quantum mechanics simulation showed that the final energy of the interaction between CIP and birnessite was smaller under the condition when the AOS of Mn was lower, in comparison to the case when the AOS of Mn was high. The highest CIP adsorption occurred under a weak alkaline condition.

1. Introduction

Antibiotics refer to a group of substances that can effectively inhibit growth of pathogens or other active materials. Since Alexander Fleming discovered penicillin in 1928, a large number of antibiotics are not only used to treat human and animal diseases but also widely used in poultry feeding and aquaculture. Antibiotics play an important role in preventing disease and promoting growth [1]. Many antibiotics have the characteristics of low biodegradability and are persistent in the environment [2].

Nonbiodegradable quinolone antibiotics are an important type in the commonly used antibiotics. The most extensively used prescribed quinolone antibiotic is ciprofloxacin that can effectively act against a wide range of gram-negative and gram-positive bacteria. In addition, CIP has high water solubility under different pH conditions and has stability in soil and wastewater [3–7]. It can be removed by wastewater treatment, owing to its significant adsorption onto the sludge floc [3]. Although 90% of CIP could be removed by activated carbon from sludge [4], it is still found in the effluent of

sewage treatment plants. Studies of the interaction between these pollutants and soil or sediment have attracted great attention as more and more antibiotics are detected in surface and wastewater.

Birnessite was originally thought as the air oxidation product of manganese oxide in alkaline conditions in Scotland [8]. It is one of the most common manganese oxides in soil and is also a potential, yet efficient, adsorbent [9]. It has an octahedral layered structure and a large specific surface area ($63\text{--}300\text{ m}^2\text{ g}^{-1}$) [10]. The charge of Mn in octahedral sites varies with the changes of environment and leads to different number of interlayer cations [11]. The interlayer cations can be more easily replaced by other inorganic or organic cations based on the electronegative level [12]. The sodium ions in birnessite can be fully exchanged by univalent ions and partly exchanged by calcium and magnesium ions [13]. Some recent studies reported that birnessite was able to promote the decomposition of tetracycline or CIP [14–17].

The aim of this study was to study CIP adsorption on birnessite under different physicochemical conditions and to investigate the potential mechanism of CIP adsorption on

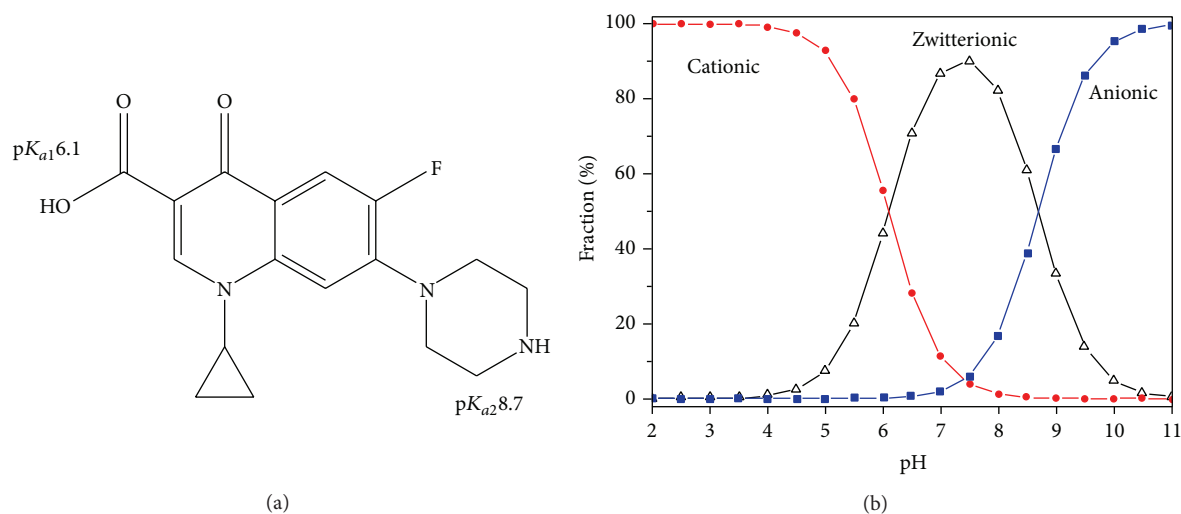


FIGURE 1: Molecular structure of ciprofloxacin (a) and speciation of CIP as a function of solution pH (b).

birnessite using X-ray diffraction (XRD), Fourier transform infrared spectroscopy (FTIR), and Material Studio simulation.

2. Materials and Methods

2.1. Experimental Materials. Sodium hydroxide, manganese chloride ($\text{MnCl}_2 \cdot 4\text{H}_2\text{O}$), and potassium permanganate were all purchased from Beijing Chemical Works. CIP has a water solubility of 30 g/L at 20°C and acid dissociation constants $\text{p}K_{a1}$ and $\text{p}K_{a2}$ at 6.1 and 8.7 [18]. When the pH is less than 6.1, the CIP molecule exists as a cation because of the protonation of amino in the triazine part. Between pH 6.1 and 8.7, zwitterion is the main form of CIP due to protonation of amino in the piperazine part and deprotonation of carboxyl. An anion is a dominant species when pH is greater than 8.7, as a result of the loss of amino group proton in piperazine moiety [19] (Figure 1).

2.2. Preparation of Birnessite with Different Average Oxidation States (AOS) of Mn. In this paper, a liquid-phase reaction method was used to prepare birnessite. The first step was to mix 0.02 mol $\text{MnCl}_2 \cdot 4\text{H}_2\text{O}$ and 0.25 mol NaOH in 100 mL distilled water. In order to form a homogeneous solution, the mixture was stirred for 1 min at room temperature. And then solution was mixed with 50 mL KMnO_4 solution in different molar ratio (61.76%, 57.89%, 54.76%, 52.17%, 50.00%, and 48.15%) relative to $\text{MnCl}_2 \cdot 4\text{H}_2\text{O}$ and stirring continued for 30 min to insure the reaction was complete. The product was aged for 24 h at room temperature. At last, the products were washed with distilled water for ten times and dried at 60°C for 24 h. Then series of birnessites with different AOS of Mn were obtained, named (I, II, III, IV, V, VI).

2.3. CIP Adsorption on Birnessite. Kinetics of CIP adsorption were carried out to evaluate the parameters of CIP removal from water by birnessite and to provide guides for further

studies on equilibrium CIP adsorption and effect of solution pH on CIP adsorption.

The study of the kinetics of CIP adsorption on birnessite was performed by mixing 0.1 g dry weight of birnessite with 25 mL of 1000 mg/L CIP solution on a horizontal shaker at 150 rpm for the following shaking times: 0.5, 1, 2, 10, 20, 30, 60, 120, 180, 240, and 300 min.

For CIP adsorption isotherm study, 0.1 g (dry weight) of birnessite was mixed with 10 mL CIP solution in each 50 mL centrifuge tube at initial concentrations of 500, 1000, 2000, 3000, 4000, and 6000 mg/L on a horizontal shaker at 150 rpm for 24 h.

The pH of the equilibrium solution was kept about 6.4 for the kinetics and isotherm study.

For the study of influence of solution pH on CIP adsorption, 0.1 g (dry weight) of birnessite and 25 mL of 2000 mg/L CIP solution were mixed in each 50 mL centrifuge tube. Then, solution pH was measured and readjusted with HCl or NaOH every 8 h until the pH stabilized at the desired final solution pH of 1–11 with an increment of 2. The total time of mixing was 24 h.

For the three experiments mentioned above, a duplicate was performed for each variable. After desired time, the mixture was centrifuged for 10 min at 7500 rpm and the supernatant passed through $0.45 \mu\text{m}$ syringe filters before being analyzed for equilibrium CIP concentrations using a UV-Vis method.

All experiments mentioned above were carried out to provide guidance for the following experiment: the effect of AOS of Mn in birnessites (different molar ratio of KMnO_4 and $\text{MnCl}_2 \cdot 4\text{H}_2\text{O}$) on CIP adsorption. 0.1 g dry weight of different kind of birnessite and 25 mL of 6000 mg/L CIP solution were mixed in each 50 mL centrifuge tube under the conditions of pH = 7.

2.4. Methods of Analyses. We determined the equilibrium CIP concentrations via a UV-Vis spectrophotometer at the wavelength of 280 nm; the calibration curve was established

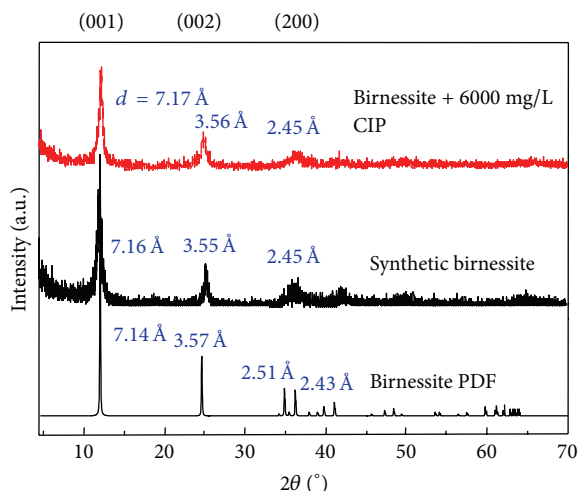


FIGURE 2: X-ray diffraction patterns of birnessite (V) and birnessite (V) which was reacted with the concentration of 6000 mg/L CIP solution.

by 10 standards in the range of 1–10 mg/L and the coefficient of regression r^2 was 0.997. For the experiment of influence of solution pH on CIP adsorption especially, we established 6 calibration curves with the pH of 1, 3, 5, 7, 9, and 11 to determine the equilibrium CIP concentrations.

For the crystal structure of manganese dioxides, X-ray powder diffraction analysis was used to characterize it. And it was performed at 40 kV and 100 mA. Oriented samples were scanned from 2θ 3° to 70° with a scanning speed of $8^\circ/\text{min}$.

The FTIR spectra were collected by accumulating 16 scans at a resolution of 4 cm^{-1} in the range of 450 to 4000 cm^{-1} on a Spectrum 100 spectrometer equipped with a mercury cadmium telluride detector.

Molecular simulation of binding energy between birnessite of different AOS of Mn and CIP was studied by means of the module Forcite of Materials Studio 5.0 software. During simulation, the quantum chemical module of Materials Studio CASTEP was used to calculate the interaction energy between CIP and birnessite. By comparing the energies, the ease of interaction between CIP and birnessite on edge surface could be determined. The lower the energy is, the more easy the interaction is.

Birnessite is a layered manganese oxide mineral. Each layer consists of edge-shared MnO_6 octahedron. In the inter-layer space, there are metal cations and water molecules. The birnessite model was constructed and the atomic coordinates were derived from the space group of C1 with $a = 5.175\text{ \AA}$, $b = 8.93\text{ \AA}$, $c = 7.38\text{ \AA}$, and $\beta = 103.18^\circ$ [20]. And we chose the (010) plane of birnessite as a demonstrational edge surface and (001) plane as the basic surface in this study.

3. Results and Discussion

3.1. Characterization of Birnessite (V) by XRD. The original sample of birnessite (V) and the birnessite (V) reacted with the concentration of 6000 mg/L CIP solution were characterized by XRD (Figure 2). The results showed that

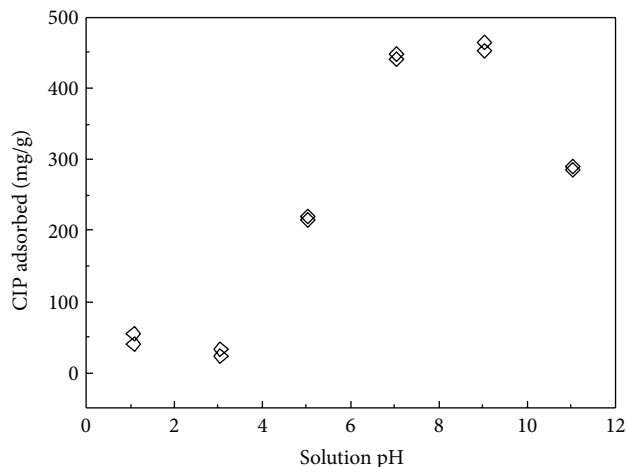


FIGURE 3: Adsorption of CIP on birnessite (V) affected by solution pH.

the synthetic material agreed well with the standard cards of birnessite, indicating that the synthetic material was relatively pure birnessite. On the other hand, compared with the two XRD diffraction patterns, the corresponding peak of (001) crystal planes was not moved and the layer spacing remained the same, proving that surface adsorption instead of interlayer adsorption was the main form of CIP uptake on birnessite.

3.2. Influence of Solution pH on CIP Removal by Birnessite. The electric charges of CIP vary with pH and lead to different CIP adsorption capacity. Under strong acidic conditions, changes in solution pH had a minimal effect on CIP removal. And then CIP adsorption increased gradually with the increase of pH. Above pH 8.7, a further increase in solution pH resulted in a remarkable decrease in CIP removal (Figure 3). This trend was similar to CIP adsorption on Camontmorillonite and kaolinite [21, 22].

Considering that the $\text{p}K_a$ values of CIP were 6.1 and 8.7, the CIP was in its zwitterionic form when solution pH was between 6.1 and 8.7. Even though the net charge of the whole molecule was zero, the positively charged amino was still able to contribute to the adsorption of CIP on birnessite. Therefore, a higher adsorption capacity occurred in the range of pH 3 to 8.7. The adsorption was lower when solution pH was 3 or less, because the negative charge of birnessite surface decreased under low pH [27] and brought repulsion with the positively charged CIP. When solution pH was greater than 8.7, an anion played a dominant role in CIP speciation. Significant repulsion was induced between the negatively charged surfaces of birnessite and CIP. Thus CIP removal on birnessite was significantly reduced in this case.

3.3. Kinetics of CIP Removal by Birnessite. The fast adsorption rate was observed in this experiment, and it could reach the adsorption equilibrium in 240 min (Figure 4), proving that the shaking time of 24 h was enough for other experiments. Kinetic characteristics of CIP removal agreed well with

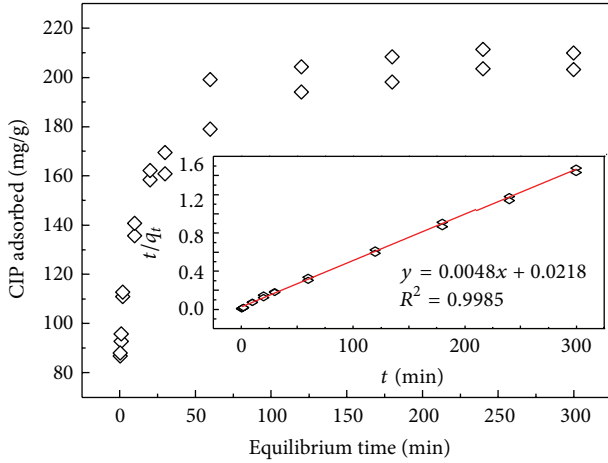


FIGURE 4: Kinetics of CIP adsorption on birnessite (V). The solid line is pseudo-second-order fit to the observed data. Inserts are plot of t/q_t against t for birnessite (V).

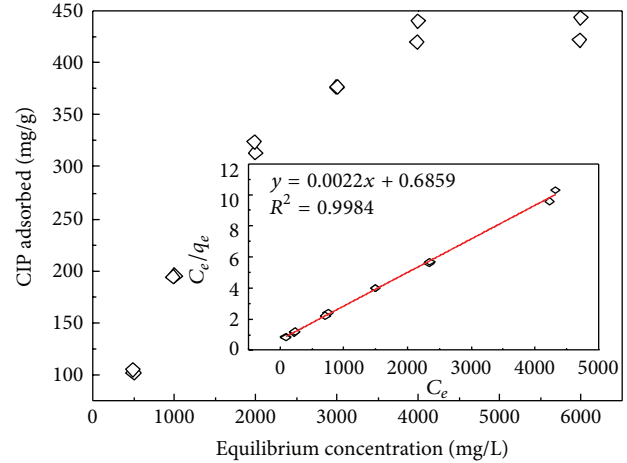


FIGURE 5: CIP adsorption on birnessite (V). The solid line is the Langmuir fits to the observed data.

the pseudo-second-order model. The integrated rate laws of the pseudo-second-order kinetics are [23, 24]

$$\frac{t}{q_t} = \frac{1}{K_s q_e^2} + \frac{1}{q_e} t, \quad (1)$$

$$q_t = \frac{C_0 - C_t}{M} V,$$

in which t (min) is the time of adsorption, q_t (mg/g) is the amount of solute adsorbed on the adsorbent surface at time t , q_e (mg/g) is the amount of solute adsorbed at equilibrium, K_s {mg/(g·min)} is the rate constant for adsorption, and C_t and C_0 are the concentrations of solute at time t and time zero.

The calculated q_e was 208 mg/g close to the experimental value of 203 mg/g. The pseudo-second-order kinetics with a coefficient of correlation $r^2 = 0.999$.

3.4. Equilibrium of CIP Removal by Birnessite. The equilibrium of CIP removal was described by the adsorption isotherm. The observed CIP adsorption capacity was about 419–442 mg/g at room temperature and the adsorption data was fitted to the Langmuir isotherm (Figure 5).

The linear forms of Langmuir isotherm model can be represented as follows:

$$\frac{C_e}{q_e} = \frac{C_e}{q_m} + \frac{1}{q_m K_L}, \quad (2)$$

in which C_e is the concentration of CIP at equilibrium (mg/L); q_e is the amount of CIP adsorbed per gram of birnessite (mg/g); q_m is the maximum adsorption in theory; and K_L is the constant of isotherm equation.

The calculated q_m was 455 mg/g close to the experimental value of 442 mg/g. And the r^2 of pseudo-second-order kinetics was greater than 0.99.

The analysis suggested that the thermodynamic characteristics of CIP adsorption were well fitted to the Langmuir model.

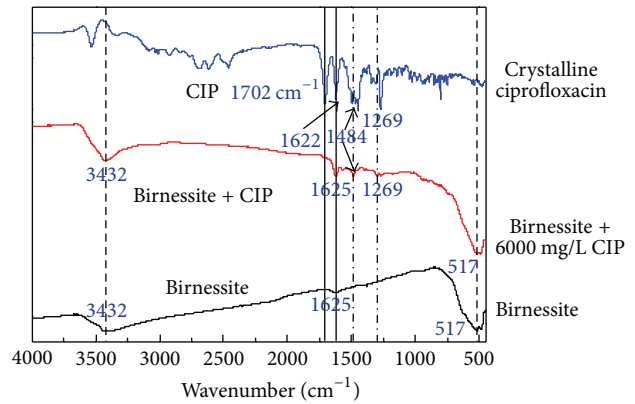


FIGURE 6: FTIR spectra of CIP (6000 mg/L) adsorbed birnessite (V) at 450–4000 cm^{-1} .

3.5. FTIR Analyses. Figure 6 presents the FTIR spectra of CIP, raw birnessite, and 6000 mg/L CIP adsorbed birnessite.

Compared with the FTIR spectra of raw birnessite and birnessite with adsorbed CIP, there was no significant change in the vibration of the backbone of birnessite before and after CIP adsorption, which indicated that the adsorbed CIP did not alter the structure, consistent with XRD observation.

Crystalline CIP had many characteristic peaks at the finger print (1200–1800 cm^{-1}). There was a peak that appeared in 1703–1699 cm^{-1} due to the fact that the ν (carboxylic acid C=O) and the ν (Ketone C=O) were located at 1622 cm^{-1} [18, 25]. And two relatively strong peaks appeared in 1269 cm^{-1} and 1484 cm^{-1} .

Because of MnO_6 octahedral, the FTIR spectra of original and CIP-adsorbed birnessite had a strong absorption peak at about 520 cm^{-1} . A broad weak and a strong broad peaks appeared in 1624 and 3431 cm^{-1} with the former attributed to less ordered water and the latter to OH, H_2O adsorbed on birnessite [26]. The other explanation of these phenomena was the bending mode of H_2O and the stretching mode of the OH groups.

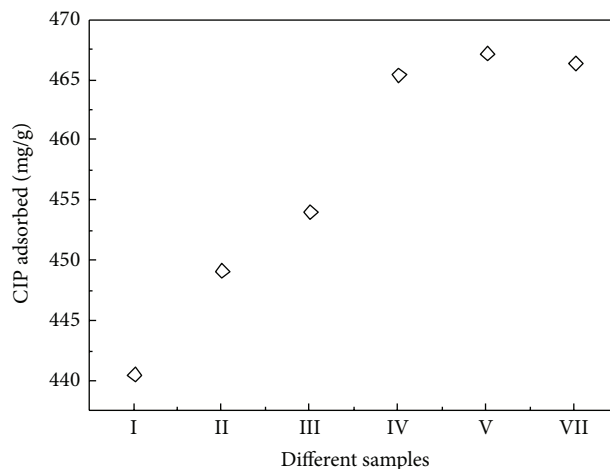


FIGURE 7: CIP adsorption on birnessite samples of different $\text{MnCl}_2/\text{KMnO}_4$ ratios.

The most obvious changes are those in $1200\text{--}1500\text{ cm}^{-1}$. At wave numbers 1269 cm^{-1} and 1484 cm^{-1} , which were the characteristic peaks of crystalline CIP, the CIP-adsorbed birnessite showed the two new peaks compared with the original material, characterizing the reaction between birnessite and CIP.

3.6. Influence of Birnessite with Different AOS on CIP Removal. Based on the study of influence of solution pH on CIP removal by birnessite, we chose the same acidity condition (pH = 7) to carry out this experiment.

Adsorption capacity of CIP increased gradually with the increase of the molar ratio of MnCl_2 and KMnO_4 (Figure 7). Consider that birnessite has a hexagonal symmetry layer structure and may possess a variable number of octahedral cationic vacancies within its layers. Manganese oxide octahedral vacancies lead to the production of the negative charge on the birnessite surface [27]. When solution pH was 7, part of the CIP was in its cationic form. And the interaction between CIPH^+ and negative surface charge resulted in the adsorption of CIP on birnessite. The increase of the ratio of MnCl_2 and KMnO_4 leads to the decrease of Mn AOS and the increase of surface electronegativity in birnessite. Thus the adsorption capacity of CIP increased from sample I to V.

3.7. Molecular Simulation. As birnessite had two-dimensional morphology microscopically, it could be presumed that the large and flat surfaces on the basic plane would be the sites for adsorption of CIP. And the charge of birnessite is deeply dependent on the ratio of Mn (II) to Mn (VII). If the adsorption of CIP on birnessite was from electrostatic interaction, the location of charge on birnessite would play an important role on the sorption sites of CIP.

We simulated the interactions between CIP and birnessite on (010) surfaces under 3 different conditions for AOS of Mn (Figure 8). To judge which condition is more stable, we calculate the total energy of the 3 different conditions for AOS of Mn. After that, we set the total energy of the highest AOS of Mn ($n(\text{KMnO}_4) : n(\text{MnCl}_2) = 61.76\%$) as the standard; when

the ratio of KMnO_4 to MnCl_2 was in sequence of 54.76% and 50.00%, the differences between the 2 energy values and the standard were in order of -6.55 and -7.47 KJ/mol . With the increase of the ratio of Mn (II) to Mn (VII), the difference of total interaction energy decreased more, showing that the system was more stable and leads to higher adsorption capacity of CIP.

The simulations showed that CIP could interact with the (010) edge surfaces more easily under a lower AOS of Mn due to the comparison among the final energy. And the simulation results agreed well with the experimental phenomenon about birnessite with different AOS on CIP removal.

3.8. Discussion. Because the pH of the equilibrium solution was 6.4, under which CIP would be a monovalent cation CIPH^+ . And the birnessite edge would be negatively charged. Therefore, the interaction between birnessite and CIP may cause CIP adsorption by birnessite.

We used Material Studio to simulate CIP removal by birnessite of different AOS of Mn and calculate the binding energy between birnessite and CIP. Quantum mechanics simulation under different proportions of Mn^{2+} conditions showed that CIP could interact with the (010) edge surfaces more securely when the AOS of Mn decreased, in which case the total negative charges of birnessite increased. This phenomenon suggested again that the removal of CIP by birnessite was due to surface adsorption and it was similar to the adsorption of oxytetracycline on montmorillonite, which confirmed that the dominant mechanism of interaction was the hydrogen bonding [28].

4. Conclusions

Kinetic and thermodynamics experiments showed that CIP adsorption fitted to the pseudo-second-order kinetics and Langmuir isotherm model well. We carried out another two experiments of changing the electric charge of CIP (the pH experiment) and the charge of birnessite (the experiment

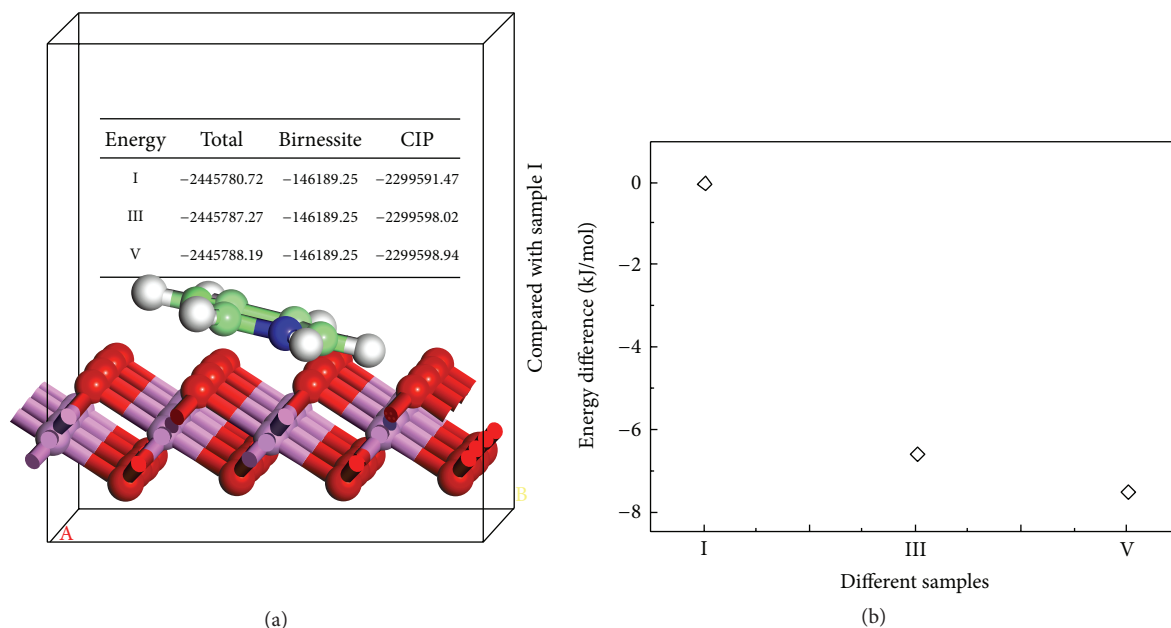


FIGURE 8: Energy (KJ/mol) of birnessite and CIP in the system of different samples (a) and energy difference compared with the energy of sample I (b).

using birnessite of different AOS of Mn), and the results showed that CIP adsorption changed as the electric charge of CIP and birnessite changed. This phenomenon proved that it was surface adsorption that caused the removal of CIP on birnessite. And the XRD, FTIR analysis, and molecular simulations confirmed this mechanism again.

Conflict of Interests

The authors declare that there is no conflict of interests regarding the publication of this paper.

Authors' Contribution

Xuebing Xing and Jingwen Feng contributed equally to this paper.

Acknowledgments

This research was jointly funded by Beijing Higher Education Young Elite Teacher Project, the University Students' Innovative Undertaking Training Program, and International S&T Cooperation (no. S2014ZR0062).

References

- [1] M. Min and G. Lu, "Antibiotics in the water environment," *Chemical and Biological Engineering*, vol. 30, no. 11, pp. 19–22, 2013.
- [2] J. Kagle, A. W. Porter, R. W. Murdoch, G. Rivera-Cancel, and A. G. Hay, "Chapter 3 biodegradation of pharmaceutical and personal care products," *Advances in Applied Microbiology*, vol. 67, pp. 65–108, 2009.
- [3] E. M. Golet, I. Xifra, H. Siegrist, A. C. Alder, and W. Giger, "Environmental exposure assessment of fluoroquinolone antibacterial agents from sewage to soil," *Environmental Science & Technology*, vol. 37, no. 15, pp. 3243–3249, 2003.
- [4] X. Yang, R. C. Flowers, H. S. Weinberg, and P. C. Singer, "Occurrence and removal of pharmaceuticals and personal care products (PPCPs) in an advanced wastewater reclamation plant," *Water Research*, vol. 45, no. 16, pp. 5218–5228, 2011.
- [5] C. Miège, J. M. Choubert, L. Ribeiro, M. Eusèbe, and M. Coquery, "Fate of pharmaceuticals and personal care products in wastewater treatment plants-conception of a database and first results," *Environmental Pollution*, vol. 157, no. 5, pp. 1721–1726, 2009.
- [6] A. J. Carrasquillo, G. L. Bruland, A. A. Mackay, and D. Vasudevan, "Sorption of ciprofloxacin and oxytetracycline zwitterions to soils and soil minerals: influence of compound structure," *Environmental Science and Technology*, vol. 42, no. 20, pp. 7634–7642, 2008.
- [7] D. Vasudevan, G. L. Bruland, B. S. Torrance, V. G. Upchurch, and A. A. MacKay, "pH-dependent ciprofloxacin sorption to soils: Interaction mechanisms and soil factors influencing sorption," *Geoderma*, vol. 151, no. 3-4, pp. 68–76, 2009.
- [8] L. H. P. Jones and A. A. Milne, "Birnessite: a new manganese oxide mineral from Aberdeenshire, Scotland," *Mineral Magazine*, vol. 151, pp. 283–288, 1956.
- [9] R. M. McKenzie, "The manganese oxides and hydroxides," in *Minerals in Soil Environments*, J. B. Dixon and S. W. Weeds, Eds., pp. 439–465, Soil Science Society of American Madison, Madison, Wis, USA, 1989.
- [10] J. A. Davis and D. B. Kent, "Surface complexation modelling in aqueous geochemistry," *Reviews in Mineralogy*, vol. 23, no. 1, pp. 177–260, 1990.
- [11] J. E. Post and D. R. Veblen, "Crystal structure determinations of synthetic sodium, magnesium, and potassium birnessite using

- TEM and the Rietveld method,” *American Mineralogist*, vol. 75, no. 5-6, pp. 477-489, 1990.
- [12] L. Zhao, Y. Sun, and L. Yu, “The organic montmorillonite intercalated modified and performance study,” *China Mining*, vol. 19, no. 11, pp. 1101-1204, 2010.
- [13] L. Al-Attar and A. Dyer, “Ion exchange in bimessite,” *Land Contamination and Reclamation*, vol. 15, no. 4, pp. 427-436, 2007.
- [14] H. Zhang and C.-H. Huang, “Oxidative transformation of fluoroquinolone antibacterial agents and structurally related amines by manganese oxide,” *Environmental Science and Technology*, vol. 39, no. 12, pp. 4474-4483, 2005.
- [15] K. F. Rubert IV and J. A. Pedersen, “Kinetics of oxytetracycline reaction with a hydrous manganese oxide,” *Environmental Science and Technology*, vol. 40, no. 23, pp. 7216-7221, 2006.
- [16] W.-R. Chen and C.-H. Huang, “Transformation kinetics and pathways of tetracycline antibiotics with manganese oxide,” *Environmental Pollution*, vol. 159, no. 5, pp. 1092-1100, 2011.
- [17] G. Chen, L. Zhao, and Y. H. Dong, “Oxidative degradation kinetics and products of chlortetracycline by manganese dioxide,” *Journal of Hazardous Materials*, vol. 193, pp. 128-138, 2011.
- [18] C. Gu and K. G. Karthikeyan, “Sorption of the antimicrobial ciprofloxacin to aluminum and iron hydrous oxides,” *Environmental Science and Technology*, vol. 39, no. 23, pp. 9166-9173, 2005.
- [19] C.-J. Wang, Z. Li, and W.-T. Jiang, “Adsorption of ciprofloxacin on 2:1 dioctahedral clay minerals,” *Applied Clay Science*, vol. 53, no. 4, pp. 723-728, 2011.
- [20] M. N. G. James and G. J. B. Williams, “Structural studies of histamine RB effector molecules: the crystal structure of the antihistaminic drug (+)-chlorpheniramine maleate,” *Canadian Journal of Chemistry*, vol. 30, pp. 1249-1257, 1974.
- [21] C. J. Wang, Z. Li, W. T. Jiang, J. S. Jean, and C. C. Liu, “Cation exchange interaction between antibiotic ciprofloxacin and montmorillonite,” *Journal of Hazardous Materials*, vol. 183, no. 1-3, pp. 309-314, 2010.
- [22] Z. Li, H. Hong, L. Liao et al., “A mechanistic study of ciprofloxacin removal by kaolinite,” *Colloids and Surfaces B: Biointerfaces*, vol. 88, no. 1, pp. 339-344, 2011.
- [23] G. Blanchard, M. Maunaye, and G. Martin, “Removal of heavy metals from waters by means of natural zeolites,” *Water Research*, vol. 18, no. 12, pp. 1501-1507, 1984.
- [24] Y. S. Ho and G. McKay, “Sorption of dye from aqueous solution by peat,” *Chemical Engineering Journal*, vol. 70, no. 2, pp. 115-124, 1998.
- [25] P. Trivedi and D. Vasudevan, “Spectroscopic investigation of ciprofloxacin speciation at the goethite-water interface,” *Environmental Science and Technology*, vol. 41, no. 9, pp. 3153-3158, 2007.
- [26] A. Jokic, A. I. Frenkel, and P. M. Huang, “Effect of light on birnessite catalysis of the Maillard reaction and its implication in humification,” *Canadian Journal of Soil Science*, vol. 81, no. 3, pp. 277-283, 2001.
- [27] R. M. McKenzie, “The surface charge on manganese dioxides,” *Australian Journal of Soil Research*, vol. 19, no. 1, pp. 41-50, 1981.
- [28] L. Aristilde, C. Marichal, J. Miehe-Brendlé, B. Lanson, and L. Charlet, “Interactions of oxytetracycline with a smectite clay: a spectroscopic study with molecular simulations,” *Environmental Science and Technology*, vol. 44, no. 20, pp. 7839-7845, 2010.

Research Article

Seismic Earth Pressures of Retaining Wall from Large Shaking Table Tests

Changwei Yang, Jian Jing Zhang, Qu Honglue, Bi Junwei, and Liu Feicheng

School of Civil Engineering, Key Laboratory of Transportation Tunnel Engineering, Ministry of Education, Southwest Jiaotong University, Chengdu 610031, China

Correspondence should be addressed to Jian Jing Zhang; zhangzhangjianjing@163.com

Received 25 March 2014; Revised 6 June 2014; Accepted 12 June 2014

Academic Editor: Zhaohui Li

Copyright © 2015 Changwei Yang et al. This is an open access article distributed under the Creative Commons Attribution License, which permits unrestricted use, distribution, and reproduction in any medium, provided the original work is properly cited.

To ascertain seismic response of retaining wall in the Wenchuan earthquake, large shaking table tests are performed and an acceleration record is acted in 3 directions. In the tests, acceleration time history recorded at Wolong station in the Wenchuan earthquake is used to excite the model wall. Results from the tests show that the location of dynamic resultant earth pressure is 0.35–0.49 H from toe of the wall for road shoulder retaining wall on rock foundation, 0.33–0.42 H for embankment retaining wall on rock foundation, and 0.46–0.77 H for road shoulder retaining wall on soil foundation. Besides, dynamic earth pressure increases with the increase of ground shaking from 0.1 g to 0.9 g and the relationship is nonlinear. The distribution is closed to for PGA less than 0.4 g but larger for PGA larger than and equal to 0.4 g, especially on the soil foundation. After the comparison of measured earth pressures and theoretical results by pseudodynamic method and pseudostatic method, results of the former are consistent with those of the shaking table test, but results of the latter method are smaller than measured.

1. Introduction

The Wenchuan earthquake seriously damaged retaining structures of highway and railway in the disaster areas, which not only brings direct economic losses, but also delays the process of rescue and relief. To support the postdisaster reconstruction and complement the code for seismic design of retaining structures, Zhang et al. [1] carried out a number of field survey and analyses and mainly focused on the seismic damages of retaining structures. Results from the field survey show that the number of damaged gravity retaining walls is up to 97.1% of all damaged retaining walls. The result stipulates us to carry out seismic performance of gravity walls. Besides, estimation of the seismic earth pressure is an important topic of research for the safe design of retaining wall in the seismic zone. It is a common practice to the seismic accelerations in both horizontal and vertical directions in terms of equivalent static forces, called pseudostatic accelerations. Using the pseudostatic approach, several researchers have developed different methods to determine the seismic earth pressure on a rigid retaining wall due to earthquake loading starting from the pioneering works by Okabe [2] and Mononobe [3],

commonly known as Mononobe-Okabe method [4] based on the pseudostatic approach, which gives the linear earth pressure distribution in a very approximate way irrespective of static and seismic conditions. Kumar [5] had determined the seismic passive earth pressure coefficients for sands using limit equilibrium method. Dewaiker and Halkude [6] have proposed a pseudostatic numerical analysis of seismic active and passive thrust on retaining wall, using Kotter's equation. Kumar and Chitikela obtained the seismic passive earth pressure coefficients using method of characteristics. Madhav and Kameswara Rao [7], Choudhury et al. [8], Choudhury [9], and Subba Rao and Choudhury [10] have adopted limit equilibrium for determining individually the seismic passive earth pressure coefficients corresponding to unit weight, surcharge, and cohesion components. Choudhury and Singh [11] have determined active earth pressure coefficients under static and seismic conditions using modified Culmann method. However, all the above methods are based on pseudostatic method of analysis, which does not consider the time effect of the applied earthquake load and the effect of shear and primary waves passing through the soil media. To overcome these drawbacks, the analytical method based on

pseudodynamic approach as given by Steedman and Zeng [12] and modified by Choudhury and Nimbalkar [13, 14] is used for the present analysis for calculation of seismic passive and active earth pressure.

Steedman and Zeng [12] considered in their analysis a vertical rigid retaining wall supporting a particular value of soil friction angle and a particular value of seismic horizontal acceleration (k_{hg} , where g is the acceleration due to gravity) only. Again they have considered the effect of horizontal seismic acceleration due to vertically propagating shear waves through the backfill behind retaining wall. In an improvement over this method, Choudhury and Nimbalkar [14] have incorporated effect of vertical seismic acceleration due to vertically propagating primary waves through the backfill soil. Again, they have studied the effect of various parameters such as wall friction angle, soil friction angle, shear wave velocity, primary wave velocity, and both the horizontal and vertical seismic accelerations on the seismic active earth pressure behind a rigid retaining wall by the pseudodynamic method. Choudhury and Nimbalkar [13] have extended this modified work for estimation of seismic passive earth pressure.

In the pseudodynamic method, vertically propagating shear and primary waves through the backfill generate vibrations in horizontal and vertical directions, respectively. These horizontal and vertical vibrations correspond to horizontal and vertical time dependent seismic inertia forces, respectively. Time dependent nature of these seismic inertia forces is considered in the present analysis.

After the pseudodynamic method, the dynamic method which is finite element method and the shaking table test are used to the safe design of retaining wall in the seismic zone [15, 16].

In the procedure of the development of pseudostatic method, pseudodynamic method, and dynamic method, achievements have been obtained, but some problems have not been understood, such as the location of resultant earth pressure and relationships between earth pressure and ground shaking intensity. As a result, large shaking table tests are performed in order to effectively help us improve the understanding of characteristics of retaining structures in highway and railway engineering. The reason for performing the large shaking table tests is that the tests are the most direct research approach [17, 18].

2. Shaking Table Tests

2.1. Shaking Table Test. The tests were performed on a large shaking table with an advanced CNC system, data acquisition, and analysis system in the Nuclear Power Research and Design Institute of China. The shaking table, 6 m by 6 m, has 6 degrees of freedom; the maximum weight is 60 ton, the maximum horizontal displacement is ± 150 mm, and the maximal vertical displacement is ± 100 mm. The full-loaded horizontal and vertical maximum acceleration is 1.0 g and 0.8 g and the horizontal and vertical maximum acceleration for no loading is 3.0 g and 2.6 g with frequency ranges from 0.1 Hz to 80 Hz. And in the shaking table tests, a 128 channel BBM data acquisition system with a maximum referenced error $\leq 0.5\%$,



FIGURE 1: Systems of CNC, data acquisition, and analysis.

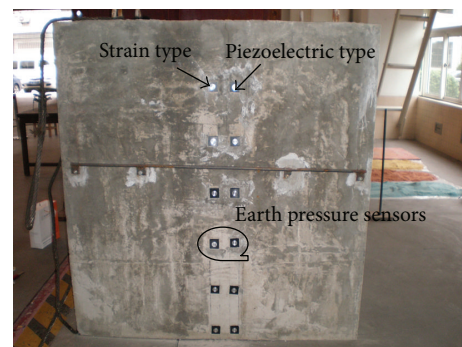


FIGURE 2: Gravity retaining wall model and earth pressure sensor installation diagram.

is used to perform data acquisition, monitoring signal and analysis online synchronously, as shown in Figure 1.

2.2. Retaining Wall Model. In the shaking table tests, three different gravity retaining wall models are constructed in the tests: road shoulder retaining wall on rock foundation, road shoulder retaining wall on soil foundation, and embankment retaining wall on rock foundation.

The internal size of model boxes is $3.7 \text{ m} \times 1.5 \text{ m} \times 2.1 \text{ m}$ and the model box is made of steel frame with steel plate on the bottom. In order to observe movement of the retaining wall and backfill, lateral walls of the steel frame are made of organic glass, and a type of absorbing material is set up on the lateral walls perpendicular to horizontal movement direction for reducing the reflection of seismic wave on the boundary. The height of the model wall is 1.6 m with a similitude ratio of 6 for modeling a wall with 9.6 m high and the backfill used in the test is granite sand, as shown in Figure 2. The similitude ratios for density and acceleration are 1, respectively, and similitude relationships of other parameters can be deduced based on Buckingham π theorem [19, 20]. The test model panorama is shown in Figure 3.

Data acquisition includes displacements, accelerations, and total and dynamic earth pressures. The sensor location arrangements are presented in Figure 4, and the sensor installation diagrams of earth pressures and displacements are shown in Figure 2 and Figure 5, respectively.

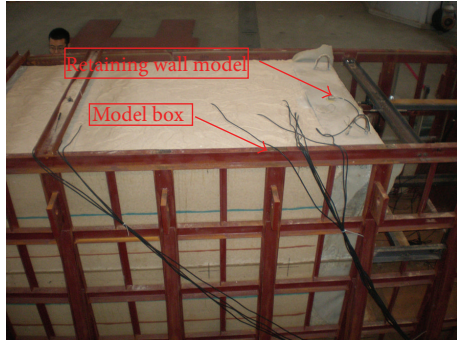


FIGURE 3: Test model panorama.

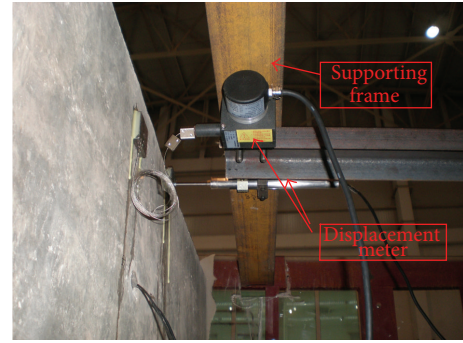


FIGURE 5: Displacement sensor installation diagram.

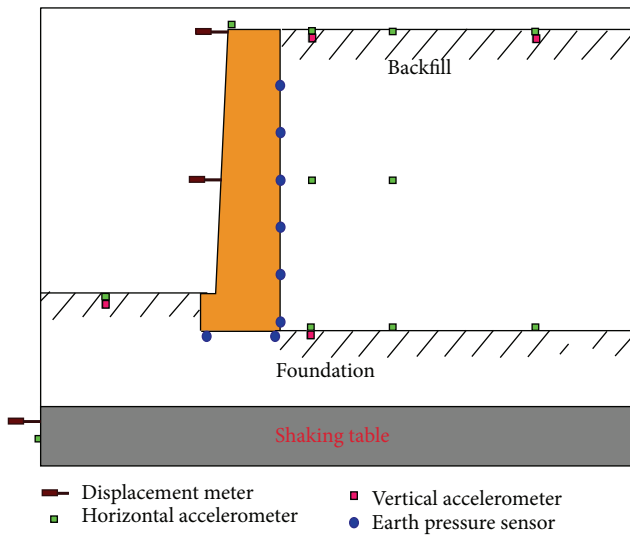


FIGURE 4: The instrument configuration.

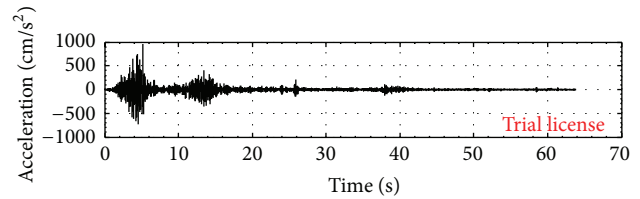


FIGURE 6: Scaled acceleration time history on duration and amplitude.

2.3. *Loading Cases.* Horizontal and vertical accelerations recorded at Wolong station in the Wenchuan earthquake are used to excite the model wall, which are scaled in the duration according to the similitude ratio used, as shown in Figure 6. Then the scaled seismic accelerations are scaled again on required amplitudes. The scaled seismic accelerations on duration and amplitude are used as input motions to excite the platform from the horizontal and vertical directions. The loading sequence in the test is white noise, PGA 0.1 g, PGA 0.2 g, PGA 0.4 g, PGA 0.7 g, and PGA 0.9 g.

3. Experimental Result Analyses

3.1. *Earth Pressure Distribution on Backwall.* The measured distributions of total and dynamic earth pressures, as shown in Figures 7 and 8, present that the distributions are nonlinear along the wall height and the amplitude of the earth pressures are proportional to the excited seismic peak accelerations [21, 22]. The dynamic earth pressures are comparatively small for PGA less than 0.4 g but increase obviously for PGA larger than and equal to 0.4 g. Besides, the rate of earth pressure intensity change is related to geometric position,

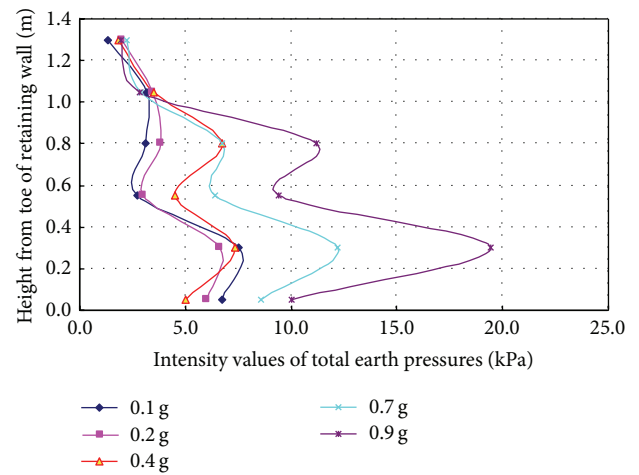


FIGURE 7: The distribution of total earth pressure.

comparatively smaller above 2/3 H from toe of the wall but larger below.

3.2. *Resultant Earth Pressures on Backwall.* Resultant dynamic and total earth pressures are proportional to the excited seismic peak acceleration and increase more obviously with the increase of excited seismic peak accelerations [23], as shown in Figures 9 and 10. The foundation condition of retaining wall is an important influence factor to resultant total and dynamic earth pressure. Compared with retaining walls constructed on rock foundation, the dynamic and total earth pressures of retaining walls on soil foundation are larger. The influence of foundation condition is not obvious when the excited seismic coefficient is low, and the difference

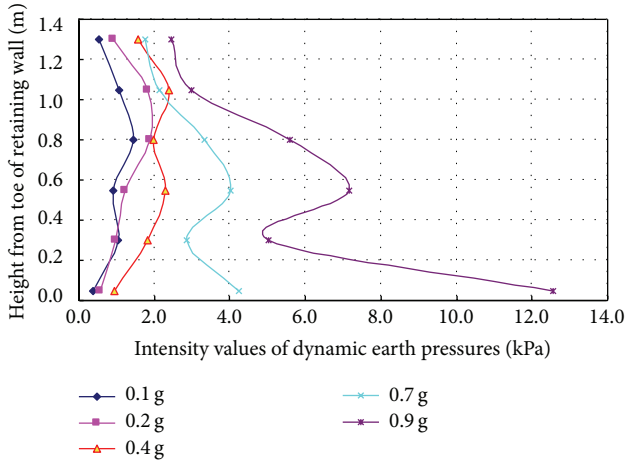


FIGURE 8: The distribution of dynamic earth pressure.

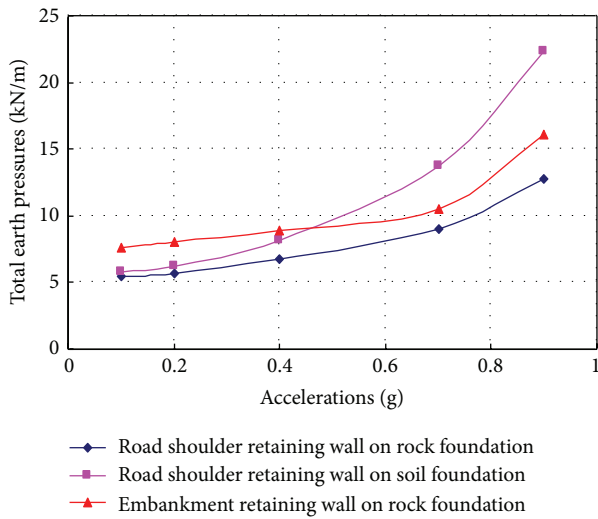


FIGURE 9: Resultant total earth pressures.

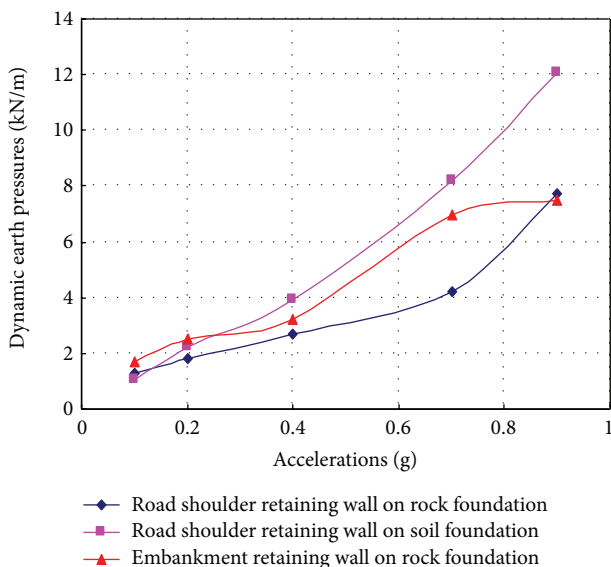


FIGURE 10: Resultant dynamic earth pressures.

TABLE 1: Location of resultant earth pressure of road shoulder retaining wall on rock foundation (h/H).

Seismic coefficient	Location of resultant total earth pressure	Location of resultant dynamic earth pressure
0.1	0.34	0.46
0.2	0.38	0.49
0.4	0.39	0.48
0.7	0.34	0.4
0.9	0.33	0.35

* H : height of wall; h : height of location of resultant earth pressure from toe of wall.

TABLE 2: Location of resultant earth pressure of embankment retaining wall on rock foundation (h/H).

Seismic coefficient	Location of resultant total earth pressure	Location of resultant dynamic earth pressure
0.1	0.44	0.38
0.2	0.44	0.42
0.4	0.39	0.38
0.7	0.35	0.33
0.9	0.32	0.36

of total earth pressure is less than 15% for PGA less than or equal to 0.3 g but respectively, 20.56%, 52.84%, and 75.02% for PGA equal to 0.4 g, 0.7 g, and 0.9 g. It is clear that the impact of foundation condition becomes greater with the increase of excited seismic peak accelerations. As a result, the influence of foundation on a seismic performance of retaining wall should be considered according to the regions where the retaining wall locates. Comparing to the regions of seismic intensities below 8 degrees if a retaining wall locates, the influence of foundation in the regions with seismic intensities above 8 degrees should be carefully concerned [24].

In addition, the values of total and dynamic earth pressures are relevant to backfill form. The total and dynamic earth pressures of an embankment retaining wall are larger than those of shoulder retaining wall. The differences from the forms of backfill reduced with the increase of excited seismic peak acceleration but should not be ignored, as the embankment earth pressures are still larger.

3.3. Location of Resultant Earth Pressure on Backwall. The measured locations of resultant earth pressures (h/H) are summarized in Tables 1, 2, and 3. Obviously, when the seismic coefficient is low, measured locations of resultant total and dynamic earth pressure are above 0.33 H from the toe of wall. With the increase of seismic coefficient, the locations become close to 0.33 H, which is provided by M-O formula [2, 3]. Figure 11 presents the results of the locations of resultant total earth pressures (h/H) with excited seismic coefficients of three different test models, and Figure 12 presents the results of the locations of resultant dynamic earth pressures (h/H) with excited seismic coefficients of three different test models.

TABLE 3: Location of resultant earth pressure of road shoulder retaining wall on soil foundation (h/H).

Seismic coefficient	Location of resultant total earth pressure	Location of resultant dynamic earth pressure
0.1	0.63	0.77
0.2	0.61	0.76
0.4	0.55	0.64
0.7	0.48	0.46
0.9	0.4	0.46

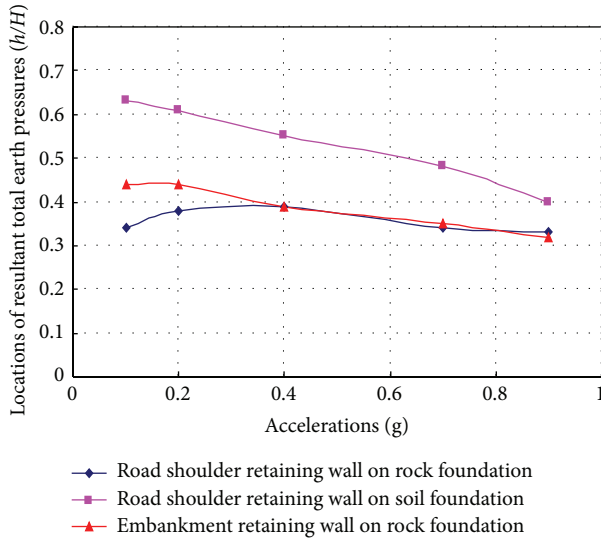


FIGURE 11: Locations of resultant total earth pressures (h/H).

From Figures 11 and 12, we can see that, for a road shoulder retaining wall, the locations of resultant total earth pressure are lower than those of resultant dynamic earth pressure, and the difference gradually reduces with the increase of seismic coefficient [25]. Table 1 shows that the locations are between 0.33 H and 0.39 H for total earth pressures, while they are between 0.35 H and 0.49 H for dynamic earth pressures. For embankment retaining wall, the locations of resultant total and dynamic earth pressures are lower when compared with those for the road shoulder retaining wall, and when seismic coefficient is lower, the locations of resultant total earth pressure are higher than those of resultant dynamic earth pressure. With the increase of seismic coefficient, the locations of resultant total and dynamic earth pressure become close [26]. Table 2 shows that the locations are between 0.32 H and 0.44 H for total earth pressures, while they are between 0.33 H and 0.42 H for dynamic earth pressures.

The foundation conditions of retaining wall have a strong impact on the locations of resultant earth pressure. Normally, the softer the foundation is, the higher the locations are. For the shoulder retaining wall constructed on soil foundation, the resultant locations are between 0.4 H and 0.63 H for total earth pressures, while they are between 0.46 H and 0.77 H for dynamic earth pressures, as shown in Table 3.

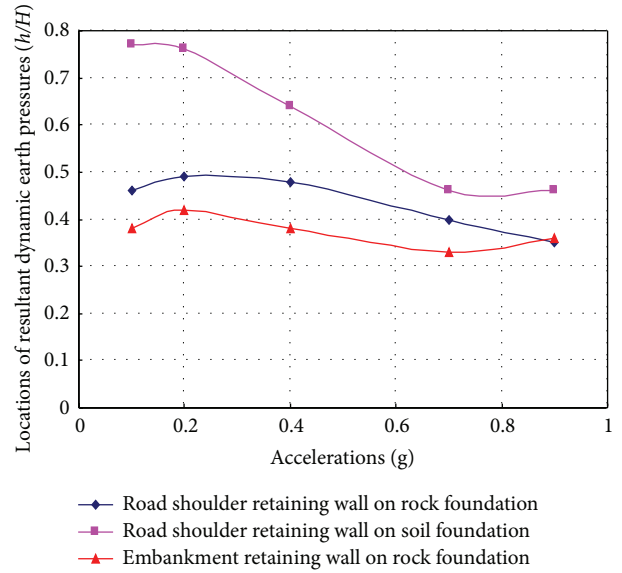


FIGURE 12: Locations of resultant dynamic earth pressures (h/H).

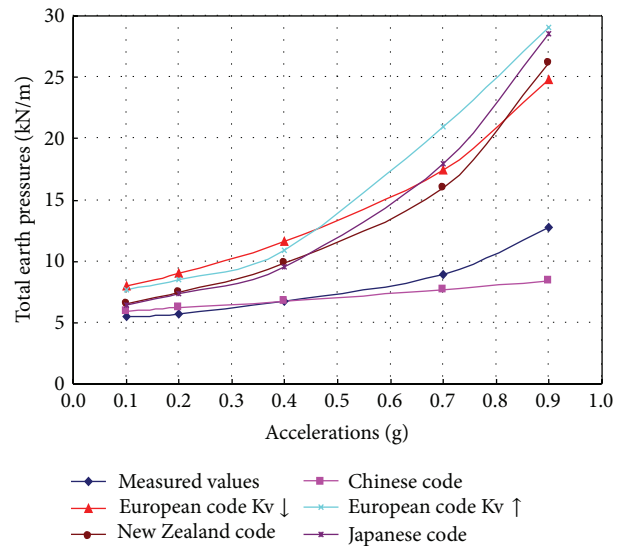


FIGURE 13: Comparison of measured earth pressures and theoretical results by codes for rock foundation.

3.4. Comparison of Measured Earth Pressures and Theoretical Results by Codes.

The diagrams of comparison between measured earth pressures and theoretical results by codes on rock and soil foundation, respectively, are shown in Figures 13 and 14.

Figures 13 and 14 show that, for rock foundation, the results by Chinese code are close to the measured earth pressures in the regions of seismic intensities below 8 degrees and smaller in the regions of seismic intensities above 8 degrees, while the results from European, Japanese, and New Zealand codes are conservative, contrast to Chinese code.

For soil foundation, the theoretical method by Chinese code for design of aseismic retaining wall is reasonable in the regions of seismic intensities below 8 degrees but is dangerous

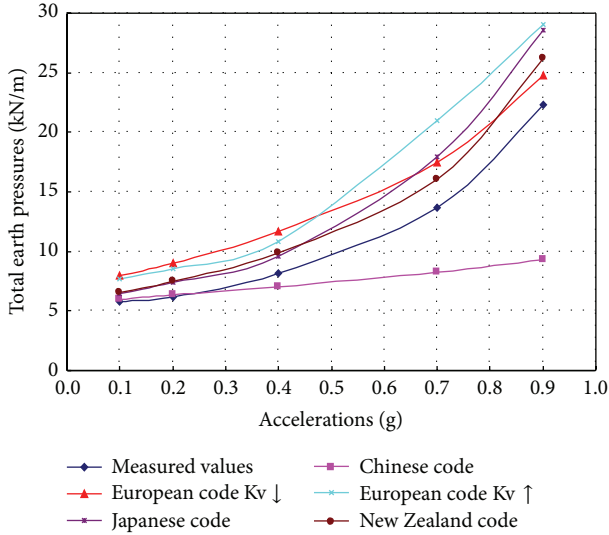


FIGURE 14: Comparison of measured earth pressures and theoretical results by codes for soil foundation.

in the regions of seismic intensities above 8 degrees, as the theoretical results are obviously smaller than measured. Nevertheless, the other theoretical results by the European, Japanese, and New Zealand codes are slightly larger than the measured, and the difference between the codes is slight with seismic acceleration. In contrast to the Chinese code, these foreign codes are comparatively reasonable, and the results from the New Zealand code are closest to the measured ones.

3.5. Comparison of Measured Earth Pressures and Theoretical Results by Pseudostatic Method (Mononobe-Okabe Method) and Pseudodynamic Method [27]. In order to make a comparison of measured earth pressures and theoretical results by pseudostatic method and pseudodynamic method, this paper uses the same material parameters, earthquake wave, and the analysis model with the shaking table test for the rock foundation. The results are shown in Figures 15 and 17.

Figures 15, 16, and 17 show that, for the measured earth pressures, the results for the pseudostatic method and the pseudodynamic method are closed to shaking table test; for the total earth pressures and the location of resultant total earth pressures, the results for the pseudodynamic method are obviously closer to the shaking table test than those for pseudostatic method.

Therefore, the results of pseudodynamic method are consistent with those of the shaking table test, but the results of pseudostatic method are smaller than measured.

4. Conclusions

(1) The distribution of total and dynamic earth pressure is nonlinear along the backwall. The dynamic earth pressures increase obviously for PGA larger than and equal to 0.4 g. Besides, the earth pressure intensity change speeds are related to geometric position, comparatively smaller above $2/3 H$ from toe of the wall but larger below.

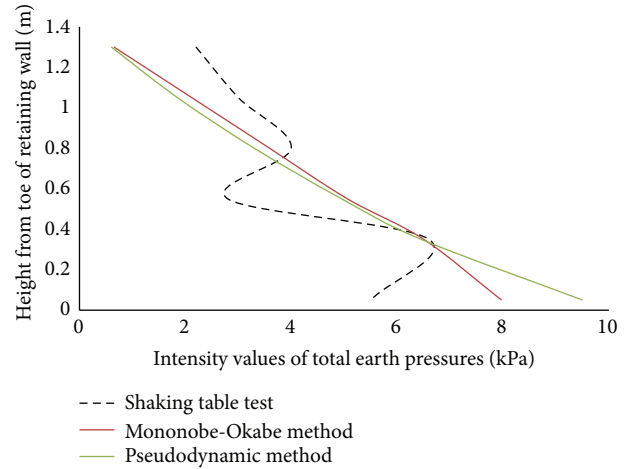


FIGURE 15: Comparison of measured earth pressures and theoretical results by pseudostatic method and pseudodynamic method for rock foundation (PGA of the input seismic wave is 0.4 g).

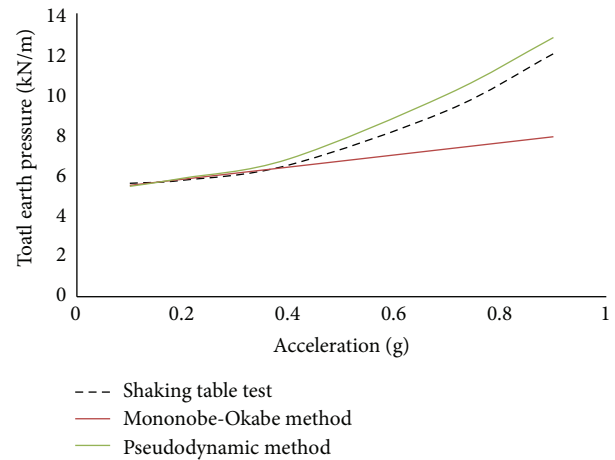


FIGURE 16: Comparison of measured total earth pressures and theoretical results by pseudostatic method and pseudodynamic method for rock foundation.

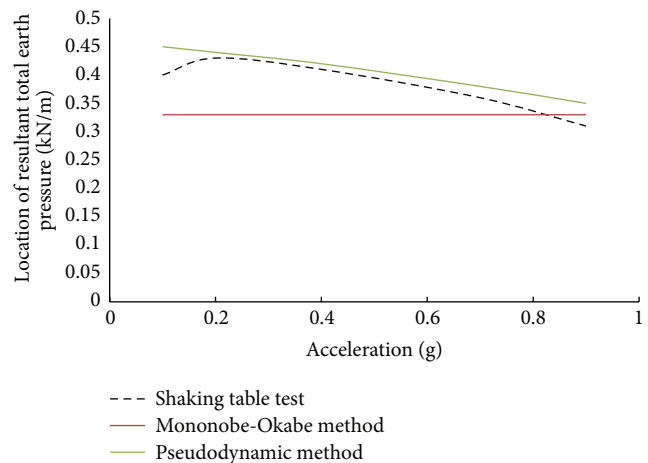


FIGURE 17: Comparison of locations of resultant total earth pressures (h/H) and theoretical results by pseudostatic method and pseudodynamic method for rock foundation.

(2) Resultant dynamic and total earth pressures grow more obviously along with the increase of seismic accelerations.

Comparing to rock foundation retaining wall, the dynamic and total earth pressures of soil foundation are larger. The foundation influence to design of aseismic retaining wall should be considered according to the regions and in the regions of seismic intensities above 8 degrees it should be carefully concerned.

The values of total and dynamic earth pressures are relevant to backfill form. The earth pressures of retaining wall on embankment are larger than on road shoulder. The influence from the form of backfill becomes less obvious along with seismic acceleration increasing but should not be ignored, as the numerical values are totally greater.

(3) When the seismic coefficient is low, measured locations of resultant total and dynamic earth pressure are above 0.33 H from the toe of wall, which is provided by M-O formula. With the rising of seismic coefficient, the locations become close to 0.33 H.

For retaining wall on road shoulder, the locations of resultant total earth pressure are lower than those of resultant dynamic earth pressure, and the gaps become closer with seismic coefficient rising. For retaining wall on embankment, the locations of resultant total and dynamic earth pressure are lower comparing to the retaining wall on road shoulder, and when the seismic coefficient is low, the locations of resultant total earth pressure are higher than those of resultant dynamic earth pressure. With the rising of seismic coefficient, the locations of resultant total and dynamic earth pressure become close.

The foundation condition has a strong impact on the locations of resultant earth pressure. At the same time, the softer, the locations higher.

(4) For rock foundation, the theoretical method for design of aseismic retaining wall provided by Chinese code is reasonable in the regions of seismic intensities below 8 degrees and smaller in the regions of seismic intensities above 8 degrees, while the results from those compared codes are too conservative.

For soil foundation, the method by Chinese code is reasonable in the regions of seismic intensities below 8 degrees but is dangerous in the regions of seismic intensities above 8 degrees. In contrast to the Chinese code, these foreign codes are comparatively reasonable, and the results from the New Zealand code are closest to the measured ones.

(5) The results of pseudodynamic are consistent with those of the shaking table test, but the results of pseudostatic method are smaller than measured.

Conflict of Interests

The authors of this paper do not have any conflict of interests regarding the publication of this paper.

Acknowledgments

The authors wish to thank Dr. Hongsheng Ma and Bo Xiang for providing help in their field trip and survey. This study is

supported in part by NSF of China (Contract no. 51408510), Guangxi Science Foundation, and the Program for Science and Technology.

References

- [1] J. J. Zhang, J. Feng, S. G. Xiao, and C. Q. Liu, "Discussions on two key technical problems for seismic design of retaining structures," *Journal of Southwest Jiaotong University*, vol. 44, no. 3, pp. 321–326, 2009.
- [2] N. Okabe, "General theory on earth pressure and seismic stability of retaining wall and dam," *Journal of Japan Society of Civil Engineers*, vol. 10, no. 6, pp. 1277–1323, 1924.
- [3] N. Mononobe, "Considerations on vertical earthquake motion relevant vibration problems," *Journal of Japan Society of Civil Engineerings*, vol. 10, no. 5, pp. 1063–1094, 1924.
- [4] S. L. Kramer, *Geotechnical Earthquake Engineering*, Prentice Hall, New Jersey, NJ, USA, 1996.
- [5] J. Kumar, "Seismic passive earth pressure coefficients for sands," *Canadian Geotechnical Journal*, vol. 38, no. 4, pp. 876–881, 2001.
- [6] D. M. Dewaikar and S. A. Halkude, "Seismic passive/active thrust on retaining wall-point of application," *Soils and Foundations*, vol. 42, no. 1, pp. 9–15, 2002.
- [7] M. R. Madhav and N. S. V. Kameswara Rao, "Earth pressure under seismic conditions," *Soils and Foundations*, vol. 9, no. 4, pp. 33–47, 1969.
- [8] D. Choudhury, K. S. SubbaRao, and S. Ghosh, "Passive earth pressures distribution under condition," in *Proceedings of the 15th International conference of Engineering Mechanics Division*, ASCE, New York, NY, USA, June 2002.
- [9] D. Choudhury, "Seismic passive resistance at soil-wall interface," in *Proceedings of the 17th ASCE Engineering Mechanics Conference*, University of Delaware, Newark, Del, USA, 2004.
- [10] K. S. Subba Rao and D. Choudhury, "Seismic passive earth pressures in soils," *Journal of Geotechnical and Geoenvironmental Engineering*, vol. 131, no. 1, pp. 131–135, 2005.
- [11] D. Choudhury and S. Singh, "New approach for estimation of static and seismic active earth pressure," *Geotechnical & Geological Engineering*, vol. 24, no. 1, pp. 117–127, 2006.
- [12] R. S. Steedman and X. Zeng, "Centrifuge modeling of the effects of earthquakes on free cantilever walls," in *Centrifuge*, vol. 91, pp. 425–430, Balkema, Rotterdam, The Netherlands, 1991.
- [13] D. Choudhury and S. Nimbalkar, "Seismic passive resistance by pseudo-dynamic method," *Geotechnique*, vol. 55, no. 9, pp. 699–702, 2005.
- [14] D. Choudhury and S. S. Nimbalkar, "Pseudo-dynamic approach of seismic active earth pressure behind retaining wall," *Geotechnical and Geological Engineering*, vol. 24, no. 5, pp. 1103–1113, 2006.
- [15] T. Xia, W. Hua, and Z. Wang, "Analysis of seismic active earth pressure of cohesive soil behind inclined retaining wall," *World Earthquake Engineering*, vol. 26, no. 1, pp. 315–321, 2010.
- [16] W. Liyan and L. Hanlong, "Study of seismic active earth pressure acted on gravity wall in backfill sand," *China Journal of Highway and Transport*, vol. 22, no. 6, pp. 26–33, 2009.
- [17] R. Siddharthan, S. Ara, and G. Norris, "Simple rigid plastic model for seismic tilting of rigid walls," *Journal of structural engineering New York, N.Y.*, vol. 118, no. 2, pp. 469–487, 1992.
- [18] X. Zeng, "Seismic response of gravity quay walls. I: centrifuge modeling," *Journal of Geotechnical and Geoenvironmental Engineering*, vol. 124, no. 5, pp. 406–417, 1998.

- [19] M. Celebi, "Seismic responses of two adjacent buildings. II. Interaction," *Journal of Structural Engineering*, vol. 119, no. 8, pp. 2477–2492, 1993.
- [20] H. A. Smith and W.-H. Wu, "Effective optimal structural control of soil-structure interaction systems," *Earthquake Engineering & Structural Dynamics*, vol. 26, no. 5, pp. 549–570, 1997.
- [21] N. M. Newmark, "Effects of earthquakes on dams and embankments," *Geotechnical*, vol. 15, no. 2, pp. 59–139, 1965.
- [22] Y. Z. Wang, "Distribution of earth pressure on a retaining wall," *Geotechnique*, vol. 50, no. 1, pp. 83–88, 2000.
- [23] R. Richards and D. G. Elms, "Seismic behavior of gravity retaining walls," *Journal of Geotechnical Engineering*, vol. 105, no. 4, pp. 444–449, 1979.
- [24] D. C. Yao, "Retaining wall seismic failure analysis," *Engineering Journal of Wuhan University*, vol. 36, no. 2, pp. 82–87, 2003.
- [25] J. H. Wood, "Earthquake-induced pressures on a rigid wall structure," *Bulletin of the New Zealand Society for Earthquake Engineering*, vol. 8, no. 3, pp. 86–175, 1975.
- [26] X. Zeng and R. S. Steedman, "Rotating block method for seismic displacement of gravity walls," *Journal of Geotechnical and Geoenvironmental Engineering*, vol. 126, no. 8, pp. 709–717, 2000.
- [27] B. Munwar Basha and G. L. Sivakumar Babu, "Reliability assessment of internal stability of reinforced soil structures: a pseudo-dynamic approach," *Soil Dynamics and Earthquake Engineering*, vol. 30, no. 5, pp. 336–353, 2010.

Research Article

Preparation and Coagulation Behavior of a Novel Multiple Flocculant Based on Cationic Polymer, Hydroxy Aluminum, and Clay Minerals

Feng-shan Zhou, Xi Wang, Lin Zhou, and Yang Liu

School of Materials Science and Technology, China University of Geosciences, Beijing 100083, China

Correspondence should be addressed to Feng-shan Zhou; zhoufs@cugb.edu.cn

Received 12 July 2014; Revised 22 August 2014; Accepted 22 August 2014

Academic Editor: Zhaohui Li

Copyright © 2015 Feng-shan Zhou et al. This is an open access article distributed under the Creative Commons Attribution License, which permits unrestricted use, distribution, and reproduction in any medium, provided the original work is properly cited.

Cationic polymer, hydroxy aluminum, and clay minerals are three flocculants with different action mechanisms and a more cost-efficient multiple flocculant can be prepared by compositing them through appropriate technology. All of attapulgite (ATP), clay minerals containing magnesium, aluminum, and silicate, are porous environmental mineral material with good absorbability and have found wide applications in industrial sewage treatment. With polyaluminum chloride (PAC), poly(dimethyl diallyl ammonium chloride) (PDMDAAC), and attapulgite (ATP) clay being the main raw materials, multiple flocculant CMHa (liquid) with good storage stability was prepared and its optimized blending mass percent was PDMDAAC of 2%–3%, ATP of 4%–6%, and PAC of 20%–30%. The liquid poly(dimethyl diallyl ammonium chloride) (PDMDAAC) was firstly loaded on solid material in kneader and then mixed in certain proportion with PAC and ATP to prepare solid CMHa convenient for storage and transportation. The optimized mass ratio is PAC : ATP : PDMDAAC = 80 : 10 : 2.4. When this multiple flocculant was used to treat domestic sewage, coal washing sewage, dyeing wastewater, and papermaking wastewater, its equivalent dosage was just 50% of PAC, while overall production cost has been reduced to about 40%, viewing showing broad application prospect.

1. Introduction

Flocculants have found wide application due to their good coagulation and purification behavior, low price, and convenience and have been the most widely used water treatment agent with the largest consumption [1, 2].

Micromolecular inorganic salt flocculants, for example, aluminium chloride ($\text{AlCl}_3 \cdot 6\text{H}_2\text{O}$), ferrous sulfate ($\text{FeSO}_4 \cdot 7\text{H}_2\text{O}$), and ferric chloride ($\text{FeCl}_3 \cdot \text{H}_2\text{O}$), have advantage in low cost but their alum grains are small and are strongly corrosive, so they are generally replaced by inorganic polymer flocculants. Polyaluminum chloride (PAC), polyferric sulfate (PFS), polyferric chloride (PFC), and polyaluminium ferric chloride (PAFC) are popular inorganic polymer flocculants. Relatively speaking, inorganic polymer flocculants have better flocculation performance

and cheaper than organic flocculants; however their storage stability is poor and will produce plenty of sludge; thus it is difficult for subsequent treatment [1, 3].

Organic flocculants have advantage in low dosage, fast flocculation velocity, being affected little by coexisting salts, pH of medium, and environment temperature, small amount of sludge, and good decolorization performance, but they are costly and their hydrolyzed or degraded products are toxic. Organic polymer flocculant is classified as natural and multiple [3, 4].

Multiple flocculants can be classified as inorganic-organic multiple, organic-organic multiple, inorganic-inorganic multiple, multinuclear inorganic polymer flocculant, and so forth. Among them, multiple of polymeric aluminum, polymeric iron, and polyacrylamide is the most popular, which integrates the merits of inorganic and organic flocculants

and makes good use of electrical neutralization, adsorption, bridging, and furl mechanism, thus improving flocculation performance, reducing costs, decreasing flocculant dosage and the amount of sludge, promoting the stability of multiple flocculant, and broadening its application. Consequently, it has been the research focus in developing new flocculant [5–13].

Mineral flocculants remove organics and metal ions in water through adsorption and thus no secondary contamination exists, particularly suitable for the treatment of seriously polluted domestic and industrial sewage [7, 10, 11, 13, 14]. However, mineral flocculants also have some disadvantages in practical application. At first, the dosage is large. When treating the same water sample, dosage of mineral flocculants is far larger than that of conventional flocculants (e.g., PAC). In addition, the large dosage makes larger amount of alum grain sediments after treatment than that produced by conventional flocculants. Thirdly, its treatment efficiency is low. Conventional flocculants can flocculate rapidly, while mineral flocculants remove organics and metal ions in water through adsorption and adsorption often takes some time, thus making the treatment efficiency of mineral flocculants lower.

By combining structural features and flocculation performance of organic cationic polymer (C), inorganic hydroxy aluminium (Ha), and clay mineral (M), this paper aims at developing a multiple flocculant CMHa with good performance and low cost.

2. Materials and Methods

2.1. Instruments. SGE-2 Digital Turbidity Meter (Shanghai Yuefeng Instruments Co., Ltd.), TDL-5A High-Speed Centrifuge (Shanghai Fulgor Analysis Instruments Co., Ltd.), and NH-1 Kneader (Shandong Laizhou Longhe Chemical Industrial Equipment Co., Ltd.) are used.

2.2. Materials. Attapulgate (ATP) (Mingguang, Anhui); bentonite (Ningcheng, Inner Mongolia); polyaluminum chloride (PAC) (liquid sample PAC; solid sample SPAC) (Gongyi, Henan); kaolinite (Karamay, Xinjiang); poly(dimethyl diallyl ammonium chloride) (PDMDAAC) (Kemira, Jiangsu); cationic polyacrylamide (CPAM) (Xitao, Beijing); poly(dimethyl diallyl ammonium chloride-acrylamide) (PDA) (Kemira, Jiangsu); diatomite (Linjiang, Jilin); cellulose graft starch (PPS) (Pinggu, Beijing); puffing modified starch (EPPS) (Pinggu, Beijing); and silane graft starch membrane-forming agent (SIM) (Pinggu, Beijing) are used. All of the samples are industrial products obtained from China chemical market.

2.3. Methods

2.3.1. Hydration of Mineral Material. Prepare suspension of clay minerals with various concentrations and then the prepared suspension was stirred for 20 min in high speed stirrer (10000 rpm) followed by hydrating for 16 h.

2.3.2. Preparation of Liquid CMHa. Blend PAC, cationic polymer, and hydrated mineral suspension in various proportions at first and then the mixture was stirred at certain temperature to form uniform solution, that is, liquid CMHa sample.

2.3.3. Load and Solidification of PDMDAAC. Add some support materials into kneader and then add liquid PDMDAAC sample slowly. Keep heating and kneading until water in PDMDAAC evaporates almost completely; then take out the sample for crushing, that is, solidified PDMDAAC sample, recorded as PDMDAAC-S.

2.3.4. Preparation of Solid CMHa. Mix dry solid PAC, PDMDAAC-S, and clay mineral uniformly, that is, solid CMHa sample CMHa-S.

2.4. Evaluations

2.4.1. Evaluation on Flocculant Stability. Leave it stand and observe its stability. And then evaluate its stability by mechanical centrifugation. Take some prepared samples and centrifuge them for 5 min at rotation speed of 2000 rpm, 3000 rpm, 4000 rpm, and 5000 rpm, respectively. The rotation speed at which sample begins separating out water or layering is selected as stability evaluation indicator. The faster rotation speed indicates better stability.

2.4.2. Evaluation on Flocculation Performances. Diatomite suspension with turbidity of 1000 NTU was prepared to simulate water sample (600 g water mixed with 1.1 g diatomite). Then add certain amount of flocculant sample into 100 mL simulated water sample and stir rapidly for 2 min at first and then stir slowly for another 2 min. After that, add certain amount of polyacrylamide and stir slowly for 2 min. Observe and record the size and settling time of alum grain. After 30 min, measure the turbidity of supernatant.

3. Results and Discussion

3.1. Influence Factors on Stability and Coagulation Behavior of CMHa

3.1.1. Mineral Materials Types. It can be known through investigating the stability of CMHa prepared by different mineral materials (shown in Table 1) that the presence of bentonite in ternary system makes the system layer and yellow liquid separate out in upper layer; precipitates can be observed in the system in the presence of kaolinite as kaolinite tends not to suspend; ATP makes the ternary system very stable, so it is selected as mineral material used in following tests.

3.1.2. Cationic Polymers. The presence of PDA makes CMHa ternary system layer, while adding PDMDAAC will not affect the system's stability. However, if content of PDMDAAC exceeds 3%, viscosity of the system will increase and thus it cannot flow easily after standing, while low content will

TABLE 1: The stability of different kinds of minerals in the CMHa.

PAC	PDMDAAC	CMHa (%)			Sample appearance after standing
		Bentonite	Kaolinite	ATP	
15	1		15		Settling
15	2		10		Settling
20	1	4.0			Obvious separated layer
20	1	5.0			Obvious separated layer
25	1	5.0			Obvious separated layer
15	1	5.0	5.0		Separated layer
15	1	3.0	3.0	3.0	Separated layer
15	1			5.0	Stable
15	1		6.0	4.0	Settling
15	1	3.5	1.5		Separated layer

TABLE 2: The influence of different kinds of cationic polymers on the stability of CMHa.

PAC	CMHa (%)			Sample appearance after standing
	PDMDAAC	PDA	ATP	
20	1		5	Relatively stable
20	2		5	Relatively stable
20	3		5	Thick and viscous
20		1	5	Obvious separated layer
20		2	5	Obvious separated layer
20		3	5	Obvious separated layer

TABLE 3: The influence of attapulgite on the stability of CMHa.

PAC	CMHa (%)		Sample appearance after standing
	PDMDAAC	ATP	
25	2	3.7	A little water separated in the upper part
25	2	4.2	Uniform
25	2	4.8	Uniform
25	2	5.2	Uniform
25	2	5.5	Uniform
25	2	6.0	Difficult to flow
25	2	7.0	Difficult to flow

degrade the flocculation performance of products. Consequently, the suitable dosage of PDMDAAC is 2%-3%, as shown in Table 2.

3.1.3. Mineral Material Content. When content of ATP was lower than 4%, viscosity of product is low and water tends to separate out in upper layer, and thus layering is observed; while content of ATP is greater than 6%, viscosity of product is too high and its flow ability becomes poor after standing. Consequently, appropriate content of ATP ranges from 4% to 6%, as seen in Table 3.

3.1.4. Reaction Temperature. Influence of reaction temperature on stability, viscosity, and flocculation behavior can be seen in Tables 4 and 5. Increasing temperature promotes

stability, increases viscosity of system, and enhances flocculation performance. However, solidification will be observed after standing some time due to high viscosity and poor flow ability. Therefore, optimal temperature should be 40°C~60°C.

3.1.5. Polyaluminum Chloride (PAC). PAC exerts great influence on the stability and flocculation behavior of CMHa. Results in Table 6 show that PAC content of 35% makes the flow ability of product poor. Content of PAC affects the performance of multiple flocculant directly and it should be as high as possible if stability allows for it. Therefore, the optimal content of PAC should be 25%~30%.

3.2. Effects of Treating Water with Different Turbidities Used Liquid CMHa. Compare the flocculation performance of solid PAC (SPAC) with that of liquid CMHa sample prepared at 60°C in the selected optimal blending ratio with good stability (25% PAC + 2% PDMDAAC + 5% ATP) according to results in Table 6. Results in Table 7 show that, when compounding with CPAM, turbidity removal performance of liquid CMHa with two times of dosage was better than that of solid PAC and settling velocity also accelerates. When singly used, turbidity removal performance of liquid CMHa with two times of dosage was improved significantly and settling velocity also accelerated considerably.

3.3. Solidification of CMHa

3.3.1. Selecting Carrier for PDMDAAC. To address the inconvenient storage and transportation of liquid CMHa, porous

TABLE 4: The influence of reaction temperature on the stability and the coagulation behavior for the produced samples (1000 NTU diatomite suspension).

PAC	CMHa (%)		Reaction temperature (°C)	Centrifugal stability (rpm)	Residual turbidity (NTU)
	PDMDAAC	ATP			
25	2	5	25	3000	1.1
25	2	5	40	3000	0.80
25	2	5	60	4000	0.63
25	2	5	80	5000	0.42

TABLE 5: The influence of reaction temperature on the appearance viscosity of produced samples.

PAC	CMHa (%)		Reaction temperature (°C)	Sample appearance
	PDMDAAC	ATP		
20	3	6	40	Thin liquid
20	3	6	60	Thick liquid
20	3	6	80	Difficult to flow
25	2	6	40	Thin liquid
25	2	6	60	Viscous liquid
25	2	6	80	Difficult to flow

TABLE 6: The influence of PAC in CMHa on the stability of produced flocculants.

PAC	CMHa (%)		Reaction temperature (°C)	Centrifugal stability (rpm)
	PDMDAAC	ATP		
15	2	5	60	3000
20	2	5	60	3000
25	2	5	60	4000
30	2	5	60	4000
35	2	5	60	Difficult to flow

solid materials are used to carry PDMDAAC solution with active ingredient content of 40% at first. Then compounding with solid PAC and solid CPAM, solid CMHa can be prepared, that is, CMHa-S. Solid carriers used in tests as shown in Table 8 were selected from natural mineral materials (Attapulgit, Diatomite, Kaolinite, Bentonite) and natural polymeric materials (PPS, EPPS, and SIM). Flocculation performance of SPAC and CMHa-S sample with optimal blending ratio was compared, as seen in Table 9. By comparing the capacity of carriers, status being loaded by PDMDAAC, flocculation performance, and costs, SIM was finally selected as the carrier for liquid PDMDAAC. CMHa-S sample prepared by SIM being as carrier is the best option.

3.3.2. Comparing Flocculent Performance of CMHa with Different PDMDAAC Contents. CMHa samples with different PDMDAAC contents were prepared as seen in Table 10. These samples were used to treat diatomite suspension of 1000 NTU to compare their flocculation performance and results shown in Table 11. Results show that higher PDMDAAC content meant better flocculation performance of CMHa in the presence/absence of CPAM. Coagulation behavior of CMHa-S-PDMDAAC24 sample in the absence of CPAM was similar to that of SPAC with three times higher dosage than it and

the settling velocity accelerates considerably, while its flocculation performance in the presence of CPAM was similar to that of SPAC with two times higher dosage than it. It is suggest that SPAC mixed mineral material and cationic polymer with an enhanced coagulation performance. However, increasing PDMDAAC content in samples made kneading difficult, so CMHa-S-PDMDAAC24 was an optimized formula considering both cost efficiency and technology.

3.3.3. Economic Efficiency of CMHa-S. Taking CMHa-S-PDMDAAC24 as an example and according to current price of raw materials, it can be known that total cost of raw materials is 2100 yuan/ton, comprehensive processing charge is 300 yuan/ton, total production cost is 2400 yuan/ton, and selling price is 3000 yuan/ton. As the equivalent dosage of SPAC is 2~3 times higher than that of CMHa-S and the price of good SPAC is about 2500 yuan/ton, the price of CMHa-S is only 40% lower than that of PAC. And therefore CMHa-S is more cost-efficient.

3.4. Results of CMHa Treating Industrial Sewage. The industrial solid CMHa-S-PDMDAAC24 sample was diluted by water to 32% and then the solution was used to treat domestic sewage, coal washing sewage, and dyeing wastewater. Then

TABLE 7: The coagulation behaviors of CMHa versus PAC (100–1000 NTU diatomite suspension).

Turbidity of diatomite suspension (NTU)	Flocculants (mg/L)	CPAM (mg/L)	Settling time (s)	Residual turbidity (NTU)	Coagulation behaviors
1000	SPAC (30)	3	50	5.7	Larger alum floc
1000	CMHa (60)	3	40	4.5	Larger alum floc
1000	SPAC (60)	—	130	7.6	Larger alum floc
1000	CMHa (120)	—	90	5.9	Larger alum floc
500	SPAC (20)	2	60	2.7	Larger alum floc
500	CMHa (40)	2	50	2.3	Larger alum floc
500	SPAC (40)	—	150	4.5	Smaller alum floc
500	CMHa (80)	—	100	3.1	Larger alum floc
100	SPAC (15)	2	80	1.8	Larger alum floc
100	CMHa (30)	2	70	1.6	Larger alum floc
100	SPAC (30)	—	180	2.5	Smaller alum floc
100	CMHa (60)	—	120	1.9	Larger alum floc

TABLE 8: The carried dosage of different carrier materials for PDMDAAC.

Carrier materials (g)	PDMDAAC (g)	Content of PDMDAAC in solidified samples (%)	Characteristics of solidified samples
Attapulgite (100)	100	28.6	High viscosity and difficulty to kneading reaction
Bentonite (100)	100	28.6	High viscosity and difficulty to kneading reaction
Diatomite (100)	200	44.4	Low viscosity and easiness to kneading reaction
EPPS (100)	80	24.0	High viscosity and difficulty to kneading reaction
PPS (100)	80	24.0	Low viscosity and easiness to kneading reaction
SIM (100)	80	24.0	Low viscosity and easiness to kneading reaction

TABLE 9: The influence of different carrier materials on the coagulation behaviors of CMHa-S (1000 NTU diatomite suspension).

Flocculants (mg/L)	CPAM (mg/L)	Settling time (s)	Residual turbidity (NTU)
SPAC (30)	2	20	0.9
SPAC (45)	2	20	0.6
CMHa-S-SIM (15)	2	20	0.8
CMHa-S-diatomite (15)	2	30	1.5
CMHa-S-PPS (15)	2	25	1.3
SPAC (100)		150	5.5
SPAC (150)		90	2.5
CMHa-S-SIM (50)		90	2.4
CMHa-S-diatomite (50)		100	2.6
CMHa-S-PPS (50)		110	3.7

evaluate its flocculation performance and compare with that of SPAC.

3.4.1. Treating Domestic Sewage. Results in Table 12 show that when CMHa was used to treat the domestic sewage of a sewage treatment plant in Changzhou the residual turbidity of treated water is lower than that treated by PAC, and alum

TABLE 10: CMHa-S with different carried dosage of PDMDAAC.

Samples number	CMHa (%)			
	SPAC	ATP	SIM	PDMDAAC
CMHa-S-PDMDAAC8	80	10	9.2	0.8
CMHa-S-PDMDAAC16	80	10	8.4	1.6
CMHa-S-PDMDAAC24	80	10	7.6	2.4

grain produced by CMHa is larger and its settling velocity is faster.

3.4.2. Treating Dyeing Wastewater. Flocculation behaviors of CMHa versus PAC for treating dyeing wastewater of a textile dyeing and printing plant in Shandong were shown in Table 13. The original wastewater with turbidity of 52 NTU is neutral pH and looks light yellow. Turbidity removal performance of CMHa with only half dosage of PAC can approach that of PAC, while settling velocity of CMHa is faster than that of PAC and its floccules were larger.

3.4.3. Treating Papermaking Wastewater. Flocculation behaviors of CMHa versus PAC for treating papermaking wastewater of a paper mill in Zhejiang were shown in Table 14. Being used singly, the turbidity removal performance and settling velocity of CMHa and PAC are close to each other. However,

TABLE 11: The coagulation behaviors of CMHa-S carried different dosage of PDMDAAC (1000 NTU diatomite suspension).

Dosage of flocculants (mg/L)	CPAM (mg/L)	Settling time (s)	Residual turbidity (NTU)	Characteristics of alum floc during coagulation reaction
SPAC (100)		150	5.5	Alum floc slow and minor
SPAC (150)		100	2.2	Alum floc quick and larger
CMHa-S-PDMDAAC8 (50)		100	4.5	Alum floc quick and larger
CMHa-S-PDMDAAC16 (50)		90	3.1	Alum floc quick and larger
CMHa-S-PDMDAAC24 (50)		80	2.1	Alum floc quick and larger
SPAC (30)	2	20	1.4	Alum floc quick and larger
CMHa-S-PDMDAAC8 (15)	2	20	1.2	Alum floc quick and larger
CMHa-S-PDMDAAC16 (15)	2	25	1.1	Alum floc quick and larger
CMHa-S-PDMDAAC24 (15)	2	20	0.8	Alum floc quick and larger

TABLE 12: Coagulation behaviors of CMHa versus PAC for domestic-sewage treatment (original wastewater 50 NTU).

Dosage of flocculants (mg/L)	CPAM (mg/L)	Settling time (s)	Residual turbidity (NTU)	Coagulation behaviors
SPAC (20)	5	80	2.7	Smaller alum floc
CMHa (10)	5	70	2.3	Larger alum floc
SPAC (30)	5	70	1.4	Larger alum floc
CMHa (15)	5	70	1.1	Larger alum floc
SPAC (20)		300	5.8	Smaller alum floc
CMHa (10)		200	5.6	Smaller alum floc
CMHa (20)		180	4.6	Larger alum floc

TABLE 13: Coagulation behaviors of CMHa versus PAC for dyeing-wastewater treatment (original wastewater 52 NTU).

Dosage of flocculants (mg/L)	CPAM (mg/L)	Settling time (s)	Residual turbidity (NTU)	Coagulation behaviors
SPAC (200)	10	120	20.2	Smaller alum floc
CMHa (100)	10	100	20.5	Smaller alum floc
SPAC (400)	10	100	10.3	Smaller alum floc
CMHa (200)	10	80	10.8	Larger alum floc
Solid PFS (400)	10	—	—	Without effect
Solid FeSO ₄ (400)	10	—	—	Without effect

TABLE 14: Coagulation behaviors of CMHa versus PAC for paper-making wastewater treatment (original wastewater 850 NTU).

Dosage of flocculants (mg/L)	CPAM (mg/L)	Settling time (s)	Residual turbidity (NTU)	Coagulation behaviors
SPAC (100)	3	50	50	Smaller alum floc
SPAC (120)	3	40	42	Larger alum floc
CMHa (50)	3	50	65	Larger alum floc
CMHa (100)	3	40	52	Larger alum floc
SPAC (200)		70	43	Smaller alum floc
SPAC (250)		60	40	Larger alum floc
CMHa (100)		60	45	Larger alum floc
CMHa (150)		60	42	Larger alum floc

when compounding with CPAM, the settling velocity of CMHa is faster than that of PAC and its floccules were larger.

Turbidity removal performance of CMHa with only half dosage of PAC is far better than that of PAC.

3.4.4. *Treating Coal Washing Sewage.* Flocculation behaviors of CMHa versus PAC for treating coal washing sewage of a coal washing plant in Shanxi were shown in Table 15.

3.5. *Action Mechanism of Multiple Flocculant.* The three components of CMHa work differently. CMHa makes full use of the comprehensive characteristics of inorganic and

TABLE 15: Coagulation behaviors of CMHa versus PAC for coal-washing wastewater treatment (original wastewater 1200 NTU).

Dosage of flocculants (mg/L)	CPAM (mg/L)	Settling time (s)	Residual turbidity (NTU)	Coagulation behaviors
SPAC (50)	5	20	19	Larger alum floc
CMHa (30)	5	15	9.4	Larger alum floc
CMHa (20)	5	15	17	Larger alum floc
SPAC (80)		150	40	Smaller alum floc
CMHa (50)		60	14	Larger alum floc
CMHa (40)		80	22	Larger alum floc

organic polymer flocculants and adsorption, bridging, and flocculation aid capacity of natural porous mineral materials, which is not simple arithmetical addition of flocculation performance of single component. Combining the previous research and results of this paper, action mechanism of multiple flocculant includes the following three aspects.

3.5.1. Role of Mineral Material in CMHa. Being as flocculant, mineral material contains exchangeable inorganic cations in its interlayer and some oxygen atoms exposed on its crystal surface. This special molecular structure and irregular crystal defect of mineral material enable it to adsorb contaminants in water well. Clay mineral is characterized as being porous, having large specific surface area, and having strong polarity and its price is often lower than that of conventional flocculants. Some unwieldy contaminants in water (e.g., organics and metal ions) can be removed through adsorption of minerals and secondary pollution can be avoided [10, 11].

3.5.2. Role of Hydroxyl Aluminum in CMHa. Polyaluminum chloride is an intermediate from hydrolyzation and its flocculation performance is related to its degree of alkalization. It is often expressed by the formula $Al_2(OH)_nCl_{(6-n)}$ and n means degree of alkalization. Hydroxyl aluminum contains polyhydroxy complex-ions and these ions will form multinuclear complex-ions using OH^- as bridge. So it can adsorb colloidal particles strongly and then promote the agglomeration of colloid through adsorption, bridging, and cross-linking. Meanwhile, physicochemical changes will occur and then charges on the surface of colloidal particles and suspended solids can be neutralized and Zeta potential is reduced, which makes the repulsive colloid particles become attractive, destroys the stability of micelles, and promotes the collision of colloidal particles, and therefore flocculant coagulative precipitation is produced and its surface area can be as large as $(200-1000) m^2/g$, having adsorption capacity [12, 15-18]. In short, polyaluminum chloride plays various roles including adsorption, destabilization, adhesion, bridging, and furl flocculation.

3.5.3. Role of Polymer in CMHa. The molecular mass, molecular structure, shape, and groups of polymer can affect the activity of flocculant. In addition, organic flocculant carried charge and thus can play electrical neutralization. Due to its large molecular mass, polymer can be regarded as a bridge helping produce flocs with structure of "colloidal particle-polymer-colloidal particle" and the flocs will settle. It can be

interpreted as that two colloidal particles with like charges are connected together by a colloidal particle with unlike charges to form precipitate. Polymer flocculant with linear structure can be absorbed on the surface of colloidal particles and can enlarge the volume of alum grains and accelerate settling through furl mechanism [19, 20].

4. Conclusions

Cationic polymer, hydroxy aluminum, and clay minerals are three flocculants with different action mechanisms and a more cost-efficient multiple flocculant can be prepared by compositing them through appropriate technology.

With polyaluminum chloride (PAC), poly(dimethyl diallyl ammonium chloride) (PDMDAAC), and attapulgite (ATP) clay being the main raw materials, multiple flocculant CMHa (liquid) with good storage stability was prepared and its optimized blending mass percent was PDMDAAC of 2%-3%, ATP of 4%-6%, and PAC of 20%-30%.

The liquid poly(dimethyl diallyl ammonium chloride) (PDMDAAC) was firstly loaded on solid material in kneader and then mixed in certain proportion with PAC and ATP to prepare solid CMHa convenient for storage and transportation. The optimized mass ratio is PAC:ATP:SIM:PDMDAAC = 80:10:7.6:2.4. When this multiple flocculant was used to treat domestic sewage, coal washing sewage, dyeing wastewater, and papermaking wastewater, its equivalent dosage was just 50% of PAC, while overall production cost has been reduced about 40%. Consequently, multiple flocculant CMHa shows broad application prospect.

Conflict of Interests

The authors declare that there is no conflict of interests regarding the publication of this paper.

Acknowledgment

This research was supported by National High Technology Research and Development Program of China (863 Program 2012AA06A109).

References

- [1] K. E. Lee, N. Morad, T. T. Teng, and B. T. Poh, "Development, characterization and the application of hybrid materials in

- coagulation/flocculation of wastewater: a review,” *Chemical Engineering Journal*, vol. 203, pp. 370–386, 2012.
- [2] S. H. Yang, F. L. Yang, and G. H. Ai, “Advances in research and application of water treatment flocculant,” *Chemical Industry Times*, vol. 20, no. 2, pp. 73–75, 2006.
- [3] F. S. Zhou, S. H. Wang, J. Y. Li, and J. G. Wu, “Progress in researches of polysilicate-containing composite inorganic polymer flocculants,” *Oilfield Chemistry*, vol. 19, no. 4, pp. 391–394, 2002.
- [4] A. K. Verma, R. R. Dash, and P. Bhunia, “A review on chemical coagulation/flocculation technologies for removal of colour from textile wastewaters,” *Journal of Environmental Management*, vol. 93, no. 1, pp. 154–168, 2012.
- [5] J. Xia, R. Q. Su, and X. W. He, “Water resources problems in china and their countermeasures & suggestions,” *Bulletin of Chinese Academy of Sciences*, vol. 23, no. 2, pp. 116–120, 2008.
- [6] F. S. Zhou, S. H. Wang, J. Z. Su et al., “The infrared spectra and characteristics of PMC—a multicore inorganic polymer flocculant,” *Fine Chemicals*, vol. 20, no. 10, pp. 615–620, 2003.
- [7] Y. Yang, *Synthesis and application of surface modification of attapulgite and its polymer composite flocculants, assistant-coagulate [Ph.D. dissertation]*, Lanzhou University, Lanzhou, China, 2007.
- [8] R. R. Lu, Y. H. Zhang, F. S. Zhou, X. Wang, Q. An, and Z. Meng, “Novel polyaluminum ferric chloride composite coagulant from Bayer red mud for wastewater treatment,” *Desalination and Water Treatment*, vol. 2013, Article ID 831791, 9 pages, 2013.
- [9] M. Yan and J. Ni, “Enhanced coagulation for high alkalinity and micro-polluted water: the third way through coagulant optimization,” *Water Research*, vol. 42, no. 8-9, pp. 2278–2286, 2008.
- [10] R. Srinivasan, “Advances in application of natural clay and its composites in removal of biological, organic, and inorganic contaminants from drinking water,” *Advances in Materials Science and Engineering*, vol. 2011, Article ID 872531, 17 pages, 2011.
- [11] Y. Wang and D. F. Zeng, “Compound clay’s application in water-treatment flocculants,” *Environmental Study and Monitoring*, vol. 21, no. 4, pp. 53–54, 2008.
- [12] L. Gao, *Study on preparation and application of polyaluminum ferric chloride [Ph.D. thesis]*, Harbin University of Science & Technology, Harbin, China, 2007.
- [13] D. An, *Study on the removal of algae with coagulation by polymeric aluminum chloride compounded with different size of clay [Ph.D. thesis]*, Qingdao University, Qingdao, China, 2008.
- [14] K. L. Yeap, T. T. Teng, and B. T. Poh, “Preparation and characterization of coagulation/flocculation behavior of a novel inorganic-organic hybrid polymer for reactive and disperse dyes removal,” *Chemical Engineering Journal*, vol. 243, pp. 305–314, 2014.
- [15] G. Ovejero, A. Rodríguez, A. Vallet, and J. García, “Catalytic wet air oxidation of a non-azo dye with Ni/MgAlO catalyst,” *Chemical Engineering Journal*, vol. 215–216, pp. 168–173, 2013.
- [16] W. Y. Yang, J. W. Qian, and Z. Q. Shen, “A novel flocculant of Al(OH)₃-polyacrylamide ionic hybrid,” *Journal of Colloid and Interface Science*, vol. 273, no. 2, pp. 400–405, 2004.
- [17] P. A. Moussas and A. I. Zouboulis, “A study on the properties and coagulation behaviour of modified inorganic polymeric coagulant-Polyferric silicate sulphate (PFSiS),” *Separation and Purification Technology*, vol. 63, no. 2, pp. 475–483, 2008.
- [18] F. El-Gohary and A. Tawfik, “Decolorization and COD reduction of disperse and reactive dyes wastewater using chemical-coagulation followed by sequential batch reactor (SBR) process,” *Desalination*, vol. 249, no. 3, pp. 1159–1164, 2009.
- [19] K. E. Lee, B. T. Poh, N. Morad, and T. T. Teng, “Synthesis and characterization of hydrophobically modified cationic acrylamide copolymer,” *International Journal of Polymer Analysis and Characterization*, vol. 13, no. 2, pp. 95–107, 2008.
- [20] M. Ng, A. E. Liana, S. Liu et al., “Preparation and characterisation of new-polyaluminum chloride-chitosan composite coagulant,” *Water Research*, vol. 46, no. 15, pp. 4614–4620, 2012.

Research Article

Composition Optimization of Glass-Like Casing and Its Novel Application in Mending Instable Borehole Wall

Zhi-jun Li,¹ Yu Wang,¹ Bao-lin Liu,¹ and Chun Yang^{1,2}

¹Key Laboratory on Deep Geodrilling Technology of the Ministry of Land and Resources, China University of Geosciences, Beijing 100083, China

²Sinomine Resource Exploration Co., Ltd, Beijing 100083, China

Correspondence should be addressed to Yu Wang; wangyu203@cugb.edu.cn

Received 21 August 2014; Revised 2 January 2015; Accepted 7 January 2015

Academic Editor: Hanlie Hong

Copyright © 2015 Zhi-jun Li et al. This is an open access article distributed under the Creative Commons Attribution License, which permits unrestricted use, distribution, and reproduction in any medium, provided the original work is properly cited.

A glass-like casing was developed to mend the instable borehole due to its great similarities in compositions and structure. In order to boost the casing's mechanical properties and lower its cost, different wt% additions of aluminum and quartz sand are added into the composition. Based on the outcomes of differential scanning calorimeter (DSC), it is suggested to be sintered at the temperature of 700°C. The results of X-ray diffraction (XRD) show that aluminum and SiO₂ are its main crystalline phases. Its compression strength and the tensile strength range 5–14 Mpa and 0.5–4.5 Mpa, respectively, with the relative densities of between 1.00 g/cm³ and 1.19 g/cm³. In the end, a glass-based formula with 30 wt% aluminum and 40 wt% quartz sand is developed and experimentally applied.

1. Introduction

Nowadays, wellbore instability has severely influenced the drilling efficiency [1]. In the past, the casing running is most frequently used to protect the well from being damaged. Mostly, however, the holes will be damaged at some certain parts; therefore, there is little point in practically mending the whole borehole wall. However, in most practical cases, the casing running will be applied from hole's bottom to the orifice, a huge waste of steel casing. In order to reduce the huge cost, a novel technology of hot melting casing is developed. The original concept of this technology is derived from Subterrene drilling, which makes holes in rocks and soils through progressive melting instead of mechanical chipping. During the process of the Subterrene drilling, a glass-like casing can be formed according to the research conducted by Los Alamos National Lab [2–5].

However, there are few attempts that have been made to research the composition as the glass-like casing. It is also a new attempt that combines the advanced material with the earth science—especially in geological engineering. Therefore, in order to make matters more understandable,

a rough sketch Figure 1 is sketched to show the process of the casing forming through the technology of hot melting [5, 6].

As is shown in Figure 1, the heat is primarily generated from a center that is made of Carbon-Carbon. The heat is sequentially transferred to the crust and the glass-like material. When the glass-like material is heated to the transition temperature (T_g), it gradually gets transformed into liquid with certain liquidity so that the glass-like casing can be formed. However, the thermal diffusivities of the glass-like casing and the borehole wall are different, leading to a temperature gap at their interface, which makes the glass-like casing forming a reality [5].

In this process, the heating temperature of the composition should be researched first since it has close relationships with the heating temperature and the design of other parts of the device. A relatively approximate melting temperature can be easily determined through the results of the DSC of the compositions.

This heating temperature is the key to optimize the makings of other components of the hot melting machine, especially the coating of the heater shell. This heating temperature is primarily related to the composition's fluidity.

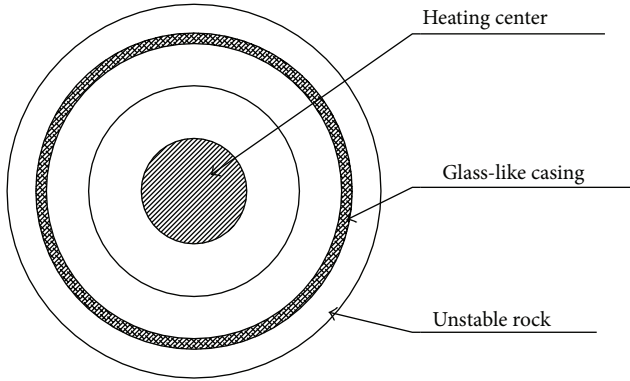


FIGURE 1: Heat distribution during developing a hot melting casing.

If the fluidity is lower enough, the glass-like composition will consequently stick to the shell. As a consequence, a coat has to be made onto the shell to prevent it from being damaged. Therefore, the research on the properties of the glass ceramic can be of great significance when it comes to the overall design of this technology.

In this paper, a composition that is similar to the shale has been developed. It is the first time to apply this glass-like casing to mend the broken borehole wall and many problems have come into being [7]. For example, in field, there is commonly no time to make the material insulated for a long time; therefore, it is highly suggested to cool it down in one minute. This makes the heat treatment more complicated to be under control, especially when the heat treatment happens underground. In order to make experiments conditions similar to the actual field conditions as much as possible, the heat insulation has been gave up, and the material has been cooled down directly in air. Furthermore, the glass-like casing is formed in an irregular shape, making some researches, the electron probe, for example, inaccurately unavailable. Although it is uneasy to deal with the natural problems above, the influence of different additives on the compositions in terms of heating stability, crystal phase growth, and field application has also been researched [8].

2. Experiments

In terms of any material, lower cost shall be an essential requirement for its future application in field. The composition provided by Zhuhai Xuanyang Limited is selected to be the raw material (RM). Due to the raw material's poor toughness and relatively high cost (RMB140 per 500 g), different wt% additives, aluminum (Al, RMB15 per 500 g), and quartz sand (QS, RMB 0.09 per 500 g) are added into the raw material. The components of different compositions are shown in Table 1.

There are some advantages both in Al and in quartz sand as for a high-quality additive, due to not only its lower cost but also good toughness [9]. As a matrix in bulk metallic glass due to its good performance in good toughness, the addition of Al also predominately contributes to the mechanical properties

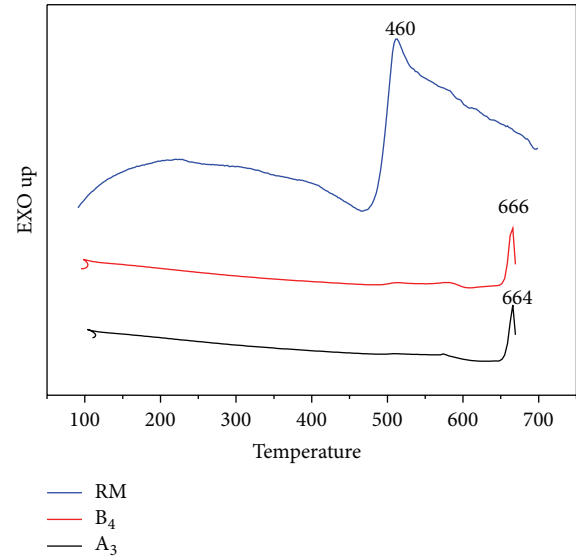


FIGURE 2: DSC results of samples RM, A₃, and B₄, respectively.

TABLE 1: Components of different compositions for making a bore-hole casing.

Sample	RM (wt%)	Al (wt%)	QS (wt%)
A ₁	90	10	0
A ₂	80	20	0
A ₃	75	25	0
A ₄	70	30	0
B ₁	70	10	20
B ₂	50	20	30
B ₃	40	30	30
B ₄	30	30	40

of the compositions in our research [8]. Similarly, quartz sand has good performance in wear resistance and lower cost [10].

XRD was applied to analyze the crystal phase because whether the crystal phase is beneficial for practical use or not is still unknown. For example, in our research, the crystal phase plays a positive role because it can boost material's mechanical properties while having little influence on fluidity. In addition, in order to figure out the influence of adding different additives on the crystalline phase growth, the scanning electron microscope (SEM) was also applied. For its future practical use, the optimized composition was applied in a model prototype [7].

3. Results and Discussions

In order to heat the composition at a proper temperature, the DSC was applied to find out the specific T_g . The results are plotted as in Figure 2 and Table 2.

The results show that the T_g increases with the add-in Al, while the melting point decreases in terms of RM and A₃. That mainly accounted for the lower melting point of Al—660°C, which is so close to the T_g of A₃ and B₄. So the add-in Al makes great contribution to lower the melting

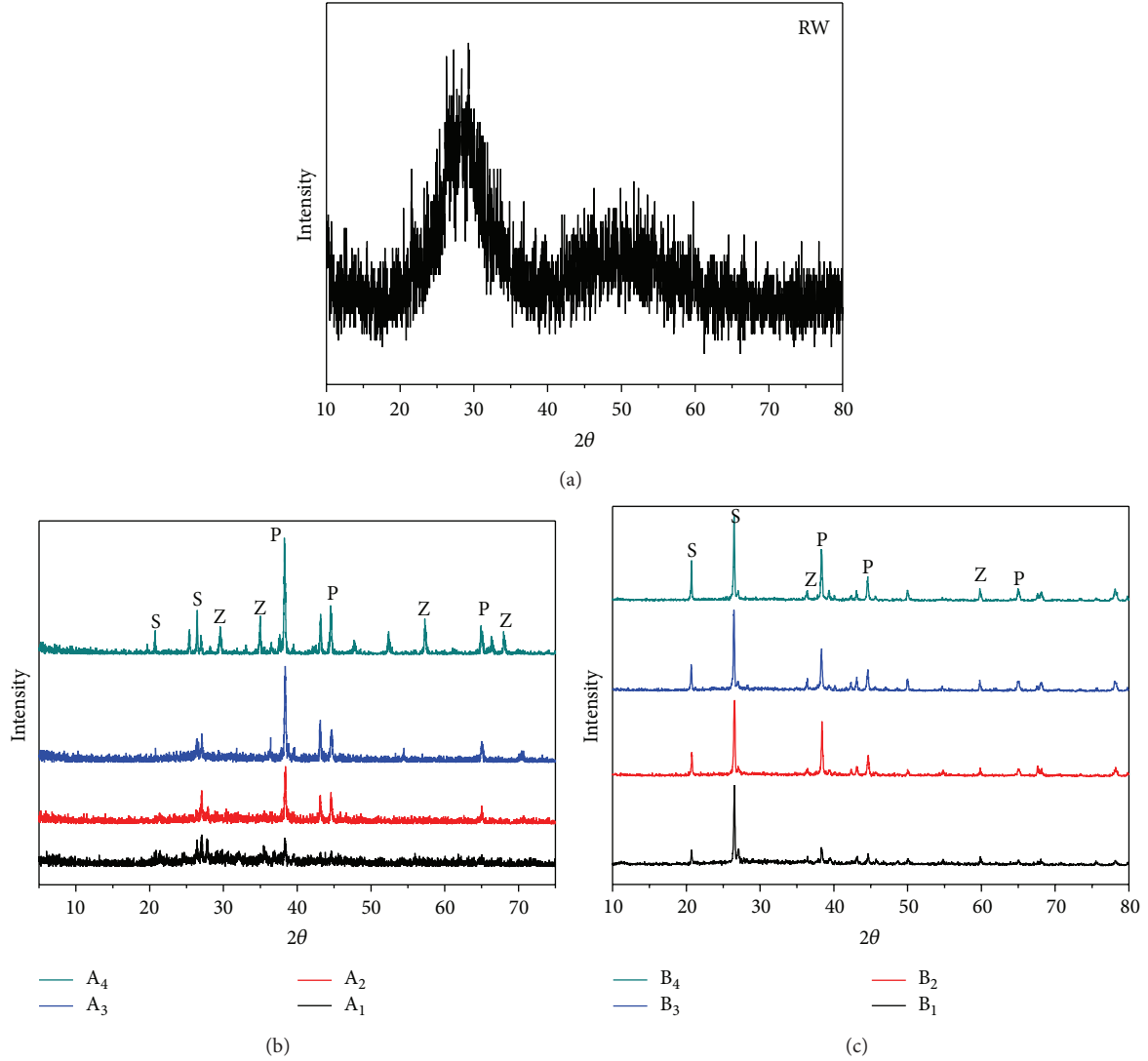


FIGURE 3: XRD patterns of different samples under the same condition, marked (a), (b), and (c).

TABLE 2: T_g and melting point performance of different compositions.

Samples	T_g ($^{\circ}\text{C}$)	Melting point ($^{\circ}\text{C}$)
RW	460	770
A ₃	657	664
B ₄	657	666

points of the compositions. The results above make great sense in figuring out a proper heating temperature (700°C). In addition, 7°C/second was selected to heat the composition, the maximum heating rate that our device can reach.

However, whether the add-in Al or the newly generated crystal can improve the composition's physical properties is still unknown. Therefore, the XRD (shown in Figure 3) is performed on the samples.

The results in Figure 3(a) show that there is no typical crystal phase in RM, though it has a trend to form a peak,

which is one of the typical properties of glass. However, the composition with add-in Al performs well in crystal phase (Figure 3(b)). Three different peaks represent different compounds phases: label "P" stands for the distribution of Al, label "S" stands for the distribution of SiO₂, and label "Z" stands for the distribution of ZnO. This actually proves that the add-in Al contributes to the appearance of the crystal phases, including ZnO and SiO₂, both of which did not actually appear in the RM.

After QS is added into the composition, the "S" peak greatly goes up. Similarly, this is mainly because SiO₂ is the main making of the QS. At the same time, the "Z" peak goes down with the addition of QS. However, whether the newly appearing crystal phase is beneficial for the composition's mechanical properties or not is still unknown so far.

In order to make a better comparison to the rock, the Brazilian Formula experiment for testing the tensile strength of the rock was applied to the samples of three. Since the tensile strength is far greater than the compressive strength

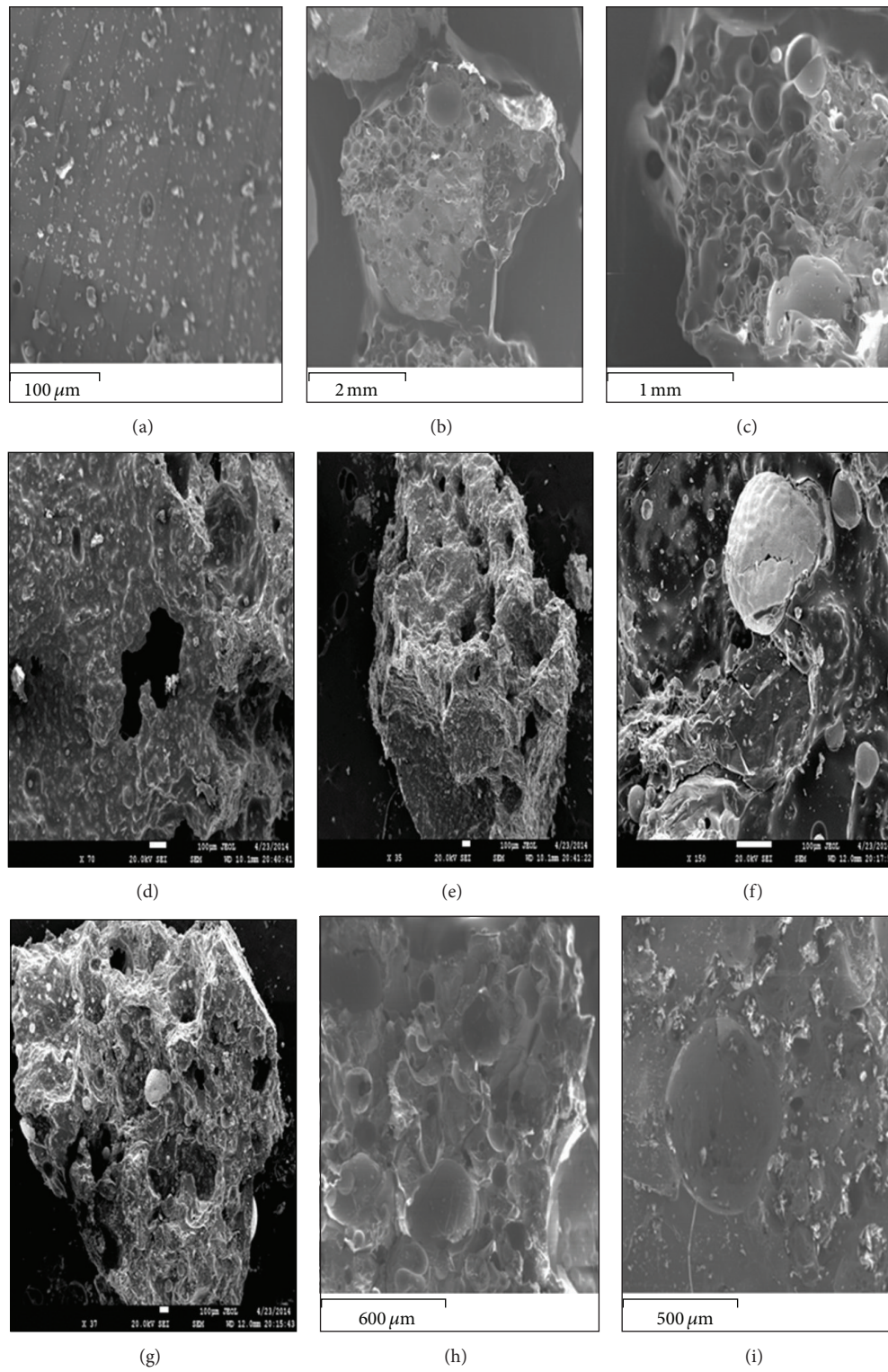


FIGURE 4: SEM micrographs of (a) RM, (b) A₁, (c) A₂, (d) A₃, (e) A₄, (f) B₁, (g) B₂, (h) B₃, and (i) B₄.

TABLE 3: Physical and mechanical characteristics of the samples.

Samples	Bulk density, ρ (g/cm^3)	Compressive strength (Mpa)	Tensile strength (Mpa)
RW	3.20	6.5	1.5
A ₁	1.11	5.7	1.3
A ₂	1.03	6.0	1.4
A ₃	1.10	10.1	2.1
A ₄	1.12	6.9	1.7
B ₁	1.03	5.7	0.6
B ₂	1.12	11.3	2.8
B ₃	1.16	11.5	4.2
B ₄	1.19	14.0	4.4

of the rock, the sample at this condition is always in tension rather than compression failure of damage. This is the Brazilian method to test the tensile strength of brittle material mechanics theory.

The results in Table 3 show that the bulk density generally decreases with the add-in Al and QS, no matter for sample A or B. This is probably associated with the large porosity rates of the compositions. The results shown in the following SEM are also another proof to illustrate this. The compressive and tensile strength are roughly boosted by the addition of Al and QS. This is another proof that shows that the newly generated crystal definitely contributes to the increased the values of the compositions.

The outcomes of SEM (Figure 4) suggest that samples A and B have much more porosity in comparison to RM. The lower bulk density, representing higher porosity, is accounted for as a consequence of different compositions and physical characteristics of the viscous flow during the heat treatment [11]. Interestingly, the overall rate of pores goes up at first and then down at the point of adding in 25 wt% Al. The increased pore rate is associated with the difficult in releasing CO₂, due to the lack of insulation or the deformation of calcite (probably from the RM). The add-in Al also boosts the process of deformation, causing CO₂ encapsulated by the crystal of Al [12–14]. When the Al is the only additive added into the composition, the interconnected pore is characterized by layered shape with the same size.

However, the layered shape of the pore is broken into more irregular ones with the add-in QS, reducing the overall porosity rate of the composition. This greatly contributes to the improved bulk density and mechanical properties. As is shown in Figure 4(i), the pore line is obscure to be seen, of which the mechanical properties perform best among the all compositions.

The results of Table 3 and Figure 4 show that, with the increasing add-in Al, both of the compressive and tensile strength perform better, with the maximum 14.0 Mpa and 4.4 Mpa in B₄ (30% RW, 30% Al, and 40% QS). In addition, its cost is relatively lower than others due to the greatest proportion of add-in QS, whose cost is comparatively lower than Al and RW. Taking the compressive and tensile strength and the lower cost together, the B₄ with 30% Al, 30% RW,



FIGURE 5: Device for conducting this laboratory experiment.

and 40% QS is eventually selected as the composition to be initially used in laboratory experiment.

4. Practical Application in Laboratory Experiment

In order to check whether the composition of the sample B₄ can be successfully applied in practice, as has been suggested as the most excellent candidate up to now, a device intended for this novel application was developed (shown in Figure 5). The composition was performed in different borehole wall using this device.

The laboratory experiment was conducted on a novel machine that was developed by our team. A carbon-carbon (C/C) was applied to generate heat, which is the original source for heating our selected compositions. The heat head consists of heat element of high strength graphite and external shell of GH742 alloy. The high strength graphite can work under 1200°C. Although the carbon-carbon composite is characterized by high strength and large thermal conductivity, it performs badly in resisting high temperature oxidation. Due to the special experiment equipment, the experimental test can be currently finished in our lab; however, the theoretically compressive and tensile pressure can be repeatedly obtained by the ordinary equipment to test mechanical properties.

The results of Figure 6 indicate that the compositions can be successfully used to form a glass-like casing with certain strength, no matter in rock or soil. However, many problems need to be solved through our further study, including the influences of heat treatment and components of compositions on its physical and mechanical properties.

5. Conclusions

Based on the researching results, the composition of sample B₄ (30 wt% Al + 40 wt% QS + 30 wt% RM) has turned out to be a high potential for making glass-like casing. The add-in Al and QS contributes to the lower cost and the high-quality mechanical properties of the compositions due to the newly generated crystal, which has a positive influence



FIGURE 6: Experimental photos of the glass-like casing, (a) and (b) composition used in granite, heating up to 700°C, and (c) and (d) composition used in soil, heating up to 700°C.

on the composition that is intended for glass-like casing. Meanwhile, the addition of QS can boost the properties of the compositions by compressing its interconnected pores, lowering the overall porosity rate.

Conflict of Interests

The authors declare that there is no conflict of interests regarding the publication of this paper.

Acknowledgments

The authors gratefully acknowledge the support by the Beijing Organization Department Outstanding Talented Person Project (no. 2013D009015000002), the Beijing Higher Education Young Elite Teacher Project (Grant no. YETP0645), the Fundamental Research Funds for the Central Universities (no. 2652015), and the National Natural Science Foundation of China (no. 51272241). Meanwhile, great thanks also go to former researchers for their excellent works, which give great help for the academic study.

References

- [1] H. Zhu, Q. Liu, J. Deng, G. Wang, and J. Liao, "Rock-breaking mechanism of rotary-percussive drilling," *Journal of Basic Science and Engineering*, vol. 20, no. 4, pp. 622–631, 2012.
- [2] D. E. Armstrong, J. S. Coleman, B. B. McInteer, R. M. Potter, and E. S. Robinson, "Rock melting as a drilling technology," Los Alamos National Laboratory Report LA-3243, Los Alamos National Laboratory, 1962.
- [3] G. E. Cort, S. J. Goff, and J. C. Rowley, "The rock melting approach to drilling," in *Proceedings of the Energy-Sources Technology Conference and Exhibition (ETCE '94)*, p. 280, American Society of Mechanical Engineers (ASME), New Orleans, La, USA, 1994.
- [4] S. K. Garg and J. Combs, "Slim holes for geothermal exploration and reservoir assessment in Japan," *GRC Bulletin*, vol. 23, pp. 89–96, 1994.
- [5] X.-F. Wang, Z.-P. Zhang, and C. Chen, "A new drilling technique—subterrene drills," *Geotechnical Engineering Technique*, vol. 17, no. 2, pp. 123–125, 2002.
- [6] L. U. Chun-hua, W. U. Xiang, and W. Qiang, "Study on hot-melt sidewall strengthening technology," *Geology and Exploration*, vol. 48, pp. 1034–1038, 2012.

- [7] A. Christogerou, T. Kavas, Y. Pontikes, S. Koyas, Y. Tabak, and G. N. Angelopoulos, "Use of boron wastes in the production of heavy clay ceramics," *Ceramics International*, vol. 35, no. 1, pp. 447–452, 2009.
- [8] D. Jiang, L. Cui, Y. Zheng, and X. Jiang, "Effects of thermal cycling on the temperature memory effect of TiNiNb alloy," *Journal of Materials Engineering and Performance*, vol. 19, no. 7, pp. 1022–1024, 2010.
- [9] R. W. Cahn, "Aluminium-based glassy alloys," *Nature*, vol. 341, no. 6239, pp. 183–184, 1989.
- [10] *A Preparation and Study on High Expansion Coefficient Glass Ceramics of Li₂O-ZnO-SiO₂ System*, vol. 27, Shan Dong Ceramics, 2004.
- [11] R. V. Manukyan and N. S. Davydova, "Use of waste in the ceramics industry," *Glass and Ceramics*, vol. 53, no. 7-8, pp. 247–248, 1996.
- [12] A. Escardino, J. Garcia-Ten, and C. Feliu, "Kinetic study of calcite particle (powder) thermal decomposition: part I," *Journal of the European Ceramic Society*, vol. 28, no. 16, pp. 3011–3020, 2008.
- [13] J. Liebault, J. Vallayer, D. Goeuriot, D. Treheux, and F. Thevenot, "How the trapping of charges can explain the dielectric breakdown performance of alumina ceramics," *Journal of the European Ceramic Society*, vol. 21, no. 3, pp. 389–397, 2001.
- [14] B. Cicek, A. Tucci, E. Bernardo, J. Will, and A. R. Boccaccini, "Development of glass-ceramics from boron containing waste and meat bone ash combinations with addition of waste glass," *Ceramics International*, vol. 40, no. 4, pp. 6045–6051, 2014.

Research Article

The Experimental Investigation of Hydraulic Fracture Propagation Characteristics in Glutenite Formation

Zhihong Zhao,¹ Jianchun Guo,¹ and Shou Ma^{1,2}

¹State Key Laboratory of Oil and Gas Reservoir Geology and Exploitation, Southwest Petroleum University, Chengdu 610500, China

²Production Technology Research Institute, Shengli Oilfield, SINOPEC, Dongying 257000, China

Correspondence should be addressed to Zhihong Zhao; swpuzzh@163.com

Received 13 June 2014; Revised 12 November 2014; Accepted 15 November 2014

Academic Editor: Guocheng Lv

Copyright © 2015 Zhihong Zhao et al. This is an open access article distributed under the Creative Commons Attribution License, which permits unrestricted use, distribution, and reproduction in any medium, provided the original work is properly cited.

Hydraulic fracture propagation characteristics in glutenite formation are studied by a series of servo-controlled triaxial large-scale fracturing experiments. The experimental results show that the fractures extend along the gravel and sandstone cementing face, and fracture geometry in glutenite formation is complex, which is similar to network fractures. The phenomenon of the gravel being split has not been observed. In the process of the fracture extension, the extension pressure is fluctuating, and the degree of fluctuation is more drastic with the gravel diameter increase. This paper suggests that using large rate and multislug technology would increase the flow ability of the carrying fluid. The conclusions are significant to hydraulic fracturing in glutenite formation.

1. Introduction

Glutenite reservoir is widely distributed in China, such as the Sheng Li oil field and Xinjiang oil field. Hydraulic fracturing is the key technology used in the exploitation of this kind of reservoir. But the hydraulic fracture extension pressure is influenced by the gravel in glutenite reservoir, which usually leads to the failure of the fracturing treatment. When the hydraulic fracture meets gravels in the process of propagation, as the lithology mutations, the hydraulic fracture propagation direction and geometry would be altered.

Many scholars use large-scale triaxis hydraulic fracturing simulation experiment device to simulate the hydraulic fracture extension and geometry under various reservoir conditions. Chen et al. [1, 2] and Jin et al. [3] performed a series of large-scale triaxial experiments to investigate the influence of natural fractures and earth stress on the induced fractures. They took into account the influence of the natural fracture strike and dip. Bohlooli and de Pater [4] performed a series of large-scale triaxial experiments to study the hydraulic fracturing in soft rocks. They observed that fractures obtained at high stress were short, branched, and tortuous while those obtained at low stress were mainly longer, straight, and less tortuous. Chen et al. [5] studied

the dynamic fracture propagation in hydraulic refracturing. Yan et al. [6] conducted scaled laboratory experiments to investigate hydraulic fracture initiation mechanisms in porous reservoirs and fractured reservoirs. They observed that the fracture propagation pressure is smooth and steady. Liu et al. [7] simulated the influence of natural fracture network on the propagation geometry of hydraulic fractures.

This paper conducted a series of hydraulic fracture initiation tests with a large-scale triaxis hydraulic fracturing simulation experiment device and artificial glutenite core with different gravel diameters. Through the observation and analysis of fracture profile and pressure curve, the characteristics of hydraulic fracture geometry and propagation in glutenite reservoir were analysed, and we can draw some significant conclusions which can be adapted to improve the fracturing response in glutenite formation.

2. Experimental Setup and Procedure

2.1. Experimental Setup. The experiments are performed in a large-scale triaxial simulation test system. The system is composed of a triaxial assembly, a servo-booster pump, an acoustic emission instrument, a data acquisition system,

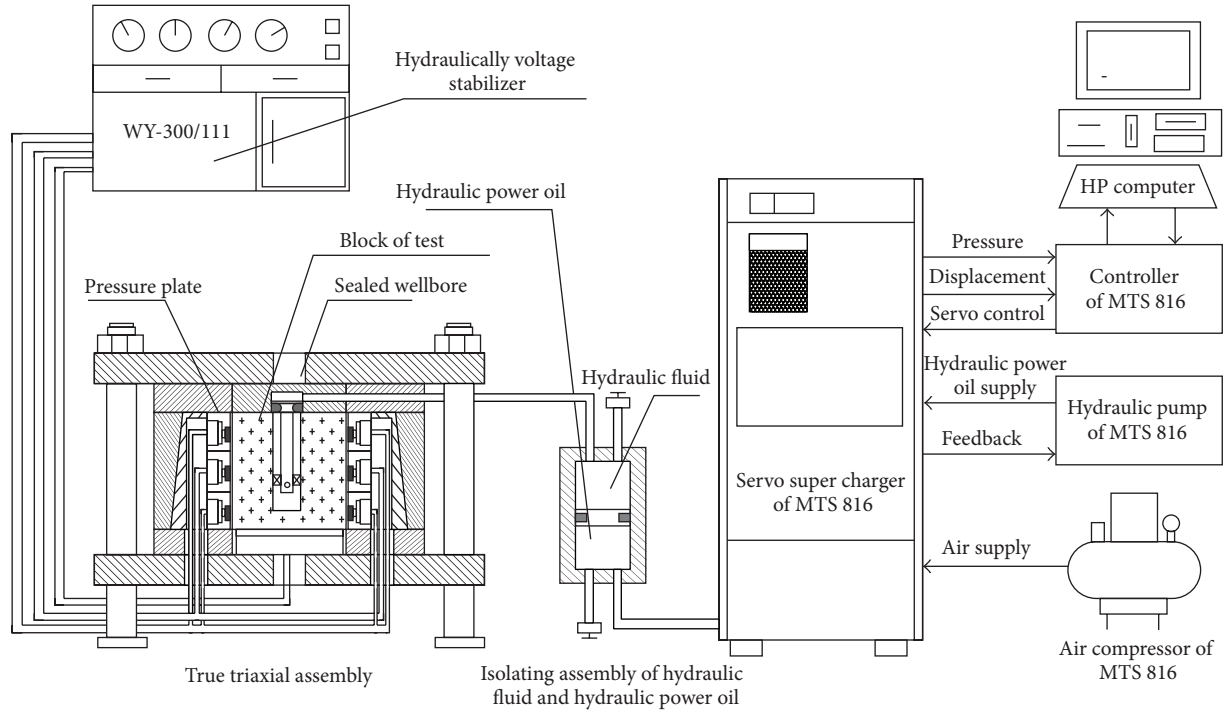


FIGURE 1: Schematic of a triaxial hydraulic fracturing test system.

a laboratory stabilized power supply unit, an oil-water isolating device, and other auxiliary devices (Figure 1).

Cubic blocks of 300 mm on a side are positioned between the pressure plates. In order to simulate the horizontal minimum principal stress, we add pressure, respectively, to the fractured interval and the top and bottom interlayer by three pairs of pressure plates in one horizontal direction. In the other horizontal and vertical direction, we simulate the vertical stress and horizontal maximum principal stress by a pair of pressure plates, respectively. The multichannel hydraulically voltage stabilizer provides pressure plates hydraulic pressure, and the pressure of every channel could be controlled (each channel for the biggest liquid pressure can reach 27 MPa).

The pressure platens are equipped with four square sheets to ensure equal pressure distribution. We used 0.1 mm thick Teflon sheets greased with Vaseline to reduce friction between the sample and the loading platens. The fluid injection pressure is provided by a servo-hydraulic pump (MTS 816).

Natural blocks or artificial blocks could be used for hydraulic fracturing experiment. Considering the difficulty of obtaining natural rock and the condition of processing, this paper conducts hydraulic fracturing with artificial rock. The experiment blocks were prepared with a special mould (Figure 2). The 10 cm section around the open hole was using the mixture of Chinese cement number 425, quartz sand, and gravel, and the other parts of the glutenite samples were mixed with Chinese cement number 425 and quartz sand. The mass ratio of cement to quartz sand was 1:1.

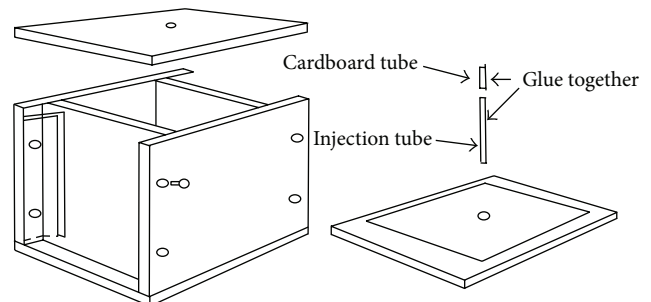


FIGURE 2: Artificial blocks moulds and bottom board assembly diagram.

2.2. Experiments Sample Preparation. A highly viscous (135 mPa·s) guar gum fracturing fluid was used to initiate hydraulic fracture. We mixed a red dye in the fluid to improve detection of the hydraulic fracture.

The steps of preparing the glutenite samples are as follows. Firstly, cast a basement about 5 cm with cement and quartz sand at the bottom of the sample. Secondly, put a wellhole in the center of the sample. Then, the wellhole was perforated along 50 mm with 4 mm diameter perforations at 180-degree phasing, putting a fine screen mesh around the wellbore about a radius of 10 cm thin and casting with cement, quartz sand, and gravel inside the fine screen mesh (Figure 3). Thirdly, cast 15 cm high outside the fine screen mesh with cement and quartz. Finally, put out the fine screen mesh slowly, and cast the other parts of the sample with cement

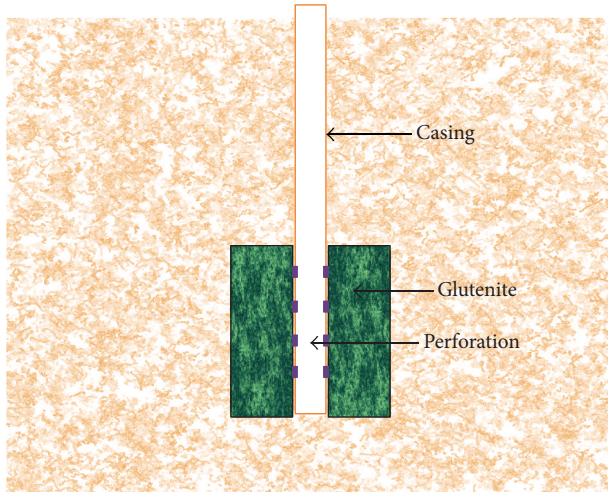


FIGURE 3: Artificial glutenite rock schemes.

and quartz. So the whole sample casting is completed. These model blocks were cured in a special mold for 5 days and then they were transferred outside for a fortnight at room temperature.

2.3. Test Procedure. We conducted our experiments in a normal-faulting stress regime. Guar gum fracturing fluid was used for the fracturing. The fluid was pumped into the bore hole with a constant rate until a fracture initiates and propagates after breakdown. The pressure decline was then recorded. After the experiment, each block was split open along the fracture plane to reveal the fracture geometry, which was subsequently photographed.

3. Experimental Program

In this paper, the primary purpose is to study the influence, caused by the gravel size, on the hydraulic fracture extension. So we prepare six artificial glutenite cores with different diameter range of gravel and prepare one sandstone core without gravel in contrast with the glutenite cores (Table 1). In our experiments, the value of the vertical compressive stress and the maximum horizontal principal stress is constant, and the value of the minimum horizontal principal stress is changed in some experiments, the purpose of which is to understand the minimum horizontal principal stress impact on the hydraulic fracture geometry and the fracture propagation pressure.

4. Experimental Results and Analysis

4.1. The Geometry of Hydraulic Fracture. In a series of experiments, the propagating direction of the hydraulic fracture in the glutenite reservoir is along the direction of maximum principal stress, which is consistent with the fracture in sandstone [5]. Yet there are large differences in fracture surface morphology. Figure 4 is the fracture cross-section of experimental sample along the maximum principal stress

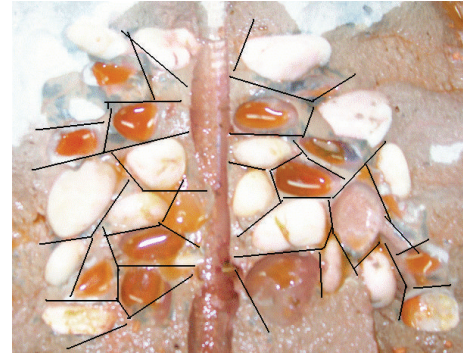


FIGURE 4: Fracture photo of sample number 1.

direction. This sample has the gravel diameter from 20 to 25 millimeters. The phenomenon of the gravels being splitted is not observed. The fractures propagate along the cement face of sandstone and glutenite, and the profile of fracture in glutenite formation looks like a spider's web. In the process of hydraulic fracture propagation, when the fracture encounters gravel, the direction of fracture propagation would be transformed, which causes roughness of the fracture surface. At the gravel, the width of the hydraulic fracture is narrower than elsewhere. The fracturing fluid mainly flows between the gravels and the channel that the fluid flow is narrow and bend, which is against the flow of the sand-carrying fluid. Characteristics of these fractures are significantly different from that in sandstone reservoir [8], in which the fissure surface is relatively smooth.

Therefore, in order to increase the liquidity of the carrier fluid and considering the complexity of the hydraulic fractures in glutenite formation, the hydraulic fracturing engineers should design larger rate to create a wider fracture and use multislug to smooth the hydraulic fracture.

4.2. The Characteristics of Extension Pressure. The distinct characteristic of hydraulic fracture propagation in glutenite formation is the sharp variation of extensions pressure. Figure 5 is the extending pressure curve of sample without gravel rock. The extension pressure is smooth, which is consistent with the experimental results as Yan et al. [6]. The pressure curve of these core samples with gravels is fluctuating, and the bigger the gravel diameter, the larger the variation of extensions pressure. Figure 6 is the pressure curve of sample with gravel diameter 16–22 mm, in which the fracture extending pressure is very fluctuation.

The fracture pressure is mainly influenced by minimum principal stress, and the greater the minimum principal stress, the more the fracture pressure. Simultaneously, the value of gravel diameter influences the fracture pressure too. The bigger the gravel diameter, the greater the fracture pressure when the minimum principle pressures are equal. For example, the fracture pressure of number 5 core sample is greater than number 6 core sample (Table 2).

Table 2 describes crustal stress and net pressure of seven samples. The value of fracture propagation is influenced by the diameter of the gravel. The greater the diameter of gravel,

TABLE 1: The parameters of hydraulic fracturing experiment.

Number	Loading speed (mm/sec)	Fluid viscosity (mPa·s)	Vertical compressive stress (MPa)	Maximum horizontal principal stress (MPa)	Minimum horizontal principal stress (MPa)	Principal stress difference (MPa)	Particle size range (mm)
1	0.1	135	15	12	9	3	20–25
2	0.1	135	15	12	7	5	16–22
3	0.1	135	15	12	7	5	Nongravel
4	0.1	135	15	12	5	7	12–18
5	0.1	135	15	12	5	7	10–15
6	0.1	135	15	12	3	9	8–12
7	0.1	135	15	12	3	9	6–10

TABLE 2: The pressure characteristics of the hydraulic fracture propagation.

Number	σ_H (Mpa)	σ_h (Mpa)	Fracture pressure (Mpa)	Extension pressure (Mpa)	Net pressure (Mpa)	Particle size range mm
1	12	9	14.24	11.9	2.9	20–25
2	12	7	13.52	9.8	2.8	16–22
3	12	7	12.27	8.7	1.7	non-gravel
4	12	5	12.27	7.6	2.6	12–18
5	12	5	9.27	7.4	2.4	10–15
6	12	3	7.30	5.2	2.2	8–12
7	12	3	6.01	4.9	1.9	6–10

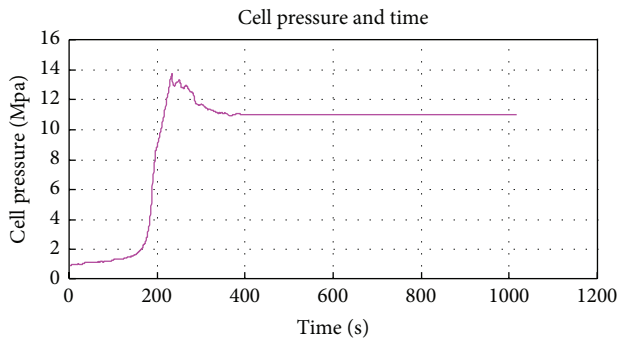


FIGURE 5: Pressure curve of sample number 2.

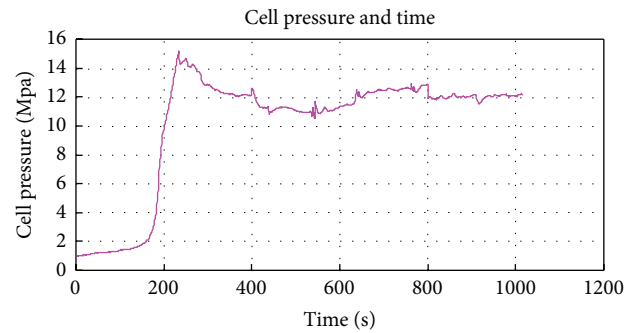


FIGURE 6: Pressure curve of sample number 3.

the larger the extension pressure. For example, the extension pressure of number 1 core sample, whose gravel diameter is 20–25 millimeter, is the greatest, and the extension pressure of number 6 core sample without gravel is the minimum (Table 2).

Consequently, it is necessary for hydraulic fracturing engineers to prepare for the extension pressure fluctuating when they design the fracturing treatment, and more propellant slugs should be adopted to smooth the fracture in glutenite formation, which would reduce the influence of the pressure fluctuating on fracturing and increase the exactness of the estimated fracturing operation by extension pressure.

5. Conclusions

Based on the experimental study, the following major conclusions are made for fracturing in glutenite formation.

- (1) Propagation of hydraulic fractures in glutenite formation has been analyzed by experiments. It is found that the fracture morphology in glutenite formation is more complex and rough, which is different from that of sandstone reservoir.
- (2) Fractures in glutenite formation would propagate along the cement face instead of splitting the gravel. The face of fracture is relatively rough, which leads to the increase of flow resistance of fracturing fluid and higher injection pressure with heavy fluctuation.

These characteristics have an important meaning to the fracturing design in glutenite formation.

- (3) Large injection rate should be applied, based on the characteristic of fracture propagation. Wider fracture should be generated so that carrying fluid can pass easily. And the number of proppant slugs which is used to polish the faces of fracture should be increased to reduce injection pressure and pressure fluctuation.
- (4) The risk of fracturing in glutenite formation can be reduced and thus success rate can be increased with the knowledge of fracture propagation characteristics in glutenite formation.

Conflict of Interests

The authors declare that there is no conflict of interests regarding the publication of this paper.

Acknowledgments

The paper is supported by Southwest Petroleum University (SWPU) Science and Technology Fund: Project name is hydraulic fracture and natural fracture interaction mechanism (no. 2013XJZ001). The authors would like to acknowledge the support of the Modeling of Fracture Network Conductivity in Shale Reservoir project (no. 51374178) which is sponsored by the National Natural Science Fund. This work was financially supported by the National Science and Technology Major Projects of China (no. 2008ZX05006).

References

- [1] M. Chen, X. Z. Chen, and R. Z. Huang, "Hydraulic fracturing of highly deviated wells," *Journal of University of Petroleum*, vol. 19, no. 2, pp. 30–35, 1995 (Chinese).
- [2] M. Chen, F. Pang, and Y. Jin, "Experiments and analysis on hydraulic fracturing by a large-size triaxial simulator," *Chinese Journal of Rock Mechanics and Engineering*, supplement 19, pp. 868–872, 2000 (Chinese).
- [3] Y. Jin, X.-D. Zhang, and M. Chen, "Initiation pressure models for hydraulic fracturing of vertical wells in naturally fractured formation," *Acta Petrolei Sinica*, vol. 26, no. 6, pp. 113–118, 2005 (Chinese).
- [4] B. Bohloli and C. J. de Pater, "Experimental study on hydraulic fracturing of soft rocks: influence of fluid rheology and confining stress," *Journal of Petroleum Science and Engineering*, vol. 53, no. 1-2, pp. 1–12, 2006.
- [5] M. Chen, H. Jiang, G. Q. Zhang, and Y. Jin, "The experimental investigation of fracture propagation behavior and fracture geometry in hydraulic fracturing through oriented perforations," *Petroleum Science and Technology*, vol. 28, no. 13, pp. 1297–1306, 2010.
- [6] T. Yan, W. Li, and X. Bi, "An experimental study of fracture initiation mechanisms during hydraulic fracturing," *Petroleum Science*, vol. 8, no. 1, pp. 87–92, 2011.
- [7] Z. Liu, M. Chen, and G. Zhang, "Analysis of the influence of a natural fracture network on hydraulic fracture propagation in carbonate formations," *Rock Mechanics and Rock Engineering*, vol. 47, no. 2, pp. 575–587, 2014.
- [8] B. Huang, P. Li, J. Ma, and S. Chen, "Experimental investigation on the basic law of hydraulic fracturing after water pressure control blasting," *Rock Mechanics and Rock Engineering*, vol. 47, no. 4, pp. 1321–1334, 2014.

Research Article

Compositional Effects and Mechanical Parametric Analysis of Outwash Deposits Based on the Randomised Generation of Stone Blocks

Chong Shi^{1,2} and Jinzhou Bai^{1,2}

¹Key Laboratory of Ministry of Education for Geomechanics and Embankment Engineering, Hohai University, Nanjing 210098, China

²Institute of Geotechnical Engineering, Hohai University, Nanjing 210098, China

Correspondence should be addressed to Chong Shi; shichong81@126.com

Received 17 September 2014; Accepted 25 November 2014

Academic Editor: Zhaohui Li

Copyright © 2015 C. Shi and J. Bai. This is an open access article distributed under the Creative Commons Attribution License, which permits unrestricted use, distribution, and reproduction in any medium, provided the original work is properly cited.

Based on the distribution of the stone blocks in outwash deposits, the paper present a modeling method for the random structure of outwash deposits, in which the long axis of the stone blocks is supposed obeying a lognormal distribution. Then numerical experiments of biaxial compression using the granular discrete element method are used in the macro- and micro parametric analysis. The influences of strength of the cementation, the sizes of stone blocks, and the content of stone blocks on the peak compressive and shear strength are discussed. The micromechanical parameters of the outwash deposits are also analyzed. The proposed method offers a supplement to the mechanical characterization of outwash deposits and accounts for the limitation that indoor experiments cannot consider large stone blocks.

1. Introduction

Outwash deposits are a particular type of geological medium and are formed by glacial movement. The media are composed primarily of irregular stone blocks with high strength and weak, fine-grained debris, as shown in Figure 1. They are widely distributed in southwestern China, where the water resources are rich and the geological conditions are suitable for the construction of hydropower plants. According to the program “accelerating the development of hydropower project in China,” outwash deposits should be an important and difficult issue and will receive more attention from the departments of geological engineering, geotechnical engineering, and hydropower engineering. However, due to the composition of outwash deposits, the mechanical parameters of outwash deposits are difficult to be determined by current analysis methods, as well as reinforcement measures.

Outwash deposits are different from common homogeneous materials because of the presence of stone blocks and the cementation of fine-grained debris. For any structural characteristics and material composition, the mechanical properties and the water-physical properties of them are

unique. At present, most studies consider the outwash deposit as a homogeneous medium. The analytical approaches rely mainly on indoor experiments and numerical simulations. However, because large stone blocks cannot be used in the indoor experiments, the mechanical characterization of outwash deposits has some limitations. Some scholars [1, 2] found that the existence of boulders increased the strength and density of outwash deposits, which also leads to deviations in their mechanical properties. Others studied the relationships among the cementation of fine-grained debris, dry density, water content, block shapes, block distribution, and the shear strength of the stone and debris mixture by experimental tests, such as the large triaxial shear experiment, the medium-sized triaxial shear experiment, and the large horizontal push shear experiment [3–7]. The results demonstrate that the stress-strain of this medium is approximately taken on nonlinear hardening characteristics, which agrees well with the hyperbola assumption of Duncan-Chang model, and the shear strength of the stone and debris mixture is related closely to the concentration and distribution of the stone blocks. However, it is difficult to gain a thorough understanding of outwash deposits without

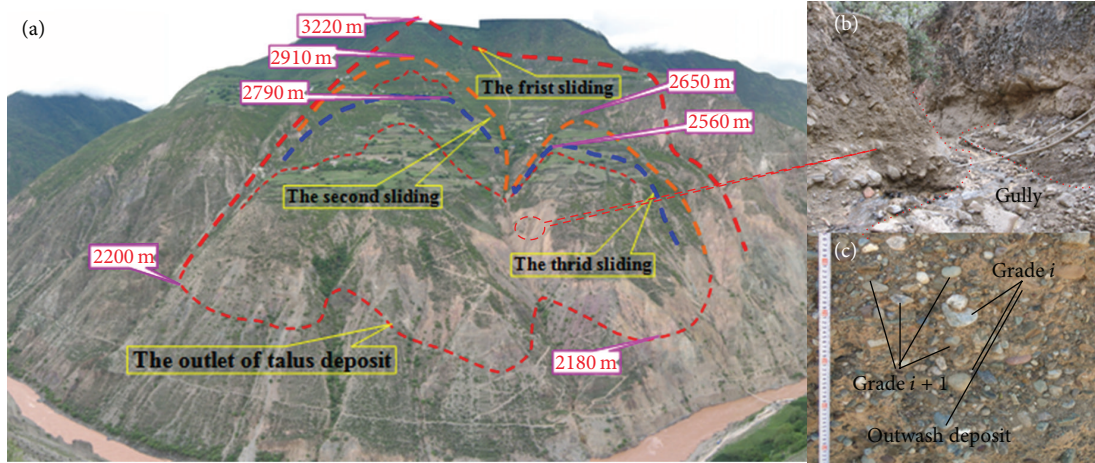


FIGURE 1: A typical outwash deposit formed by glacial movement.

considering the effects of heterogeneity and randomness on the distribution and concentration of stone blocks in the conventional geotechnical experiments. The limited field tests are discrete and not representative. Therefore, it is necessary to consider the composition of the outwash deposit in the experiments and numerical calculations when studying the mechanical characteristics. Digital image processing is a convenient tool. The sizes and shapes of the debris in outwash deposits were studied by Lebourg et al. [8]. The real internal structure of geological materials was also detected by such technology [9–12]. So it can provide an effective approach for research into the composition of outwash deposits [13, 14]. Because the structure composition of outwash deposits is mainly determined by stone blocks, a model considering the distribution and randomness of stone blocks is meaningful.

According to the field statistics, the geometric shapes of the stone blocks are assumed to be approximately elliptic-polygon and obey a normal distribution in this work. Then a geomechanical model for biaxial compression is established using the particle flow code. The effects of the stone blocks and fine-grained debris on the mechanical properties of outwash deposit are studied. The changes in the macroscopic compressive strength and shear strength of the medium are also discussed.

2. Structural Characteristics of Outwash Deposits

2.1. The Structural Composition of Outwash Deposits. Outwash deposits are a type of binary mixture medium consisting of fine-grained debris and stone blocks, where both the debris and stone blocks are made of the same material and are distinguished by the grain size but not by the composition. However, not all sizes of stone blocks have a positive influence on the strength of the medium. There is a threshold that distinguishes debris from stone blocks. The threshold size of stone blocks can be determined only in certain geological conditions and scales, which shows that the large grains play a greater role in the macroscopic mechanical properties

during the smaller scale studies. When the scale of research is increased, the former large grains will lose their dominant effect to mechanical property and can be regarded as debris. The following criterion to distinguish stones from debris is proposed [15]:

$$f = \begin{cases} R & d \geq d_{\text{thr}} \\ S & d < d_{\text{thr}}, \end{cases} \quad (1)$$

where d_{thr} is the threshold of stone and debris ($d_{\text{thr}} = 0.05L_c$), L_c is the characteristic engineering size, R denotes the stone, and S denotes the debris.

In addition, the indoor geotechnical test on similar media, the direct shear test, and triaxial compression test can only consider grains below 2 cm due to the limitations of the instruments. Therefore, d_{thr} is set to be 2 cm in this work, which means that if the grain size is less than 2 cm, the grain will be defined as debris. Conversely, if the grain size is greater than 2 cm, the grain will be considered as a stone block.

By above measure, grains of debris and stone blocks will be endowed attributes separately to reflect the change rule of medium composition and mechanical property.

2.2. The Aggregate Gradation of Outwash Deposits. The sizes and shapes of stone blocks differ greatly at different part, as shown in Figure 1(c). The microstructure of outwash deposits, which can be explained as grain contact and interaction, is just related to content, size, and roughness of stone blocks. In order to construct a stochastic model of outwash deposits, the grains regarded as stone can be divided into several gradation according to the grain size. Then according to the results of the grain size analysis and field statistics, the proportion, quality, volume, and area of the stone blocks in the research region can be obtained easily. The grains smaller than the threshold will be considered as debris and can be described using the conventional geotechnical experiments. Numerical simulation method will be used to reflect its influence on mechanical property of outwash deposit, in which the stone blocks are supposed to be unbroken.

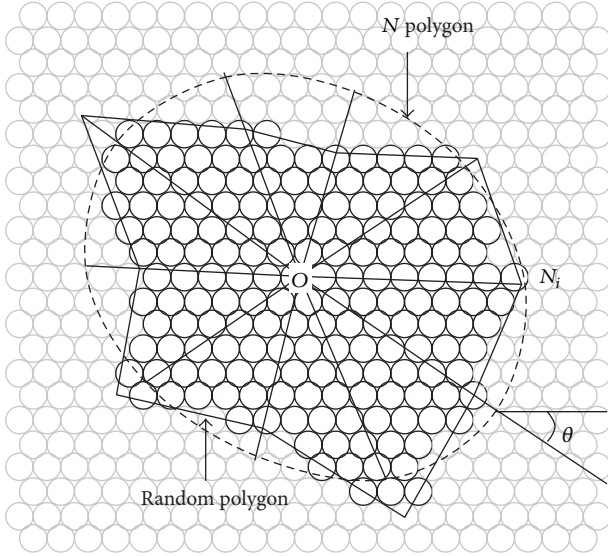


FIGURE 2: An arbitrarily shaped stone block depicted by a particles cluster.

If the density of the stone blocks is ρ_R , the debris density is ρ_S . Therefore, the 2D area of the stone blocks in grade i can be written as follows:

$$A_i = \frac{4r^2 G_i / \rho_R}{G_0 / \rho_S + \sum_{k=1}^n G_k / \rho_R}, \quad (2)$$

where A_i is the 2D area percentage of stone blocks in grade i , G_0 is the weight of the medium with grain sizes below the threshold and $\sum_{k=1}^n G_k / \rho_R$ is the total weight of stone blocks.

2.3. The Randomised Generation of Aggregates. Each stone block can be regarded as an arbitrary polygon in the plane, so a number of polygons are generated randomly in the designated region to simulate blocks. During the generation process, every polygon should be judged to avoid overlapping with others. Then the area in the polygons is regarded as stone blocks of different grades. When the polygon is convex, it has difficulty in considering the interaction force due to mosaic effect of rough block surface, which will lead to deviations in the mechanical parameter research, so the polygon generation should consider convexity and concavity at the same time.

To generate the arbitrary shapes of the stone blocks, the stone blocks are assumed to be initially elliptical, then the outline is divided as polygon and the vertices of polygon are random, as shown in Figure 2. The ellipses can be determined using three parameters: the length of long axis a , length of the short axis b (or the axis ratio defined as ratio of the short axis length to the long axis), and the azimuth of the long axis θ . Field investigation shows that the angle of long axis azimuth is in poor statistical correlation, so it can be regarded as obeying uniform distribution over $0 \sim 360^\circ$.

As shown in Figure 3(a), the lengths of the long axis and the axis ratio are approximately obeying normal distribution with variance as shown in Figures 3(c) and 3(d). So the length

of the long axis, the axial ratio, and the azimuth angle of long axis whose definition is shown in Figure 3(b) are given as shown in the following formula:

$$\begin{aligned} a &= a_0 + 2\sigma_a (\text{rand}(1) - 1), \\ r &= r_0 + 2\sigma_r (\text{rand}(1) - 1), \\ \theta &= 360 \cdot \text{rand}(1), \end{aligned} \quad (3)$$

where a , σ_a , r , σ_r are the mean of the long axis, the variance of the long axis, the mean of the axial ratio, and the variance of axial ratio, respectively; θ is the azimuth of long axis. $\text{rand}(1)$ returns a random number between 0 and 1. a , σ_a , r , σ_r should be obtained using the statistics according to the stone blocks in outwash deposit medium. Here, 0.5 times the corresponding mean value is used as an empirical parameter for variance if there is no statistical information.

Then, every stone block is hypothesised to be a polygon composed of N sides as shown in Figure 2. The elliptical arc is accordingly divided into N arcs. Each point of the arc can be moved towards the centre of the ellipse. The corresponding coordinate of each point can be defined as follows:

$$\begin{aligned} x_i &= x_0 + a \cdot \cos(\theta + N\Delta\varphi), \\ y_i &= y_0 + a \cdot r \cdot \sin(\theta + N\Delta\varphi), \end{aligned} \quad (4)$$

where x_i and y_i are the coordinates of the i th node in a polygon, x_0 and y_0 are the coordinates of the centre of the ellipse, φ_0 is the azimuth of ellipse, and $\Delta\varphi$ is the angle between two vertexes of the polygon where $\Delta\varphi = 360/N$.

The steps of the random structure generation are shown in Figure 4. The generated polygons can be convex or concave. The polygons are divided into n triangles using the centre and vertexes of the polygon. Therefore, once the centre of an element is determined to be within one triangle, the element can be set as a stone block and numbered.

To ensure that the stone blocks do not overlap, the elements are set as debris by default. Once one of the elements in the current trial has been defined as a stone block, the current step will end and a new position will be tried as the centre of the generated polygon until all of the elements in the generated polygon are no longer debris. When all of the generated polygons are finished in this way, the numerical model is complete.

To avoid setting adjacent polygons as the same stone block, each stone block should be numbered a unique number. The particle contact parameters within one stone block are endowed the parameters of the stone blocks, and the contact parameter between two stone blocks is taken as that of debris. Therefore, the contact characteristics between stone blocks can be approximately simulated.

The content rate of stone block of grade i in a two-dimension model can be defined as the ratio of the stone block area within grade i to the total area of the model. It can be expressed as follows:

$$n_i = \frac{\sum A_j}{A}, \quad (5)$$

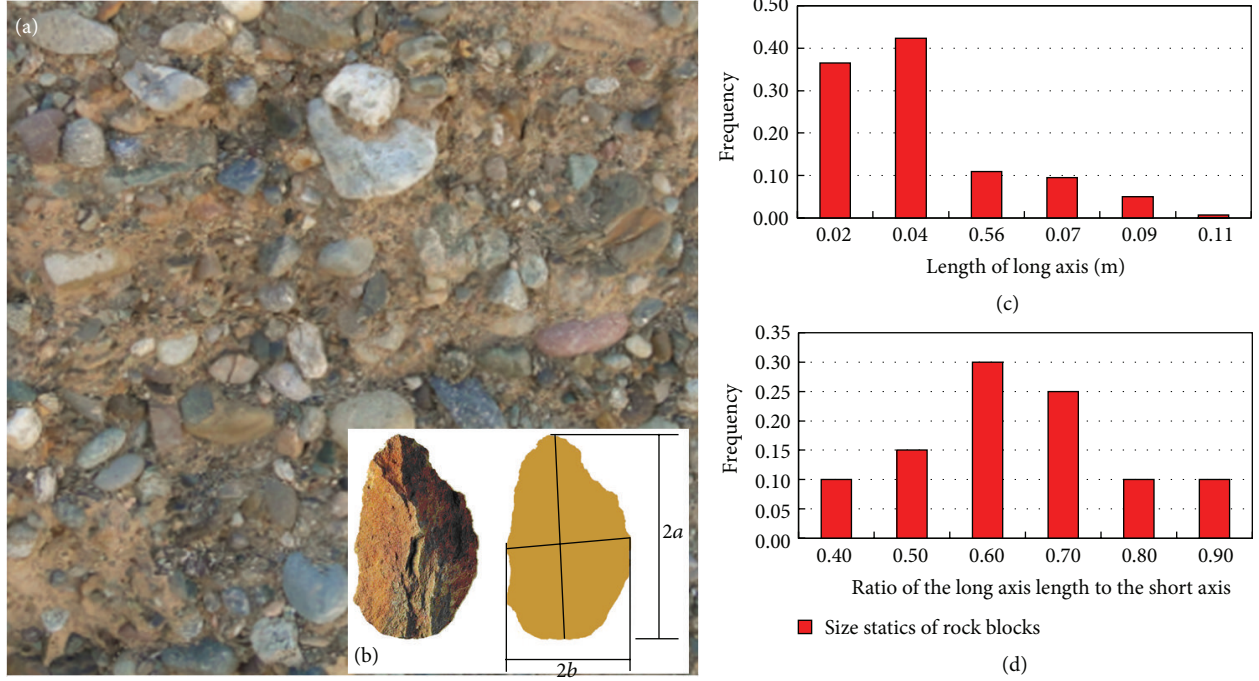


FIGURE 3: The statistical results of the size and the lengths of the long axis of stone blocks. (a) the in situ outwash deposits; (b) definition of the long axis and short axis for stone blocks; the long axis is the largest distance between vertices along the stone outline, while the short axis is the maximum segment length normal to the long axis direction; (c) the statistical results of the size of stone blocks; (d) the statistical results of the lengths of the long axis of stone blocks.

where A is the total area of the model, A_j is the area of the j th stone block and grade i , and n_i is the content rate of stone blocks of grade i .

The area of the total stone blocks is counted until the grade requirement is met.

The structure of the outwash deposit model is generated randomly according to the method of multigradations. The influences of the azimuth, concavity, and convexity of the stone blocks on the outwash deposit are also taken into consideration. The generation of stone blocks occurs from the largest to the smallest size according to the grain size accumulation curve.

3. Analysis Based on Micromechanical Model

3.1. The Principle of the Granular Discrete Element Method. The granular discrete element method is adopted to simulate the micromechanical properties of the granular materials in the form of discs or spherical particles using the explicit difference algorithm [16]. Newton's Second Law is used in order to determine the particle movement that is caused by contact or the force of a body, while the force-displacement law is used to calculate the contact force that is changing relative to movement. The two laws are then used alternately until the total system reaches equilibrium as shown in Figure 5(a). The particles can be combined into any shape or combination to simulate the stone or debris mass structures.

As shown in Figure 5(b), when there is no bonding between particles, the mechanical behaviour of the particles

in contact is determined by their own normal stiffness (k_n), tangential stiffness (k_s), and friction coefficient (μ). When two particles are in contact, the contact and tangential stiffness can be calculated as follows:

$$k_n = \frac{k_n^{(A)} k_n^{(B)}}{k_n^{(A)} + k_n^{(B)}}, \quad (6)$$

$$k_s = \frac{k_s^{(A)} k_s^{(B)}}{k_s^{(A)} + k_s^{(B)}}.$$

The normal force of contact particles is depicted as

$$F_n = K_n U_n, \quad (7)$$

where U_n is the normal contact depth.

In the calculation process, the tangential force is zero initially, so the incremental form of the equation is used as follows:

$$\Delta F_s = -k_s \Delta U_s. \quad (8)$$

If $U_n \leq 0$, a gap exists between the particles, the normal and shear force are both zero, and the slipping force between the particles should be calculated with the friction coefficient. This coefficient is calculated as $\mu = \min(\mu^{(A)}, \mu^{(B)})$, where $\mu^{(A)}$ and $\mu^{(B)}$ are the particle friction coefficients of A and B , respectively, and $F_s = \mu F_n$ is used when $F_s \geq \mu F_n$.

The stiffness contact model is adopted for the outwash deposit in this work because the point contact and the

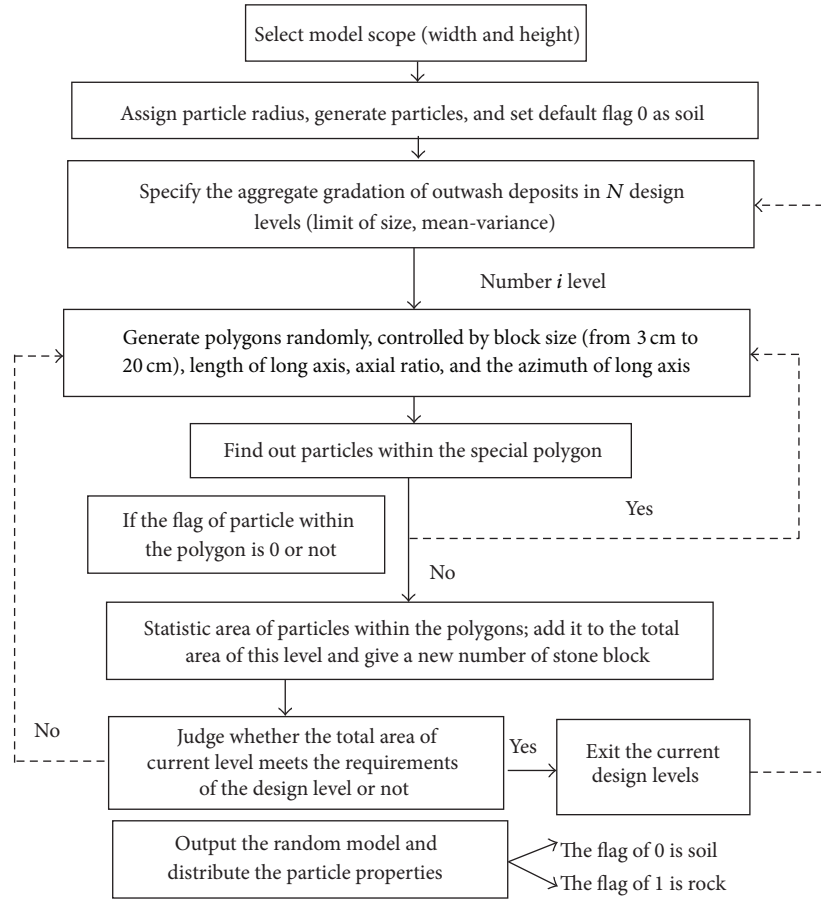


FIGURE 4: The flowchart for the randomised generation of stone blocks.

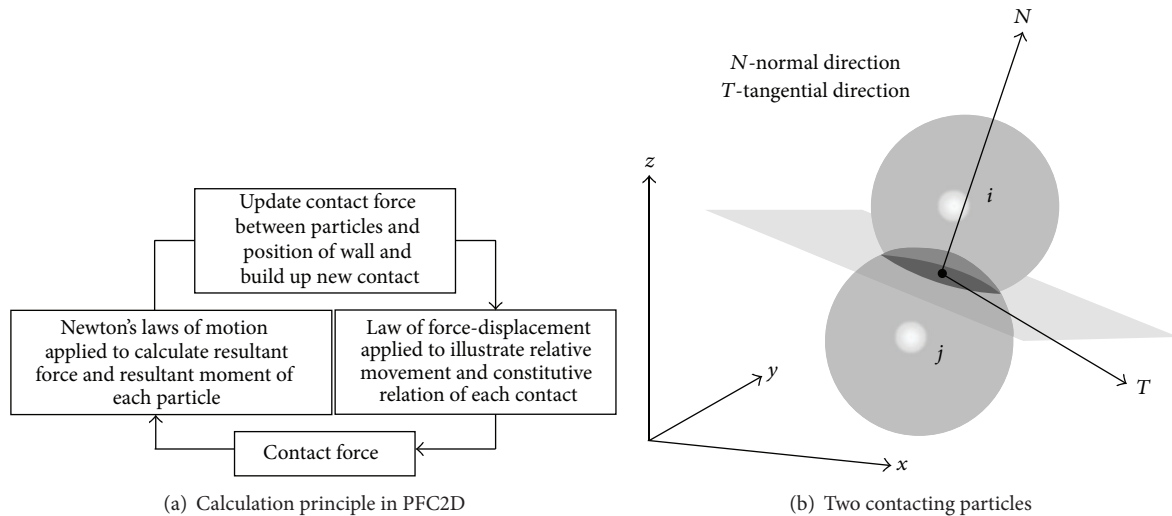


FIGURE 5: Contact force between particles and calculation principle.

linear contact in the debris-debris, debris-stone, and stone-stone are the main kind of contact types; the point contacts are especially dominant. Five microparameters need to be calibrated: the normal stiffness, the stiffness ratio of tangent stiffness and normal stiffness, the friction coefficient, the

normal bonding strength, and the tangent bonding strength according to PFC2D manual [17].

3.2. The Conversion from the Geological Model to a Mechanical Model. According to the theory of granular discrete element

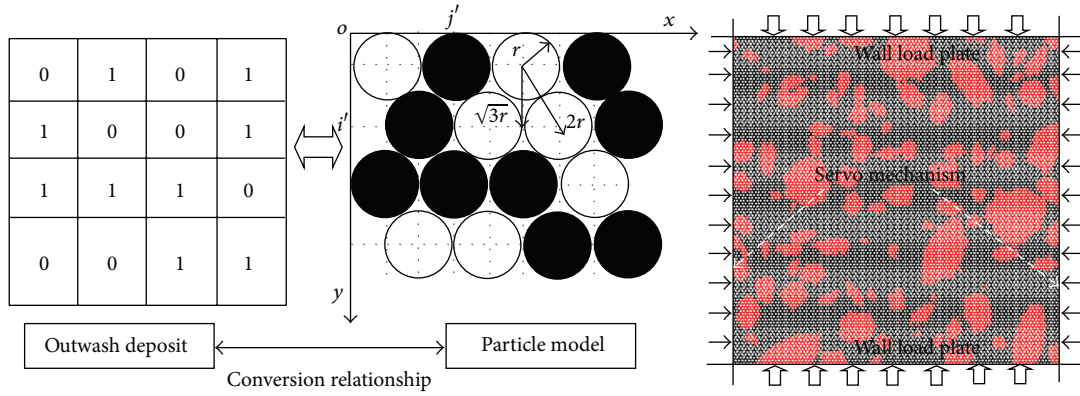


FIGURE 6: Construction of a debris-stone micromodel using a spot matrix and PFC2D.

method, 2D disk particles are used to transform the geological model to a mechanical model. If the particle is too large in the model, the shape of stone block and microstructure characteristic will be distorted. However, the larger number of particles in a model will lead to very slow calculation speed. A significant amount of time will be sacrificed, which may not be tolerable. So a proper particle size should be determined empirically.

The width and the height of the model in this work are taken to 0.50×0.50 m, the constant radius of particles is 2.5 mm, and the arrangement of the particles is shown in Figure 6. The distance between the centres of two adjacent particles in the vertical direction is $\sqrt{3}r$ (r is the radius of particle). The distance between the centres of adjacent particles in the horizontal direction is $2r$. Therefore, the coordinates of the particle centre $(x_{i',j'}, y_{i',j'})$ in the i' line and j' column can be expressed as follows:

$$x_{i',j'} = \begin{cases} (2j' - 1)r & (i' = 2k + 1), \\ 2j'r & (i' = 2k), \end{cases} \quad (k \in N), \quad (9)$$

$$y_{i',j'} = r + \sqrt{3}r(i' - 1).$$

According to the modelling steps, the particles are arranged initially as shown in Figure 6. The even rows are dislocated to ensure that the particles are tangential with adjacent rows. When a particle model filling the research zone is generated, every particle within the model will be judged to determine whether its centre is located in some random polygon. If it is in a polygon, the particle belongs to a stone block with a certain flag. If it is not in any polygon, the particle is regarded as debris. The initial structural information can be obtained from site research or by random generation.

Several particles with the same polygon flag are assembled together by the high bonding force to simulate the characteristics of the stone blocks. The structural effect of the outwash deposit is thus simulated. The separation of the debris from the stone is also convenient for the determination of the mechanical parameters.

3.3. The Relationship between the Macro- and Micromechanical Parameters. Young's modulus and Poisson's ratio

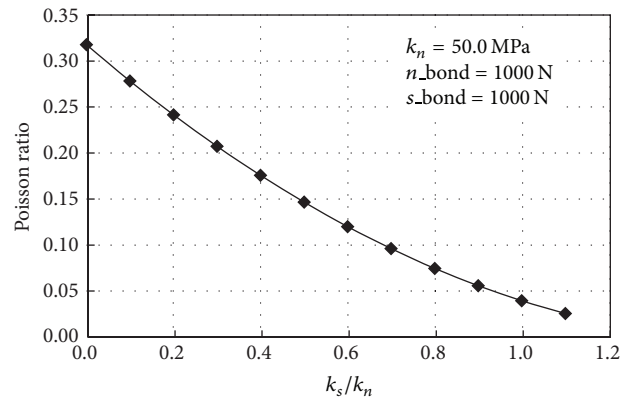


FIGURE 7: The relationship between Poisson's ratio and the stiffness ratio.

determined in the indoor geotechnical tests are used to describe the macrodeformation properties of the materials. Many studies have shown that Young's modulus is related to the microparameter k_n and the stiffness ratio k_s/k_n , while Poisson's ratio is mainly related to the stiffness ratio [18, 19]. However, these changes are all affected by the particle compositions, such as the mean radius and the ratio of the maximum radius to the minimum radius. Since a constant radius is used in this work, the problem can be neglected.

To reflect the relation between Poisson's ratio and the stiffness ratio, k_s/k_n , the normal stiffness is initially fixed at a constant 50 MPa. The relationship between Poisson's ratio and the stiffness ratio is shown in Figure 7. It can be found that Poisson's ratio in the debris shows a nonlinear, inverse relationship with the stiffness ratio of debris when the particle radius is unchanged.

It can also be concluded in Figure 7 that the tangent stiffness is usually less than the normal stiffness. Once the tangent stiffness is equal to or greater than the normal stiffness, Poisson's ratio will reach zero. This situation only exists in very loose cellular structures. However, for outwash deposits, it is obviously unreasonable when the medium is in a compacted state. Poisson's ratio declines as the stiffness ratio increases. When the tangent stiffness is equal to the

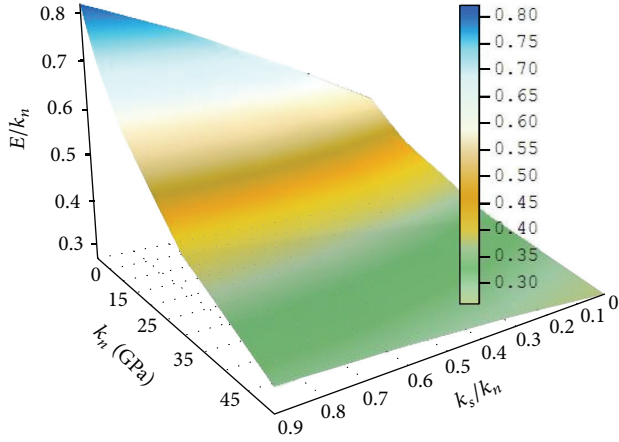


FIGURE 8: The changes in Young's modulus with the microdeformation parameters.

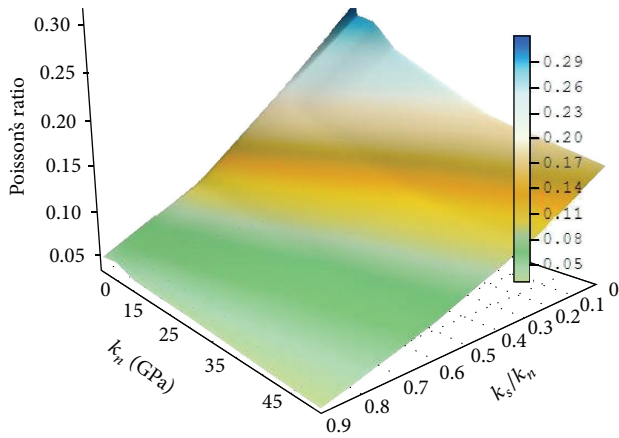


FIGURE 9: The changes in Poisson's ratio with the microdeformation parameters.

normal stiffness, Poisson's ratio is close to zero. When the stiffness ratio decreases, the lateral deformation increases. When the tangent stiffness is zero, Poisson's ratio reaches its maximum value. The relationship between Poisson's ratio and the stiffness ratio based on a series of numerical tests can be expressed using the following equation:

$$\mu_0 = 0.1278\eta^2 - 0.4061\eta + 0.3177, \quad (10)$$

where μ is Poisson's ratio and $\eta = k_s/k_n$ is the ratio of the tangent stiffness to the normal stiffness, which lies in the range 0~0.5. Once η is greater than 1.0, Poisson's ratio may be greater than 1.0 or negative, which disagrees with the properties of common solid media.

It should be noted that (10) does not consider the influence of the stiffness. If the stiffness is taken into consideration, Young's modulus and Poisson's ratio can be estimated with different normal stiffness as follows:

$$\begin{aligned} E &= (0.2259\eta - 0.0058k_n - 0.0042\eta k_n + 0.5346) k_n, \\ \mu &= -0.2760\eta - 0.0029k_n + 0.0031\eta k_n + 0.3200. \end{aligned} \quad (11)$$

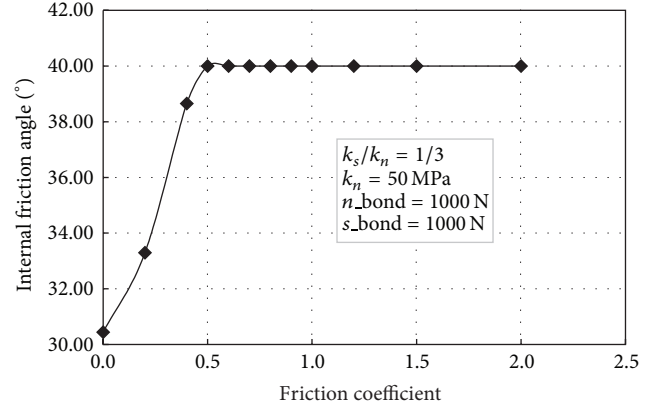


FIGURE 10: The changes in the internal friction angle at different coefficients of friction.

The changes in Young's modulus and Poisson's ratio with the changes in the microparameters are shown in Figures 8 and 9. The figures illustrate that the relationship between Young's modulus of an outwash deposit and the corresponding Poisson's ratio is not a simple linear relation but a double linear correlation in the calculation of the granular discrete element method. When the microparameters need to be determined, Young's modulus and Poisson's ratio can initially be assumed. Then, more reasonable values can be determined using (11). The steps should be repeated many times until Young's modulus and Poisson's ratio agree with the results of the macroscopic tests. In addition, the debris and stone blocks should be calibrated separately to obtain proper microparameters.

3.4. The Micromechanical Parameters of the Outwash Deposits.

The normal contact force (n_{bond}), tangent contact force (s_{bond}), and the coefficient of friction μ are the main microparameters related to macrostrength in a granular model based on PFC2D. These parameters correspond to the macrocohesion and the internal friction in the Mohr-Coulomb criterion. The coefficient of friction is the pure frictional force when the outwash deposit is completely destroyed. It determines the residual strength of the medium and can be approximately equal to the pure friction coefficient $\tan \varphi$ of the stone and debris mass.

As shown in Figure 10, when the coefficient of friction is low, the deformation of the stone and debris mass shows a linear variation. By contrast, when the friction coefficient is high, the deformation of the stone and debris mass shows a nonlinear variation. The internal friction angle of the medium first increases and then remains unchanged as the coefficient of friction increases. The cohesion shows similar behaviour, but it remains constant if the coefficient of friction is low. The cohesion will increase as the coefficient of friction increases, as shown in Figure 11.

It is not difficult to find that the microcoefficient of friction is sensitive to the macro-internal-friction angle. When the microparameters need to be determined, the bonding forces should initially be set to zero, then the friction

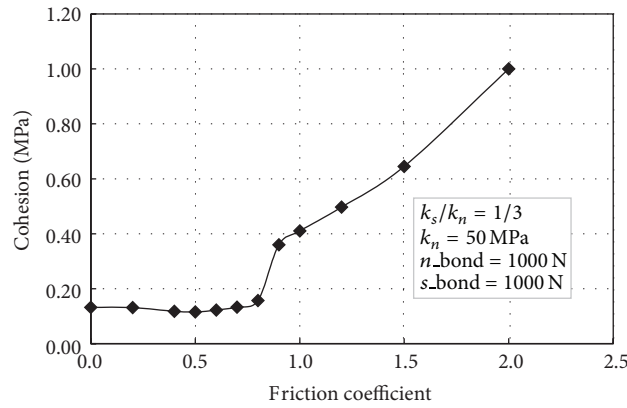


FIGURE 11: The cohesion remains constant if the coefficient of friction is low.

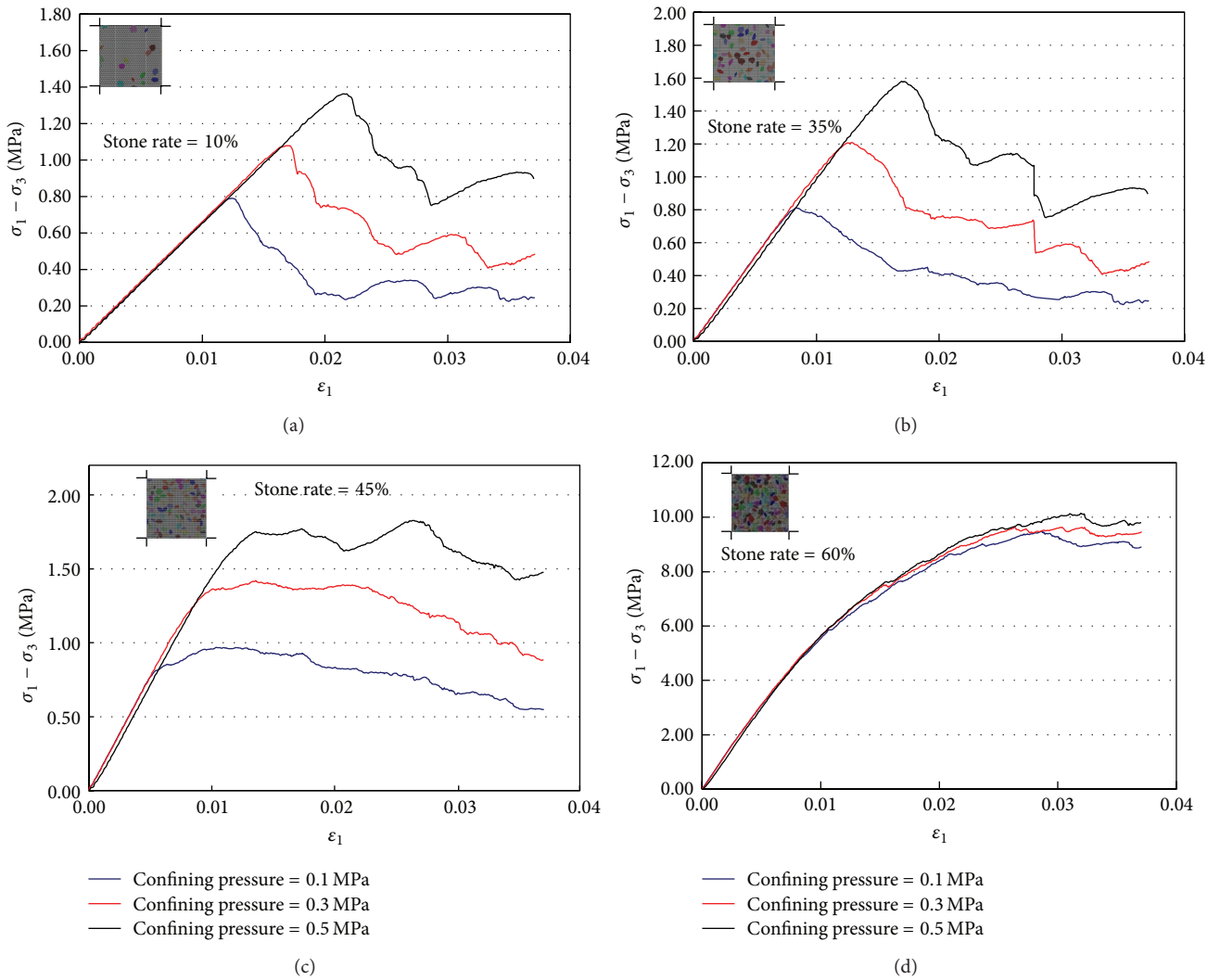


FIGURE 12: The biaxial compression curve at different confining pressures and stone block content. (a) Stone block content is 10%; (b) stone block content is 35%; (c) stone block content is 45%; and (d) stone block content is 60%.

TABLE 1: The micromechanical parameters of outwash deposits.

Material	Density (kg/m ³)	Bonding force (N)		Stiffness ratio	Normal stiffness (N/m)	Friction coefficient
		Normal	Tangential			
Debris	2200	1e3	1e3	0.0	1e8	0.25
Stone	2700	2e6	2e6	0.2	9.5e9	1.20

TABLE 2: The macromechanical parameters of outwash deposits.

Material	Young's modules (MPa)	Poisson's ratio	Internal friction angel (°)	Cohesion (MPa)
Debris	55.9	0.32	27.94	0.07
Stone	4950	0.20	56	12.0

coefficient can be determined using trial calculations until the macromechanical properties are in line with the experimental results. Finally, the bonding forces are adjusted so that the parameters are consistent with the macromechanical properties of the outwash deposit.

When the bonding force is zero, the internal friction angle will reach its minimum value. Therefore, the determination of the internal friction angle should take the effect of the stiffness ratio into consideration. If the internal friction angle is unchanged when the coefficient of friction increases, the bonding force can be adjusted to be in agreement with the peak strength of the stress. In this work, the microparameters are shown in Table 1, and the corresponding macroparameters are shown in Table 2.

4. The Analysis of the Mechanical Behaviour of the Outwash Deposits

As a case study shown in Figure 1, the stone rate of outwash based on the statistical results is about 30% to 40%, the mean length of long axis is about 4.13 cm with a variance 0.15, and the mean axis ratio is 0.64 with a variance 0.17. Then the random structure models of outwash deposits are generated according to the above information. Finally, numerical simulation and comparison are executed in order to analyse the effect of comprehensive mechanical behaviour.

4.1. The Stress-Strain Curve Based on the Biaxial Compression Test. The stress-strain curves from the numerical simulation tests of an outwash deposit under biaxial compression conditions can be divided into three stages: the elastic stage, the hardening stage, and the residual strength stage (shown in Figure 12). In the elastic stage, the deformation modulus is determined by the undamaged debris particles and stone block assemblies. As the deformation increases, fractures will first appear in the debris because of its low modulus and strength. When the outwash deposit enters into the hardening stage the debris particle bonding forces will fail gradually, and the deformation modulus will decrease slowly. However, the strength will increase continually due to the interaction force caused by mosaic effect between the debris particles and the stone blocks. When the stress reaches its peak strength, the outwash deposit will enter into the residual strength stage. The cementation ability between the debris

particles is almost completely lost. The compressive-bearing capability of the sample cannot continue to increase. The compressive-bearing capability is controlled mainly by the interparticle friction. When the strain continues to increase, the stone blocks may rotate and tumble, which leads to the complete destruction of the structure of the outwash deposit. However, there is still some compression-bearing capability, which causes the residual strength of the outwash deposit. The residual strength shows fluctuations because of the contact action between the debris and the stone blocks.

As shown in Figure 13, the damage of a model with content ratio of stone block 40%, length of long axis about 2 to 6 cm, and the axial ratio 0.5 to 0.8 is compared in the loading process. It shows that cracks occur firstly between some blocks and then develop among the boundary of stone blocks and fill with the debris particles. The crack number will increase shapely with the strain increase until all bond contacts between debris particles are destroyed.

The curves for different debris bonding forces in Figure 14 show that the cementation strength of the debris particles decides the strength of outwash deposit and has a dominant role in the mechanical properties when the other conditions are fixed. With a stronger cementation force of debris particles, there is a smaller increase in the internal friction angle and a bigger increase for the cohesion. The mechanical properties of an outwash deposit with high cementation strength are more similar to the properties of the stone blocks. Conversely, if the cementation strength of the debris particles is weak, there is a bigger increase in the internal friction angle and a smaller increase in the cohesion. The mechanical properties of the outwash deposit are much closer to the elastic-plastic debris.

4.2. The Influence of the Aggregate Size. As shown in Figure 15, the larger the size of stone blocks is, the smaller the peak strength is. This situation can be interpreted by the perimeter ratio, which is defined as the ratio of all boundaries' perimeters of stone blocks and the model area. The perimeter ratio under the same stone ratio varies greatly. The smaller aggregate size has more stone blocks, so the perimeter ratio will reach a high level and form larger contact areas. The compressive strength also increases. When the number of stone blocks increases, the contact area of the debris and stone blocks and the interaction force between the debris and the

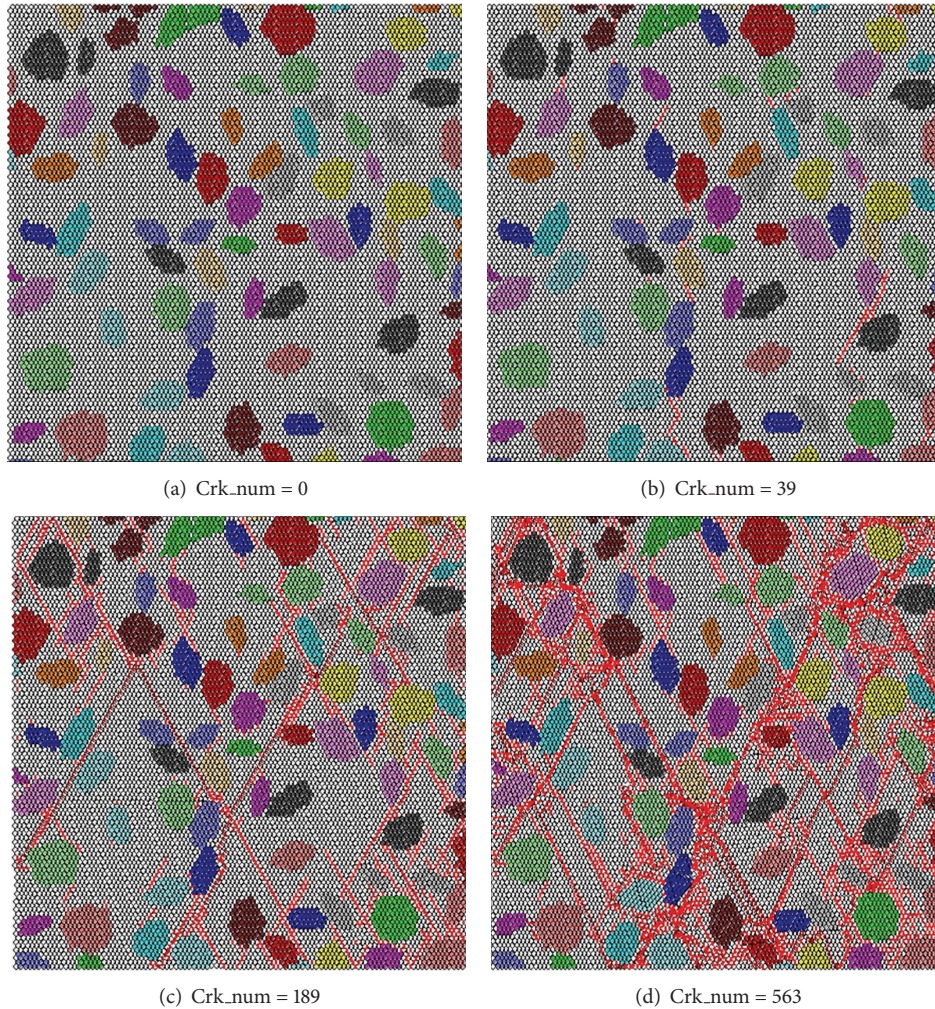


FIGURE 13: The damage of outwash deposits with different stone block content; (a) shows a model with the initial content rate of stone block 40%; (b) shows the cracks which first appear between some blocks; (c) shows fracture development among the boundary of stone blocks; and (d) shows the damaged outwash deposits.

stone blocks will increase, which just explains the reason why the macromechanical properties of the outwash deposit are improved with the number of stone blocks.

4.3. The Influence of the Stone Block Content. As shown in Figure 16, when there are few stone blocks in the outwash deposit, the debris-debris contact between particles will be the main contact type. The existence of stone blocks leads to the concentration of stress along their boundaries, which can aggravate the debris contacts to damage; the peak compressive strength keeps close to the pure debris with slight fluctuation. Meanwhile, due to the stress concentration, the outwash deposits become more brittle. The shear strength is decreased. Many experiments show that when the content of stone blocks is less than 25%, the characteristic is more close to pure debris. By contrast, when the content of stone blocks is greater than 25%, there is not only debris-stone contact in the outwash deposits but also stone-stone contact.

The compressive and shear strengths are improved. When the content of stone blocks is more than 50%, the main contact type in the outwash deposits is stone-stone. The mechanical properties are better in stone-filled materials. The compressive and shear strengths are significantly improved in the stone-filled materials.

However, when the stress-strain curves enter the residual strength stage, there is an obvious fluctuation after the peak of the curve, the amplitude of which is related to the size and content ratio of stone blocks, so in order to study the macro-shear strength, the peak value of stress-strain curves is used to calculate shear property.

4.4. The Macroparameter Analysis of the Outwash Deposits. In terms of the stress-strain curves, for any content rate of stone block, cementation strength, and block size, the major factor that influences the mechanical properties of the

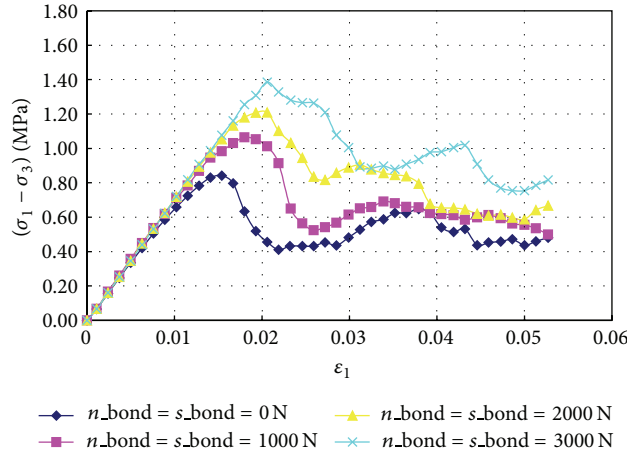


FIGURE 14: The biaxial compression curves with different debris bonding force.

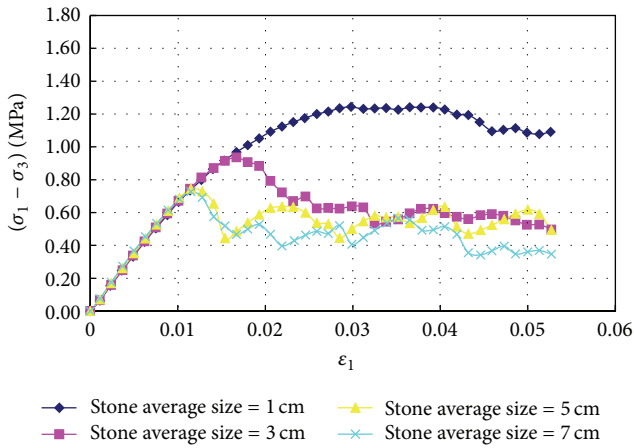


FIGURE 15: The biaxial compression curves with different average sizes of stone blocks.

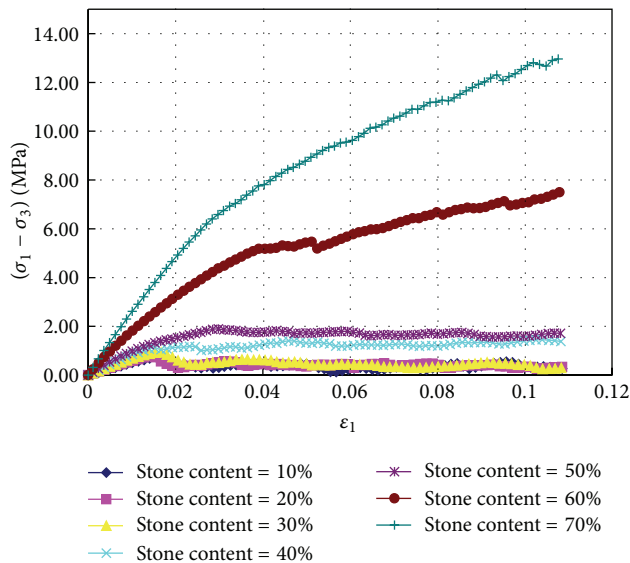


FIGURE 16: The biaxial compression curve with different stone block contents.

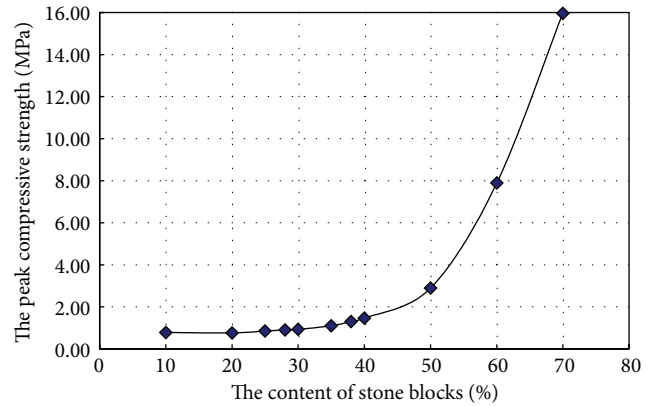


FIGURE 17: The peak compressive strength with different stone block contents.

outwash deposits can be attributed to the dominant contact type, which is defined as the ratio of some particle contact number and total contact number in numerical models. The particle contact can be divided into three kinds, respectively, the debris-debris, debris-stone, or stone-stone contact.

If ratio of stone block is high enough to make stone-stone contact becoming dominant contact type, the characteristic of outwash deposit is close to rockfill. For the nature medium, several kinds of contacts exist at that time, which will affect the comprehensive mechanical property greatly. Although the different geometries and distributions also affect the mechanical properties, the content of stone blocks is the decisive factor. For the different stone block contents, the peak strength under the confining pressure of 1.5 MPa can be calculated approximately using formula (12) as a cubic parabola curve (shown in Figure 17):

$$P_k = 141.84\alpha^3 - 90.44\alpha^2 + 16.00\alpha + 0.2894, \quad (12)$$

where α is the content ratio of stone blocks and P_k is the peak strength.

It should be noted that the compressive strength of the outwash deposit increases slowly when content ratio of stone

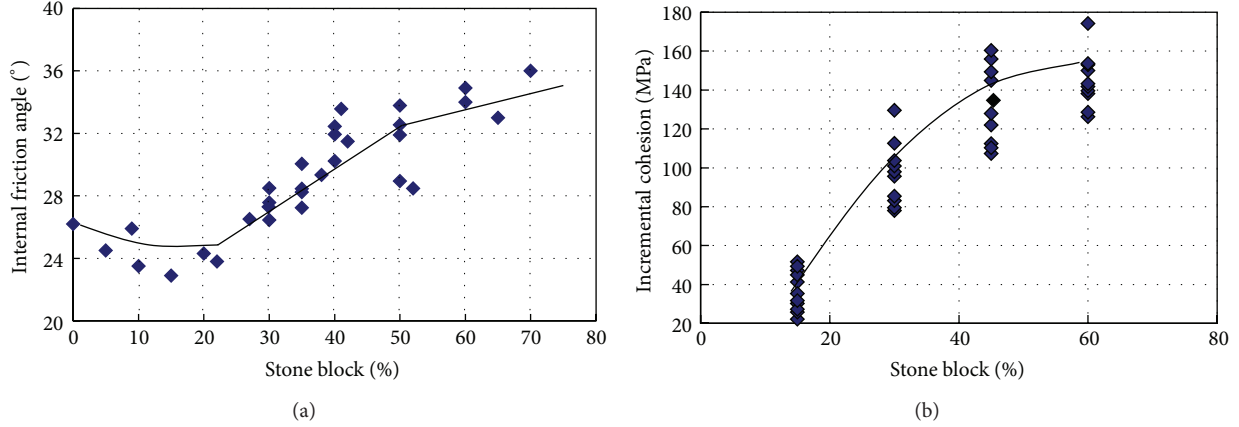


FIGURE 18: Changes of shear strength of outwash deposits with different contents and distributions of stone blocks; (a) shows changes of the internal friction of outwash deposit; (b) shows changes of the cohesion of outwash deposit.

blocks lies between 25 and 50%. Once the content of stone blocks is greater than 50%, the stone-stone contact becomes the dominant factor, which causes the compressive strength to increase sharply. The internal friction angle versus the stone block content can be described using three stages, as shown below:

$$\varphi = \begin{cases} 180.9393\alpha^2 - 49.5165\alpha + 26.5026, & \alpha < 25\%, \\ 19.4271\alpha + 22.1719, & 25\% < \alpha < 50\%, \\ 23.4286\alpha + 19.1429, & \alpha > 50\%, \end{cases} \quad (13)$$

where φ is the internal friction angle of the outwash deposit and α is the stone block content.

Furthermore, it can be observed from Figure 18(a) that the fluctuation of the internal friction angle is approximately $0\sim 8^\circ$ for the same stone blocks content, which agrees with the fluctuations in the stress-strain curves. By contrast, the cohesion of outwash deposit increases clearly with the stone block content due to the interaction force between stone blocks as shown in Figure 18(b). The amplitude of variation will increase significantly with the content of stone blocks. However, it is usually difficult to quantify the amplitude due to roughness, size, characteristic of stone block, and so on.

Therefore, for outwash deposits with extremely uneven shapes and distributions of stones, the compressive strength and shear strength are primarily controlled by the stone block content. The randomness of the stone block distributions causes large deviations in the mechanical parameters. For example, the internal friction angle may have a large fluctuation at the same stone block content. This feature is the cause of the poor results of the geotechnical experiments.

5. Discussions

Outwash deposits are a type of debris-stone mixture. The mechanical properties of these deposits are affected by the composition of the debris and stone blocks. As the debris cementation increases, the compressive strength increases. However, the internal friction angle has a negative correlation

with the cementation force. The stone block content is the decisive factor for the mechanical properties of outwash deposits. The randomness of the structural composition leads to significant fluctuations in the properties, which also creates large discrepancies in the mechanical parameters.

The major influences of the particle sizes, geometric distribution, and stone block content are to determine the contact type in the outwash deposits. When the debris-debris contact is the dominant contact type, there is little influence from the stone blocks on the mechanical properties of the outwash deposits. When the debris-stone contact is the dominant contact type, the stone block content has a positive influence on the compressive and shear strengths. When the stone-stone contact is the dominant contact type, the roles of the debris and stone blocks are reversed and the properties of the outwash deposits are much closer to a rock-filled material.

Although it is difficult to determine the mechanical parameters of an outwash deposit using indoor experiments, the properties of the medium can still be researched using indirect approaches. The mechanical parameters of the debris and stone blocks can be determined from the indoor experiments. Then, the biaxial compression numerical experiment using the granular discrete element method can be carried out to analyse the influence of the stone blocks on the properties of outwash deposits, which makes up for the limitation that the indoor experiments cannot consider the large stone blocks and offers a beneficial supplement to aid in the geological parameter determination.

6. Conclusions

According to the grain size and shape statistics from field statistics, the numerical granular discrete element model with randomised generation of stone blocks can be used with hypothesis that the length of the long axis and the axial ratio all follow normal distributions and the azimuth of the long axis follows uniform distribution in $0\sim 360^\circ$. The relationships between the macro- and micromechanical parameters are discussed and the mechanical behaviour of the outwash

deposit is affected by the cementation strength, the size of stone blocks, the stone block content, and the distribution of the stone blocks. These properties are analysed so that they can be better understood by the geologists working on the democratisation of the Engineering Project.

Conflict of Interests

The authors declare that there is no conflict of interests regarding the publication of this paper.

Acknowledgments

The work was supported by the National Natural Science Foundation of China (no. 51309089 and no. 51379065), the National Key Technology R&D Program (no. 2013BAB06B00), the National Basic Research Program of China (973 Program) (no. 2015CB057903), the Natural Science Foundation of Jiangsu Province (no. BK20130846) and the Fundamental Research Funds for the Central Universities (no. 2014B04914).

References

- [1] W. G. Holtz and H. J. Gibbs, "Triaxial shear tests on pervious gravelly soils," *Journal of the Soil Mechanics and Foundations Division*, vol. 82, no. 1, pp. 1–22, 1956.
- [2] R. J. Chandler, "The inclination of Talus, Arctic Talus Terraces, and other slopes composed of granular materials," *The Journal of Geology*, vol. 81, no. 1, pp. 1–14, 1973.
- [3] X. H. You, *Stochastic structural model of the earth-rock aggregate and its application [Ph.D. thesis]*, Beijing Jiaotong University, Beijing, China, 2001.
- [4] X. H. You and J. S. Tang, "Research on horizontal push-shear in-situ test of debris and rock-mixture," *Chinese Journal of Rock Mechanics and Engineering*, vol. 21, no. 10, pp. 1537–1540, 2002.
- [5] X. H. You, G. He, and X. Li, "Micro-handling technology of earth-rock aggregate slope," *Hydrogeology and Engineering Geology*, vol. 30, no. 1, pp. 18–21, 2003.
- [6] J. M. He, *Study of deformation and failure mechanisms of rock-debris aggregate in three gorges reservoir area [Ph.D. thesis]*, China University of Mining and Technology, Beijing, China, 2004.
- [7] X. Li, Q. L. Liao, J. M. He, and J. Chen, "Study on in-situ tests of mechanical characteristics on soil-rock aggregate," *Chinese Journal of Rock Mechanics and Engineering*, vol. 26, no. 12, pp. 2377–2384, 2007.
- [8] T. Lebourg, J. Riss, and E. Pirard, "Influence of morphological characteristics of heterogeneous moraine formations on their mechanical behaviour using image and statistical analysis," *Engineering Geology*, vol. 73, no. 1–2, pp. 37–50, 2004.
- [9] T. R. Reid and J. P. Harrison, "A semi-automated methodology for discontinuity trace detection in digital images of rock mass exposures," *International Journal of Rock Mechanics and Mining Sciences*, vol. 37, no. 7, pp. 1073–1089, 2000.
- [10] Z. Q. Yue, S. Chen, and L. G. Tham, "Finite element modeling of geomaterials using digital image processing," *Computers and Geotechnics*, vol. 30, no. 5, pp. 375–397, 2003.
- [11] Z. Q. Yue, S. Chen, H. Zheng, and G. H. Tang, "Digital image proceeding based on finite element method for geomaterials," *Chinese Journal of Rock Mechanics and Engineering*, vol. 23, no. 6, pp. 889–897, 2004.
- [12] Q. L. Liao, X. Li, W. C. Zhu, and J. S. Liu, "Structure model construction of rock and soil aggregate based on digital image technology and its numerical simulation on mechanical structure effects," *Chinese Journal of Rock Mechanics and Engineering*, vol. 29, no. 1, pp. 155–162, 2010.
- [13] W. J. Xu, R. L. Hu, Z. Q. Yue, and R. J. Tan, "Mesostructural character and numerical simulation of mechanical properties of soil-rock mixtures," *Chinese Journal of Rock Mechanics and Engineering*, vol. 26, no. 2, pp. 300–311, 2007.
- [14] W. J. Xu, Z. Q. Yue, and R. L. Hu, "A current status of digital image based quantitative analysis of internal structures of debris, rock and concretes and associated numerical simulation," *Journal of Engineering Geology*, vol. 15, no. 3, pp. 289–313, 2007.
- [15] W. J. Xu, R. L. Hu, Z. Q. Yue, R. Zhang, and G. L. Wang, "Research on relationship between rock block proportion and shear strength of soil-rock mixtures based on digital image analysis and large direct shear test," *Chinese Journal of Rock Mechanics and Engineering*, vol. 27, no. 5, pp. 996–1007, 2008.
- [16] P. A. Cundall and O. D. L. Strack, "A discrete numerical model for granular assemblies," *Geotechnique*, vol. 29, no. 1, pp. 47–65, 1979.
- [17] Itasca Consulting Group, *PFC2D (Particle Flow Code in 2 Dimensions) (Version 3.1)*, Itasca Consulting Group, Minneapolis, Minn, USA, 2004.
- [18] J. Yoon, "Application of experimental design and optimization to PFC model calibration in uniaxial compression simulation," *International Journal of Rock Mechanics and Mining Sciences*, vol. 44, no. 6, pp. 871–889, 2007.
- [19] Y. C. Wang and P. Mora, "Macroscopic elastic properties of regular lattices," *Journal of the Mechanics and Physics of Solids*, vol. 56, no. 12, pp. 3459–3474, 2008.

Research Article

Effect of Sintering Temperature on Membranes Manufactured with Clays for Textile Effluent Treatment

Mirele Costa da Silva,¹ Hélio de Lucena Lira,¹
Rosa do Carmo de Oliveira Lima,¹ and Normanda Lino de Freitas²

¹Unidade Acadêmica de Engenharia de Materiais, Universidade Federal de Campina Grande, Avenida Aprígio Veloso 882, 58429-900 Campina Grande, PB, Brazil

²Academic Unit of Development Technology, Federal University of Campina Grande, Rua Luiz Grande, S/N, 58540-000 Sumé, PB, Brazil

Correspondence should be addressed to Mirele Costa da Silva; mirelecsilva@hotmail.com

Received 5 September 2014; Accepted 25 November 2014

Academic Editor: Guocheng Lv

Copyright © 2015 Mirele Costa da Silva et al. This is an open access article distributed under the Creative Commons Attribution License, which permits unrestricted use, distribution, and reproduction in any medium, provided the original work is properly cited.

The aim of this work is to use cheap raw materials, such as kaolin and ball clay, for the manufacture of ceramic membranes for application in effluent treatment from textile industry and to evaluate the influence of sintering temperature in the structural and morphological characteristics of those membranes. The ceramic mass was characterized by X-ray diffraction and thermal analysis. The membranes were characterized by scanning electron microscopy, Hg porosimetry, and water permeability with desalinated water. The variation in the sintering temperature directly affected the structural and morphological characteristics of the membranes. The increase in sintering temperature of the membranes has raised the average pores diameter from 0.116 to 0.179 μm but decreased the porosity of the membrane, from 40.30 to 25.16% for temperatures from 900 to 1100°C, respectively. The reduction in porosity of the membrane affected the water permeated flux and decrease from 35.82 Kg/h·m² (at 1000°C) to 15.68 Kg/h·m² (at 1100°C). All the membranes have been applied with success in the effluent treatment from textile industry, resulting in the decrease in turbidity and discoloration, reaching approximately 100% of rejection of solid particles.

1. Introduction

Despite all the advantages that the processes involving ceramic membranes exhibit the search for making these articles with the minimum possible cost is still under consideration. The clays are natural materials that have grown in importance and have interested the scientists in this area. These materials are abundant in nature and require low temperatures during sintering process, when compared, for example, with metal oxides.

The first researches on the preparation of ceramic membranes used $\alpha\text{-Al}_2\text{O}_3$ as a precursor and then $\gamma\text{-Al}_2\text{O}_3$, zirconia, silica, and titania, valuable materials, when compared to those used in recent work where some researchers began working with natural raw materials and residues, such as apatite, ash powder, and kaolin, to reduce the cost of the membrane [1].

Among some recent works reported in the literature that refer to the use of natural raw materials for the manufacture of membranes, can be cited, for example, the study done by Fakhfakh et al. [2] who dedicated their work to the study of ceramic membranes prepared from mineral oxides for use on tubular support of clay.

Jana et al. [1] prepared ceramic membranes for microfiltration using clay. They prepared two different membranes; the first was done with pure clay and the second with clay and small amounts of sodium carbonate, boric acid, and sodium metasilicate. In its results the authors showed membranes with potential for use in the treatment of effluents containing heavy metals. Recently Zuhairun et al. [3] used clay for the preparation of membranes to be used in gas permeation processes, and the results showed that the gas permeation rate increased with increasing clay content in the mass composition used to prepare the membranes. Khemakhem

and Amar [4] developed a membrane for microfiltration with clay from Tunisia and the rejection rates results were superior to 99% of salt. From the various applications for which the use of membrane technology is intended, the treatment of effluents is distinguished by excellent results presented. A large amount of these effluents is from industries that make the disposal of these products without a proper pretreatment.

Textile industry, which generally uses large volumes of water and hence long sequence of wet processing stages, consumes many resource inputs and produces quantities of wastewater. The main sources of wastewater are rinsing waters from fiber preparation and continuous dyeing, alkaline waste from preparation, and batch dyeing waste containing large amounts of salts, acid, or alkali chemicals [5]. In this way, the interest in applied membrane for reuse of waste water from textile processes is increasing thanks to technological innovations which make them reliable and viable compared to other systems [6]. Membrane technology is today the dominant technique in the treatment of several types of wastewater: wastewater from some industries, such as electronic [7], petrochemical [8], treatment of radioactive waste [9], effluents containing natural organic matter [10], heavy metals [11], and aqueous samples containing pesticides and herbicides [12] industries.

According to this context, the aim of this work is to obtain microfiltration membranes from raw materials of low cost and simple processing, such as kaolin and ball clay, evaluate the effect of different sintering temperatures (900, 1000, and 1100°C), in structural and morphological characteristics of these membranes, and apply these membranes to the textile industry effluent treatment.

2. Materials and Methods

The composition used for preparation of ceramic mass to obtain membranes was composed of ball clay (44% w/w) and clay (56% w/w) from the state of Paraíba (Brazil).

To obtain the ceramic mass, the kaolin and ball clay were passed in a sieve with aperture of 0.074 mm, according to ABNT standard, and homogenized in a blender manufactured by METVISA Company, for a period of 6 hours. After that, water (20% w/w) and lubricant (diesel oil, 3% w/w) were added to the mass, to acquire the proper texture for extrusion.

The ceramic mass processing was conducted in a vacuum of extruder from Verdés, 051 model, in tubular format with internal and external diameters of 7.0 and 10.0 mm, respectively. After that, the extruded parts were dried in two stages, at room temperature for a period of 7 days and at 100°C for a period of 24 hours.

The membranes were sintered on electric oven, model LF0914, from Jung Industry, with the following temperature program during the firing process: from room temperature to 400°C with heating rate of 2°C/min, from 400 to 700°C with a heating rate of 1°C/min, and from 700 to maximum temperature at a heating rate of 3°C/min, staying at this maximum temperature for period of 1 hour. Maximum temperatures were 900, 1000, and 1100°C.

The ceramic mass was characterized by thermal analysis performed in a thermal analyzer, model RB-3000-20,

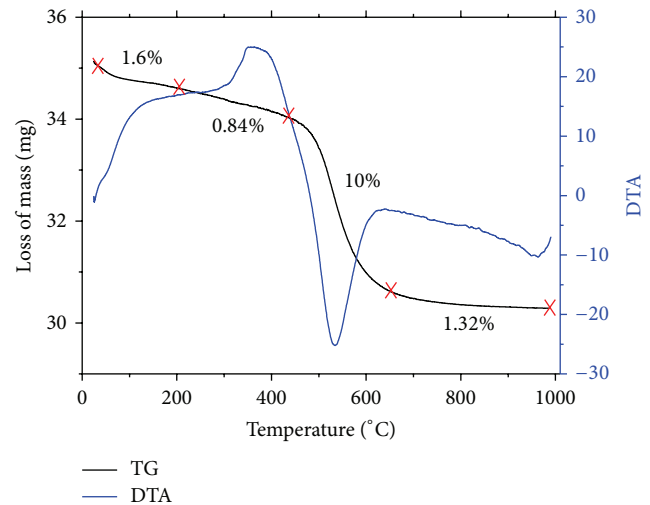


FIGURE 1: Thermogravimetric and differential thermal analysis of the mass before the sintering.

manufactured by the BP Company, with heating rate of 12.5°C/min, in nitrogen atmosphere, using a platinum crucible and range from room temperature to a maximum temperature of 1000°C. The ceramic mass was also submitted to an X-ray diffractometer XRD-6000 model Shimadzu, with α radiation from copper with scanning of 2θ from 2 to 80°.

The membranes were characterized by scanning electron microscopy using model SSX-550, from Shimadzu and mercury porosimetry through an Analyzer Autopore model IV, from Micromeritics, and permeated flow tests were conducted with distilled water, with tangential flow at 25°C.

The membranes have been applied to the treatment of effluent from the dyeing step of a textile industry from Fortaleza city, Brazil.

3. Results and Discussion

3.1. Characterization of Massiness Ceramics. Figure 1 shows the graph for the thermal analysis of the ceramic mass before the sintering stage.

According to the thermogravimetric curve a first event which begins from 25°C up to 200°C was observed showing a loss in mass of 1.6% of the adsorbed water that is eliminated from the surface of the mass. From 200 to 435°C there is a discrete mass loss equivalent to 0.84%, due to elimination of organic matter, confirmed by differential thermal curve that shows an exothermic peak at the same interval of temperature, indicating the combustion of organic matter. At 435°C starts the third and biggest event that follows up to 625°C, showing a 10% mass loss due to elimination of hydroxyls groups of the clay fraction. From 630°C until the end of the analysis there is a slight loss of 1.32% mass, caused by decomposition and loss of carbonates and hydroxides. The last endothermic peak appears in differential thermal curve at 960°C and is due to nucleation of mullite. In total the mass loss has reached a value of 13.8%.

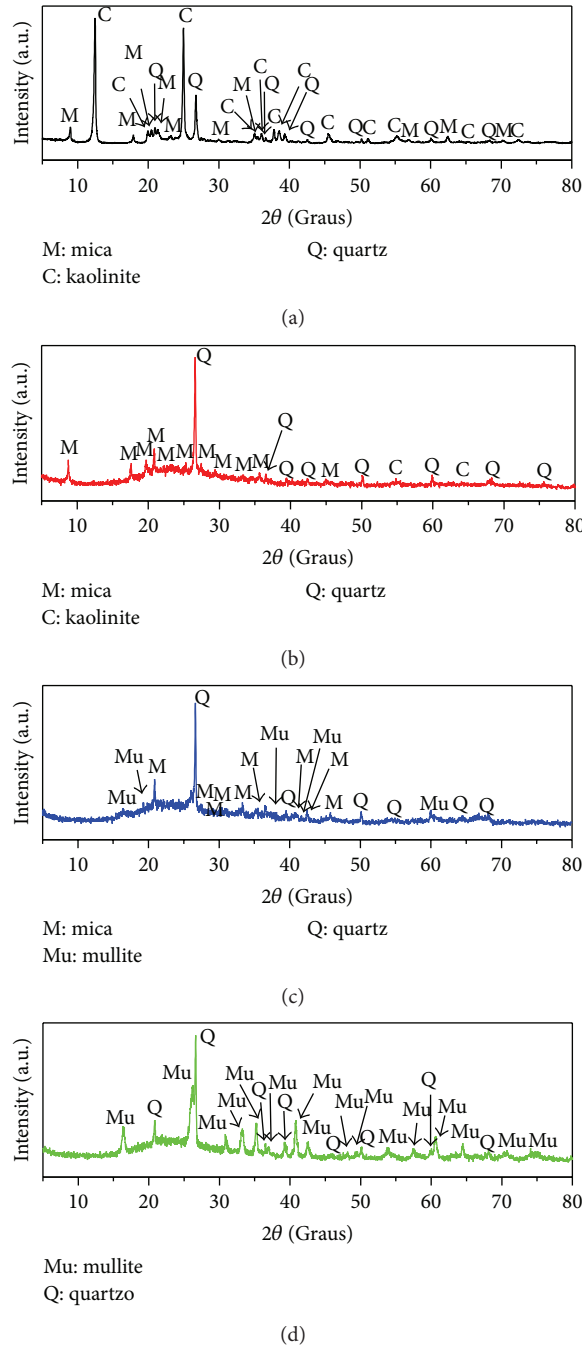


FIGURE 2: X-ray patterns of (a) ceramic mass before the sintering and sintered mass at (b) 900°C, (c) 1000°C, and (d) 1100°C.

Figure 2 shows the X-ray curves of the ceramic mass before and after the sintering stage at temperatures of 900, 1000, and 1100°C.

It is observed through Figure 2 that, for the first sintering temperature, at 900°C, the peaks presented in curves were the same crystalline phases presented to the mass before the sintering, with the presence of quartz and mica. The kaolinite was present in just a few traces due to its transformation into a metakaolinite. The increase in temperature in

sintering process causes a reaction between silica (SiO_2) and alumina (Al_2O_3) present in the raw materials forming mullite ($3\text{Al}_2\text{O}_3 \cdot 2\text{SiO}_2$) (standard sheet JCPDF 15-0776) as shown in the curve for sintered mass at 1000°C. As for the curve of sintered mass at 1100°C, there is also the presence of the quartz and mullite, differentiating from the curve of sintered mass at 1000°C, by presenting more intense and defined peaks and the absence of mica, due to probably the destruction of its structure and/or its contribution to formation of mullite.

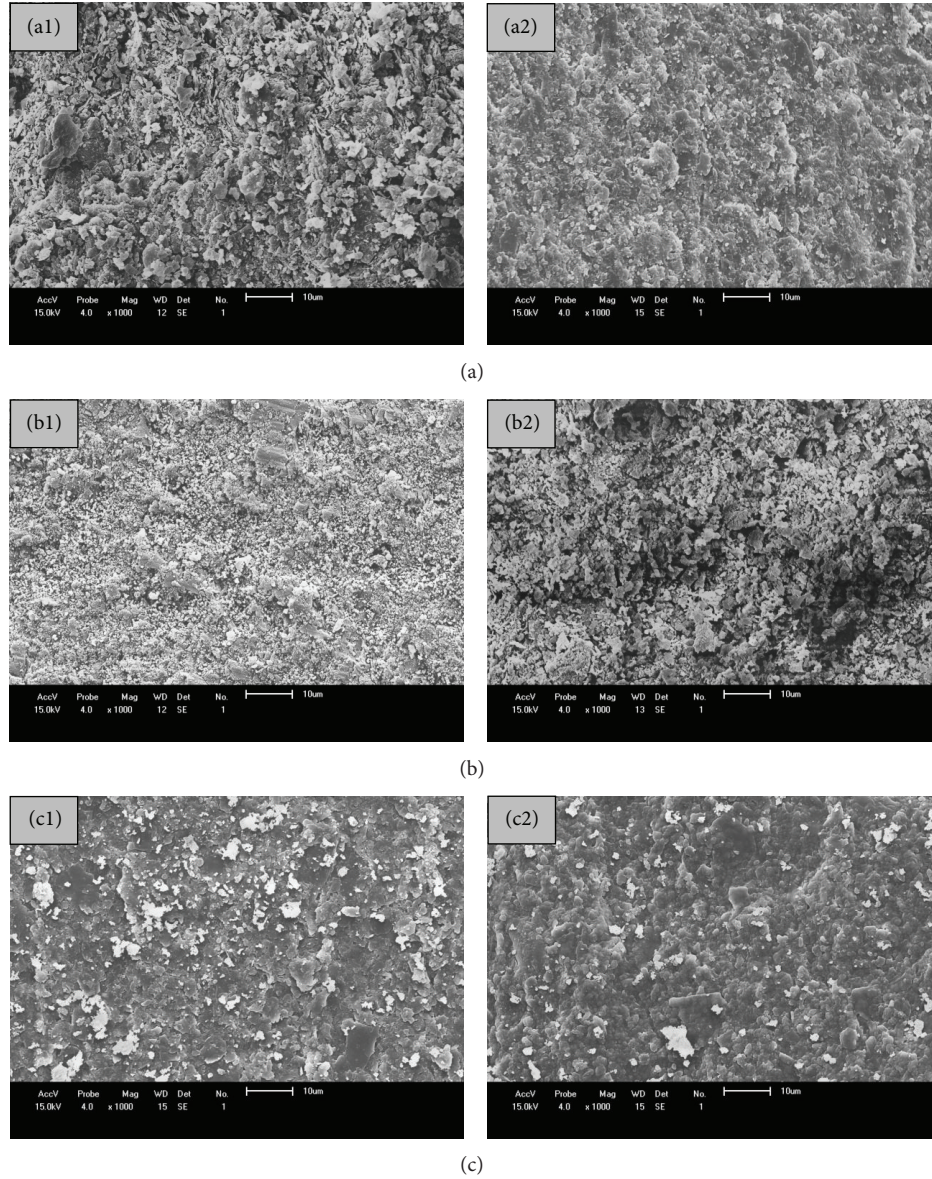


FIGURE 3: SEM images of longitudinal (1) and transversal (2) sections of the sintered ceramic membranes at 900 (a), 1000 (b), and 1100°C (c).

3.2. Characterization of Ceramic Membrane. Figure 3 shows the SEM images of the cross-sectional and longitudinal sections of the membranes sintered at 900, 1000, and 1100°C.

The image illustrated in Figure 3 allows the indication of the porous structure of the membrane, with the presence of grains with irregular plates formats, randomly distributed, with sizes larger than $2\ \mu\text{m}$.

From Figure 3(a) it is realized that the sintering temperature was not enough to promote good sintering, since it is possible to show isolated grains, also in the form of irregular plates. Despite the structure being porous, the micrographs do not allow estimating with accuracy the pore size and the degree of porosity of the membranes. It can be evaluated from Figure 3(b) that the increase in 100°C in the sintering temperature has caused the increase of grain size, but there is still the presence of some grains with distinct geometries,

different sizes, distributed along the membrane. These images when compared with the images from Figure 3(a) make possible the observation that the rise in the sintering temperature provided a better visualization of pores present in the membrane. The images allow the evaluation that the increase in sintering temperature caused a difference in the superficial aspect of the membranes. Despite the presence of grains well sintered, it is still possible to note a few isolated and scattered grains along the membrane. The grains are spread in a more homogeneous way when compared with the images of the sintered membranes at 900 and 1100°C.

Figure 4 presents the variation of pores diameter of ceramic membranes as a function of the accumulated intrusion volume of mercury.

In Figure 4 the three curves corresponding to three sintering temperatures show that the vast majority of pores

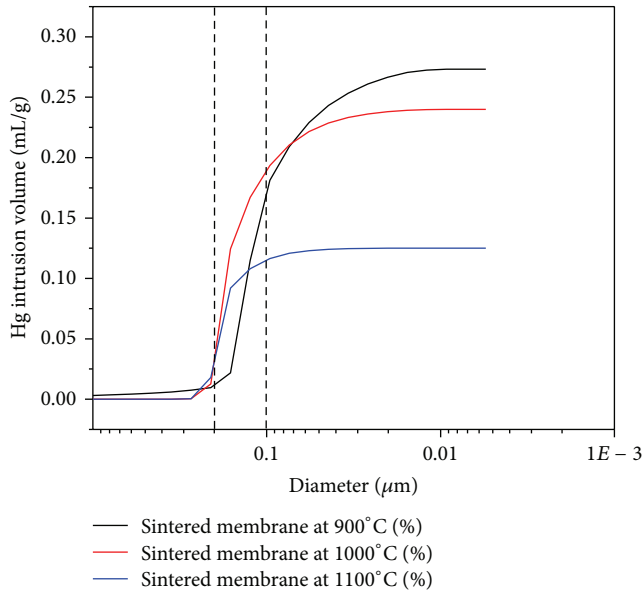


FIGURE 4: Variation of pore diameter versus mercury intrusion volume of the membranes sintered at 900, 1000, and 1100°C.

TABLE 1: Values of the average pore diameter and porosity of sintered ceramic membranes at 900, 1000, and 1100°C.

Sintering temperature (°C)	Average pore diameter (μm)	Porosity (%)
900	0.116	40.30
1000	0.164	38.75
1100	0.179	25.16

have sizes ranging from 0.1 to 0.2 μm, which characterizes membranes for microfiltration processes. Table 1 presents the values of the average pore diameter and porosity of ceramic membranes in relation to sintering temperature.

It can be observed that the increase in temperature of sintering from 900 to 1100°C led to a small increase in the average pore diameter from 0.116 to 0.179 μm. But as regards the porosity, the difference between sintered membranes from 900 and 1100°C reached 15.14%.

The increasing temperature increases the amount of liquid phase formed during the sintering process, which by capillarity effect penetrates the pores of smaller diameter leading to the reduction or even the disappearance of them. According to Nandi et al. [13] the capillary strains cause the liquid to redistribute itself between the particles and into the small pores, leading to further rearrangement and enlargement of the size of big pores. According to Germman [14] the formation of liquid phase can also lead to the growth of grain. In this way, there has been an increase in the values of the size of the average pore diameter and the decrease in the values of porosity.

Figure 5 illustrates the flow curves of distilled water permeated through the membrane as a function of time.

The membrane that obtained greater water permeated flow was sintered membrane at 1000°C, showing stabilized

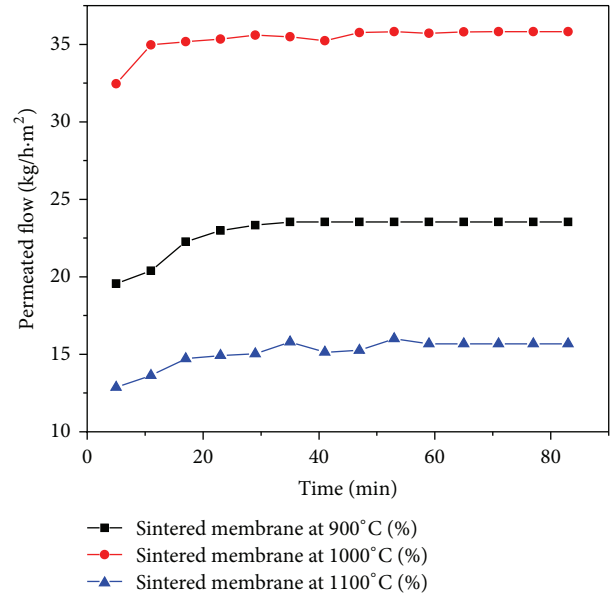


FIGURE 5: Distilled water permeated flows to the ceramic membranes sintered at 900, 1000, and 1100°C.

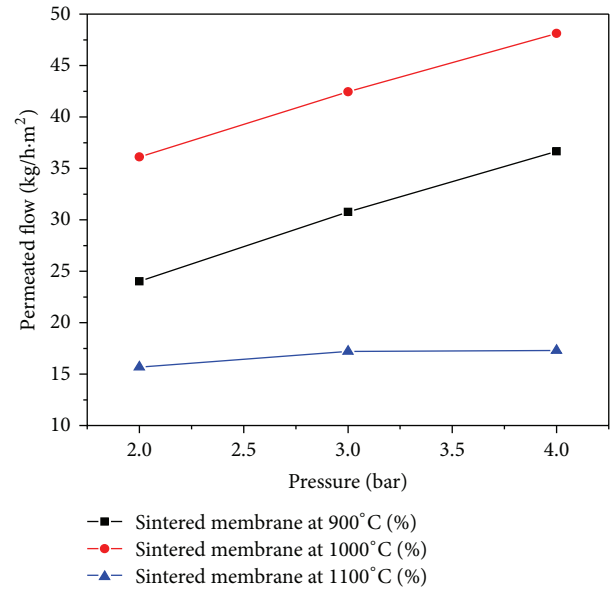


FIGURE 6: Water permeated flow versus applied pressure for the membrane sintered at 900, 1000, and 1100°C.

value of 35.82 kg/h·m² after 30 min, followed by the membrane sintered at 900°C with 23.54 kg/h·m² and 1100°C with 15.68 kg/h·m². Obviously, for same pressure and very close pore sizes, the porosity features greater influence in the permeated flow with distilled water through the membrane.

Figure 6 shows the water permeated flow versus applied pressure for the membranes sintered at 900, 1000, and 1100°C.

From Figure 6 the water permeated flow increases with the increase in transmembrane pressure. The values obtained for the permeability of ceramic membranes were 6.32, 6.00, and 0.81 Kg/h·m²·bar for sintered membranes at 900, 1000,

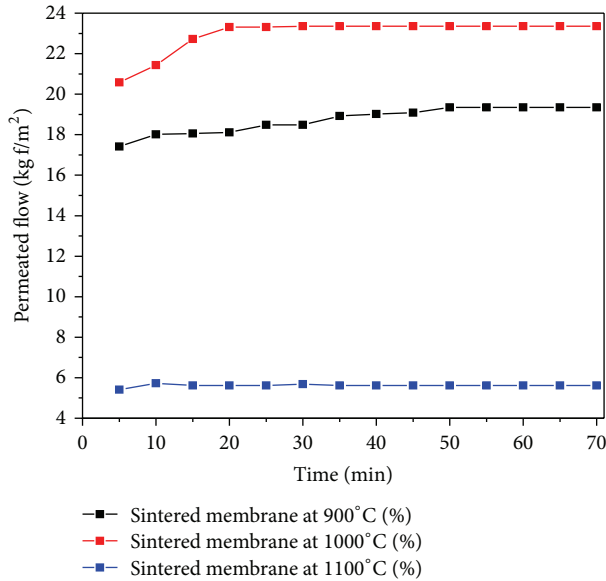


FIGURE 7: Textile effluent permeated flow of the ceramic membranes sintered at 900, 1000, and 1100°C.

TABLE 2: Comparative values between the permeated flows from distilled water and industrial effluent.

Sintered temperature (°C)	Permeated flow (kg/h·m ²)	
	Distilled water	Effluent from textile industry
900	23.54	19.35
1000	35.82	23.62
1100	15.68	5.62

and 1100°C, respectively. According to Vasconcelos [15] the permeability of porous materials is a function of the volumetric fraction of pores, as well as the average pore diameter. The greater permeability was achieved by sintered membrane at 1000°C, due to higher product value between average pore diameter and porosity reached at this temperature. The lowest permeability presented by the membrane sintered at 1100°C is due to the lower porosity caused by shrinkage when compared with membranes sintered at 900 and 1000°C.

3.3. Application of Membrane. The results of the behavior of the permeated flow of textile effluent by ceramic membranes using a pressure of 2 Bar are presented in Figure 7.

According to Figure 7 it was verified that the permeated flows stabilized in values of 19.35, 23.62, and 5.62 Kg/h·m² for the sintered membranes at 900, 1000, and 1100°C, respectively, and the largest permeated flow was achieved by the membrane sintered at 1000°C.

Table 2 presents the average values of the permeated flows of the ceramic membranes using distilled water by comparing them with the values of permeated flows using the industrial effluent.

It is observed that the industrial effluent permeated flows decreased when compared with distilled water permeated

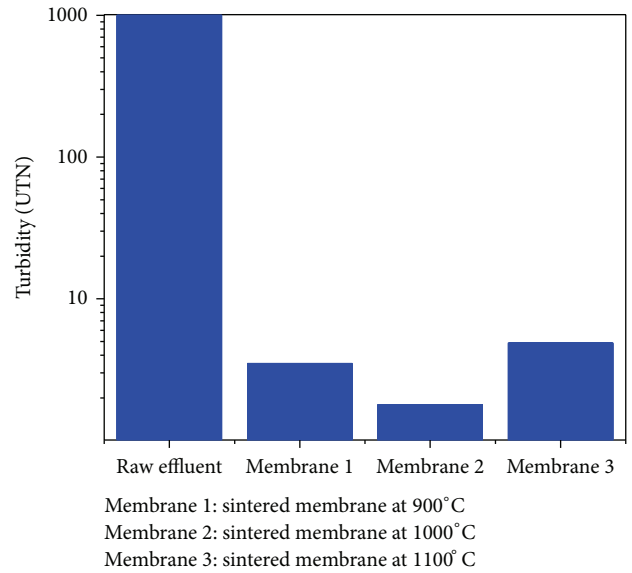


FIGURE 8: Turbidity of textile effluent before and after permeation through the sintered ceramic membranes at 900, 1000, and 1100°C.

flows, this decrease being more pronounced for sintered membrane at 1100°C, and this occurs due to clogging of the pores of the membrane with suspended particulates from the effluent. The particles size distribution of the effluent showed average diameter of 2.22 μm and 10% of the particles have sizes smaller than 0.26 μm . These values are close to those of membrane pore diameters sintered at 1100°C (0.179 μm), which can penetrate the pores, causing an obstruction.

Figure 8 presents the results of turbidity for the industrial raw effluent and after permeation through membranes sintered at 900, 1000, and 1100°C.

The results obtained of turbidity for the effluent after passing through the ceramic membranes showed that the separation was efficient, retaining solid particles present in the effluent. The values after permeation were 3.49, 1.79, and 4.85 UTN for sintered membranes at 900, 1000, and 1100°C, respectively. Fersi and Dhabhi [16] studied two treatments with membrane, the first with ultrafiltration and the second with nanofiltration, and reached retention of textile effluent color with approximately 95%. This confirms the potential of the membranes obtained through this research, which significantly reduced the turbidity.

Figure 9 presents the images of textile effluent before and after permeation by ceramic membranes.

Through visual analysis of Figure 9 the difference found for the industrial effluent before and after permeation through membranes is clear. It is possible to observe the high turbidity of raw effluent and the removal of solid particles of permeated.

4. Conclusions

The preparation of ceramic membranes with kaolin and ball clay is a viable alternative, with excellent results for the treatment of effluent from textile industry. The sintered

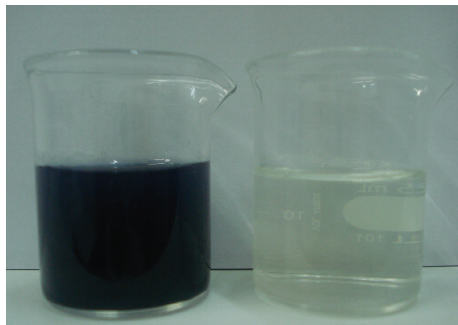


FIGURE 9: Images of the textile effluent before and after permeation through ceramic membranes.

ceramic membranes at three temperatures, 900, 1000, and 1100°C, presented in the pore diameter for use in microfiltration processes, showing efficiency in treating effluent from textile industry, reaching solid rejection rate close to 100%. The increase in sintering temperature of the membranes has raised the average pores diameter from 0.116, 0.164 to 0.179 μm but decreased the porosity of the membrane, from 40.30 to 25.16% for temperatures from 900 to 1100°C, respectively. The reduction in porosity of the membrane with the increase in sintering temperature affected the water permeated flux and decrease from 35.82 $\text{Kg/h}\cdot\text{m}^2$ (at 1000°C) to 15.68 $\text{Kg/h}\cdot\text{m}^2$ (at 1100°C). All the membranes have been applied with success in the effluent treatment from textile industry, resulting in the decrease in turbidity and discoloration, reaching approximately 100% of rejection of solid particles.

Conflict of Interests

The authors declare that there is no conflict of interests regarding the publication of this paper.

References

- [1] S. Jana, M. K. Purkait, and K. Mohanty, "Preparation and characterization of low-cost ceramic microfiltration membranes for the removal of chromate from aqueous solutions," *Applied Clay Science*, vol. 47, no. 3-4, pp. 317-324, 2010.
- [2] S. Fakhfakh, S. Baklouti, and J. Bouaziz, "Preparation, characterization and application in BSA solution of silica ceramic membranes," *Desalination*, vol. 262, no. 1-3, pp. 188-198, 2010.
- [3] A. K. Zuhairun, A. F. Ismail, T. Matsuura, M. S. Abdullah, and A. Mustafa, "Asymmetric mixed matrix membrane incorporating organically modified clay particle for gas separation," *Chemical Engineering Journal*, vol. 241, pp. 495-503, 2014.
- [4] S. Khemakhem and R. B. Amar, "Grafting of fluoroalkylsilanes on microfiltration Tunisian clay membrane," *Ceramics International*, vol. 37, no. 8, pp. 3323-3328, 2011.
- [5] P. Bhattacharya, S. Dutta, S. Ghosh, S. Vedajnananda, and S. Bandyopadhyay, "Crossflow microfiltration using ceramic membrane for treatment of sulphur black effluent from garment processing industry," *Desalination*, vol. 261, no. 1-2, pp. 67-72, 2010.
- [6] P. Schoeberl, M. Brik, R. Braun, and W. Fuchs, "Treatment and recycling of textile wastewater—case study and development of a recycling concept," *Desalination*, vol. 171, no. 2, pp. 173-183, 2005.
- [7] A. Majouli, S. Tahiri, S. A. Younsi, H. Loukili, and A. Albizane, "Elaboration of new tubular ceramic membrane from local Moroccan Perlite for microfiltration process. Application to treatment of industrial wastewaters," *Ceramics International*, vol. 38, no. 5, pp. 4295-4303, 2012.
- [8] S. S. Madaeni, H. Ahmadi Monfared, V. Vatanpour et al., "Coke removal from petrochemical oily wastewater using $\gamma\text{-Al}_2\text{O}_3$ based ceramic microfiltration membrane," *Desalination*, vol. 293, pp. 87-93, 2012.
- [9] A. K. Pabby, "Membrane techniques for treatment in nuclear waste processing: global experience," *Membrane Technology*, vol. 2008, no. 11, pp. 9-13, 2008.
- [10] L. M. Corneal, S. J. Masten, S. H. R. Davies, V. V. Tarabara, S. Byun, and M. J. Baumann, "AFM, SEM and EDS characterization of manganese oxide coated ceramic water filtration membranes," *Journal of Membrane Science*, vol. 360, no. 1-2, pp. 292-302, 2010.
- [11] J. Llanos, P. M. Williams, S. Cheng et al., "Characterization of a ceramic ultrafiltration membrane in different operational states after its use in a heavy-metal ion removal process," *Water Research*, vol. 44, no. 11, pp. 3522-3530, 2010.
- [12] F. J. Benitez, J. L. Acero, F. J. Real, and C. Garcia, "Removal of phenyl-urea herbicides in ultrapure water by ultrafiltration and nanofiltration processes," *Water Research*, vol. 43, no. 2, pp. 267-276, 2009.
- [13] B. K. Nandi, R. Uppaluri, and M. K. Purkait, "Preparation and characterization of low cost ceramic membranes for microfiltration applications," *Applied Clay Science*, vol. 42, no. 1-2, pp. 102-110, 2008.
- [14] R. M. Germman, *Sintering Theory and Practice*, John Wiley & Sons, New York, NY, USA, 1996.
- [15] W. L. Vasconcelos, "Descrição da Permeabilidade em Cerâmicas Porosas," *Cerâmica*, vol. 43, pp. 119-122, 1997.
- [16] C. Fersi and M. Dhahbi, "Treatment of textile plant effluent by ultrafiltration and/or nanofiltration for water reuse," *Desalination*, vol. 222, no. 1-3, pp. 263-271, 2008.

Research Article

Tunable Upconversion Luminescence and Energy Transfer Process in $\text{BaLa}_2\text{ZnO}_5:\text{Er}^{3+}/\text{Yb}^{3+}$ Phosphors

Lefu Mei, Jing Xie, Libing Liao, Ming Guan, and Haikun Liu

Beijing Key Laboratory of Materials Utilization of Nonmetallic Minerals and Solid Wastes, National Laboratory of Mineral Materials, School of Materials Science and Technology, China University of Geosciences, Beijing 100083, China

Correspondence should be addressed to Lefu Mei; mlf@cugb.edu.cn and Libing Liao; clayl@cugb.edu.cn

Received 17 August 2014; Accepted 29 August 2014

Academic Editor: Zhaohui Li

Copyright © 2015 Lefu Mei et al. This is an open access article distributed under the Creative Commons Attribution License, which permits unrestricted use, distribution, and reproduction in any medium, provided the original work is properly cited.

$\text{BaLa}_2\text{ZnO}_5:\text{Er}^{3+}/\text{Yb}^{3+}$ has been synthesized via a high temperature solid-state method, and the tunable upconversion luminescence and energy transfer process between Yb^{3+} and Er^{3+} in this system have been demonstrated. Upon 980 nm laser excitation, the intense green and red emission around 527, 553, and 664 nm were observed for $\text{BaLa}_2\text{ZnO}_5:\text{Er}^{3+}/\text{Yb}^{3+}$, which can be assigned to the characteristic energy level transitions of $^2\text{H}_{11/2} \rightarrow ^4\text{I}_{15/2}$, $^4\text{S}_{3/2} \rightarrow ^4\text{I}_{15/2}$, and $^4\text{F}_{9/2} \rightarrow ^4\text{I}_{15/2}$ of Er^{3+} , respectively. The critical Er^{3+} quenching concentration (QC) was determined to be about 5 mol%, and the power studies indicated that mixture of 2- and 3-photon process was responsible for the green and red upconversion luminescence.

1. Introduction

It is believed that the appearance of photon upconversion (UC) luminescence phenomenon has attracted numerous attentions focused on the UC phenomena and UC luminescent materials because of their potential applications in medical labels, multicolor displays [1–4]. The upconversion (UC) luminescence process is achieved through the sequential absorption of two or more excitation photons, which is accorded with the anti-Stokes emission phenomenon. Consequently, UC processes can be induced by low power, continuous wave lasers, obviating the need for high-cost, high-intensity pulsed lasers that are required for simultaneous multiphoton absorption experiments such as simultaneous two-photon absorption and second harmonic generation [5, 6]. Up to now, efficient photon UC process has been observed to occur primarily in the rare-earth elements, namely, those of the Ln series. Lanthanide ions are very suitable to be used in UC process as they have the rich energy level structure that allows for efficient spectral conversion. Among all the lanthanides, Er^{3+} ion has abundant energy level structures, and always acting as the luminescent center can emit intense green and red light. In contrast, Yb^{3+} ion has a strong and broad near-infrared absorption cross section around 980 nm

with relatively simple electronic structure of two energy level manifolds: $^2\text{F}_{7/2}$ ground state and $^2\text{F}_{5/2}$ excited state around $10,000\text{ cm}^{-1}$ in NIR region [7]. Additionally, the similar value of energy level of excited $^2\text{F}_{5/2}$ state of Yb^{3+} is close to the $^4\text{I}_{11/2}$ levels of Er^{3+} ions. Accordingly, cooperative UC process has also been reported for $\text{Tm}^{3+}/\text{Yb}^{3+}$, $\text{Ho}^{3+}/\text{Yb}^{3+}$, and $\text{Tm}^{3+}/\text{Ho}^{3+}/\text{Yb}^{3+}$ couples in many host materials [8–11].

The ternary oxides XY_2ZO_5 ($X = \text{Ba}$, $Y = \text{rare-earth}$, and $Z = \text{Cu}$, Zn) are receiving much attention because of their very interesting structural, excellent physical, and chemical stability and special magnetic, optical, and superconducting properties. As a member of these compounds, BaY_2ZnO_5 and $\text{BaGd}_2\text{ZnO}_5$ have been proved to be efficient UC hosts [12–15]. However, the UC properties of $\text{BaLa}_2\text{ZnO}_5$ based phosphor have not been investigated. Based on the effective ionic radii and charge balance of cations with different coordination number (CN), the rare-earth $\text{Er}^{3+}/\text{Yb}^{3+}$ ions are expected to occupy the La^{3+} sites randomly in the $\text{BaLa}_2\text{ZnO}_5$ host. Therefore, $\text{BaLa}_2\text{ZnO}_5$ can be an excellent host doped with various ions, and they are promising candidates for practical applications. In this paper, $\text{Er}^{3+}/\text{Yb}^{3+}$ codoped $\text{BaLa}_2\text{ZnO}_5$ UC materials are synthesized via a solid-state reaction process, and the structure and UC luminescent

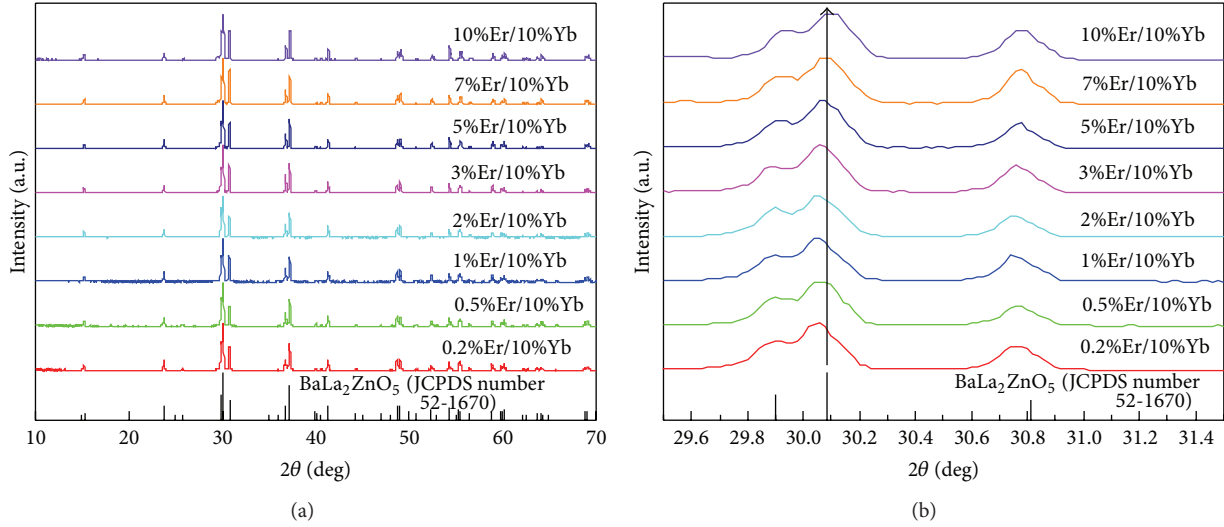


FIGURE 1: XRD patterns of the $\text{BaLa}_{1.9-x}\text{ZnO}_5:x\%\text{Er}^{3+}/0.10\text{Yb}^{3+}$ ($x = 0.2\%$, 0.5% , 1% , 2% , 3% , 4% , 5% , 7% , and 10%) and the standard PDF diffraction lines of $\text{BaLa}_2\text{ZnO}_5$ as a reference: (a) $10^\circ \leq 2\theta \leq 70^\circ$ and (b) $29.5^\circ \leq 2\theta \leq 32^\circ$.

characteristics of these phosphors have been discussed in detail.

2. Experimental

A series of polycrystalline phosphors $\text{BaLa}_2\text{ZnO}_5:x\%\text{Er}^{3+}/\text{Yb}^{3+}$ were synthesized by a solid-state reaction technology. The raw materials were Ba_2CO_3 (AR), La_2O_3 (99.99%), ZnO (99.99%), Er_2O_3 (99.99%), and Yb_2O_3 (99.99%), which were used directly without any treatment. The selected starting materials were mixed and ground thoroughly. The homogeneous mixtures were calcined at 1250°C for 3 hours, with the heating rate of $5^\circ\text{C}/\text{min}$, and then the samples were cooled to room temperature naturally. After that, the samples were washed three times by the deionized water and dried for the following measurement.

The phase and crystal structure of the samples were recorded by X-ray diffraction (XRD, D8 Advance diffractometer, Bruker Corporation, Germany) with Cu-K α radiation ($\lambda = 0.15406$ nm, 40 kV, 30 mA). The morphology of the as-prepared samples was characterized by a field emission scanning electron microscopy (FE-SEM, JSM-7001F). The UC luminescence spectra were recorded on a Hitachi F-4600 spectrophotometer (Hitachi High Technologies Corporation, Tokyo, Japan) equipped with an external power-controllable 980 nm semiconductor laser (Beijing Viasho Technology Company, China) as the excitation source. All the measurements were carried out at room temperature.

3. Results and Discussion

The crystallization and morphology of the as-prepared samples were checked by XRD and SEM measurements. Figure 1 shows the XRD patterns of the $\text{BaLa}_{1.9-x}\text{ZnO}_5:x\%\text{Er}^{3+}/0.10\text{Yb}^{3+}$ ($x = 0.2\%$, 0.5% , 1% , 2% , 3% , 4% , 5% , 7% , and 10%)

and the standard PDF diffraction lines of $\text{BaLa}_2\text{ZnO}_5$ as a reference. It can be seen that all of the diffraction peaks are matched well with the standard data of $\text{BaLa}_2\text{ZnO}_5$ (JCPDS number 52-1670) indicating the introduction of $\text{Er}^{3+}/\text{Yb}^{3+}$ ions into the $\text{BaLa}_2\text{ZnO}_5$ host lattice is completely dissolved in the $\text{BaLa}_2\text{ZnO}_5$ host lattice by substitution for the La^{3+} owing to their similar ionic radii and properties. Moreover, the diffraction peaks of the as-prepared samples shift toward the larger 2θ side owing to the small size of Yb^{3+} ion and Er^{3+} ion substituting for La^{3+} in the compound.

Figure 2 shows the SEM micrographs of the typical $\text{BaLa}_2\text{ZnO}_5:0.05\text{Er}^{3+}/0.10\text{Yb}^{3+}$ powders prepared at 1250°C with different plotting scale. SEM result shows sheet-like phosphor grains with an average diameter of about $30\ \mu\text{m}$. Compared to the as-prepared samples via high temperature solid-state technology, we can find that the current samples have smooth surface and better crystallinity in the form of two-dimensional flaky states, which indicate that they should own better luminescence properties because of the decreased particle surface defects [16].

Upon the 980 nm laser excitation, strong visible emission was observed in codoped crystals due to the result of the upconversion process. Figure 3(a) shows the comparison of UC luminescence spectra of the as-prepared $\text{BaLa}_2\text{ZnO}_5:x\%\text{Er}/\text{Yb}10\%$ ($x = 0.2\%$, 0.5% , 1% , 2% , 3% , 4% , 5% , 7% , and 10%) samples. The emission consists of two strong bands: the red one peaked at 664 nm associated with $^4\text{F}_{9/2} \rightarrow ^4\text{I}_{15/2}$ transition and the green band centered at 553 nm assigned to the mixed transition $^2\text{H}_{11/2} + ^4\text{S}_{3/2} \rightarrow ^4\text{I}_{15/2}$ of the acceptor Er^{3+} ion [17]. To date, a wide variety of Er^{3+} doped $\text{BaLa}_2\text{ZnO}_5$ have been generated that are capable of emitting a wide range of colors within the visible spectral region. The above result testified the UC process in the $\text{Er}^{3+}/\text{Yb}^{3+}$ doped $\text{BaLa}_2\text{ZnO}_5$. Additionally, as shown in Figure 3(b), it can be seen that either the green

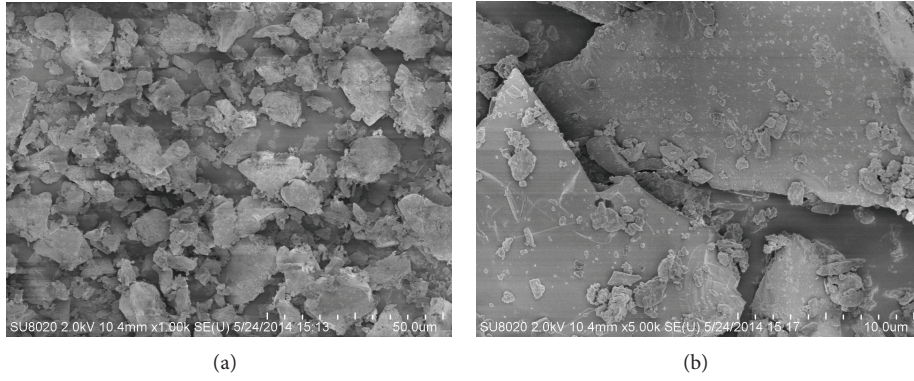


FIGURE 2: SEM images of the $\text{BaLa}_2\text{ZnO}_5:0.05\text{Er}^{3+}/0.10\text{Yb}^{3+}$ plotting scale $\times 1000$ (a) and plotting scale $\times 5000$ (b).

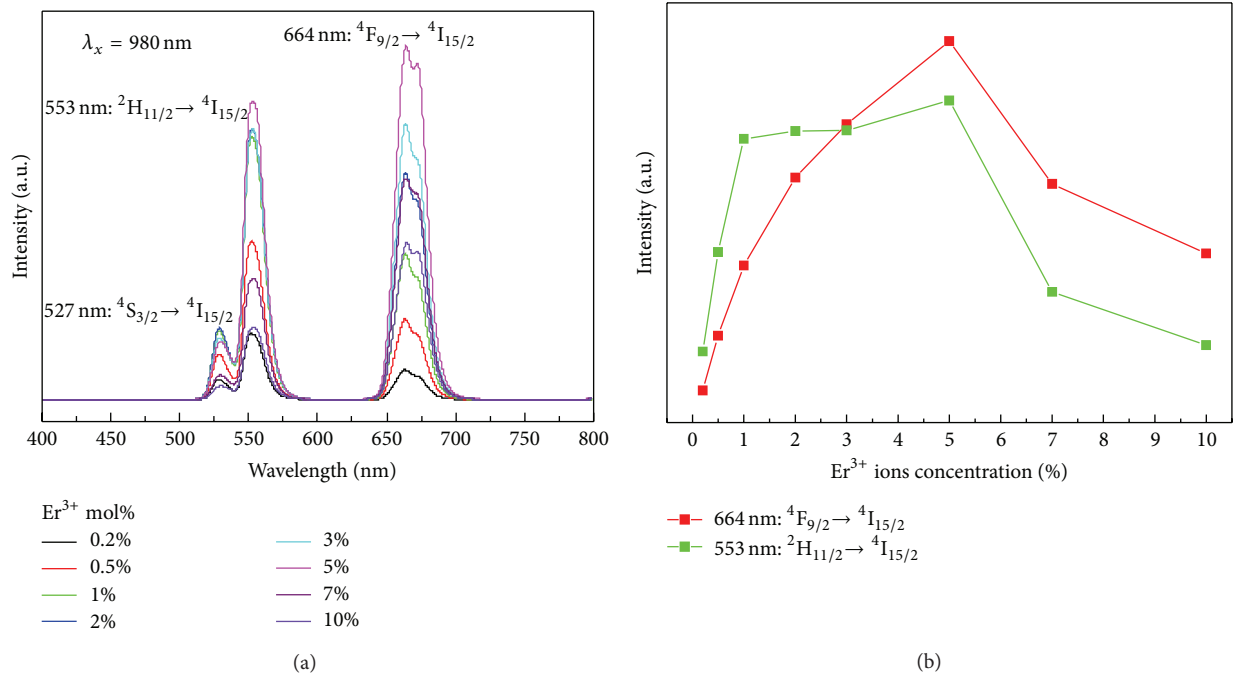


FIGURE 3: Comparison of UC luminescence spectra of the $\text{BaLa}_2\text{ZnO}_5:x\text{Er}^{3+}/0.10\text{Yb}^{3+}$ ($x = 0.2\%$, 0.5% , 1% , 2% , 3% , 4% , 5% , 7% , and 10%) under 980 nm laser excitation (a), and the variation of green and red emission intensities corresponds to different Er^{3+} doping concentration (b).

(553 nm) or the red (664 nm) emission band intensities of $\text{BaLa}_2\text{ZnO}_5:x\text{Er}^{3+}/0.10\text{Yb}^{3+}$ increase first and then decrease with the increasing concentration of Er^{3+} ion, which is attributed to the concentration quenching effect [18]. With increasing the Er^{3+} contents, the distance between Er^{3+} and Yb^{3+} (or Er^{3+}) ions decreased to promote nonradiative ET approach and decreased the luminescent intensity of Er^{3+} ions. After a critical concentration, $5.0\text{ mol}\%$ of Er^{3+} , both bands are quenched but the intensity of the green one is quenched stronger than that of the red one.

The physical mechanism involved in the upconversion processes can be elucidated by analyzing the dependence of the integrated upconverted intensity (I_{em}) as a function of

the pumping intensity (P_{pump}), which is suggested to obey the following empirical equation [19–21]:

$$I_{\text{em}} \propto (P_{\text{pump}})^n, \quad (1)$$

where n is the number of pump photons required for the transition from ground state to the upper emitting state. A plot of $\log I_{\text{em}}$ versus $\log P_{\text{pump}}$ yields a straight line with slope n . Figure 4(a) shows the UC emission spectra of $\text{BaLa}_2\text{ZnO}_5:5\%\text{Er}^{3+}/10\%\text{Yb}^{3+}$ with different pumping power, and dependence of green and red UC luminescence intensities upon pumping power is shown in Figure 4(b). With the increasing pumping power, UC emission intensities

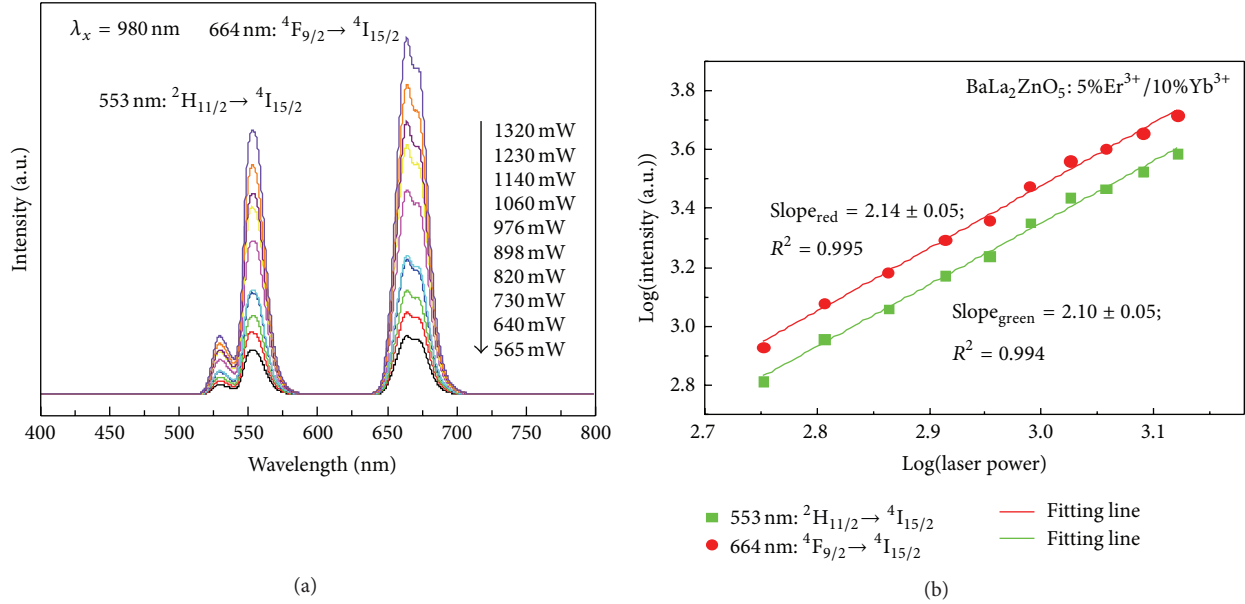


FIGURE 4: UC emission spectra of $\text{BaLa}_2\text{ZnO}_5:0.05\text{Er}^{3+}/0.10\text{Yb}^{3+}$ with different pumping power (a) and dependence of green and red UC emission intensities upon pumping power (b).

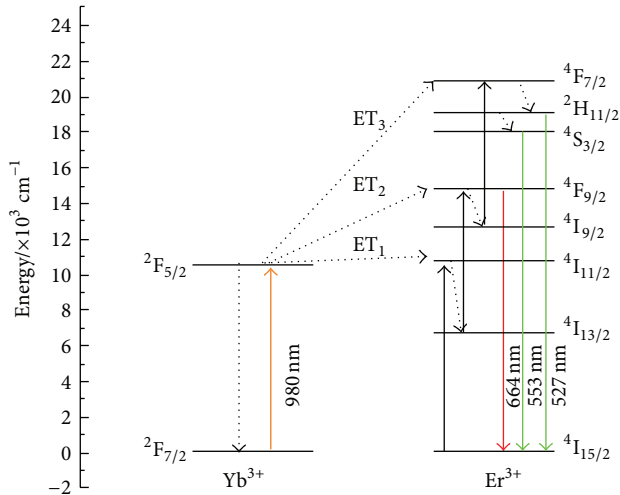


FIGURE 5: Energy level diagram of Er^{3+} and Yb^{3+} ions and the proposed UC luminescence mechanisms in $\text{BaLa}_2\text{ZnO}_5:\text{Er}^{3+}/\text{Yb}^{3+}$.

of $\text{BaLa}_2\text{ZnO}_5:5\%\text{Er}^{3+}/10\%\text{Yb}^{3+}$ increased. The calculated slopes were 2.14 for the red emission ($664\text{ nm}: 4\text{F}_{9/2} \rightarrow 4\text{I}_{15/2}$) and 2.10 for the green emission ($553\text{ nm}: 4\text{S}_{3/2} \rightarrow 4\text{I}_{15/2}$), indicating that both red and green emission are the mixture of 2- and 3-photon process which were responsible for the green and red upconversion luminescence. The corresponding energy levels scheme for the infrared excitation and upconversion emission is demonstrated in the schematic energy level diagram of Er^{3+} and Yb^{3+} ions, as shown in Figure 5. According to the above-mentioned three-photon process in $\text{BaLa}_2\text{ZnO}_5:\text{Er}^{3+}/\text{Yb}^{3+}$, the Yb^{3+} ions act as sensitizer and the Er^{3+} ions as activators. Under 980 nm

laser excitation, a Yb^{3+} ion can be excited by one of the near-infrared photons and transitioned from the ground state of $2\text{F}_{7/2}$ to the only excited state of $2\text{F}_{5/2}$ and then transfers the energy to Er^{3+} ion and promotes the transition of $4\text{I}_{15/2} \rightarrow 4\text{I}_{11/2}$ of Er^{3+} ion. Furthermore, Er^{3+} in $4\text{I}_{11/2}$ level is easy to reach a lower excited level of $4\text{I}_{13/2}$ by a nonradiative relaxation as the similar value of energy level. Then, the second step of ET₂ from Yb^{3+} can promote an excited state absorption (ESA) of Er^{3+} from $4\text{I}_{13/2}$ to the $4\text{F}_{9/2}$ level. In this case, the emission band located in the red region which associated with the transition of $4\text{F}_{9/2} \rightarrow 4\text{I}_{15/2}$. The third energy transfer step (ET₃) are followed as: Er^{3+} ions at $4\text{F}_{9/2}$ level relax nonradiatively again and back to another lower excited level of $4\text{I}_{9/2}$, and then the Er^{3+} are excited from $4\text{I}_{9/2}$ to $4\text{F}_{7/2}$ by another ESA process. In this case, the emission band located in the green region which associated with the $2\text{H}_{11/2} \rightarrow 4\text{I}_{15/2}$ and $4\text{S}_{3/2} \rightarrow 4\text{I}_{15/2}$ transitions of Er^{3+} ions, respectively. Accordingly, green emission concerted at 527 and 549 nm was detected in the UC spectra.

4. Conclusions

UC phosphors of $\text{Er}^{3+}/\text{Yb}^{3+}$ codoped $\text{BaLa}_2\text{ZnO}_5$ were synthesized by a traditional solid-state reaction method. Under 980 nm near-infrared laser excitation, both green (527 nm and 553 nm) and red (664 nm) emission bands have been found in the UC spectra, and these emission peaks are assigned to the characteristic level transition of $2\text{H}_{11/2} \rightarrow 4\text{I}_{15/2}$, $4\text{S}_{3/2} \rightarrow 4\text{I}_{15/2}$, and $4\text{F}_{9/2} \rightarrow 4\text{I}_{15/2}$ of Er^{3+} , respectively. The influence of Er^{3+} doped concentration on UC luminescence intensities has been studied, which

depicts that the optimum Er^{3+} doped concentration is 5%. The dependence of the UC luminescence on pumping power indicates that the energy transfer from Yb^{3+} to Er^{3+} in the $\text{BaLa}_2\text{ZnO}_5$ host is a three-photon process. The mechanisms for the green and red UC luminescence were discussed in detail.

Conflict of Interests

The authors declare that there is no conflict of interests regarding the publication of this paper.

Acknowledgments

This present work was supported by the National Natural Science Foundations of China (Grant nos. 51202226, 41172053, and 51172216), the Fundamental Research Funds for the Central Universities (Grant nos. 2652013043 and 2652013128), Science and Technology Innovation Fund of the China University of Geosciences (Beijing), and the Fundamental Research Funds for the Central Universities (53200959276).

References

- [1] S. Das, A. A. Reddy, S. S. Babu, and G. V. Prakash, "Tunable visible upconversion emission in $\text{Er}^{3+}/\text{Yb}^{3+}$ -codoped KCaBO_3 phosphors by introducing Ho^{3+} ions," *Materials Letters*, vol. 120, pp. 232–235, 2014.
- [2] G. Y. Chen, H. L. Qiu, P. N. Prasad, and X. Y. Chen, "Upconversion nanoparticles: design, nanochemistry, and applications in theranostics," *Chemical Reviews*, vol. 114, pp. 5161–5214, 2014.
- [3] H. K. Liu, Y. Y. Zhang, L. B. Liao, Q. F. Guo, and L. F. Mei, "Synthesis, broad-band absorption and luminescence properties of blue-emitting phosphor $\text{Sr}_3\text{La}_2(\text{PO}_4)_6\text{O}_2:\text{Eu}^{2+}$ for n-UV white-light-emitting diodes," *Ceramics International*, vol. 40, no. 8, pp. 13709–13713, 2014.
- [4] J. Zhang, Y. Wang, L. Guo, and P. Dong, "Up-conversion luminescence and near-infrared quantum cutting in $\text{Y}_6\text{O}_5\text{F}_8:\text{RE}^{3+}$ (RE = Yb, Er, and Ho) with controllable morphologies by hydrothermal synthesis," *Dalton Transactions*, vol. 42, no. 10, pp. 3542–3551, 2013.
- [5] F. Auzel, "Upconversion and anti-stokes processes with f and d ions in solids," *Chemical Reviews*, vol. 104, no. 1, pp. 139–173, 2004.
- [6] M. V. DaCosta, S. Doughan, Y. Han, and U. J. Krull, "Lanthanide upconversion nanoparticles and applications in bioassays and bioimaging: a review," *Analytica Chimica Acta*, vol. 832, pp. 1–33, 2014.
- [7] M. Guan, L. F. Mei, Z. H. Huang, C. X. Yang, Q. F. Guo, and Z. G. Xia, "Synthesis and near-infrared luminescence properties of $\text{LaOCl}:\text{Nd}^{3+}/\text{Yb}^{3+}$," *Infrared Physics & Technology*, vol. 60, pp. 98–102, 2013.
- [8] W. Zheng, H. Zhu, R. Li et al., "Visible-to-infrared quantum cutting by phonon-assisted energy transfer in $\text{YPO}_4:\text{Tm}^{3+}, \text{Yb}^{3+}$ phosphors," *Physical Chemistry Chemical Physics*, vol. 14, no. 19, pp. 6974–6980, 2012.
- [9] J. Y. Sun, B. Xue, G. C. Sun, and D. P. Cui, "Yellow upconversion luminescence in $\text{Ho}^{3+}/\text{Yb}^{3+}$ co-doped $\text{Gd}_2\text{Mo}_3\text{O}_9$ phosphor," *Journal of Rare Earths*, vol. 31, no. 8, pp. 741–744, 2013.
- [10] J. Sun, B. Xue, and H. Du, "White upconverted luminescence of $\text{Ho}^{3+}/\text{Yb}^{3+}/\text{Tm}^{3+}$ tri-doped $\text{Gd}_2\text{Mo}_3\text{O}_9$ phosphors," *Materials Science and Engineering B: Solid-State Materials for Advanced Technology*, vol. 178, no. 12, pp. 822–825, 2013.
- [11] Z. Xia, W. Zhou, H. Du, and J. Sun, "Synthesis and spectral analysis of $\text{Yb}^{3+}/\text{Tm}^{3+}/\text{Ho}^{3+}$ -doped $\text{Na}_{0.5}\text{Gd}_{0.5}\text{WO}_4$ phosphor to achieve white upconversion luminescence," *Materials Research Bulletin*, vol. 45, no. 9, pp. 1199–1202, 2010.
- [12] I. Etchart, I. Hernández, A. Huignard et al., "Efficient oxide phosphors for light upconversion; green emission from Yb^{3+} and Ho^{3+} co-doped $\text{Ln}_2\text{BaZnO}_5$ (Ln = Y, Gd)," *Journal of Materials Chemistry*, vol. 21, no. 5, pp. 1387–1394, 2011.
- [13] C. Guo, J. Yu, J.-H. Jeong, Z. Ren, and J. Bai, "Effect of Eu^{3+} contents on the structure and properties of $\text{BaLa}_2\text{ZnO}_5:\text{Eu}^{3+}$ phosphors," *Physica B: Condensed Matter*, vol. 406, no. 4, pp. 916–920, 2011.
- [14] G. Y. Dong, C. C. Hou, Z. P. Yang et al., "Color-tunable, single phased $\text{BaLa}_{2-x-y}\text{ZnO}_5:\text{xBi}^{3+}, \text{yEu}^{3+}$ phosphors with efficient energy transfer under ultraviolet excitation," *Ceramics International*, vol. 40, pp. 14787–14792, 2014.
- [15] I. Etchart, M. Berard, M. Laroche et al., "Efficient white light emission by upconversion in Yb^{3+} -, Er^{3+} - and Tm^{3+} -doped Y_2BaZnO_5 ," *Chemical Communications*, vol. 47, no. 22, pp. 6263–6265, 2011.
- [16] Z. G. Xia, J. Li, Y. Luo, and L. B. Liao, "Comparative investigation of green and red upconversion luminescence in Er^{3+} doped and $\text{Yb}^{3+}/\text{Er}^{3+}$ Codoped LaOCl ," *Journal of the American Ceramic Society*, vol. 95, no. 10, pp. 3229–3234, 2012.
- [17] T. Li, C. F. Guo, Y. R. Wu, L. li, and J. H. Jeong, "Green upconversion luminescence in $\text{Yb}^{3+}/\text{Er}^{3+}$ co-doped $\text{ALn}(\text{MoO}_4)_2$ (A=Li, Na and K; Ln=La, Gd and Y)," *Journal of Alloys and Compounds*, vol. 540, pp. 107–112, 2012.
- [18] B. P. Singh, A. K. Parchur, R. K. Singh, A. A. Ansari, P. Singh, and S. B. Rai, "Structural and up-conversion properties of Er^{3+} and Yb^{3+} co-doped $\text{Y}_2\text{Ti}_2\text{O}_7$ phosphors," *Physical Chemistry Chemical Physics*, vol. 15, no. 10, pp. 3480–3489, 2013.
- [19] Y. C. Yang, C. Mi, F. Yu et al., "Optical thermometry based on the upconversion fluorescence from $\text{Yb}^{3+}/\text{Er}^{3+}$ codoped $\text{La}_2\text{O}_2\text{S}$ phosphor," *Ceram. Inter.*, vol. 40, no. 7, pp. 9875–9880, 2014.
- [20] P. Du, Z. Xia, and L. Liao, "Tunable upconversion luminescence and energy transfer process between Yb^{3+} and Er^{3+} in the $\text{CaY}_4\text{F}_{14}$," *Journal of Luminescence*, vol. 133, pp. 226–229, 2013.
- [21] Y. F. Jiang, R. S. Shen, X. P. Li et al., "Concentration effects on the upconversion luminescence in $\text{Ho}^{3+}/\text{Yb}^{3+}$ co-doped NaGdTiO_4 phosphor," *Ceramics International*, vol. 38, no. 6, pp. 5045–5051, 2012.

Research Article

The Evaluation of Groundwater Resources Value of Beijing Based on Emergy Theory

Ling Wang^{1,2} and Qing He^{1,2}

¹School of Humanities and Economic Management, China University of Geosciences, Beijing 100083, China

²Key Laboratory of Carrying Capacity Assessment for Resource and Environment, Ministry of Land and Resources, Beijing 100083, China

Correspondence should be addressed to Ling Wang; wang006699@163.com

Received 11 August 2014; Revised 15 October 2014; Accepted 24 October 2014

Academic Editor: Hanlie Hong

Copyright © 2015 L. Wang and Q. He. This is an open access article distributed under the Creative Commons Attribution License, which permits unrestricted use, distribution, and reproduction in any medium, provided the original work is properly cited.

Accurate yet valid evaluation of values of groundwater resources is difficult. However, it is of an urgent need. Based on water resource system, the emergy synthesis of the ecological economics was used to make a systematic study on the assessment of the quantity of groundwater resources. Taking Beijing in 2012 as an example, the values of groundwater for residents life subsystem, the industrial subsystem, and the agricultural subsystem are 7.64, 6.00, and 3.25 billion Yuan, accounting for 45.24, 35.5, and 19.24% of the total value, respectively. The total value of the underground water accounts for 1.51% of the GDP in Beijing for that year. Meanwhile, Contribution Rate of Groundwater Resources (GWCR) in Beijing decreased in the following order: groundwater contribution rate for industry (GWCRI 4.52%), groundwater contribution rate for agriculture (GW CRA 3.24%), and groundwater contribution rate for residential life (GW CRL 0.71%). The conclusions will provide important basis for the government's scientific decision to improve the level of comprehensive management of water resource.

1. Introduction

As a part of the natural resources, the groundwater provides valuable water for most people to support agricultural and industrial production activities. About two-thirds of people in China use groundwater as their drinking water, and about two-thirds of cities and farmlands take groundwater as their main water supply, especially in Northern China, where the development is heavily dependent on the exploitation of groundwater [1]. The evaluation of groundwater resources is a practical problem to be solved in social development. It is important to use the groundwater reasonably and to realize the coordinated development between economic society and environment.

The evaluation of groundwater resource value is a scientific issue remaining to be solved. At present, the methods widely accepted to value the water resources are (1) *system model method*, such as the fuzzy mathematic model [2–5], CGE model [6], and shadow price model [7–12]; (2) *market analysis method*, such as the supply and demand pricing model [13] and the marginal opportunity cost model [14–17];

and (3) nonmarket method, such as the contingent valuation method [18].

The above-mentioned methods all attempt to monetize water resources and human economy activities, to use the currency as the only way to measure wealthy, but currency cannot measure everything, particularly the essence of nature and laws. Water (groundwater) is a kind of natural resource and its value cannot be measured by money totally because the currency in circulation does not pass through natural world. Currency is only a tool to measure human's role and contribution in economic activities, not the role and contribution of economy and nature. Groundwater provides the vast majority of people with valuable water resource and sustains agriculture and industry. At the same time, the pollution of water mainly arises from human's activities [19]. Therefore, research on groundwater resource value can be made from its contribution to industrial production, agricultural production, and residential life.

The new method of groundwater evaluation is the emergy theory of ecological economics. Emergy theory is reviewed as the value theory of environment and natural resources.

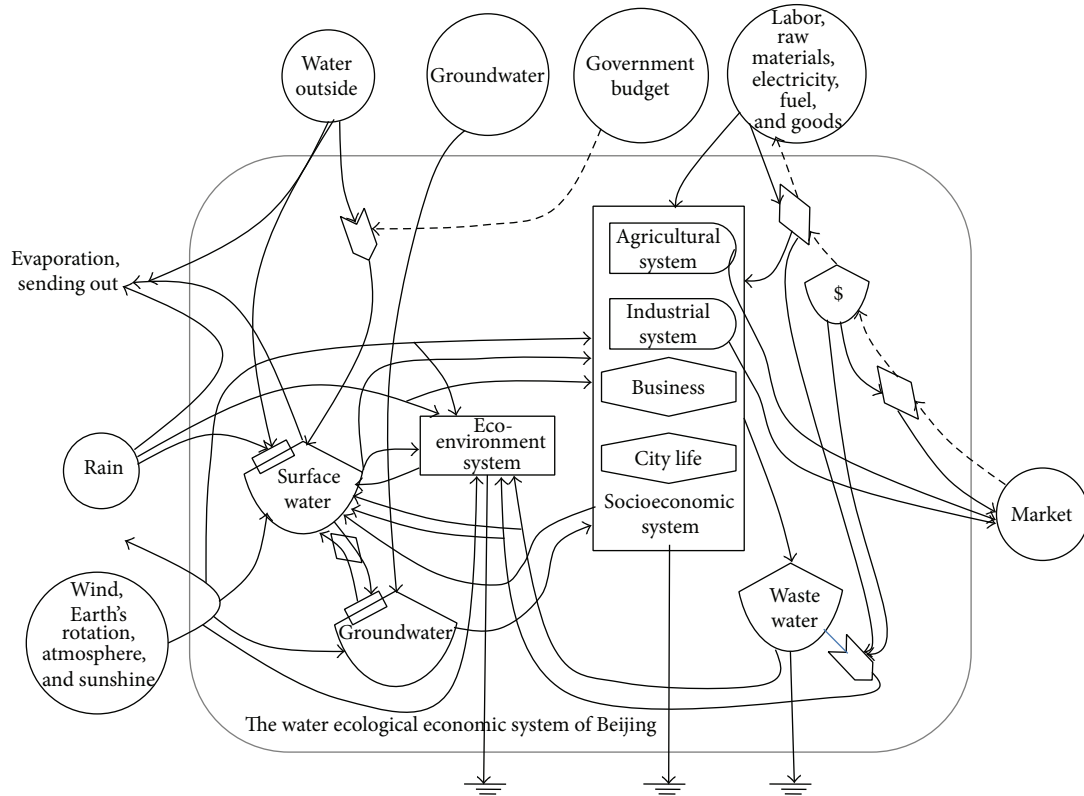


FIGURE 1: Diagram of eco-economic inputs and outputs within and outside the RWEEES (regional water ecological-economic system).

The essence of the energy theory is translating different forms of energy and materials into solar energy. In 2000, the energy theory was applied to the field of water resources by *Buenfil* for the first time. *Buenfil* simulated and optimized the allocation of water in city, agriculture, and environment of Florida, America. In 2001, *Buenfil* calculated the energy transform rates of the main rivers, aquifers, and eight water plants in Florida. Xie [20] analyzed the water environment value of *Tumen River Basin* using the energy theory. Chen [21] applied the energy method to the evaluation of natural water resources and regarded coastal county in southern China as an example for practical application. Lv [22] conducted a systematic study of energy evaluation of ecological economic value of water resources.

Based on the energy recycling and transformation in water eco-economic system and the construction principles of energy and energy network, the energy and energy network of water eco-economic system and its subsystems are constructed in this paper, including industrial subsystem, agricultural subsystem, and residential subsystem. In the light of the current situation of economy development and water exploitation in Beijing, the groundwater resource value was checked from 2008 to 2012, which will provide theoretical basis and techniques for the proper decision and evaluation of water exploitation.

2. Theory and Method

Emergy, specifically *solar emergy*, is the available solar energy used up directly and indirectly to make a service of product

[23]. Therefore we can measure the emergy of all kinds of energy based upon the solar energy. The solar emergy owned by any sources, products, or services is the amount of solar energy they used directly or indirectly for their formation, and its unit is solar emjoules (sej).

2.1. The Energy Network of Water Resource System and Its Subsystem

(1) *The Energy and Emergy Network of Water Eco-Economic System*. According to the basic structure of water resources eco-economic system and the main condition of ecological-economic flow including energy sources, material, and information, the energy network of water resources ecological-economic system is constructed (Figure 1). The basic structure of regional water ecological-economic system, the relationship of ecological and economic flow and its main direction, water circulation flow path, and the relationship between economic-social production and ecological environment will be clear. And then emergy/dollar ratio (EDR) is calculated as follows:

$$\begin{aligned} \text{EDR (sej/¥)} &= \frac{EM_U}{\text{GDP Comparison Price}} \\ &= \frac{EM_R + EM_N + EM_F - EM_{EX}}{\text{GDP Comparison Price}}, \end{aligned} \quad (1)$$

where EM_U is total emery used; EM_R is renewable emery; EM_N is nonrenewable emery; EM_F is feedback emery; and EM_{EX} is export emery.

(2) *The Energy and Emery Network of Industrial, Agricultural, and Residential Subsystem.* According to the directions of main energy flow, material flow, and monetary flow of industrial, agricultural, and residential subsystem, each subsystem's energy and emery network can be constructed and the emery flow of each subsystem will be calculated. Three more indices emphasizing the contribution rate of groundwater resources (GWCR) were developed:

$$GWCR_I = \frac{\text{Emery of Groundwater within Industry}}{\text{All Emery Input within Industry}}, \quad (2)$$

$$GWCR_A = \frac{\text{Emery of Groundwater within Agriculture}}{\text{All Emery Input within Agriculture}}, \quad (3)$$

$$GWCR_L = \frac{\text{Emery of Groundwater within Residents life}}{\text{All Emery Input within Residents life}}. \quad (4)$$

2.2. *Transformity of Different Water Bodies with the Method of Emery Calculation.* The biggest challenge of the emery analysis is the calculation of transformity (Tr) of all sorts of energy, material, information, and service. So far, lots of significant achievements of the international emery research have been accomplished. *Odum* and other researchers over the world (*such as* Brown et al. [24]) calculated the transformity of the emery of the main energies and substances. With this transformity of the emery we can do some generic systematic emery analysis that could be conducted. It is necessary to calculate more detailed transformity of the emery between resources and substances according to professional systems. For example, for the ecologically economical systems of the water resources, just the rainwater emery transformity is not enough; calculating more detailed classifications of the water solar emery transformity is required. The UEV (*unit of emery value*) of a system can be considered as an efficiency indicator. For example, Brown et al. [24] stated that "UEVs are inversely related to the system efficiency on the scale of the biosphere." In other terms, a more efficient overall use of resources by the coupled human-natural system has a lower UEV. The UEVs of the natural water, the engineering water, and the recycled water were calculated, respectively, as follows:

$$\begin{aligned} &\text{UEV of Natural water} \\ &= \frac{\text{Total Emery of the watershed rainfall (sej/a)}}{\text{Mass of The catchment water capacity per year (m}^3\text{/a)}} \\ &= (\text{Rainfall per year} \times \text{Gibbs energy of rain} \\ &\quad \times \text{Tr of the Rain}) \end{aligned}$$

$$\begin{aligned} &\times (\text{Mass of Total water per year} \\ &\quad \div \text{Refresh Cycle Time})^{-1}, \end{aligned} \quad (5)$$

$$\begin{aligned} &\text{UEV of Engineering water} \\ &= (\text{Total Emery of Engineering water} \\ &\quad \text{Input per year (sej/a)}) \\ &\quad \times (\text{Mass of Total water per year (m}^3\text{/a)})^{-1}, \end{aligned} \quad (6)$$

$$\begin{aligned} &\text{UEV of Recycled Water} \\ &= (\text{Total Emery input within Waste} \\ &\quad \text{water treatment per year (sej/a)}) \\ &\quad \times (\text{Mass of Total Recycled water per year (m}^3\text{/a)})^{-1}. \end{aligned} \quad (7)$$

3. Case Study

3.1. *Study Area.* Beijing, the capital of China, located in the northwest of the North China Plain, is a municipality directly under the control of the central government and also the political and economic center. Its geographic coordinates for longitude and latitude are $115^{\circ}25' - 117^{\circ}30' E$ and $39^{\circ}28' - 41^{\circ}05' N$, with a total area of 16410.54 km^2 . In 2012, the GDP of Beijing is 1787.94 billion yuan, with a population of 20.693 million. The population density is 1251 capita/km^2 . And per-capita water supply is 173 m^3 , which is lower than the world average (Figure 2). Groundwater resource is not only a basic resource for the development of Beijing, but also strategic resources and the important guarantee for Beijing's development. With groundwater accounting for 1/2 of the city's water supply, Beijing is one of the few big cities that regard groundwater as the main source of water supply. With the rapid development of the urban construction and the process of rural urbanization, an increase of the urban population, the conflict between supply and demand of water in the city is more serious. The excessive exploitation of groundwater has caused a series of environmental problems, such as land subsidence and ground fissure, and shortage of groundwater has become a bottleneck of the economic and sustainable development of Beijing.

3.2. Results and Discussion

(1) *Calculation of EDR in Beijing Based on the Regional System Emery Analysis.* According to a comprehensive analysis of the main energy flow, material flow, and monetary flow inside and outside of Beijing water resources ecological-economic system, the emery index datum, including renewable resources emery (EM_R), nonrenewable resources emery (EM_N), feedback input emery (EM_F), and the system emery export (EM_{EX}), the total emery used (EM_U) of

TABLE 1: The Summary of the main energy indexes about the water system of Beijing (unit: 10^{20} sej).

Energy indexes	2008	2009	2010	2011	2012
EM_R	459	324.2	378.12	397.98	508.66
EM_N	1202.36	1287	1318.71	1107.09	976.8
Renewable environmental resources products	712.77	727.47	711.05	698.29	687.95
EM_F	8138.62	8618.9	11371.8	14863.4	17508.9
EM_{EX}	3918.5	3998.3	5528.98	7296.26	8367.11
EM_U	5881.48	6231.8	7539.61	9072.26	10627.2
EM_Y	75465.1	83250	89993.4	96928.6	96935.7
Annual water energy consumption EM_W	333.65	364.63	383.55	351.5	385.67
Water from external EM_{WE}	1.83	6.12	6.72	8.03	9.58
Water from local EM_{WL}	284.06	310.52	324.03	303.37	332.97
Emergy/\$ EDR (10^{11} sej/\$)	46.29	44.31	48.51	51.35	59.84
Emergy/RMB EDR (10^{11} sej/¥)	6.76	6.49	7.26	8.11	9.51

The data of Table 1 have been summarized. The regional data reference is from the following books: [25, 26].

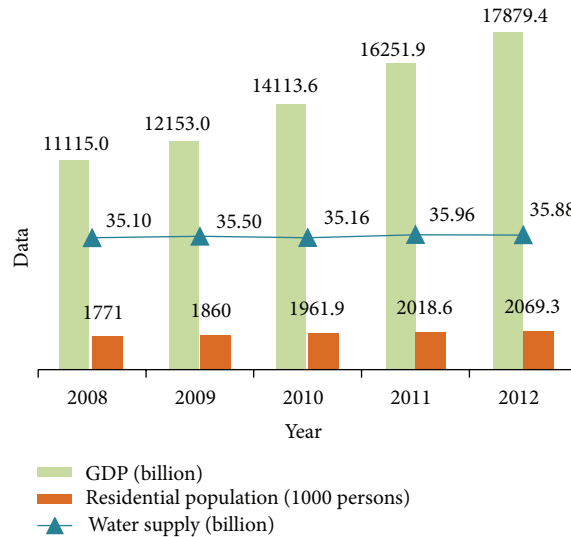


FIGURE 2: The population of permanent residents, water supply, and gross domestic product (GDP) of Beijing. Source: [25].

the system energy yield (EM_Y), and annual water energy (EM_W), was calculated. The complex energy network chart of the regional water ecological-economic system (RWEES) in Beijing was constructed (Figure 3).

After arranging the raw data, analysis of energy, material, and monetary flows in Beijing, the emergy flow of all kinds of resources, material, and monetary in the system was classified and established. EDR (emergy/RMB) was calculated (Table 1).

(2) *Calculation of Transformity of Different Water Bodies in Beijing.* The natural water in Beijing can be generally divided into two kinds: surface water and groundwater. Based on the method of the calculation of transformity of different water bodies, transformity of surface water, groundwater, and engineering water from 2008 to 2012 in Beijing was counted (Table 2).

In accordance with the scale of the water supply of the 9th Water Plant which takes the surface water as source water and the 8th Water Plant which takes groundwater as the source water in Beijing, based on the Standards of Urban Water Supply Construction Project, the input and output amounts of emergy of the water plant were reckoned. The emergy transformity of different water bodies in Beijing was calculated as shown in Table 3 with formulas (5), (6), and (7) above and the original data reference from the following references: [30–35].

(3) *Emergy Analysis of Groundwater Resources Value regarding the Industrial Subsystem as an Example.* According to the main directions of energy flow, material flows in the industrial subsystem, and the relations of production in the system in Beijing, the industrial subsystem emergy network was established (Figure 4).

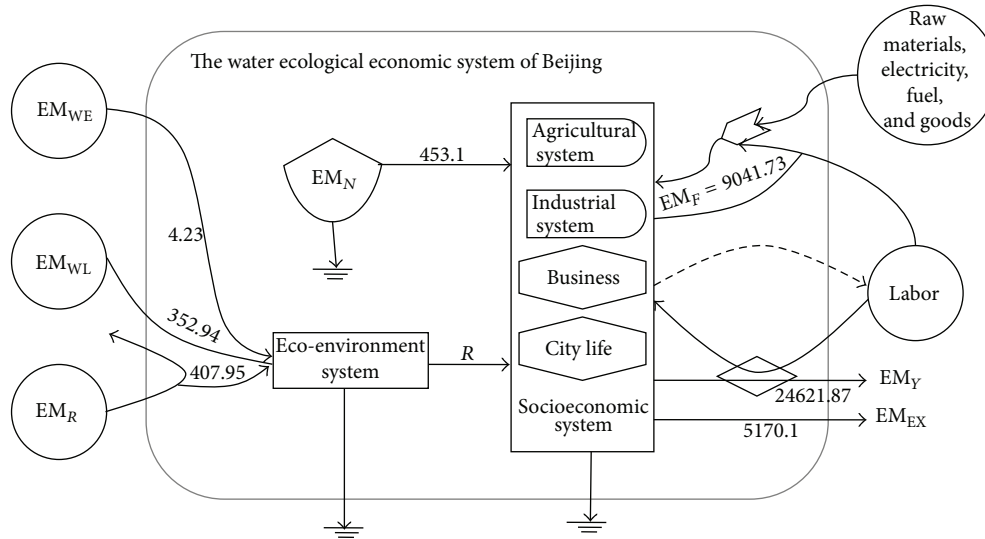


FIGURE 3: Aggregated figure of emergy flows for RWEES (units: emergy 10^{20} sej).

TABLE 2: Transformity of the engineering water of Beijing, 2008–2012.

Item	2008	2009	2010	2011	2012
Raw surface water (10^{11} sej/m ³)	4.27	7.77	7.37	5.6	5.09
Raw groundwater (10^{11} sej/m ³)	24	28.39	29.04	28.93	29.04
The raw south-to-north diversion project water (Raw SNDP water) (10^{11} sej/m ³)	1.99	1.99	1.99	1.99	1.99
Water diversion costs (¥/m ³)	0.39	0.39	0.39	0.39	0.39
Reservoir construction costs (¥/m ³)	1.53	1.53	1.53	1.53	1.53
Tube and wells pumping station construction costs (¥/m ³)	0.32	0.32	0.32	0.32	0.32
The south-to-north diversion project water investment (¥/m ³)	3.35	3.35	3.35	3.35	3.35
EM\$ (10^{11} sej/¥)	6.76	6.49	7.26	8.11	9.51
Engineering surface water (10^{11} sej/m ³)	17.21	20.2	21.28	21.14	23.3
Engineering surface water (10^{11} sej/m ³)	28.77	32.97	34.17	34.66	35
Engineering SNDP water (10^{11} sej/m ³)	24.61	23.71	26.3	29.15	33.8

Original source: Beijing Water Statistical Yearbook [26–29].

TABLE 3: Engineering water, tap water, and recycled water emergy per volume.

Item	Tap water		Recycled water
	From surface water	From groundwater	
Emergy per volume (sej/m ³)	$3.13E + 13$	$3.25E + 13$	$1.19E + 13$

Through the collection, classification, and collation of the original data of energy, material, and money flows of Beijing industrial subsystem, the emergy flow of the industrial subsystem from 2008 to 2012 was obtained. Taking 2012 as an example, the calculation result was shown in Table 4.

Among them, the solar energy and the wind energy are obtained from all the Beijing area. Nonrenewable resources are calculated on the basis of the data of standard coal given in the Beijing Statistical Yearbook. The raw materials,

labor, operation expenses, and fixed assets are expressed in currencies.

With formula (2) and summarizing the data in Table 4 (the data of 2008–2011 can't be shown in this paper, for the limited space), the emergy of groundwater for industry and $GWCR_I$ of Beijing from 2008 to 2012 was shown in Table 5. For the better comparison of different years, the amount of money involved in the process of calculation is based on the comparable prices calculated of 2008.

TABLE 4: Emery inputs and outputs within and outside BIS (Beijing industrial system), 2012.

	Item	Raw data	Unit	Transformity (sej/unit)	Emery (10^{20} sej)
1	Total inputs				3592.76
1.1	Renewable environmental resources				67.43
1.1.1	Solar	$7.19E + 19$	J	1*	0.72
1.1.2	Wind	$1.38E + 17$	J	632*	0.87
1.1.3	Industrial water	$48.9E + 07$	m ³		65.84
1.1.3.1	Tap water	$12.05E + 07$	m ³		40.40
1.1.3.1.1	From surface water	$6.17E + 07$	m ³	$3.29E + 13$	20.34
1.1.3.1.2	From groundwater	$5.87E + 07$	m ³	$3.41E + 13$	20.06
1.1.3.2	Engineering water from surface water	$5.77E + 07$	m ³	$0.23E + 13$	1.34
1.1.3.3	Engineering water from groundwater	$15.4E + 07$	m ³	$0.35E + 13$	5.40
1.1.3.4	Recycled water	$15.7E + 07$	m ³	$1.19E + 13$	18.70
1.2	Nonrenewable environmental resources				3525.33
1.2.1	Energy	$6.67E + 17$	J	39800*	265.44
1.2.2	Raw material, labor, and other fees	$26.75E + 10$	¥	$9.51E + 11$ *	2543.08
1.2.3	*Fixed assets depreciation	$7.54E + 10$	¥	$9.51E + 11$ *	716.81
2	Total outputs				8051.12
2.1	Farm and sideline food	$3.5E + 10$	¥	$9.51E + 11$ *	332.33
2.2	Textile and garment industry	$1.92E + 10$	¥	$9.51E + 11$ *	182.44
2.3	Wood and furniture	$0.81E + 10$	¥	$9.51E + 11$ *	76.92
2.4	Chemical products	$3.46E + 10$	¥	$9.51E + 11$ *	328.76
2.5	Chemical	$5.43E + 10$	¥	$9.51E + 11$ *	516.44
2.6	Rubber and plastic	$1.1E + 10$	¥	$9.51E + 11$ *	104.57
2.7	Raw coal	$1.57E + 17$	J	39800*	62.41
2.8	Crude oil	$4.41E + 17$	J	66000*	291.11
2.09	Electricity	$10.47E + 17$	J	$1.59E + 05$ *	1664.66
2.10	Steel	26000	t	$1.78E + 15$ *	0.46
2.11	Glass	$2.54E + 06$	t	$8.4E + 13$ *	2.13
2.12	Cement	$8.75E + 06$	t	$1.98E + 15$ *	173.15
2.13	General equipment industry outputs	$5.25E + 10$	¥	$9.51E + 11$ *	498.77
2.14	Special equipment industry outputs	$5.1E + 10$	¥	$9.51E + 11$ *	485.07
2.15	Transportation equipment manufacturing industry	$27.22E + 10$	¥	$9.51E + 11$ *	2586.97
2.16	Electrical machinery and equipment manufacturing	$6.70E + 10$	¥	$9.51E + 11$ *	636.54
2.17	Other manufacturing	$0.56E + 10$	¥	$9.51E + 11$ *	53.46
	Industrial waste water	$1.46E + 15$	J	$3.76E + 06$ *	54.92
	Contribution rate of groundwater resources %				1.83

Original source: [25, 26].

Transformity of Table 4 marked with "*" sited from Lv [22] and Odum [23]. Other Tr without "*" are calculated with the original data.

Similarly, the emery value of the groundwater for agricultural and living subsystems can be obtained. The summary of groundwater resources value in Beijing was shown in Table 6.

According to the results, the groundwater emery value and monetary value of the industrial subsystem both show a steady trend from 2008 to 2012. Monetary value per volume of groundwater for industry was slightly decreased in the later 2 years because of the promotion of water-saving awareness and the implementation water saving action.

The groundwater emery value and monetary value of the agricultural subsystem in Beijing kept a stationary fluctuation trend. Compared to a year earlier, the emery value of the agricultural subsystem in the last three years rose slightly. This is due to the effect of agricultural irrigation and water saving policies; in addition, an increase in efficiency of farming is another reason.

In addition, a rising trend in these years of groundwater resources value can be seen in general, although there were slight fluctuations in the middle years. For example, monetary

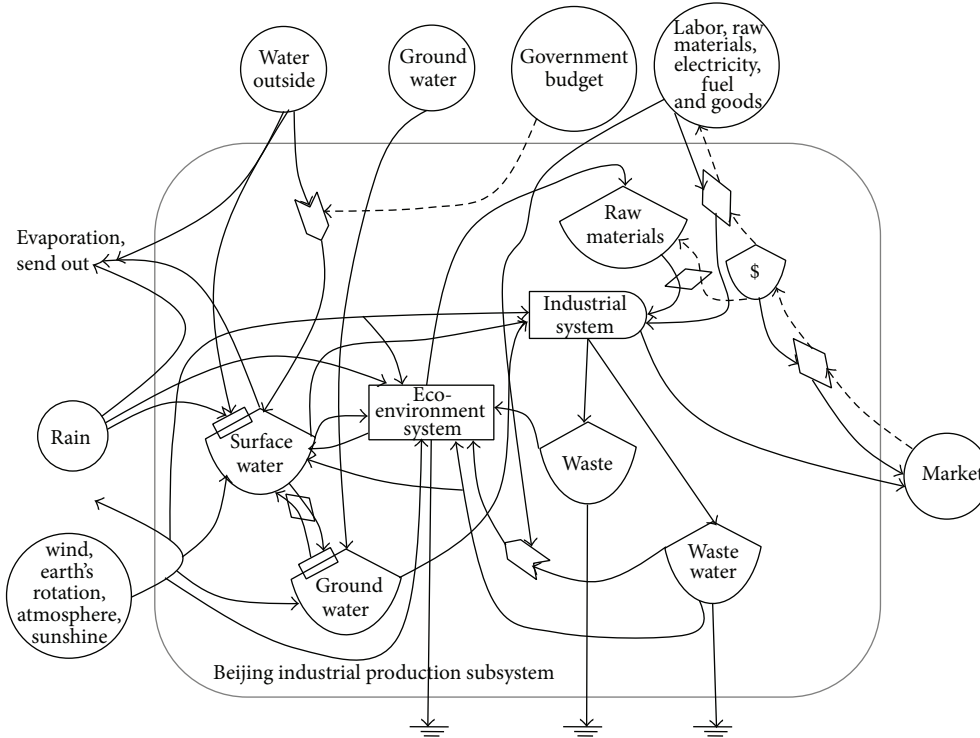


FIGURE 4: Figure of energy flows for Beijing industrial subsystem network.

TABLE 5: The water resource contribution rate and value of Beijing industry system (2008–2012) (unit: 10^{20} sej).

Item	2008	2009	2010	2011	2012
Emergy of water for industry	56.30	60.74	59.51	63.05	65.84
Emergy of groundwater for industry	24.97	25.24	23.17	23.69	25.45
Total emergy inputs for industry	1511.70	2938.67	3020.52	3254.55	3592.76
Total emergy outputs of industry	3068.95	5164.62	6832.95	7050.51	5805.11
WCR for industry (%)	3.73	2.07	1.97	1.93	1.83
GWCR for industry (%)	1.65	0.86	0.77	0.73	0.71
Emergy value of water resource for industry	114.38	106.74	134.62	136.59	147.55
Emergy value of groundwater resource for industry	50.70	44.36	52.43	51.33	57.04
EDR emergy/RMB (10^{11} sej/¥)	6.76	6.49	7.26	8.121	9.51
Monetary value of water resource for industry (10^9 ¥)	16.92	16.45	18.53	16.83	15.52
Monetary value of groundwater resource for industry (10^9 ¥)	7.50	6.83	7.22	6.33	6.00
Total volume of water resource for industry (10^8 m ³)	5.2	5.23	5.06	5.01	4.89
Volume of water resource for industry (10^8 m ³)	2.42	2.29	2.11	2.1	2.13
Emergy transformity of water used in industry (10^{13} sej/m ³)	22.0	20.4	26.6	27.3	30.2
Emergy transformity of groundwater used in industry (10^{13} sej/m ³)	2.09	1.94	2.48	2.45	2.68
The monetary value of water resource per volume for industry (¥/m ³)	32.55	31.45	36.63	33.60	31.74
The monetary value of groundwater resource per volume for industry (¥/m ³)	30.97	29.83	34.14	30.19	28.19

value per volume of groundwater for residential life in 2008 is 14.22 ¥/m³, which is as much as 14.99 ¥/m³ in 2012 which is much lower than the average price of residents water (5 ¥/m³) in Beijing.

(4) *The Summary of GWCR in Beijing.* Comparing $GWCR_I$ and $GWCR_A$ in Beijing, for 5 years the average $GWCR_I$ was

0.944% and the average $GWCR_A$ was 4.38% (Table 7). This is because agricultural production is generally dependent on the supply of water, but the degree of industrial production relying on water is low. In addition, urban water supply is mostly from reservoir water but rural wells water supply is mostly from groundwater in Beijing.

TABLE 6: The summary table of Beijing groundwater value.

Item	2008	2009	2010	2011	2012	
Total emergy value (10^{20} sej)	Groundwater for industry	50.70	44.36	52.43	51.33	57.04
	Groundwater for agriculture	30.81	27.45	30.48	33.43	30.89
	Groundwater for residential life	44.2	43.9	52.1	57.2	72.6
	Total	125.71	115.71	135.01	141.96	160.53
Total monetary value (10^9 ¥)	Groundwater for industry	7.50	6.83	7.22	6.33	6.00
	Groundwater for agriculture	4.56	4.23	4.20	4.12	3.25
	Groundwater for residential life	6.54	6.77	7.17	7.05	7.64
	Total	18.6	17.83	18.59	17.5	16.89
Monetary value per volume (¥/m ³)	Groundwater for industry	30.97	29.83	34.14	30.19	28.19
	Groundwater for agriculture	5.02	4.82	5.10	5.19	4.44
	Groundwater for residential life	14.22	14.19	14.88	14.61	14.99

TABLE 7: The Summary table of contribution rate of water resources (unit: %).

Item	2008	2009	2010	2011	2012
Contribution rate of water resources for industry (C-RWRI)	3.73	2.07	1.97	1.93	1.83
Contribution rate of groundwater resources for industry (C-RGRI)	1.65	0.86	0.77	0.73	0.71
Contribution rate of water resources for agriculture (C-RWRA)	9.94	8.60	9.92	10.83	8.84
Contribution rate of groundwater resources for agriculture (C-RGRA)	4.35	3.81	4.34	4.86	4.52
Contribution rate of water resources for residential life (C-RWRR)	13.41	13.57	13.01	10.44	10.03
Contribution rate of groundwater resources for residential life (C-RWRR)	4.42	4.10	3.91	3.38	3.24

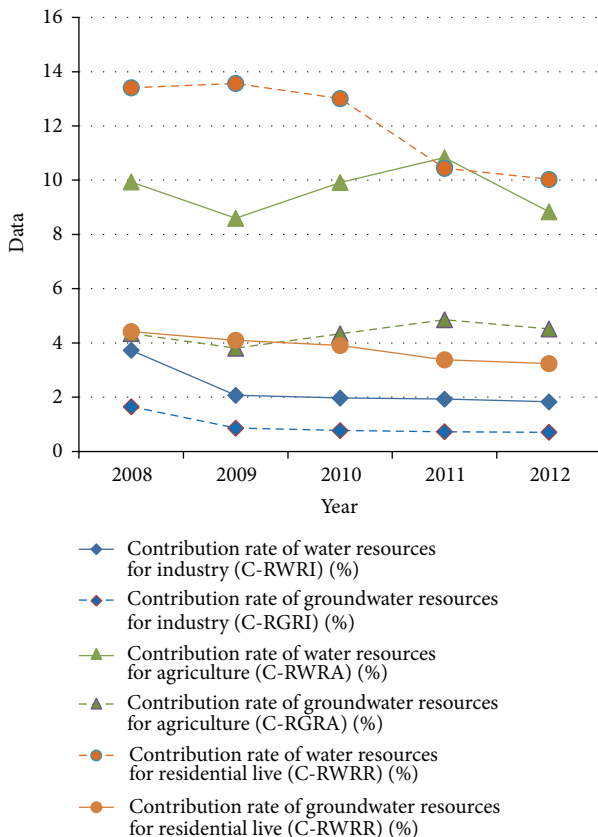


FIGURE 5: The summary table of contribution rate of water resources.

GWCR_L in Beijing showed a downward trend (Figure 5), falling from 4.42% in 2008 to 3.24% in 2012. On the one hand, the residents' awareness of water saving is strengthened, and the South to North Water Diversion Project is gradually put into use.

4. Conclusions

Based on the principle of water cycle and the emergy theory of ecological economy, the frame of emergy evaluation of groundwater resources is constructed.

(1) *The Evaluation of the Importance of Groundwater as a Basic Elements Involved in Each Subsystem.* As a basic element for the residents' life, groundwater also supports the industry's production activities. Taking Beijing in 2012 as an example, in terms of monetary value of groundwater from big to small sorting, followed by groundwater for residents, for industrial, and for agricultural, its monetary value was 7.64, 6.00, and 3.25 billion yuan, accounting for 45.24%, 35.52%, and 19.24% of the total value, respectively. The total monetary value of the groundwater (16.89 billion yuan) accounts for 1.51% of the GDP (1118.059 billion yuan based on the comparable price of 2008) in Beijing.

(2) *Predicting the GWCR of Each Subsystem.* In 2012, the GWCR of each subsystem including GWCR_A, GWCR_L, and GWCR_I are 4.52%, 3.24%, and 0.71%, respectively. By further understanding the true value of groundwater and strengthening integrated management to water resources, the

results can provide an important basis for scientific decision-making of the government.

Conflict of Interests

The authors declare that there is no conflict of interests regarding the publication of this paper.

Acknowledgments

The study is supported by the Social Science Foundation of China (13BJY063) and Beijing Planning Office of Philosophy and Social Science (12JGB065).

References

- [1] F. Liu, "Brief review on achievements of groundwater contamination monitoring and remediation," *Rock and Mineral Analysis*, vol. 31, no. 4, pp. 645–646, 2012.
- [2] Y. Hu and S. L. Cao, "On fuzzy comprehensive appraisal model for water resources worth," *Journal of Shandong University (Engineering Science)*, vol. 33, no. 3, pp. 341–345, 2003.
- [3] L. J. Wei, J. Q. Bao, and X. Y. Fu, "Application of the fuzzy mathematical model in evaluation of water resources value," *Journal of Lanzhou Jiaotong University (Natural Sciences)*, vol. 25, no. 3, pp. 73–76, 2006.
- [4] P. F. Lin, L. Q. Wang, and J. S. Zhang, "Modification and application of fuzzy mathematics model in evaluating loss of water resource value," *Environmental Science and Technology*, vol. 30, no. 1, pp. 66–68, 2007.
- [5] C. Chen, *Research on the value of quaternary groundwater based on GIS [Dissertation for doctoral degree]*, China University of Geosciences, Beijing, China, 2012.
- [6] Y. Wang, "Study and simulation on water resources regulation in Zhangye City based on CGE model," *Journal of Natural Resources*, vol. 25, no. 6, pp. 959–966, 2010.
- [7] C. M. Mao and R. H. Yuan, "Calculation and analysis of the theory value of water resources of Huanghe River," *Resources and Environment*, vol. 13, no. 3, pp. 25–29, 2003.
- [8] I. A. Curtis, "Valuing ecosystem goods and services: a new approach using a surrogate market and the combination of a multiple criteria analysis and a Delphi panel to assign weights to the attributes," *Ecological Economics*, vol. 50, no. 3–4, pp. 163–194, 2004.
- [9] S.-K. Ning and N.-B. Chang, "Watershed-based point sources permitting strategy and dynamic permit-trading analysis," *Journal of Environmental Management*, vol. 84, no. 4, pp. 427–446, 2007.
- [10] L. Diaz-Balteiro and C. Romero, "Valuation of environmental goods: a shadow value perspective," *Ecological Economics*, vol. 64, no. 3, pp. 517–520, 2008.
- [11] W. Yang, J. Chang, B. Xu, C. Peng, and Y. Ge, "Ecosystem service value assessment for constructed wetlands: a case study in Hangzhou, China," *Ecological Economics*, vol. 68, no. 1–2, pp. 116–125, 2008.
- [12] A. Tilmant, D. Pinte, and Q. Goor, "Assessing marginal water values in multipurpose multireservoir systems via stochastic programming," *Water Resources Research*, vol. 44, no. 12, 2008.
- [13] H. Wang, *Research of water resources value based on the theory of marginal utility [Dissertation for master degree]*, Beijing University of Technology, Beijing, China, 2012.
- [14] J. T. Warlord, "Resources, environment and economic development. China population," *Resources and Environment*, vol. 1, pp. 78–83, 1992.
- [15] M. L. Nieswiadomy, "Estimating urban residential water demand: effects of price structure, conservation, and education," *Water Resources Research*, vol. 28, no. 3, pp. 609–615, 1992.
- [16] Z. H. Chen, "Positive analysis of water resource pricing B a sed on marginal opportunity cost," *Journal of South-Central University for Nationalities (Natural Sciences)*, vol. 22, no. 3, pp. 75–77, 2003.
- [17] M. H. Ali, M. R. Hoque, A. A. Hassan, and A. Khair, "Effects of deficit irrigation on yield, water productivity, and economic returns of wheat," *Agricultural Water Management*, vol. 92, no. 3, pp. 151–161, 2007.
- [18] D. N. Barton, "The transferability of benefit transfer: contingent valuation of water quality improvements in Costa Rica," *Ecological Economics*, vol. 42, no. 1–2, pp. 147–164, 2002.
- [19] F. Liu, S.-M. Wang, and H.-H. Chen, "Progress of investigation and evaluation on groundwater organic contaminants in western countries," *Geological Bulletin of China*, vol. 29, no. 6, pp. 907–917, 2010.
- [20] Z. Y. Xie, "Research on water environment value of Tumen river basin in the way of emergy," *Journal of Jilin Agricultural University*, vol. 24, no. 3, pp. 68–72, 2002.
- [21] D. Chen, J. Chen, and Z.-H. Luo, "Evaluation method of natural water resources based on energy theory and its application," *Journal of Hydraulic Engineering*, vol. 37, no. 10, pp. 1188–1192, 2006.
- [22] M. C. Lv, *Emergy evaluation of ecological economic value of regional water resources [M.S. thesis]*, Zhengzhou University, 2009.
- [23] H. T. Odum, *Environmental Accounting: Emergy and Environmental Decision Making*, John Wiley & Sons, New York, NY, USA, 1996.
- [24] M. T. Brown and S. Ulgiati, "Energy quality, emergy, and transformity: H.T. Odum's contributions to quantifying and understanding systems," *Ecological Modelling*, vol. 178, no. 1–2, pp. 201–213, 2004.
- [25] Beijing Statistical Yearbook, *Beijing Water Statistical Yearbook*, China Industrial Economy, Beijing Water Authority, 2008–2012.
- [26] National Bureau of Statistics of the People's Republic of China, *China Industrial Economy Statistics Yearbook*, China Statistics Press, 2008–2012.
- [27] J. C. Li, W. L. Jiang, and L. S. Jin, *The Ecological Value Theory*, Chongqing University Press, 1999.
- [28] Q. K. Li, S. Y. Miao, and B. Z. Chen, "Well irrigation cost analysis of three areas in Hebei Province," *Water Conservancy Planning and Analysis*, vol. 4, pp. 41–45, 1994.
- [29] H. Xu, *Study on water price of multi-water resources in the reception basin of the south-north water transfer project: in Beijing as a case [Ph.D. thesis]*, China Institute of Water Resources and Hydropower Research, 2013 (Chinese).
- [30] *Beijing Water Statistical Yearbook (2008–2012)*, GB3838, 2014.
- [31] *Standards of the Surface Water Environment Quantity*, GB8978, 2002.
- [32] *Integrated Wastewater Discharge Standard*, Construction-Standard, 1994/1574, 1996.
- [33] *Standards of Urban Water Supply Construction Project*, Construction-Standard, 1994/1574, 1994.
- [34] *Standards of Urban Sewage Treatment*, GB/T14848.93, 1994.
- [35] *Standards of the Groundwater Quantity*, 1993.

Research Article

Critical Damage Analysis of WC-Co Tip of Conical Pick due to Coal Excavation in Mines

Saurabh Dewangan,¹ Somnath Chattopadhyaya,¹ and Sergej Hloch²

¹Department of Mechanical Engineering, Indian School of Mines, Dhanbad 826004, India

²Faculty of Manufacturing Technologies, Technical University of Košice with a Seat in Prešov, 080 01 Prešov, Slovakia

Correspondence should be addressed to Saurabh Dewangan; saurabh22490@gmail.com

Received 21 August 2014; Revised 7 December 2014; Accepted 10 December 2014

Academic Editor: Guocheng Lv

Copyright © 2015 Saurabh Dewangan et al. This is an open access article distributed under the Creative Commons Attribution License, which permits unrestricted use, distribution, and reproduction in any medium, provided the original work is properly cited.

WC-Co based tools are widely used in the field of coal and rock excavation because of their unique combination of strength, hardness, and resistance to abrasive wear. Conical pick is one of the coal cutting tools. The tip of the pick is made of WC-Co material. As coal and rock are heterogeneous elements, they pose various constraints during excavation. As a result the tools wear out during the process. Other parameters like cutting techniques, tool orientation, and environmental conditions also affect the tool significantly. The wearing phenomenon greatly reduces the service life of the tools and thereby cuts down the production rate. To prevent such wearing process, it is important to investigate the different wear mechanisms in WC-Co. Simultaneously, there has to be an ongoing endeavour for the development of better quality WC-Co. This paper focuses on different wear mechanisms in a conical pick which has been used in a continuous miner machine for coal cutting. The worn out surface has been observed by using FE-SEM (field emission scanning electron microscopy) and EDS (energy dispersive X-ray spectroscopy). The mechanisms, namely, coal/rock intermixing, cracking and crushing of WC grains, and adhesion of rock particles, have been predominantly investigated in this study. A little indication of corrosive decay in the WC grain has also been reported. The EDS has detected material concentration in a selected area or point of the worn-out surface. The spectrograph confirms the presence of coal/rock materials. Elements such as W, C, Ca, K, O, and Co have been mainly found in different concentrations at different positions.

1. Introduction

Conical pick is an essential tool in the field of coal/rock excavation. The abrasive cone tip is made of cemented carbide material and is inserted in a steel body. Cemented carbide is a binary composition of WC and Co. It is extensively used in excavating machines, such as continuous miner, roadheader, and shearer. Picture of a continuous miner is shown in Figure 1(a). Cemented carbide has the ideal combination of hardness and toughness. Tungsten carbide possesses strength and hardness whereas the cobalt is responsible for toughness [1, 2]. The grain size of carbide affects wear-resistance property of the cemented carbide. The coarse-grained carbides usually have a lower abrasive wear-resistance than that of a fine or medium grain size [3–8]. By increasing the granule size of carbides, the fracture toughness increases [9]. Factors such as rock types, abrasiveness, drilling temperature, rock penetration, and corrosive environment

around tool can result in various wear mechanisms [10, 11]. Different drilling patterns can also be the cause of different failure mechanisms. If percussion drilling is carried out, then it causes fatigue impact wearing as the main failure mechanism. Again, when the rotary/crushing is the drilling pattern, it is abrasion and crack that become the primary characteristics of failure mechanism [12–14]. Beste et al. (2006) have studied mainly two deterioration mechanisms in rock drill buttons. They are binder phase degradation and rock intermixing [15]. Larsen-Basse (1973) has concluded in a review that rock drill bit wear can be explained by the following mechanisms: surface impact spalling, surface impact fatigue spalling, thermal fatigue, and abrasion [16]. However, the generated heat during drilling process greatly affects the sustainability of tools. Fish et al. (1957) have found that hard rock drilling leads to a process of tool material softening due to high button temperature. Moreover, the necessary high load generates high frictional heat [17]. The

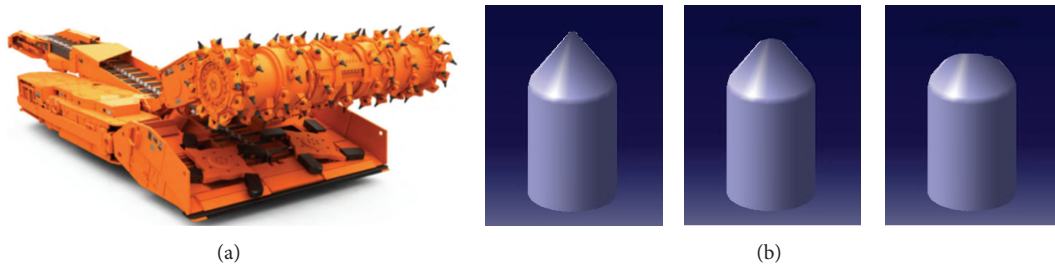


FIGURE 1: (a) Continuous miner machine (courtesy: joy global) [27]; (b) gradual wear of WC-Co tip.

actual surface temperature of the drill button is difficult to measure. However, the average temperature has been reported to be between 300°C and 400°C [10]. Also, oxidation of Co takes place near the crack tips at higher temperature which results in brittle-ductile transitions [18]. The thermal fatigue crack propagation in WC-Co has been studied by Lagerquist [19] and the rate-controlling factor has been found to be the width of Co layers between the adjacent WC grains. Many researchers have studied wear mechanisms of CC tool with SEM (scanning electron microscopy) and high resolution field emission gun SEM analysis. They have found different types of damage in the cemented carbide buttons, namely, microspalling, abrasion wear, cracks, WC grain pullout, extrusion of binder metal, and reptile skin [11, 13, 14, 16, 20–23]. In an experiment, Olovsjö et al. (2013) have concluded that the controlling parameters of the wearing process in CC are plastic deformation and cracking and crushing of individual WC grains. Cobalt depletion and rock material penetration may also affect the drill button life to a great extent [24]. Gupta et al. (2012) have carried out SEM analysis of worn out diamond cutting tool and unused tool to compare the microstructure after rock cutting. The new tool has displayed properly bonded diamond particles in nickel matrix. However, channels or grooves can be seen in the worn-out part due to combined effect of excessive loading and bit rotation. It has also been noticed that the matrix is plastically deformed due to the high temperature produced during core drilling [25]. After investigating various wear mechanisms in CC drill bits, researchers believe that there have to be further studies in this area [24, 26].

The present paper studies wear mechanisms in the WC-Co tip of a worn-out conical pick, which has been used in a coal cutting operation by a continuous miner machine. A sketch of gradual wearing of the WC-Co tip is given in Figure 1(b). It is important to organize adequate samples of worn-out tools for critical investigation. The field emission scanning electron microscopy (FESEM) and energy dispersive X-ray spectrography (EDS) have been used to observe the severity of damage and deterioration. FESEM has more advantages over SEM in terms of better quality images with higher magnification. EDS helps to find the exact amount of material concentration in the selected point/area. Hence, the detection of rock/coal materials in the selected part of WC-Co structure can be made properly.

2. Experimental Work

The experimental work primarily consisted of organizing a worn-out sample to make critical observation. It required a small-sized sample of the work piece for getting correct results in SEM analysis. If the tip is inserted deeply into the tool body, it becomes difficult to cut the hard WC-Co material properly. Therefore, the tip was cut by electric discharge machining (EDM). The microscopic analysis was done with the FE-SEM Supra 55 (Carl Zeiss, Germany). The worn-out conical pick and the sample, which were observed through SEM, are shown in Figures 2(a), 2(b), and 2(c).

The cracks and crushed parts in the tip surface could be seen by naked eyes as in the referred figure but the microstructural damage inside could not be seen. By using SEM and EDS, different types of wear mechanisms were found.

3. Observation

The SEM is capable of detecting the microstructural damage. Simultaneously, the factors causing the damage in a particular area can be detected through EDS. For taking SEM images of different parts, some adjustments had to be made, regarding the magnification, accelerating voltage or electron high tension (EHT), working distance (WD) between the sample surface and the lower portion of the lens, and so forth. These are shown in each of the SEM images. Different types of wear mechanisms could be observed in the surface of the worn-out sample. Cracking and crushing of WC grains, interruption of coal and rock particles, and adhesion of rock materials into the surface were found to be the main wear mechanisms.

Hard rocks are always present in between coals in a mine. These undesirable rock materials are the main cause behind tool damage. With the drum of the continuous miner machine rotating at 54 rpm, the tool is hit by coal and rock during cutting. The sudden high impact leads to cracking and crushing of the WC grains, rendering the tool absolutely useless. The cracks in the WC grains are shown in Figure 3. During this process, some sharp edges of rocks penetrate the cracks, thereby crushing the WC grains. In some cases, small fragments of crushed WC grains come out, making a hole in the original structure (Figure 4). Sometimes these holes are filled with coal/rock material.

Coal/rock interruption in between the WC-Co structures is a common wear mechanism in any coal cutting equipment.

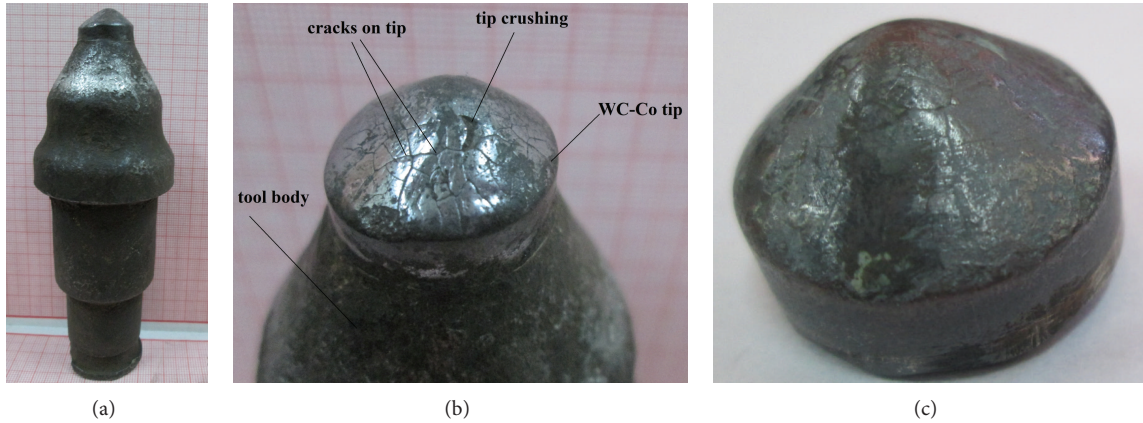


FIGURE 2: (a) Worn-out conical pick; (b) crushing and cracking of WC-Co tip; (c) sample to be tested on SEM.

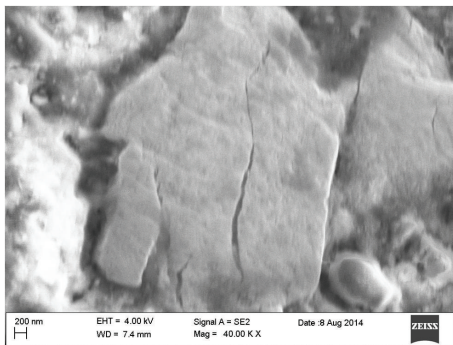


FIGURE 3: Crack on WC grain.

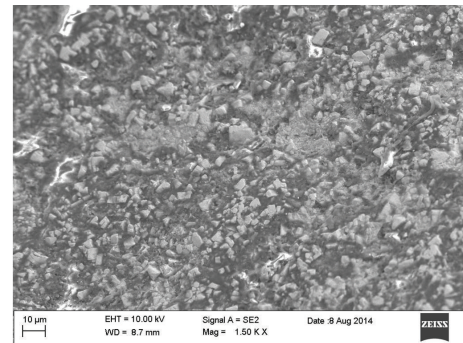


FIGURE 5: Coal/rock particle interruption (black portion) in between the WC grains.

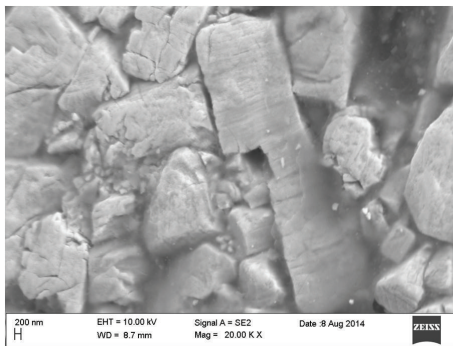


FIGURE 4: Crushing of WC grains; hole due to penetration of sharp edge of hard rock.

The Co binder phase is ductile in nature and due to the massive impact, the rock/coal particles enter into the binder phase and get mixed with them. This results in the degradation of the Co phase. As a result, it can no longer bind the WC grains properly. Rock/coal intermixing can be assumed to be the main factor which triggers other types of deterioration in the tool. The presence of coal/rock has been confirmed by the EDS analysis. The spectra plotted by EDS are capable

of showing the percentage concentration of mixed rock/coal materials. The coal and rock interrupted zone (black part) in the surface of the tip is shown in Figure 5. Coal intermixing at another part of the sample is shown in Figure 6. For capturing this image, the magnification and accelerating voltage had to be adjusted at 2.00 Kx and 10.00 kV, respectively. For the purpose, an area marked spectrum 1 was selected for observation of the concentration of coal and rock materials through EDS. The data obtained through EDS reveals that mainly W, C, and O are in excess and their weights (%) are 39.53, 35.89, and 20.81, respectively. Ca (0.77%) and Co (3.00%) are also present in small amount. Here C represents the coal particles and Ca and O are the sign of rock parts. As the tool was used in a coal mine, mainly coal interruption was observed.

A comparative analysis of EDS spectra at three different zones of the crushed WC surface was done (Figures 7(a), 7(b), and 7(c)). All the three figures are the same but the points/areas selected for taking EDS were different. Spectra 1, 2, and 3 have been marked on the solid WC grain, binder material (dark part), and crushed WC grains, respectively. The pertaining EDS images are given in Figures 8(a), 8(b), and 8(c). Also, the weight percentage and atomic percentage of the elements of the corresponding images have been noted

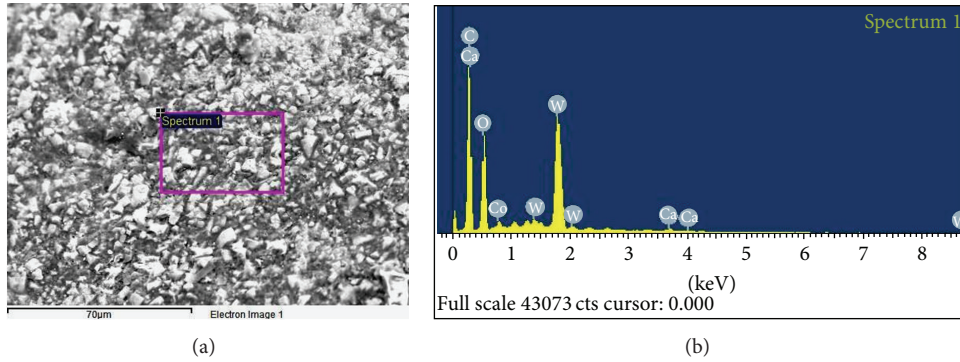


FIGURE 6: (a) Coal/rock intermixed zone (dark coloured); (b) EDS spectra of selected area showing the presence of coal and rock material.

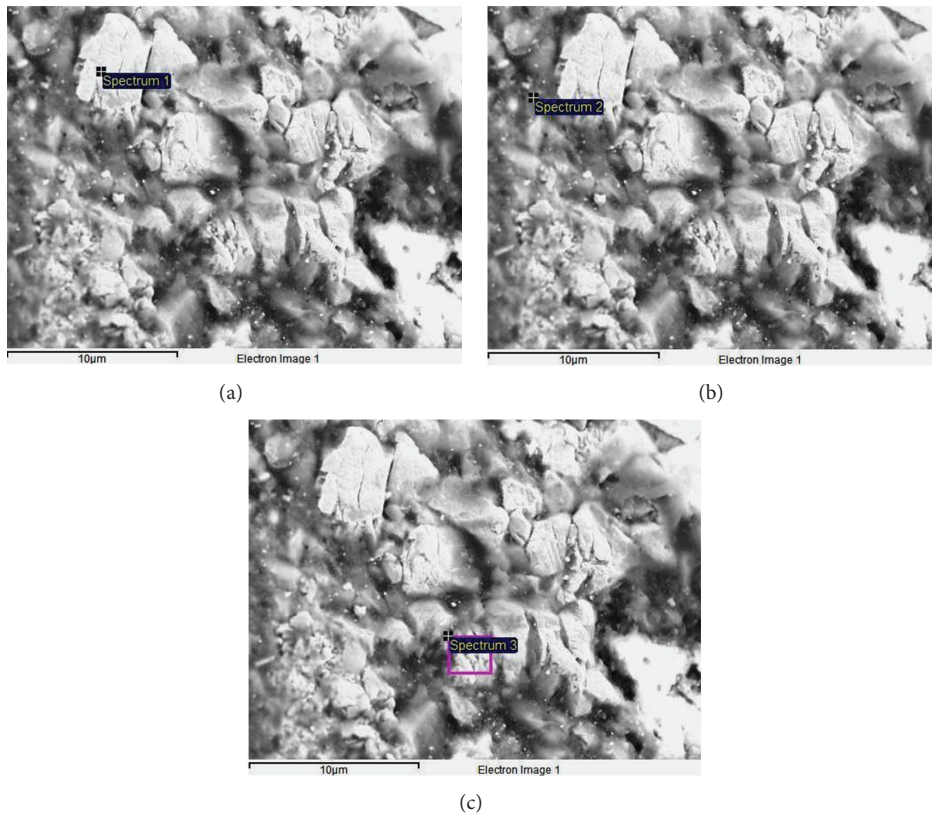


FIGURE 7: Crushed part of tool tip; different points/area selected for EDS analysis.

down. This process verifies the presence of coal and rock in the damaged tip surface. The damaged part shows very little amount of Co indicating that it has been degraded by coal/rock materials.

The homogeneous α -tungsten carbide contains tungsten and carbon in an exact stoichiometric ratio of 49.5–50.5 mol% carbon [28]. Pure tungsten powder is mixed with pure carbon (lamp black) in the ratio of 94% and 6% by weight at a high heat of about 1400–2000°C [28, 29]. Hence, it is natural to find a concentration of C in the WC grain. On the basis of the spectrum 1 (a point on solid WC grain) it can be concluded that the W and C are the main constituent of

the WC grain, although a small amount of O is also present due to the deteriorated condition of the surface. Spectrum 2 (a point selected on binder (black) part) shows a comparatively high amount of carbon and oxygen content and also a little amount of Mg, Ca, and Al, indicating intermixing of coal and rock material with the binder phase. The area of spectrum 3 in the crushed WC grains also shows the presence of penetrated coal and rock materials (see Figure 8).

The adhesion of coal/rock particle into the surface of cemented carbide is another wear mechanism. The observed rock material is shown in Figure 9 (magnification = 14.00 Kx). This phenomenon enhances the rock interruption in between

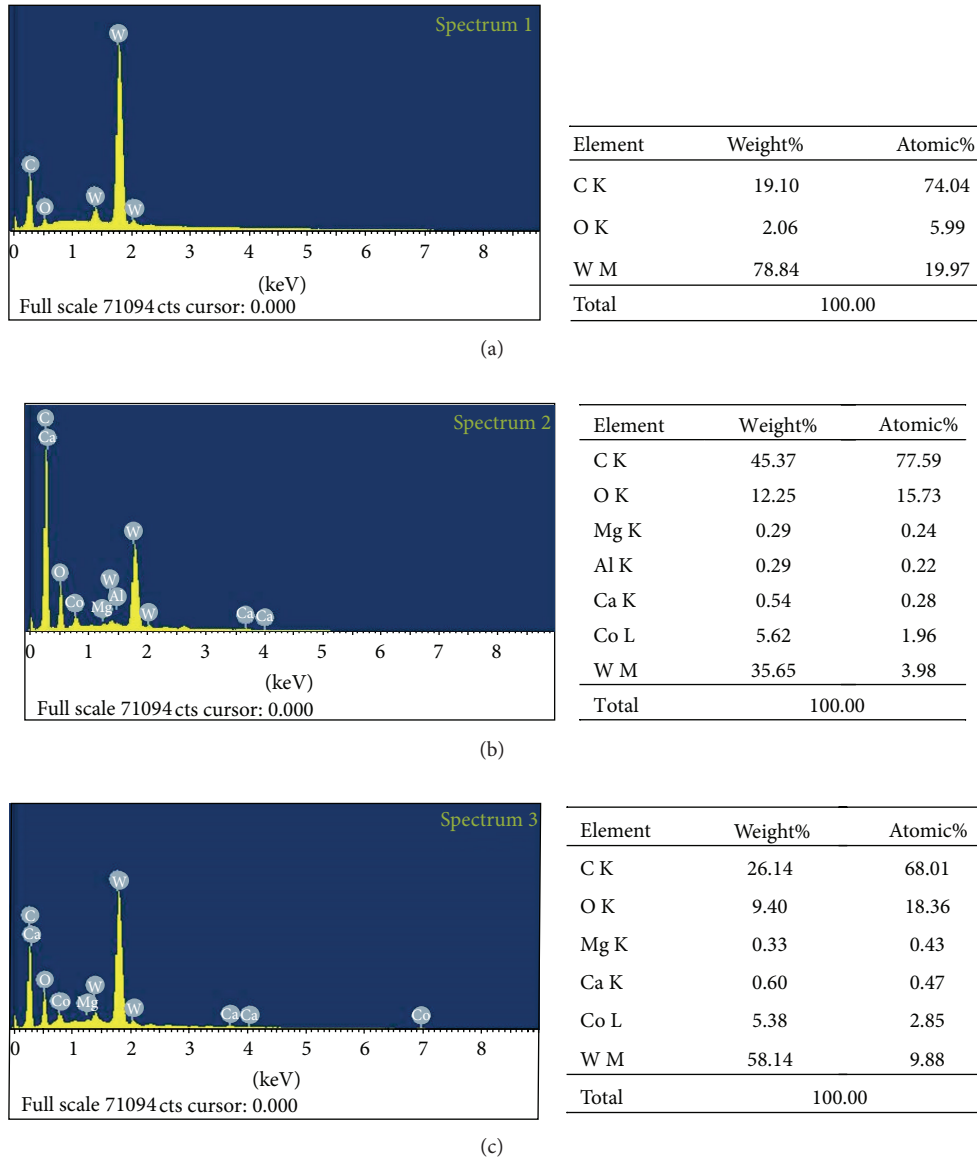


FIGURE 8: EDS pertaining to area selected in Figure 7; (a) EDS of a point selected in Figure 7(a) on WC grain; (b) EDS of a point selected in Figure 7(b) on dark part; (c) EDS of an area selected in Figure 7(c) on crushed WC grain.

the binder contents. The rock and coal materials adhere to the surface due to the high impact caused by moving roller of continuous miner machine at the time of coal cutting. As the number of rotations increases, the rock particle begins to enter into the WC-Co bond by replacing the Co binder phase. The rectangular area (spectrum 1) was selected for observing the EDS result (Figure 9). Excess carbon indicates presence of the coal materials. Rock materials like N and O were also significantly visible.

Beste and Jacobson (2008) explained the chemical and oxidative degradation of the WC grains by SEM images in which the oxides were shown in the form of white circular spots. They also pointed out decay of the WC grains due to corrosive environment [26]. Similar corrosive decay to

an extent was reported in the present experiment as well. However, the oxide layers or spots are not present in this experimented sample. The corrosive degradation has been shown inside the white oval (Figure 10).

4. Conclusion

For a long time, the wearing mechanisms of CC have been under study. In order to enhance the quality of CC, it is important to understand the wearing process of CC under different working conditions. In the present study, an attempt has been made to understand the deterioration mechanisms in a worn out conical pick. The pick was being used in continuous miner machine for coal mining. The tool sample was

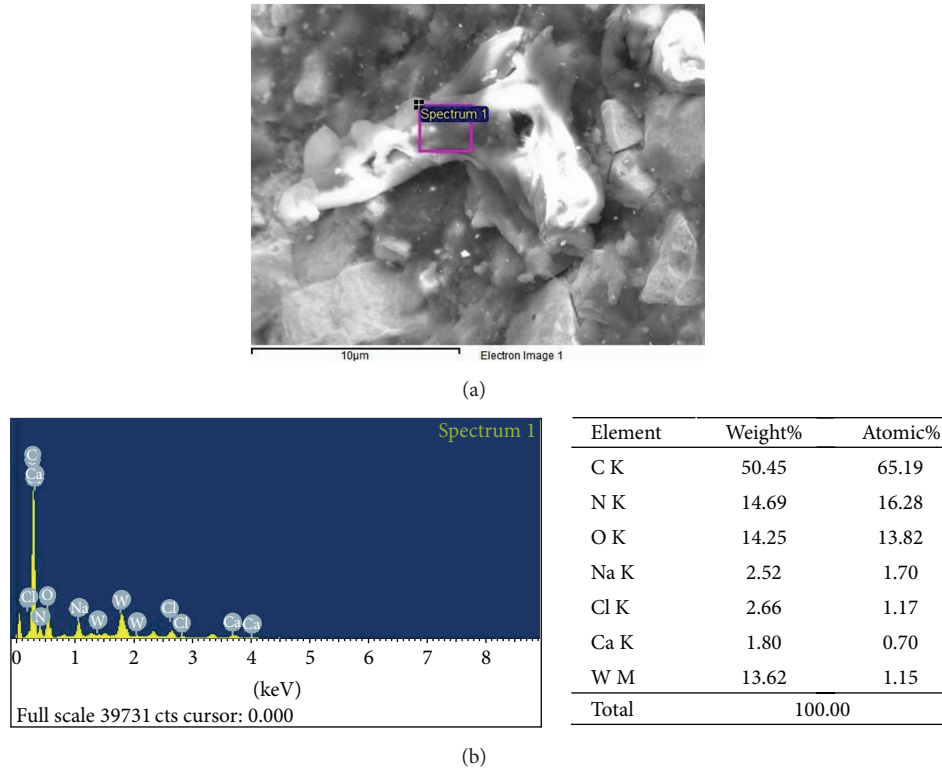


FIGURE 9: Adhering of rock particle; EDS spectra showing the concentration of elements.

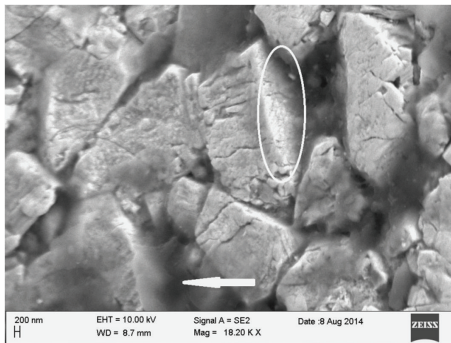


FIGURE 10: Corrosive degradation of WC grain (white oval); white arrow shows the coal/rock intermixed binder material.

carefully investigated through FE-SEM and EDS for a thorough understanding of the wearing mechanism. Although cracks and crushed parts in the surface were clearly visible by naked eyes, the severity of damage could be assessed only by using SEM. Also, the material (element) concentrations in the damaged part were detected by EDS. Different types of wear mechanisms, namely, coal/rock interruption, cracking and crushing of WC grains, adhesion of rock particles, and a small indication of corrosive decay in the WC grains, were reported. Predominantly, WC grain cracking and crushing could be detected. The conclusion that could be made at the end of the study was that coal/rock materials penetrate the cracks of the coal cutting tools to enter inside the base material and

degrade it. A small percentage of intermixed rock material in the present investigation indicated that the quality of coal is good in this particular mine under study and has very little amount of rock present in between the coals.

Conflict of Interests

The authors declare that there is no conflict of interests regarding the publication of this paper.

References

- [1] A. Mukhopadhyay and B. Basu, "Recent developments on WC-based bulk composites," *Journal of Materials Science*, vol. 46, no. 3, pp. 571–589, 2011.
- [2] G. S. Upadhyaya, "Materials science of cemented carbides—an overview," *Materials and Design*, vol. 22, no. 6, pp. 483–489, 2001.
- [3] K. Bonny, P. De Baets, Y. Perez, J. Vleugels, and B. Lauwers, "Friction and wear characteristics of WC-Co cemented carbides in dry reciprocating sliding contact," *Wear*, vol. 268, no. 11-12, pp. 1504–1517, 2010.
- [4] J. Pirso, S. Letunoviš, and M. Viljus, "Friction and wear behaviour of cemented carbides," *Wear*, vol. 257, no. 3-4, pp. 257–265, 2004.
- [5] T. Kagnaya, C. Boher, L. Lambert, M. Lazard, and T. Cutard, "Wear mechanisms of WC-Co cutting tools from high-speed tribological tests," *Wear*, vol. 267, no. 5–8, pp. 890–897, 2009.
- [6] J. Deng, J. Zhou, H. Zhang, and P. Yan, "Wear mechanisms of cemented carbide tools in dry cutting of precipitation hardening

- semi-austenitic stainless steels," *Wear*, vol. 270, no. 7-8, pp. 520–527, 2011.
- [7] G. List, M. Nouari, D. Géhin et al., "Wear behaviour of cemented carbide tools in dry machining of aluminium alloy," *Wear*, vol. 259, no. 7-12, pp. 1177–1189, 2005.
- [8] J. Y. Sheikh-Ahmad and J. A. Bailey, "The wear characteristics of some cemented tungsten carbides in machining particleboard," *Wear*, vol. 225–229, no. 1, pp. 256–266, 1999.
- [9] X. Deng, B. R. Patterson, K. K. Chawla et al., "Mechanical properties of a hybrid cemented carbide composite," *International Journal of Refractory Metals and Hard Materials*, vol. 19, no. 4–6, pp. 547–552, 2001.
- [10] U. Beste, T. Hartzell, H. Engqvist, and N. Axén, "Surface damage on cemented carbide rock-drill buttons," *Wear*, vol. 249, no. 3-4, pp. 324–329, 2001.
- [11] U. Beste and S. Jacobson, "Micro scale hardness distribution of rock types related to rock drill wear," *Wear*, vol. 254, no. 11, pp. 1147–1154, 2003.
- [12] L. C. Duan, X. Y. Liu, B. S. Mao, K. H. Yang, and F. L. Tang, "Research on diamond-enhanced tungsten carbide composite button bits," *Journal of Materials Processing Technology*, vol. 129, no. 1–3, pp. 395–398, 2002.
- [13] J. Larsen-Basse, "Binder extrusion in sliding wear of WC-Co alloys," *Wear*, vol. 105, no. 3, pp. 247–256, 1985.
- [14] K. J. Swick, G. W. Stachowiak, and A. W. Batchelor, "Mechanism of wear of rotary-percussive drilling bits and the effect of rock type on wear," *Tribology International*, vol. 25, no. 1, pp. 83–88, 1992.
- [15] U. Beste, E. Coronel, and S. Jacobson, "Wear induced material modifications of cemented carbide rock drill buttons," *International Journal of Refractory Metals and Hard Materials*, vol. 24, no. 1-2, pp. 168–176, 2006.
- [16] J. Larsen-Basse, "Wear of hard-metals in rock drilling: a survey of the literature," *Powder Metallurgy*, vol. 16, no. 31, pp. 1–32, 1973.
- [17] B. G. Fish, G. A. Guppy, and J. T. Ruden, "Abrasive wear effects in rotary rock drilling," *Transactions of the Institutions of Mining and Metallurgy*, vol. 63, pp. 357–383, 1959.
- [18] P. Kindermann, P. Schlund, H.-G. Sockel et al., "High-temperature fatigue of cemented carbides under cyclic loads," *International Journal of Refractory Metals and Hard Materials*, vol. 17, no. 1, pp. 55–68, 1999.
- [19] M. Lagerquist, "A study of the thermal fatigue crack propagation in WC-Co cemented carbide," *Powder Metallurgy*, vol. 18, no. 35, pp. 71–88, 1975.
- [20] U. Beste and S. Jacobson, "Friction between a cemented carbide rock drill button and different rock types," *Wear*, vol. 253, no. 11-12, pp. 1219–1221, 2002.
- [21] K. G. Stjernberg, U. Fischer, and N. I. Hugoson, "Wear mechanisms due to different rock drilling conditions," *Powder Metallurgy*, vol. 18, no. 35, pp. 89–106, 1975.
- [22] J. Larsen-Basse, C. M. Perrott, and P. M. Robinson, "Abrasive wear of tungsten carbide-cobalt composites. I. Rotary drilling tests," *Materials Science and Engineering*, vol. 13, no. 2, pp. 83–91, 1974.
- [23] J. Larsen-Basse, "Effect of composition, microstructure, and service conditions on the wear of cemented carbides," *Journal of Metals*, vol. 35, no. 11, pp. 35–42, 1983.
- [24] S. Olovsjö, R. Johanson, F. Falsafi, U. Bexell, and M. Olsson, "Surface failure and wear of cemented carbide rock drill buttons—the importance of sample preparation and optimized microscopy settings," *Wear*, vol. 302, no. 1-2, pp. 1546–1554, 2013.
- [25] A. Gupta, S. Chattopadhyaya, and S. Hloch, "Critical investigation of wear behaviour of WC drill bit buttons," *Rock Mechanics and Rock Engineering*, vol. 46, no. 1, pp. 169–177, 2013.
- [26] U. Beste and S. Jacobson, "A new view of the deterioration and wear of WC/Co cemented carbide rock drill buttons," *Wear*, vol. 264, no. 11-12, pp. 1129–1141, 2008.
- [27] 14CM Series Continuous Miner Product Review, <http://www.joyglobal.com/>.
- [28] H. Tullhoff, "Carbides. Metal like carbides of industrial importance," in *Ullmann's Encyclopedia of Industrial Chemistry*, Wiley-VCH, Weinheim, Germany, 2000.
- [29] R. K. Rajput, *A Textbook of Manufacturing Technology: Manufacturing Process*, Firewall Media, 2007.

Research Article

Preparation of N-Doped TiO₂-ZrO₂ Composite Films under Electric Field and Heat Treatment and Assessment of Their Removal of Methylene Blue from Solution

Lefu Mei, Ranfang Zuo, Jing Xie, Libing Liao, and Hao Ding

School of Material Sciences and Technology, China University of Geosciences, Beijing 100083, China

Correspondence should be addressed to Lefu Mei; mlf@cugb.edu.cn and Libing Liao; clayl@cugb.edu.cn

Received 23 July 2014; Revised 21 August 2014; Accepted 22 August 2014; Published 28 August 2014

Academic Editor: Zhaohui Li

Copyright © 2014 Lefu Mei et al. This is an open access article distributed under the Creative Commons Attribution License, which permits unrestricted use, distribution, and reproduction in any medium, provided the original work is properly cited.

TiO₂-ZrO₂ composite film with the grain size of 50 nm was synthesized by electric field and heat (EF&H) treatments. Portions of O atoms in the TiO₂ network structure were replaced by N atoms as revealed by X-ray photoelectron spectroscopy (XPS) and X-ray diffraction (XRD) analyses, suggesting formation of a nonstoichiometric compound TiO_{2-x}N_x on the composite film. The UV-Vis spectra of the film suggested that the visible light with wavelength of 550 nm could be absorbed for the N-doped composite film after EF&H treatment in comparison to a cutoff wavelength of 400 nm for the composite film without EF treatment. Photocatalytic experiments showed that the degradation rate of methylene blue by N-doped composite films increased significantly under visible light irradiation. The partial replacement of O by doped N played a very important role in narrowing the band gap and improving the visible light photocatalytic reactivity.

1. Introduction

TiO₂ films are widely used in many fields, ranging from transforming solar energy into chemical energy and electric energy to environmental remediation, including photocatalytic degradation of pollutants in atmosphere and water, sterilization, and self-cleaning, and so forth [1–3]. The TiO₂ has low thermal expansion coefficient making it inferior to metal materials that have high thermal expansion. This drawback results in a lower TiO₂ film efficacy compared to metal surfaces, and thus, limited its practical applications. TiO₂-ZrO₂ composite film has the advantages of adjustable thermal expansion rate. It can be applied to a variety of metal surface modifications. But the photocatalytic reactivity of TiO₂ under visible light condition (wavelength greater than 387.5 nm) still remains low after the addition of ZrO₂ to TiO₂. In order to utilize the visible part of the solar spectrum, or under general illumination conditions, two approaches could be undertaken with one being doping transition metals into TiO₂ [4, 5], and the other being forming defects of

TiO_x catalyst compounds [6, 7]. Although doping transition metals can improve the reactivity of TiO₂ under visible light, the TiO₂ reactivity under ultraviolet light would decrease correspondingly. In addition, the reactivity under visible light was much lower than that under UV because of the metal ions becoming the recombination centers. In addition, stability of TiO₂ would be reduced due to doping [8]. The TiO₂ reactivity under visible light condition could be increased by incorporation of nitrogen atoms into TiO₂ [9]. But, it was not until 2001, when Sato et al. [8] reported in science that substitution of a small quantity of lattice O by N could narrow the TiO₂ band gap, thus increasing the TiO₂ reactivity under visible light condition, while maintaining its UV light reactivity. This discovery attracted great attention for nonmetallic elements doped TiO₂ [10, 11].

In this paper, the N-doped TiO₂-ZrO₂ composite film with relatively high photocatalytic reactivity under visible light was prepared by a sol-gel method followed by treating the products under electric field and heat in nonequilibrium state. It is anticipated that this simple process could gain wide

popularity in the field of surface treatment of various daily use.

2. Experimental Methods

2.1. Sol Preparation. The TiO_2 sol was prepared through hydrolyzing the tetrabutyl titanate ($\text{Ti}(\text{OBU})_4$) under acidic condition. To do so, 10 mL tetrabutyl titanate (98%) was dissolved in 40 mL absolute alcohol (99.7%) and 10 mL acetyl acetone (99.9%) was added to inhibit premature hydrolyses of tetrabutyl titanate. The mixture was stirred for 30 min using a magnetic stirrer. Then, 10 mL deionized (DI) water was added slowly and the mixture stirred vigorously to form a uniform dispersion. During this process, dilute hydrochloric acid (3.6%) was continuously added to maintain the pH value of the solution at 1.8.

Similarly, the ZrO_2 sol was prepared using a molar ratio of $\text{Zr}(\text{OPr})_4$ (99%):n-propyl alcohol (99.8%):acetyl acetone:water at 1:4:2:2. A period of 12 h aging is needed for the ZrO_2 sol, before it was fully mixed with the prepared TiO_2 sol at a ratio of 1:4 (ZrO_2 sol: TiO_2 sol). Then, 1 g NH_4NO_3 (99%) was added to the mixture. The mixture was stirred for 2 h and allowed to stand for 12 hours, before being used for coating film.

2.2. Film Preparation. Silex glass with a diameter of 1.5 cm was used as the substrate for film coating at a thickness of 1 mm. The substrate was washed in ether under ultrasound and then rinsed with DI water. The cleaned substrate was dried at 80°C for 1 h in an oven. A dip-coating method with a pulling speed of 0.5 mm/s was adopted. After dip-coating the substrate was dried in an oven at 80°C for 4 h. The dried sample was placed in electric furnace (Figure 1) and treated under external direct current electric field with voltages of 0 or 600 V, respectively (the calculated electric field strength was 0 or 6000 V/cm). Heat treatment was carried out in N_2 atmosphere at 500°C for 1 h.

2.3. Photocatalytic Performance. The performance of the N-doped TiO_2 - ZrO_2 composite film was evaluated by assessing the photocatalytic degradation of methylene blue (MB) in 10 mg/L. The N-doped TiO_2 - ZrO_2 composite film was added to 100 mL MB solutions of 10 mg/L followed by exposure to different light sources for 3 h. The tests were conducted under a wavelength irradiation of 365 nm created by a high pressure mercury lamp or under continuous wavelength ranging from 400 to 760 nm generated by a 40 W fluorescent lamp. The residual MB concentration in solution was measured at the maximum absorption wavelength of 660 nm using the UV-1901 type UV-Vis spectrophotometer. The MB removal was determined by the differences between the initial and equilibrium MB concentrations.

2.4. Instrumentation Analyses. The XPS was obtained using the PHI5300 type X-ray photoelectron spectrometer; the X-ray diffraction was performed by a D/max-rB X-ray diffractometer; the UV-Vis diffuse reflectance spectrogram was

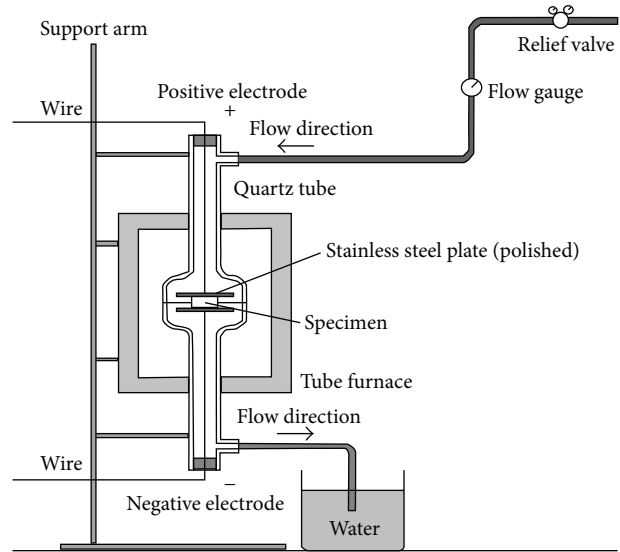


FIGURE 1: The heating apparatus and specimen arrangement.

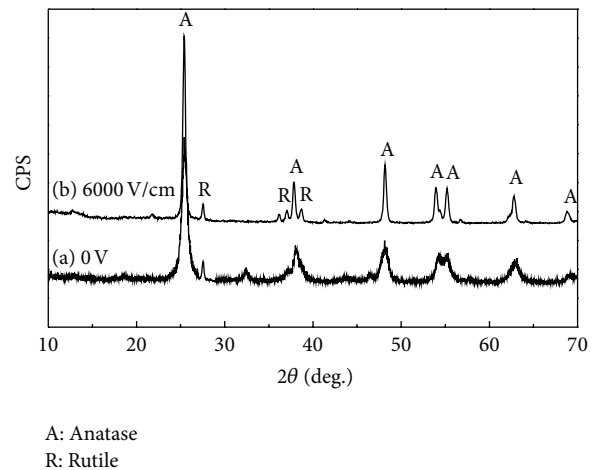


FIGURE 2: X-ray diffraction patterns of the composite film annealed at 500°C for 1 h: (a) 0 V and (b) 6000 V/cm.

recorded by the UV-1901 ultraviolet visible spectrophotometer. The surface morphology of the films was observed by the JSM-6301F scanning electron microscope (SEM).

3. Results and Discussion

3.1. Phase Analyses of the Doped Film. Figure 2 showed the XRD patterns of the composite film with heat treatment in the presence and absence of electric field. Without EF treatment, the phase of the film was mainly made of anatase with trace amount of rutile. The rutile phase increased substantially in the composite film after EF&H treatment, suggesting that the external EF promoted crystal transformation on the film. Moreover, the crystallinity of the composite film increases significantly after EF treatment. Meanwhile, no TiN phase was observed in the two XRD patterns (Figure 2).

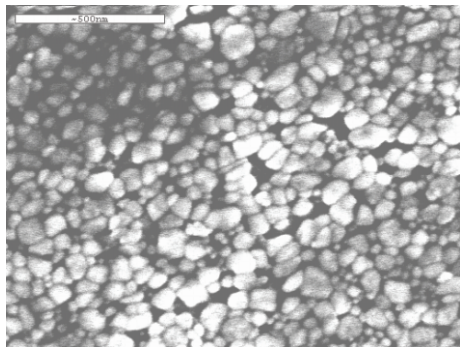


FIGURE 3: SEM surface micrograph of the samples after EF&H treatment at 6000 V/cm and 500°C for 1 h.

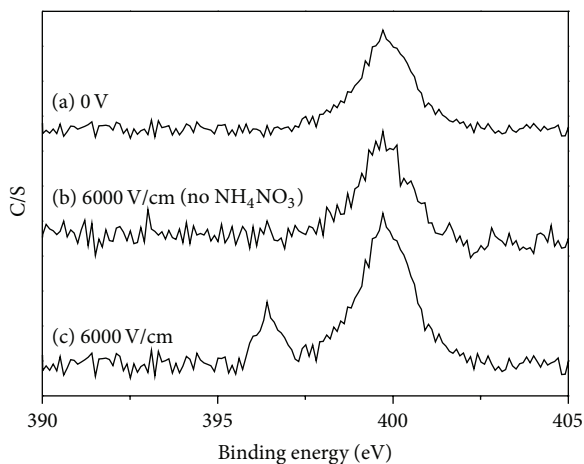


FIGURE 4: XPS of the N1s in composite film treated at 500°C for 1 h: (a) 0 V, (b) 6000 V/cm (no NH_4NO_3) and (c) 6000 V/cm with addition of NH_4NO_3 .

3.2. The Mean Grain Size of the Films. After EF&H treatment the mean grain size of the film surface was about 50 nm as revealed by the SEM micrograph of the composite film (Figure 3).

3.3. XPS Energy Spectrum Analysis. The XPS energy spectra of N1s of the composite film produced in the absence and presence of EF are shown in Figures 4(a) and 4(c). Figure 4(a) shows a peak shoulder at 399.7 eV and Figure 4(c) shows two peak shoulders at 399.7 eV and 396.4 eV, respectively. The binding energy at 399.7 eV indicates the presence of gap state of N element and the binding energy at 396.4 eV corresponded to the Ti-N bond or the O-Ti-N bond [12]. As the XRD analysis did not reveal the TiN phase, the chemical bond corresponding to the peak at 396.4 eV should be assigned to O-Ti-N bond instead of Ti-N bond, which suggested the formation of nonstoichiometric compounds $\text{TiO}_{2-x}\text{N}_x$ in the composite film prepared under EF&H treatment. This suggested that N successfully replaced some of the O atoms near the surface region of the O-Ti-O network under DF&H treatment, forming the N-Ti-O network. Because of the slight difference in electronegativity between

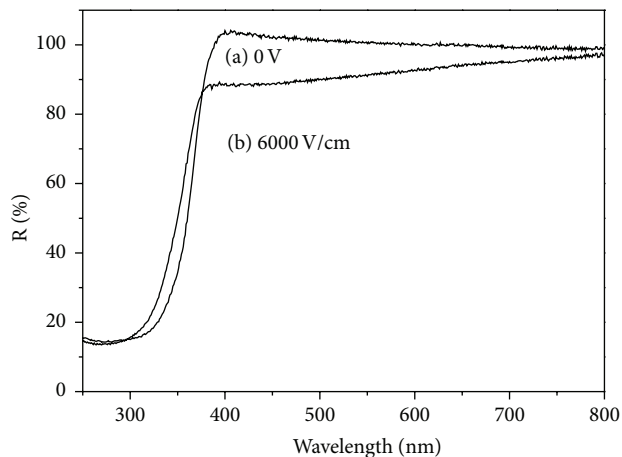


FIGURE 5: UV-Vis DRS of the composite film annealed at 500°C for 1 h: (a) 0 V and (b) 6000 V/cm.

O and N atoms, the electron cloud had a small tendency deflecting towards O atoms, resulting in a slight decrease in the electronic cloud density of N atom. Figure 4(b) is the XPS curve of N1s in the coextruded film prepared under the same EF&H condition without addition of NH_4NO_3 . Only a peak shoulder at 399.7 eV was observed, suggesting the absence of nonstoichiometric compounds $\text{TiO}_{2-x}\text{N}_x$. In comparison to Figures 4(a) and 4(c), the N element in the $\text{TiO}_{2-x}\text{N}_x$ was derived from NH_4NO_3 .

3.4. UV-Vis Spectra of the Thin Film. Figure 5 is the UV-Vis DRS of the composite film without EF and with EF of 6000 V/cm at 500°C heat treatment for 1 h. The composite film prepared without external EF showed no absorption of light whose wavelength was above 400 nm. In comparison, the visible light with wavelength of 550 nm can be absorbed by the composite film prepared with EF&H treatment and contained $\text{TiO}_{2-x}\text{N}_x$, suggesting a red shift in the absorption edge. This red shift of the absorption edge could be attributed to the increased photocatalytic reactivity of the N-doped $\text{TiO}_2\text{-ZrO}_2$ composite film under visible light after EF&H treatment.

3.5. Photocatalytic Performance. Photocatalytic performance test was conducted on the composite film produced in the absence and presence of EF. The degradation rate of MB is listed in Table 1. The degradation rate of composite film prepared under EF of 6000 V/cm was higher than that prepared in the absence of EF. Under the irradiation condition of 365 nm by the high-pressure mercury lamp, the MB degradation rate by the film after EF&H treatment was as high as 95%. Under the irradiation by 40 W fluorescent lamp, the degradation rate was as high as 83%, in comparison to only 39% without treatment. This result showed that the composite film prepared under EF&H treatment possessed excellent visible light catalytic reactivity.

TABLE 1: Degradation rate of the coextruded film annealed at 500°C for 3 h: (a) 0 V and (b) 6000 V/cm.

Sample	Degradation rate (%)	
	Fluorescent lamp (40 W)	High-voltage mercury lamp (365 nm)
(a) 0 V	39	91
(b) 6000 V/cm	83	95

4. Discussion

The improved performance of photocatalytic degradation of MB by the film under visible light condition could be attributed to the following effects. Doping of the film in N_2 atmosphere generated $TiO_{2-x}N_x$ in the presence of EF&H treatment, which increased the impurity levels and decreased the band gap of TiO_2 [8]. Doping of N can narrow band gap as the increase in impurity level could result in band gap reduction of TiO_2 after mixing the 2p state of N atom and 2p state O atom. Theoretical calculation shows that the red shift of absorption edge could be achieved via N-doping. This is mainly due to the potential transition of N atoms to d_{xy} state of Ti by replacing the electrons of $2p\pi$ state in TiO_2 [8, 13]. Additionally, doping of N could generate Ti^{3+} on the surface of TiO_2 film. As the Ti^{3+} on the surface increases, the Fermi level of TiO_2 increases, resulting in an increase in light absorbing potential for catalyst.

5. Conclusion

The EF promoted the phase transformation. When the external EF is 6000 V/cm and the heat treatment is 500°C for 1 h, $TiO_{2-x}N_x$ was generated in the ZrO_2 - TiO_2 composite film. The XPS and XRD analyses indicated that partial N atoms appear in TiO_2 resulting from the replacement of O by N atoms. The composite film containing $TiO_{2-x}N_x$ could absorb visible light around 550 nm, as reviewed by the UV-Vis DRS analyses. The N-doped ZrO_2 - TiO_2 composite had a higher UV and visible light catalytic reactivity. The doped N partially replaced O, which plays a very significant role in narrowing the band gap and improving the photocatalytic reactivity of the film under visible light conditions.

Conflict of Interests

The authors declare that there is no conflict of interests regarding the publication of this paper.

Acknowledgment

This present work was supported by the Fundamental Research Funds for the Central Universities (Grant no. 2652013043).

References

- [1] A. Fujishima and K. Honda, "Electrochemical photolysis of water at a semiconductor electrode," *Nature*, vol. 238, no. 5358, pp. 37–38, 1972.
- [2] M. R. Saleem, P. Silfsten, S. Honkanen, and J. Turunen, "Thermal properties of TiO_2 films grown by atomic layer deposition," *Thin Solid Films*, vol. 520, no. 16, pp. 5442–5446, 2012.
- [3] B. Barrocas, O. C. Monteiro, M. E. M. Jorge, and S. Sério, "Photocatalytic activity and reusability study of nanocrystalline TiO_2 films prepared by sputtering technique," *Applied Surface Science*, vol. 264, pp. 111–116, 2013.
- [4] R. Su, R. Bechstein, J. Kibsgaard, R. T. Vang, and F. Besenbacher, "High-quality Fe-doped TiO_2 films with superior visible-light performance," *Journal of Materials Chemistry*, vol. 22, no. 45, pp. 23755–23758, 2012.
- [5] M. Khan, J. N. Xu, W. B. Cao, and Z. K. Liu, "Mo-doped TiO_2 with enhanced visible light photocatalytic activity: a combined experimental and theoretical study," *Journal of Nanoscience and Nanotechnology*, vol. 14, p. 6865, 2014.
- [6] M. Khan, Y. Song, N. Chen, and W. Cao, "Effect of v doping concentration on the electronic structure, optical and photocatalytic properties of nano-sized V-doped anatase TiO_2 ," *Materials Chemistry and Physics*, vol. 142, no. 1, pp. 148–153, 2013.
- [7] Y. X. Wang, H. Liu, Z. Q. Li, X. X. Zhang, R. K. Zheng, and S. P. Ringer, "Role of structural defects on ferromagnetism in amorphous Cr-doped TiO_2 films," *Applied Physics Letters*, vol. 89, no. 4, 2006.
- [8] S. Sato, R. Asahi, T. Morikawa, T. Ohwaki, K. Aoki, and Y. Taga, "Photocatalysts sensitive to visible light," *Science*, vol. 295, no. 5555, pp. 626–627, 2002.
- [9] S. Sato, "Photocatalytic activity of NO_x -doped TiO_2 in the visible light region," *Chemical Physics Letters*, vol. 123, no. 1-2, pp. 126–128, 1986.
- [10] J. L. Gole, J. D. Stout, C. Burda, Y. Lou, and X. Chen, "Highly efficient formation of visible light tunable $TiO_{2-x}N_x$ photocatalysts and their transformation at the nanoscale," *Journal of Physical Chemistry B*, vol. 108, no. 4, pp. 1230–1240, 2004.
- [11] M. Maeda and T. Watanabe, "Visible light photocatalysis of nitrogen-doped titanium oxide films prepared by plasma-enhanced chemical vapor deposition," *Journal of the Electrochemical Society*, vol. 153, no. 3, pp. C186–C189, 2006.
- [12] K. Tanaka, K. Kashima, K. Hirao, N. Soga, A. Mito, and H. Nasu, "Second harmonic generation in electrically poled $Li_2ONb_2O_5TeO_2$ glasses," *Journal of Non-Crystalline Solids*, vol. 185, no. 1-2, pp. 123–126, 1995.
- [13] R. Asahi, Y. Taga, W. Mannstadt, and A. J. Freeman, "Electronic and optical properties of anatase TiO_2 ," *Physical Review B*, vol. 61, no. 11, pp. 7459–7465, 2000.

Research Article

Experimental Study and Numerical Solution of Poly Acrylic Acid Supported Magnetite Nanoparticles Transport in a One-Dimensional Porous Media

M. Golzar,¹ S. F. Saghravani,¹ and M. Azhdari Moghaddam²

¹ Department of Civil Engineering, University of Shahrood, Shahrood 3619995161, Iran

² Department of Civil Engineering, University of Sistan and Baluchestan, Zahedan, Iran

Correspondence should be addressed to M. Golzar; golzarmohsen@yahoo.com

Received 3 March 2014; Revised 30 May 2014; Accepted 2 June 2014; Published 23 June 2014

Academic Editor: Zhaohui Li

Copyright © 2014 M. Golzar et al. This is an open access article distributed under the Creative Commons Attribution License, which permits unrestricted use, distribution, and reproduction in any medium, provided the original work is properly cited.

Recently, iron nanoparticles have attracted more attention for groundwater remediation due to its potential to reduce subsurface contaminants such as PCBs, chlorinated solvents, and heavy metals. The magnetic properties of iron nanoparticles cause to attach to each other and form bigger colloid particles of iron nanoparticles with more rapid sedimentation rate in aqueous environment. Using the surfactants such as poly acrylic acid (PAA) prevents iron nanoparticles from forming large flocs that may cause sedimentation and so increases transport distance of the nanoparticles. In this study, the transport of iron oxide nanoparticles (Fe_3O_4) stabilized with PAA in a one-dimensional porous media (column) was investigated. The slurries with concentrations of 20, 100 and 500 (mg/L) were injected into the bottom of the column under hydraulic gradients of 0.125, 0.375, and 0.625. The results obtained from experiments were compared with the results obtained from numerical solution of advection-dispersion equation based on the classical colloid filtration theory (CFT). The experimental and simulated breakthrough curves showed that CFT is able to predict the transport and fate of iron oxide nanoparticles stabilized with PAA (up to concentration 500 ppm) in a porous media.

1. Introduction

There are various compositions of iron nanoparticles with wide range of applications in environmental engineering, especially in contaminant removal processes. One of the advantages of using iron nanoparticles for in situ processes is that they can be injected directly into the environment and contrary to millimetric iron particles, so there is no need for underground installation as in the case of permeable reactive barriers (PRBs) that makes it economically affordable [1]. Moreover, the extremely large specific surface area (SSA) of nanoparticles provides a much higher surface reactivity compared to the more widely used millimetric iron [2–4].

Nanoscale zerovalent iron (NZVI) has demonstrated high reactivity in remediation of aquifers contaminated by nonaqueous phase liquids, heavy metals, and other hazardous compounds. However, observations in laboratory and field scales disclosed the fact that the application of NZVI

in porous media faces critical problems including short travel distances, pore plugging, and significant loss of porosity and permeability especially when used in high concentrations [5, 6]. This is attributed to the strong tendency of NZVI bare particles to aggregation, agglomeration, and consequent rapid settlement or filtration on the solid phase surface [7]. Researches showed that bare iron nanoparticles may travel in porous media only a few centimeters from the injection point under typical groundwater conditions [8, 9]. To overcome this limitation and to improve NZVI transport in porous media, researchers have used electrostatic, steric, and depletion stabilization mechanisms generating stabilized NZVI colloids by stabilizers like polystyrene sulfonate (PSS), carboxymethyl cellulose (CMC), poly acrylic acid (PAA), triblock, xanthan gum, and emulsified iron [10–15].

Phenrate et al. [16, 17] examined transport of poly-electrolyte-stabilized NZVI at different particle concentration (0.03, 0.3, 1, 3 and 6 g/L) in saturated sand column.

They demonstrated that slurry with low concentrations is in agreement with the assumptions of CFT model. In the slurries with higher concentrations ($C > 1 \text{ g/L}$), they modified CFT model by providing empirical corrections. The empirical corrections are capable of estimating the agglomerate size and deposition during injection of slurry of polyelectrolyte-stabilized NZVI of high particle concentration in saturated sand [16, 17]. In the CFT model, the removal of suspended particles is described by first-order kinetics, resulting in concentrations of suspended and retained particles that decay exponentially with distance [18, 19]. In addition, other researchers such as Tosco et al. and Hosseini et al. [20, 21] developed another form of nanoparticles transport model that can be considered the pore blocking, clogging, and ripening processes during transport in porous media.

In addition to NZVI, iron oxide nanoparticles (Fe_3O_4) can also be used in remedial processes for environmental engineering purposes. Although iron oxides nanoparticles have less reactivity than NZVI, the use of iron oxides nanoparticles, as powerful adsorbents and more stable to oxidation in groundwater treatment, provides a convenient approach for contaminant remediation. In addition, iron oxide nanoparticles can be easily separated and collected by applying external magnetic fields. Hu et al. [22] have used nanoparticles of iron oxide (Fe_3O_4) in order to remove Cr(VI) from an aqueous media through absorption process. Also, Su and Puls and Yavuz et al. [23, 24] showed that iron oxides nanoparticles can be effective in the removal of arsenic from groundwater through the sorption of arsenite ($\text{As}(\text{III})$) on the magnetite surface. Moreover, iron oxide nanoparticles were shown to be effective sorbents for a number of other heavy metals such as Hg, Ag, Pb, Cd, and Ti [25]. In addition, iron oxides nanoparticles can promote the transformation of carbon tetrachloride [26, 27]. Pan et al. [28] showed that iron oxides nanoparticles stabilized with sodium carboxymethyl cellulose can immobilize phosphorous in soils.

The objective of this study is to investigate the transport of iron oxide nanoparticles (Fe_3O_4) stabilized with poly acrylic acid (PAA) in one-dimensional porous media. Transport tests in columns packed with glass beads were performed by injecting the iron oxide nanoparticles (Fe_3O_4) stabilized with poly acrylic acid dispersed in deionized water with different concentrations ($C_0 = 20, 100, \text{ and } 500 \text{ ppm}$) and injection rates (hydraulic gradients = 0.125, 0.375, and 0.625 which represents 9 Darcian velocity due to the difference in viscosity of slurries). This research aimed to contribute to a better understanding of important parameters in the transport of the nanoparticles in porous media by providing the experimental data in order to evaluate the proposed model for nanoparticles transport. The experimental results were further analyzed by using a numerical one-dimensional model of advection-dispersion transport equation based on the classical colloid filtration theory (CFT).

2. Methodology

2.1. Materials. All chemicals used in these experiments were laboratory grade. Nano iron oxide (Fe_3O_4) was obtained

From Pasteur Institute of Iran with 99.5% purity and average particle size of 44.5 nanometers. For determination of particle size distribution of the nano iron oxide (Fe_3O_4), particle size distribution test has been conducted. The results are shown in Figure 1(a). The existence of trivalent iron nanoparticles has been investigated using X-ray diffraction (XRD) device with 40 KV energy, 30 mA current, and copper anodes and the results are presented in Figure 1(b). Poly acrylic acid (PAA, mean M.W. = 1.8 kg/mole) was purchased from Sigma Aldrich Company. Both materials (nano iron oxide (Fe_3O_4) and poly acrylic acid) were in the powder form.

2.2. Synthesize a Slurry of Iron Oxide Nanoparticles Stabilized with PAA. Three slurries of iron oxide nanoparticles, with the concentrations of 20, 100, and 500 mg/L stabilized with poly acrylic acid. The optimum weight ratio of 2:1 (1 g nano iron oxide and 2 g poly acrylic acid) was selected based on findings by Saghraani et al. [29]. Preparation process included several steps as follows. The required iron oxide nanoparticles were placed in a flask and then distilled water was added up to one-fifth of the final volume of required slurry solution. The flask was put in an ultrasonic shaker (40 KHz frequency, 50 W power) for 5 periods of 6 minutes shaking and 1 minute rest to obtain a uniform mixture. Having PAA twice the weight of nano Fe_3O_4 in another flask, the remaining volume of distilled water was added to have the desired concentration and then placed on a shaker, 500 rpm for 1 hour. The solutions were added to each other and placed in the ultrasonic shaker for another 1 hour. The result was a uniform solution of stabilized nano iron oxide with PAA. The solution was kept in the room temperature for another 24 hours and was shaken with an ultrasonic shaker for another half an hour before conducting the experiments. In order to specify the particle size distribution of iron oxide nanoparticles stabilized with PAA, samples were from the solutions of different concentrations. Using the particle size distribution test, the variation of amplitude and the average size of particles were specified. Figure 2 illustrates the particle size distribution in the samples. Zeta potential was measured in order to investigate the stability of the nanoparticles in the fluid. Since absolute value of zeta potential is greater than 30 for all samples ($|\zeta| \geq 30$), it can be concluded that slurries of iron oxide nanoparticles stabilized with PAA were stable (Table 1). By summarizing the data provided in Table 1 and Figure 2 one can conclude that the size of particles would remain in the nano range after addition of PAA.

2.3. Porous Media. The experiments were conducted in a pyrex glass column with internal diameter of 3.5 cm and 40 cm height. The column was filled with glass bead (8–20 mesh, average diameter $d_{50} = 1.8 \text{ mm}$). Two porous glass diffuser plates with 1 cm height were placed on each end of pyrex glass column to provide an even distribution of iron oxide nanoparticles stabilized with PAA in the experiment column. The pore (void) volume was measured at 110 mL then the porosity was calculated to be 0.30. For all tests, the column was prewashed with 2.2 L (20 times of pore volume) of 0.5 normal HCL and then washed through with distilled water

TABLE 1: Average diameter of iron oxide nanoparticles stabilized with PAA and zeta potential (ζ) in slurries with concentrations (A) 20, (B) 100, and (C) 500 mg/L.

Concentration (mg/L)	Average diameter of iron oxide nanoparticles stabilized with PAA (nm)	Zeta potential (ζ) (mV)
Bare nanoparticles	44.52	-23.88
Nanoparticles stabilized with PAA		
20	85.14	-30.37
100	51.30	-46.44
500	48.99	-51.10

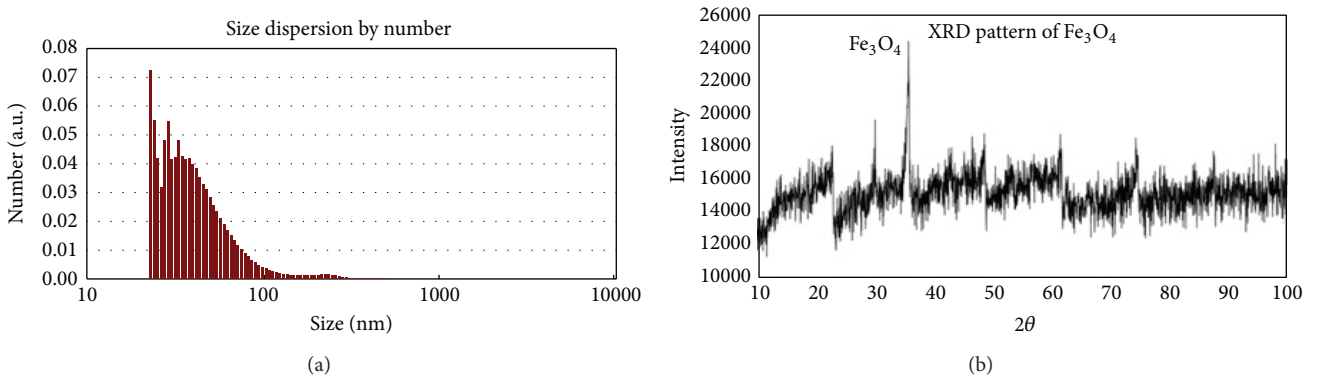


FIGURE 1: Diagram of size distribution of iron oxide nanoparticles (Fe₃O₄) and the result of XRD analysis of iron oxide nanoparticles (Fe₃O₄).

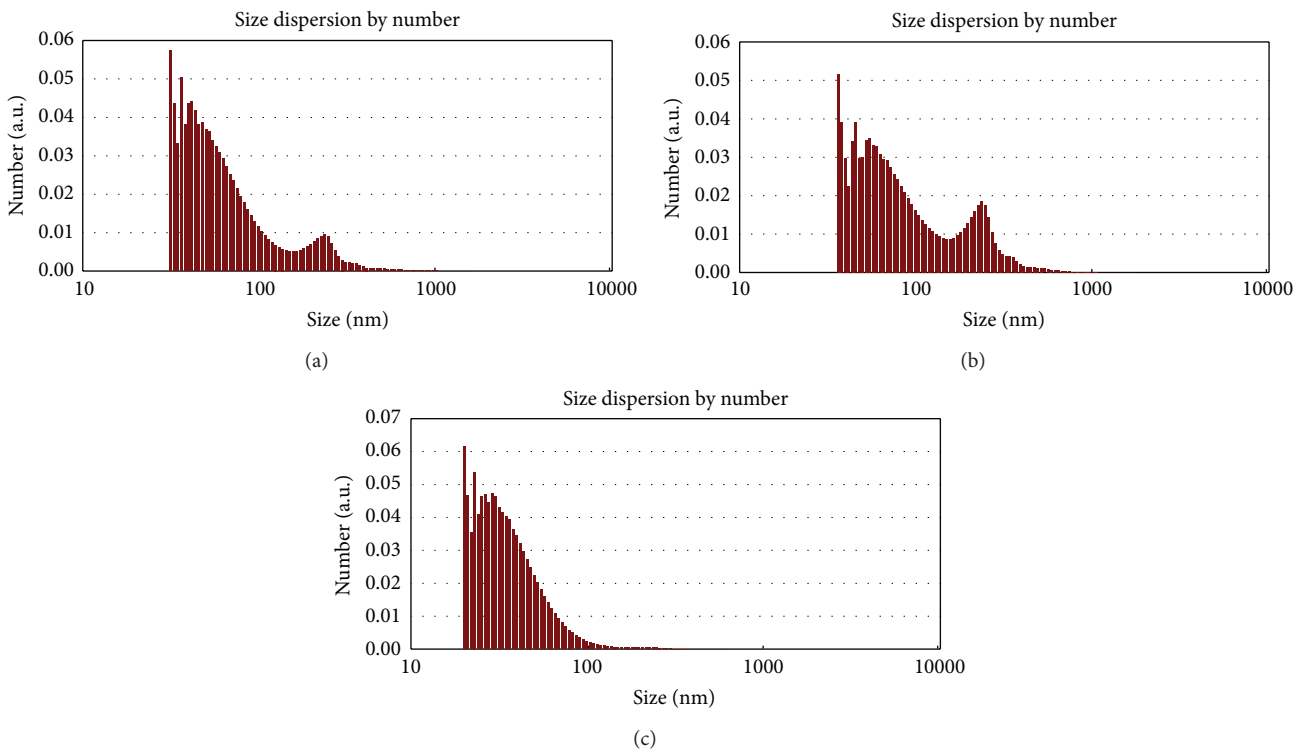


FIGURE 2: Diagram of size distribution of iron oxide nanoparticles stabilized with PAA in slurries with concentrations (a) 20, (b) 100, and (c) 500 mg/L.

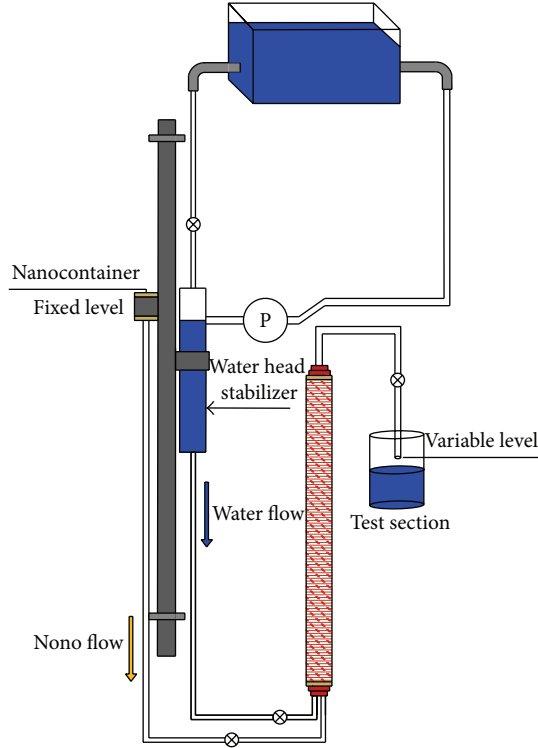


FIGURE 3: Schematic of the experimental setup.

until pH = 7 was confirmed in effluent so that we obtained a uniform, homogenous, and saturated porous media.

2.4. Transport Experiment. In these experiments 220 mL (approximately two times of empty pores volume) of iron oxide nano slurries stabilized with PAA (with different concentrations of 20, 100, and 500 ppm) was injected to the porous media by applying hydraulic gradients equal to 0.125, 0.375, and 0.625. The injections of water and slurry of iron oxide nanoparticles were made separately from the bottom of the column to avoid the errors due to trapped air bubbles. Simultaneously, from the beginning of the injection, samples were taken from the effluent at equal time intervals. Concentrations nanoparticles in the samples were measured through spectrophotometry by Jenus UV 1200-Spectrophotometer. The breakthrough curves for the concentration (of nanoparticles (C/C_0) versus time) for all tests were then plotted (Figure 3). Each experiment was repeated three times and the breakthrough curves were provided based on the average of the concentration of samples.

2.5. The Advection-Dispersion Equation with Respect to Surface Absorption Conditions. The temporal and spatial variations of colloid concentration in a homogenous, granular porous media are described by the advection-dispersion equation:

$$\frac{\partial C}{\partial t} = D \frac{\partial^2 C}{\partial x^2} - U \frac{\partial C}{\partial t}. \quad (1)$$

Here, C is the colloid concentration in the aqueous phase at a distance of x and time t , U is the interstitial particle velocity, and D is the hydrodynamic dispersion coefficient. In (1), only the physical transport processes of advection and hydrodynamic dispersion are considered. In granular media, colloids are removed from the fluid-phase by physico-chemical filtration or attachment to sediment grain surfaces. Physicochemical filtration of microbes has been modeled as either an irreversible (no detachment) or reversible process. In the case of reversible attachment, both equilibrium and kinetic mechanisms have been considered [30]. When an attachment mechanism is used to describe removal of particles from the liquid phase, the general equation for colloid transport and fate in a one-dimensional, homogeneous, granular porous media becomes

$$\frac{\partial C}{\partial t} + \frac{\rho_b}{\varepsilon} \frac{\partial S}{\partial t} = D \frac{\partial^2 C}{\partial x^2} - U \frac{\partial C}{\partial t}, \quad (2)$$

where S is the retained particle concentration, ρ_b is the dry bulk density of the porous media, and ε is the porosity.

In the classical colloid filtration theory (CFT), originally presented in 1971 [30], the attachment of colloids to sediment surfaces is considered irreversible, neglecting the release of particles [31]. Thus the equation based on CFT can be written as

$$\frac{\rho_b}{\varepsilon} \frac{\partial S}{\partial t} = K_d C, \quad (3)$$

where K_d is the particles sedimentation rate coefficient (or the particle attachment rate coefficient). Considering the effect of the attachment of colloids to sediment surfaces, (2) for colloid transport and fate in a one-dimensional, homogeneous, granular porous media based on the classical colloid filtration theory (CFT) becomes

$$D \frac{\partial^2 C}{\partial x^2} - U \frac{\partial C}{\partial x} - K_d C = \frac{\partial C}{\partial t}, \quad (4)$$

where the particle attachment rate coefficient is related to η_0 and α via [18]. Consider

$$K_d = \frac{3(1-\varepsilon)U}{2d_c} \alpha \eta_0. \quad (5)$$

Here, d_c is the average sediment particles size. Due to limitations in the proposed theory for predicting the attachment efficiency (α), measurement techniques are usually employed instead [18]. The normalized fluid-phase colloid concentration (C/C_0) at the length $x = L$ were calculated after the measured values of C_0 were obtained. Then the attachment efficiency (α) can be calculated using (6). In this work, the theoretical value of the single-collector contact efficiency (η_0) was calculated by using a closed-form of the equation and data from Table 2 [18, 30]. Consider

$$\alpha = \frac{-2d_c}{3(1-\varepsilon)L\eta_0} \ln \left(\frac{C}{C_0} \right). \quad (6)$$

TABLE 2: Required values of data for calculation of the single collector content efficiency (η_0).

d_c (mm)	d_p (nm)			A (j)	μ (Pa·s)			P_p (g/cm ³)	D_ω (m ² /s)
	20 (ppm)	100 (ppm)	500 (ppm)		20 (ppm)	100 (ppm)	500 (ppm)		
1.8	85.14	51.30	48.99	2.1×10^{-19}	0.0106	0.00713	0.0106	5.1	5.7×10^{-13}

TABLE 3: The values of particles sedimentation rate coefficient (K_d) and hydrodynamic dispersion coefficient (D) calculated for each experiment.

Test number	Concentration (ppm)	Density of slurry (g/cm ³)	ε	Hydraulic gradients	U_0 (m/s)	C/C_0	K_d (1/s)	D (m ² /s)
1	20	1.005	0.3	0.125	0.000800	0.88	0.000256	9.000×10^{-7}
2	20	1.005	0.3	0.375	0.001950	0.90	0.000514	1.020×10^{-6}
3	20	1.005	0.3	0.625	0.002650	0.95	0.000340	2.500×10^{-5}
4	100	1.021	0.3	0.125	0.000253	0.93	0.000046	9.250×10^{-8}
5	100	1.021	0.3	0.375	0.000400	0.95	0.000051	1.000×10^{-6}
6	100	1.021	0.3	0.625	0.001000	0.97	0.000076	2.000×10^{-6}
7	500	1.045	0.3	0.125	0.000172	0.90	0.000045	7.500×10^{-7}
8	500	1.045	0.3	0.375	0.000340	0.88	0.000109	1.500×10^{-7}
9	500	1.045	0.3	0.625	0.000480	0.92	0.000100	1.750×10^{-6}

Substituting (6) into (5), the particle attachment rate coefficient (K_d) can be expressed in a simpler form as shown in the following:

$$\begin{aligned}
K_d &= \frac{3(1-\varepsilon)U}{2} \frac{1}{d_c} \alpha \eta_0 \\
&= \frac{3(1-\varepsilon)U}{2} \frac{1}{d_c} \times \left(\frac{-2d_c}{3(1-\varepsilon)L\eta_0} \ln\left(\frac{C}{C_0}\right) \right) \times \eta_0 \quad (7) \\
&= -\frac{U}{L} \times \ln\left(\frac{C}{C_0}\right).
\end{aligned}$$

To have an initial guess about hydrodynamic dispersion coefficient (D) with regard to the experimental data plotted as a breakthrough curve, the method proposed by Charbeneau was employed [32]. In this method, the time values (on the abscissa) changed to a dimensionless parameter, ξ , and $\xi = (T-1)/\sqrt{2T}$ and $T = tU/L$. U is the interstitial particle velocity, L is the length of the column, and t is time from the beginning of the experiment. The breakthrough curves (BTC) then were redrawn with ξ on abscissa and normalized fluid-phase colloid concentration at output column experiment (C/C_0) on the ordinate. Initial approximate values for the hydrodynamic dispersion coefficients (D) were obtained from (8) (Table 3). After having initial guess of value of hydrodynamic dispersion coefficient (D), it was used as the initial value for the numerical solution of the advection-dispersion equation. The simulated and experimentally obtained breakthrough curves were plotted in the same diagram then any further justifications needed to reach to a match were performed. Consider

$$D = \frac{UL}{4} (\xi_{0.84} - \xi_{0.16}). \quad (8)$$

Here, $\xi_{0.84}$, $\xi_{0.16}$: the values of ξ when the ratios (C/C_0) are equal to 0.84 and 0.16, respectively

2.5.1. Discretization Method and Numerical Solution of the Advection-Dispersion Equation. The transport equation for the classical colloid filtration theory (CFT) (4) was nondimensionalized as follows:

$$\begin{aligned}
D^* &= \frac{D}{LU_0}, & K_d^* &= \frac{K_d L}{U_0}, \\
U^* &= \frac{U}{U_0}, & C^* &= \frac{C}{C_0}, \\
X^* &= \frac{X}{L}, & t^* &= \frac{tU_0}{L}.
\end{aligned} \quad (9)$$

U_0 is the interstitial particle velocity, L is the length of the column, t is time from the beginning of the experiment, and C_0 is fluid-phase colloid concentration. Hence,

$$D^* \frac{\partial^2 C^*}{\partial x^{*2}} - U^* \frac{\partial C^*}{\partial x^*} - K_d^* C^* = \frac{\partial C^*}{\partial t^*}. \quad (10)$$

Laasonen method, which is unconditionally stable, was employed to solve (10). The Laasonen method uses the second-order central difference approximation for space derivatives and the first-order forward approximation for time derivate. With discretization of derivatives and further simplifications, (10) was converted to (11) which was solved through tridiagonal system of equations by applying appropriate boundary and initial conditions for each experiment. The results of the numerical solutions were drawn accordingly [33]. Consider

$$\begin{aligned}
&\left[-\frac{D^* \Delta t^*}{\Delta x^{*2}} - \frac{U^* \Delta t^*}{2\Delta x^*} \right] C_{i-1}^{*n+1} \\
&+ \left[1 + \frac{2D^* \Delta t^*}{\Delta x^{*2}} + K_d^* \Delta t^* \right] C_i^{*n+1} \\
&+ \left[-\frac{D^* \Delta t^*}{\Delta x^{*2}} + \frac{U^* \Delta t^*}{2\Delta x^*} \right] C_{i+1}^{*n+1} = C_i^{*n}.
\end{aligned} \quad (11)$$

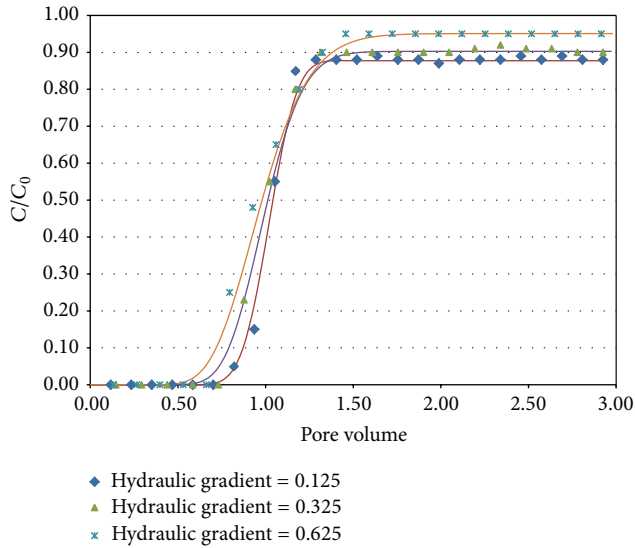


FIGURE 4: The normalized breakthrough curves (C/C_0) of iron oxide slurry stabilized with poly acrylic acid at concentration 20 ppm. Colored symbols and lines indicate the observed and simulated values, respectively.

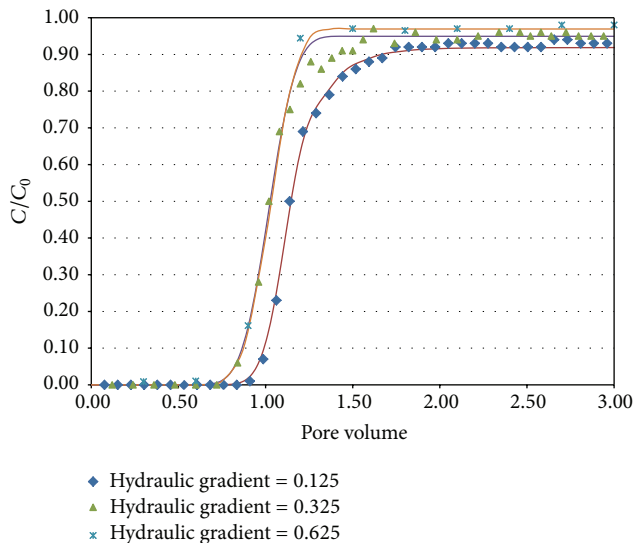


FIGURE 5: The normalized breakthrough curves (C/C_0) of iron oxide slurry stabilized with poly acrylic acid at concentration 100 ppm. Colored symbols and lines indicate the observed and simulated values, respectively.

3. Results

Figures 4, 5, and 6 demonstrate the breakthrough curves obtained from the experiments of transport of iron oxide slurry stabilized with PAA, in different concentrations under variety of hydraulic gradients along with the simulated breakthrough curves obtained from numerical solution of the advection-dispersion equation with corresponding initial and appropriate boundary conditions for each experiment. All breakthrough curves, obtained from laboratory tests

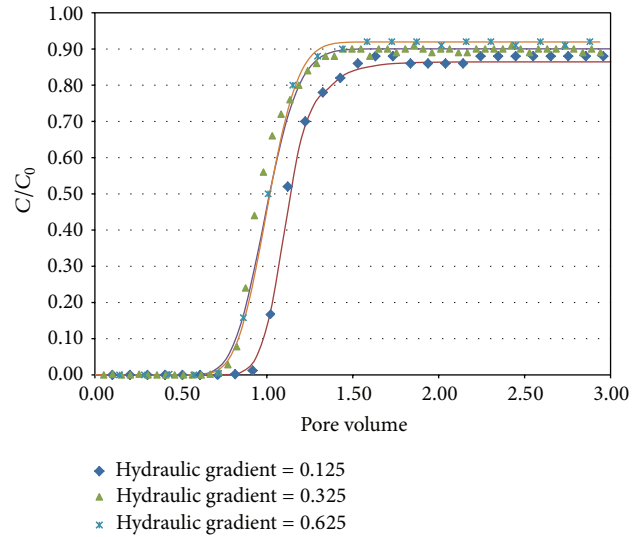


FIGURE 6: The normalized breakthrough curves (C/C_0) of iron oxide slurry stabilized with poly acrylic acid at concentration 500 ppm. Colored symbols and lines indicate the observed and simulated values, respectively.

and the numerical simulations, are in a good agreement which indicates the classical colloid filtration theory (CFT) has the ability of prediction of the transport and fate of iron oxide nanoparticles (Fe_3O_4) stabilized with poly acrylic acid. As seen in Figures 4–6 an increase in the hydraulic gradients of injection of slurry inflow into the experiment column, causes the increase in the ratio of (C/C_0) in the outflow from the experiment column. The agglomerate size is a result of the balance between van der Waals forces and magnetic attractions between iron oxide nanoparticles, electrostatic repulsive forces from the adsorbed PAA, and the induced fluid shear in the pore spaces. The agglomerates then transport and deposit onto a surface of collector (e.g., a sand grain). The agglomerates with large size yield higher attachment efficiency because the drag force due to the fluid flow (which promotes detachment) is less than the adhesive force which promotes particle attachment when the size of the retained particles/agglomerates increases. Increasing the hydraulic gradients of slurry inflow to the experiment column (increasing injection rates) reduces the possibility of the formation of large agglomerate due to higher shear force applied from the fluid. Hence in a high-speed flow field the size of agglomerates is less than in low-speed flow fields. Increasing injection rates lead to greater drag forces of the fluid therefore causes more absorbed agglomerates remove of surface of collectors, and it can lead to increase of ratio of C/C_0 at outflow.

4. Conclusions

In this study, the transport of iron oxide nanoparticles (Fe_3O_4) stabilized with poly acrylic acid in saturated porous media under different hydraulic heads was investigated. Based on the characterizations of the slurry, breakthrough

tests, and numerical simulation, the following conclusions can be made.

- (1) A good prediction of transport and fate of iron oxide nanoparticles (Fe_3O_4), stabilized with poly acrylic acid in a 1D porous media, can be obtained from numerical solution of advection-dispersion equation based on the classical colloid filtration theory (CFT).
- (2) The particles sedimentation rate coefficient (K_d) can be calculated based on the CFT to predict the effluent concentration of the slurry.
- (3) Increasing hydraulic gradient causes the rate of media absorption to decrease, which in turn makes its transfer to the polluted area more feasible.
- (4) The capability of Charboneau's method for prediction of hydrodynamic dispersion coefficient (D) was verified for slurries.

Conflict of Interests

The authors declare that there is no conflict of interests regarding the publication of this paper.

References

- [1] E. K. Wilson, "Zero-valent metals provide possible solution to groundwater problems," *Chemical and Engineering News*, vol. 73, no. 27, pp. 19–23, 1995.
- [2] W.-X. Zhang, "Nanoscale iron particles for environmental remediation: an overview," *Journal of Nanoparticle Research*, vol. 5, no. 3-4, pp. 323–332, 2003.
- [3] X. Li, P. Zhang, C. L. Lin, and W. P. Johnson, "Role of hydrodynamic drag on microsphere deposition and re-entrainment in porous media under unfavorable conditions," *Environmental Science and Technology*, vol. 39, no. 11, pp. 4012–4020, 2005.
- [4] F. S. Freyria, B. Bonelli, R. Sethi, M. Armandi, E. Belluso, and E. Garrone, "Reactions of acid orange 7 with iron nanoparticles in aqueous solutions," *Journal of Physical Chemistry C*, vol. 115, no. 49, pp. 24143–24152, 2011.
- [5] K. J. Cantrell, D. I. Kaplan, and T. J. Gilmore, "Injection of colloidal Fe0 particles in sand with shear-thinning fluids," *Journal of Environmental Engineering*, vol. 123, no. 8, pp. 786–791, 1997.
- [6] J. Zhan, T. Zheng, G. Piringer et al., "Transport characteristics of nanoscale functional zerovalent iron/silica composites for in situ remediation of trichloroethylene," *Environmental Science and Technology*, vol. 42, no. 23, pp. 8871–8876, 2008.
- [7] T. Phenrat, N. Saleh, K. Sirk, R. D. Tilton, and G. V. Lowry, "Aggregation and sedimentation of aqueous nanoscale zerovalent iron dispersions," *Environmental Science and Technology*, vol. 41, no. 1, pp. 284–290, 2007.
- [8] A. Tiraferri, K. L. Chen, R. Sethi, and M. Elimelech, "Reduced aggregation and sedimentation of zero-valent iron nanoparticles in the presence of guar gum," *Journal of Colloid and Interface Science*, vol. 324, no. 1-2, pp. 71–79, 2008.
- [9] E. D. Vecchia, M. Coisson, C. Appino, F. Vinai, and R. Sethi, "Magnetic characterization and interaction modeling of zerovalent iron nanoparticles for the remediation of contaminated aquifers," *Journal of Nanoscience and Nanotechnology*, vol. 9, no. 5, pp. 3210–3218, 2009.
- [10] N. D. Berge and C. A. Ramsburg, "Oil-in-water emulsions for encapsulated delivery of reactive iron particles," *Environmental Science and Technology*, vol. 43, no. 13, pp. 5060–5066, 2009.
- [11] S. Comba and R. Sethi, "Stabilization of highly concentrated suspensions of iron nanoparticles using shear-thinning gels of xanthan gum," *Water Research*, vol. 43, no. 15, pp. 3717–3726, 2009.
- [12] F. He, D. Zhao, J. Liu, and C. B. Roberts, "Stabilization of Fe-Pd nanoparticles with sodium carboxymethyl cellulose for enhanced transport and dechlorination of trichloroethylene in soil and groundwater," *Industrial and Engineering Chemistry Research*, vol. 46, no. 1, pp. 29–34, 2007.
- [13] S. R. Kanel, R. R. Goswami, T. P. Clement, M. O. Barnett, and D. Zhao, "Two dimensional transport characteristics of surface stabilized zero-valent iron nanoparticles in porous media," *Environmental Science and Technology*, vol. 42, no. 3, pp. 896–900, 2008.
- [14] T. Phenrat, H.-J. Kim, F. Fagerlund, T. Illangasekare, R. D. Tilton, and G. V. Lowry, "Particle size distribution, concentration, and magnetic attraction affect transport of polymer-modified Fe0 nanoparticles in sand columns," *Environmental Science and Technology*, vol. 43, no. 13, pp. 5079–5085, 2009.
- [15] N. Saleh, T. Phenrat, K. Sirk et al., "Adsorbed triblock copolymers deliver reactive iron nanoparticles to the oil/water interface," *Nano Letters*, vol. 5, no. 12, pp. 2489–2494, 2005.
- [16] T. Phenrat, A. Cihan, H.-J. Kim, M. Mital, T. Illangasekare, and G. V. Lowry, "Transport and deposition of polymer-modified Fe0 nanoparticles in 2-D heterogeneous porous media: effects of particle concentration, Fe 0 content, and coatings," *Environmental Science and Technology*, vol. 44, no. 23, pp. 9086–9093, 2010.
- [17] T. Phenrat, H.-J. Kim, F. Fagerlund, T. Illangasekare, and G. V. Lowry, "Empirical correlations to estimate agglomerate size and deposition during injection of a polyelectrolyte-modified Fe0 nanoparticle at high particle concentration in saturated sand," *Journal of Contaminant Hydrology*, vol. 118, no. 3-4, pp. 152–164, 2010.
- [18] N. Tufenkji and M. Elimelech, "Correlation equation for predicting single-collector efficiency in physicochemical filtration in saturated porous media," *Environmental Science and Technology*, vol. 38, no. 2, pp. 529–536, 2004.
- [19] S. C. Kim, M. S. Harrington, and D. Y. H. Pui, "Experimental study of nanoparticles penetration through commercial filter media," *Journal of Nanoparticle Research*, vol. 9, pp. 117–125, 2007.
- [20] T. Tosco and R. Sethi, "Transport of non-newtonian suspensions of highly concentrated micro- and nanoscale iron particles in porous media: a modeling approach," *Environmental Science and Technology*, vol. 44, no. 23, pp. 9062–9068, 2010.
- [21] S. M. Hosseini and T. Tosco, "Transport and retention of high concentrated nano-Fe/Cu particles through highly flow-rated packed sand column," *Water Research*, vol. 47, no. 1, pp. 326–338, 2013.
- [22] J. Hu, G. Chen, and I. M. C. Lo, "Selective removal of heavy metals from industrial wastewater using maghemite nanoparticle: performance and mechanisms," *Journal of Environmental Engineering*, vol. 132, no. 7, pp. 709–715, 2006.
- [23] C. Su and R. W. Puls, "Arsenate and arsenite sorption on magnetite: relations to groundwater arsenic treatment using zerovalent iron and natural attenuation," *Water, Air, and Soil Pollution*, vol. 193, no. 1–4, pp. 65–78, 2008.

- [24] C. T. Yavuz, J. T. Mayo, W. W. Yu et al., "Low-field magnetic separation of monodisperse Fe_3O_4 nanocrystals," *Science*, vol. 314, no. 5801, pp. 964–967, 2006.
- [25] W. Yantasee, C. L. Warner, T. Sangvanich et al., "Removal of heavy metals from aqueous systems with thiol functionalized superparamagnetic nanoparticles," *Environmental Science and Technology*, vol. 41, no. 14, pp. 5114–5119, 2007.
- [26] M. L. McCormick and P. Adriaens, "Carbon tetrachloride transformation on the surface of nanoscale biogenic magnetite particles," *Environmental Science and Technology*, vol. 38, no. 4, pp. 1045–1053, 2004.
- [27] P. J. Vikesland, A. M. Heathcock, R. L. Rebodos, and K. E. Makus, "Particle size and aggregation effects on magnetite reactivity toward carbon tetrachloride," *Environmental Science and Technology*, vol. 41, no. 15, pp. 5277–5283, 2007.
- [28] G. Pan, L. Li, D. Zhao, and H. Chen, "Immobilization of non-point phosphorus using stabilized magnetite nanoparticles with enhanced transportability and reactivity in soils," *Environmental Pollution*, vol. 158, no. 1, pp. 35–40, 2010.
- [29] S. F. Saghraani, F. Daneshgar, and M. Golzar, "Investigation on stability of slurry of iron oxide nanoparticles (Fe_3O_4) stabilized with poly acrylic acid," in *Proceedings of the 7th National Congress on Civil Engineering*, Shahid Nikbakht Faculty of Engineering, Zahedan, Iran, 2013.
- [30] K.-M. Yao, M. T. Habibian, and C. R. O'Melia, "Water and waste water filtration: concepts and applications," *Environmental Science and Technology*, vol. 5, no. 11, pp. 1105–1112, 1971.
- [31] N. Tufenkji and M. Elimelech, "Deviation from the classical colloid filtration theory in the presence of repulsive DLVO interactions," *Langmuir*, vol. 20, no. 25, pp. 10818–10828, 2004.
- [32] R. J. Charbeneau, *Groundwater Hydraulics and Pollutant Transport*, Waveland Press, 2008.
- [33] K. A. Hoffmann and S. T. Chiang, *Computational Fluid Dynamics*, vol. 1, Engineering Education System, 2000.

Research Article

Photocatalytic Degradation of Methylene Blue Using TiO₂ Impregnated Diatomite

Ranfang Zuo,¹ Gaoxiang Du,¹ Weiwei Zhang,¹ Lianhua Liu,¹
Yanming Liu,¹ Lefu Mei,¹ and Zhaohui Li²

¹ School of Material Science and Technology, China University of Geosciences, Beijing 100083, China

² Geosciences Department, University of Wisconsin-Parkside, Kenosha, WI 53144, USA

Correspondence should be addressed to Gaoxiang Du; dgx@cugb.edu.cn and Zhaohui Li; li@uwp.edu

Received 6 March 2014; Accepted 12 May 2014; Published 11 June 2014

Academic Editor: Hanlie Hong

Copyright © 2014 Ranfang Zuo et al. This is an open access article distributed under the Creative Commons Attribution License, which permits unrestricted use, distribution, and reproduction in any medium, provided the original work is properly cited.

Nano-TiO₂ showed a good catalytic activity, but it is easy to agglomerate, resulting in the reduction or even complete loss of photocatalytic activity. The dispersion of TiO₂ particles on porous materials was a potential solution to this problem. Diatomite has high specific surface and absorbability because of its particular shell structure. Thus, TiO₂/diatomite composite, prepared by loading TiO₂ on the surface of diatomite, was a good photocatalyst, through absorbing organic compounds with diatomite and degrading them with TiO₂. Scanning electron microscopy (SEM), energy dispersive spectrum (EDS), X-ray diffraction (XRD), chemical analysis, and Fourier transform infrared spectrometry (FTIR) indicated that TiO₂ was impregnated well on the surface of diatomite. Furthermore, TiO₂/diatomite was more active than nano-TiO₂ for the degradation of methylene blue (MB) in solution. MB at concentrations of 15 and 35 ppm can be completely degraded in 20 and 40 min, respectively.

1. Introduction

With the progression of global industrialization, environmental pollution becomes a more serious issue and, thus, has received considerable attention. The treatment of colored wastewaters produced by the textile industry has recently been heavily researched. Titanium dioxide (TiO₂) is a well-established *n*-type semiconductor used as a photocatalyst to decompose pollutants in water and air as well as produce self-cleaning materials [1, 2]. In recent years, TiO₂ has been widely investigated and used because of its nontoxicity, chemical inertness, high photocatalytic activity, and low cost. TiO₂ has a significant degradation effect as a good photocatalyst of organic and inorganic pollutants in the air and water, which has a broad prospect of application [3].

The photocatalytic activity of TiO₂ is influenced by its crystal structure, particle size, specific surface area, and porosity. Ultrafine powders of TiO₂ show a good catalytic activity. However, agglomeration often takes place, resulting in reduction or even complete loss of photocatalytic activity. The dispersion of TiO₂ particles on porous materials

is a potential solution to this problem. Porous materials impregnated with TiO₂ show high thermal stability and larger pore sizes that afford better incorporation of the species without diffusion problems and increased specific surface area [4]. In order to facilitate its recycling and reuse, considerable efforts have been made to load TiO₂ particles on various substrates, such as mica, graphite, glass, diatoms stone, fly-ash, and attapulgite [5, 6]. Diatomite is an important nonmetallic resource with nontoxic and good chemical stability. Diatomite has high specific surface and absorbability because of its particular shell structure [7]. It could serve as an effective substrate for TiO₂ impregnation. This study presents the preparation and characterization of TiO₂-supported diatomite and its photodegradation of methylene blue (MB) in solution.

2. Experimental

2.1. Materials. Diatomite was supplied by Changbai Mountain, Ltd., Jilin Province, China. The medium diameter of diatomite powder, d_{50} , is 34 μm , and the specific surface is

10 m²/g. Its SiO₂ content was 87%, with other elements, such as Al, Fe, Ca, K, Mg, and Na. Tetrabutyl titanate was obtained from commercially available.

2.2. Preparation of TiO₂/Diatomite Composite. Tetrabutyl titanate was dissolved by ethanol and the solution was gradually added to diatomite. The mixture was stirred for 2 h by magnetic stirrers and then dried in the oven at 80 °C. Finally, the dried mixture was further heated to 550 °C for about 2 h, before it was cooled naturally. The specific surface of TiO₂/diatomite composite is 32 m²/g.

2.3. Characterization. The particle size of diatomite powder was measured by a laser particle analyzer Mastersizer 2000. The morphologies of pure diatomite and TiO₂/diatomite composite were examined by scanning electron microscopy (SEM). X-ray diffraction analysis was performed using a D5000 Diffractometer (Siemens) with a Ni filter and CuKα (λ = 1.54 Å) radiation. The UV-Vis absorbance spectra were recorded using Varian Cary 5000. BET surface area was determined at liquid nitrogen temperature (77.3 K) using QUADRASORB SI-MP.

3. Result and Discussion

3.1. The Microstructure and EDS Analysis of Diatomite and TiO₂/Diatomite Composite. Diatomite has porous structure and rough surface after acid treatment (Figure 1(a)). The pore size of diatomite is between 2 and 5 μm. After impregnation, TiO₂ particles formed a dense coating on the surface of the orifice, which presents honeycomb with smaller pore (Figure 1(b)). Compared with raw diatomite, Ti element appeared in the EDS analysis of TiO₂/diatomite composite, indicating that TiO₂ was successfully coated on the surface of diatomite. This result corroborates the high TiO₂ content detected by EDS analysis.

3.2. Chemical Analysis and XRD Patterns. Chemical composition analyses showed that the content of TiO₂ increased from 0.15 to 8.71% after TiO₂ impregnation (Table 1). The result together with that from the EDS analysis indicates that TiO₂ was coated on the surface of diatomite successfully. The reflections of TiO₂ were characteristics of anatase. Diatomite is made of amorphous SiO₂ with only trace amount of quartz. The XRD pattern of TiO₂/diatomite composite revealed mixed phases of anatase TiO₂ and amorphous SiO₂ (Figure 2). The coating of diatomite particles by TiO₂ does not cause any change in their peak positions and shapes compared with the pure TiO₂ and diatomite. The results of XRD analysis and chemical analysis were consistent with that of SEM analysis totally.

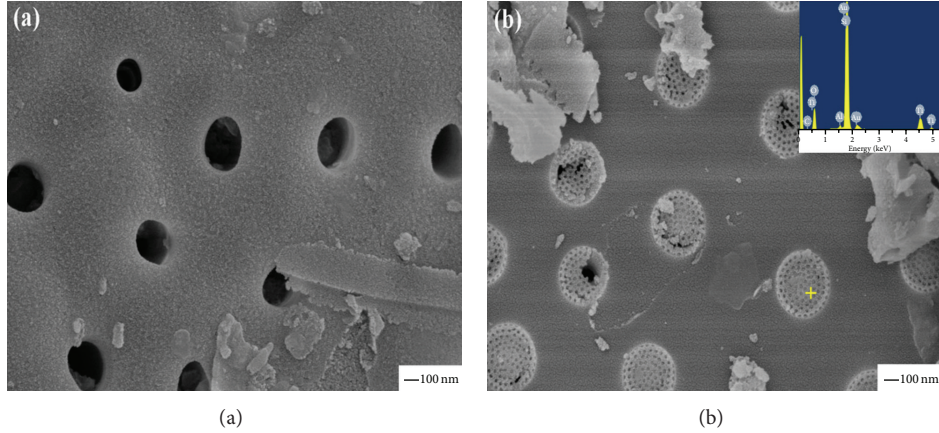
3.3. FTIR Analysis. The FTIR spectrum of TiO₂/diatomite composite consists of the characteristic peaks of TiO₂ and diatomite (Figure 3). The band at 1089 cm⁻¹ was assigned to the asymmetric stretching vibration modes of Si–O–Si bond [8, 9] and the band at 1633 cm⁻¹ was attributed to the stretching mode of O–H bonds on the surface of TiO₂

[10]. The band at 797 cm⁻¹ was assigned to the symmetric stretching vibration modes of Si–O bond and the strong absorption peak at 400–600 cm⁻¹ was attributed to the vibration mode of Si–O–Ti and Ti–O–Ti bonds [11].

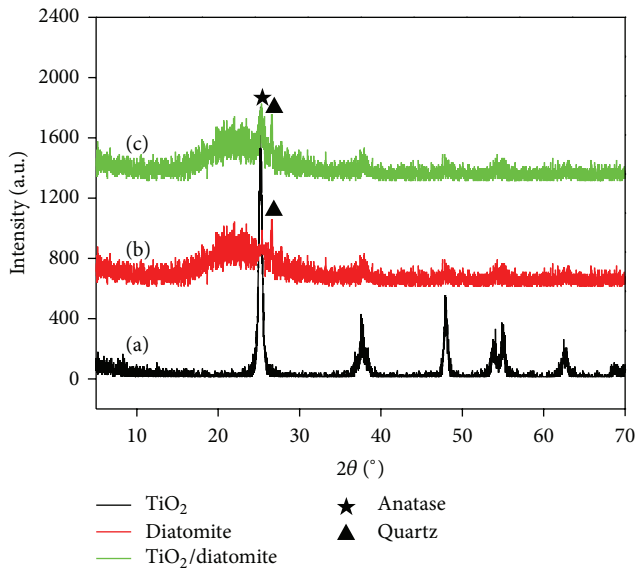
3.4. Adsorption of MB on Different Catalysts and Characterization of Photocatalytic Activity. TiO₂ almost had no adsorption as well as no photocatalyst for MB and the adsorption of TiO₂/diatomite on MB was much lower than pure diatomite for MB (Figure 4). The adsorption reached equilibrium after 30 min in dark. Under dark conditions, TiO₂/diatomite composite removed more MB in comparison to TiO₂ and control, showing almost no activity as well as no photocatalyst for TiO₂ and the control (Figure 5), agreeable to the results presented in Figure 4. In the presence of UV, the rate of MB degradation by TiO₂/diatomite composite was higher than that by TiO₂, attributing to its high surface area and high adsorbability. The MB at concentrations 15 and 35 ppm could be completely degraded after irradiating 20 and 40 min, respectively. The control had the lowest MB self-degradation under UV light. The photoactivity of TiO₂ loaded on diatomite was evidently increased because the high surface area of diatomite effectively concentrates MB around the deposited TiO₂ and produces high concentrations of organic compounds for the TiO₂ photocatalysis. The diatomite might improve the thermal stability of TiO₂ and the surface area and preserve a higher content of surface hydroxyl groups [12].

3.5. UV-Vis Absorption Analysis of MB Solution. Two major absorbance peaks of methylene blue were located at 292 and 664 nm, due to benzene ring and heteropolyaromatic linkage (Figure 6). In addition, the aqueous solution of MB molecules exhibited a double-peak feature at 664 and 615 nm, which correspond to monomers and dimers, respectively [13]. Upon irradiation, the peak at 664 nm has a progressively blue shift to shorter wavelength (Figure 6(b)) because of hypsochromic effect [14, 15]. The absorbance of MB solution was about 2.5 a.u. at time zero. In the presence of TiO₂ the absorbance of MB remained the same after 30 min (Figure 6(a)), agreeing well with the results in Figure 5, while the absorbance of MB decreased sharply after 30 min in the presence of TiO₂/diatomite composite, indicating that TiO₂/diatomite composite has good adsorbability (Figure 6(b)). The absorption peak at 615 nm becomes higher than the peak at 664 nm after 30 min, indicating that the degradation rate of monomers is much higher than that of dimers [14]. Besides, a parallel decrease in intensities and slight blue shift of the bands located at 664 nm also could be observed. These are caused by the N-demethylated degradation concomitantly with the degradation of the phenothiazine [16], as shown in Figure 6(a). And MB was degraded completely after irradiating 60 min and 20 min by TiO₂ and TiO₂/diatomite composite, respectively.

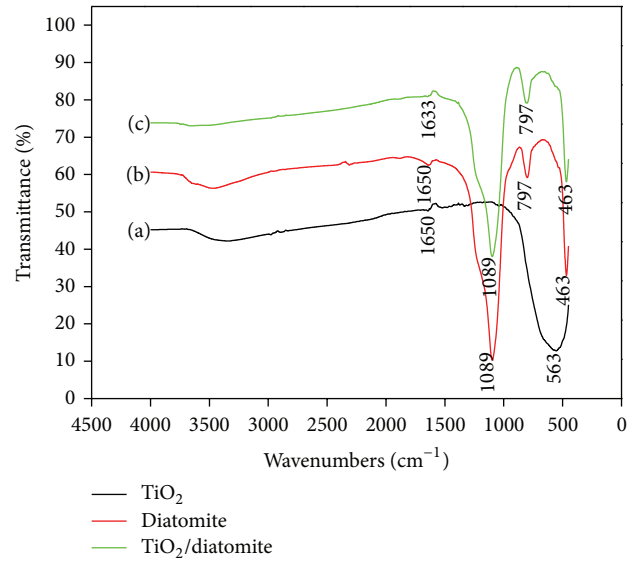
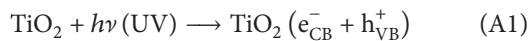
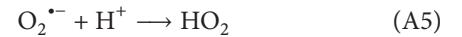
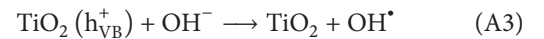
3.6. Mechanism of TiO₂ Activation with UV Light and Photosensitized Oxidation for MB and Its Identification of Intermediate Products. The electron and the hole are generated

FIGURE 1: The microstructure of diatomite and TiO₂/diatomite composite.TABLE 1: Chemical analyses of diatomite and TiO₂/diatomite composite.

Composition %	SiO ₂	Al ₂ O ₃	Fe ₂ O ₃	MnO	MgO	CaO	Na ₂ O	K ₂ O	H ₂ O ⁻	TiO ₂	P ₂ O ₅
Diatomite	86.82	3.21	1.60	0.011	0.43	0.46	0.25	0.56	0.011	0.15	0.22
TiO ₂ /diatomite	84.66	2.22	0.61	0.15	1.31	0.23	0.15	0.33	0.45	8.71	0.012

FIGURE 2: XRD patterns of TiO₂ (a), diatomite (b), and TiO₂/diatomite composite (c).

in the conduction band and in the valence band of TiO₂ by UV irradiation, respectively, as shown in (A1) [17]. The positive hole can oxidize hydroxide ions (or water molecule) adsorbed on the surface of TiO₂ particles to produce hydroxyl radical [18], as presented in (A2) and (A3) [17]. The electrons of conduction band can react with the oxygen to produce superoxide radical anions (A4) [19]. The superoxide radical anion reacts with a proton to form hydroperoxyl radical (A5):

FIGURE 3: FTIR spectra of TiO₂ (a), diatomite (b), and TiO₂/diatomite composite (c).

For the mechanism of photosensitized oxidation, in the presence of catalysts the excited state of MB injects an electron into the conduction band (B1). The MB dye is then converted to a cationic dye radical that undergoes degradation to yield products according to (B2) to (B5) [17].

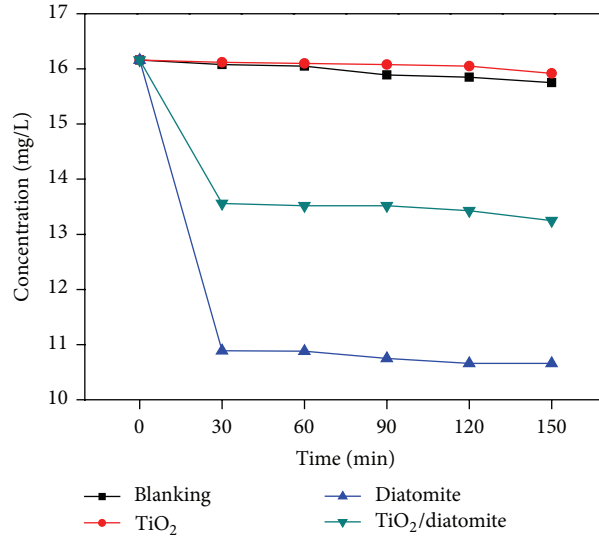


FIGURE 4: Removal of MB by different sorbents due to adsorption.

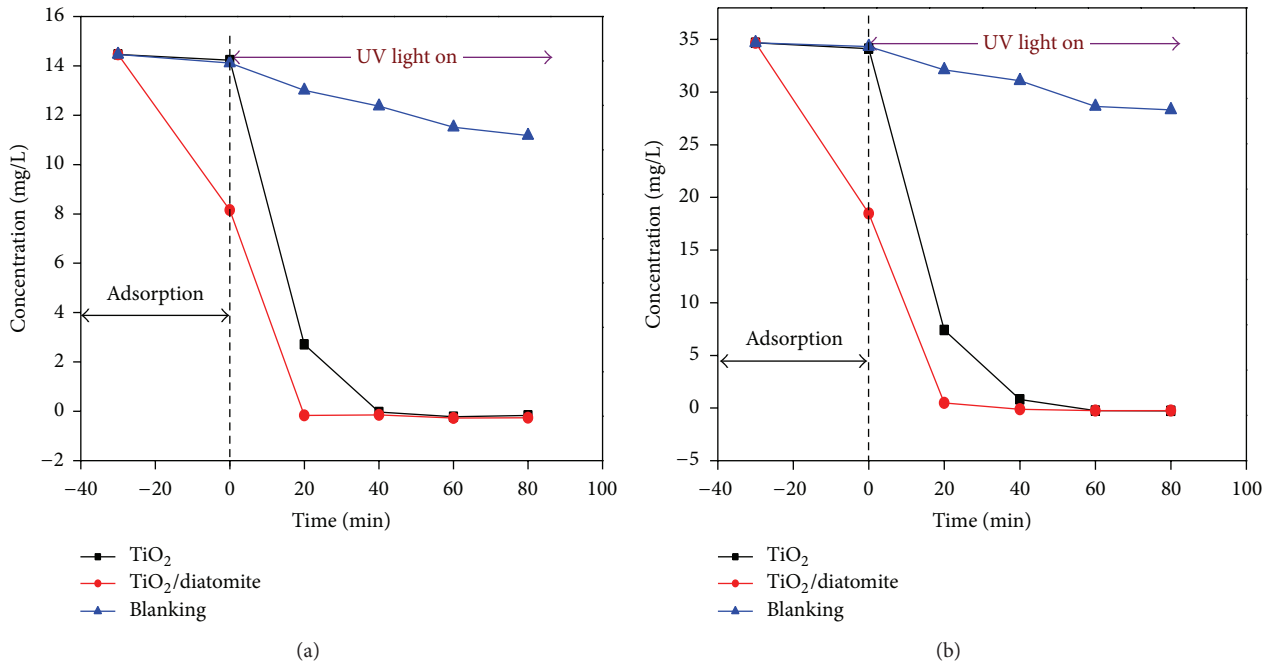
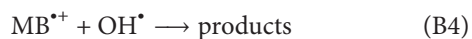
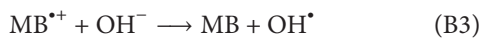
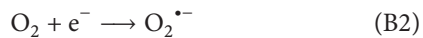
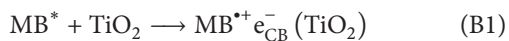


FIGURE 5: Kinetics of photocatalytic MB degradation from initial MB concentrations of 15 (a) and 35 mg/L (b).

The hydroxyl radical existing on the surface of diatomite accelerated the degradation of MB (B3):



The typical HPLC chromatograms of MB degraded by TiO₂/diatomite under UV light were shown in Figure 7. HPLC analyses showed no degradation products of MB under the condition of adsorption (Figure 7(a)). The decrease in peak height was just caused by adsorption of MB on TiO₂/diatomite (Figure 7(b)). However, the adsorption of the dye molecules over the TiO₂ surface directly affects the occurrence of electron transfer between the excited dye and TiO₂ which further accelerated the degradation rate [20]. In the inserts, peak number 1 represented the retention time of MB, peak number 2 was the self-degradation intermediate metabolite of MB, while peaks number 3 and 4 were further

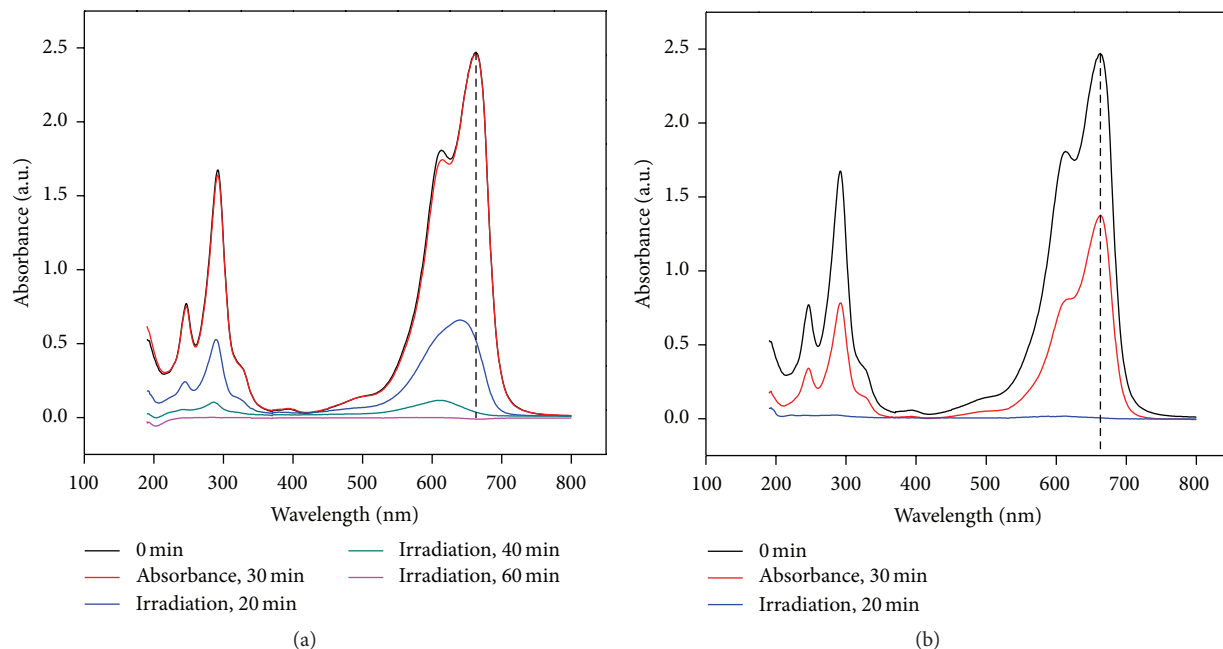


FIGURE 6: UV absorption spectra of MB solution after reacting with TiO_2 (a) or TiO_2 /diatomite composite (b) at different time.

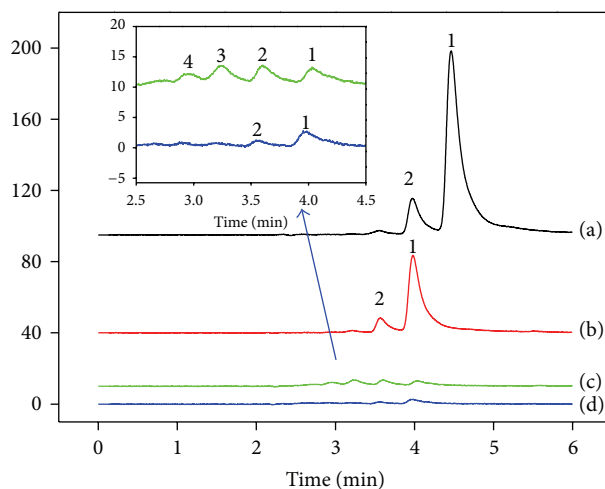


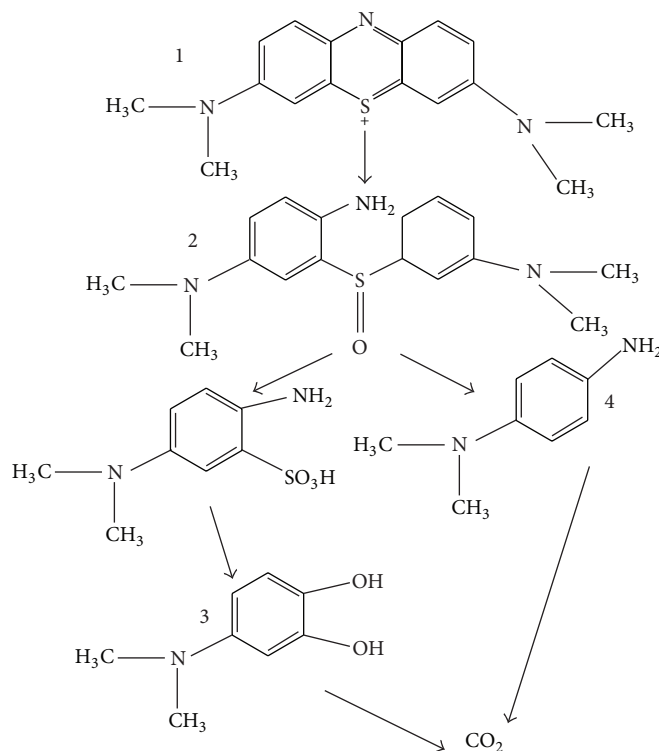
FIGURE 7: HPLC analyses of MB. (a) Initial MB solution at 15 ppm, (b) equilibrium MB solution after 30 min absorption in the dark, (c) after UV irradiation for 5 min, and (d) after irradiation for 20 min.

degradation products of MB (Figure 7(c)). Peaks number 3 and 4 were further degraded to CO_2 completely in addition to further reduction of peak height of peaks number 1 and 2 after UV irradiation for 20 min. These results are in agreement with the results shown in Figures 5 and 6(b). The MB and its progressive degradation products corresponding to the peaks of 1, 2, 3, and 4 were reported in Scheme 1. The OH^\bullet radicals can attack the $\text{C}-\text{S}^+=\text{C}$ functional group in MB, which is in direct Coulombic interaction with the surface of TiO_2 /diatomite. Therefore, the initial step of MB degradation can be ascribed to the cleavage of the bonds of the $\text{C}-\text{S}^+=\text{C}$ functional group in MB. The passage from $\text{C}-\text{S}^+=\text{C}$ to $\text{C}-\text{S}(=\text{O})-\text{C}$ requires the conservation of the

double bond conjugation, which induces the opening of the central aromatic ring containing both heteroatoms, S and N. The origin of H atoms necessary to $\text{C}-\text{H}$ and $\text{N}-\text{H}$ bond formation can be proposed from the proton reduction by photo-generated [21].

4. Conclusion

Impregnation of diatomite with TiO_2 yielded supported anatase catalyst for MB photodegradation. The diatomite supported anatase catalysts were more active than the nano- TiO_2 , probably due to the adsorption of MB on diatomite



SCHEME 1: Photocatalytic degradation pathway of MB.

and the hydroxyl radicals existing on its surface, which accelerated the degradation of MB. At an initial concentration of 15 ppm MB can be completely degraded in 20 min. The results demonstrate that TiO_2 /diatomite photocatalysis is a good candidate for color removal in wastewater treatment.

Highlights

- (1) Diatomite has high specific surface and absorbability.
- (2) The TiO_2 /diatomite facilitates the recycling and reuse of TiO_2 .
- (3) TiO_2 /diatomite adsorbs organic compounds with diatomite and degrades them with TiO_2 .

Conflict of Interests

The authors declare that there is no conflict of interests regarding the publication of this paper.

Acknowledgment

This work was supported by the Fundamental Research Funds for the Central Universities (no. 2652013037 and no. 2652013043).

References

- [1] H. Choi, S. R. Al-Abed, D. D. Dionysiou, E. Stathatos, and P. Lianos, "TiO₂-based advanced oxidation nanotechnologies for water purification and reuse," *Sustainability Science and Engineering*, vol. 8, pp. 229–254, 2010.
- [2] D.-J. Kim, H.-C. Pham, D.-W. Park, and K.-S. Kim, "Preparation of TiO₂ thin films on polypropylene beads by a rotating PCVD process and its application to organic pollutant removal," *Chemical Engineering Journal*, vol. 167, no. 1, pp. 308–313, 2011.
- [3] W. Mekprasart and W. Pecharapa, "Synthesis and characterization of nitrogen-doped TiO₂ and its photo-catalytic activity enhancement under visible light," in *Proceedings of the Eco-Energy and Materials Science and Engineering Symposium*, vol. 9, pp. 509–514, 2011.
- [4] C. Suwanchawalit and S. Wongnawa, "Influence of calcination on the microstructures and photocatalytic activity of potassium oxalate-doped TiO₂ powders," *Applied Catalysis A*, vol. 338, no. 1-2, pp. 87–99, 2008.
- [5] P. Huo, Y. Yan, S. Li, H. Li, and W. Huang, "Preparation of poly-o-phenylenediamine/TiO₂/fly-ash cenospheres and its photo-degradation property on antibiotics," *Applied Surface Science*, vol. 256, no. 11, pp. 3380–3385, 2010.
- [6] S. Zhou, J. Lv, L. K. Guo et al., "Preparation and photocatalytic properties of N-doped nano-TiO₂/muscovite composites," *Applied Surface Science*, vol. 258, no. 16, pp. 6136–6141, 2012.
- [7] G. X. Du, R. F. Zuo, L. F. Mei, J. H. Liao, and W. J. Guo, "Surface modification of diatomite by silane coupling agent and its effect

- on the reinforcing efficiency of NB/SBR blend,” *Rare Metal Materials and Engineering*, vol. 42, pp. 412–417, 2013 (Chinese).
- [8] Y. Liu, C. Ge, M. Ren et al., “Effects of coating parameters on the morphology of SiO₂-coated TiO₂ and the pigmentary properties,” *Applied Surface Science*, vol. 254, no. 9, pp. 2809–2819, 2008.
- [9] Y. Zhang, H. Yin, A. Wang et al., “Deposition and characterization of binary Al₂O₃/SiO₂ coating layers on the surfaces of rutile TiO₂ and the pigmentary properties,” *Applied Surface Science*, vol. 257, no. 4, pp. 1351–1360, 2010.
- [10] H.-X. Guo, K.-L. Lin, Z.-S. Zheng, F.-B. Xiao, and S.-X. Li, “Sulfonic acid-modified P25 TiO₂ nanoparticles with improved photocatalytic degradation on Congo red under visible light,” *Dyes and Pigments*, vol. 92, no. 3, pp. 1278–1284, 2012.
- [11] X. F. Hou, H. Ding, Y. X. Zheng, and M. M. Wang, “Preparation and characterisation of amorphous silica/anatase composite through mechanochemical method,” *Materials Research Innovations*, vol. 17, pp. 234–239, 2013.
- [12] X. Wang, Z. Hu, Y. Chen, G. Zhao, Y. Liu, and Z. Wen, “A novel approach towards high-performance composite photocatalyst of TiO₂ deposited on activated carbon,” *Applied Surface Science*, vol. 255, no. 7, pp. 3953–3958, 2009.
- [13] C. An, S. Peng, and Y. Sun, “Facile synthesis of sunlight-driven AgCl:Ag plasmonic nanophotocatalyst,” *Advanced Materials*, vol. 22, no. 23, pp. 2570–2574, 2010.
- [14] F.-T. Li, Y. Zhao, Y. Liu, Y.-J. Hao, R.-H. Liu, and D.-S. Zhao, “Solution combustion synthesis and visible light-induced photocatalytic activity of mixed amorphous and crystalline MgAl₂O₄ nanopowders,” *Chemical Engineering Journal*, vol. 173, no. 3, pp. 750–759, 2011.
- [15] N. C. Castillo, A. Heel, T. Graule, and C. Pulgarin, “Flame-assisted synthesis of nanoscale, amorphous and crystalline, spherical BiVO₄ with visible-light photocatalytic activity,” *Applied Catalysis B*, vol. 95, no. 3-4, pp. 335–347, 2010.
- [16] F. Wang, S. Min, Y. Han, and L. Feng, “Visible-light-induced photocatalytic degradation of methylene blue with polyaniline-sensitized TiO₂ composite photocatalysts,” *Superlattices and Microstructures*, vol. 48, no. 2, pp. 170–180, 2010.
- [17] H. A. Le, L. T. Linh, S. Chin, and J. Jurng, “Photocatalytic degradation of methylene blue by a combination of TiO₂-anatase and coconut shell activated carbon,” *Powder Technology*, vol. 225, pp. 167–175, 2012.
- [18] R.-J. Wu, C.-C. Chen, C.-S. Lu, P.-Y. Hsu, and M.-H. Chen, “Phorate degradation by TiO₂ photocatalysis: parameter and reaction pathway investigations,” *Desalination*, vol. 250, no. 3, pp. 869–875, 2010.
- [19] G. Wang, F. Wu, X. Zhang, M. Luo, and N. Deng, “Enhanced TiO₂ photocatalytic degradation of bisphenol E by β -cyclodextrin in suspended solutions,” *Journal of Hazardous Materials*, vol. 133, no. 1–3, pp. 85–91, 2006.
- [20] K. Natarajan, T. S. Natarajan, H. C. Bajaj, and R. J. Tayade, “Photocatalytic reactor based on UV-LED/TiO₂ coated quartz tube for degradation of dyes,” *Chemical Engineering Journal*, vol. 178, pp. 40–49, 2011.
- [21] A. Houas, H. Lachheb, M. Ksibi, E. Elaloui, C. Guillard, and J.-M. Herrmann, “Photocatalytic degradation pathway of methylene blue in water,” *Applied Catalysis B*, vol. 31, no. 2, pp. 145–157, 2001.